

**Residual Strength and Repair of Damaged and Deteriorated  
Offshore Structures**

**Area Three**

**REPAIR OF DENTED TUBULAR COLUMNS -  
WHOLE COLUMN APPROACH**

By  
J.M. Ricles  
W.M. Bruin  
T.K. Sooi

Research Sponsored by

Exxon Production Research Company  
Minerals Management Service (U.S. Dept. of the Interior)  
(Technical Assessment and Research Branch)  
Mobil Technology Company  
Shell Offshore, Inc.

ATLSS Report No. 97-13

December 1997  
[Distribution restricted until December 1998]

ATLSS Engineering Research Center  
Lehigh University  
117 ATLSS Dr., Imbt Laboratories  
Bethlehem, PA 18015-4729  
(610) 758-3525

An NSF Sponsored Engineering Research Center



## **DISCLAIMER**

This report has been reviewed by the Sponsors and approved for publication. Approval does not signify that the contents necessarily reflect the views and policies of the Sponsors, nor does mention of trade names or commercial products constitute endorsement or recommendation for use.





# EXECUTIVE SUMMARY

## Introduction

Numerous offshore platforms are known to have suffered dent damage from collision with either marine vessels or dropped objects. Previous research has been conducted on the behavior of dent-damaged tubular members, where the dent damage was more than 25% of the member's diameter  $D$ . This research has determined that dent damage causes a loss of tubular member capacity. Furthermore, previous experimental research involving dent depths up to 15% of their diameter determined that the internal grout repair of damaged members can restore their strength to a capacity of a non-damaged member.

The objective of this study was to investigate the behavior of dent-damaged tubulars having severe dent depths ( $>0.25D$ ) and to evaluate the capacity of such members after having been repaired by placing grout inside the tubular. A series of experimental tests and analyses were conducted to achieve this objective. The results were used to evaluate the reliability of different analytical methods to predict residual and repaired strength. Because of the prior lack of experimental data, these existing analytical models had not been calibrated for more severely dent damaged tubulars.

## Workscope

The scope of this study was limited to *long columns* subjected to compressive, concentric axial load at their ends. Dent depths of 25% and 50% of the member's diameter were investigated.

**Tests** - The experimental program included nine specimens - four as-dented, four dented and internally grouted, and one repaired using an external grouted sleeve. For each dent depth value, two diameter-to-thickness ( $D/t$ ) ratios - 34.5 and 69 - were used. The sleeve repair was tested to compare the relative effectiveness of internal versus external grouted repairs. The geometry of each specimen is summarize in Table 1.

All specimens had a nominal diameter of 8.625 in. and were made of ERW, ATSM A53 Grade B pipe. The dents were made at mid span of the column, opposite to the seam weld, by controlled pressing of a steel wedge onto the tubular section (Figure 1(a)). The resulting dented section was flat at the dent trough (Figure 1(b)). The repaired specimens were subsequently injected with a grout slurry and cured prior to testing. The tests were set up with both ends of the column simulating a pinned boundary condition (Figure 1 (c)).

**Analysis** - The analytical part of this project involved predicting the ultimate capacities and/or load-deformation behavior of the dented and dented-grouted test specimens subjected to pure compressive loads. The methods of analysis used included: (1) a theoretical formulation based on the cross-sectional behavior of a dent in a beam-column [1,2,3]; (2) semi-empirical formulations in the form of conventional unity checks and based on test data [4,5]; (3) numerical solutions using a phenomenological model, also based on test data and implemented in DENTA - a commercially available computer program for dented members; (4) a moment-thrust-curvature ( $M-P-\phi$ ) formulation, that is a numerical integration method of analysis that requires short column load-deformation behavior input and for which computer programs are available, such as DDAM [6] and DGROUT [7]; and (5) ABAQUS [8], a non-linear finite element (FE) program. The methods were used for both as-dented and dented-grouted specimens, except that the DENTA computer program was not used for the latter (i.e., for internal grout repaired or grouted sleeve repaired members). In addition to the specimens of this project, specimens from the literature were also analyzed in order to evaluate the robustness of the analytical methods in predicting member capacity and/or behavior for a variety of dent depths and

D/t ratios. The geometry and experimental capacity of these other specimens is summarized in Appendix E.

## Test Results

The compression tests of as-dented specimens showed that the dents grew deeper under the application of axial load due to the folding of the dent under the bending moment resulting from load eccentricity at the dent section. This resulted in yielding of the tubular wall in the vicinity of the dented cross section, leading to a reduction in stiffness and axial load carrying capacity. The depth of the dent, out-of-straightness, and diameter-to-thickness ratio were found to influence specimen residual strength, with larger values leading to a further reduction in capacity. Figure 2(a) shows the trend of the reduction in ultimate capacity, for various D/t ratios, as the depth of the dent  $d_d$  increases.

Internal grouting of the dented members inhibited the dent growth during testing, resulting in an increase in specimen capacity, relative to the as-dented condition. Figure 3 illustrates the load-deformation behavior of a deep dented specimen for the as-dented (Specimen A12) and grout-dented conditions (Specimen A13), indicating the increase in ultimate capacity due to grouting. The failure of the internal grout repaired specimens consisted of yielding of the steel tubular in the vicinity of the dented cross section and the formation of a plastic hinge as global buckling occurred. Again, the out-of-straightness and diameter-to-thickness ratio of the damaged tubular was found to have an effect on the capacity of the grouted specimens as well.

In Figure 2(b) the ratio of the as-dented to grouted-dented capacities are shown from tests conducted under the current study and other studies reported in the literature [9]. Dented specimens of larger diameter-to-thickness ratio benefited more from internal grouting. The increase in strength was approximately 1.5 and 3 times the as-dented strength for the tubulars with nominal diameter-to-thickness ratios of 34.5 and 69, respectively. The external grouted sleeve resulted in an increase of over five times the as-

dented strength of the tubular with a dent depth of  $0.50D$  and  $D/t$  ratio of 69. The failure of the grouted sleeve repaired specimen was outside and adjacent to the sleeve, where yielding and local buckling occurred. Therefore, external grouted sleeves are more efficient than internal grouting in restoring the strength of dented members. The capacity results from the tests ( $P_{TEST}$ ) are presented in Table 2.

An examination of the data generated in this study and other data from the literature [9] involving simply supported columns subjected to axial load indicates that dent-damaged tubulars with a dent depth less than  $0.20D$  and out-of-straightness less than 0.2% of their length can have their strength restored to that of a corresponding undamaged tubular by the use of internal grout repair (Figure 2(c)). Specimens with deeper dents would require the use of an external grouted clamp or sleeve, in order to restore their strength to that of a corresponding non-damaged tubular.

## **Analytical Results**

The experimental results in terms of ultimate strength were compared with predictions based on analytical and semi-empirical formulations, a numerical M-P- $\phi$  method and nonlinear finite element analysis. For the latter two methods, load-deformation characteristics were also compared.

**Analytical and Semi-empirical Formulations** - An assessment of the analytical methods to predict capacity was made by comparing calculated strengths with test data ( $P_{TEST}$ ) obtained from this project and other pertinent data extracted from the literature. As shown in Figure 4, a comparison of predicted-to-experimental capacity ratios indicate that analytical methods based on sectional behavior of beam columns tend to underpredict capacities. The Ellinas beam-column formulation [1] underpredicts on average by 13%, whereas Ricles' formulation [9] does it by 29%. Loh's empirical formulation [3], which is patterned after the well know AISC unity check format, has about the same statistics as

Ellinas', but is too unconservative for dent depths of 50% of their diameter (it should be noted that Loh's formulation is only defined for dent depths up to about 0.2D).

Ellinas' formulation appears to be the most appropriate predictor of axial capacity for deep-dented ( $\geq 0.30D$ ) members left in the as-dented condition, with Loh's formulation being more accurate for dents less than 0.30D. However, unlike Loh's formulation that explicitly includes member end moments, as it is the case in practical design, Ellinas' formulation does not accommodate moments directly. Hence, there is an incentive to extend Loh's formulation by obtaining data on short column behavior with deep dents, which is a requirement for Loh's formulation in predicting the capacity of long columns.

For the internal-grout repaired specimens, an assessment of the analytical methods was also made. A comparison of predicted-to-experimental capacity ratios of test specimens from the database is given in Figure 5. It is seen in this figure that the beam-column formulation of Parsanejad [2] and the empirical formulation of Loh [5] both predict the capacity with similar scatter (Figures 5(a) and (b)). However, Loh's formulation, being reasonably conservative at deep dents (0.50D) and having the ability to explicitly accommodate end moments, makes it the formulation of choice.

**Moment-Thrust-Curvature (M-P- $\phi$ )** - As illustrated in Figures 4(d) and 5(c), ultimate strength predictions by the M-P- $\phi$  integration methods were conducted using computer programs DDAM [6] and DGROUT [7]. The former program is similar to BCDENT. It is known that BCDENT predicts well the capacity of tubulars with shallow dents, for which empirical M-P- $\phi$  data exist [10].

The capacity prediction of unrepaired dented specimens by M-P- $\phi$  exhibit more scatter than those obtained by either Ellinas' analytical or Loh's empirical formulations for the same range of dent depths and D/t ratios (see Figure 4). In particular, the scatter increases for specimens with dents deeper than 0.20D or D/t greater than 90. Similar

comments apply to the predictions of the grouted-dented capacities, as shown in Figure 5(c), with the additional uncertainty of the grout properties that appear to significantly influence the capacity predictions. In fact, using values of artificially reduced grout modulus seems to improve predictions.

The M-P- $\phi$  method should provide, in principle, the most robust means to predict dented member capacity in that it can accommodate more than one dent at different locations along the member and in different orientations around the cross section, as well as various support conditions and intermediate concentrated and/or linearly distributed loads. However, the method requires empirical relationships between moment, axial force and associated deformations with various D/t ratios. Since such empirical relationships are not available for grouted-dented tubulars, the M-P- $\phi$  predictions presented here for internal grout repaired dented members are based on calculated relationships. Furthermore, empirical relationships are also not available for deep-dented non-repaired tubulars. For the M-P- $\phi$  analysis of specimens of this research program the empirical M-P- $\phi$  relationships for tubulars of dent depths less than 0.2D were consequently used. Therefore, it is not surprising to find a scatter in accuracy when the predictions are compared to test data.

**DETA** - As indicated in Table 2, this computer program, which is popular within the industry, conservatively underpredicts capacity by up to 28% for the two as-dented specimens with 0.25D dent depths (Specimens A10 and C10). For deep dents, the program had convergence problems. This is not surprising, since the model used in the program is phenomenological and is only calibrated to tests of dents up to about 0.25D.

**Finite Element Analysis** - Overall, the finite element method using ABAQUS was found to be the most accurate predictor of capacity for the specimens in the as-dented condition (Figure 4(d)), although it tends to have a large scatter at deep dents. For shallow dents (less than 0.30D), the finite element method is an excellent predictor. However, the

analysis are time consuming in that the denting process is also simulated, and a new dent depth requires a complete new analysis.

The analysis of the grouted-dented specimens assumed full composite action between grout and the steel. The comparisons shown in Figure 5(d) suggest that the grout modulus can have a significant effect on the predicted behavior. In fact, an assessment of the finite element analysis of some of the specimens in the database indicates that capacity is over-predicted when the true grout modulus is used. Furthermore, the predicted load-deformation response tends to be stiffer than the experimental result. As in the M-P- $\phi$  method, the finite element method predicts capacity better, if the value for the grout modulus is artificially reduced to 1 ksi. Finite element solutions could not be carried much beyond the peak load, due to the nonlinear nature of the problem on both steel and grout materials and overall geometry. The need to substantially soften the grout to improve the capacity prediction makes the finite element method highly suspect for strength prediction of internal grout repaired members until a rigorous calibration is made.

## **Recommendations**

The new data obtained in this project suggest the following methods to predict ultimate axial capacity of as-dented and grouted-dented members:

### **As-Dented Members:**

- Use Loh's formulation [4] up to dents of depth  $0.30D$ .
- For dents between 30% and 50% of the member's diameter  $D$  use Ellinas' formulation [1]. However, provisions should be made to incorporate the effect of the end moments.

- To estimate the capacity for multiple-dent cases, in which dents are present at different longitudinal locations and in different circumferential orientations, check each dent at midspan, as indicated above, subjected to axial load and the moment components resolved about the dent cross-sectional axes.
- If more accurate estimates are required for the multiple-dent case, use BCDENT, provided that dent depths are less than  $0.30D$ .
- For single-dent members at midspan deeper than  $0.50D$ , conduct a finite element analysis that includes the denting process. For deep dented cases, the shape of the dent cross section becomes important - flat versus a hammock-shaped dent trough. Use of flat dents is conservative.

#### **Grouted Dented Members:**

- Use Loh's formulation [5] up to dent depths of  $0.50D$  with the end moments decomposed unto the dent cross sectional axes. Assume grouts typical of those used offshore. In absence of specific data, use a cube strength of 40 MPa and a steel-grout modular ratio of 18.
- Use of the current version of BCDENT with calculated  $M-P-\phi$  input for grout filled tubulars is only recommended to obtain an indication of capacity.
- Unless further calibration is made, finite element analyses are not recommended due to cost, effort, and uncertainty.

#### **Future Work**

Based on the research results, it is recommended that future research address the following topics:



- Experimental tests of *short* as-dented and grouted-dented tubular columns with dent depths between 30% and 50% of their diameter to determine the moment-rotation behavior at constant axial load for a given D/t ratio. These test results will acquire information on the M-P- $\phi$  relationships needed to fully utilize BCDENT.
- Additional tests as above to study the effect of the dent cross-sectional shape likely to occur in tubulars with relatively large D/t ratio. In this case, the dent trough is not flat but hammock-shaped. Members with more realistic dent shape should have significantly higher residual strength than those with flat dents.
- More extensive non-linear finite element studies of existing experimental results in order to more thoroughly evaluate the sensitivity of predicted behavior to modeling assumptions and to develop calibrated models.

## References

1. Ellinas, C. P. (1984), "Ultimate Strength of Damaged Tubular Bracing Members", *Journal of Structural Engineering*, ASCE, Vol. 110, No.2.
2. Parsanejad, S. (1987), "Strength of Grout-Filled Damaged Tubular Members", *Journal of Structural Engineering*, ASCE, Vol. 113, No. 3.
3. Loh, J. T. (1993), "Ultimate Strength of Dented Tubular Steel Members", *Proceedings of the Third International Offshore and Polar Engineering Conference*, Vol. IV, Singapore.
4. Loh, J. T., Kahlich, J. L., and Broekers, D. L. (1992), "Dented Tubular Steel Members", EXXON Production Research Company Internal Report, Houston, Texas.

5. Loh, J. T. (1991), "Grout-Filled Undamaged and Dented Tubular Steel Members", EXXON Production Research Company Internal Report, Houston, Texas.
6. Ricles, J.M. and Fan, C.H. (1997), "Analysis of Dent-Damaged and Internally Grout Repaired Tubular Steel Bracing Using Moment Curvature-Based Integration Methods", ATLSS Report 97-xx, ATLSS Engineering Research Center, Lehigh University, Bethlehem, Pennsylvania (in press).
7. Ricles, J. (1996), "Chapter 7 - Analysis of Internally Grout Repaired Damaged Members", *Analysis and Software of Cylindrical Members*, CRC Press.
8. *ABAQUS User's Manual (Version 5.3)* (1993), Copyright Hibbitt, Karlsson and Sorensen, Inc., 100 Medway Street, Providence, Rhode Island, 02906.
9. Ricles, J., Bruin, W., and Sooi, T. K (1997), "Residual Strength and Grout Repair of Dent-Damaged Offshore Tubular Bracing - Phase II Study", ATLSS Report No. 97-12, ATLSS Engineering Research Center, Lehigh University, Bethlehem, Pennsylvania (in press).
10. Chen, W.F. (1995), "Strength of Damaged Cylindrical Members Under Combined Axial Load and Bending," Structural Stability Research Council, *Proceedings of the 1995 Theme Conference on Stability Problems Related to Aging, Damaged, and Deteriorated Structures*, Kansas City, Missouri.

Table 1 - Dented and Grouted-Dented Specimen Description

Test Series	Specimen	Condition	Dia. OD (in.)	OD/t	Length L (in.)	Initial Ovality* (%)	Initial OSS** $\delta/L$	Dented OSS $\delta/L$	Dent-Depth, (%OD)	Dent Width (in.)	Yield Stress (ksi)	KL/r	$\lambda^{***}$	Grout Strength (ksi)
1	A10	As-Dented	8.629	33.8	177.2	0.4	0.0002	0.0064	25.3	7.0	36	59.9	0.622	-
	C10	As-Dented	8.585	67.6	180.1	0.4	0.0001	0.0052	25.0	7.0	37	59.9	0.670	-
2	A12	As-Dented	8.625	34.1	177.0	0.1	0.0005	0.0174	49.1	8.5	34	59.8	0.644	-
	C12	As-Dented	8.608	68.9	180.0	0.3	0.0003	0.0152	49.5	8.5	38	59.8	0.676	-
3	A11	Grouted	8.633	34.5	177.9	0.4	0.0007	0.0059	25.1	7.0	36	60.1	0.663	5.97
	C11	Grouted	8.582	68.1	180.5	0.3	0.0001	0.0051	25.5	7.0	36	59.9	0.661	5.90
4	A13	Grouted	8.625	34.1	177.5	0.1	0.0001	0.0211	50.0	8.5	34	59.9	0.645	7.69
	C13	Grouted	8.598	68.8	179.8	0.3	0.0002	0.0166	49.8	8.5	39	59.7	0.685	7.55
5	C15	Ext. Sleeve	8.601	68.8	180.5	0.3	0.0003	0.0150	49.9	8.5	35	59.9	0.650	3.77

\*  $(D_{MAX}-D_{MIN})/D_{MEAN}$

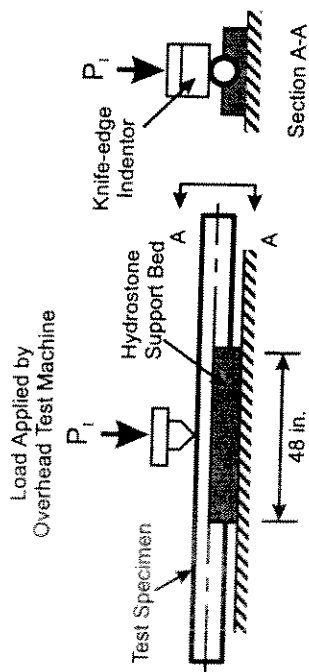
\*\* Out of Straightness

\*\*\* Slenderness parameter,  $\lambda = \frac{KL}{r} \sqrt{\frac{\sigma_y}{E}}$

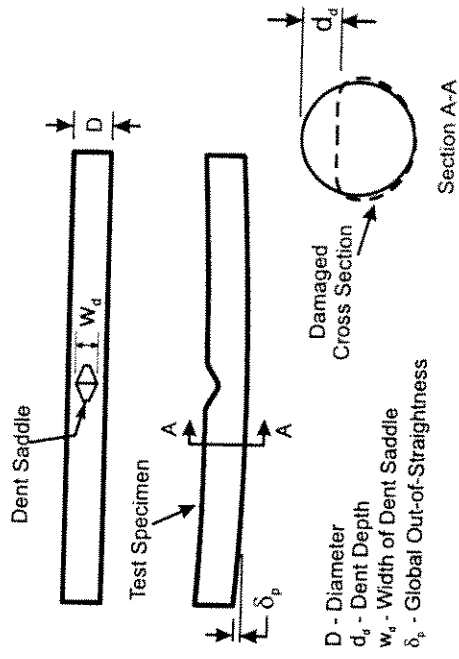
Table 2 - Comparison of Test Results to Calculated Ultimate Capacity

CAPACITY CALCULATION METHOD												
Test Series	Spec.	Specimen Condition	OD/t	Dent Depth, (%OD)	P <sub>TEST</sub> (kips)	CRC Eqn. Intact Column	THEORY Ellinas Ref. 1	THOERY Parsanejad Ref. 2	Unity Check Loh Ref. 4 & 5	M-P-φ Ricles Ref. 6 & 7	"DENTA"	FE ABAQUS Ref. 8
						P <sub>TEST</sub> /P <sub>CALC</sub>	P <sub>TEST</sub> /P <sub>CALC</sub>	P <sub>TEST</sub> /P <sub>CALC</sub>	P <sub>TEST</sub> /P <sub>CALC</sub>	P <sub>TEST</sub> /P <sub>CALC</sub>	P <sub>TEST</sub> /P <sub>CALC</sub>	P <sub>TEST</sub> /P <sub>CALC</sub>
1	A10	As-Dented	33.8	25.3	98	0.42	0.67	-	0.87	0.90	0.72	1.01
	C10	As-Dented	67.6	25.0	37	0.32	0.85	-	1.07	0.68	0.87	0.99
2	A12	As-Dented	34.1	49.1	39	0.18	0.71	-	1.33	0.86	Did not work	0.81
	C12	As-Dented	68.9	49.5	14	0.12	0.92	-	1.93	0.37	Did not work	1.24
3	A11	Grouted	34.5	25.1	158	MEAN	0.79	-	1.25	0.70	-	1.01
	C11	Grouted	68.1	25.5	104	COV	0.149	-	0.349	0.341	-	0.174
4	A13	Grouted	34.1	50.0	50	0.68	-	1.02	1.10	1.19	-	1.15
	C13	Grouted	68.8	49.8	40	0.93	-	1.05	1.09	1.19	-	1.37
5	A15	Ext. Sleeve	68.8	49.9	72	0.23	-	1.26	0.96	0.98	-	1.22
	C15	Ext. Sleeve	68.8	49.9	72	0.32	-	1.14	0.87	0.81	-	1.23
5	A15	Ext. Sleeve	68.8	49.9	72	MEAN	-	1.12	1.01	1.05	-	1.24
	C15	Ext. Sleeve	68.8	49.9	72	COV	-	0.093	0.113	0.179	-	0.065

(a) Denting Process



(b) Dent Damage



(c.) Test Setup

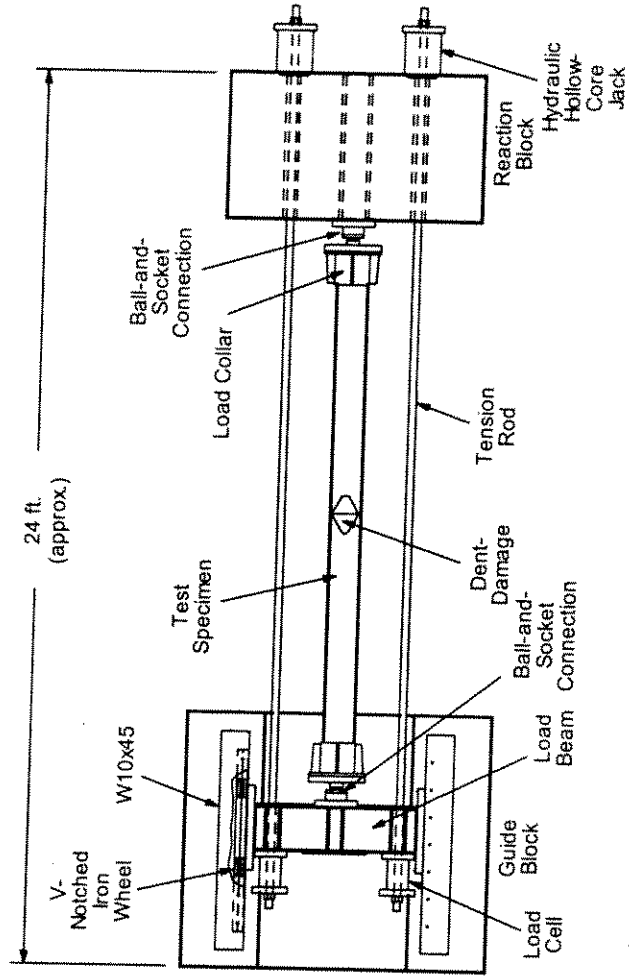
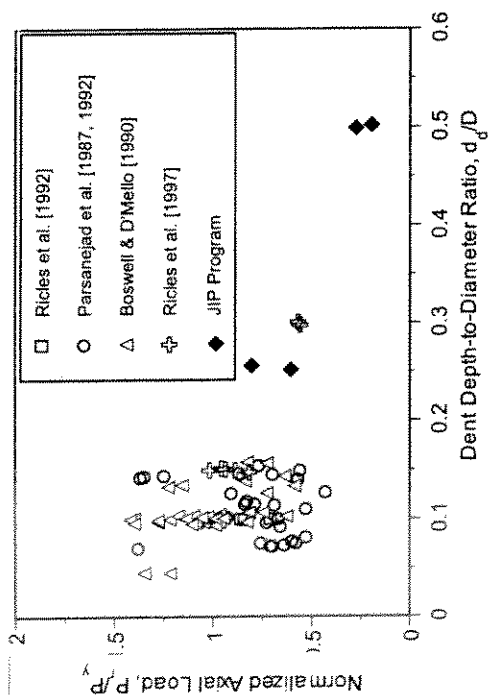
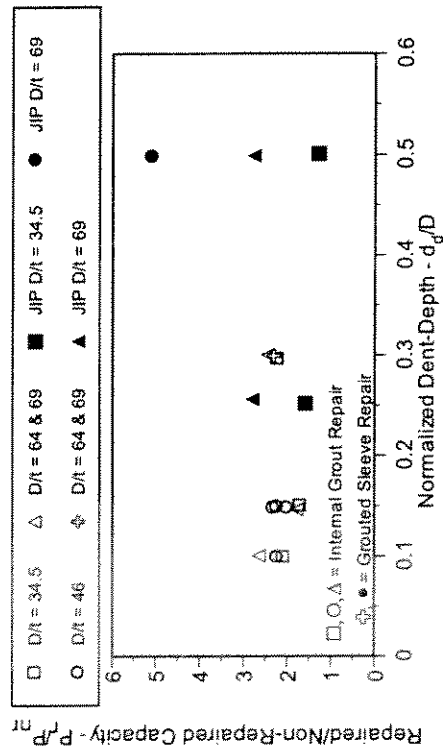


Figure 1 Schematics of (a) Denting Process, (b) Dent Damage, and (c.) Test Setup.

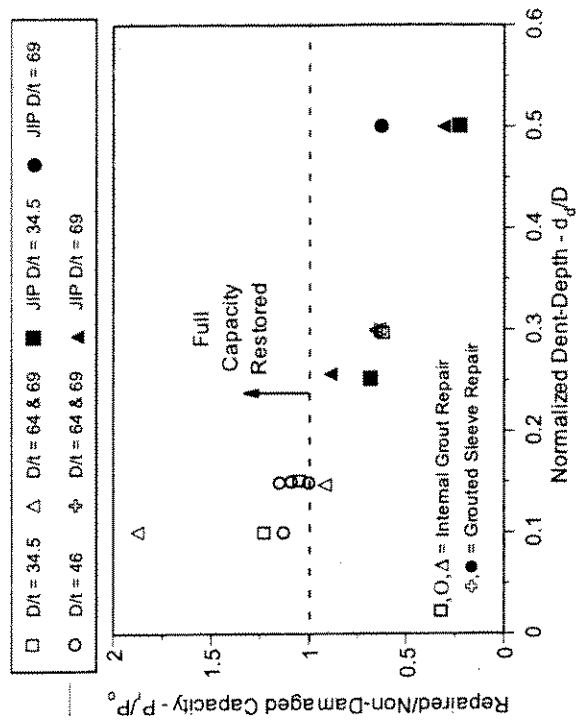


(a) Capacity Degradation Due to Denting



(b) Capacity Increase Due to Grouting

$P_0$  = Intact capacity  
 $P_{nt}$  = As-dented capacity  
 $P_r$  = Grouted-dented capacity  
 $P_y$  = yield capacity



(c) Grouted-Dented vs. Intact Ultimate Capacities

Figure 2 Effect of Denting and Grouting on Axial Capacity

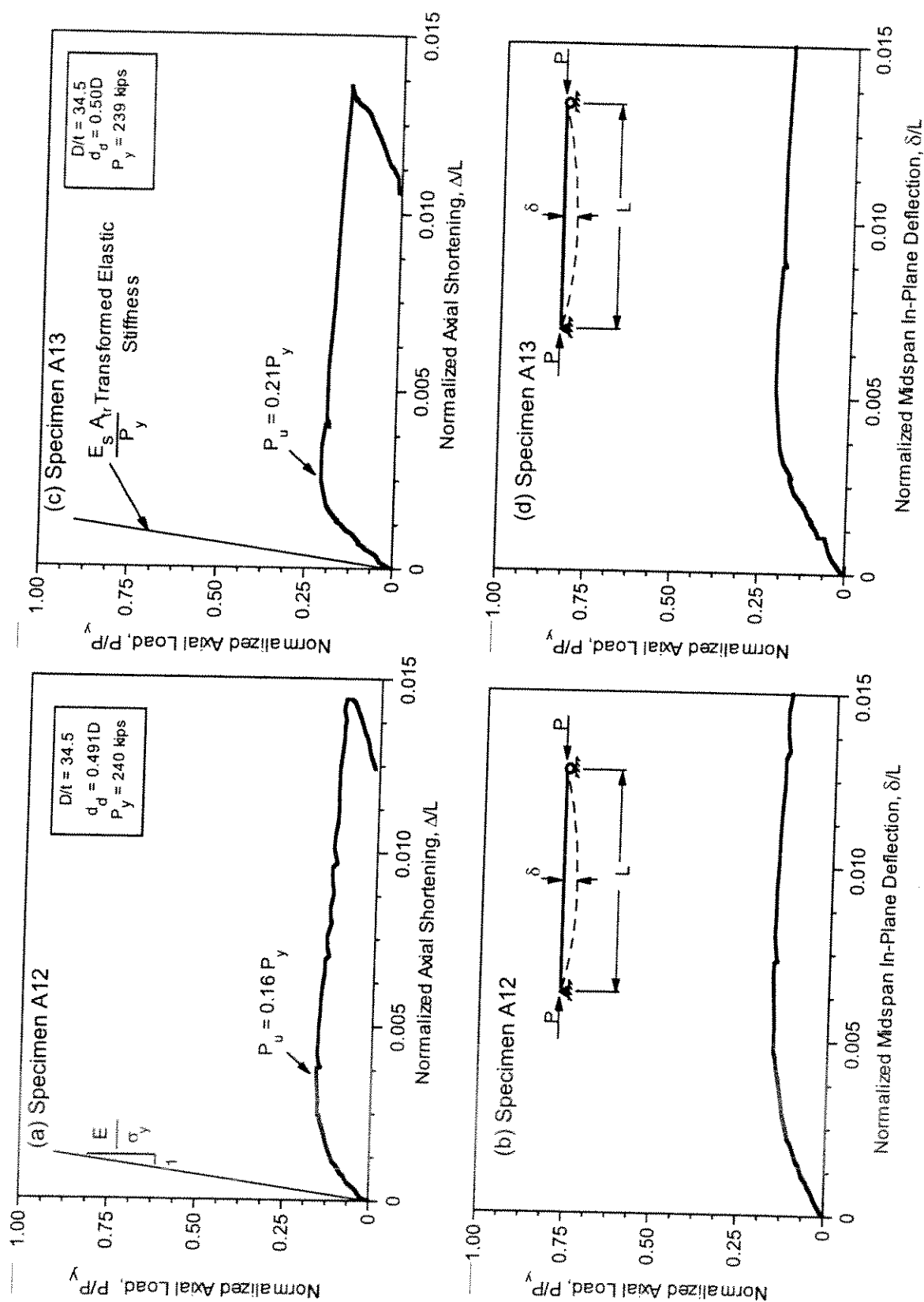
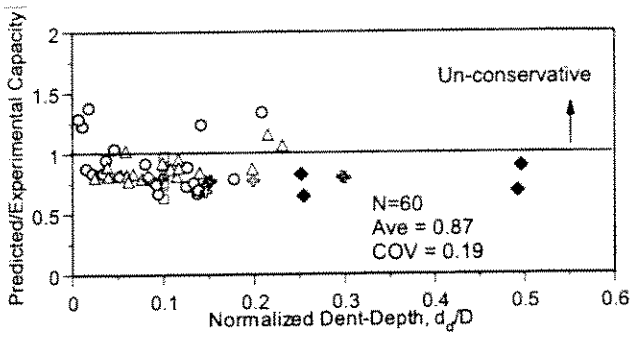
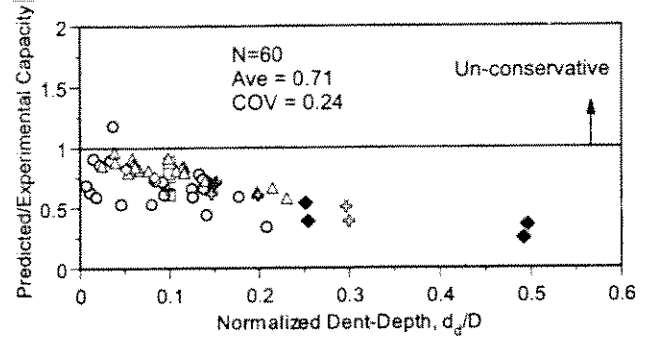


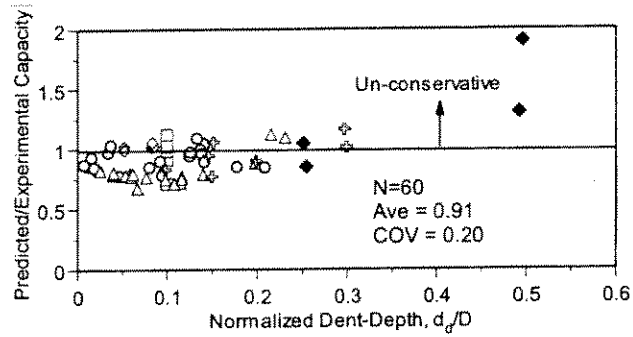
Figure 3 Load-Displacement Behavior for As-Dented (Specimen A12) and Grout-Dented (Specimen A13) Tubular, Deep Dent: 50%OD.



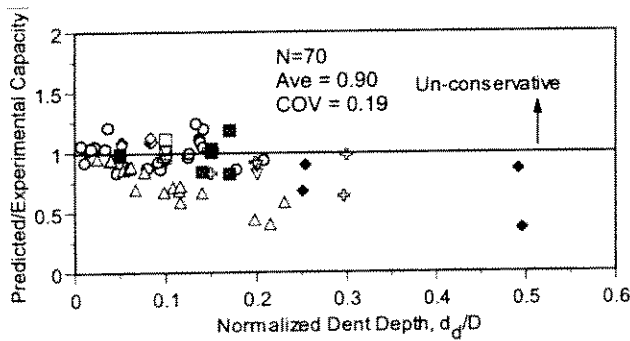
(a) Ellinas' Beam-Column Formulation [1]



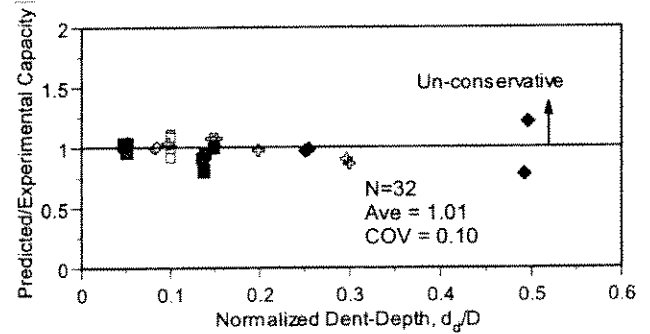
(b) Ricles' Beam-Column Formulation [9]



(c) Loh's Beam-Column Formulation [3]



(d) Numerical Moment-Curvature Approach  
(Program DDAM) [6]



(E) Nonlinear Finite Element Analysis [8]

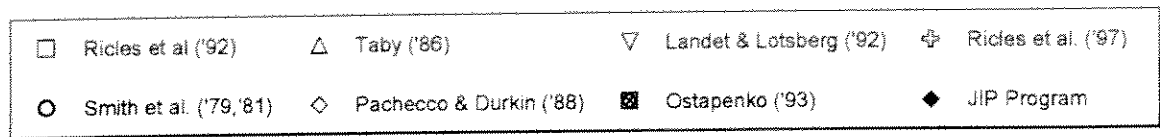
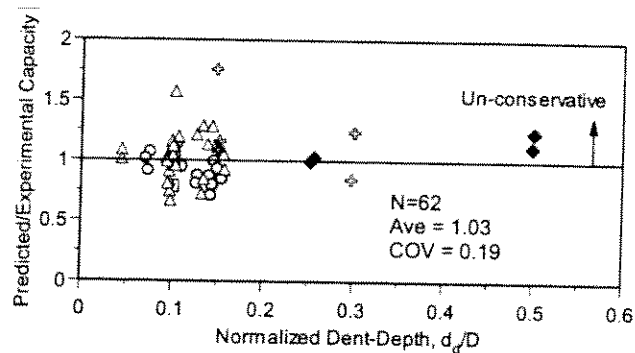
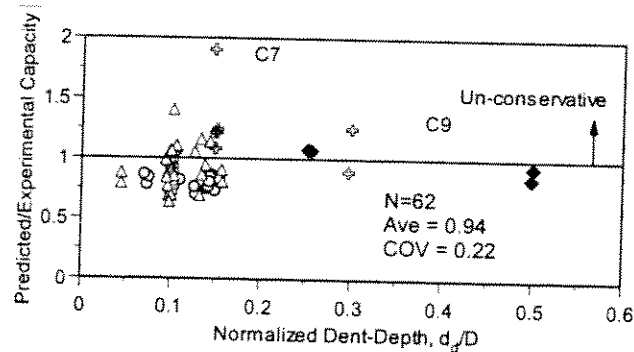


Figure 4 Comparison of Various Methods to Calculate Capacity of Dented Tubular Members.

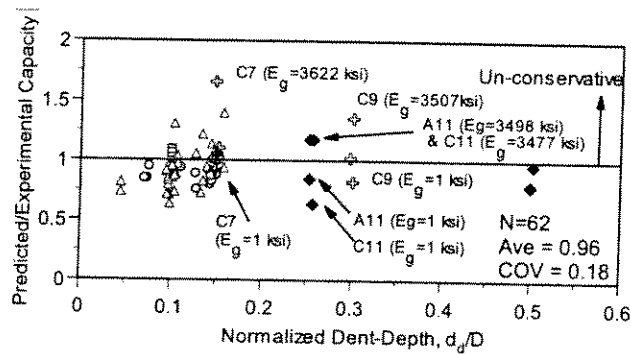




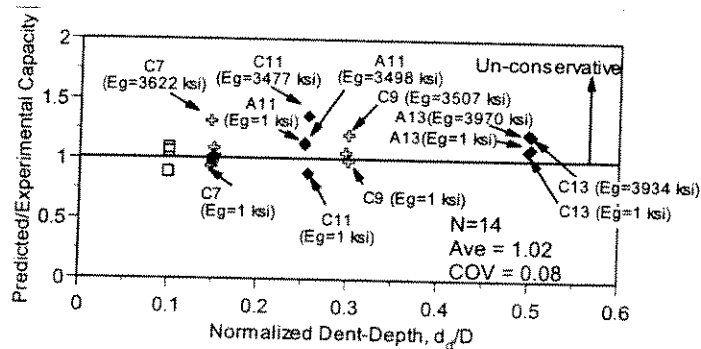
(a) Parsanejad's Analytical Formulation [2]



(b) Loh's Semi-Empirical Formulation [5]



(c) Numerical Moment-Curvature Approach  
(Program DGROUT) [7]



(d) Nonlinear Finite Element Analysis [8]

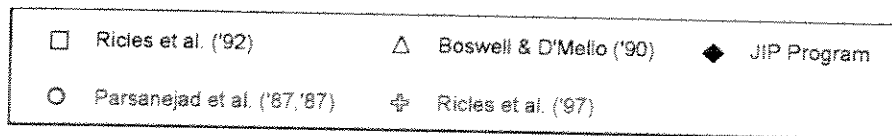


Figure 5 Comparison of Various Methods to Calculate Capacity of Grouted- Dented Tubular Members.



## ACKNOWLEDGMENTS

This report describes the work performed in Area Three of the project "Residual Strength and Repair of Damaged and Deteriorated Offshore Structures" at Lehigh University, Department of Civil and Environmental Engineering (Le-Wu Lu, Chairman). The project was within the managerial structure of ATLSS (Advanced Technology for Large Structural Systems, John W. Fisher, Director). Area Three entitled "Repair of Dented Tubular Columns - Whole Column Approach" was directed by Dr. James M. Ricles and was one of three areas, with Area One directed by Dr. Alexis Ostapenko and Area Two directed by Dr. Stephen P. Pessiki. The tests of Area Three were all conducted in the Imbt Laboratory located at ATLSS. The computations were conducted using the computer facilities located at ATLSS as well as at the Lehigh University Computer Center.

The project was sponsored as a Joint Industry Project by the following: EXXON Production Research Company (Contract: PR-14257), Minerals Management Service (DOI) (Contract: 14-35-0001-30719), Mobil Technology Company (Contract: 055-20-017), and Shell Offshore, Inc. (Contact: ANE-090193-KAD). The financial support provided by these organizations is greatly appreciated. The authors of this report are indebted for the advice and guidance of the following representatives of these organizations: Jaime Buitrago (EXXON), Douglas R. Angevine (Mobil), Charles E. Smith (MMS/DOI), and Kris A. Digre (Shell).

The authors are thankful to Perry S. Green, a graduate student in the Department of Civil and Environmental Engineering who assisted in conducting the grouted sleeve test and gave valuable guidance on the use of the computer program ABAQUS. The authors are also thankful to undergraduate students Trevor Dolena, John Matthew, Lisa Rios, and Peter Schönwetter who assisted in various aspects of this study. Thanks are also expressed to Frank Stokes, Robert Dales, John Hoffner, and others of the technical staff of the Imbt Laboratory.



# TABLE OF CONTENTS

EXECUTIVE SUMMARY	i
ACKNOWLEDGMENTS	xviii
TABLE OF CONTENTS	xix
CHAPTER 1 - INTRODUCTION	1-1
1.1. Project Organization	1-1
1.2. Research on Tubular Columns with Dent Damage	1-1
1.3. Description of Current Study	1-3
1.4. Outline of the Report	1-4
CHAPTER 2 - EXPERIMENTAL PROGRAM	2-1
2.1. Test Matrix	2-1
2.2. Test Specimens	2-3
2.2.1. Specimen Geometry	2-3
2.2.1.1. Initial Geometry	2-4
2.2.1.2. Infliction of Dent-Damage	2-5
2.2.1.3. Damaged Geometry	2-5
2.2.2. Material Properties	2-7
2.2.2.1. Tensile Coupon Tests	2-8
2.2.2.2. Stub-Column Tests	2-9
2.2.2.3. Grout Compressive Strength Tests	2-11
2.2.2.4. Bond Tests	2-13
2.3. Internal Grout Repair Methodology	2-14
2.4. Grouted Sleeve Repair Design	2-15
2.5. Experimental Test Set-up	2-17
2.6. Instrumentation and Data Acquisition	2-20
2.7. Test Procedure	2-22
CHAPTER 3 - EXPERIMENTAL BEHAVIOR	3-1
3.1. Behavior of Damaged, Non-repaired Specimens	3-2
3.1.1. Test Series 1 - 0.25D Dent-Depth	3-2
3.1.2. Test Series 2 - 0.50D Dent-Depth	3-6
3.1.3. Summary of Behavior for Damaged, Non-repaired Specimens	3-9
3.2. Behavior of Damaged, Internal Grout Repaired Specimens	3-9
3.2.1. Test Series 3 - 0.25D Dent-Depth	3-10
3.2.2. Test Series 4 - 0.50D Dent-Depth, Internal Grout Repair	3-15
3.2.3. Test Series 5 - 0.5D Dent-Depth, Grouted Sleeve Repair	3-18
3.2.4. Dissection of Grout Repaired Specimens	3-21

3.2.5. Summary of Behavior for Damaged, Grout Repaired Specimens	3-21
CHAPTER 4 - ANALYSIS OF EXPERIMENTAL RESULTS	4-1
4.1. General	4-1
4.2. Moment-Axial Load Interaction	4-2
4.2.1. Non-repaired Specimens	4-2
4.2.2. Internal Grout Repaired Specimens	4-4
4.3. Specimen Residual and Repaired Strength Assessment	4-5
4.3.1. Effect of Dent-Damage on Ultimate Capacity	4-5
4.3.2. Effectiveness of Internal Grout and Grouted Sleeve Repair	4-7
4.4. Comparison of Experimental Results with Theoretical Predictions	4-9
4.4.1. Analysis of Non-repaired Specimens	4-10
4.4.1.1. Simplified Strength Equations and Beam-Column Analysis Methods	4-11
4.4.1.2. Moment-Thrust-Curvature (M-P- $\Phi$ ) Based Method	4-17
4.4.1.3. Finite Element Method (FEM)	4-20
4.4.2. Analysis of Internal Grout Repaired Specimens	4-23
4.4.2.1. Simplified Strength Equations	4-23
4.4.2.2. Moment-Thrust-Curvature (M-P- $\Phi$ ) Based Method	4-26
4.4.2.3. Finite Element Method (FEM)	4-30
4.5. Repair Feasibility Study	4-34
CHAPTER 5 - SUMMARY AND RECOMMENDATIONS	5-1
5.1. Summary	5-1
5.2. Recommendations	5-7
5.2.1. Recommendations for Application of Completed Research	5-7
5.2.2. Recommendations for Future Research	5-9
REFERENCES	6-1
TABLES	
FIGURES	
APPENDIX A - SPECIMEN MEASURED OUT-OF-STRAIGHTNESS FOLLOWING DENTING	A-1
APPENDIX B - SPECIMEN MEASURED DENT PROFILES	B-1
APPENDIX C - ABAQUS INPUT FILE FOR SPECIMEN A10 - DENTED, NON-REPAIRED SPECIMEN ANALYSIS	C-1
APPENDIX D- ABAQUS INPUT FILE FOR SPECIMEN A11 - DENTED, INTERNAL GROUT REPAIRED SPECIMEN ANALYSIS	D-1

APPENDIX E- DATABASE OF UNREPAIRED AND INTERNAL GROUT  
REPAIRED DENT-DAMAGED TEST SPECIMENS

E-1





# **CHAPTER 1**

## **INTRODUCTION**

### **1.1. Project Organization**

This Joint Industry Project “Residual Strength and Repair of Damaged and Deteriorated Offshore Structures” at Lehigh University covered the following three areas of research:

Area One -

“Corrosion Damage - Effect on Strength”

with Dr. Alexis Ostapenko, Principal Investigator

Area Two -

“Corrosion Damage - Assessment in the Field”

with Dr. Stephen P. Pessiki, Principal Investigator

Area Three -

“Repair of Dented Tubular Columns - Whole Column Approach”

with Dr. James M. Ricles, Principal Investigator

This report describes the research conducted in Area Three on the general topic entitled “Tubular Columns with Deep Dents.”

### **1.2. Research on Tubular Columns with Dent Damage**

Tubular steel members are the primary type of structural element used in an offshore structure because their shape tends to minimize lateral hydrodynamic forces, provide high member torsional rigidity, and possess the same structural properties in all

directions. Under lateral impact loading however the circular cross-section of these members is susceptible to localized denting. Statistics have indicated that the largest single type of offshore accident, accounting for nearly 30% of all incidents, involves collisions or impacts into platform members [Ellinas and Valsgard, 1985]. The effect of dent damage is a reduction in member capacity. The residual strength of dent-damaged members must therefore be determined in order to evaluate the structural reliability of the structural system as well as identify the need for repair. To ensure that repairs are adequate for maintaining the structure's safety, the residual strength of repaired members must also be determined.

Numerous studies have been conducted on the residual strength of dented tubulars. These studies have included both analytical and experimental investigations, which have focused primarily on the behavior of non-repaired, dent damaged tubular members. Most of the experimental effort has involved small scale specimens, with a few tests involving large scale specimens [Smith et al. 1979, 1981; Taby et al. 1981, 1985, 1986, 1988; Pacheco and Durkin 1988; Ueda and Rashed 1985; Landet and Lotsberg 1992; Ricles et al, 1992, 1994a; Ostapenko et al. 1993]. A majority of the specimens had the damage limited primarily to a dent depth of 15% of the tubular's diameter. A few tests have been conducted with the specimens having a dent depth of approximately 20% of the member's diameter. More recently, Ricles et al. [1997] conducted two large-scale tests on specimens having dent depths of 30% of their diameter.

The above experimental research all found that dent-damage causes the wall of the cross-section in the dent saddle to grow inwards under the application of axial load, causing yielding in the tubular which leads to a reduction in member capacity. The residual strength was found to be smaller in specimens of greater dent depth.

In addition to the above experimental studies, several analytical studies on non-repaired dent-damaged tubulars have also been conducted [Ellinas 1984; Taby et al. 1981, 1985, 1986, 1988; Loh et al. 1992; Loh 1993; Ricles et al. 1992, 1994a, 1996; Duan et al.

1993; Kim 1992; Pacheco and Durkin 1988; MacIntyre 1991; Salman 1994; Ostapenko et al. 1993]. These analytical investigations have included approaches that ranged in complexity from simple closed-form beam column solutions to extensive non-linear finite element analysis.

Fewer studies have been conducted to evaluate the repair of dent-damaged tubulars. A majority of these studies have focused primarily on the effectiveness of injecting grout inside a tubular to improve strength. Tests have been conducted where the dent depths were up to 15% of the member's diameter [Parsanejad 1987; Parsanejad and Gusheh 1992; Tebbet and Forsyth 1987; Boswell and D'Mello 1988; Ricles et al. 1992; 1994a]. More recent tests have been conducted by Ricles et al [1997] on internal grout filled tubulars having dent damage as large as 30% of their diameter. These tests were complemented by analytical studies on the predicted performance of internal grout repaired damaged tubulars [Parsanejad 1987; Parsanejad and Gusheh 1992; Loh 1991; Ricles and Fan 1996; Ricles 1996]. The results of these studies indicated that internal grout repair can increase a dent-damaged tubular's residual strength.

A review of previous research indicates that there is a lack of test data associated with the residual strength and internal grout repair of dented tubulars with more severe damage. In addition, there is a lack of comparison of the predicted behavior of non-repaired and repaired dent-damaged tubulars of more severe damage using existing analytical models. The topic of this study addresses these aspects.

### **1.3. Description of Current Study**

The project described herein included nine tests on dent-damaged long tubulars under concentric axial loading. The dent depth of the specimens was 25% and 50% of their diameter. Four of the tests were on non-repaired tubulars, with an additional four tests conducted on internal grout repaired tubulars. One of the tests was on a damaged tubular with a dent depth of 50% of the diameter, in which the specimen was repaired

using a grouted sleeve. Each repaired specimen had dent damage and a geometry that corresponded to a non-repaired specimen.

Measurements taken during the tests enabled the general behavior and residual strength of the non-repaired specimens to be established. The effectiveness of internal grout repair for a given dent depth was made by directly comparing the measured response of corresponding non-repaired and repaired specimens. The influence of the extent of damage on the effectiveness of the use of grout to rehabilitate a dent damaged tubular was performed by comparing the results of the repaired specimens having different amounts of damage.

Analysis of the non-repaired and repaired specimens were conducted using several different existing methods. These analytical methods included: (1) beam-column formulations; (2) moment-thrust-curvature integration; and (3) non-linear finite element analysis. The analysis results, combined with those of analysis of specimens conducted in previous studies, were used to evaluate the effectiveness of the various analytical methods in predicting member capacity.

#### **1.4. Outline of the Report**

Four chapters of this report are used to document the description of the test program and the results of the tests and analytical study.

Chapter 2 describes the four non-repaired test specimens and five repaired test specimens, test setup, instrumentation, and test procedure.

Chapter 3 presents the test observations of the non-repaired and repaired specimens. Results for each specimen's load-deformation relationships, dent growth, and dented cross-sectional strain data are given and discussed.

Chapter 4 gives an evaluation of the moment-axial load interaction of each specimen at its dented cross-section. An assessment of the specimen residual strength and repaired strength is presented. In addition, the results of the comparison of the experimental results with theoretical predictions is also presented.

Finally, Chapter 5 summarizes the work performed in this project and lists the general conclusions as well as recommendations for the use of the results of the study. Recommendations for future research that is needed is also given in this chapter.



## CHAPTER 2

### EXPERIMENTAL PROGRAM

This chapter describes the test matrix, experimental test set-up, repair methodologies, test procedures, and reports the geometric and material properties for specimens. The experimental program involved the testing of 9 large-scale tubular bracing members having a nominal  $D/t$  ratio of 34.5 and 69. Non-repaired specimens as well as grout repaired specimens, and a grouted sleeve repaired specimen were tested. Each specimen was loaded in compression under concentric axial force to failure in order to study the influence of dent-damage on member performance. Following their denting to a specified dent-depth, each of the repaired specimens were either internally grouted or a sleeve placed over the dented region and the annulus grout filled. The effectiveness of the repair of these specimens was evaluated by comparing their response to that of the corresponding non-repaired specimens. The nominal dent-depths of the specimens was 0.25D to 0.5D.

#### 2.1. Test Matrix

The matrix of the test specimens is summarized in Table 2.1, with the specimen diameter-to-thickness ( $D/t$ ) ratio and normalized dent-depth ( $d_d/D$ ) plotted in Figure 2.1. Of the nine specimens in the test matrix, four were repaired by internal grouting and one by a grouted sleeve. These repaired specimens had geometric properties (i.e.,  $D/t$  ratio and thickness  $t$ ), as well as degree of damage (i.e., dent depth  $d_d$  and out-of-straightness  $\delta_p$ ) that were similar to that of corresponding non-repaired specimens. The evaluation of the repair methodology was achieved by comparing the performance of the non-repaired specimens with that of the repaired specimens which had a similar dent-depth ( $d_d$ ) and global out-of-straightness ( $\delta_p$ ). In addition, the lost in member strength from denting was evaluated by comparing the damaged, unrepaired specimen capacity with the theoretical capacity based on SSRC's Column Curve 1 [Galambos, 1988].

To facilitate the discussion, the specimens have been classified by dent-depth and repair methodology, resulting in five test series. Each of the test series are summarized below:

**Series 1** - Testing of two dent-damaged, non-repaired specimens (Specimens A10 and C10) with a nominal dent-depth of  $0.25D$ . The nominal  $D/t$  ratio for the specimens was 34.5 and 69, respectively.

**Series 2** - Testing of two dent-damaged, non-repaired specimens (Specimens A12 and C12) with a nominal dent-depth of  $0.50D$ . The nominal  $D/t$  ratio for the specimens was equal to 34.5 and 69, respectively.

**Series 3** - Testing of two internally grout repaired specimens (Specimens A11 and C11) with a nominal dent-depth of  $0.25D$ . The nominal  $D/t$  ratio for the specimens was equal to 34.5 and 69.

**Series 4** - Testing of two internally grout repaired specimens (Specimens A13 and C13) with a nominal dent-depth of  $0.5D$ . The nominal  $D/t$  ratio for the specimens was equal to 34.5 and 69.

**Series 5** - Testing of one grouted sleeve repaired specimen (Specimens C15) with a nominal dent-depth of  $0.50D$  and nominal  $D/t$  ratio of 69.

All internally grout repaired specimens had their inside wall surface in a clean, painted condition (i.e., no corrosion or mill scale existed). The effect of surface condition on the strength of the repair was investigated under the companion study by Ricles et al, [1997], where it was found not to significantly affect the repair. The outside surface of Specimen C15 of the present study was sand blasted over the area where the external grouted sleeve was fitted. The sand blasting was done in order to achieve a uniform roughness of approximately 3 mils which could be used as a reference for any subsequent



tests by either the investigators or other researchers.

## **2.2. Test Specimens**

The 9 test specimens were fabricated from hot-rolled electric resistance welded (ERW) carbon steel structural tubing of ASTM A53 Grade B Type E material. A pair of specimens, having the same  $D/t$  ratio, were cut from the same 40 foot long tubular as shown in Figure 2.2, with the remaining portions of the tubular being used for tensile coupon and stub column material tests. An exception to this was the fabrication of Specimens A12 and A13. For these specimens, the lack of availability of material made it necessary to cut the undamaged outer third portions of specimens tested under the companion study [Ricles et al. 1997]. These cut segments were then welded together, as shown in Figure 2.3, to form Specimens A12 and A13. In joining the segments, their longitudinal welds were aligned.

Dent-damage was imposed at the midspan of each specimen, directly opposite of the longitudinal weld seam. The measured cross-sectional dimensions, global imperfections, and material properties of all test specimens conformed to all API minimum standards for structural steel tubulars before being damaged [API RP-2A-LRFD, 1993].

### **2.2.1. Specimen Geometry**

The specimens were designed to model dent-damaged diagonal bracing members of fixed offshore platforms. The size of each test specimen was chosen to closely represent a large-scale model of a typical prototype bracing member found in fixed platforms existing in U.S. waters. Nominal values for the slenderness ratio ( $KL/r$ ) and the column slenderness parameter ( $\lambda$ ) were selected from typical design parameters and set at 60 and 0.65 to 0.70, respectively. The outer diameter ( $D$ ) to wall thickness ( $t$ ) ratios ( $D/t$ ) of 34.5 and 69 selected for the specimens covers the range of most fixed offshore

platforms in the Gulf of Mexico. A nominal outside diameter of 8.625 inches was selected for all specimens in order to accommodate the test frame fixture and facilitate testing. With this diameter, each specimen of this study represented a two-thirds to full-scale model of typical diagonal bracing, depending on the platform geographic location and water depth. The length ( $L$ ) of the specimens was approximately 15 feet, and was based on the prototype slenderness ratio of  $kL/r = 60$ . A summary of measured specimen dimensions, initial out-of-straightness ( $\delta_o$ ), and geometric test parameters are presented in Tables 2.2 and 2.3, respectively.

#### **2.2.1.1. Initial Geometry**

Measurements of specimen diameter ( $D$ ) and thickness ( $t$ ) were taken, the former by means of caliper measurements at 90 degree spacing around the circumference of the cross-section, at five locations along the length of the tube. The mean thickness was determined from the average of four micrometer readings at each end of the tube. Mean values and statistical parameters for all measurements are reported in Table 2.2. All cross-sectional measurements were found to be well within standard tolerances [API RP-2A-LRFD, 1993].

Initial out-of-straightness ( $\delta_o$ ) was measured using a surveying level with a leveling rod of 1/100 inch gradients. Each test specimen was placed in its horizontal test position and supported only at its ends, as it would be during a test. At fifteen stations along the length of the tube measurements were taken at four positions around the circumference of the cross-section, spaced at 90 degree intervals and originating at the weld. Corrections to the recorded data were made to account for any slope in the laboratory floor. A typical plot of member out-of-straightness ( $\delta_o$ ) prior to damage is shown in Figure 2.4. Maximum values for out-of-straightness ( $\delta_o$ ) for each specimen are reported in Table 2.2 where they have been normalized by their length ( $L$ ). The measured member initial out-of straightness ( $\delta_o$ ) of all of the members fall well below the API tolerance of  $\delta_o < L/960$  [API RP-2A-LRFD, 1993].

#### 2.2.1.2. Infliction of Dent-Damage

During denting to the targeted dent depth ( $d_d$ ) global bending was minimized by uniformly supporting the tube throughout the middle section during the denting sequence. For the specimens to be dented to a depth of 0.25D this support was provided by a bed of Hydrostone (Hydrostone Gypsum Cement, United States Gypsum, Chicago, IL) over a length of 48 inches. The specimens to be dented to 0.5D depth were supported by a neoprene pad. The latter was found to produce less out-of-straightness damage during denting to a depth of 0.5D.

The method of denting of the specimens to 0.25D is shown schematically in Figure 2.5 and photographed in Figure 2.6. The dent was imposed using a 600 kip Satec universal testing machine (Satec Systems Inc., Garden City, PA) under displacement control. The dent was applied along the top longitudinal surface of the tube such that the fold of the dent saddle was perpendicular to the tube axis. The dent was formed by loading the tubular under displacement control with a knife-edge device having a tip radius of approximately one-quarter of an inch. Figures 2.7 shows this knife edge device. The sharp edge simulated the geometry of a sharp, rigid structure which might impact the prototype brace in the field. The denting load was imposed until the dent-depth ( $d_d$ ) reached the targeted amount. A caliper was used to measure the dent-depth, by measuring the distance from the middle of the dent saddle to the underside of the tubular and subtracting this dimension from the original measured diameter ( $D$ ). Because a some elastic rebound was experienced when denting the tubes, in some specimens several trials were necessary to carefully obtain the correct dent-depth. Typical load-displacement relationships during denting to a depth of 0.25D for specimens with  $D/t = 34.5$  and 69 are shown in Figures 2.8(a) and (b), respectively.

#### 2.2.1.3. Damaged Geometry

After imposing the dent-damage, the dent geometry and damaged out-of-

straightness ( $\delta_p$ ), (i.e., global bending), were measured for each specimen. The measurements are summarized in Table 2.4. In addition to dent-depth ( $d_d$ ), the dent-width ( $w_d$ ) was also measured using a caliper in conjunction with a scale with gradients of 0.01 inch. Figure 2.9 illustrates these recorded geometric dimensions used to describe the dent-damage of each specimen. Damaged out-of-straightness was measured in the same manner as that used for the initial out-of-straightness. The dent profile for each specimen was measured at 1 inch increments along the top surface of the tube over a distance of 24 inches on either side of the center of the dent. The method used to measure the dent profile was the same as that used for measuring the dent depth during the denting of the tube.

A typical plot of member out-of-straightness ( $\delta_p$ ) after the infliction of dent-damage is shown in Figure 2.10. Typical measured dent profiles for each dent-depth are shown in Figure 2.11. Photographs of the dent-profile of specimens with dent-damage of 0.25D and 0.5D in depth are given in Figure 2.12. Dent profiles of specimens with different D/t ratios for a given dent-depth were observed not to vary by any appreciable amount. Plotted measurements for all specimens are given in Appendices A and B for the out-of-straightness and dent depth, respectively.

As a point of interest, Figure 2.13 shows a plot of the normalized measured member out-of-straightness ( $\delta_p/L$ ) as a function of measured dent-depth ( $d_d/D$ ). Included in this figure are the measurements for the companion study [Ricles et al. 1997], which used the same denting procedure in conjunction with a Hydrostone support bed. Figure 2.13 illustrates, despite efforts to control global bending during denting, that an approximate parabolic increase in the out-of-straightness ( $\delta_p/L$ ) occurs as the depth ( $d_d$ ) of applied dent-damage increases. Members with larger D/t ratios are shown in Figure 2.13 to have less out-of-straightness at a specified dent-depth.

### 2.2.2. Material Properties

As noted previously, all test specimens were fabricated from hot rolled electric resistance welded (ERW) carbon steel structural tube of ASTM A53 Grade B Type E material. The ASTM A53 specification mandates a minimum yield stress ( $\sigma_y$ ) of 34 ksi, however, it does not specify a maximum yield strength. Over the past few years, the introduction of recycled steels containing diverse alloys to the production process has become more popular by the mills that manufacture the majority of steel tube and pipe produced today. In addition, pressure to optimize the quantity of material being produced at these facilities has increased the rate at which the steel tubulars are fabricated, and subsequently has increased the rates at which these members are cooled. As a result, the yield strength of newly fabricated ASTM A53 tubes has on average increased to stresses that typically range from 55 to 70 ksi. Tensile coupons taken from the tubulars of this test program confirmed that the groups of specimens with D/t ratio of 34.5 had a yield strength of 60 ksi with an ultimate tensile strength of 70 ksi, virtually no yield plateau, and 23 percent elongation (see Figure 2.14). This material was not representative of the steel commonly used in the construction of many existing offshore platforms. A majority of U.S. platforms are at an age of at least fifteen years old [Leblanc, 1994]. Many of these older platforms, the focus of this program, were constructed of a mild grade steel, such as ASTM A7 or ASTM A36, although some were constructed of relatively higher strength grades like ASTM A441. These milder grade steels, however, typically had a yield stress in the range of 33 to 42 ksi, a well defined yield plateau that reaches a strain of approximately 10 to 20 times the yield strain, and 25 to 35 percent total elongation. For the current test program, tubulars with D/t = 34.5 possessing these mild steel characteristics were not readily available from any supplier, therefore, it was necessary to have the tubulars annealed to create material properties more representative of the prototype structures. On the contrary, as shown in Figure 2.14, the material for the tubulars with a D/t ratio of 69 possessed a more representative stress-strain relationship in terms of yield strength, tensile strength, and elongation, and therefore was not annealed.

Several sample tensile coupons were annealed and tested to confirm the annealing procedure to be used for the specimens with  $D/t = 34.5$  (see Section 2.2.2.1. for tensile coupon test procedures). After confirming the process, the specimens were then annealed in a vertical hanging position to minimize distortions of the cross-section. The annealing process consisted of heating the tubes to 1650° F for thirty minutes and then furnace cooling (turning off the furnace and allowing the specimens to cool very slowly over a twenty-four hour period) to below 750° F. After annealing, additional tensile coupons were tested and the steel yield and tensile strengths were observed to have been lowered to 40 ksi and 60 ksi, respectively. The steel also developed a yield plateau that had a length that reached a strain ten times the yield strain, with total elongation of over 25%. The annealed tubes with  $D/t = 34.5$  therefore had material properties more representative of the in-situ material found in the older offshore platforms studied in this program.

In addition to tensile coupon tests, other material tests were performed to obtain additional mechanical properties of the test specimens. Stub-column tests were performed to evaluate the compressive yield strength and the degree of residual stresses in the tubulars tubes, the latter being more applicable to the specimens not annealed. Compression tests were conducted on all grout mixtures in order to determine their respective compressive strengths ( $f'_g$ ). The average bond stress between the internal grout and steel tubular was estimated by a series of bond tests. Procedures and results from these material tests are described below, with results reported in Table 2.5.

#### **2.2.2.1. Tensile Coupon Tests**

Tensile properties of the steel tubular specimens were determined by conducting standard tensile coupon tests. Tensile coupons were machined according to ASTM Specification E8-91 ["Standard" 1991] with a width of 1.5 inches and a gage length of 8 inches. Three coupons were taken from the end regions of each specimen. As shown in Figure 2.2, the coupons were cut in the longitudinal direction of the tube at an angle of 90

degrees from each other around the circumference of the cross-section, originating at, but not including the weld.

The coupons were tested according to SSRC Technical Memorandum B.7 [Galambos, 1988] in a 120 kip Tinius-Olsen (Tinius-Olsen Machine Co., Willow Grove, PA) displacement controlled universal testing machine. An eight inch mechanical extensometer incorporating two linear transducers, one on each side of the coupon, was used to measure the average strain over the coupon gage length and to eliminate effects of longitudinal curvature in the coupon measurements (see Figure 2.15). The coupons were tested at a strain rate of 0.0025 inches per minute for dynamic measurements. A static reading was taken in the yield plateau of the stress-strain curve by holding the axial displacement and allowing the load resisted by the specimen to stabilize over a duration of approximately five minutes. Several static readings were taken in the yield plateau to establish the static yield stress. Elongation measurements were taken after testing. Typical stress-strain plots for each D/t ratio are shown in Figures 2.16(a) and (b).

Reported in Table 2.5 are the measured Young's modulus ( $E_s$ ), yield stress ( $\sigma_y$ ), ultimate stress ( $\sigma_u$ ), strain at the onset of strain hardening ( $\epsilon_{sh}$ ); strain at maximum stress ( $\epsilon_u$ ); strain at fracture ( $\epsilon_{max}$ ), and the slope  $E_{sh}$  of the stress-strain relationship at the onset of strain hardening. These values in Table 2.5 are the average of the three tensile coupons of each specimen after annealing. Also included in Table 2.5 is the compressive yield stress, based on stub-column tests.

#### **2.2.2.2. Stub-Column Tests**

One stub-column for each tubular from which a pair of specimens were cut were tested to determine the effect of local buckling and longitudinal residual stresses on the strength of the fabricated tubulars. The stub-column tests were performed in accordance with SSRC Technical Memorandum B.3 [Galambos, 1988]. The stub-columns were saw cut from the end of the tubular from which two specimens were obtained (see Figure 2.2),

and annealed along with the specimens. Since the test specimens with a  $D/t$  ratio equal to 69 were not annealed, the corresponding stub columns were also not annealed. Each stub column was thirty inches in length, or approximately  $3.5D$ , and had a ten inch gage length. Each stub-column specimen was placed directly on the pedestal of the 600 kip Satec universal testing machine. Cardboard bearing material was used at both ends to eliminate any stress concentrations due to burrs at the saw cut ends. A machine plate was then placed on the top of each stub-column. A wet Hydrostone grout mixture was placed on top of the plate and the machine head was lowered until the Hydrostone grout squeezed out from all sides of the plate, leaving approximately  $1/16$  to  $1/8$  inches between the machine and the plate. Using Hydrostone in this manner enabled a proper alignment of a stub-column to be achieved, resulting in a uniform longitudinal stress distribution.

Instrumentation of the stub-columns consisted of four 1.5 inch linear transducers placed over the gage length, at 90 degree spacing around the circumference of the stub-column to record axial shortening during the compressive testing. Head travel and applied load were also recorded. The stub-column test set-up is shown in Figures 2.17 and 2.18. For the stub columns with  $D/t = 34.5$  the displacement transducers were held in place by tack welding studs to the tube, whereas for the stub columns with  $D/t = 69$  the instrumentation was held in place by using wood blocking and metal straps tensioned around the circumference of the tube (not shown).

During the testing of the stub-columns a loading rate of 0.01 inches per minute was used for the dynamic measurements. Several static readings were taken by stopping the loading and holding head displacement until the load maintained by the specimen had stabilized, requiring a pause of approximately five minutes.

Typical stress-strain curves for the two values of  $D/t$  are shown in Figures 2.19(a) and (b). The stub-column test results for the annealed tubulars with  $D/t$  of 34.5 show that the annealing process had eliminated all residual stresses from fabrication. For these stub



columns their elastic slope abruptly ends when the overall yield capacity is reached. In contrast, the elastic slope of the specimens with a  $D/t$  of 69 began to show softening around 86 percent of the overall compressive yield capacity. This implies that the level of compressive residual stress was about 14 percent of the overall yield stress of the material. After yielding developed across the entire section, a yield plateau became present in all stub-columns and was used to measure the overall compressive yield stress. At this point, the stub-columns with  $D/t = 69$  locally buckled at their ends and the axial load deteriorated. The stub-columns with a  $D/t$  ratio of 34.5 exhibited a stress-strain curve that reached approximately 12 times the yield strain. At this strain, the stub-columns began to strain harden before developing multiple local buckles at midspan. The compressive yield stress obtained from the stub-columns are shown in Table 2.5 to corresponded well to those results from the tensile coupon tests.

#### **2.2.2.3. Grout Compressive Strength Tests**

Grout mixes of API Class A portland cement combined with densified microsilica and high water/cement ( $w/c$ ) ratios were used to achieve a targeted 28 day compressive strength of 6000 psi. The densified microsilica flour provided good pumpability and replaced cement to increase the  $w/c$  ratio, while increasing hydration of the remaining cement. The internally grouted and grouted sleeve specimens each required approximately 5.5 and 1.9 cubic feet of grout, respectively. A typical grout mix consisted of a 65 to 70 percent  $w/c$  ratio by weight. Microsilica flour per weight of cement was set at 20 percent.

A sample of grout was taken from the grout batch after each specimen was pumped full and used to mold two inch cube specimens in accordance with ASTM C109-92 ["Standard" 1992] for subsequent determination of the grout compressive strength ( $f'_g$ ). All cubes were cured in a water-lime bath at ambient temperature until immediately before testing in a 60 kip Tinius-Olsen displacement controlled universal testing machine. Compressive strengths are given in Table 2.6 and are based on the average of three to six

cubes on the day of testing the corresponding repaired specimen.

The grout elastic modulus ( $E_g$ ) was initially measured directly from the stress-strain curves of the grout cube compressive test. A typical measured compressive stress-strain relationship for a grout cube is shown in Figure 2.20. This method tended to vary greatly from cube to cube and was determined to be unreliable. In addition, this method did not allow easy correlation with modulus values measured from cylinder tests used in some capacity prediction equations [Loh 1991]. A more effective method to estimate the grout elastic modulus ( $E_g$ ) was proposed by Lamport [1988]. This method is based on a modified version of ACI Equation 8.5.1 ["American" 1992] which relates the concrete cylinder compression strength ( $f'_c$ ) and density ( $w_c$ ) to the elastic modulus of concrete ( $E_c$ ). Lamport showed that a reasonable approximation of the grout elastic modulus ( $E_g$ ) could be obtained by using the grout density ( $w_g$ ) in place of the concrete density ( $w_c$ ) and by substituting the grout cube's compressive strength ( $f'_g$ ) with an 20 percent reduction for the concrete cylinder strength ( $f'_c$ ) into the ACI equation. The resulting modified version of ACI Equation 8.5.1 is therefore:

$$E_g = w_g^{1.5} \cdot 33 \sqrt{0.8 \cdot f'_g} \quad (2.1)$$

Shown in Figure 2.21 is data of the elastic modulus from the grout cylinder tests by Lamport [1988] plotted against corresponding grout cube compression strengths from the companion study by Ricles et al. [1977]. Good correlation is seen in Figure 2.21 between test data and Equation (2.1), where a value of 133 pounds per cubic foot was used for the grout density ( $w_g$ ) in the modified ACI equation.

To provide an independent verification of Equation (2.1), in the companion study by Ricles et al. [1977] two - 4 by 8 inch cylinders were cast with grout in accordance with the procedures outlined in ASTM Specification C192-90a ["Standard" 1990]. Both cylinders were tested in accordance with ASTM Specification C39-86 ["Standard" 1986] after 28 days of curing to determine their compressive cylinder strength and directly measure the grout elastic modulus. The results of both of these tests are presented in

Table 2.7 and the measured stress-strain curves shown in Figure 2.22.

The results for  $E_g$  from these tests were used in conjunction with  $f'_g$  from grout cube tests to develop data points that are included in Figure 2.21, and designated as "Bruin 2-inch cube". These results also showed good agreement with Equation (2.1). Satisfied with the agreement, the elastic modulus of grout for all internal grout repaired specimens were calculated using Equation (2.1) and are reported in Table 2.6.

#### **2.2.2.4. Bond Tests**

The average bond stress between the internal grout and steel tubular was estimated in the companion study by Ricles et al. 1997 by testing a series of bond specimens for standard and simulated poor bond conditions. In this study, each of the bond test specimens consisted of a fifteen inch long segment of tube with  $D/t = 46$ , with its longitudinal axis oriented vertically and subjected to compression. The interior surface of the specimens were cleaned of any loose mill scale and debris. To create the "poor bond" condition a light 90 weight hydraulic oil was spread uniformly on the interior surface of the steel tube prior to casting of grout.

All specimens were filled with thirteen inches of grout, where at the top surface the grout was cast flush with the steel tube, while at the bottom a two inch space was left between the grout and the end of the steel tube (see Figures 2.23(a) and (b)). Each bond test specimen was placed onto the pedestal of the 600 kip Satec universal testing machine with the bare steel end downward and prepared for testing in the same fashion as the stub-columns (see Section 2.2.2.2.). Axial compressive load was applied directly to the internal grout at the top of the bond test through the placement of a circular steel plate on a bed of Hydrostone which rest exclusively on the interior grout. An additional plate was placed on the circular plate and the Satec head was lowered before the Hydrostone completely solidified to seat all components and to ensure even distribution of load in the

grout. This configuration allowed the applied load to transfer from the grout to the steel tube exclusively by the shear action developed in the bond between the inside face of the steel tube and the internal grout. Instrumentation was set-up such that the applied axial load, Satec head travel, and relative axial displacements between the steel and internal grout were recorded. The relative axial displacement was measured by averaging the readings over a gage length of 10 inches of four displacement transducers spaced at 90 degrees intervals around the circumference of the bond test specimen (see Figure 2.23).

The average bond stress-axial displacement relationship of a standard and lubricated bond specimen is shown in Figure 2.24, where the average bond stress is equal to the applied load divided by the surface area of the grout in contact with the steel tube. This figure shows that the relationship between the average shear stress and axial displacement is linear up to the critical stress at which the bond between the grout and steel fails. For the standard bond specimen, the critical stress was 132 psi, while the reduced bond specimen achieved a maximum capacity of only 31 psi, representing a reduction of 76 percent in the maximum average bond stress. After initial failure, each test specimen resisted approximately 60 percent of its peak capacity through sliding friction.

### **2.3. Internal Grout Repair Methodology**

Following the infliction of damage to the internal grout repaired specimens, each tube was then fitted with two end plates to provide containment of the grout at its ends. Each of these end plates had machined and tapped holes to facilitate the installation of grout ports. A standard one-inch gate valve was inserted into the inlet port to enable pressurized injection of the grout into the specimens. The outlet port consisted of a three-foot vertical standing pipe. The end plates were tensioned into position and secured by the means of tightening four lengths of all thread rod that passed through both end plates which had been fitted onto each end of the specimen. In addition, foam spacers were placed inside of the specimen and prior to placement of the end plates. These foam

spacers would create a void in the grout at each of the specimen's ends (see Figure 2.25) to allow the direct application of the axial load through the ends of the steel tubular during testing.

A grout pump with a one-inch diameter hose was utilized in the grout injection. The specimens were inclined approximately 45 degrees to simulate field conditions and the grout was injected from the low end and pumped to the high end. The grouting set-up is shown in Figure 2.26. Grout was pumped under low pressure and allowed to completely flush through the tube, overflowing out of the standing pipe. Grouting continued until a consistent mix was flowing out of the standing pipe. The inlet valve was then closed and the grout pumping was stopped. The grout-filled specimens were subsequently cured inside the laboratory, sheltered from the sun and from any drastic temperature variations.

#### **2.4. Grouted Sleeve Repair Design**

Following the infliction of damage to Specimen C15 to a dent depth of  $0.5D$ , a steel sleeve was placed over the dented portion of the tube and grouted. The steel sleeve was used in place of a conventional steel clamp in order to test the concept of providing an exterior repair by confined grout using a steel member, while reducing the cost for purposes of laboratory testing. Specimen C15 was selected for a grouted sleeve repair, since if the method was successful for a specimen that had a  $D/t$  ratio of 69, then it could be hypothesized that the repair would also be successful for tubulars with a smaller  $D/t$  ratio. The steel sleeve consisted of a tubular of 12.75 inch outer diameter and 0.1875 inch wall thickness, resulting in a  $D/t$  ratio of 68. This  $D/t$  ratio was approximately the same as that of the dented specimen. The inner diameter of the sleeve ( $D_i$ ) was 12.375 inches, which was large enough to enable the sleeve to pass over the dented cross-section, whose width was 11.5 inches. The grout annulus was therefore seven-sixteenths of an inch at this location.

The length of the sleeve  $L_s$  was based on meeting two criteria. The first of these was that the sleeve must be able to resist by itself the undamaged axial capacity  $P_0$  of the tubular. Therefore, the length of the sleeve had to be large enough to allow stresses to develop in the sleeve by bond action between the inner surface of the sleeve and the grout annulus, where the total stress transferred by bond action was equivalent to the undamaged capacity  $P_0$ . On this basis, assuming a uniform bond stress  $f_b$ , the required sleeve length  $L_s$  is:

$$L_s \geq \frac{2 P_0}{\pi D_i f_b} \quad (2.2)$$

For a bond stress of 132 psi (based on the results of the bond tests reported in Section 2.2.2.4), a undamaged capacity  $P_0$  of 126 kips (based on SSRC Column Curve 1), and  $D_i$  equal to 12.375 inches, the required sleeve length based on Equation (2.2) was 49 inches.

While this length is conservative, since the dented tubular has some residual strength, it was found that the length of the sleeve was controlled by the second criteria. This second criteria is based on having the cross-sectional distortion of the portion of the damaged tubular within the tolerances of API RP-2A [API RP-2A - LRFD 1993] for ovality. It was determined that the ovality of the cross-section was within the API limits at a distance of 35.5 inches to each side of the center of the dent, therefore requiring a total sleeve length of 71 inches.

A section view of the sleeve is shown schematically in Figure 2.27, where internal ring stiffeners have been placed at 1.5 inches from the edge of the sleeve (the length of the sleeve has been increased to 74 inches to accommodate the end distance for the ring stiffeners). The purpose of the ring stiffeners was to provide a water tight encasement for the grout annulus, where an o-ring gasket was placed between the ring stiffener and a second loose ring that was bolted to the ring stiffener (see Figure 2.27(a)). As noted previously, prior to placing the sleeve over the specimen, the outer surface of the

damaged member and inner surface of the sleeve were sand blasted to achieve a uniform roughness of 3 mils.

Grout ports were located at each end of the sleeve. During grout placement the member was inclined at a 45 degree angle and grout was injected into the lower port until it flushed through the sleeve, overflowing out of a standing pipe placed at the upper port. The specimen was then cured inside the laboratory, sheltered from the sun and any drastic temperature variations.

## **2.5. Experimental Test Set-up**

A 500 kip self-reacting test frame ,shown schematically in Figure 2.28 was designed and fabricated for the purpose of testing the specimens under compressive axial load. Care was taken in the development of the design criteria for the test frame to appropriately model assumed experimental parameters including: (1) specimen pinned-end conditions, with unrestrained rotation of specimen ends about any axis; (2) adequate clearance for lateral displacement of the specimen; and (3) sufficient test frame capacity. Components of the test frame included: two frictionless, precision machined ball-and-socket bearing connections; a frictionless sliding load beam and track system located by a reinforced concrete guide block; a reinforced concrete reaction block; two high strength tension rods; and a pair of 150 ton hollow core hydraulic cylinders. A photograph of the test frame is given in Figure 2.29.

A compressive axial load was applied to the specimen through the use of a 150 ton capacity hollow plunger hydraulic cylinder reacting against each tension rod (see Figure 2.28). The pair of hydraulic cylinders were connected to a 10,000 psi air-cooled hydraulic pump, using a common hydraulic line to synchronize the pressure in each cylinder. A pressure relief valve was used to limit pressure developed by the pump in the hydraulic line, thus limiting the force developed on the tension rods and enabling load control during testing. An in-line needle valve enabled the tight metering of flow into

each cylinder, subsequently allowing displacement control in the post-ultimate region of loading during testing.

The spherical ball-and-socket bearing connection, shown in Figure 2.30, was designed to effectively model true pinned-end conditions by allowing free rotation of an end of a specimen. The ball-and-socket were machined to a tolerance of 0.003 inch. The ball was coated with high-pressure grease before being fastened to the socket with high strength bolts. The grease minimized any friction from developing in the bearing.

The load beam shown in Figure 2.31 was designed to accommodate a ball-and-socket bearing connection, transfer the tension rod force to the specimen, and slide in a controlled, relatively friction-free horizontal manner on the sliding-track system installed on the guide block. This beam was built up from two standard C15x50 channel shapes placed back to back with a 3-inch gap which provided passage for the tension rods, and secured by welded plates. Various web stiffeners were located in the regions of applied loads and reactions. A 3 x 2 x 1/4 inch structural tube of 28 inches in length was welded at each end of the load beam, to which four cast iron V-notched wheels were attached. These V-notched wheels rode on rails that were anchored to the guide block. Each pair of these wheels was located at 26 inches on center at the ends of the structural tubes to provide a wide wheel base in order to minimize any horizontal or vertical racking of the load beam during testing.

The guide block was designed to support the sliding track system for the load beam as well as resist any accidental racking forces that may develop in the load beam. Extreme care was taken in the construction of the guide block to ensure that the tracks guiding the V-notched wheels, and subsequently the load beam, were installed parallel and level with each other to minimize load beam racking. Each track consisted of a W10x45 beam that had two pieces of angle placed between its flanges. On the lower inside face of the flange, a 60 inch length of 2 x 2 x 3/8 inch angle was laid with its apex side up and welded along its edges over its entire length to the inside face of the lower



flange of the W10x45. A second 60 inch length of angle having threaded rods welded to the inside face at its apex, was fitted into the upper flange of the W10x45 and bolted. This two angle arrangement allowed adjustment of the double sided track that supported and guided the V-notched wheels of the load beam from above and below (see Figure 2.32).

The reaction block of the test frame was designed to resist the moments and shear imposed on it by the two hydraulic cylinders and the bearing of the ball-and-socket connection from the test specimen. Additional steel plates were placed in the block behind each hydraulic cylinder and the ball-and-socket connection to resist local crushing of the concrete and to provide positive bearing for the attached elements. A photograph of the reaction block with the tension rods and hollow core hydraulic cylinders in place is shown in Figure 2.33.

Both the reaction and guide blocks were spaced and leveled in the test configuration on the laboratory floor to accommodate a specimen 14 to 16 feet in length. A surveyor's level was used to align and level the two blocks, before being Hydrostoned to the laboratory floor. The Hydrostone ensured even bearing on the floor.

The two high strength threaded tension rods were each 2 inches in diameter and comprised of two lengths coupled together and extending a total of 20 feet. The rods each had a working load rating of 250 kips.

Load collars, indicated in Figure 2.28 and displayed in Figure 2.30, transferred the axial load to the ends of the specimen from the sliding load beam. A similar collar was used to transfer the load from the reaction block to the other end of the specimen. Each load collar was fabricated from a 9.625 inch diameter steel tube section that was 10 inches in length. The tube section was welded at one end to a 16 inch square mounting plate, which had a drilled hole pattern to match the ball-and-socket connection. Prior to placement of the load collar on a specimen, end platens were first inserted into each end of the specimen to provide uniform bearing pressure over only the steel portion of the

cross-section of the tubular. Then, a load collar was slipped over each end of the specimen and centered with the use of several set screws drilled into the collar. Hydrostone was then injected into the collars to provide a uniform bearing surface between the load collars and the end platens as well as the outer wall of the specimen. The specimen was then installed into the test frame by bolting the mounting plate of the load collar to the ball-and-socket connection. The mounting plate was aligned prior to bolting such that the center of the load collar coincided with the center of the spherical bearing to apply concentric axial loading of the specimen.

## **2.6. Instrumentation and Data Acquisition**

Each specimen was instrumented to monitor its response under loading. Figure 2.34 shows the instrumentation set-up employed for the non-repaired and internal grout repaired specimen tests. Axial shortening was measured over the gage length ( $L_g$ ) of the specimen, using two displacement transducers located at the south end and attached to targets at the north end. Table 2.8 lists the gage lengths over which axial shortening was measured for each of the test specimens. The two shortening transducers were averaged together to obtain the axial shortening at the centerline of the specimen. Electric inclinometers were mounted on each end of the specimen to record end rotation.

Vertical displacements in the plane of bending of the specimen were measured by five equally spaced transducers along the length of the specimen. The dent growth was monitored using two vertical transducers, one measuring the displacement of the bottom of the dented section while the other measuring the displacement of the saddle of the dent, as shown in Figure 2.34. These two readings were subtracted from each other to obtain the dent-depth growth. A displacement transducer was also placed at the dented section to monitor any horizontal movement of the specimen out of the plane of bending.

Strain gages were placed around the circumference of the tube at its quarter points along the span to monitor longitudinal and hoop strains. The longitudinal gages at each

end were also used to align a specimen during its installation into the test frame. Two strain gages were also placed on the top face of the specimen on either side of the dent to monitor longitudinal strain in the dent saddle.

The instrumentation plan for the grouted sleeve repaired specimen (Specimen C15) is shown schematically in Figure 2.35. Basically, the instrumentation plan was the same as that for the testing of the non-repaired and internal grout repaired specimens, with some additional strain gages placed on the sleeve and specimen to measure longitudinal and hoop stress. In addition, at each end of the sleeve four linear displacement transducers were equally spaced around the circumference of the sleeve and used as slip gages to measure any relative movement between the ends of the sleeve and the dented tubular (see Figure 2.36). Any growth in dent depth was monitored by placing a metal rod through a void in the grout annulus, where one end of the rod was in contact with the dent and the other attached to a displacement transducer mounted on the sleeve (see Figure 2.37). The void in the grout was created by casting a greased bolt in the grout, which passed through a threaded hole in the sleeve directly above the dent. This bolt was subsequently removed after the grout was cured.

A pair of calibrated load cells, located between the load beam and each nut of the tension rod, monitored the load applied to each tension rod. The separate readings were combined to provide the total applied axial load.

A specimen installed into the test frame, instrumented for response, and ready to test is shown photographed in Figure 2.29. Specimens were whitewashed prior to testing with a hydrated lime solution to display yield patterns.

All data from the instrumentation was collected using the DATACQ 3.1 computer-controlled data acquisition system software developed for this experimental test program [Mihalic, 1992]. The system utilized a 386 personal computer to run DATACQ 3.1, which is capable of continuously scanning a total of 64 channels with 12 bit



accuracy. This was accomplished by multiplexing a 16 channel National Instruments AT-MIO-16 A/D board with two 32 channel National Instruments Multiplexing boards. During a test, protection against a power failure was provided by the use of a back-up power supply capable of powering all instrumentation, the data acquisition system, and the hydraulic pump for ten minutes in the event of a power outage.

## **2.7. Test Procedure**

After the installation and instrumentation of a test specimen, the data acquisition was configured by execution of the data acquisition software and taking a zero scan of all channels. The transducers were checked against known displacements to verify system operation. Another zero scan was taken and written to disk. A shunt calibration of the strain gages was performed to confirm their operation. Channels and their associated increments in signal output readings were then selected to trigger the system to record the acquired data to disk. Display channels for real time display and printer output were also defined.

Prior to each test, the axial alignment of a specimen was verified by applying an initial load of 25% of the expected ultimate axial load  $P_{max}$ . Longitudinal axial strains were monitored during alignment to check for uniformity around the circumference of the cross-section at several locations. This verification ensured that no accidental eccentricity was introduced into the specimen during its installation into the test frame. The alignment also provided a force necessary to firmly seat all components of the test frame and ready the system for testing. Strain readings within 5% of each other were considered acceptable for alignment, else the specimen misalignment was corrected. After the alignment check was shown to be satisfactory, the specimen was unloaded and all instruments were zeroed in the data acquisition program.

A compressive axial load during testing was initially applied at an approximate rate of 1 ksi per minute under load control. The loading rate was controlled by limiting

the pressures developed by the pump and released to the hydraulic cylinders. Load control was attained in the ascending branch of the load-shortening curve by slowly increasing the pressure delivered to the cylinders through the use of the pressure relief valve.

Scan triggers were set within the data acquisition software to record to disk all instrumented channels at increments of approximately 2 kips of the total applied load or specimen axial shortening of approximately 0.03 inches. An axial shortening signal was fed into an XY recorder, together with the load cell signal, to provide a real-time graphic display of the load-shortening curve. During loading on the ascending branch of the specimen's axial load-deformation response, triggering was typically controlled by the load increments.

The applied loading was halted frequently to allow the load to stabilize and static readings to be scanned. The load stabilization in the ascending portion of the load-shortening curve was accomplished by locking in the current pressure of the system. The loading was continued until the ultimate capacity of the specimen was reached and the maximum static load was recorded. Frequent manual scans were taken near the peak load to ensure that the maximum load and all instrument readings were recorded. Beyond ultimate capacity, displacement control was introduced into the loading system by the tight metering of an in-line needle valve which controlled the flow of hydraulic fluid into the hollow-core cylinders. With the pressure decreasing, increased hydraulic fluid flow was allowed, subsequently increasing the cylinder stroke. The triggering for recording of the data by the acquisition software by axial shortening typically began to occur just prior to attaining the peak load, as a specimen's axial shortening became large.

The test was continued until a specimen's strength approached zero, or a total displacement of five times the displacement at peak load was reached. Typically the latter controlled. After the loading was discontinued, the data was saved to disk in binary form with the name extension \*.DAQ, and the program was exited. The file created by

DATAcq 3.1 was then post-processed by the program DATARED.EXE to create a group of individual channel files in ASCII format for subsequent data reduction and analysis.

## CHAPTER 3

### EXPERIMENTAL BEHAVIOR

This chapter discusses the observed behavior of the 9 damaged bracing specimens that were axially compressed to failure. The discussion related to each of the tests is described herein under sections pertaining to the 5 test series defined previously in Section 2.1. Observations and specimen response are presented, along with a summary of the experimental behavior for each test series. The behavior of each specimen is described by the axial load-shortening ( $P-\Delta$ ) response, the growth in dent-depth ( $d_d$ ), the lateral displacements of the specimen along its length ( $\delta_x$ ), and by the development of longitudinal strains in the dent-damaged region. These measured displacements and strains are also correlated to observed signs of yielding and local buckling that occurred during the course of testing. In the presentation of the experimental data, the applied axial load  $P$  has been normalized by the yield strength  $P_y$ , where  $P_y$  is based on the specimen dynamic measured yield stress reported in Chapter 2.

All references to the test specimens and dent-damage are made in relation to Figure 3.1, which defines the nomenclature describing the orientation, specific features, and response quantities of a typical test specimen. Each specimen was oriented in the test frame such that its longitudinal axis was oriented parallel to the laboratory floor and coincided with the north-south direction. The sliding load beam and the fixed reaction were located north and south, respectively. All specimens had their longitudinal weld seam facing the laboratory floor, thus defining the bottom surface of the tubular. In this position, the dent-damage being 180 degrees opposite of the weld seam defined the top surface of the tubular. The east and west surfaces of the specimen were located 90 degrees clockwise and counter-clockwise from the top surface, respectively, and corresponded with the east and west directions. The lateral displacements ( $\delta_x$ ) coincided



with downward deformation of the specimen toward the laboratory floor, as shown in Figure 3.1.

### **3.1. Behavior of Damaged, Non-repaired Specimens**

A total of four tests were conducted to assess the affect of dent-damage of a depth of 0.25D and 0.50D on member behavior, where D is the measured specimen diameter. The measured geometry for these specimens is listed in Tables 2.2, 2.3 and 2.4 for the initial and damaged states, respectively. Measured steel material properties for all specimens are given in Table 2.5. As noted in Table 2.4, the global out-of-straightness ( $\delta_p$ ) of these specimens ranged from 0.0052L (Specimen C10) to 0.0174L (Specimen A12), where L is the measured length of the specimen. The results from these tests were also used to evaluate state-of-the-art analytical methods for predicting the residual strength of dent-damaged members which is presented in Chapter 4.

#### **3.1.1. Test Series 1 - 0.25D Dent-Depth**

**Specimen A10** - Specimen A10 modeled a bracing member having a nominal D/t ratio of 34.5 subjected to concentric axial loading with dent depth  $d_d$  measuring 0.253D in depth. The measured out-of-straightness ( $\delta_p$ ) of the specimen in its damaged state was 0.0064L. A photograph of Specimen A10 prior to testing is shown in Figure 3.2.

The ascending portion of the normalized axial load-shortening response of Specimen A10 prior to achieving its peak load ( $P_u$ ) was linear and in close agreement with elastic theory, as shown in the normalized axial load-shortening relationship of Figure 3.3. Initial yielding of the specimen was first noticed at approximately 65% of  $P_u$ , and initiating at the crest of the dent and attenuating along the sides of the tubular to a distance of about 5 inches from the centerline of the dent. This yielding was a result of the compressive stress flow around the dent saddle, combined with the compressive

residual stresses introduced into the cross-section from the denting process. A slight linear growth in dent-depth was observed prior to reaching the ultimate capacity of the specimen, as indicated in Figure 3.4.

The lateral stiffness of the specimen began to decrease at about 60% of  $P_u$ , prior to achieving ultimate load, as indicated by the slope of the normalized axial-load midspan deflection response curve shown in Figure 3.5. At failure, this stiffness greatly decreased as the specimen laterally displaced at midspan to approximately  $0.0045L$ . At the peak load of 98 kips ( $P_u = 0.37 P_y$ ), the dent-depth rapidly increased by approximately  $0.015D$ .

The history of longitudinal strains around the circumference of the damaged section are shown in Figure 3.6. The bottom longitudinal gage in the dented cross-section developed a reversal in strain at approximately 60% of  $P_u$ , leading to tensile strain as the dent-depth grew and second-order effects increased due to growth in the lateral displacement ( $\delta$ ) at midspan. The strains measured by the south strain gage located inside the dent saddle, shown in Figure 3.7, approached the yield strain ( $1320 \mu\epsilon$ ) of the steel tubular as the specimen was loaded to  $P_u$ . At the axial load of  $P_u$ , the dent growth and ovalization of the cross-section that had occurred forced compressive stresses to flow directly to the stiffer east and west sides of the dented section, leading to a reduction in strain within the dent saddle.

The application of axial shortening after achieving  $P_u$  resulted in continued dent-growth and formation of a plastic hinge in the dent-damaged region due to the loss of cross-sectional depth, resulting in a capacity reduction and increasing second-order bending effects. Photographs showing the dented region and overall deflected shape of Specimen A10 after achieving  $P_u$  are shown in Figures 3.8 and 3.9. Measured lateral displacements of the specimen revealed a concentration of curvature in the dented region following the application of peak load, as shown in Figure 3.10. Extensive yielding of the steel around the circumference of the damaged cross-section continued as

plastification of the dent occurred. Yielding also spread along both sides of the tubular, away from the dented region to a distance of 22 inches from dent centerline of the tubular and 12 inches on either side of the dent centerline along the bottom surface. Dimples were observed to form at the ends of the dent saddle when gross ovalization of the section occurred after the plastic hinge developed (see Figure 3.11).

The peak load of 98 kips which developed in Specimen A10 corresponded to an axial load capacity that was 44% of that for a corresponding non-damaged member, whose capacity is estimated using the SSRC Column Strength Curve 1 [Galambos 1988].

**Specimen C10** - Specimen C10 modeled a bracing member having a nominal  $D/t$  ratio of 69 subjected to concentric axial loading. The measured dent-damage consisted of a dent-depth of  $0.250D$  and a maximum out-of-straightness of  $0.0052L$ . A photograph of Specimen C10 prior to testing is shown in Figure 3.12.

The axial load-shortening relationship shown in Figure 3.13 displayed a deviation from linearity at about 33% of the peak load  $P_u$ , as the second-order bending effects on the specimen increased due to growth in the midspan lateral deflection. Prior to achieving  $P_u$ , the lateral stiffness of the member, related to the ascending slope of the normalized axial load-midspan lateral deflection curve, began to decrease, as shown in Figure 3.14. At the peak load of 37 kips ( $P_u = 0.28 P_y$ ), the midspan lateral displacement of the member had grown to nearly  $0.003L$ . A photograph of Specimen C10 taken at peak load is shown in Figure 3.15, where lateral displacement of the specimen can be seen. The normalized lateral displacement profile along the length of the member is shown in Figure 3.16 at various stages of loading, and clearly indicates the extent of global bending prior to and after failure of the member occurred. The normalized axial load-dent growth relationship for Specimen C10 is shown in Figure 3.17. A photograph is given in Figure 3.18 which shows the dented region following the development of peak axial load. Similar to the previously tested specimens, a large growth in dent-depth

initiated in Specimen C10 near peak load, reducing the member's ability to resist the applied compressive load. Initial yielding at the ends of the dent fold were observed to simultaneously occur at the attainment of ultimate capacity of the member.

The longitudinal strain history developed around the circumference of the dented section and in the dent saddle for Specimen C10 are shown in Figures 3.19 and 3.20, respectively. Prior to reaching the peak load, the exterior top surface of the tube in the dent saddle developed compressive strain under the applied load, as shown in Figure 3.19. As the dent grew in depth, local bending of the wall of the tubular occurred that resulted in tensile strains in the dent saddle. As in the response of Specimen A10, a reversal from compression to tension longitudinal strain occurred at the bottom of the tubular in the dented region (see Figure 3.20).

Continued axial shortening resulted in extreme lateral deflections as indicated in Figure 3.16. As a result of this excessive deflection, large compressive strains developed as the stress flow necessary for equilibrium passed around the dent saddle along the east and west sides of the tubular. As the dent continued to grow inwards, a local outward dimple developed at both ends of the dent saddle, as shown in Figure 3.21. These dimples continued to grow outward until the test was discontinued, at which time the axial shortening had exceeded 10 times the shortening corresponding to ultimate load. A photograph of the lateral displacement of Specimen C10 at the end of the test is shown in Figure 3.22.

The peak load of 37 kips which developed for Specimen C10 corresponded to a capacity that was 28% of that for a corresponding non-damaged member, as estimated using SSRC Column Strength Curve 1.

### 3.1.2. Test Series 2 - 0.50D Dent-Depth

**Specimen A12** - Specimen A12 modeled a bracing member having a nominal  $D/t$  ratio of 34.5 subjected to concentric axial loading. The measured dent-damage consisted of a dent depth  $d_d$  of  $0.491D$  and maximum out-of-straightness ( $\delta_p$ ) of  $0.0174L$ . A photograph of Specimen A12 before testing is shown in Figure 3.23.

The normalized axial load-shortening response of Specimen A12 is presented in Figure 3.24. The response from the onset of the test from shows a deviation from the predicted elastic axial stiffness of a similar, yet non-damaged tubular. Since the inflicted damage significantly reduced the cross-sectional properties of the tubular in the dented region, the member began to loose axial stiffness as soon as the axial load was applied. The midspan lateral deflection increased at a faster rate than that seen in the previously tested specimens with nominal dent-depths of  $0.25D$ , as shown in Figure 3.25. The normalized axial load-dent depth growth relationship is shown in Figure 3.26. Just prior to attaining peak load, the dent-depth had grown by  $0.02D$ , representing an increase of 4% from its original depth.

The history of longitudinal strains around the circumference of the dented cross-section is shown in Figure 3.27. Unlike the previous specimens having smaller initial dent-depths, tensile strains are shown to develop at the bottom of the damaged cross-section of Specimen A12 from the onset of the test. Initial yielding of the cross-section was observed along the bottom surface of the dented section as the specimen approached its peak load  $P_u$  of 39 kips ( $P_u = 0.16 P_y$ ). Figure 3.27 shows the strain at the bottom of the cross-section to approach the yield strain near peak load and is consistent with the above observation. The measured strains in the dent saddle, located along the top of the dented segment, are shown in Figure 3.28 to remain elastic and are relatively low compared to Specimen A10, which had the same  $D/t$  ratio but a smaller dent depth of  $d_d$  of  $0.25D$ . The lateral displaced profile of Specimen A12 at selected levels of applied

axial load is given in Figure 3.29, and shows the existence of large lateral defections prior to peak load. A photograph of Specimen A12 at peak load is shown in Figure 3.30, where the pronounced lateral deflection at midspan is visible.

Axial shortening of the specimen beyond attainment of the peak load resulted in a gradual decrease in capacity and continued yielding around the dented region, especially along the bottom surface of the tubular in the dented region. The yielding spread symmetrically to a distance of nearly 22 inches to each side of the dent. Lateral displacements of the specimen also continued to grow as the specimen folded about the plastic hinge that had formed at the midspan dent. Figure 3.31 shows a close up of the dent-damaged region following the development of peak axial load. A plastification of the dented section occurred as the lateral displacement increased. The overall lateral deflection of the specimen at the conclusion of the test is shown in Figure 3.22.

The peak load of 39 kips which developed in Specimen A12 was 18% of that for a corresponding non-damaged member, estimated using the SSRC Column Strength Curve 1.

**Specimen C12** - Specimen C12 modeled a bracing member having a nominal  $D/t$  ratio of 69 subjected to concentric axial loading. Following denting, the measured dent-damage consisted of a dent-depth of  $0.495D$  and a maximum out-of-straightness ( $\delta_p$ ) of  $0.0152L$ . A photograph of Specimen C12 taken prior to testing is given in Figure 3.33.

The normalized axial load-shortening response of Specimen C12 is presented in Figure 3.34, where from the onset of loading it is shown to deviate from the predicted elastic axial stiffness. The dent-depth also grew from the onset of the application of axial load, as shown in Figure 3.35. As indicated in the normalized axial load-midspan lateral displacement relationship given in Figure 3.36, the member possessed very little lateral stiffness and subsequently the deflection at midspan had increased to nearly  $0.0065L$  prior

to developing its peak load. Figure 3.37 shows a photograph of the dented region of the specimen when peak load was applied, where the overall lateral deflection of the member can be noted when a comparison of the bottom surface of the specimen is made to the horizontal tension rod.

At the ultimate capacity of 14 kips ( $P_u = 0.10 P_y$ ), yielding of the specimen occurred at the ends of the dent fold, indicating high compressive strains passing around the dent saddle. The longitudinal strain history around the circumference of the dented cross-section is shown in Figure 3.38 and confirms the increase in compressive strains on the east and west sides of the damaged tubular at ultimate load. Strains in the dent saddle never developed to the level of yield and elastically decrease after failure of the specimen, as shown in Figure 3.39.

Continued axial shortening of the specimen resulted in a gradual decrease in capacity and continued yielding in the dented region. Lateral displacements of the specimen also continued to grow as the specimen folded about the plastic hinge that had formed at the dented cross-section at midspan. Figure 3.40 shows the lateral deflection profile of the specimen at various levels of applied axial load and indicates concentrations of curvature in the heavily plastified dent-damaged region. A photograph of the dented region near the end of the test is shown in Figure 3.41. No yield lines or flaking of the whitewash occurred during testing since the specimen was painted after fabrication.

The peak load of 14 kips which developed for Specimen C12 corresponded to a capacity that was approximately 11% of that for a corresponding non-damaged member estimated using the SSRC Column Strength Curve 1.

### **3.1.3. Summary of Behavior for Damaged, Non-repaired Specimens**

All four non-repaired specimens experienced a significant reduction in axial capacity due to the midspan dent-damage, with a greater reduction occurring in the members with the deeper dent-damage. Each of the specimens tested failed shortly after yielding occurred in the dent-damaged region, where the axial load resistance deteriorated with continued axial shortening. For the two specimens with dent-damage having a nominal depth of 0.25D (Specimens A10 and C10), the dent consistently was shown to rapidly grow inwards as the cross-section ovalized upon attaining peak load, reducing the sectional capacity of the dented region. For the two specimens with the deeper dent-damage of nominal depth of 0.50D (Specimens A12 and C12) the dent also grew during testing. The significant reduction in cross-sectional properties in the dented region and greater damaged out-of-straightness ( $\delta_p$ ) of the specimen led to a significant loss of member strength, as second-order bending effects occurred under the application of axial load.

Yielding was observed to initiate in the dent or at the ends of the dent fold near peak load. Increased axial shortening of the specimen resulted in an attenuation of this yielding along the sides of the tubular, away from the dent as well as through the thickness of the dented cross-section. Eventually, second-order bending effects became prominent, leading to further yielding in the dent-damaged region and resulting in the formation of a plastic hinge at midspan where the member was dented.

### **3.2. Behavior of Damaged, Internal Grout Repaired Specimens**

Five tests were conducted to assess the ability of grout repair to restore member strength, where the tubular had midspan dent-damage of nominal depth from 0.25D and 0.50D. Four of the tests involved internal grout repair. The measured damaged out-of-straightness ( $\delta_p$ ) of these repaired specimens ranged from 0.0051L (Specimen C11) to



0.0211L (Specimen A13). The internal grout repair extended along the full length of the specimen and was applied after the infliction of the dent, except at both ends of each repaired specimen where a grout void of 4 inch length was created in order to directly apply axial load to the steel cross-section of the specimen. Axially loading the steel directly simulated prototype conditions where a diagonal brace is axially loaded by force transfer from the steel chord member of the platform jacket to the steel section of the brace.

The remaining repaired specimen (Specimen C15) consisted of a grouted sleeve repair. As noted in Chapter 2, the sleeve was fabricated from a steel tubular of  $D/t = 68$ , where the outside diameter  $D$  was 12.75 inches. The length of the sleeve was 71 inches (equivalent to 8.2 diameters of the dented specimen), with a 1.5 inch extension beyond the internal ring stiffener at each end of the sleeve. The measured dent depth and midspan out-of-straightness after denting was  $0.499D$  and  $0.015L$ , respectively.

Initial and damaged geometry for all repaired specimens are included in Tables 2.2, 2.3, and 2.4. Steel material properties are summarized in Table 2.5. The grout compressive strength of the repair was determined for each specimen on the day of test and reported in Table 2.6.

Behavior of the repaired specimens is evaluated in the same manner as that for the non-repaired tests, namely the axial load-shortening response, growth in dent-depth, lateral displacement response, and longitudinal strain history in the damaged region are discussed. The yield capacity  $P_y$  of only the steel section is used to normalize the results.

### 3.2.1. Test Series 3 - 0.25D Dent-Depth

**Specimen A11** - Specimen A11 modeled an internal grout repaired bracing member having a nominal  $D/t$  ratio of 34.5 and subjected to concentric axial load. Inflicted dent-

damage was  $0.251D$  in depth, while the maximum out-of-straightness ( $\delta_p$ ) measured  $0.0059L$ . The average grout strength on the day of testing was 5970 psi. A photograph of Specimen A11 prior testing is shown in Figure 3.42.

The normalized axial load-shortening response of Specimen A11 is shown in Figure 3.43. At 8% of the axial load capacity ( $P_u$ ) of the specimen, which corresponds to  $P = 0.05 P_y$ , the response of the specimen began to deviate from the transformed elastic axial stiffness ( $A_{tr} \cdot E_s / P_y$ ) that was computed based on transformed sections, where  $A_{tr}$  and  $E_s$  are the transformed cross-sectional area and Youngs modulus, respectively, of the steel tubular. The transformed elastic axial stiffness assumes full-composite action between the steel tube and the internal grout. At this point of loading, initial yield lines in the tubular were observed to have formed on either side of the dent centerline and cracking sounds were heard within the internal grout. These observations, along with the measured deviation of the axial load-shortening response of the specimen from the predicted elastic stiffness, indicated that the composite action between the steel and grout was deteriorating. At  $P = 0.29 P_y$ , symmetrical yield lines were noted to have developed on both sides of the tubular, centered around the dented region and spreading longitudinally nearly 17 inches to each side of the dent. Dent growth at this stage was minimal as shown in Figure 3.44 and remained so throughout the test. Midspan lateral deflection of the specimen continued to grow as the load was increased (see Figure 3.45). At a lateral deflection ( $\delta$ ) at midspan of approximately  $0.0035L$ , corresponding to an axial load of  $P = 0.47 P_y$ , the yielding of the tubular had spread longitudinally along the sides of the dented section as well as on the top surface of the tubular to a distance of approximately 20 inches from the dent centerline.

The longitudinal strain history measured by the strain gages around the circumference of the dented cross-section is shown in Figure 3.46. At the load of  $P = 0.5P_y$ , the longitudinal strains on the east and west faces of the dented cross-section were at about the yield strain of  $1220 \mu\epsilon$ , indicating that yielding was taking place on the sides

of the dented cross-section. Yielding in the dent saddle was also occurring as indicated by the south strain gage readings shown in Figure 3.47.

A peak load of 158 kips ( $P_u = 0.62 P_y$ ) was attained for Specimen A11, at which the longitudinal strain gages on the bottom surface of the tubular indicated tensile strains were equivalent to the yield strain (see Figure 3.46). The grout was preventing the growth of the dent into the cross-section of the member. Without dent growth, the stabilized dent saddle was able to develop large compressive strains, as shown in Figure 3.46. Preventing the loss of cross-sectional properties by inhibiting dent-growth also resulted in the specimen maintaining a larger stiffness to resist second-order lateral deflections, where a  $\delta$  of nearly  $0.006L$  developed under the maximum axial applied load. A photograph of Specimen A11 showing the lateral deflection at maximum applied load is given in Figure 3.48.

Further shortening of the specimen beyond the peak load resulted in the development of curvature along the length of the specimen, as shown in Figures 3.49 and 3.50. Heavy yielding accompanied the curvature at the dented cross-section at midspan. This yielding attenuated longitudinally away from the dent along the top and side surfaces of the tubular to a distance of 22 inches from the dent centerline. Smaller yield lines on the sides of the tube began to form a dense cross-hatch pattern along the entire length of the dented section. Yielding on the bottom surface was confined to a 20 inch region centered about the dented region. With continued imposed axial displacement beyond that corresponding to  $P_u$ , a local outward buckle formed in the dent saddle at an axial shortening of  $\Delta = 0.0055L$ , corresponding to an axial load of  $0.55P_y$ . This local buckle developed on the top surface of the dented section having an approximate wave length of approximately 4 inches. Figures 3.51 and 3.52 show photographs of the dented region of Specimen A11 near the end of the test, where specimen yielding and local outward buckling can be seen.

The peak load of 158 kips which developed in Specimen A11 corresponded to a capacity that was 71% of that for a corresponding non-damaged tubular member, estimated using the SSRC Column Strength Curve 1. By comparing this result with that of Specimen A10, indicates that the internal grout repair was successful at increasing the axial capacity of the member above that of a corresponding member having not been repaired.

**Specimen C11** - Specimen C11 modeled an internal grout repaired bracing member having a nominal  $D/t$  ratio of 69 and subjected to concentric axial load. Inflicted dent-damage was  $0.255D$  in depth, while maximum out-of-straightness ( $\delta_p$ ) measured  $0.0051L$ . The average grout strength on the day of testing was 5900 psi. A photograph of Specimen C11 prior to testing is shown in Figure 3.53.

The normalized axial load-shortening response of Specimen C11 is given in Figure 3.54, where it is shown to deviate from the theoretical transformed elastic axial stiffness at approximately 0.37% of the ultimate load. The axial and lateral stiffness of Specimen C11 both began to deteriorate as the axial load increased, however the dent-depth growth was completely restrained up to the attainment of ultimate load as shown in Figure 3.55. Lateral displacements of the member at midspan continued to increase as the lateral stiffness decreased under the applied axial load, as shown in Figure 3.56. At  $P = 0.70 P_y$  the first audible crack was heard and a corresponding change in the slope in the axial load-shortening response occurred (see Figure 3.54), which indicated that the composite action between the internal grout and the steel sleeve was beginning to degrade.

Upon reaching the ultimate load of 104 kips ( $P_u = 0.82 P_y$ ), the midspan deflection of the specimen was nearly  $0.004L$ . Figure 3.57 shows the history of measured longitudinal strains from the strain gages placed around the circumference of the dented section. The development of tensile strains on the bottom surface of the tubular and high

compression strains beyond yield on the east and west sides of the dented section at maximum applied load, which can be seen in Figure 3.57, indicate that large second-order bending stresses were occurring in the cross-section. Failure of the member was extremely ductile as load was gradually shed with increased axially applied shortening. The growth in dent-depth slowly increased after peak load, but remained restricted from growing by the internal grout at rates previously observed of the non-repaired specimens.

As the axial shortening was applied beyond the ultimate load, longitudinal strains within the dent saddle continued to develop large compressive strains, as shown in Figure 3.58. This data indicated that compressive strains continued to pass through the saddle of the dent-damaged region. Cracking in the grout continued to occur, resulting in increases in both the axial shortening and the lateral deflection of the member, with a corresponding decline in axial load capacity. Figure 3.59 shows the lateral displacement profile of the specimen, where beyond ultimate load a greater concentration of curvature is shown to occur in the dent at midspan, providing evidence that plastification of the dented section was occurring. A photograph showing the overall deflected shape of Specimen C11 at  $0.57P_u$  following failure is given in Figure 3.60. The formation of a local buckle occurred in the dent saddle at an axial shortening of  $\Delta = 0.0089L$ . Figure 3.61 shows a photograph of the local buckle near the end of testing. The half wavelength of this local buckle was observed to be approximately 3 inches in length. A photograph showing the overall deflected shape of the specimen at the end of the test is given in Figure 3.62.

The maximum load of 104 kips developed by Specimen C11 was approximately 88% the capacity of a corresponding non-damaged steel tubular based on SSRC's Column Curve 1. This resistance was however over 2.8 times that of corresponding unrepaired Specimen C10, indicating that the internal grout repair provided a substantial increase in strength of a damaged member.

### 3.2.2 Test Series 4 - 0.50D Dent-Depth, Internal Grout Repair

**Specimen A13** - Specimen A13 resembled an internal grout repaired bracing member having a nominal  $D/t$  ratio of 34.5 and subjected to concentric axial load. Inflicted dent-damage was 0.50D in depth, while the maximum out-of-straightness ( $\delta_p$ ) measured 0.0211L. This initial out-of-straightness of the specimen is quite pronounced as seen in Figure 3.63, where Specimen A13 is photographed prior to the application of axial load. The average grout strength on the day of testing was 7690 psi.

Figure 3.64 shows the axial load-shortening response of Specimen A13, where the initial ascending portion of the response curve is less than the theoretical transformed axial stiffness for an non-damaged member with similar geometry. This reduction in stiffness is attributed to the pronounced out-of-straightness  $\delta_p$  that lead to significant shortening due to lateral displacement and geometric effects. The lateral stiffness of Specimen A13, shown in Figure 3.65, is initially smaller relative to the other repaired specimens of less depth. Figure 3.65 also shows the lateral stiffness to have rapidly deteriorated from the start of the test. This deterioration was a result of the severe deformation of the dented cross-section, resulting in a significant out-of-straightness and consequently a greater eccentricity between the axis of loading and the centroid of the dented section causing bending. The eccentricity at the dent, the initial out-of-straightness of the specimen, and the lateral deflection all combined to cause an increase in the amount of bending stresses developed within the section under the applied axial load. The longitudinal strain history around the circumference of the damaged section is shown in Figure 3.66, and indicates that tensile strains developed on the bottom surface of the tubular from the onset of testing due to bending stresses generated from second-order effects. Cracking of the internal grout was audible prior to failure when the lateral displacement at midspan exceeded 0.002L.

At the maximum load of 50 kips ( $P_u = 0.21 P_y$ ), the lateral deflection of the member at midspan was approximately equal to  $0.005L$ . Figure 3.67 shows a photograph of the specimen at ultimate load, where the lateral deflection of the specimen can be seen. Growth in dent-depth was insignificant, being arrested by the grout as shown in Figure 3.68. At peak load, the compressive strains developed in the dent saddle were approximately equal to the yield strain, as shown in Figure 3.69, indicating that plastification of the section was beginning to take place. The lateral displacement profile, shown in Figure 3.70, indicates that a concentration of curvature in the dented region had developed at peak load due to the plastification of the dented cross-section. Flaking of the applied white wash was not observed in Specimen A13, due in part to the lack of mill scale on the outer surface of the tubular. With continued axial shortening beyond maximum axial load the capacity of Specimen A13 gradually deteriorated, as shown in the load-displacement relationships (Figures 3.64 and 3.65). Photographs of the dented region and overall view of Specimen A13 at the end of the test are shown in Figures 3.71 and 3.72.

The maximum load of 50 kips developed by Specimen A13 was approximately 23% of the capacity of a corresponding non-damaged tubular member based on SSRC's Column Curve 1. This indicated that the repair was marginally successful at restoring the axial capacity of a dent-damaged specimen with dent depth  $0.5D$ . However, the resistance of Specimen A13 was 28% greater than that of corresponding non-repaired Specimen A12.

**Specimen C13** - Specimen C13 modeled an internal grout repaired bracing member having a nominal  $D/t$  ratio of 69. Inflicted dent-damage was  $0.498D$  in depth, while maximum out-of-straightness ( $\delta_p$ ) measured  $0.0166L$ . The average grout strength on the day of testing was 7550 psi. A photograph of Specimen C13 prior to testing is shown in Figure 3.73, where the initial out-of-straightness  $\delta_p$  is evident.

From the onset of loading, the normalized axial load-shortening curve for Specimen C13 deviated from a linear response, as shown in Figure 3.74. Upon achieving an axial load of  $0.17P_y$  the first audible cracking sounds from the grout occurred. Continued loading increased the frequency of cracking as the lateral stiffness of the member deteriorated, resulting in larger lateral deflection, as shown in Figure 3.75. At an axial load of  $P = 0.21 P_y$  the midspan lateral displacement was approximately  $0.004L$ . Second-order effects caused the longitudinal strains at the bottom the tube of the dented cross-section to develop tensile strains from the onset of testing (see Figure 3.76). Immediately prior to the application of the maximum axial load  $P_u$  cracking of the grout was accompanied by a sudden increase in both the axial shortening and lateral deflection.

At the ultimate load of 40 kips, corresponding to  $P_u = 0.29 P_y$ , the midspan lateral deflection of the specimen was about  $0.01L$ . Figure 3.77 shows a photograph of the specimen when the peak load was reached, where the lateral bending is quite prominent. As in the other internal grouted specimens, the dent growth was minimal as shown in Figure 3.78. Yielding at the bottom of the dented cross-section was observed at ultimate load and consistent with recorded longitudinal strain shown in Figure 3.76. However, the strain on the top of the dented cross-section remained elastic, with a tensile strain reversal occurring before reaching ultimate load (see Figure 3.79).

Continued axial shortening of the specimen resulted in extreme lateral deflections, as shown in the lateral displacement profile in Figure 3.80 and the photograph in Figure 3.81 that was taken at the end of the test. Load shedding was gradual and ductile behavior was observed. Cracking of the internal grout continued to be heard with increasing frequency as the midspan deflection reached  $0.015L$ . A photograph of the dented region of Specimen C13 at the end of the test is given in Figure 3.82. No yield lines in the whitewash are visible because of the lack of specimen mill scale.



The maximum load of 40 kips developed by Specimen C13 was approximately 30% of the capacity of a corresponding non-damaged tubular based on SSRC's Column Curve 1. The repair resulted in an resistance that was over 2.8 times that of the corresponding non-repaired specimen (Specimen C12). This indicated that the repair was successful in partially restoring the axial capacity of the dent-damaged member.

### **3.2.3 Test Series 5 - 0.5D Dent-Depth, Grouted Sleeve Repair**

**Specimen C15** - Specimen C15 was a grouted sleeve repaired member having a nominal D/t ratio of 69. The inflicted dent damage consisted of a dent depth and out-of-straightness at midspan of 0.499D and 0.015L. The sleeve was placed over the specimen, covering the dented segment, where the out-of-straightness at the end of the sleeve in the specimen was 0.011L. The out-of-straightness of the damaged member before testing is evident in the photograph given in Figure 3.83. The average grout strength on the day of the test was 3770 psi.

The normalized axial load-shortening curve for Specimen C15 is shown in Figure 3.84. The member responded initially linear, with an initial axial stiffness slightly greater than that associated with a bare steel tube. At an axial load of approximately 50% of the peak load  $P_u$ , corresponding to  $0.29P_y$ , grout cracking in the annulus along the sleeve was audible. As the load was increased the axial stiffness began to soften, as seen in Figure 3.84 where a decrease in stiffness is evident. An increase in the lateral deflection at midspan was also recorded, as shown in the axial load-midspan deflection relationship presented in Figure 3.85. As the axial load was increased to  $0.75P_u$  (corresponding to  $0.43P_y$ ), the specimen along the sleeve developed a lateral displacement of  $0.002L$ , where minimal curvature occurred in the sleeve while a more noticeable amount developed in the specimen outside the sleeve. This is apparent in the plot of the measured lateral displacement profile presented in Figure 3.86, as well as in a photograph of the specimen

shown in Figure 3.87, where the latter was taken just prior to the application of the ultimate load.

At the maximum applied axial load of 72 kips, corresponding to  $0.57P_y$ , the strain gages indicated that yielding occurred on the top of the cross-section along a segment of the specimen outside the sleeve (see Figures 3.88 and 3.89). This yielding was associated with the greater compressive stress that developed at the top of the specimen's cross-section due to the combined effects of axial load and second order bending moment from the lateral displacement of  $0.004L$  in the specimen at the south end of the sleeve. Longitudinal strains around the circumference of the specimen at a longitudinal distance of about 15 inches from outside the sleeve showed tensile strain to develop on the bottom of the specimen's cross-section from the onset of testing (see Figures 3.87 and 3.88).

At the peak applied axial load a local outward buckle developed in the specimen at the south edge of the sleeve where the prior yielding had occurred the top of the specimen resulted, and is shown photographed in Figure 3.90. This led to a deterioration of the axial load capacity with further imposed axial deformation. Continued imposed deformations caused the local buckle, which resembled an elephant's buckle, to attenuate around the circumference of the cross-section. In addition, the lateral displacements became greater, where a concentration of curvature developed at the buckled section, which was located at a distance of approximately  $0.30L$  from the south end of the specimen. This concentration of curvature is evident in the measured lateral displacement profile of the specimen (see Figure 3.86) as well as the photograph of the specimen shown in Figure 3.91. No significant slip was measured between the sleeve and tubular, however, the local buckling caused a shortening of the gage length of the slip gages. This phenomena is seen in Figure 3.92. Upon achieving an axial shortening of 4 inches, corresponding to  $0.022L$ , the test was terminated.

The longitudinal strains around the circumference of the steel tube and sleeve at the dented cross-section were found to remain relatively small throughout the test (less than about 100  $\mu\epsilon$ ), as shown in Figure 3.93 and 3.94. This was also found at the other strain measurement locations which were beneath, as well as on the sleeve (e.g., at 0.42L and 0.58L from the south end of the specimen), as shown in Figure 3.95 to 3.98. The inner radial pressure exerted on the sleeve by the radial expansion of the specimen caused by the Poisson effect and restraint of the sleeve to inhibit dent growth of the specimen led to tensile transverse strains on the sleeve (see Figures 3.99 through 3.101).

It was determined from the measured transverse and longitudinal strains of the sleeve that the maximum bond stress which developed between the grout and the sleeve was approximately 25 to 50 psi (see Figures 3.102 and 3.103). This bond stress represents the stress developing over 15 inches to the South (Figure 3.102) and North (Figure 3.103) of the dent. Based on these results, and assuming a uniform bond stress over the length of the sleeve, the axial force resisted by the sleeve was 36 kips (25 psi bond stress) to 72 kips (50 psi bond stress).

Through radial constraint, the sleeve was found to completely restrain the dent from growing inwards, for no growth in dent depth was measured as shown in Figure 3.104. The reinforcement by the sleeve thereby forced most of the inelastic deformation and failure to occur in the steel tubular outside the sleeve.

The maximum load of 72 kips which developed in Specimen C15 was 80% greater than that of corresponding internally grout repaired Specimen C13, and was approximately 54% of the capacity of a corresponding non-damaged member based on the SSRC Column Strength Curve 1. The strength of Specimen C15 was over five times the strength of corresponding non-repaired Specimen C12. The above results indicated that although the capacity of Specimen C15 was less than that of a corresponding non-damaged tubular, the use of a grouted sleeve provided a significant increase in strength

relative to the strength of a corresponding non-repaired member with dent depth of  $0.5D$ . The behavior of Specimen C15 indicated that the out-of-straightness  $\delta_p$  of the damaged member at the termination point of the sleeve must be considered in the design length of the sleeve, for the cross-section of the tubular at this location is subjected to the maximum stress due to the combined effects of axial load and second order bending as is the likely location where failure will occur.

#### **3.2.4. Dissection of Grout Repaired Specimens**

Following the completion of testing, the internal grout repaired specimens were cut open in the dent zone in order to expose the grout. This was accomplished by using a flame torch to burn through the wall thickness of the steel tube. The exposed grout of the specimens (Specimens A11, C11, A13 and C13) are shown in Figures 3.105 through 3.108. During the dissection the steel wall of each tube was found to be rather easily removed, indicating a weak radial bond existed between the steel tube and grout. In all cases, the exposed grout showed an area of intact grout that was directly beneath the dent saddle where the steel tube had remained in contact with the grout. Adjacent to this area, loose, cracked grout was found where the steel tube had locally buckled outwards.

The cutting open of the grouted sleeve specimen (Specimen C15) revealed no grout cracking or crushing.

#### **3.2.5 Summary of Behavior for Damaged, Grout Repaired Specimens**

Internal grout repair significantly improved the load carrying capacity of all of the specimens tested through the prevention of further dent growth. The grout supported the dented section, thus eliminating this mechanism of failure. The specimens developed their peak load as the steel wall yielded in the dent saddle and along the compression surface along the top of the tubular, followed by yielding of the tubular on the bottom

face of the dented cross-section. Specimens with a nominal  $d_d = 0.25D$  failed before their respective non-damaged capacities were achieved due to a yielding of the dented section caused by second-order bending stresses. Severe reductions in the cross-sectional properties of the dented tubulars with  $d_d = 0.50D$  reduced the lateral stiffness of the specimen. This, combined with the greater out-of-straightness prior to testing, resulted in large lateral displacements and bending stresses to develop in the dented region under the applied axial loading. Post-ultimate behavior of all specimens was characterized by gradual load shedding and reasonably ductile response at large axial shortening.

The performance of the grouted sleeve repaired specimen indicated that the sleeve inhibits the dent from growing, thereby increasing the capacity of the damaged member. While the strains in the repaired segment of the specimen remained small, large strains outside the sleeve developed in the specimen. The ability of the sleeve repair to increase the capacity of a dent-damaged member is limited by the out-of-straightness in the tubular adjacent to the termination point of the sleeve. At this location, the member develops its greatest stress under combined axial load and second order bending effects, which causes the cross section to eventually develop a local buckle.

## CHAPTER 4

### ANALYSIS OF EXPERIMENTAL RESULTS

#### 4.1. General

In Chapter 3, observations of the experimental behavior for each of the 9 specimens tested for the experimental program were discussed in detail. In Chapter 4, a detailed evaluation of the experimental behavior will be presented by analyzing the measured data from each specimen. The axial load capacity  $P_{exp}$  for each specimen is given in Table 4.1, where  $P_{exp}$  has also been normalized by the yield capacity  $P_y$  of the steel tube, where  $P_y$  is based on the measured dynamic yield stress and material properties reported in Chapter 2. To evaluate the amount of deterioration in a member's axial capacity attributed to dent-damage, in this chapter the residual strengths  $P_{nr}$  of the non-repaired members for a range of dent-depths are compared to their original design capacity  $P_o$ . Member capacities are also compared with capacities of corresponding non-repaired and repaired test specimens in order to assess the effectiveness of the internal grout repair at restoring the axial capacity of dented bracing members with varying degrees of damage. Cross-section strength based on moment-axial load interaction analyses are presented and used to evaluate the failure of the non-repaired and internal grout repaired specimens, respectively. Finally, comparisons between several analytical methods and the experimental results are made in order to assess the accuracy of these methods to predict the non-repaired and repaired member response of dent-damaged tubular bracing members.

For the analytical models, the measured static yield strength of the specimens, grout strength, and geometry were used. The comparison of predicted and experimental capacities appearing in the various tables of Chapter 4 were directly made using the static predicted capacity and peak axial experimental load  $P_{exp}$ . Plots showing a comparison of analytical and experimental results were made by normalizing both results by specimen

capacity based on dynamic yield stress of the tubular in order to be consistent with experimental results plotted in Chapter 3 as well as in comparison with normalized data reported by other studies.

## 4.2. Moment-Axial Load Interaction

The moment-axial load surface for dent-damaged bracing members was shown in Ricles et al. [1992, 1997] to provide reasonable agreement with the response of the measured force path of experimentally tested specimens, in terms of their capacity. For the force path, the moment  $M$  of the dented cross-section at midspan of a specimen was determined at each step of axial loading history using the measured axial load  $P$ , lateral midspan displacement  $\Delta$ , and initial out-of-straightness  $\delta_p$  following denting in the following expression:

$$M = P(\delta_p + \Delta) \quad (4.1)$$

The moment  $M$  in Equation (4.1) is referenced with respect to the centroid of the undented cross-section. Equation (4.1) was used to derive the experimental force path for both the damaged and internal grout repaired specimens, which are discussed below.

### 4.2.1. Non-repaired Specimens

Plasticity theory was utilized by Ricles et al. [1997] to develop the moment-axial load capacity relationship for a steel tubular cross-section with dent-damage. The resulting expression for moment capacity  $M_u$  as a function of axial load and dented cross-section properties can be shown [Ricles et al. 1997, Taby 1986] to be

$$\frac{M_u}{M_p} - \frac{\pi F_{pd}}{2 P_y} \left( \frac{2 \eta}{D} + \cos(\alpha^*) \right) - \cos \left[ \frac{\pi}{2} \left( \frac{P - F_{pd}}{P_y} \right) + \frac{\alpha^*}{2} \right] + \frac{1}{2} \sin(\alpha^*) = 0 \quad (4.2)$$

where  $P_y$  is the yield load and  $M_p$  the plastic moment capacity for a thin-walled section, as given by

$$P_y = \sigma_y \Pi \bar{D} t \quad (4.3a)$$

$$M_p = \sigma_y \bar{D}^2 t \quad (4.3b)$$

The quantities  $\bar{D}$  and  $t$  are the specimen diameter with respect to the wall mid-thickness, and  $t$  the wall thickness.

The angle  $\alpha^*$  is that which subtends one-half around the circumference of the dent saddle. This angle is related to the dent depth by the following expression

$$\alpha^* = \cos^{-1} \left( 1 - 2 \frac{d_d}{\bar{D}} \right) \quad (4.4)$$

where  $d_d$  is the depth of the dent.

The axial resistance  $F_{pd}$  is based on a plastification of the dent saddle of the cross-section, where

$$F_{pd} = 80 \alpha^* t \sigma_y \left( \sqrt{4 \eta^2 + t^2} - 2 \eta \right) \quad (4.5)$$

In order to account for restraint effects on the dent saddle by the undamaged part of the cross-section, Equation (4.5) includes the multiplication by the empirical correction factor  $C_{dp} = 80t/\bar{D}$  based on recommendations by Taby [1986] for members with  $\bar{D}/t$  less than 80. The resistance  $F_{pd}$  acts at the centroid of the area of the original cross-section at the distance  $\eta$  above the dent saddle of the dented cross-section, where

$$\eta = \frac{\bar{D}}{2} \left( \frac{\sin(\alpha^*)}{\alpha^*} - \cos(\alpha^*) \right) \quad (4.6)$$

Equation (4.2) is only valid for members with the dent located on the compressive side of the bending moment and with the axial load in compression. Furthermore, it assumes that the initial dent-depth does not increase under applied load.

Figures 4.1 through 4.4 show the experimental force paths of the non-repaired specimens compared with their moment-axial load interactions surfaces calculated using Equation (4.2) in conjunction with measured specimen dimensions and material



properties. Each of the specimens reach their maximum axial load in the vicinity of the interaction surface. In the post-ultimate range, the force path of each specimen has a tendency to initially follow the interaction surface until elastic unloading takes place (i.e., where both the axial load  $P$  and moment  $M$  decrease). The interaction curve appears to provide better agreement with the residual strength of dent-damaged members having  $D/t = 34.5$  (i.e., Specimens A10 and A12). The capacity of Specimens C10 and C12, which have  $D/t = 69$ , is slightly over-estimated by Equation (4.2). It appears that the accuracy of Equation (4.2) could be improved by further calibration of  $F_{pd}$  for sections with higher  $D/t$  ratios.

#### **4.2.2. Internal Grout Repaired Specimens**

The capacity of the internal grout repaired specimens was also compared to their theoretical moment-axial load interaction surface. For each specimen a fiber analysis technique, similar to that used by Ricles et al. [1997], was employed to develop the interaction surface using measured material properties. An upper bound on the strength was established by assuming full composite action between the steel tubular and the grout. This analysis involved describing the dented cross-section and grout by several individual fibers, each with its own stress-strain relationship. The grout stress-strain curve is similar to that shown in Figure 4.5. Measured material properties and specimen dimensions were used in the analysis, where the grout compressive strength was set at  $0.8f'_g$  to account for the scale effects between the grout cube material tests and the in situ grout strength [Loh, 1991]. No strength enhancement due to confinement was considered, since the surrounding steel tube radially expands under axial load due to the Poisson effect. The strain  $\epsilon_o$  corresponding to peak stress  $f'_g$  was set equal to 0.004, and based on typical values for grout reported in the literature [Lamport 1988]. The grout was assumed to fail (i.e., develop a loss of strength) at a strain of  $\epsilon_{br} = 0.005$ . The stress-strain curve for the steel fibers was assumed to be elastic-perfectly plastic.

Assuming plane-sections remain plane, the moment-curvature ( $M-\Phi$ ) relationships of the dented, repaired section were determined for prescribed levels of axial load. For this section analysis the moment was referenced from the centroid of the undented cross-section.. The peak moment  $M$  and prescribed axial load  $P$  corresponding to each of the  $M-\Phi$  relationships were used to define the coordinates of the  $M-P$  interaction surface.

Specimen force paths based on Equation (4.1) are plotted against the theoretical interaction surfaces in Figures 4.6 through 4.9, where the bending moment and the applied axial load have been normalized by the plastic moment ( $M_p$ ) and the squash load ( $P_y$ ) of the steel tubular, respectively. In all of the cases except for Specimen C13 the maximum axial load that the specimens achieved occurs prior to reaching the theoretical interaction surface. Being unable to reach the strength predicted by the interaction surface indicates that the specimens did not achieve their full composite action capacity for the dent-damaged cross-section prior to failure. This occurrence is consistent with the observations presented in Chapter 3, where cracking sounds within the grouted member were noted in all of the specimens prior to attaining their peak axial load. This cracking is an indication of the separation occurring between the grout and the steel tubular, causing a reduction in the composite action between the two materials. In conclusion, the  $M-P$  capacity based on full composite action provides a upper bound for strength of the internal grout repaired members.

### **4.3. Specimen Residual and Repaired Strength Assessment**

#### **4.3.1. Effect of Dent-Damage on Ultimate Capacity**

A comparison of the damaged, non-repaired capacities ( $P_{nr}$ ) of the test specimens with the capacity ( $P_o$ ) of a similar, yet non-damaged member, is summarized in Table 4.2. The non-damaged capacity ( $P_o$ ) for specimens of the current test program was based on

the Structural Stability Research Council's Column Curve 1 [Galambos, 1988]. The current program's test data for the ratio of  $P_{nr}/P_o$ , as well as that by Ricles et al. [1992, 1997], are shown plotted in Figure 4.10 as a function of the normalized dent depth  $d_d/D$ . The prior test program by Ricles et al. [1992, 1997] had a dent depth of 0.1D, 0.15D; 0.2D, and 0.3D. It is clear from Figure 4.10 that a significant reduction in the ultimate capacity of a damaged member occurs as the depth of the dent-damage increases. More deeply dented specimens ( $d_d = 0.5D$ ) are seen to suffer a loss of capacity of as much as 82% and 88% (Specimens A12 & Specimen C12) of a corresponding member's non-damaged capacity, resulting in  $P_{nr}$  equal to  $0.18P_o$  and  $0.12P_o$ , respectively. Specimens with less severe dent-damage of nominal depth of 0.10D have residual capacities ( $P_{nr}$ ) that ranged from 50% to about 75% of  $P_o$ . Specimens A10 and C10 of the current study, having a dent depth of  $d_d = 0.25D$ , had residual capacities  $P_{nr}$  of  $0.42P_o$  and  $0.32P_o$ , respectively. For a given degree of dent-damage, specimens with nominal  $D/t$  ratios of 69 appear to suffer slightly larger strength reductions than the specimens having the smaller  $D/t$  ratios of 34.5 or 46. Figure 4.11 shows the normalized non-repaired capacities ( $P_{nr}/P_y$ ) plotted as a function of normalized dent-depth ( $d_d/D$ ) for the specimens tested in this program as well as for experimental data from similar previous studies [Ricles et al., 1992 & 1997; Smith et al., 1979 & 1981; Taby et al. 1981; Pacheco and Durkin, 1988]. Figure 4.11 further illustrates the degradation of ultimate strength associated with the increase in dent depth.

The larger reduction in member capacity associated with deeper dent-depths are attributed to the decrease in the bending resistance of the dent-damaged cross-section and increased eccentricity in the dented cross-section. The moment of inertia of the damaged section is significantly lowered after the infliction of damage, and continues to deteriorate as the dent-depth grows under the application of compressive axial load. A larger internal force couple develops across the damaged section as a result of the eccentricity that exists between the centroid of the dented and non-damaged portions of the member having a greater damaged out-of-straightness ( $\delta_p$ ). This internal couple combines with

second order effects to increase the bending demand imposed across the dent saddle, which leads to a local failure in the damaged region. Observations of this type of local failure were found in all of the non-repaired specimens tested in the current program discussed in Chapter 3 of this report.

#### **4.3.2. Effectiveness of Internal Grout and Grouted Sleeve Repair**

The experimental tests conducted for this program resulted in a dramatic increase in capacity of the internally grouted specimens compared to the non-repaired specimens. Figure 4.12 plots the normalized ultimate axial capacity ( $P_{exp}/P_y$ ) of the specimens tested herein, against the normalized dent-depth ( $d_d/D$ ). Included in Figure 4.12 are results from studies by Ricles et al. [1992, 1997], Parsanejad [1987,1992], and Boswell and D'Mello [1990]. Despite a relatively large band of scatter, this figure shows that the restoration to original non-damaged member strength by means of internal grouting is limited by the depth ( $d_d$ ) of dent-damage. It is also known, and will be discussed later, that the damaged out-of-straightness ( $\delta_p$ ) affects the repaired strength. The out-of-straightness ( $\delta_p$ ) of the specimens whose test results are shown in Figure 4.12 varied from 0.0001L to 0.0211L. The majority of the scatter in Figure 4.12 is in the small-scale tests conducted by Parsanejad et al. [1987 & 1992] and by Boswell and D'Mello [1990]. Some of these tests, especially those of the Boswell et al., are considered to be somewhat suspect because of their small scale ( $D < 3$  inches) and since the grout compressive strengths ( $f'_g$ ) reported did not vary among the measured material properties reported. Additionally, the reported elastic modulus of the grout ( $E_g$ ) for these specimens does not correlate well with the measured strengths presented herein, or with those of other studies [Lamport, 1988] that established a relationship between the elastic modulus and the strength of the grout.

A comparison of the repaired strength ( $P_r$ ) with the non-repaired residual strength ( $P_{nr}$ ), as well as with the non-damaged strength ( $P_o$ ) of the test specimens of the current program are given in Table 4.3. The non-repaired strength  $P_{nr}$  is based on the

corresponding non-repaired test specimens (see Table 4.2), while the non-damaged strength  $P_o$  is based on SSRC Curve 1 [Galambos 1988]. The relationship between normalized dent-depth ( $d_d/D$ ) and the repaired capacity-to-damaged capacity ratio ( $P_r/P_{nr}$ ) as well as between repaired capacity-to-non-damaged capacity ( $P_r/P_o$ ) is shown in Figures 4.13 and 4.14, respectively, for the test results of the current study and by Ricles et al. [1992, 1997]. Table 4.3 and Figure 4.13 both indicate that the internal grout repair of damaged members with an nominal dent-depth of 0.1D to 0.50D resulted in an increase in capacity above the non-repaired strength ( $P_{nr}$ ) for all D/t ratios tested. On average, for the results included in Figure 4.13 this increase in axial load capacity after the repair was more than twice the non-repaired strength ( $P_{nr}$ ). For the current study involving dent depths  $d_d$  of 0.25D and 0.5D, the increase ranged from  $1.61P_{nr}$  to  $2.81P_{nr}$  and  $1.28P_{nr}$  to  $5.11P_{nr}$ , respectively. The increase to  $5.11P_{nr}$  was for Specimen C15, which was a grouted sleeve repair.

As indicated in Figure 4.14, specimens with a dent-depth up to 0.15D had a repaired capacity which was equal to or exceeded the specimen non-damaged axial load capacity. Furthermore, repaired specimens with a larger D/t ratio have a greater enhancement in strength as shown in Figures 4.13 and 4.14. Internal grouting alone, however, is evidently unsuccessful in reinstating the capacity of the specimens with more severe dent-damage ( $d_d = 0.25D$  to  $0.5D$  and  $\delta_p = 0.005L$  to  $0.021L$ ) to their full non-damaged capacity ( $P_o$ ). As noted previously, for a deeper dent-depth, a greater reduction in the cross-section's moment of inertia as well as a larger amount of out-of-straightness  $\delta_p/L$  occurs, thus making it more susceptible to an overall column-type compression failure. For the values of out-of-straightness of the specimens tested that are plotted in Figure 4.14, there appears to be a  $d_d/D$  ratio between 15% and 25% beyond which internal grouting is not a viable repair method to restore a member to its original strength. The interaction of  $\delta_p$  and  $d_d$  on the residual and repaired strength will be discussed more later.

A comparison of the normalized experimental axial load-shortening relationships

between corresponding non-repaired and internal grout repaired specimens with nominal dent-depths of 0.25D and 0.50D are shown in Figures 4.15 through 4.18. The comparison for the grouted sleeve repair is included in Figure 4.18. The enhancement of axial load capacity after internal grouting can also be seen in these figures. The response of the grouted sleeve repaired specimen (Specimen C15) is shown to have a significant improvement in strength compared to the internal grout repaired specimen (Specimen C13). The capacity of Specimen C15 was  $0.64P_o$ , which is 100% greater than that of Specimen C13 (see Figure 4.18 and Table 4.3). Furthermore, the grouted sleeve repair significantly enhanced the performance of Specimen C15, where as noted previously the repaired strength was 5.11 times that of a corresponding non-repaired specimen. The failure of Specimen C15 was due to a local buckle that formed in the steel tubular, just beyond the end of the grouted sleeve. As noted in Chapter 3, the out-of-straightness ( $\delta_p$ ) at the section where local buckling occurred led to additional compressive stresses due to P- $\delta$  effects. Thus, the out-of-straightness ( $\delta_p$ ) that exists at the end of a grouted sleeve is an important variable that should be considered in repair design.

Improvements to the residual capacity after application of the grout repair is attributed to the prevention of the dent-growth and cross-sectional ovalization observed to have occurred in the non-repaired specimens, as noted in Chapter 3 of this report. The internal grouting of the damaged member was shown in Chapter 3 to stop the dent-growth and related deterioration of cross-sectional resistance. In the grouted sleeve repair the restraint of the sleeve prevented the dented section from distorting and therefore the dent from growing inwards. By inhibiting the growth in dent-depth, and thus arresting the cross-section from further distortion, the moment of inertia of the damaged steel cross-section did not decrease below its initial damaged value.

#### **4.4. Comparison of Experimental Results with Theoretical Predictions**

This section presents the results of a comprehensive effort to assess the

performance of various analytical techniques used to predict the ultimate capacity and the overall behavior of both non-repaired and internal grout repaired dent-damaged tubular bracing members. Analysis of the specimens tested under the current program as well as other studies were conducted. As noted previously, the analysis of each repaired specimen involved using the measured material and geometric properties reported in Chapter 2, which included the static yield strength of the steel tube for each specimen. For the grout compressive strength, a value of 80% of the measured average cube strength was used for each specimen in order to account for scale effects between the cube strength and in situ strength [Loh 1991].

Statistical comparisons of each analytical method are presented in Tables 4.4 through 4.6 for the analysis of the non-repaired and repaired specimens of the current program. Additional comparisons were made using data from previous studies in order to cover a range of normalized dent-depths ( $d_d/D$ ) and diameter-to-thickness ratios ( $D/t$ ) to assess the sensitivity of specimen capacity prediction for each of the analysis methods considered. The results from previous experimental studies included in these comparisons provided a total sample size of 60 specimens for non-repaired tubulars and 62 for internal grout repaired tubulars. Previously tested specimens were limited to those possessing simple-supported boundary conditions with dent-damage at midspan and axially loaded to cause single curvature.

#### **4.4.1. Analysis of Non-repaired Specimens**

Presented in this section are the analysis of the dent-damaged specimens without repair. These analysis are based several different theoretical methods, which are discussed below. The comparison between the predicted and experimental capacities for the specimens tested in this program are summarized in Table 4.4.

#### 4.4.1.1. Simplified Strength Equations and Beam-Column Analysis Methods

##### Ellinas Strength Equation

The Ellinas strength equation [Ellinas 1984] is based on beam-column theory, considering the interaction of axial load and moment and a member's out-of-straightness following denting. The ultimate member stress  $\sigma_{ud}$  of a damaged member is determined by solving the following quadratic equation

$$\frac{1}{\sigma_e} \sigma_{ud}^2 - \left[ 1 + \alpha_o \lambda_d + \frac{A_d e_d}{S_d} + \frac{f_y}{\sigma_e} \right] \sigma_{ud} + f_y + \sigma_{pd} \left[ \frac{A_d e_d}{S_d} \right] = 0 \quad (4.7)$$

where,  $e_d$ ,  $f_y$ ,  $\sigma_e$ ,  $\sigma_{pd}$ ,  $A_d$ , and  $S_d$  are equal to the eccentricity that exists in the dented region between the centroids of the damaged and non-damaged sections, the equivalent squash stress of the dented section, the Euler buckling stress, the initial plastification stress in the saddle of the dent, the dented cross-sectional area, and dented section modulus, respectively. Expressions for the geometric parameters for the imperfection and column slenderness,  $\alpha_o$  and  $\lambda_d$ , respectively, as well as section properties are given in Ellinas [1984].

The ultimate axial load capacity ( $P_{Ellinas}$ ) based on the computed ultimate stress ( $\sigma_{ud}$ ) of the damaged section found from Equation (4.7) are compared with the maximum experimental axial loads ( $P_{exp}$ ) of the current test program in column 4 of Table 4.4. Figure 4.19 plots the theoretical ultimate load normalized by the yield load ( $P_y$ ) of the non-damaged tubular cross-section against the normalized experimental capacities of the specimens tested in this experimental program. This figure shows that the Ellinas strength equation tends to provide a lower bound for the predicted capacity of the non-repaired test specimens. The mean and coefficient of variations (COV) for the ratio  $P_{Ellinas}/P_{exp}$  for the specimens is 0.79 and 0.149, respectively. Figures 4.20 and 4.21 plot the  $P_{Ellinas}/P_{exp}$  ratio for specimens of this program as well as those of previous studies involving non-repaired specimens, as a function of  $d_d/D$  and  $D/t$ , respectively. These figures show that the Ellinas



equation is not especially sensitive to neither the depth in dent damage nor the  $D/t$  ratio, and in most cases underestimates residual strength. A histogram of  $P_{Ellinas}/P_{exp}$  for all of these specimens is shown in Figure 4.22, where the mean and COV are equal to 0.87 and 0.189, respectively.

## DENTA

The DENTA II computer program was developed by Taby et al. [1986] for analyzing dent-damaged members. The program has been calibrated against test data where the dent depths were as large as  $0.23D$ . The analysis involves three stages: (1) loading to first yield; (2) inelastic response at ultimate load; and, (3) a post ultimate load and displacement response. The model neglects any increase in the dent-growth until after reaching the ultimate load. The DENTA II program predicts an increase in strength beyond first yield of the dented cross-section, but experimental findings of this study show only a small increase in axial load beyond initial yield of the specimen in the dent saddle. The experimental results also show that there exists a growth in dent-depth prior to developing the peak load.

The analysis of the test specimens resulted in converged solutions for only those specimens with a dent depth of  $0.25D$  (i.e., Specimens A10 and C10). The analysis of Specimens A12 and C12 by DENTA, both having a nominal dent depth of  $0.5D$ , gave erroneous results. The experimental axial load-shortening response for Specimens A10 and C10 are compared with that predicted by DENTA II in Figure 4.23. In this figure the elastic axial stiffness  $K_{el}$  based on  $AE/L$  is indicated, where  $A$ ,  $E$ , and  $L$  are the undented cross-sectional area, Young's modulus, and overall length, respectively. The initial elastic stiffness predicted by DENTA is shown to agree well with the experimental results as well as the value for  $K_{el}$ . The comparison between the predicted and experimental axial load-shortening response given in Figure 4.23 shows DENTA to underestimate the capacity of Specimens A10 and C10.

Numerical comparisons between the DENTA II analysis ( $P_{\text{DENTA}}$ ) and experimental ( $P_{\text{exp}}$ ) axial load capacity are given in column 5 of Table 4.4. Figure 4.24 plots the theoretical ultimate load value that has been normalized by the yield load ( $P_y$ ) against the normalized experimental values for the current experimental program.

Figures 4.25 and 4.26 plot the  $P_{\text{DENTA}}/P_{\text{exp}}$  ratio as a function of  $d_d/D$  and  $D/t$ , respectively, for the current program as well as the results from the studies by Ricles et al. [1992, 1997]. These figures indicate that the DENTA II analysis results are neither sensitive to dent-depth nor the  $D/t$  ratio for dent up to  $0.3D$  in depth (Specimens A12 and C12 are excluded from these figures). A histogram of  $P_{\text{DENTA}}/P_{\text{exp}}$  related to this same data is shown in Figure 4.27, where the mean and coefficient of variation are equal to 0.93 and 0.128, respectively. The limited sample size of 15 analyzed specimens was the result of the proprietary nature of the DENTA II program, which made extensive analysis of the complete specimen database not possible.

The comparison of the experimental capacity with predicted capacity indicates that DENTA cannot be used for members of dent depth deeper than  $0.3D$ .

## UCDENT

A quadratic equation implemented in the computer program UCDENT gives the load at first yield of the dented section for dented members with initial out-of-straightness ( $\delta_p$ ) and end eccentricity ( $e$ ) [Ricles et al. 1992, 1994]. The model is based on a damaged tubular member subjected to either concentric or eccentric axial load, and accounts for the dent occurring at any location along the axis of the member. The model is a more generalized quadratic stress resultant expression than Ellinas' approach, accounting for member out-of-straightness ( $\delta_p$ ), dented eccentricity ( $e_d$ ), and eccentric axial load effects.

The ultimate capacity of the dented member  $P_{ud}$  is predicted by the use of the following quadratic expression:

$$a P_{ud}^2 + b P_{ud} + c = 0 \quad (4.8)$$

where,

$$a = \frac{1}{P_{ed}} \left[ \frac{1}{A_d} + \frac{e + e_d}{S_d} - \frac{L_1 L_d e (1 + C_d)}{E I_d \beta S_d} P_{ed} \right] \quad (4.9 a)$$

$$b = - \left[ \frac{e + e_d}{S_d} + \left( \delta_o - \frac{L_1 L_d M_e}{E I_d \beta} \right) \frac{(1 + C_d)}{S_d} + \frac{M_e e^*}{P_{ed} S_d} + \frac{1}{A_d} + \frac{F_{pd}}{A_d P_{ed}} + \frac{\sigma_y}{P_{ed}} \right] \quad (4.9 b)$$

$$c = \sigma_y + \frac{F_{pd}}{A_d} \left( 1 + \frac{A_d e^*}{S_d} \right) \quad (4.9 c)$$

The derivation and definition of the various quantities appearing in Equation (4.9) can be found in Ricles et al. [1992 & 1994a].

UCDENT was used to assess the ultimate strength of the test specimens. Comparisons of the predicted capacity  $P_{UCDENT}$  with the experimental specimen capacity are given in column 6 of Table 4.4. The predicted results for  $P_{UCDENT}$ , which have been normalized by  $P_y$ , are compared with the normalized experimental axial load capacity in Figure 4.28. The method is shown to provide an extremely conservative lower bound for residual strength predictions, having a mean of 0.40 and a COV of 0.302. When considering all of the current four specimens and the 56 non-repaired specimens of others, Figures 4.29 and 4.30 both show that this method requires calibration to improve its accuracy. In Figure 4.29, the ultimate strength predictions are seen to become extremely conservative as the dent-depth increases. The UCDENT analysis is shown to become less conservative at higher  $D/t$  ratios (see Figure 4.30). Figure 4.31 shows the histogram of the  $P_{UCDENT}/P_{exp}$  ratios for all of the available experimental data (e.g. 4 non-repaired specimens from the current program and 56 similar specimens identified previously), where the mean and coefficient of variation are equal to 0.71 and 0.241, respectively. The large scatter of the prediction is attributed to the lack of calibration of

the formulation and the fact that failure is based on first yielding in the dent saddle.

### Loh Unity Check Equations

The experimental axial load capacity of the test specimens was compared to that predicted by two unity check expressions developed by Loh [Loh et al. 1992, Loh 1993] for dent-damaged tubular members. The unity check equations consider cases of axial loading (compression or tension) in combination with multi-directional bending with respect to dent orientation. For the load parameters addressed in this report, only compressive axial loading with uni-axial bending which place the dent into compression are considered.

The first unity check equation is referred to as the “strength check” and is associated with the strength limit state. This equation accounts for the possible failure of a short segment of a dented tubular under combined axial compression and uni-axial bending. The unity check expression is given by Equation (4.10), where an estimation of the strength of the dented section can be made by solving for  $P_{str}$ :

$$\frac{P_{str}}{P_{ud}} + \left[ \frac{M}{M_{ud}} \right]^{\frac{\alpha}{2}} = 1 \quad (4.10)$$

In Equation (4.10)  $P_{ud}$ ,  $M_{ud}$ , and  $M$  are equal to the damaged section’s axial capacity, damaged section’s flexural capacity, and the bending moment at the dented section due to applied end moments or end eccentricities, respectively. The parameter  $\alpha$  is defined as a function of dent depth  $d_d$  and diameter  $D$ , where

$$\alpha = 2 - 3 \frac{d_d}{D} \quad (4.11)$$

Expressions for the damaged section capacities ( $P_{ud}$  and  $M_{ud}$ ) are summarized in detail by Loh et al. [1992, 1993], as well as by Ricles et al. [1992].

The second unity check equation was used to assess the instability of a dented member under combined loading, and is referred to as the “stability check.” The buckling capacity  $P_{crdo}$  of a dented member without any out-of-straightness ( $\delta_p$ ) is first computed

by using a damaged slenderness parameter ( $\lambda_d$ ), which is explained further in Loh et al. [1992, 1993]. The buckling capacity  $P_{crd}$  of the damaged member, considering out-of-straightness ( $\delta_p$ ), is then determined by solving the following quadratic expression:

$$\frac{P_{crd}}{P_{crdo}} + \frac{P_{crd} \delta_p}{\left(1 - \frac{P_{crd}}{P_{ed}}\right) M_{ud}} = 1 \quad (4.12)$$

where  $P_{ed}$  is the Euler buckling load of the damaged cross-section. The stability load ( $P_{stab}$ ), which represents the residual strength of the dented tubular associated with the stability limit state is then obtained from the following expression:

$$\frac{P_{stab}}{P_{crd}} + \left[ \frac{C_m M}{\left(1 - \frac{P_{stab}}{P_{ed}}\right) M_{ud}} \right]^{\frac{\alpha}{2}} = 1 \quad (4.13)$$

where  $M$ , as in Equation (4.10), is the bending moment at the dented section due to applied end moments and any member end eccentricities, and  $\alpha$  is given by Equation (4.11). Further derivations and explanations related to Equation (4.13) can also be found in Loh et al. [1992, 1993] as well in Ricles et al. [1992].

Measured specimen material properties and dimensions were used to evaluate  $P_{str}$  and  $P_{stab}$  from Equations (4.10) and (4.13), where the smaller of the two values was taken as the predicted load-carrying capacity ( $P_{UnityChk}$ ) associated with the residual strength of a dent-damaged specimen. The results for  $P_{UnityChk}$  of the test specimens are given in column 7 of Table 4.4, where they are compared to the peak experimental capacity ( $P_{exp}$ ) for each of the specimens. The predicted capacity of the specimens of this program, in terms of the normalized ultimate strength ( $P_{UnityChk}/P_y$ ), are compared with the normalized experimental load ( $P_{exp}/P_y$ ) in Figure 4.32. For the prediction of test specimen capacity it was found that the stability limit state unity equation (i.e., Equation (4.13)) governed.

The ratio for  $P_{UnityChk}/P_{exp}$  is shown in Table 4.4 to range from 0.87 to 1.93 and have a mean of 1.25 and a COV of 0.349. Three of the four test specimens are shown in Table 4.4 and Figure 4.32 to have their capacity overestimated, where the specimens

having a dent depth  $d_d$  of  $0.5D$  (i.e., Specimens A12 and C12) have their capacity significantly overestimated.

The prediction of specimen capacity was also studied to examine the sensitivity to dent depth and diameter-to-thickness ratio. For this purpose the current as well as data obtained from previous experimental investigations were included. The results for the ratio of  $P_{\text{UnityChk}}/P_{\text{exp}}$  are shown plotted in Figures 4.33 and 4.34 as a function of the normalized depth of dent-damage ( $d_d/D$ ) and diameter-to-thickness ratio ( $D/t$ ), respectively. Figure 4.33 shows that within the range that the unity check equation has been calibrated ( $d_d \leq 0.20D$ ) the scatter is relatively small and the mean for the ratio of  $P_{\text{UnityChk}}/P_{\text{exp}}$  is conservative. However, this method tends to become unconservative as the dent-depth increases beyond the  $0.20D$  limit. The results for the ratio of  $P_{\text{UnityChk}}/P_{\text{exp}}$  plotted as a function of the  $D/t$  ratio are shown in Figure 4.34 not to be sensitive to the value of  $D/t$ , however, the specimens having a dent depth of  $0.5D$  (i.e. Specimens A12 and C12) have their capacity well overestimated. The histogram for the  $P_{\text{UnityChk}}/P_{\text{exp}}$  ratio for all of the experimental data base is given in Figure 4.35. The mean and COV for the histogram is 0.91 and 0.201, respectively.

The above results imply that the parameters appearing in the unity check expressions need calibration for deeper dent depths in order to extend the use of these equations to tubulars having dent depths greater than  $0.20D$ .

#### **4.4.1.2. Moment-Thrust-Curvature (M-P- $\Phi$ ) Based Method**

The analysis of the specimens was performed using the program DDAM, developed by Ricles and Fan [1996] and based on a moment- thrust-curvature (M-P- $\Phi$ ) formulation. In this approach the member was discretized into 21 segments, where the M-P- $\Phi$  relationships for dented [Duan et al., 1993] and undented segments [Chen and Han, 1985; Sohal and Chen, 1984, 1987, and 1988] were used in conjunction with numerical

integration to account for second order effects and to determine the axial load-deformation response of a dent-damaged specimen. The specimens with  $D/t = 69$  had the effects of residual stresses from fabrication accounted for in the  $M-P-\Phi$  relationships. The residual stress effect was neglected in the other specimens since they were annealed.

Duan's  $M-P-\Phi$  relationships are based on an assessment and regression analysis of data from over 150 experimental tests of dent-damaged specimens, and represents an empirical expression for the moment-curvature response of a dented tubular under a given axial load. It should be noted that the dent-depth ( $d_d$ ) and out-of-straightness ( $\delta_p$ ) values of the test specimens in this database were in the range of up to  $0.2D$  and  $0.01L$ , respectively. A few tests had  $d_d = 0.23D$  and  $\delta_p$  between  $0.01L$  and  $0.03L$ . Also, many of these tests were of a small scale with diameters ( $D$ ) that were typically 5 inches or less.

Duan's empirical expression for the  $M-P-\Phi$  relationship is very convenient, for during the integration analysis the curvature ( $\Phi$ ) can be obtained directly based on the current moment ( $M$ ) and axial load ( $P$ ). Further details of the  $M-P-\Phi$  based integration method of analysis are found in Ricles and Fan. [1996] and Ricles [1996].

Comparisons between the experimental axial load-shortening response of each test specimen of the current program and that generated by the  $M-P-\Phi$  based method is shown in Figures 4.36(a) through (d). The theoretical elastic axial stiffness  $K_{el} = AE/L$  is indicated in these figures. The results show that, while the specimen initial tangent axial stiffness is well estimated, the analysis does not capture the softening in the axial load-shortening response that occurs prior to reaching peak axial load. In addition, the specimen capacity is under estimated. In the post-ultimate response the  $M-P-\Phi$  based method consistently under predicts the resistance of the member after the peak load has developed. This discrepancy was similarly noted in some of the results for the load-shortening response generated by the DENTA II analysis.

Ricles and Fan [1996] noted that the tendency to underestimate axial capacity during the descending branch of analysis can be attributed to the sensitivity of the M-P- $\Phi$  analysis program to the length of the dented segment used in the model and the empirical nature of the M-P- $\Phi$  expressions. Although variation of the dented segment length was shown not to influence the ultimate capacity prediction, changes in the length of the dent segment were observed by Ricles and Fan [1996] to increase the accuracy as the length was decreased to approximately one half the member's diameter ( $0.5D$ ), and to prevent the convergence of the program in the descending branch if the length was increased beyond 3 times the member diameter ( $3D$ ). A length equal to twice the member's diameter for the dented segment, roughly corresponding to the extent of dent-damage observed on the test specimens of dent less than  $0.2D$ , was suggested by Ricles [1996] in order to provide the most reasonable estimate of behavior while ensuring program convergence. The dent segment length of  $2D$  was used in all of the analyses presented herein.

Numerical comparisons between the M-P- $\Phi$  based method predicted member capacity ( $P_{M-P-\Phi}$ ) and experimental axial load capacity ( $P_{exp}$ ) are given in column 8 of Table 4.4. Figure 4.37 plots the theoretical ultimate load value that has been normalized by the yield load ( $P_y$ ) against the similarly normalized experimental values. This figure also shows that the M-P- $\Phi$  based method underestimates specimen capacity. The mean and COV for the ratio  $P_{M-P-\Phi}/P_{exp}$  for the test specimens was 0.70 and 0.341, respectively. Figures 4.38 and 4.39 plot the value for the ratio  $P_{M-P-\Phi}/P_{exp}$  as a function of  $d_d/D$  and  $D/t$ , respectively, for specimens tested in the current as well as previous studies. Figure 4.38 shows that the M-P- $\Phi$  based method tends to increasingly underestimate specimen capacity as the dent depth becomes larger. Examination of Figure 4.39 shows that the predicted capacity is increasingly more conservative for specimens with a  $D/t$  ratio greater than 90 (i.e., test specimens of Taby [1986]). A histogram of  $P_{M-P-\Phi}/P_{exp}$  for the database is shown in Figure 4.40, where the mean and coefficient of variation are equal to 0.90 and 0.191, respectively.



The comparisons between the predicted and experimental result indicates that the M-P- $\Phi$  relationships need further calibration in order to extend the method to analyzing tubulars of deeper dent depth (i.e., the empirical moment-thrust-curvature relationships need to be refined where data from test specimens of deeper dent depth is included in the regression analysis).

#### **4.4.1.3. Finite Element Method (FEM)**

The commercially available finite element program ABAQUS [1993] was used to conduct nonlinear analyses of the non-repaired specimens. The finite element analysis was based on an updated Lagrangian formulation to capture the effects of large displacements, with Green's strain and second Piola-Kirchoff stress to model the moderate strain levels. The von Mises yield criterion with the associated flow rule and a mild amount of isotropic strain hardening was used to model the inelastic material response. For the test specimens, symmetry exists along the longitudinal z-axis in the xz-plane and at midspan in the xy-plane where the dent is located (see Figure 4.41(a)). Therefore, by taking advantage of this symmetry only one quarter of the specimen had to be modeled. The finite element model of a non-repaired specimen consisted of 422 eight-node shell elements, 1831 nodes, and approximately 10443 degrees of freedom. Five integration points through the thickness of the shell element were used. A typical mesh for the finite element model of a non-repaired specimen is shown in Figure 4.41(a). The transition from a coarse to a more finer mesh along the length of the model was achieved using multiple point constraints to ensure compatibility along the edges of adjacent elements at the point of transition.

The finite element analysis of a dented member involved four stages, similar to those of the experiments, namely: (1) supporting the member to prevent imposing excessive global out-of-straightness damage, and the loading of a knife edge indenter to create the dent-damage; (2) unloading of the indenter; (3) removal of the indenter and associated

support from the model, as well as specifying the pin-ended boundary conditions; and (4) applying the axial load and utilizing the modified RIKS solution scheme to solve for the non-linear axial force-shortening response of the member. A sample ABAQUS input file for a typical analysis of a non-repaired specimen is given in Appendix C.

The deformed mesh of the model after imposing the dent damage, but prior to applying axial load, is shown in Figure 4.41(b). Several trial runs had to be conducted to obtain the correct dent depth and damaged out-of-straightness during stages 1 through 3 of the analysis.

Longitudinal stress contours for Specimen A10 are shown in Figure 4.42. These results correspond to stage 4 of the analysis, when the peak axial load was applied to the model following denting. The stress contours plotted in Figure 4.42 shows longitudinal tensile stresses to develop at the bottom of the tube near the dent as well as locally on the top of the tube, where the longitudinal distortion in the cross section starts due to the dent. Compressive stresses are shown to develop around the remaining circumference of the cross section, with large stresses and yielding occurring outside the dent saddle and near the dimple of the cross-section created by the dent. The stress contours shown in Figure 4.42 represent typical results for the analysis of the non-repaired specimens.

The longitudinal stress contours shown in Figure 4.42 are in good agreement with the experimental results. Near the peak load the measured test specimen longitudinal strains around the circumference of the dented cross section had the compressive strains exceed the yield strain on the sides of the tube, with a smaller magnitude of tensile strain developing on the bottom of the dent (see Figure 3.6 and 3.8).

Comparisons of the normalized load-shortening curves generated by the non-linear FEM analysis with experimental data is shown in Figure 4.43(a) through (d). The theoretical elastic axial stiffness  $K_{el} = AE/L$  is indicated in the figure. The correlation of the

predicted response to the measured response is generally good, particularly for Specimen A10 which has  $D/t$  ratio of 34.5 and dent depth of  $0.25D$ . For specimens having a  $D/t$  ratio of 69 (i.e., Specimens C10 and C12) the experimental results are shown to develop a softening in the ascending branch of their response that is not predicted by the finite element model. The greatest discrepancy with the experimental data and the predicted response occurs in the descending branch of the response.

The phenomenon associated with softening prior to achieving peak axial load may be attributed to the existence of tensile residual stresses from fabrication at the weld seam along the bottom surface of the tubular. These residual stresses cause an earlier yielding at the bottom surface of the dented cross section, resulting in a reduction of stiffness in the experimental response prior to attaining ultimate load. However, analyses that included the fabrication residual stresses in the model did not result in any significant difference in the predicted load-displacement response.

Numerical comparisons between the FEM analysis and experimental axial load capacity are given in column 9 of Table 4.4. Figure 4.44 plots the values of the theoretical ultimate load of the FEM analysis ( $P_{FEM}$ ) that has been normalized by the yield load ( $P_y$ ) against the experimental values ( $P_{exp}$ ) normalized in a similar manner. The mean and COV for the ratio  $P_{FEM}/P_{exp}$  was 1.01 and 0.174, respectively. The results shown in Figure 4.44 and Table 4.4 indicate that the FEM analysis provides a good strength prediction for Specimens A10 and A12. The largest discrepancy exists with the results for Specimens A12 and C12, which had the dent depth  $d_d$  of  $0.5D$ . Figures 4.45 and 4.46 plot the ratio of  $P_{FEM}/P_{exp}$  for results of the finite element analysis of specimens as a function of  $d_d/D$  and  $D/t$  to assess the sensitivity of this method to damage and geometric properties, respectively. The specimens included in these figures are from the current and previous test programs that are indicated in the legends of the figures. Figure 4.45 shows that the non-linear finite element analysis prediction for specimen capacity in general is not especially sensitive to dent-depth, with the largest scatter occurring at the

largest dent depth of 0.5D (i.e., Specimens A12 and C12). The results in Figure 4.46 indicate that the accuracy of the FEM analysis in general is not especially sensitive to the tubular's D/t ratio. A histogram for the ratio of  $P_{FEM}/P_{exp}$  related to these test specimens is given in Figure 4.47. The relatively small scatter confined about the mean value of 1.01 with a coefficient of variation of 0.10 indicates the consistent accuracy of the prediction for member capacity.

#### 4.4.2. Analysis of Internal Grout Repaired Specimens

Presented below are the analysis of the dent-damaged specimens repaired by internal grouting. These analysis are based on several different methods, which were discussed below. Numerical comparisons between the predicted and experimental capacities for the specimens tested in this program are summarized in Tables 4.5 and 4.6.

##### 4.4.2.1. Simplified Strength Equations

###### Parsanejad Equation

Parsanejad developed an analytical expression based on beam-column theory to predict the ultimate strength of a dent-damaged specimen, repaired by internally grouting and subjected to concentric or eccentric axial compression. The expression, which appears below, is written in terms of stress, considers transformed section properties, and assumes that failure occurs when the total stress  $\sigma_{ud}$  (axial combined with bending) in the dent saddle reaches the yield stress  $\sigma_y$  of the steel tubular [Parsanejad, 1987].

$$\frac{A_{tr}}{A_{tr}^* \sigma_{ed}} \sigma_{ud}^2 - \left[ \frac{A_{tr}}{A_{tr}^*} + \frac{A_{tr}^* e_t}{S_{tr}} + \frac{\sigma_y}{\sigma_{ed}} \right] \sigma_{ud} + \sigma_y = 0 \quad (4.14)$$

In Equation (4.14)  $\sigma_{ed}$ ,  $A_{tr}$ ,  $A_{tr}^*$ ,  $S_{tr}$ , and  $e_t$  are equal to the Euler buckling stress, transformed cross-section area of the dented section, transformed cross-section area of the undented section, section modulus of the cross-section area of the dented section, and

total eccentricity between the centroid of the dented cross-section and the applied axial load at the ends of the member. Mathematical definitions of the terms appearing in Equation (4.14) can be found in Parsanejad [1987] and Parsanejad and Gusheh [1992]. A correction for the gross moment of inertia  $I_g$  was used, as pointed out by Loh [1991]. Furthermore, theoretically the areas of the undented and dented cross-section should be the same. Hence, for this study they were taken to be the same, and based on the undented, transformed cross-section area of the grout filled tubular area. Finally, better correlation was found when the transformed section properties appearing in Equation (4.14) were based on the modular ratio computed using Lamport's formulation (Equation 2.1).

For each of the internal grout repaired specimens of the current test program, the theoretical ultimate axial capacities ( $P_{\text{Parsanejad}}$ ) predicted using the Parsanejad equation (Equation (4.14)) are compared to the corresponding experimental capacities ( $P_{\text{exp}}$ ) in column 4 of Table 4.5. Figure 4.48 plots the value for  $P_{\text{Parsanejad}}$ , which has been normalized by the yield load ( $P_y$ ) of the steel tubular, against the normalized experimental result. The results show this method to overestimate the repaired capacity of all of the internal grout repaired specimens. The mean and coefficient variation for the ratio of  $P_{\text{Parsanejad}}/P_{\text{exp}}$  is 1.12 and 0.093, respectively. Additional comparisons are given in Figures 4.49 and 4.50, where the results from the analysis of the previous tests are included [Ricles et al., 1992; Parsanejad et al., 1987, 1992; Boswell and D'Mello, 1990] in order to determine the sensitivity of Parsanejad's equation to the effect of depth of dent-damage ( $d_d$ ) and diameter-to-thickness ( $D/t$ ) ratio of the member. The results in these figures suggest that the average predicted strength based on this formulation produces results for the ratio  $P_{\text{Parsanejad}}/P_{\text{exp}}$  where a consistent scatter occurs about the mean value over the range of dent-damage and the  $D/t$  ratios considered. An exception exists for two specimens of the current program (Specimens A13 and C13) which had a dent depth of  $0.5D$ . The largest discrepancy between predicted and experimental capacity appearing in Figures 4.49 and 4.50 is associated with Specimen C7 of the test program by Ricles et al. [1997]. Specimen C7 had a dent depth of  $0.15D$  and  $D/t$  ratio of 69. A histogram of the

$P_{\text{Parsanejad}}/P_{\text{exp}}$  ratio for all available test data is shown in Figure 4.51, where Parsanejad's equation is shown to have a mean and coefficient of variation of 1.03 and 0.191 for the 62 test specimens analyzed.

### **Loh Modified AISC-LRFD Equation**

Loh [1991] suggested that the AISC-LRFD provisions used to design concrete filled tubular members could be applicable to predict the ultimate strength of an internal grouted, dent-damaged tubular if it were assumed that the full length of the repaired member had a prismatic cross-section that possessed the properties of the dented section. This method assumes full-composite action is developed and that failure occurs when the overall buckling stress, or material yield stress in the case of a squat member, is reached. The result of this approach led to the following formulation, which has to be equated to unity in order to evaluate the predicted ultimate axial capacity of the member  $P$ :

$$\frac{P}{P_{cr}} + \frac{C_m M}{\left(1 - \frac{P}{P_e}\right) M_u} = 1 \quad (4.15)$$

In Equation (4.15)  $C_m$ ,  $M$ ,  $P_e$ ,  $M_u$  are equal to the AISC moment gradient coefficient, applied moment, Euler load, and modified bending capacity, respectively. In addition,  $P_{cr}$  is the reduced ultimate axial compression capacity of the damaged tubular, accounting for changes in member slenderness due to denting, and defined by the following expression:

$$P_{cr} = F(\lambda) P_u \quad (4.16)$$

The quantity  $F(\lambda)$  is a factor that is associated with a modified buckling curve which accounts for the damaged member response, and is based on modifications to the SSRC Column Curves [Galampos, 1988] used in the AISC-LRFD [1994] and API RP-2A-LRFD [1993] design provisions.

A more thorough discussion of the approach is presented in Loh [1991]. In evaluating the axial capacity using (4.15), Lamport's formula (i.e., Equation (2.1)) was used to compute the grout modulus that is required in determination of the Euler load  $P_e$ .

Numerical comparisons between the predicted results  $P_{\text{Mod-AISC}}$  using the Loh modified AISC-LRFD method and experimental axial load capacity are given in column 5 of Table 4.5. Figure 4.52 plots the theoretical ultimate load value ( $P_{\text{Mod-AISC}}$ ) calculated by Equation (4.15), which has been normalized by the yield load ( $P_y$ ) of the steel tubular against the normalized experimental values ( $P_{\text{exp}}/P_y$ ) of the tests of the current program. Reasonable good accuracy was achieved using Equation (4.15). The mean and COV for the ratio  $P_{\text{Mod-AISC}}/P_{\text{exp}}$  of the specimens tested under the current program are 1.01 and 0.113, respectively.

Figures 4.53 and 4.54 plot the ratio  $P_{\text{Mod-AISC}}/P_{\text{exp}}$  as a function of  $d_d/D$  and  $D/t$ , respectively, to assess the sensitivity of the Loh modified AISC-LRFD equation to dent depth and  $D/t$  ratio. Figure 4.53 shows that this equation is not especially sensitive to the depth of inflicted dent-damage, however, the strength estimation is unusually higher in Specimen C7 of the study conducted by Ricles et al. [1997], which have a  $D/t$  ratio of 69. Specimen C7 ( $d_d = 0.15D$ ) had a predicted strength that was 1.91 times higher than the experimental capacity, respectively. The histogram of the ratio  $P_{\text{Mod-AISC}}/P_{\text{exp}}$  for this test data is shown in Figure 4.55, where the mean and coefficient of variation is 0.94 and 0.221, respectively. These results indicate that a reasonable good prediction of the capacity of a dented tubular subjected to axial load can be achieved by Loh's modified AISC-LRFD method for members up to dent depths of  $0.5D$ .

#### **4.4.2.2. Moment-Thrust-Curvature (M-P- $\Phi$ ) Based Method**

The prediction of the capacity of the internal grout repair specimens by the moment-thrust-curvature analysis method involved the use of the computer program DGROUT

developed by Ricles [1996]. The method involves the use of numerical integration over the length of the member in conjunction with M-P- $\Phi$  relationships, where the M-P- $\Phi$  relationship of a grouted tube segment was established by a separate analysis of the cross-section. The computation involves generating data points corresponding to the moment-curvature (M- $\Phi$ ) response of the dented and undented sections of the grouted member for a specified axial force (P). Assumptions in the analysis include plane sections remaining plane and full bond (i.e. compatibility and composite action) between the steel and grout.

The cross-section of the grouted tube is first discretized into fibers, each fiber representing either steel or grout based on the fiber's location. The stress-strain curves for the grout and steel fibers are illustrated in Figures 4.56(a) and (b), respectively. The analysis was based on the assumption that no tensile stress developed in the grout. The modular ratio of the grout was set equal to the value based on Lamport's formulation (Equation (2.1)). No increase in the grout compressive strength due to confinement was considered, with the strength degradation initiating at a strain of  $\epsilon_{br} = 4\epsilon_o$  and at the rate of  $0.2f'_g$ , where  $\epsilon_o$  is the strain corresponding to maximum grout compressive strain. To account for scale effects in the grout cube tests, a value of  $0.8f'_g$  was used (in lieu of  $f'_g$ ), which produced more reasonable results.

The material properties of the steel fibers included a descending branch in the stress-strain curve to account for local buckling (see Figure 4.56(b)). This phenomena is controlled by the parameters  $\gamma$  and  $n$  in DGROUT, where a value of  $n = -0.2$  was used. By specifying the value for  $\gamma$ , the strain at the onset of local buckling of the steel tubular could be adjusted for tubular members that are more susceptible to local buckling. For specimens with a lower D/t ratio (i.e.,  $D/t = 34.5$ )  $\gamma$  was set equal to a value of 4, which allowed development of plastification before the local buckling of the steel tube occurred. In the analysis of the specimens with a D/t ratio of 69, the value for the  $\gamma$  parameter was set equal to 2 in order to account for the tendency of tubulars of higher D/t ratio to develop local buckling at a smaller strain beyond the yield strain  $\epsilon_y$ .



It was determined that the result for predicted capacity of the members was not sensitive to the material parameters associated with deterioration of the stress-strain curve, since member capacity was achieved just after yielding in the fibers of the cross-section occurred.

The cross-section of each segment was discretized into 80 fibers over the depth. Other input details used in the DGROUT to model the test specimens include defining a model with 21 individual segments, where one segment in the middle of the model represented the dent-damaged region. Other aspects of the M-P- $\Phi$  approach are similar to those discussed previously for the non-repaired member analysis M-P- $\Phi$  procedure. More complete details and a description of the theory and use of DGROUT can be found in Ricles (1996).

A sample M- $\Phi$  relationship computed for Specimen A11 corresponding to an axial load (P) of 145 kips is shown in Figure 4.57. A comparison between the experimental load-deformation response of the internal grout repaired members of the current test program with that generated by the M-P- $\Phi$  approach are shown in Figures 4.58(a) through (d). The axial load-shortening response based on the transformed elastic axial stiffness indicated in Figure 4.58 is defined by the following relationship:

$$\frac{P}{P_y} = K_{eq,tr} \frac{\Delta}{L} \quad (4.17)$$

where the equivalent elastic transformed axial stiffness ( $K_{eq,tr}$ ) of the internal grout repaired member is equal to:

$$K_{eq,tr} = \frac{E_s A_{tr}}{\sigma_y A_s} \quad (4.18)$$

In Equation (4.18),  $E_s$ ,  $A_s$ , and  $\sigma_y$  are the elastic modulus of the steel tubular, cross sectional area of the steel tubular, and yield stress of the steel tubular, respectively, and  $A_{tr}$  is the transformed cross-sectional area of the grouted member defined as:

$$A_{tr} = A_s + \frac{A_g}{n} \quad (4.19)$$

where  $n$  is the modular ration representing the ratio of steel to grout modulus.

The M-P- $\Phi$  based method is shown in Figure 4.58 to overestimate the axial stiffness of the specimens. For Specimens A11 and C11 the predicted elastic stiffness agrees with the initial tangent stiffness experimental result. However, for Specimens A13 and C13 the experimental result is softer than the predicted initial stiffness. These latter two specimens had a large out-of-straightness following denting ( $\delta_p = 0.021L$  and  $0.017L$ , respectively), and therefore the axial shortening caused by the geometric effect of bending was more significant. The over-prediction in axial stiffness of Specimens A13 and C13 is partially attributed to the assumption that full composite action is maintained up to ultimate load in the analysis, which increases the bending stiffness.

Numerical comparisons of the predicted  $P_{M-P-\Phi}$  and experimental capacity  $P_{exp}$  are given in Table 4.5, and shown plotted in Figure 4.60 where they have been normalized by the steel tubular yield load  $P_y$ . These results and the axial load-shortening results shown in Figure 4.58 both indicate that the capacity of Specimens A11 and C11 were over-predicted ( $P_{M-P-\Phi} / P_{exp} = 1.19$ ) while that of Specimens A13 and C13 ( $P_{M-P-\Phi} / P_{exp} = 0.98$  and  $0.81$ , respectively) were under-predicted.

All of the specimens of the current program were reanalyzed using a grout modulus stiffness of  $E_g = 1$  ksi. This was done in order to evaluate the sensitivity to the assumed value for grout modulus and to examine whether the grout acted mainly to prevent the dent from growing inwards as opposed to increasing the tubular stiffness. The results for the axial load-shortening predicted response are compared to that of the experimental response in Figure 4.59(a) and (d). The associated elastic ascending axial stiffness is noted. A summary of the ratio of  $P_{M-P-\Phi} / P_{exp}$  is given in column 4 of Table 4.6, where the mean and COV for the test specimens is 0.82 and 0.166. It is seen that the main effect of reducing the grout modulus is to reduce the stiffness, with the strength also being reduced in Specimens A11 and C11 to 0.86 and 0.65 of the experimental result  $P_{exp}$ . For Specimens A13 and C13, which had the more significant out-of-straightness and deeper dent depth, the predicted

strength did not change compared to the analysis based on the grout modulus using Equation (2.1). However, the axial stiffness of all specimens is reduced.

Figures 4.61 and 4.62 plot the ratio for  $P_{M-P-\Phi}/P_{exp}$  as a function of  $d_d/D$  and  $D/t$ , respectively, for the data base of internally grout repaired specimens. The specimens tested by Ricles et al. [1997] as well as the current program have been analyzed using the grout modulus based on Equation (2.1) as well as a value of  $E_g = 1$  ksi. Figures 4.61 and 4.62 show that the prediction of the capacity of specimens tested by Boswell and D'Mello [1990] have a considerable scatter when compared to experimental capacity. This scatter is suspected to be partially attributed to the constant value of 10 for the grout modulus reported by Boswell and D'Mello [1990], and which was used in the analysis. Furthermore, these figures show that the M-P- $\Phi$  based method tends to provide an un-conservative estimate of repaired member strength when the full grout modulus is used, particularly for cross-sections having  $D/t = 69$ . The histogram for the ratio of  $P_{M-P-\Phi}/P_{exp}$  for the test specimens in the data base is shown in Figure 4.63, which has a mean value of 0.96 and coefficient of variation of 0.181. The analysis results included in Figure 4.63 are solely based on a grout modulus from Equation (2.1).

In summary, the M-P- $\phi$  based method tends to provide a higher prediction of capacity compared to test results for specimens having a mild to moderate out-of-straightness when the full stiffness value of the grout modulus is used. On the contrary, for specimens with a deeper dent (which also had significant out-of-straightness) the value of the grout modulus used in the analysis did not effect the capacity but did effect the stiffness of the load-deformation response.

#### 4.4.2.3. Finite Element Method (FEM)

ABAQUS was also used to analyze the internal grout repaired specimens. The finite element mesh used for analyzing internally grout repaired members is shown in Figure 4.64,

where one-quarter of the member was modeled by taking advantage of symmetry. The planes of symmetry were identical to those of the non-repaired models, namely: along the longitudinal z-axis with respect to the xz-plane and at midspan with respect to the xy-plane. The finite element model consisted of a total of 505 elements, 1671 nodes, and 8305 degrees of freedom. A combination of eight-node shell elements and eight-node and six-node solid elements were used to model the member over a longitudinal distance from the dent to three diameters away from midspan of the test specimen. The remaining part of the member was modeled using beam-column elements. The solid elements were used to model the internal grout, whereas the shell elements were used to model the steel tube. Full bond transfer was assumed between the shell and the solid elements. As in the finite element model of the non-repaired specimens, the model for the repaired specimens utilized multiple point constraints at locations of mesh refinement to ensure compatibility between the edges of the shell elements. The beam-column elements were assigned section properties related to those of a composite grout filled beam-column. Constraint equations were used to ensure compatibility between the beam-column and the shell and solid elements at their interface.

The finite element analysis was based on an updated Lagrangian formulation to account for large displacement effects, with Green's strain and second Piola Kirchhoff stress to model the moderate strain level. For the steel tube, the von Mises yield criterion with the associated flow rule and a mild amount of isotropic strain hardening was used to model the inelastic material response. The grout was modeled using the concrete material option available in the ABAQUS material library, where the value for the grout modulus was based on Equation (2.1) using a grout strength of 80% of the measured cube strength. The concrete material model in ABAQUS consists of a compressive yield/flow surface to model the concrete response in predominantly compressive states of stress, together with damaged elasticity to represent cracks that have occurred at a material calculation point. The occurrence of cracks is defined by a crack detection failure surface which is considered to be part of the elasticity. Cracking of the concrete due to excessive tensile strain is modeled

in ABAQUS by a smeared crack approach. The concrete failure surfaces in plane stress space are shown in Figure 4.65. A 16% increase in the compressive strength under biaxial stress relative to the measured specimen grout cylinder compressive strength  $f'_g$  times 0.8 (i.e.,  $0.8f'_g$ ) was assumed in defining the failure compressive surface. The tensile surface was based on a specified value of 9% of the uniaxial compressive strength for the uniaxial tensile strength. The tension stiffening option in ABAQUS was used to simulate stress transfer across a crack, with a gradual decrease in strength with further crack opening. Complete details of the material model can be found in the ABAQUS User's Manual [1993].

The finite element analysis of an internal grout repaired dented specimen involved five stages and two models, namely: (1) imposing local dent-damage to a model of a hollow steel tubular member by laterally supporting the member and loading it with a knife-edge indenter to determine the coordinates of the shell elements and initial strain in the damaged state; (2) unloading; and (3) removing the indenter and lateral support and writing the coordinates and strain information to a file; (4) developing a new model that includes the damaged steel tubular and stress-free grout, where the coordinate and initial strains due to denting of the steel tubular are used to define this second model; and (5) applying the axial load, utilizing the modified RIKS algorithm to obtain the non-linear axial-force shortening response of the second model, and thus the behavior of a damaged member having a internal grout repair. A sample input file for an analysis of a grout repaired specimen is given in Appendix D.

Comparisons between the experimental load-deformation relationship of the internal grout repaired specimens and that predicted using the finite element analysis are shown in Figures 4.66(a) through (d). For Specimens A11 and C11 the initial tangent elastic axial stiffness of the finite element model agreed with that of the measured experimental response, while that for Specimens A13 and C13 shows disagreement. In all cases, for increased axial load towards a specimen's capacity the finite element analysis had a higher

axial stiffness than the experimental data. This discrepancy is attributed to the assumption that in the model that full composite action is maintained between the grout and steel up to and beyond ultimate load, causing a greater stiffness. The larger discrepancy between the measured stiffness of Specimens A13 and C13 and the finite element results is attributed to the more significant contribution of the bending to axial shortening due to geometric effects, and the fact that the model has too large a bending stiffness.

It was found that the convergence of the finite element solution on the descending branch of the load-deformation response was difficult to achieve. This phenomenon is associated with the simultaneous occurrence of the nonlinearities due to grout cracking and steel yielding. The descending branch of response was for that reason not computed for larger values of axial shortening than that shown in Figure 4.66. The prediction of Ultimate load ( $P_{FEM}$ ) for all of the specimens was overestimated by the analysis. A summary of the ratio of predicted-to-experimental capacity  $P_{FEM}/P_{exp}$  is given in column 7 of Table 4.5, and plotted in Figure 4.70 in normalized format. The mean and COV for the ratio  $P_{FEM}/P_{exp}$  is 1.24 and 0.065, respectively.

All of the test specimens were reanalyzed with the grout stiffness  $E_g$  assigned a value of 1 ksi in order to evaluate the contribution of the grout to preventing the dent from growing inwards without enhancing the axial stiffness of the member. The results for normalized axial load-shortening are shown plotted in Figure 4.67, where a better agreement with experimental data exists than the analysis having full grout stiffness. Numerical comparisons between the results of these latter finite element analysis ( $P_{FEM}$ ) and experimental axial load capacity ( $P_{exp}$ ) are given in column 5 of Table 4.6. The mean and coefficient of variation for the ratio of  $P_{FEM}/P_{exp}$  are 1.05 and 0.091; respectively.

Longitudinal stress contours for the steel and grout elements of the model for Specimen A11 are shown in Figures 4.68 and 4.69. These results are for the model having a reduced grout modulus and correspond to when an axial deformation of just beyond the

peak axial load was achieved in the analysis. An examination of these figures reveals the extent of compression yielding on the sides of the steel tube, maximum grout stress under and in the vicinity of the dent saddle, and tension cracking of the grout at the bottom of the dented cross-section (where the stress contours show the largest tensile stress). This yielding pattern and locations of maximum grout stress was consistent with experimental observations for tube yielding and grout crushing in the vicinity of the dent saddle (see Figure 3.46, 3.51, and 3.105).

Figures 4.71 and 4.72 plot the ratio of predicted to experimental capacity  $P_{FEM}/P_{exp}$  as a function of  $d_d/D$  and  $D/t$  to assess the sensitivity of the analyses to damage and geometric properties, respectively. Included in these plots are analysis results of specimens tested by Ricles et al. [1992, 1997] where the dent depth  $d_d$  was  $0.1D$ ,  $0.15D$ , and  $0.3D$ . Predictions based on a reduced and full grout modulus stiffness of some of the specimens are noted in Figure 4.71 and 4.72. The results shown in these figures indicate that the non-linear finite element model is in general not especially sensitive to dent-depth nor  $D/t$  ratio when using a reduced grout stiffness of  $E_g$  equal to 1 ksi. A histogram for the ratio of  $P_{FEM}/P_{exp}$  for these 14 test specimens is given in Figure 4.73, where the predicted capacity  $P_{FEM}$  is based on a full grout stiffness per Equation (2.1). The mean and coefficient of variation for the histogram is 1.02 and 0.081, respectively.

In summary, it appears that the use of the non-linear finite element method can produce reasonable predictions for specimen behavior,. However, the stiffness and capacity of members tends to be overestimated when the full stiffness of the grout is used in the model. A reduced grout modulus results in a closer upper bound prediction for member capacity.

#### 4.5. Repair Feasibility Study

The M-P- $\Phi$  based method in conjunction with numerical integration is computationally efficient compared to the nonlinear finite element method. In a previous

investigation by Ricles et al. [1997] the M-P- $\Phi$  approach was used to conduct a parametric study in order to investigate the interaction of global damaged out-of-straightness ( $\delta_p/L$ ) and dent-depth ( $d_d/D$ ) on the residual and repaired capacities of non-repaired and internal grout repaired members, respectively, having the  $D/t$  ratios of 34.5, 46 and 69. Member slenderness ( $kL/r$ ), grout compressive strength ( $f'_g$ ), and steel yield strength ( $\sigma_y$ ) were each fixed at 60, 5.0 ksi, and 35 ksi, respectively, which were values approximately equal to those of the test specimens. The full grout stiffness was used in the study.

The results for this parametric study related to a comparison of the non-repaired strength with grout repaired strength as a function of dent-depth ( $d_d/D$ ) and damaged out-of-straightness ( $\delta_p/L$ ) are shown in Figures 4.74 and 4.75. In these figures the predicted strength  $P_u$  has been normalized by the yield strength ( $P_y$ ) of the steel tubular, and the repaired surface is represented by the shaded surface. The results in Figures 4.74 and 4.75 show that both the non-repaired and repaired strengths are significantly influenced by the values of  $d_d/D$  and  $\delta_p/L$ .

The results of the parametric study that compares repaired strength and non-damaged capacity are shown plotted in Figures 4.76 and 4.77 for the normalized strength ( $P_u/P_y$ ) as a function of the variables  $\delta_p/L$  and  $d_d/D$  for members with  $D/t$  ratios of 34.5 and 69, respectively. In these figures, the shaded surface is associated with non-damaged residual capacity ( $P_o$ ) and the unshaded surface the repaired strength after internal grouting. The non-damaged strength ( $P_o$ ) was estimated using the Structural Stability Research Council's Column Curve 1 [Galambos, 1988] and a member out-of-straightness of  $\delta_o = 0.001L$ , based on the API-RP2A LFRD [1993] limit for out-of-straightness. It is seen in these figures, as in Figures 4.74 and 4.75, that a greater reduction in repaired capacity and the ability of the repair to enhance the strength of a damaged member occurs when the effects of out-of-straightness and dent-depth are both considered.

An expression  $\phi$  for the line formed by the intersection of these two surfaces was obtained through regression analysis by Ricles et al. [1997], where for  $D/t = 34.5$ ,  $kL/r = 60$ , and  $d_d/D \leq 0.33$ ,



$$\phi\left(\frac{\delta_p}{L}, \frac{d_d}{D}\right) = -\left(\frac{\delta_p}{L}\right) + 0.0099 - 0.008\left(\frac{d_d}{D}\right) - 0.0639\left(\frac{d_d}{D}\right)^2 \quad (4.20a)$$

and for  $D/t = 69$ ,  $kL/r = 60$ , and  $d_d/D \leq 0.40$ ,

$$\phi\left(\frac{\delta_p}{L}, \frac{d_d}{D}\right) = -\left(\frac{\delta_p}{L}\right) + 0.0171 - 0.0225\left(\frac{d_d}{D}\right) - 0.0501\left(\frac{d_d}{D}\right)^2 \quad (4.20b)$$

For a given  $D/t$  ratio, the internal grout repair is a viable repair technique to restore a member's capacity to its non-damaged strength ( $P_o$ ) if the values for  $\delta_p/L$  and  $d_d/D$  result in a positive value for  $\phi$  when substituted into the above limit state equations. As specifically implied by Equation 4.20(a), a member with a  $D/t$  ratio of 34.5 and having a dent-depth exceeding  $0.33D$  cannot have its full non-damaged strength reinstated by internal grout repair, no matter how small the member's out-of-straightness is. A comparison of these regression equations with the analysis data of the M-P- $\Phi$  based method, as well as with the experimental data for each  $D/t$  of the repaired specimens of the current study and those by Ricles et al. [1997], are shown in Figures 4.78 and 4.79. In these figures  $P_r$  designates repaired capacity and  $P_o$  the non-damaged capacity per SSRC Curve 1 [Galambos, 1988].

For the specimens with  $D/t$  ratios of 34.5 the function  $\phi$  is shown to be consistent with the experimental results, where experimental data points inside the limit state surface have  $P_r$  exceed  $P_o$  and outside the limit state surface  $P_r$  is less than  $P_o$ . In Figure 4.79 the M-P- $\Phi$  based method is shown to over-predict the capacity of the specimens which have a  $D/t$  ratio of 69, for the coordinates related to Specimens C7, C11, and C9 plot in the region where repair is predicted to be fully effective yet the experimental capacity  $P_r$  was equal to 92%, 93%, and 69%, respectively, of the non-damaged capacity  $P_o$ . This tendency to over-predict the axial capacity of specimens with  $D/t$  ratios of 69 was noted in the previous section discussing the accuracy of the M-P- $\Phi$  based method. The limit state function  $\phi$  in Figure 4.79 therefore needs to be calibrated in order to more accurately reflect the observed experimental trend involving specimens with  $D/t$  equal to 69. This may require reducing the stiffness of the grout.

# CHAPTER 5

## SUMMARY AND RECOMMENDATIONS

### 5.1. Summary

The research described in this report was performed with the principal objective of evaluating the residual strength and internal grout repair of long tubulars with deep dents. The work performed consisted of experimental and analytical studies, and resulted in identifying the range in which internal grout repair is effective as well as the reliability of existing analytical methods in predicting the behavior of non-repaired as well as internal grout repaired tubulars having deep dents.

In all, nine specimens were tested to evaluate the effect of severe dent damage on the residual strength and repair of tubular members. Two different dent depths were investigated, namely 25% and 50% of the tubulars diameter ( $D$ ), as well as two different diameter-to-thickness ratios ( $D/t$ ) of 34.5 and 69. The corresponding out-of-straightness ( $\delta_p$ ) following denting ranged from approximately 0.005 of the members length ( $L$ ) to 0.02 $L$ . The dent was imposed to each specimen by laterally loading a supported tubular at midspan with a steel wedge, simulating a knife-edge, under controlled displacement in order to cause a sharp dent profile. Each of the dented specimens was tested with simply supported end conditions under concentrically applied axial load.

Four of the specimens were non-repaired, where for each of the two dent depths two specimens were tested that had a  $D/t$  ratio of 34.5 and 69, respectively. Four of the specimens were repaired by internal grout, where each of these specimens had dent damage and section cross-sectional dimensions that corresponded to the non-repaired specimens. One specimen was tested that had a dent depth of 0.5 $D$  and  $D/t$  ratio of 69, and which was repaired using a grouted steel sleeve over the damaged section.

The observations drawn from this test program were as follows:

- 1) The non-repaired specimens were found to have their dent grow deeper under the application of axial load. This resulted in yielding of the tubular wall in the vicinity of the dented cross-section, leading to a reduction in stiffness and axial load carrying capacity.
- 2) The depth of the dent and the specimen's  $D/t$  ratio were found to influence the residual strength. The capacity of the non-repaired specimens with a dent depth of  $0.25D$  and  $D/t$  ratio of 34.5 and 69 was 42% and 32%, respectively, of their corresponding undamaged strength. The capacity of the non-repaired specimens having a dent depth of  $0.5D$  and  $D/t$  ratio of 34.5 and 69 was 18% and 12% of their corresponding undamaged strength.
- 3) The repair of the dented test specimens was found to inhibit the dent growth during testing, and resulted in an increase in the tubular's capacity. Dented specimens of larger  $D/t$  ratio benefited more from internal grouting. The increase in strength of the internal grout repaired specimens with a dent depth of  $0.25D$  was 1.6 and 2.8 times the non-repaired strength of tubulars with a  $D/t$  ratio of 34.5 and 69, respectively. For a dent depth of  $0.5D$  the increase in strength by internal grout repair was 1.3 and 2.9 times that of the non-repaired capacity for tubulars with a  $D/t$  ratio of 34.5 and 69. The grouted sleeve resulted in an increase of 5.1 times the non-damaged strength for the tubular with a dent depth of  $0.5D$  and  $D/t$  ratio of 69. The failure of the grouted sleeve repaired specimen was outside the sleeve, adjacent to the sleeve, where yielding and local buckling occurred. The out-of-straightness and  $D/t$  ratio of the damaged tubular at this location has a significant effect on the repaired capacity. The failure of the internal grout repaired specimens consisted of yielding of the steel tubular in the vicinity of the dented cross-section, resulting in the formulation of a plastic hinge as global buckling occurred. The

dent depth and out-of-straightness at the dented section have a significant effect on member repaired capacity.

- 4) An examination of the data of the study and that of tests from concurrent and previous experimental studies involving simply supported columns subjected to axial load indicates that dent-damaged tubulars with a dent depth of less than  $0.2D$  and out-of-straightness less than  $0.002L$  can have their strength restored to that of a corresponding undamaged tubular by the use of internal grout repair. Specimens of deeper dent depth would require the use of a grouted clamp in order to restore their strength to that of a corresponding non-damaged tubular.

The analytical study involved evaluating the ability of existing methods to predict the behavior of the test specimens, which had dent depths greater than that which the methods were calibrated for. The methods of analysis for the non-repaired specimens included beam-column formulations; the DENTA computer program; moment-thrust-curvature  $M-P-\phi$  integration (similar to that used by the computer program BCDENT); and the non-linear finite element method. For the internal grout repaired specimens the same analysis methods except for DENTA were used. The grout was accounted for in these analyses, with the  $M-P-\phi$  integration method being based on section analysis of a grout filled tubular. To assess the methods for a broader range of dent depth and member  $D/t$  ratio, the test specimens of concurrent and previous experimental studies were also analyzed.

The observations drawn from this analytical study were as follows:

- 1) The beam-column formulations for non-repaired specimens were found to underestimate the residual strength of the test specimens of the current study. However, the unity check procedure developed by Loh [1993] was found to

significantly overestimate the capacity of the specimens having a dent depth of 0.5D, where the predicted capacity was 1.33 and 1.93 times that of the experimental strength of specimens with a D/t ratio of 34.5 and 69, respectively. This can be explained by the fact that the procedure has been calibrated for specimens having dent depths up to about 0.2D. For dent depths of 0.3D to 0.5D, Ellinas' formulation [1984] is the most accurate of the beam-column analysis methods. However, unlike Loh's formulation that explicitly includes member end moments, as it is the case in practical design, Ellinas' formulation does not accommodate moments directly. The predicted capacity using the M-P- $\phi$  method was found to underestimate specimen strength, particularly for tubulars having the higher D/t ratio of 69 where the estimated strength was 0.68 and 0.37 of the experimental capacity for specimens with a dent depth of 0.25D and 0.5D, respectively. The poor estimate in specimen capacity by the M-P- $\phi$  integration method of analysis is due to the use of the empirical M-P- $\phi$  relationships developed by Duan et al. [1993] for tubulars with dent depths up to about 0.2D. The finite element method, using the non-linear computer program ABAQUS [1993], was found to provide the most accurate prediction of specimen strength and general behavior. However, the analysis are time consuming in that the denting process is also simulated and a new dent depth requires a complete new analysis. The ratio of predicted-to-experimental capacity was found to have a mean of 1.01 and a coefficient of variation of 17% using the finite element method in conjunction with measured specimen material and geometric properties.

- 2) The computer program DENTA [Taby et al. 1986] conservatively underpredicted the capacity of the two test specimens with a dent depth of 0.25D. For dent depths greater than 0.3D the program had convergence problems.

- 3) The analysis of the internal grout repaired specimens of the current study was found to be overestimated by the beam-column formulation of Parsanejad [1987]. Better accuracy was achieved using the modified AISC method recommended by Loh [1991], where the mean coefficient of variation for the ratio of predicted-to-experimental capacity was 1.01 and 11%, respectively. This accuracy was achieved using a value for the grout modulus  $E_g$  based on 80% of the measured grout cube compressive strength in conjunction with the formula by Lamport [1988]. The stiffness of the grout was found to significantly effect the predicted behavior of the repaired tubulars using the M-P- $\phi$  and finite element methods, where full composite action was assumed. Both of these methods tended to over predict the stiffness and strength of the dented tubular. More conservative predictions were achieved using a reduced grout stiffness of  $E_g = 1$  ksi. For this latter set of analysis, the mean and coefficient of variation for the ratio of predicted-to-experimental capacity was 0.82 and 17% respectively, using the M-P- $\phi$  integration method, and 1.05 and 9% using the finite element method, respectively. When using the grout stiffness based on Lamport's formulation the mean and coefficient of variation were 1.05 and 18%, respectively, for the M-P- $\phi$  integration method and 1.24 and 7%, respectively, for the finite element method.
- 4) An assessment of the analytical methods by a comparison of predicted-to-experimental capacity of test specimens from the current, concurrent and previous studies indicated that, in an average sense, Loh's formulation is the most accurate of the beam-column analysis methods for predicting the residual strength of non-repaired tubulars with dent depths and  $D/t$  ratios in the range of 0 to 0.5D and 28 to 120, respectively. However, as noted above this formulation over predicts the capacity of specimens with dent depths of 0.5D. Ellinas' beam-column formulation gave a better prediction than Loh's for specimens with a dent depth of 0.5D. The M-P- $\phi$  integration method was found to have more scatter for the same range of dent depth and  $D/t$  ratio,

particularly for specimens having dent depths greater than  $0.2D$  or  $D/t$  ratios greater than 90. The finite element method using ABAQUS was found to be the most accurate of the analysis methods for non-repaired specimens having a dent depth and  $D/t$  ratio in the range of 0 to  $0.5D$  and 28 to 90, respectively. However, as noted above, the method is time consuming.

- 5) For the internal grout repaired specimens an assessment of the analytical methods by a comparison of predicted-to-experimental capacity of test specimens from the current, concurrent and previous studies indicated that the value of the grout modulus can have a significant effect on the predicted behavior. Uncertainties in the reported values of the grout modulus of previous studies [Boswell and D'Mello 1990] led to a large coefficient of variation in the predicted strength. For the same data base, Parsanejad's formulation and Loh's modified AISC method had a coefficient of variation of 19% and 22%, respectively, however the latter was found to have a mean value (0.94) for the ratio of predicted-to-experimental capacity that was conservative and closer to unity than the results using Parsanejad's method. The analysis of the same data base using the M-P- $\phi$  integration method for internal grout filled tubulars had a coefficient of variation of 18% and mean of 0.96, indicating a smaller improvement in accuracy compared to the modified AISC method. An assessment of the analysis of some of the specimens in the data base using the finite element method and assuming full composite action indicated that the capacity of the specimens is over predicted when the grout modulus has its full stiffness (i.e., when it is assumed that  $E_g$  has a value based on Lamport's formula with 80% of the compressive capacity). As in the M-P- $\phi$  integration analysis method a more conservative and accurate prediction is achieved when using a significantly reduced value for the grout modulus of  $E_g = 1$  ksi. The M-P- $\phi$  and finite element analysis methods both appear to be sensitive to grout properties, thereby making these methods unreliable for capacity prediction until a rigorous calibration can be made.

- 6) The comparison of the test results with an analytical parametric study on the feasibility of repair by Ricles et al. [1997] in a concurrent project indicates that dent depth and out-of-straightness both influence the residual strength and repairability. This parametric study found that a parabolic formula could be used to expressive the feasibility of repair as a function of member dent depth and out-of-straightness. A comparison of this expression with the test specimens having a  $D/t$  ratio of 34.5 resulted in good agreement, while that with specimens with  $D/t = 69$  showed more of a discrepancy and the need when evaluating tubulars with such a  $D/t$  ratio to refine the  $M-P-\phi$  integration method used in the analysis.

## **5.2. Recommendations**

Recommendations are made based on the completed research of this project. These recommendations include the application of the information and results acquired in this project as well as future research that is considered to be necessary in order to improve and generalize the completed research in order to make it more valuable to industry.

### **5.2.1. Recommendations for Application of Completed Research**

#### **Repair of Dented Members:**

- 1) Depending on the level of required repair strength needed of a dented tubular, internal grout repair is recommended for tubulars with dent depths less than  $0.15D$  and out-of-straightness of  $0.002L$  when the full design strength (i.e., undamaged capacity) is required of the member. For deeper dent depths, or greater out-of-straightness, grouted clamps are recommended when the member's full undamaged capacity is required to be restored. In cases when the full undamaged strength does not have to be restored, internal grout repair



may be considered. In designing the clamp, consideration should be given to the damaged member's out-of-straightness to ensure proper fit up as well as susceptibility of the tubular to failure at the end of the clamp.

#### **Capacity Prediction of As-Dented Members:**

- 2) Because of its ease of use, Loh's unity check method for the analysis of the residual strength of non-repaired dented tubulars [Loh et al. 1992] is recommended for members with dent depths up to  $0.3D$ .
- 3) For dents between 30% and 50% of the member's diameter  $D$  use Ellinas' formulation [1984]. However, provisions should be made to incorporate the effect of the end moments.
- 4) To estimate the capacity for multiple-dent cases, in which dents are present at different longitudinal locations and in different circumferential orientations, check each dent at midspan, as indicated above, subjected to axial load and the moment components resolved about the dent cross-sectional axes.
- 5) If more accurate estimates are required for the multiple-dent case, use BCDENT or an similar M-P- $\phi$  integration based analysis program, provided that dent depths are less than  $0.30D$ .
- 6) For single-dent members at midspan deeper than  $0.50D$ , conduct a finite element analysis that includes the denting process. For deep dented cases, the shape of the dent cross section becomes important - flat versus a hammock-shaped dent trough. Use of flat dents is conservative.

### Capacity Prediction of Internal Grout Repaired Members:

- 7) Use Loh's formulation [1991] up to dent depths of  $0.50D$  with the end moments decomposed unto the dent cross sectional axes. Assume grouts typical of those used offshore. In absence of specific data, use a cube strength of 40 MPa and a steel-grout modular ratio of 18.
- 8) Use of the current version of BCDENT with calculated M-P- $\phi$  input for grout filled tubulars is only recommended to obtain an indication of capacity.
- 9) Unless further calibration is made, finite element analyses are not recommended due to cost, effort, and uncertainty.

### 5.2.2. Recommendations for Future Research

Based on the research results described on this report, the following studies are recommended for future work:

- 1) Experimental tests of *short* as-dented and grouted-dented tubular columns with dent depths between 30% and 50% of their diameter to determine the moment-rotation behavior at constant axial load for a given  $D/t$  ratio. These test results will acquire information on the M-P- $\phi$  relationships needed to fully utilize BCDENT.
- 2) Additional tests as above to study the effect of the dent cross-sectional shape likely to occur in tubulars with relatively large  $D/t$  ratio. In this case, the dent trough is not flat but hammock-shaped. Members with more realistic dent shape should have significantly higher residual strength than those with flat dents.

- 3) More extensive non-linear finite element studies of existing experimental results in order to more thoroughly evaluate the sensitivity of predicted behavior to modeling assumptions and to develop calibrated models.

## REFERENCES

- ABAQUS User's Manual (Version 5.3)* (1993), Copyright Hibbitt, Karlsson and Sorensen, Inc., 100 Medway Street, Providence, Rhode Island, 02906.
- American Concrete Institute (1992), "Building Code Requirements for Reinforced Concrete and Commentary", ACI, ACI 318-89 (Revised 1992).
- American Institute of Steel Construction (1994), "Manual of Steel Construction - Load and Resistance Factor Design", AISC, Volume I, Second Edition.
- American Petroleum Institute (1993), "Recommended Practice for Planning, Designing and Constructing Fixed Offshore Platforms - Load Resistance and Factor Design", API, RP2A-LRFD, 20th Edition.
- Banon, H., Bea, R. G., Bruen, F. J., Cornell, C. A., Krieger, W. F., and Steward, D. A. (1994), "Assessing Fitness for Purpose of Offshore Platforms. I: Analytical Methods and Inspections", *Journal of Structural Engineering*, ASCE, Vol. 120, No.12.
- Banon, H. (1994), "Assessing Fitness for Purpose of Offshore Platforms. II: Risk Management, and Repair", *Journal of Structural Engineering*, ASCE, Vol. 120, No.12.
- Boswell, L. F. and D'Mello, C. A. (1990), "Residual and Fatigue Strength of Grout-Filled Damaged Tubular Members", OTH 89 314, Offshore Technology Report, U.K. Department of Energy.
- British Standards Institution (1982), "Code of Practice for Fixed Offshore Structures", BS-6235, London, England.

Canadian Standards Association (1992), "Steel Structures", Part III of the Code for the Design, Construction, and Installation of Fixed Offshore Structures, CAN/CSA-S473-92.

Chen, W. F. and Han, D. J. (1985), *Tubular Members of Offshore Structures*, Pitman Advanced Publishing Program, London, England.

Chen, W. F. and Lui, E. M. (1987), *Structural Stability - Theory and Implementations*, Elsevier Science Publishing Company, New York, New York.

Det Norske Veritas (1984), "Rules for the Design, Construction and Inspection of Offshore Structures", DnV, Høvik, Norway.

Duan, L., Chen, W. F. and Loh, J. T. (1993), "Moment Curvature Relationships for Dented Tubular Sections", *Journal of Structural Engineering*, ASCE, Vol. 119, No.3.

Dunn, F. P. (1983), "Offshore Platform Inspection", *Proceedings of the International Symposium on the Role of Design, Inspection and Redundancy in Marine Structural Reliability*, Marine Board, National Research Council, National Academic Press.

Ellinas, C. P. (1984), "Ultimate Strength of Damaged Tubular Bracing Members", *Journal of Structural Engineering*, ASCE, Vol. 110, No.2.

Ellinas, C. P. and Valsgard, S. (1985), "Collisions and Damage of Offshore Structures: A State-of-the-Art", *Proceedings of the Fourth International Offshore Mechanics and Arctic Engineering Symposium*, OMAE, Vol. 2, Dallas, Texas.

Fan, C.H. (1994), "Assessment and Prediction of the Behavior of Dent-Damaged and Internally Grout Repaired Tubular Steel Bracing Using Moment Curvature-Based

Integration Methods”, M.S. Thesis, Department of Civil Engineering, Lehigh University, Bethlehem, Pennsylvania.

Galambos, T. V. (1988), *Guide to Stability Design Criteria for Metal Structures*, Fourth Edition, Wiley-Interscience Publication, New York, New York.

Kim, W. (1992), “Behavior and Strength of Damaged Tubular Columns with End Restraints”, Ph.D. Dissertation, Department of Civil Engineering, Lehigh University, Bethlehem, Pennsylvania.

Lamport, W. B. (1988), “Ultimate Strength of Grouted Pile-to-Sleeve Connections”, PMFSEL DISS-1, Ferguson Structural Engineering Laboratory, The University of Texas.

Landet, E. and Lotsburg, I. (1992), “Laboratory Testing of Ultimate Capacity Dented Tubular Members”, *Journal of Structural Engineering*, ASCE, Vol. 118, No. 4.

Leblanc, L. (1994), “The Field Costs that Won’t Go Away”, *Offshore Magazine*, Penn Well Publication Company, September 1994.

Loh, J. T. (1991), “Grout-Filled Undamaged and Dented Tubular Steel Members”, EXXON Production Research Company Internal Report, Houston, Texas.

Loh, J. T., Kahlich, J. L., and Broekers, D. L. (1992), “Dented Tubular Steel Members”, EXXON Production Research Company Internal Report, Houston, Texas.

Loh, J. T. (1993), “Ultimate Strength of Dented Tubular Steel Members”, *Proceedings of the Third International Offshore and Polar Engineering Conference*, Vol. IV, Singapore.

MacIntyre, J. (1991), "An Analytical Study of Damaged Tubular Member Behaviour", Ph.D. Dissertation, Department of Civil Engineering, University of Toronto, Toronto, Canada.

*MARC User Manual* (1986), MARC Research Corporation, Version K-1.

Matthew, J., Ricles, J., Bruin, W. and Sooi, T. K. (1993), "Moment-Curvature Analysis of Dented Tubular Beam Columns", NSF Research Experience for Undergraduates (REU) Report, ATLSS Engineering Research Center, Lehigh University, Bethlehem, Pennsylvania.

Mihalic, P. (1992), "DATACQ Users Manual", AMES 199 Report, Department of Applied Mechanics and Engineering Sciences, University of California at San Diego.

Newmark, N. M. (1943), "Numerical Procedure For Computing Deflections, Moments and Buckling Loads", Transaction, ASCE, Vol 108.

Ostapenko, A., Wood, B.A., Chowdury, A., and Hebor, M.F. (1993), "Residual Strength of Damaged Tubular Members in Offshore Structures", Volume 1, ATLSS Report 93-03, ATLSS Engineering Research Center, Lehigh University, Bethlehem, PA.

Pacheco, L. A. and Durkin, S. (1988), "Denting and Collapse of Tubular Members - A Numerical and Experimental Study", *International Journal of Mechanical Sciences*, Vol. 30, No. 5.

Parsanejad, S. (1987), "Strength of Grout-Filled Damaged Tubular Members", *Journal of Structural Engineering*, ASCE, Vol. 113, No. 3.

- Parsanejad, S., Tyder, S., and Chin, K.Y. (1987), "Experimental Investigation of Grout-Filled Damaged Tubular Members", *Proceedings on Steel and Aluminum Structures*, University College, Cardiff, England.
- Parsanejad, S. and Gusheh, P. (1992), "Behavior of Partially Grout-Filled Damaged Tubular Members", *Journal of Structural Engineering*, ASCE, Vol. 118, No. 11.
- Ricles, J., Gillum, T. and Lamport, W. (1992), "Residual Strength and Grout Repair of Dent-Damaged Offshore Tubular Bracing - Phase I Study", ATLSS Report No. 92-14, ATLSS Engineering Research Center, Lehigh University, Bethlehem, Pennsylvania.
- Ricles, J., Gillum, T. and Lamport, W. (1994a), "Grout Repair of Dented Offshore Tubular Bracing - Experimental Behavior", *Journal of Structural Engineering*, ASCE, Vol. 120, No. 7.
- Ricles, J., Bruin, W., Sooi, T. K., and Fan, C.P. (1994b), "Behavior, Analysis, and Repair of Dented Marine Platform Bracing Member", *Proceedings of the 50th Annual Technical Session of the Structural Stability Research Council*, SSRC, Lehigh University, Bethlehem, PA.
- Ricles, J. (1996), "Chapter 7 - Analysis of Internally Grout Repaired Damaged Members", *Analysis and Software of Cylindrical Members*, CRC Press.
- Ricles, J.M. and Fan, C.H. (1996), "Analysis of Dent-Damaged and Internally Grout Repaired Tubular Steel Bracing Using Moment Curvature-Based Integration Methods", ATLSS Report 96-xx, ATLSS Engineering Research Center, Lehigh University, Bethlehem, Pennsylvania (in press).



- Ricles, J., Bruin, W., and Sooi, T. K. (1997), "Residual Strength and Grout Repair of Dent-Damaged Offshore Tubular Bracing - Phase II Study", ATLSS Report No. 97-12, ATLSS Engineering Research Center, Lehigh University, Bethlehem, Pennsylvania (in press).
- Smith, C. S., Kirkwood, W., and Swan, J. W. (1979), "Buckling Strength and Post-Collapse Behavior of Tubular Bracing Members Including Damage Effects," *BOSS '79*, Imperial College, London, England.
- Smith, C. S., Somerville, J. W., and Swan, J. W. (1981), "Residual Strength and Stiffness of Damaged Steel Bracing Members", *Proceedings of the Offshore Technology Conference*, OTC Paper 3981, Houston, Texas.
- Smith, C. S. (1983), "Assessment of Damage in Offshore Steel Platforms", *Marine Offshore Safety, Proceedings of an International Conference*, Glasgow, Scotland, Paper 15.
- Smith, C. S. (1986), "Residual Strength of Tubulars Combining Bending and Dent Damage", *Ninth Annual Energy-Sources Technology Conference and Exhibition*, New Orleans, Louisiana.
- Salman, W. A. (1994), "Damage Assessment of Tubular Members in Offshore Structures", Ph.D. Dissertation, Department of Civil Engineering, University of Toronto, Toronto, Canada.
- Sohal, I. S., and Chen, W. F. (1984), "Moment-Curvature Expressions for Fabricated Tubes", *Journal of Structural Engineering*, ASCE, Vol. 110, No. 11.
- Sohal, I. S., and Chen, W. F. (1987), "Local Buckling and Sectional Behavior of Fabricated Tubes", *Journal of Structural Engineering*, ASCE, Vol. 113, No. 3.

- Sohal, I. S., and Chen, W. F. (1988), "Local and Post-Buckling Behavior of Tubular Beam-Columns", *Journal of Structural Engineering*, ASCE, Vol. 114, No. 5.
- "Standard Test Method for Compressive Strength of Cylindrical Concrete Specimens" (1986), *ASTM Special Technical Publication C39-86*, ASTM, Philadelphia, Pennsylvania.
- "Standard Method of Making and Curing Concrete Test Specimens in the Laboratory" (1990), *ASTM Special Technical Publication C192-90a*, ASTM, Philadelphia, Pennsylvania.
- "Standard Test Methods for Tensile Coupon Testing" (1991), *ASTM Special Technical Publication E8-91*, ASTM, Philadelphia, Pennsylvania.
- "Standard Test Methods for Compressive Strength of Hydraulic Cement Mortars" (1992), *ASTM Special Technical Publication C109-02*, ASTM, Philadelphia, Pennsylvania.
- Taby, J., Moan, T., and Rashed, S. M. H. (1981), "Theoretical and Experimental Study of the Behavior of Damaged Tubular Members in Offshore Structures", *Norwegian Maritime Research*, Vol. 9, No. 2.
- Taby, J. and Moan, T. (1985), "Collapse and Residual Strength of Damaged Tubular Members", *Proceedings, Fourth International Conference on Behavior of Offshore Structures*, Delft, Netherlands.
- Taby, J. (1986), "Residual Strength of Damaged Tubulars. Final Report," NTNF Programme for Marine Structures, SINTEF Report No. 6.10, Trondheim, Norway.

Tebbett, I. E. and Forsyth, P. (1987). "New Test Data on the Capacity of Cement-Filled Steel Tubulars", *Proceedings of the Offshore Technology Conference*, OTC Paper 5484, Houston, Texas.

Ueda, Y. and Rashed, S. M. H. (1985), "Behavior of Damaged Tubular Structural Members", *Proceedings of the Fourth International Offshore and Polar Engineering Symposium*, Vol. II, Dallas, Texas.

Wimpy Offshore (1986), "Static Testing of Grout-Filled Joints and Members", Doc. No. 2/86A, Report to EPR Co., Southwest Research Institute.

Yao, T., Taby, J., and Moan, T. (1988), "Ultimate Strength and Post Ultimate Strength Behaviour of Damaged Tubular Members in Offshore Structures", *Journal of Offshore Mechanics and Arctic Engineering*, Transactions of the ASME, Vol. 110, No. 3.

Table 2.1 - Experimental Test Specimen Matrix

Test Series	Specimen	D/t	Dent-Depth, $d_d$	Description of Specimen
1	A10	34.5 69	0.25D	Damaged, Non-repaired
	C10			Damaged, Non-repaired
2	A12	34.5 69	0.5D	Damaged, Non-repaired
	C12			Damaged, Non-repaired
3	A11	34.5 69	0.25D	Damaged, Internal Grout Repair
	C11			Damaged, Internal Grout Repair
4	A13	46 69	0.5D	Damaged, Internal Grout Repair
	C13			Damaged, Internal Grout Repair
5	C15	69	0.5D	Damaged, Grouted Sleeve Repair

Table 2.2 - Measured Specimen Pre-Damaged Geometry

Test Series	Specimen	Diameter, D (inches)		Thickness, t (inches)		Length, L (inches)	Initial Ovality $\frac{D_{max}-D_{min}}{D_{mean}}$	$\delta_o/L$
		Mean	COV	Mean	COV			
1	A10	8.629	0.004	0.255	0.007	177.2	0.004	0.0002
	C10	8.585	0.003	0.127	0.008	180.1	0.004	0.0001
2	A12	8.625	0.003	0.253	0.007	177.0	0.001	0.0005
	C12	8.608	0.004	0.125	0.008	180.0	0.003	0.0003
3	A11	8.633	0.002	0.250	0.008	177.9	0.004	0.0007
	C11	8.582	0.005	0.126	0.009	180.5	0.003	0.0001
4	A13	8.625	0.001	0.253	0.007	177.5	0.001	0.0001
	C13	8.598	0.005	0.125	0.008	179.8	0.003	0.0002
5	C15	8.601	0.005	0.125	0.008	180.5	0.003	0.0003

Table 2.3 - Test Specimen Parameters Based on Measured Specimen Geometry

Test Series	Specimen	D/t	KL/r	$\lambda = \frac{KL}{r} \sqrt{\frac{\sigma_y}{E}}$
1	A10	33.8	59.9	0.622
	C10	67.6	59.9	0.670
2	A12	34.1	59.8	0.644
	C12	68.9	59.8	0.676
3	A11	34.5	60.1	0.663
	C11	68.1	59.9	0.661
4	A13	34.1	59.9	0.645
	C13	68.8	59.7	0.685
5	C15	68.8	59.9	0.650

Table 2.4 - Measured Specimen Damaged Geometry

Test Series	Specimen	$\delta_p/L$	$d_d/D$	$w_d$ (inch)
1	A10	0.0064	0.253	7
	C10	0.0052	0.250	7
2	A12	0.0174	0.491	8.5
	C12	0.0152	0.495	8.5
3	A11	0.0059	0.251	7
	C11	0.0051	0.255	7
4	A13	0.0211	0.500	8.5
	C13	0.0166	0.498	8.5
5	C15	0.0150	0.499	8.5

Table 2.5 - Measured Specimen Steel Material Properties

Test Series	Specimen	Steel Elastic Modulus $E_s$ (ksi)	Static Yield Stress $\sigma_{y,s}$ (ksi)	Dynamic Yield Stress $\sigma_{y,d}$ (ksi)	Compressive Yield Stress $\sigma_{y,c}$ (ksi)	Ultimate Stress $\sigma_u$ (ksi)	Strain at Strain Hardening $\epsilon_{sh}$ (in/in)	Strain at Max. Stress $\epsilon_u$ (in/in)	Strain at Fracture $\epsilon_{max}$ (in/in)	Young's Modulus at $E_{sh}$ (ksi)
1	A10 C10	29870 29950	36 37	39 39	38 38	60 53	0.027 0.007	0.19 0.17	0.26 0.30	482 586
2	A12 C12	29700 30100	34 38	36 41	36 39	60 54	0.025 0.012	0.22 0.20	0.30 0.31	667 428
3	A11 C11	29985 29960	36 36	39 38	39 38	60 53	0.027 0.009	0.19 0.18	0.26 0.31	482 570
4	A13 C13	29700 29990	34 39	36 42	36 41	60 55	0.025 0.010	0.22 0.23	0.30 0.33	667 411
5	C15	30100	35	38	39	52	0.008	0.20	0.30	531

† Compressive Yield Stress Reported is Based on Static Measurement

Table 2.6 - Measured Specimen Grout Material Properties

Test Series	Specimen	Compressive Grout Stress $f'_g$ (ksi)	Grout Elastic Modulus <sup>1</sup> $E_g$ (ksi)
1	A10	-	-
	C10	-	-
2	A12	-	-
	C12	-	-
3	A11	5.97	3498
	C11	5.90	3477
4	A13	7.69	3970
	C13	7.55	3934
5	C15	3.77	2780

<sup>1</sup> Based on Equation (2.1)

Table 2.7 - Summary of Grout Cylinder Tests

Cylinder	Grout Cube Compressive Strength, $f'_g$ (psi)	Grout Cylinder Compressive Strength, $f'_c$ (psi)	Cylinder Elastic Modulus $E_c$ (ksi)
1	7550	4630	3750
2	7550	4890	3600



Table 4.1 - Test Specimen Peak Experimental Loads ( $P_{exp}$ )

Test Series	Specimen	Nominal Dent-Depth ( $d_d$ ) <sup>1</sup>	$P_{exp}$ (kips)	$\frac{P_{exp}}{P_y}$	Comments
1	A10	0.25D	98	0.37	Non-repaired
	C10		37	0.28	Non-repaired
2	A12	0.50D	39	0.16	Non-repaired
	C12		14	0.11	Non-repaired
3	A11	0.25D	158	0.62	Internal Grout Repaired
	C11		104	0.82	Internal Grout Repaired
4	A13	0.50D	50	0.21	Internal Grout Repaired
	C13		40	0.29	Internal Grout Repaired
	C15		72	0.56	Grouted Sleeve Repair

<sup>1</sup> Measured Dent-Depths are Reported in Table 2.4

Table 4.2 - Comparison of Non-Repaired Residual Strength ( $P_{nr}$ ) with Non-Damaged Specimen Capacity ( $P_o$ )

Test Series	Specimen	$P_{nr}$ (kips)	$\frac{P_{nr}}{P_o}$
1	A10	98	0.42
	C10	37	0.32
2	A12	39	0.18
	C12	14	0.12

Table 4.3 - Comparison of Repaired Strength ( $P_r$ ) with Non-Repaired ( $P_{nr}$ ) and Non-Damaged ( $P_o$ ) Specimen Capacities

Test Series	Specimen	$P_r$ (kips)	$\frac{P_r}{P_{nr}}$	$\frac{P_r}{P_o}$
3	A11	158	1.61	0.68
	C11	104	2.81	0.93
4	A13	50	1.28	0.23
	C13	40	2.86	0.32
	C15	72	5.11	0.64

Table 4.4 - Comparison of Predicted and Experimental Results for the Residual Strength of Damaged, Non-Repaired Specimens

Test Series	Spec.	$P_{exp}$ (kips)	Ellinas Equation	DENTA	UCDENT	Unity Check	M-P- $\Phi$	FEM
			$\frac{P_{Ellinas}}{P_{exp}}$	$\frac{P_{DENTA}}{P_{exp}}$	$\frac{P_{UCDENT}}{P_{exp}}$	$\frac{P_{UnityChk}}{P_{exp}}$	$\frac{P_{M-P-\Phi}}{P_{exp}}$	$\frac{P_{FEM}}{P_{exp}}$
1	A10	98	0.67	0.72	0.41	0.87	0.90	1.01
	C10	37	0.85	0.87	0.56	1.07	0.68	0.99
2	A12	39	0.71	*	0.27	1.33	0.86	0.81
	C12	14	0.92	*	0.38	1.93	0.37	1.24
Mean			0.79	0.79	0.40	1.25	0.70	1.01
COV			0.149	0.137	0.302	0.349	0.341	0.174

\* analysis did not converge.

Table 4.5 - Comparison of Predicted and Experimental Results for the Strength of Internal Grout Repaired Specimens (Grout Modulus Based on Eqn (2.1))

Test Series	Spec.	$P_{exp}$ (kips)	Parsanejad Equation	Modified AISC	M-P- $\Phi$	FEM
			$\frac{P_{Parsanejad}}{P_{exp}}$	$\frac{P_{Mod-AISC}}{P_{exp}}$	$\frac{P_{M-P-\Phi}}{P_{exp}}$	$\frac{P_{FEM}}{P_{exp}}$
3	A11	158	1.02	1.10	1.19	1.15
	C11	104	1.05	1.09	1.19	1.37
4	A13	50	1.26	0.96	0.98	1.22
	C13	40	1.14	0.87	0.81	1.23
Mean			1.12	1.01	1.05	1.24
COV			0.093	0.113	0.179	0.065

Table 4.6 - Comparison of Predicted and Experimental Results for the Strength of Internal Grout Repaired Specimens (Reduced Grout Modulus  $E_g = 1$  ksi)

Test Series	Spec.	$P_{exp}$ (kips)	M-P- $\Phi$	FEM
			$\frac{P_{M-P-\Phi}}{P_{exp}}$	$\frac{P_{FEM}}{P_{exp}}$
3	A11	158	0.86	1.13
	C11	104	0.65	0.89
4	A13	50	0.98	1.11
	C13	40	0.81	1.09
		Mean	0.82	1.05
		COV	0.166	0.091

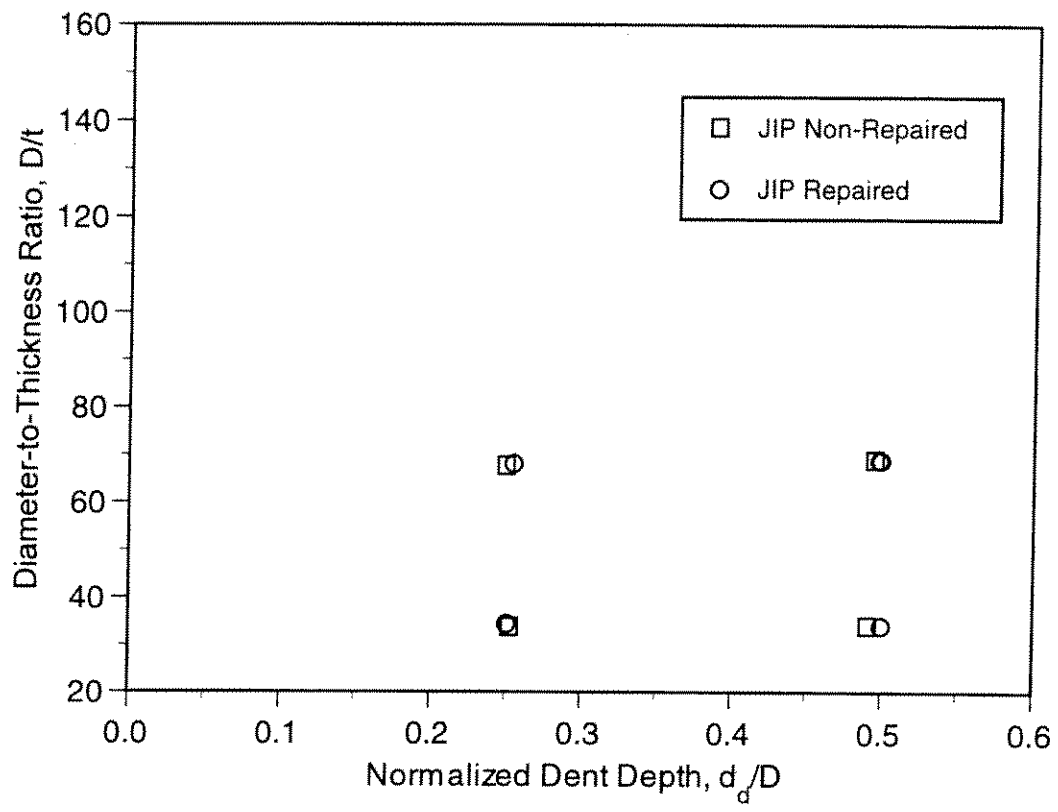


Figure 2.1 - Range of Measured Specimen  $D/t$  and  $d_d/D$  Ratios Tested in Current Program

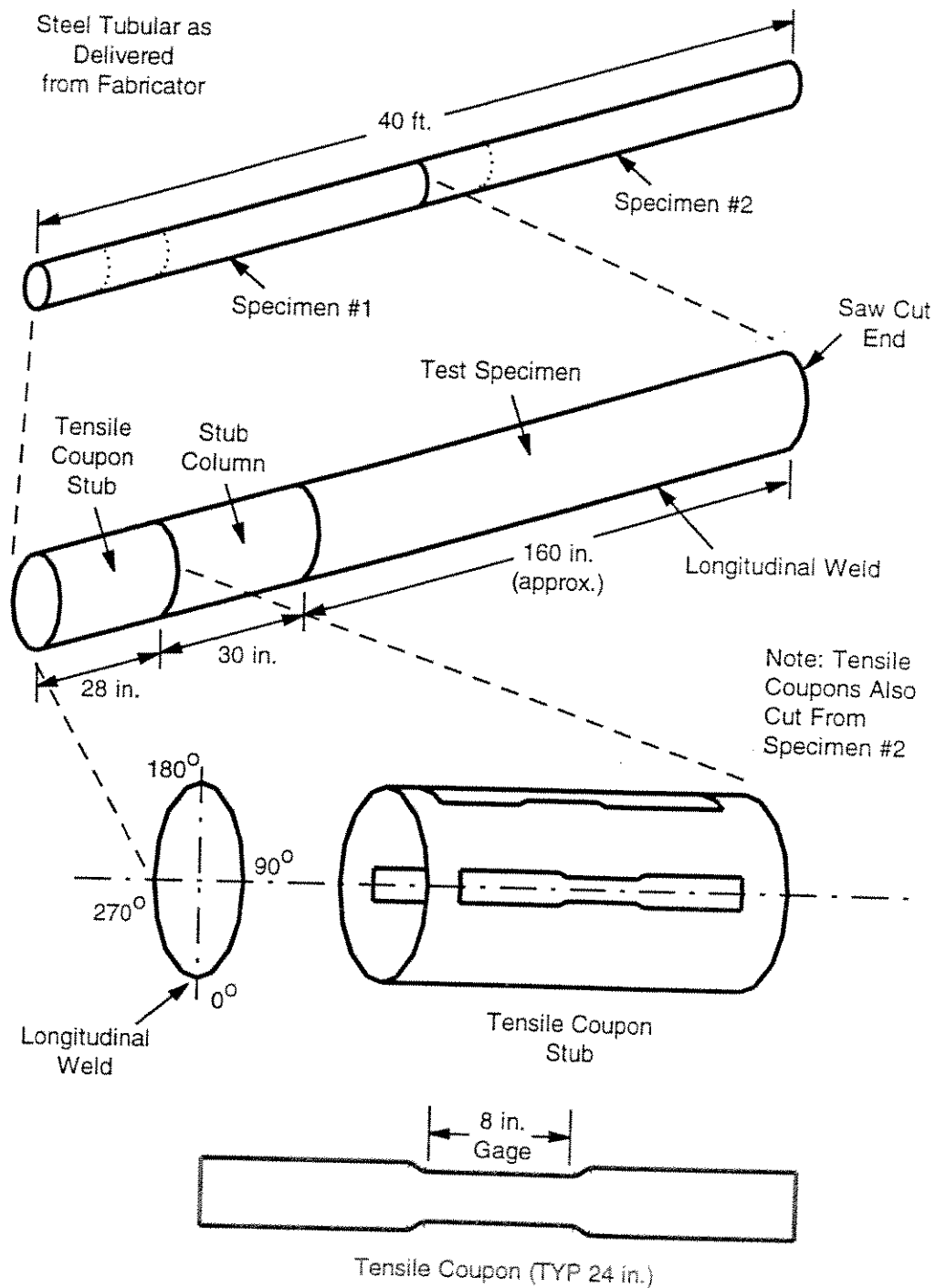
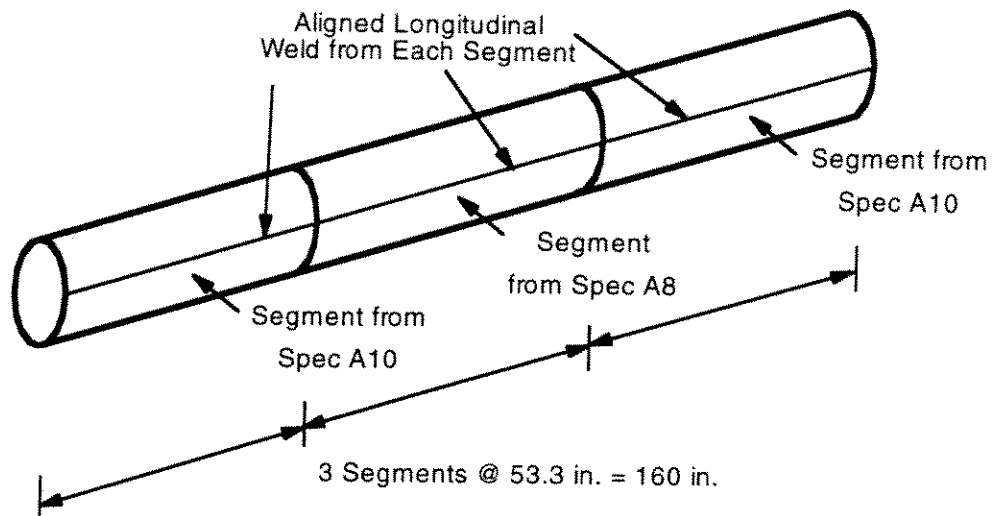


Figure 2.2 - General Description of ASTM A53 Steel Tubular Showing Location of Test Specimens and Various Material Property Specimens

### Specimen A12



### Specimen A13

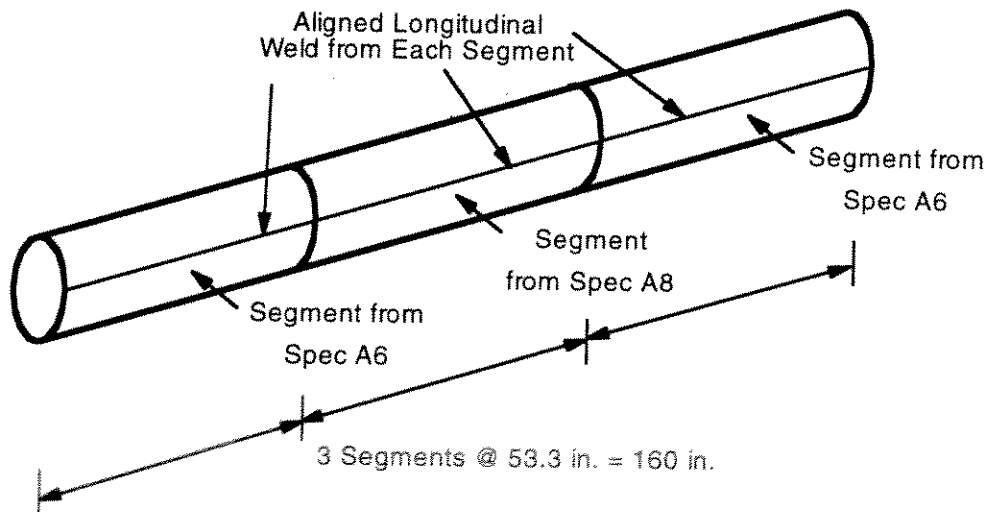


Figure 2.3 - Fabrication of Specimens A12 and A13 from Undamaged Segments of Specimens A6, A8, and A10 of Companion Study by Ricles et al. [1997]

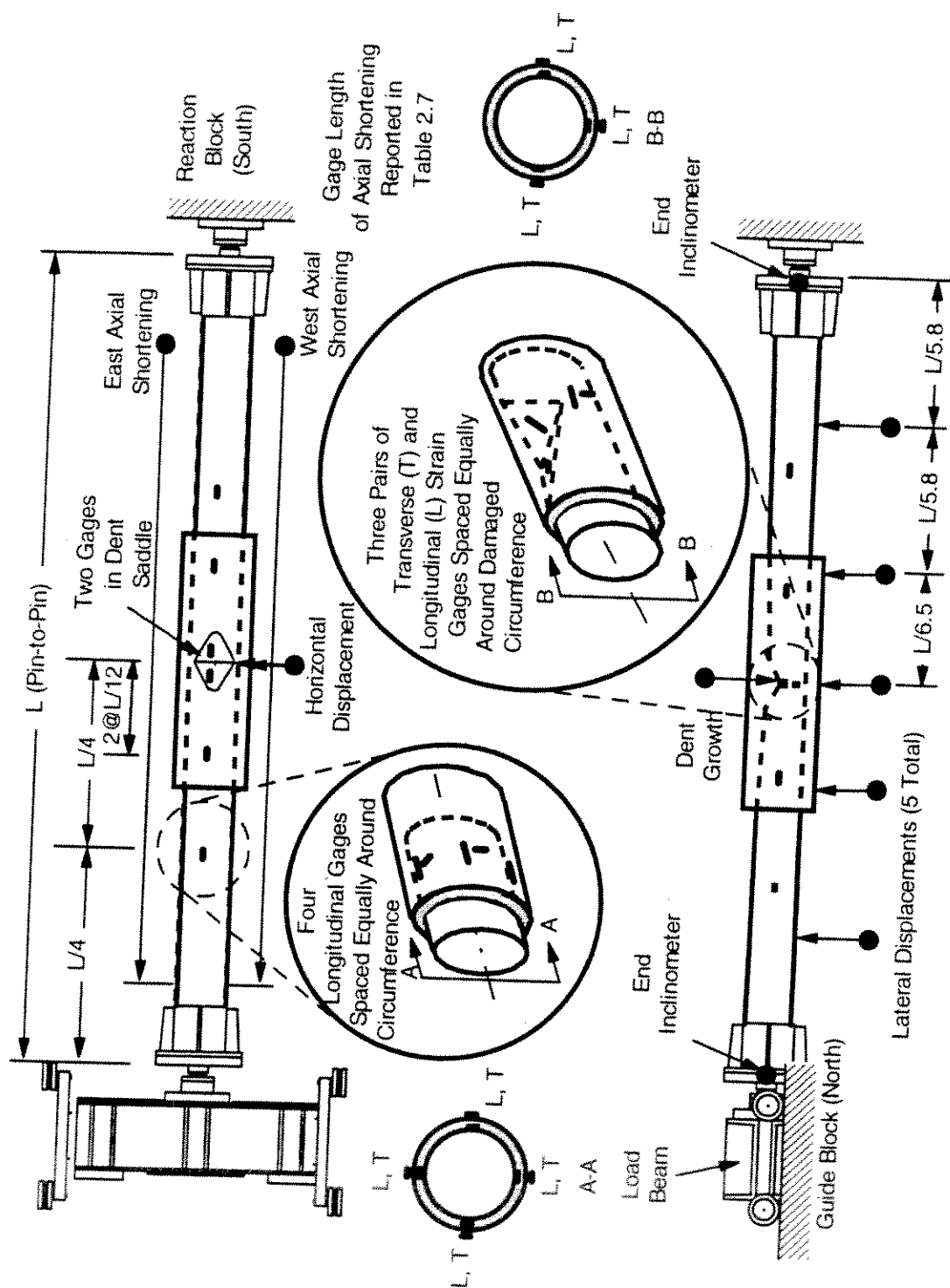


Figure 2.35 - Instrumentation for Grouted Sleeve Repaired Specimens





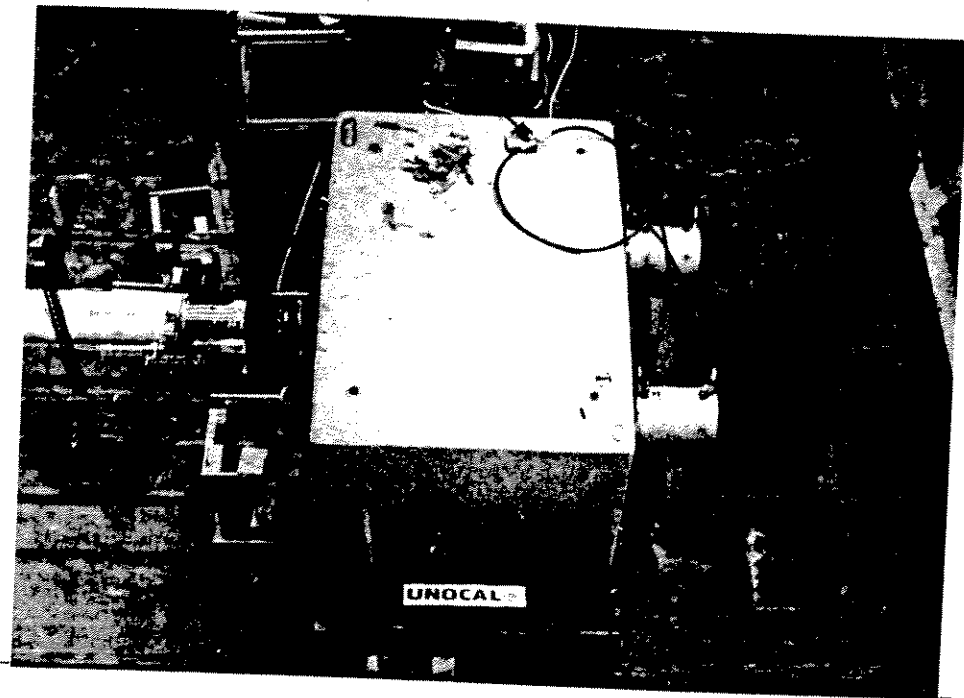


Figure 2.33 - Two 150 ton Hydraulic Cylinders Attached to Tension Rods and Reacting Against the Backside of the Reaction Block

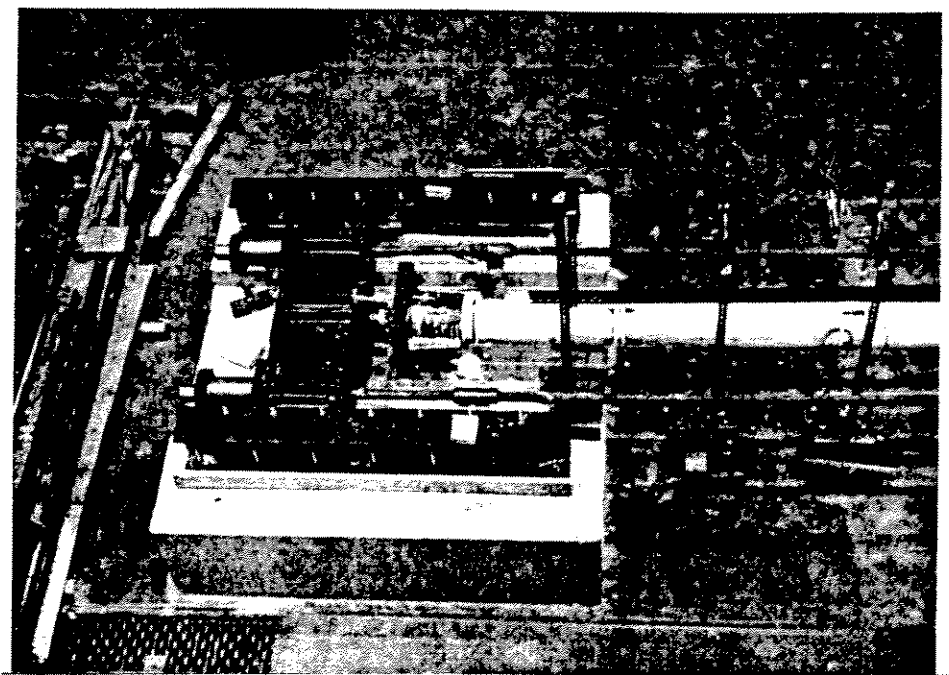


Figure 2.31 - Sliding Load Beam and Reinforced Concrete Guide Block

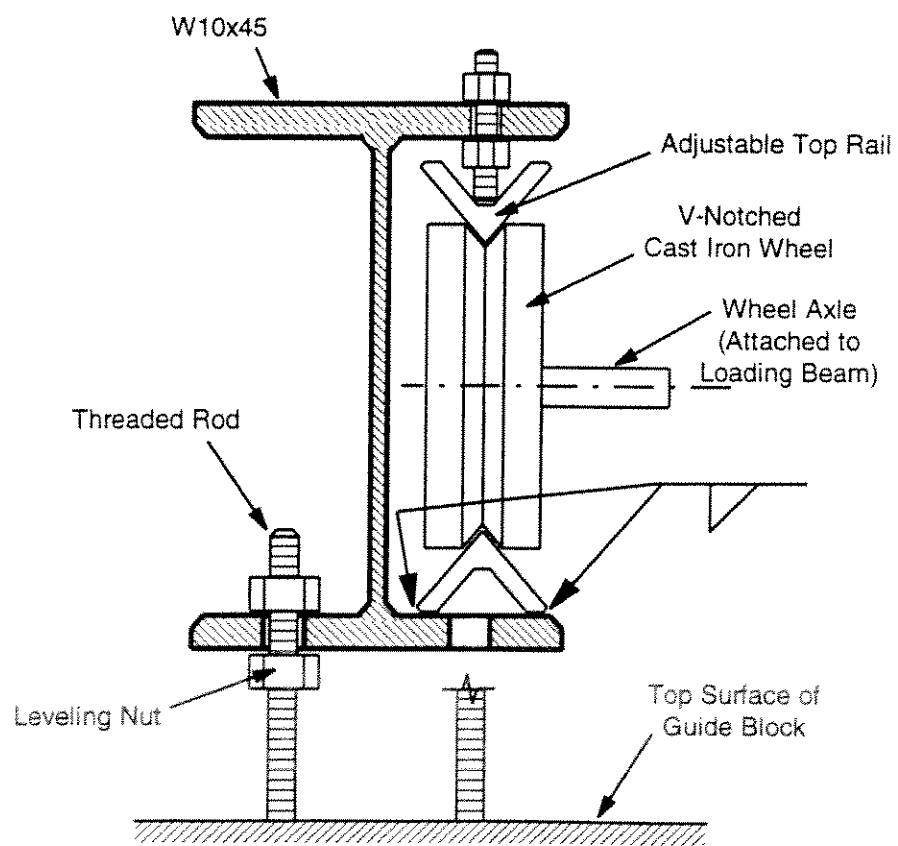


Figure 2.32 - Schematic of Sliding Track System Installed onto the Guide Block

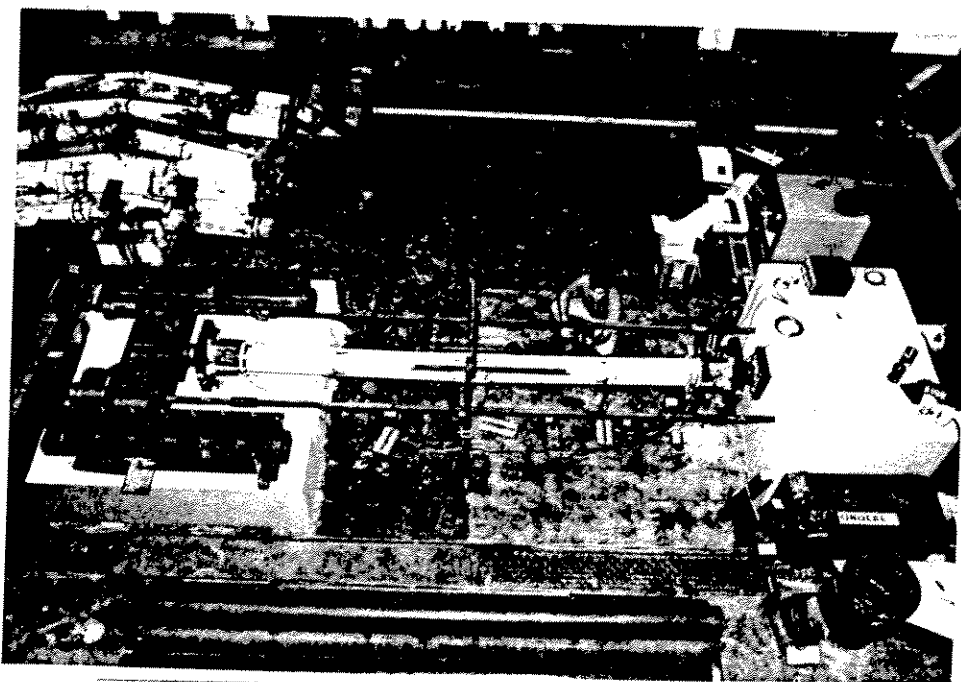


Figure 2.29 - 500 kip Self-Reacting Test Frame

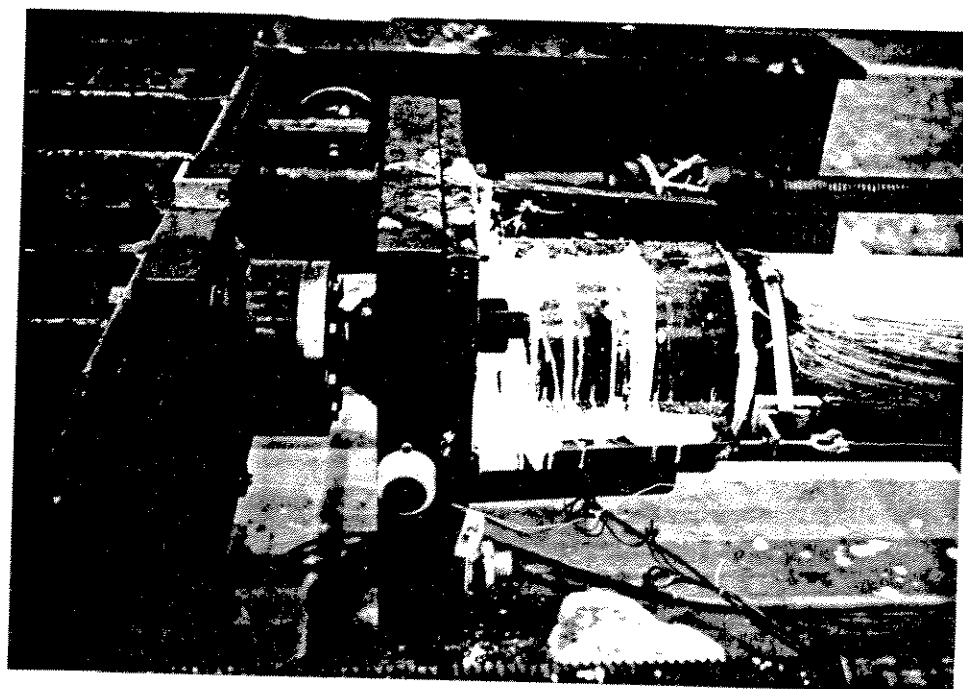


Figure 2.30 - Ball-and-Socket Bearing Connection Allowing Free Rotation of the Ends of the Specimen

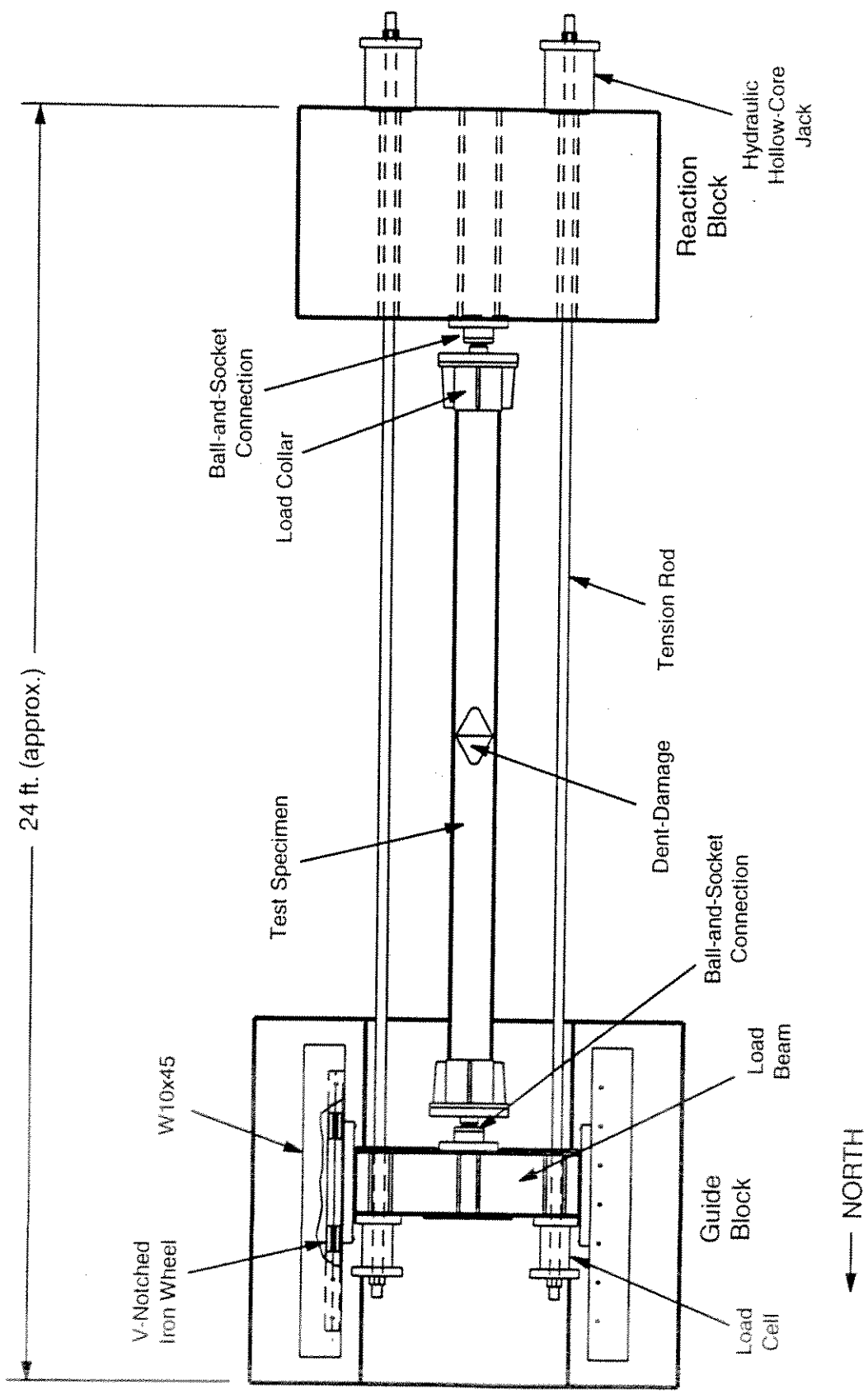


Figure 2.28 - Plan View of Experimental Test Set-up

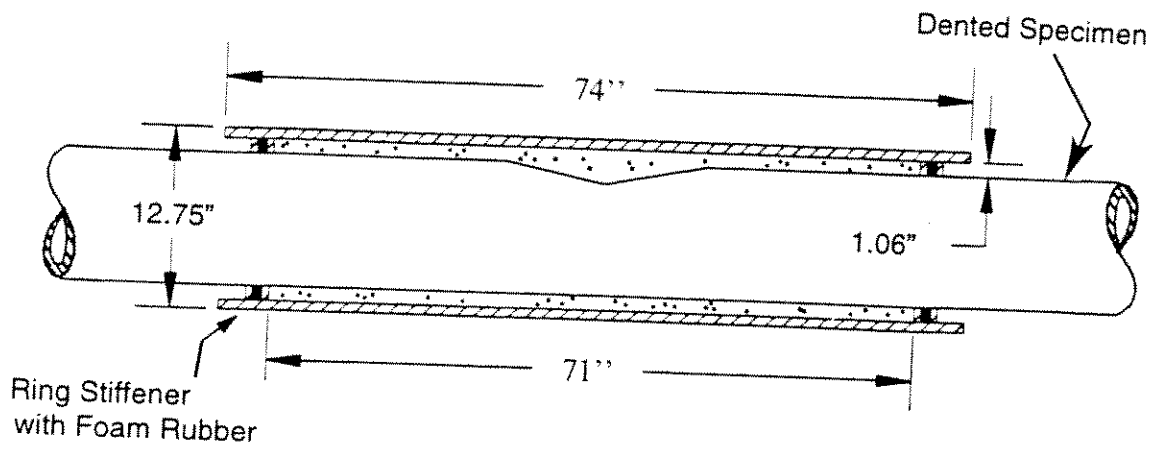


Figure 2.27(a) - Section of Sleeve Designed to Simulate Grouted Clamp

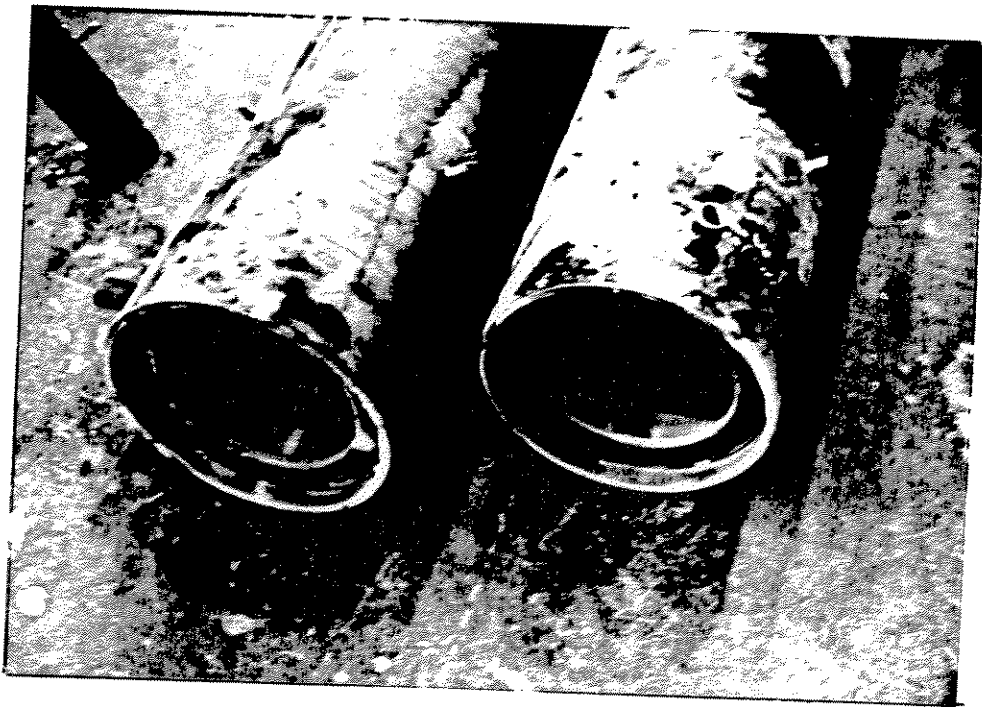


Figure 2.27(b) - End View of Sleeve Showing Ring Stiffener and Rubber Seal

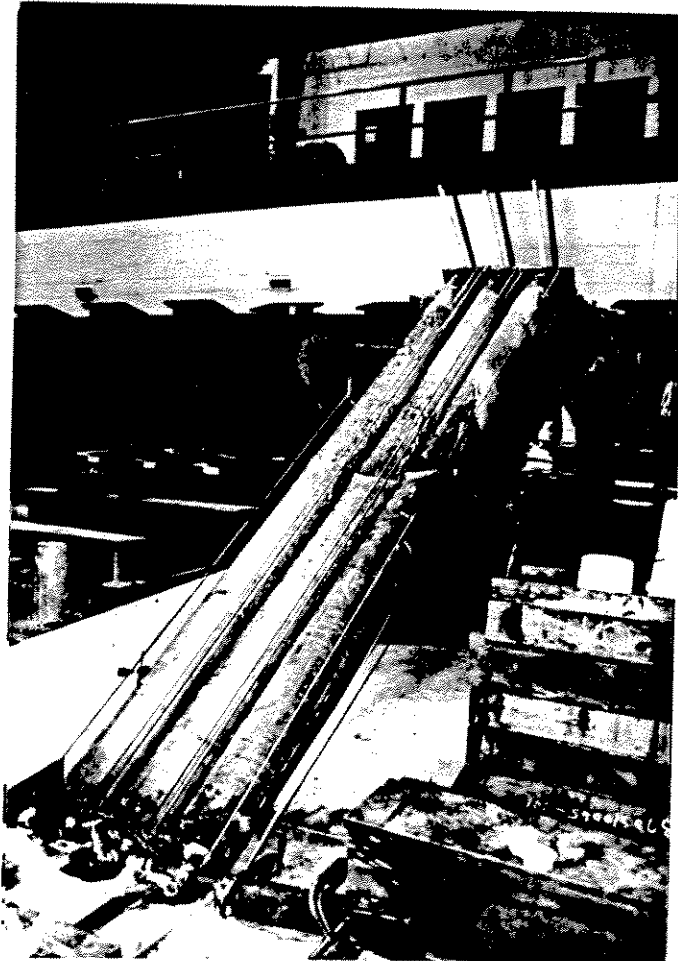


Figure 2.26 - Inclined Set-up for Internal Grouting of Repaired Specimens

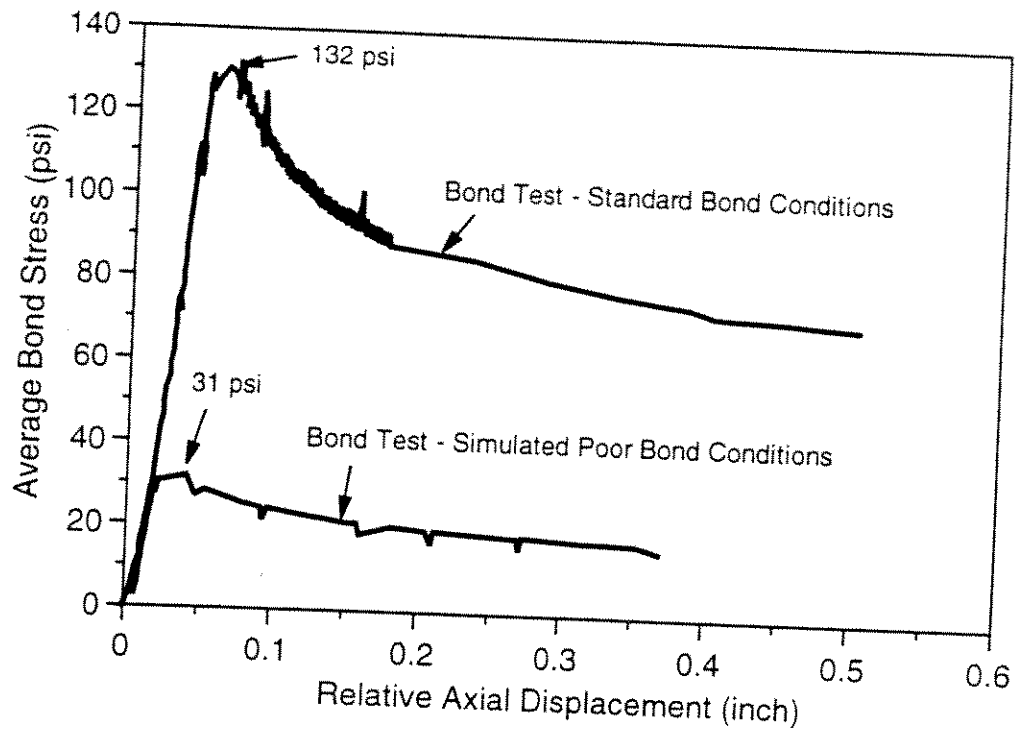


Figure 2.24 - Comparison of Average Shear Strength for Bond Test Specimens Simulating Standard and Poor Bond Conditions



Figure 2.25 - Grout Void at Ends of the Repaired Specimens Ensuring Exclusive Application of Load into the Steel Tubular



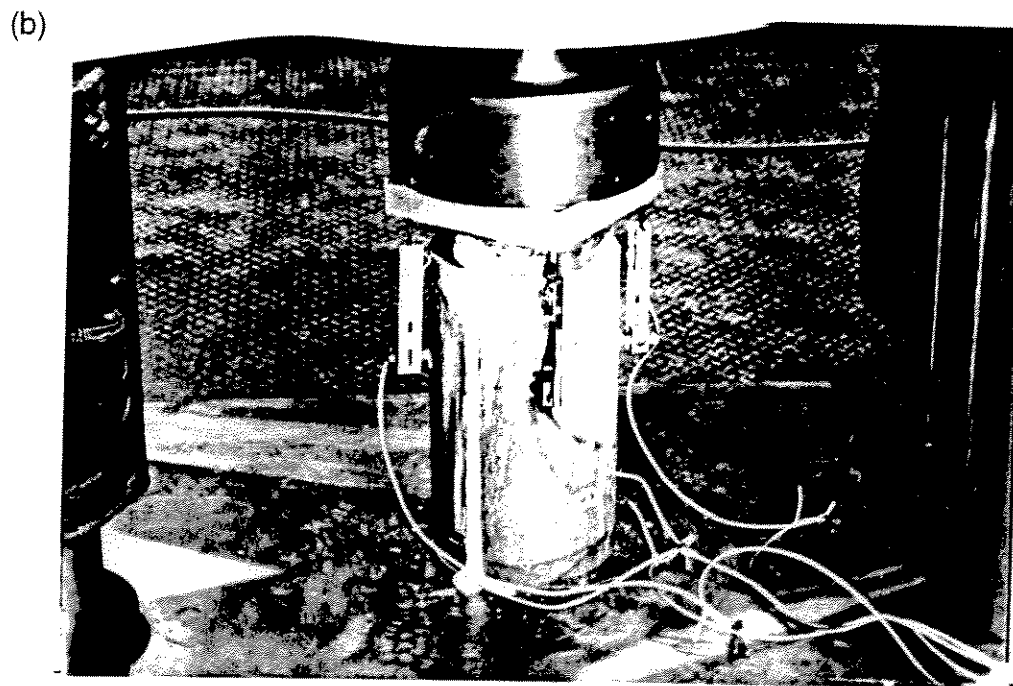
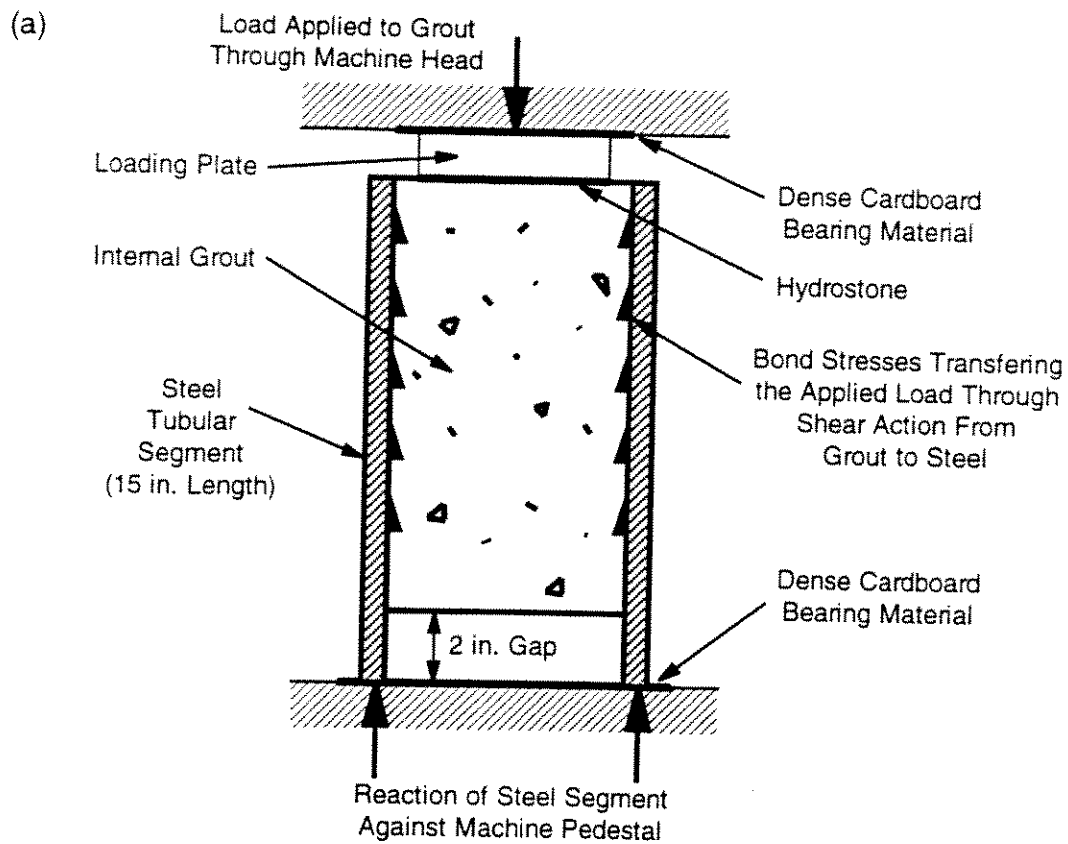


Figure 2.23 - (a) Schematic of General Set-up for Bond Specimen (Longitudinal Section Shown) and (b) Photograph of Bond Specimen in Universal Test Machine Prior to Loading

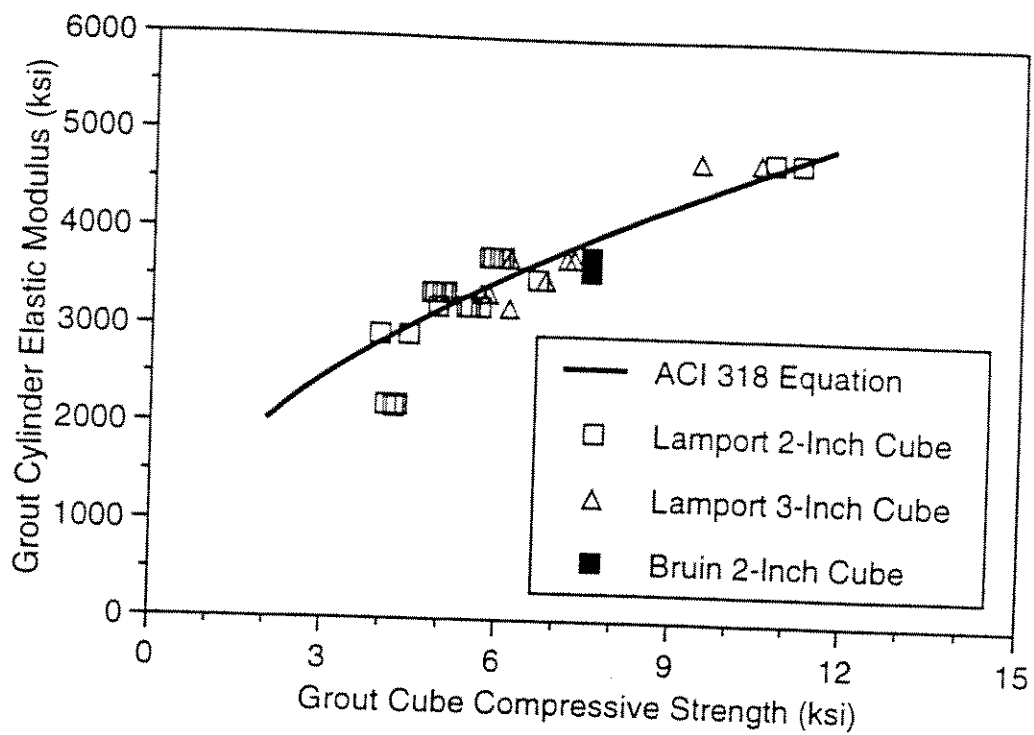


Figure 2.21 - Relationship Between Grout Elastic Modulus ( $E_g$ ) and Grout Cube Compression Strength ( $f'_g$ )

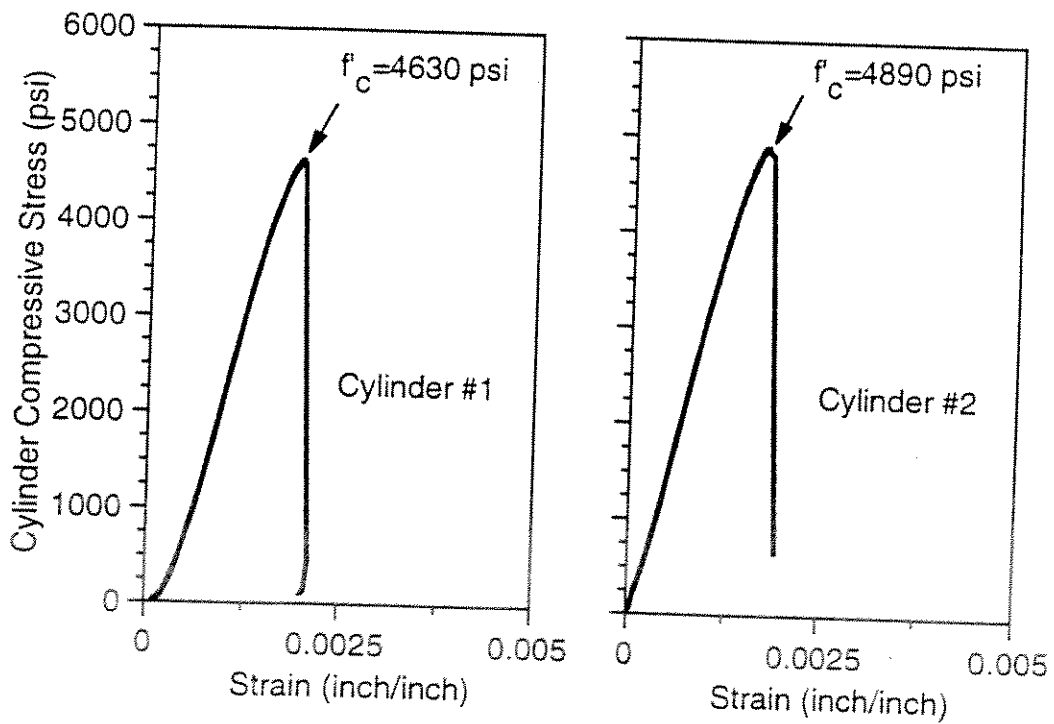


Figure 2.22 - Typical Grout Cylinder Stress-Strain Curve

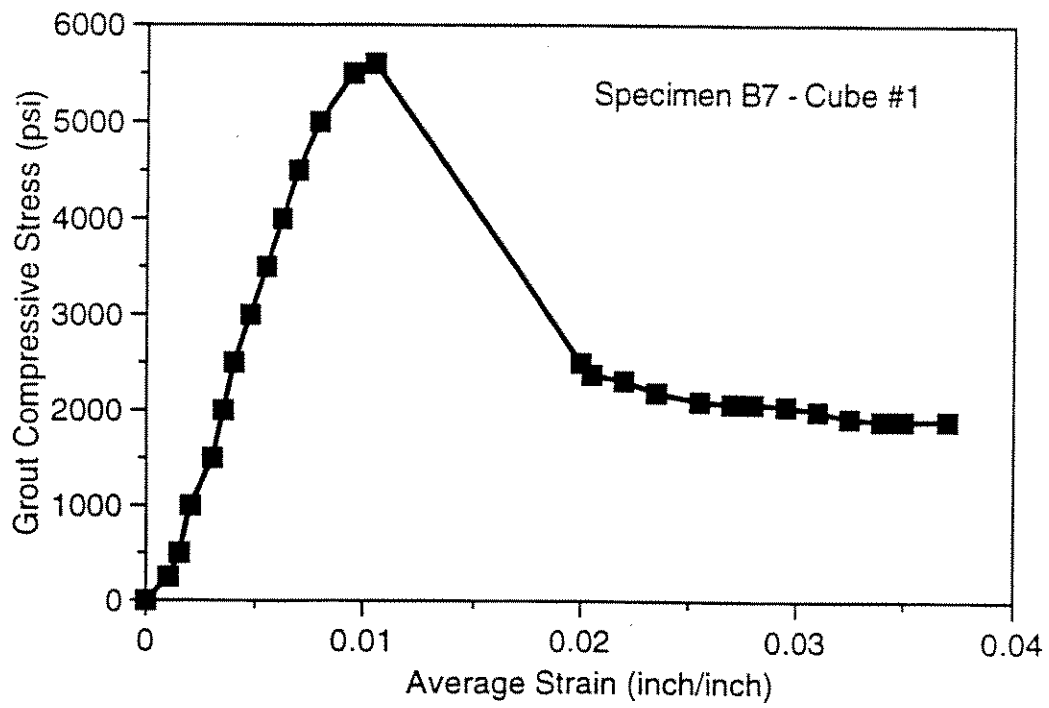


Figure 2.20 - Typical Grout Cube Stress-Strain Curve

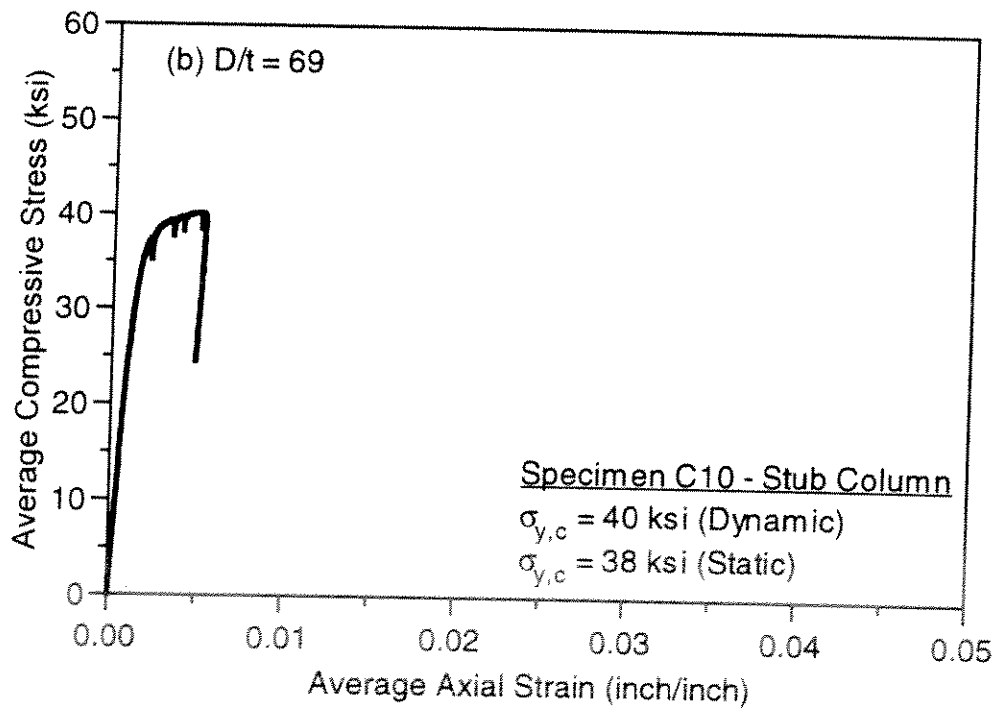
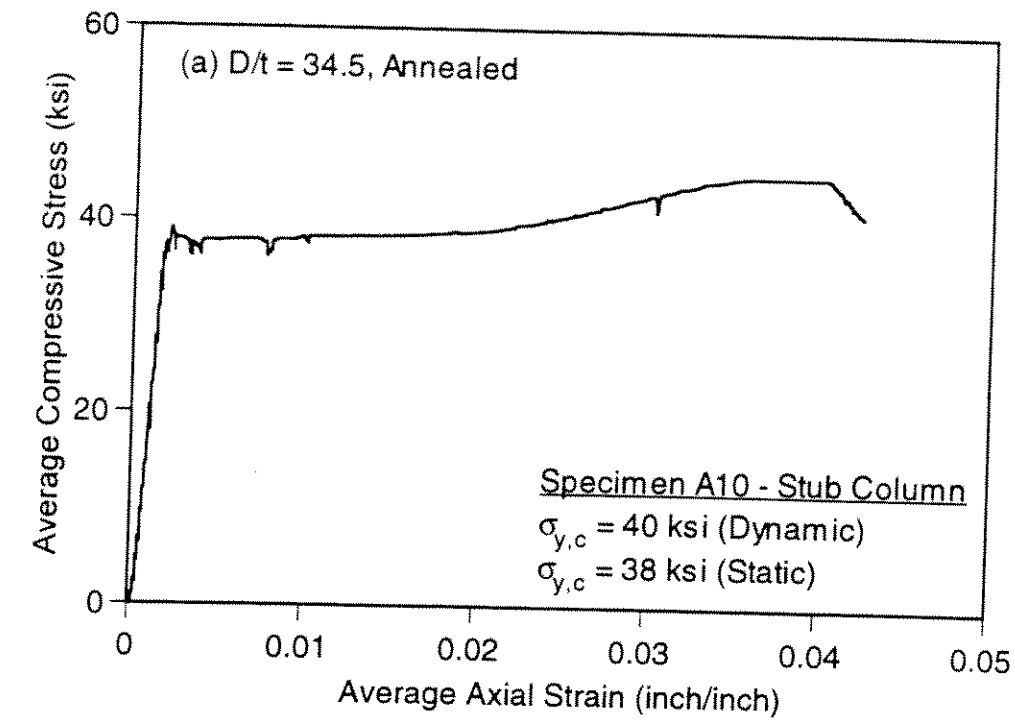


Figure 2.19 - Stub-Column Stress-Strain Curve for Specimens with (a)  $D/t = 34.5$  and (b)  $D/t = 69$

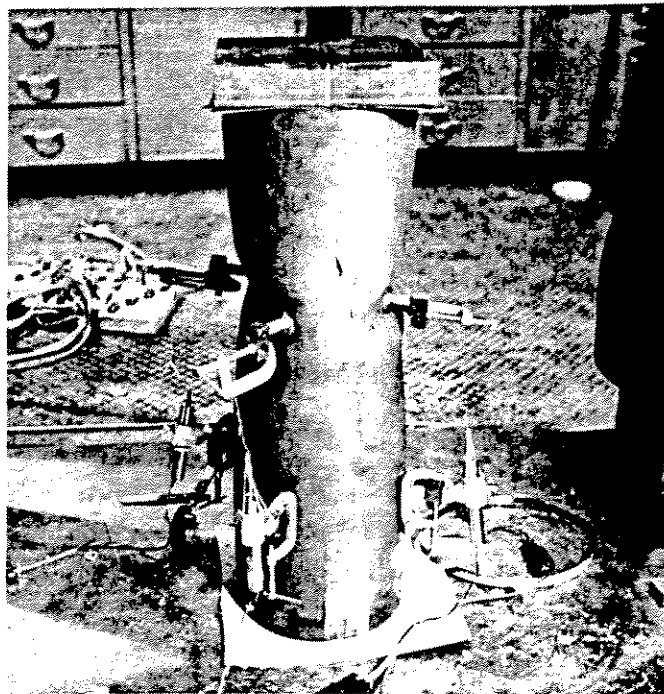


Figure 2.18 - Photograph of Stub Column Specimen After Development of Significant Local Buckling in the Post-Ultimate Load Range

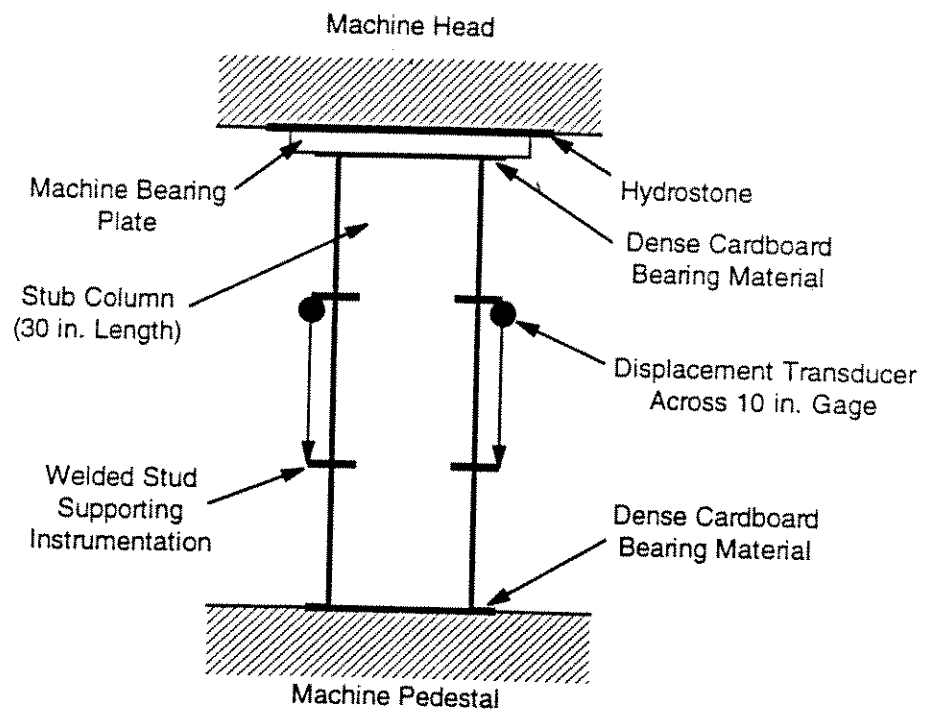


Figure 2.17 - General Stub Column Test Set-up and Instrumentation ( $D/t = 34.5$ )

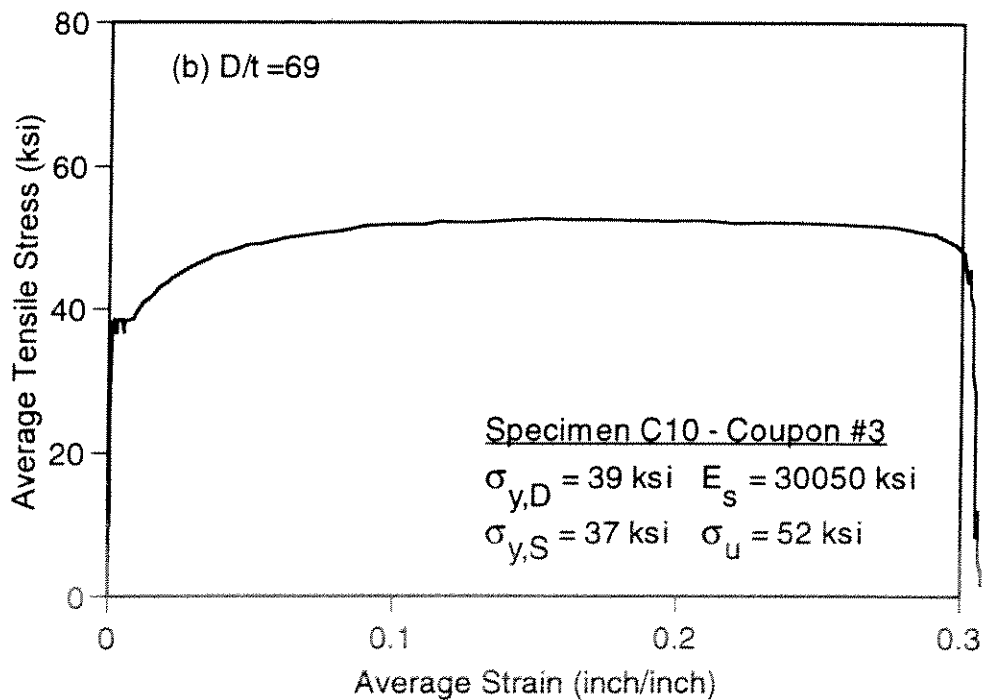
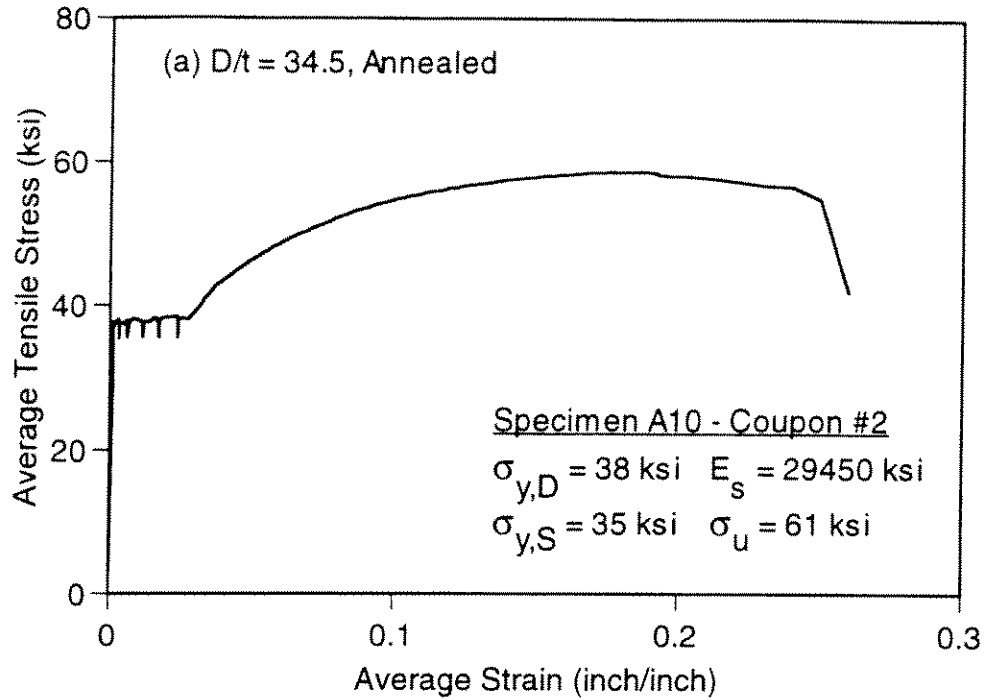


Figure 2.16 - Typical Tensile Coupon Stress-Strain Curves for Specimens with (a)  $D/t = 34.5$  and (b)  $D/t = 69$

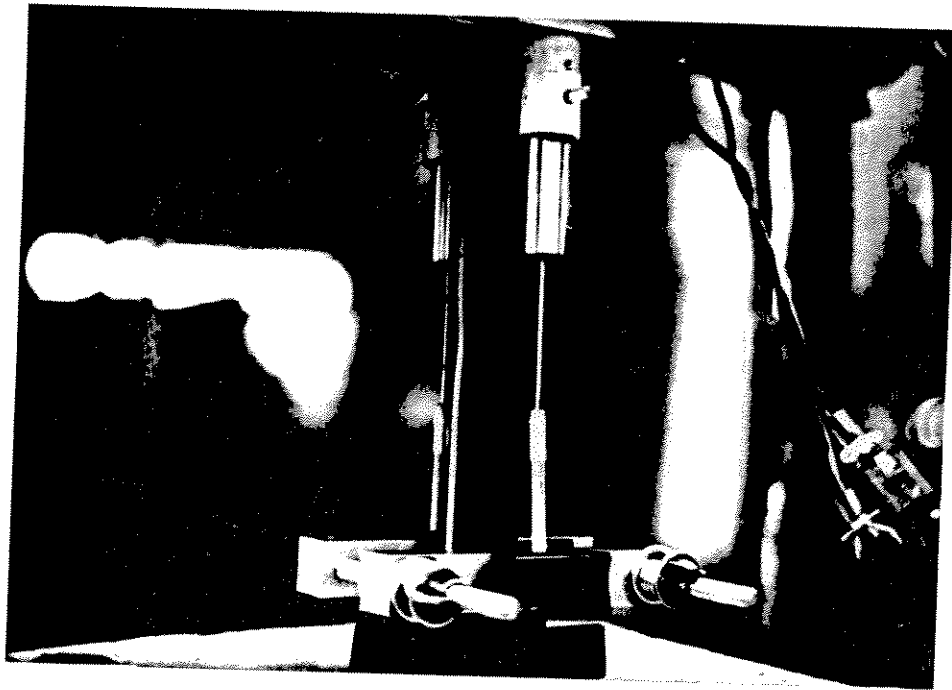


Figure 2.15 - View of Tensile Coupon During Testing



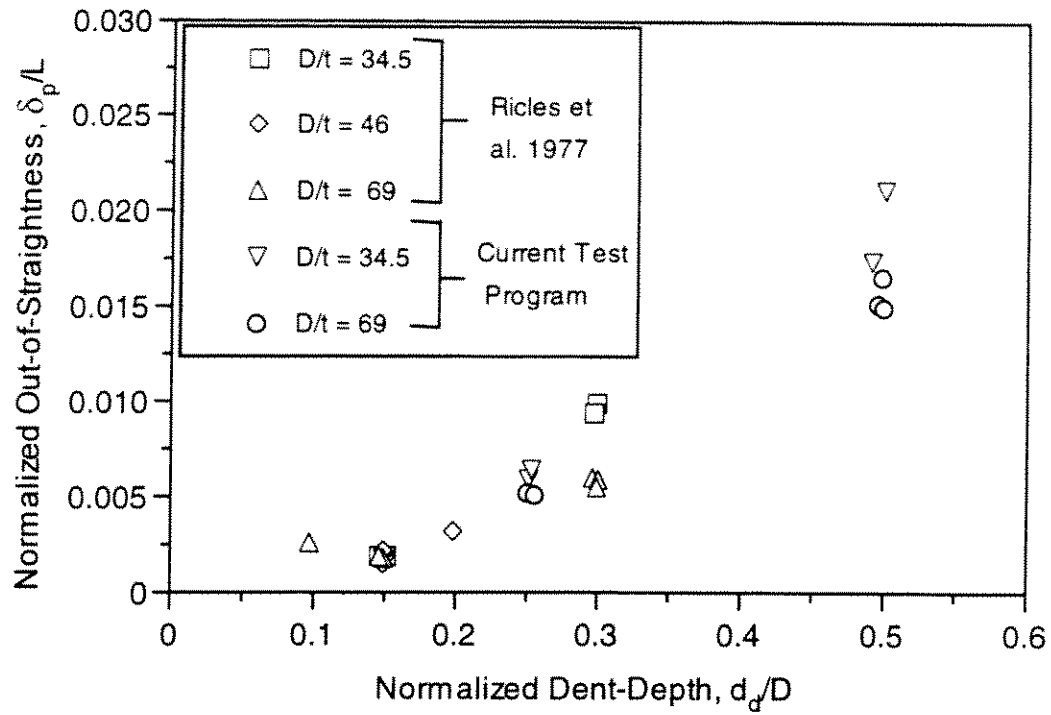


Figure 2.13 - Induced Global Out-of-Straightness After Infliction of Dent-Damage

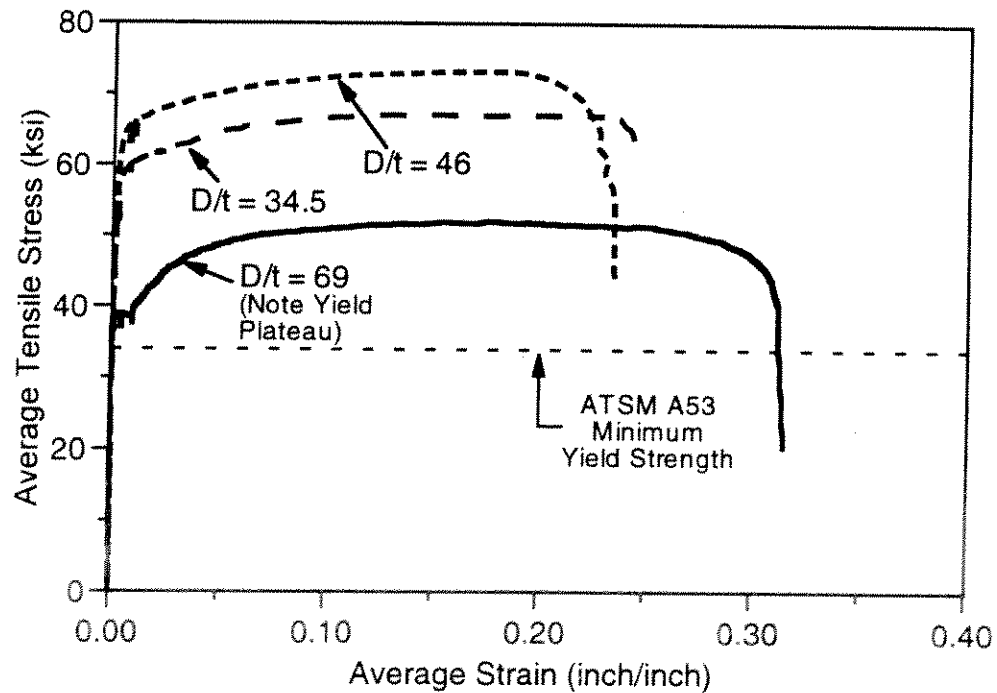


Figure 2.14 - Typical Stress-Strain Curves for Each D/t Prior to Annealing

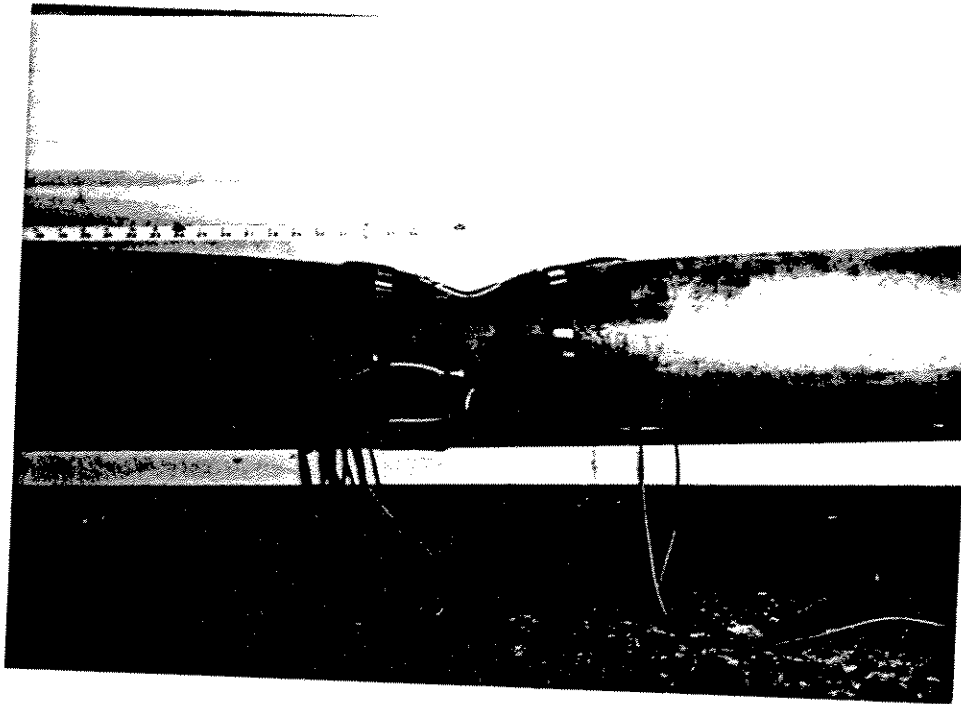


Figure 2.12(a) - Dent Profile for Specimen A11 ( $d_d = 0.25D$ )

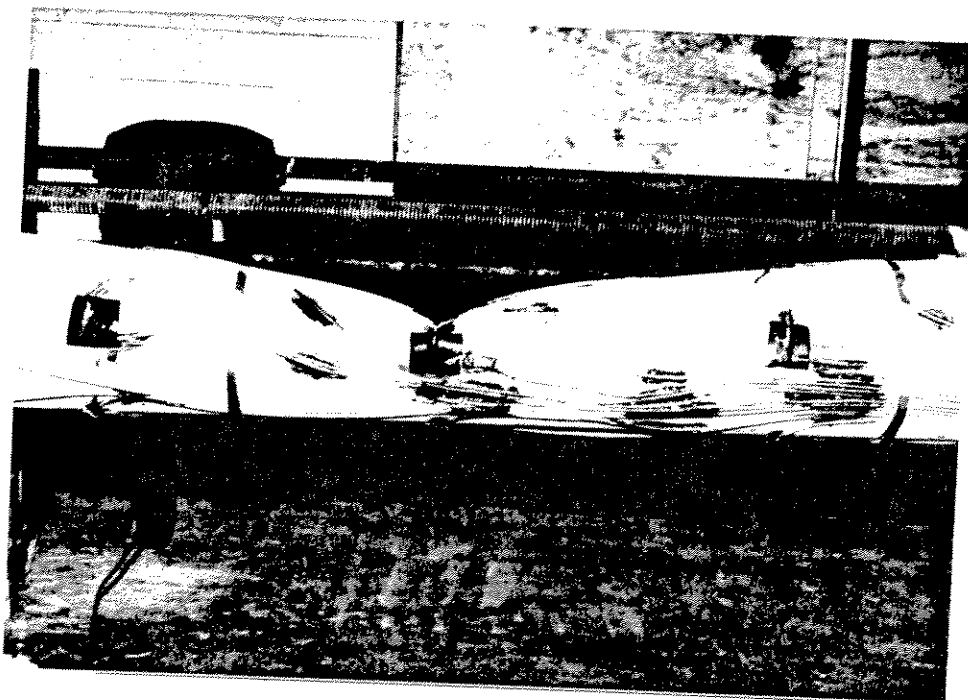


Figure 2.12(b) - Dent Profile for Specimen C15 ( $d_d = 0.5D$ )

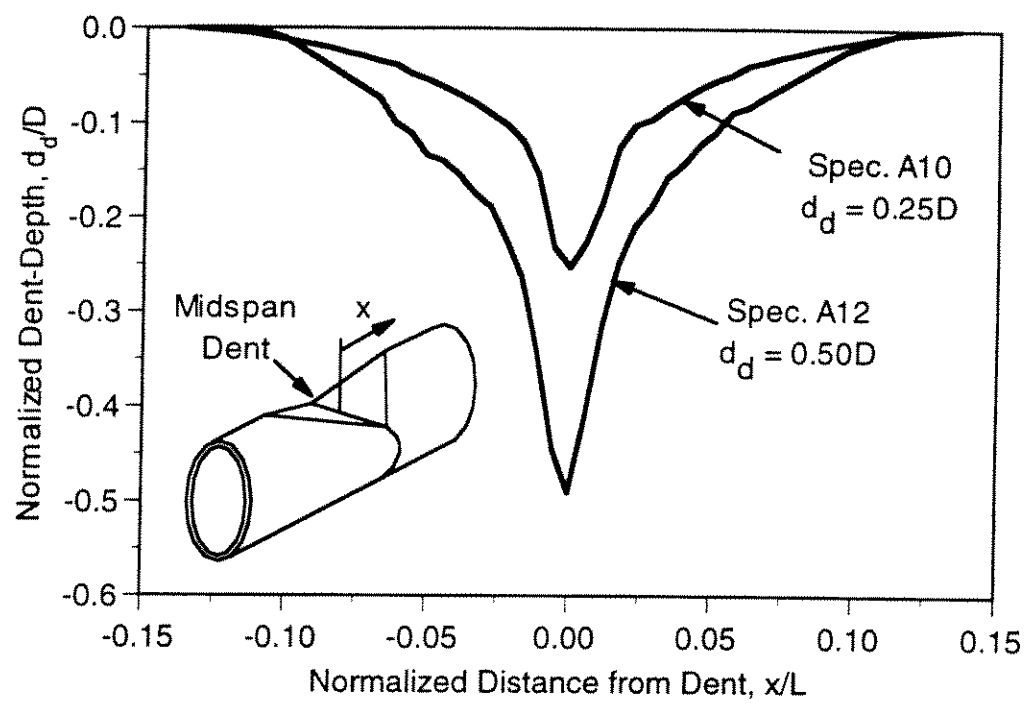


Figure 2.11 - Typical Dent Profiles for Specimens at Each Dent-Depth Tested

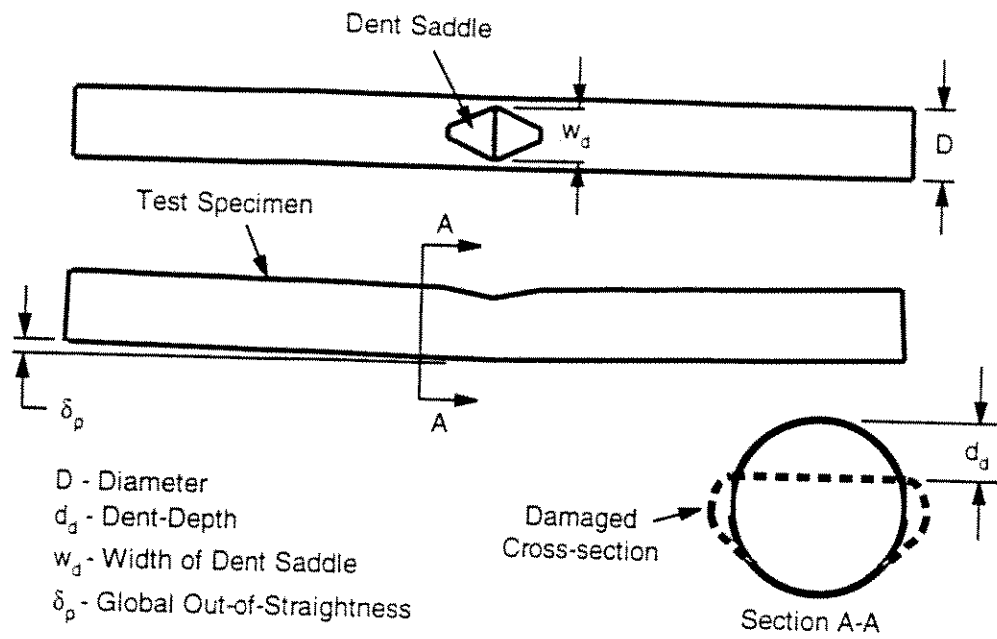


Figure 2.9 - Measured Geometric Parameters Characterizing Dent-Damage

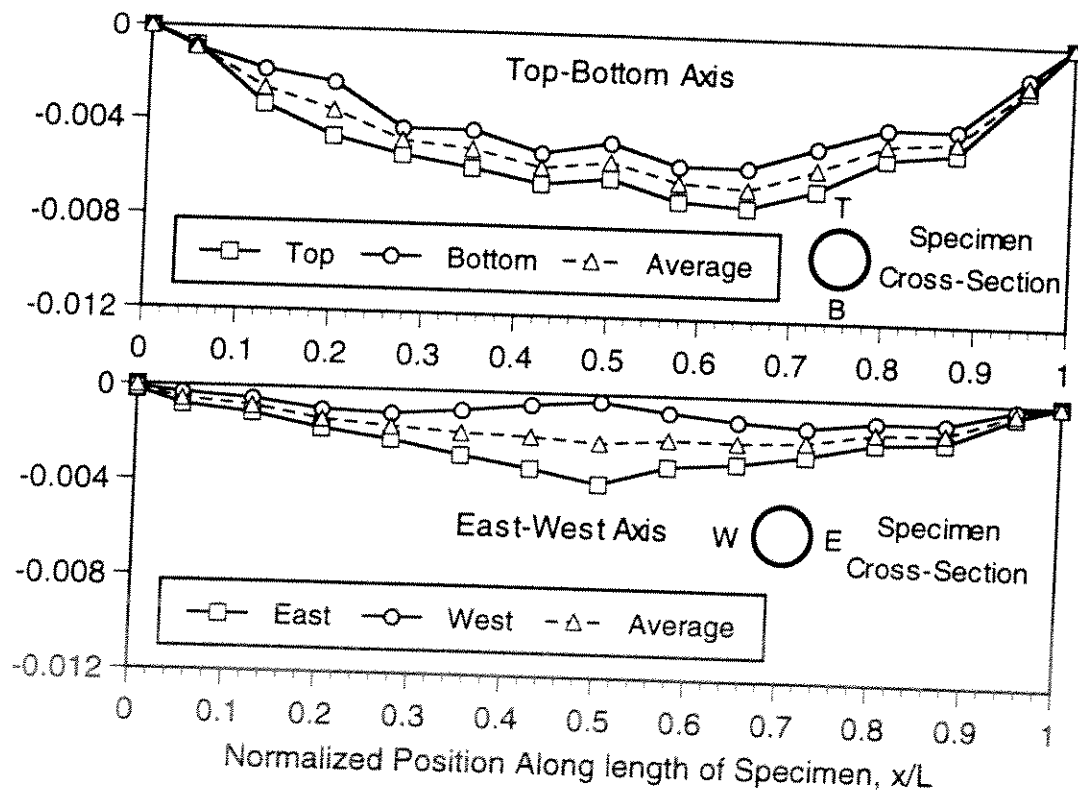


Figure 2.10 - Out-of-Straightness of Specimen A10 Measured After Infliction of Dent-Damage (Midspan Adjusted to Account for Dent-Depth)

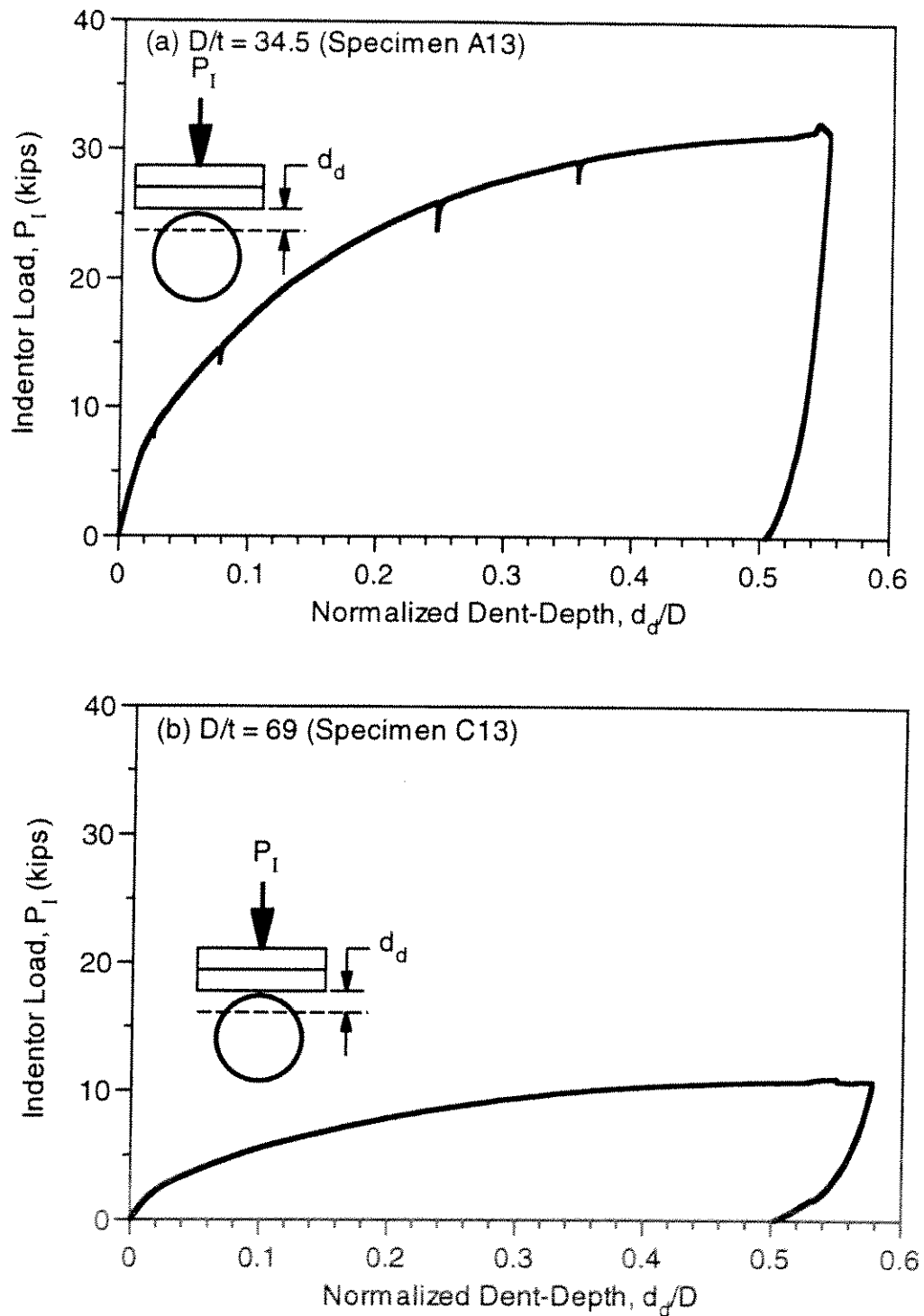


Figure 2.8 - Typical Relationship Between Applied Indentor Load and Dent-Depth for Specimens with (a)  $D/t = 34.5$  and (b)  $D/t = 69$

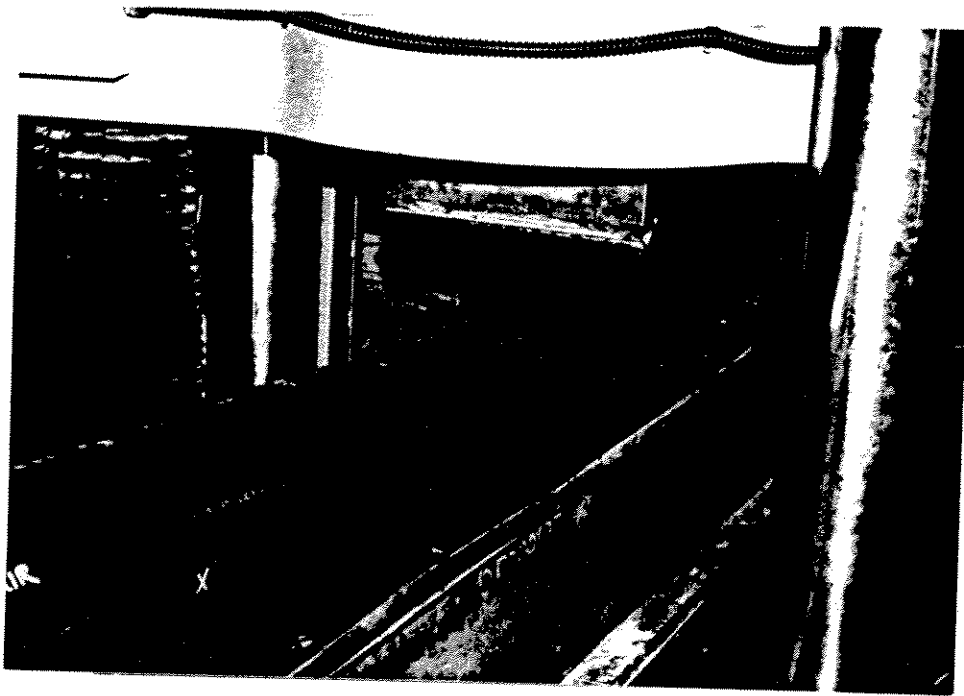


Figure 2.6 - View of Specimen in Universal Test Machine During the Application of Dent-Damage

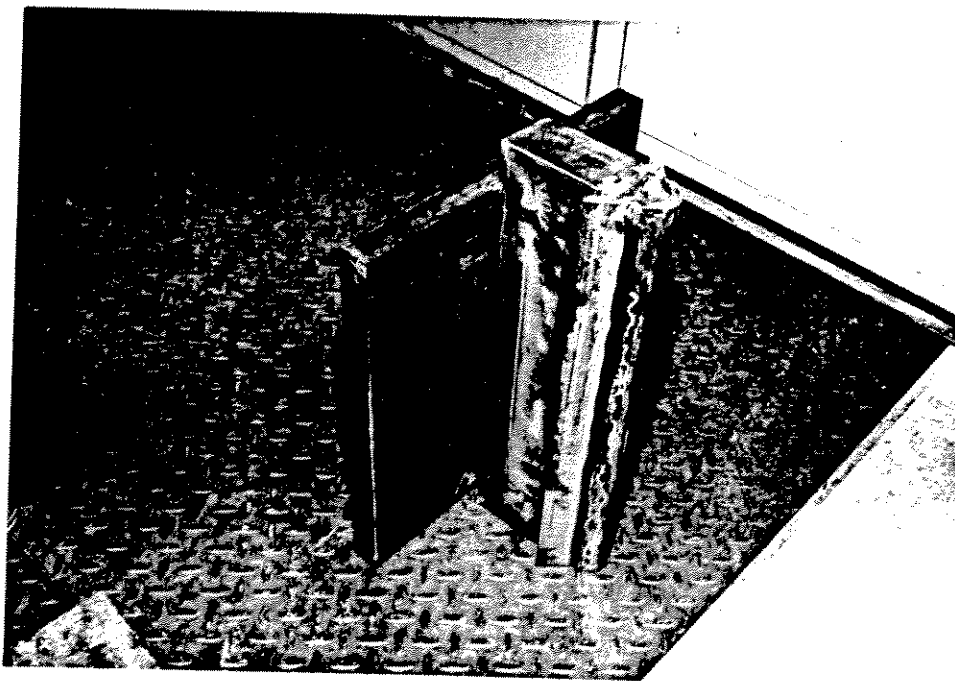


Figure 2.7 - Close-up View of Knife-edge Indentor Used to Inflict Dent-Damage

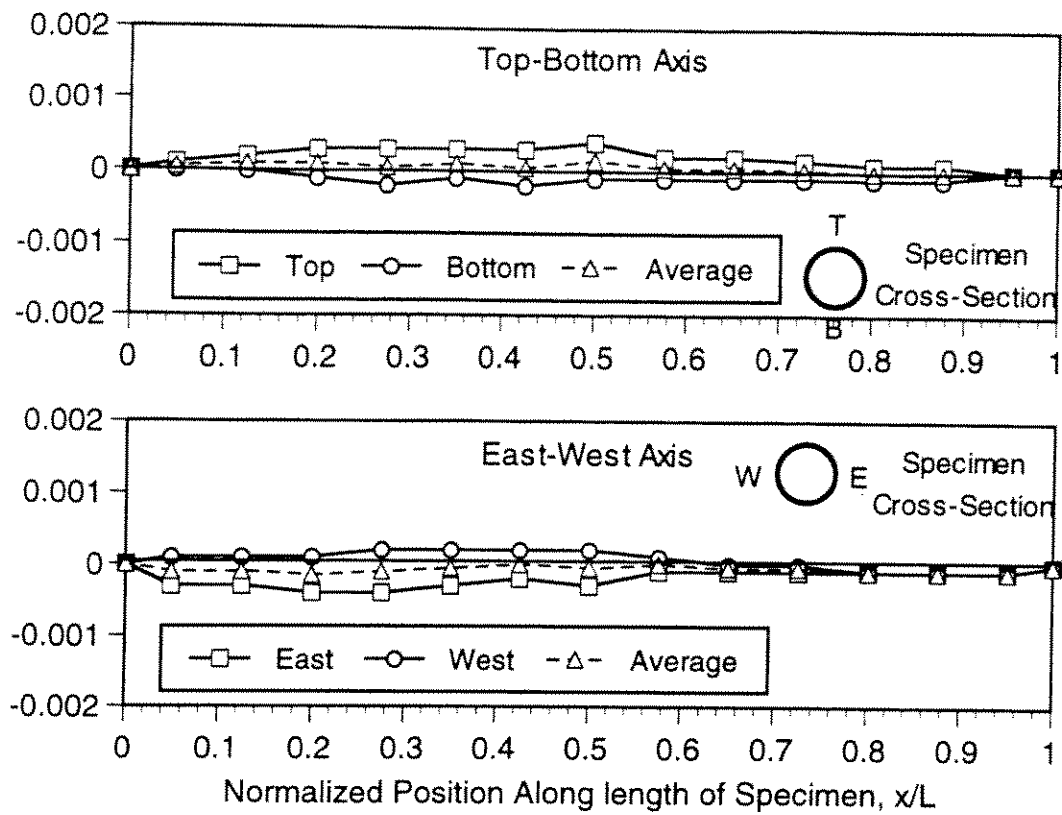


Figure 2.4 - Initial Out-of-Straightness of Specimen A10 Measured Prior to Infliction of Dent-Damage

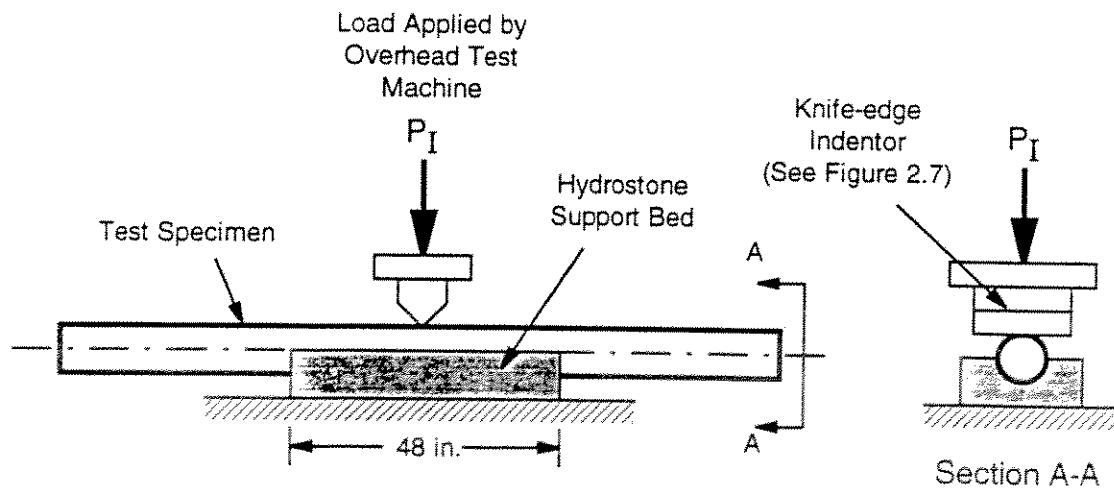


Figure 2.5 - Indentation Device Imposing Controlled Dent-Damage to a Specimen

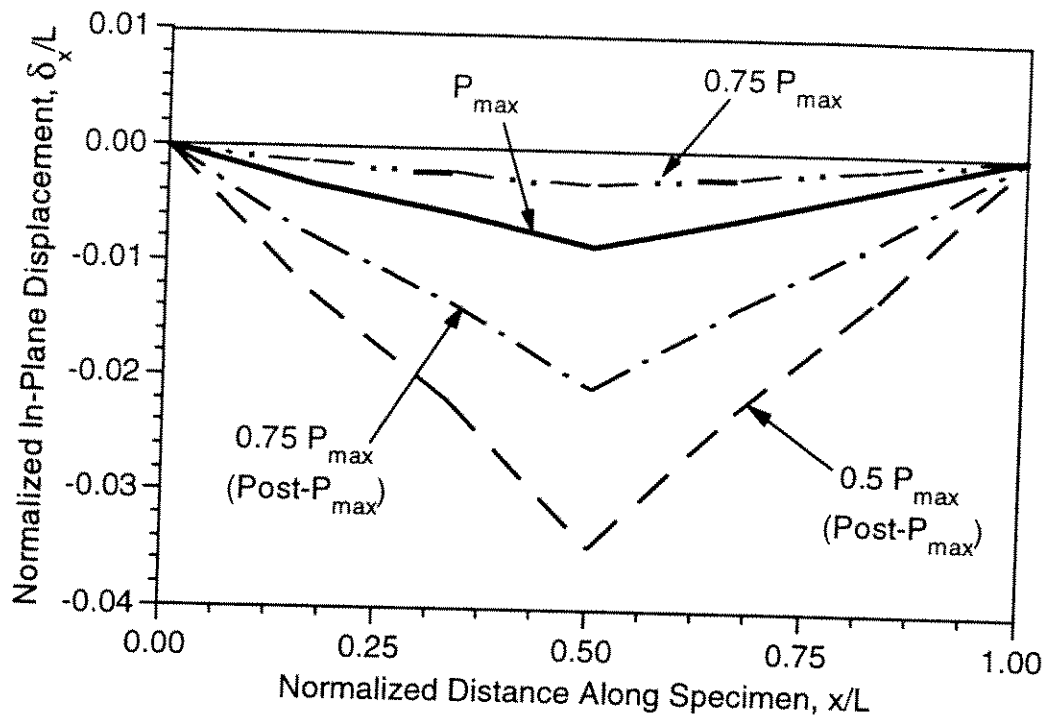


Figure 3.40 - Measured In-Plane Displacements of Specimen C12 at Various Stages of Loading

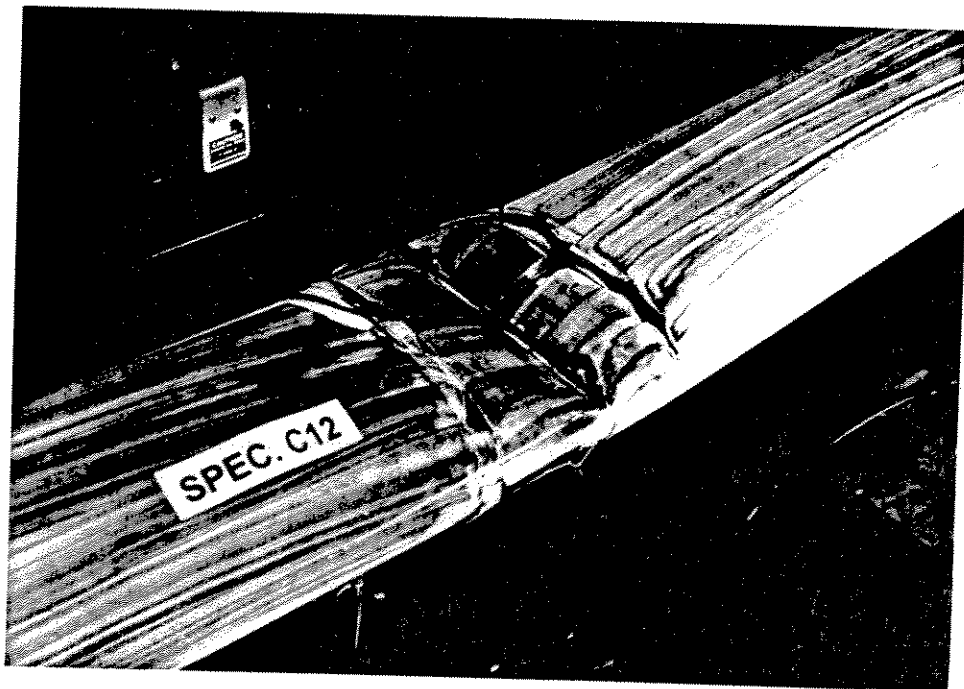


Figure 3.41 - Dented Region of Specimen C12 at Conclusion of Test



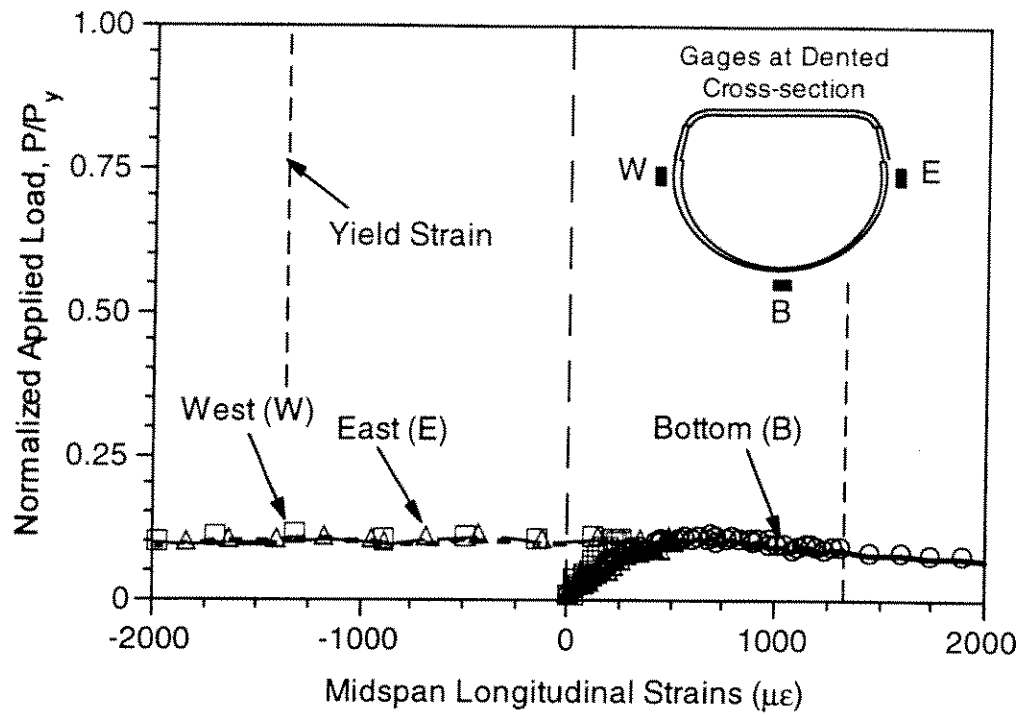


Figure 3.38 - Strain History at Midspan Dent of Specimen C12

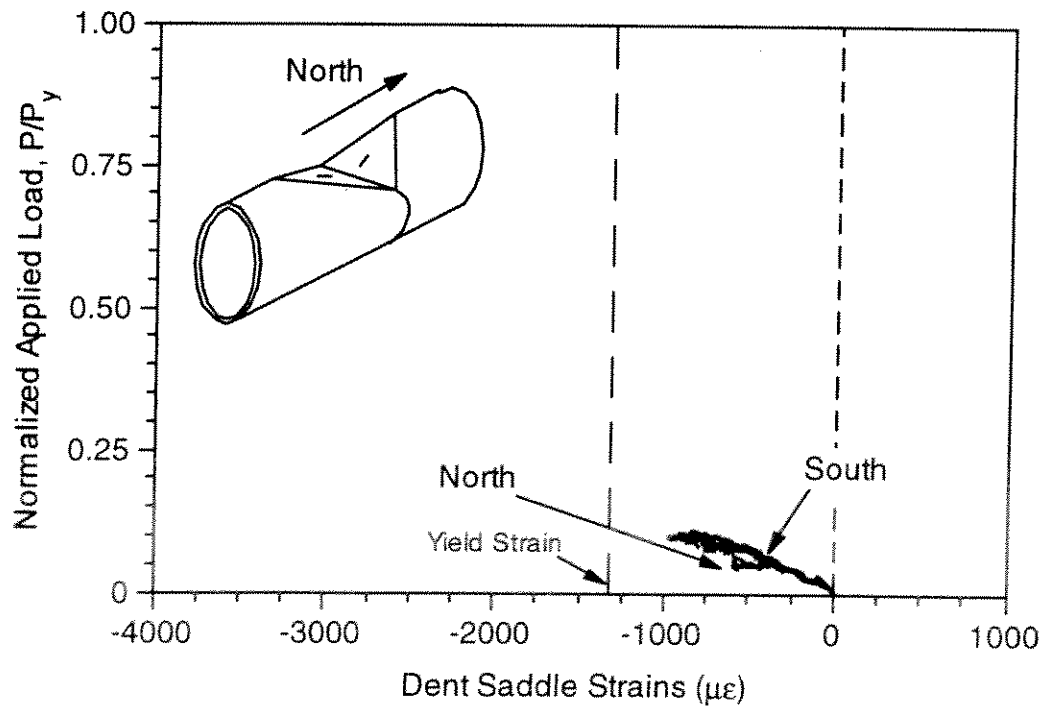


Figure 3.39 - Strain History Inside Dent Saddle of Specimen C12

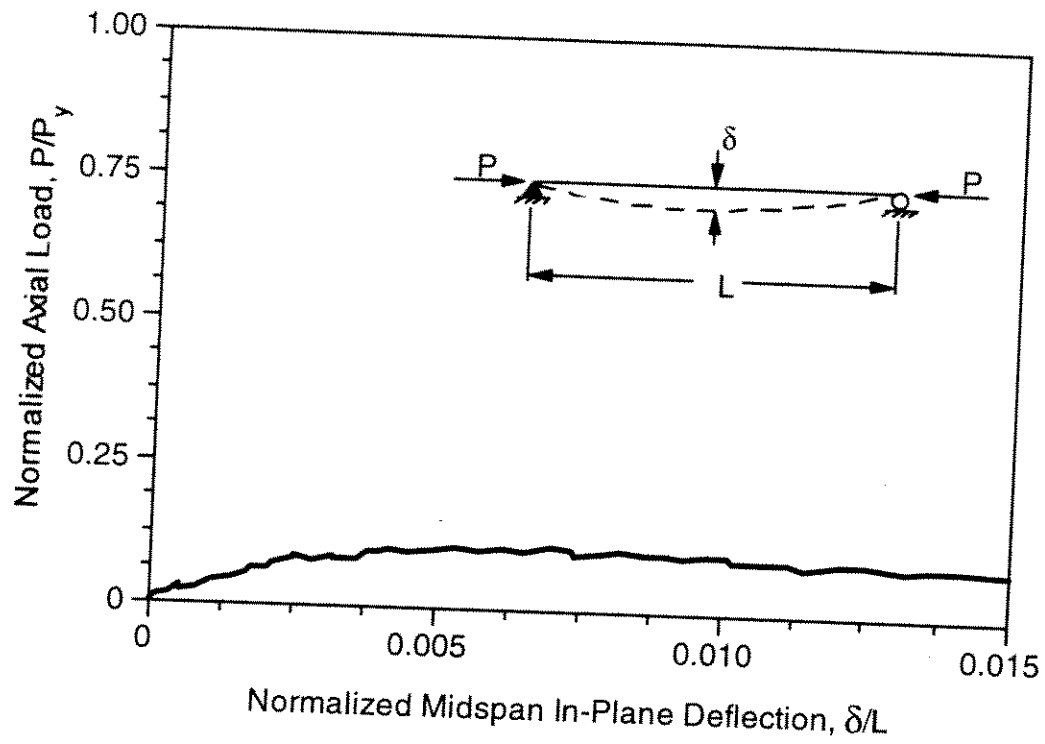


Figure 3.36 - Axial Load-Midspan Deflection Response of Specimen C12

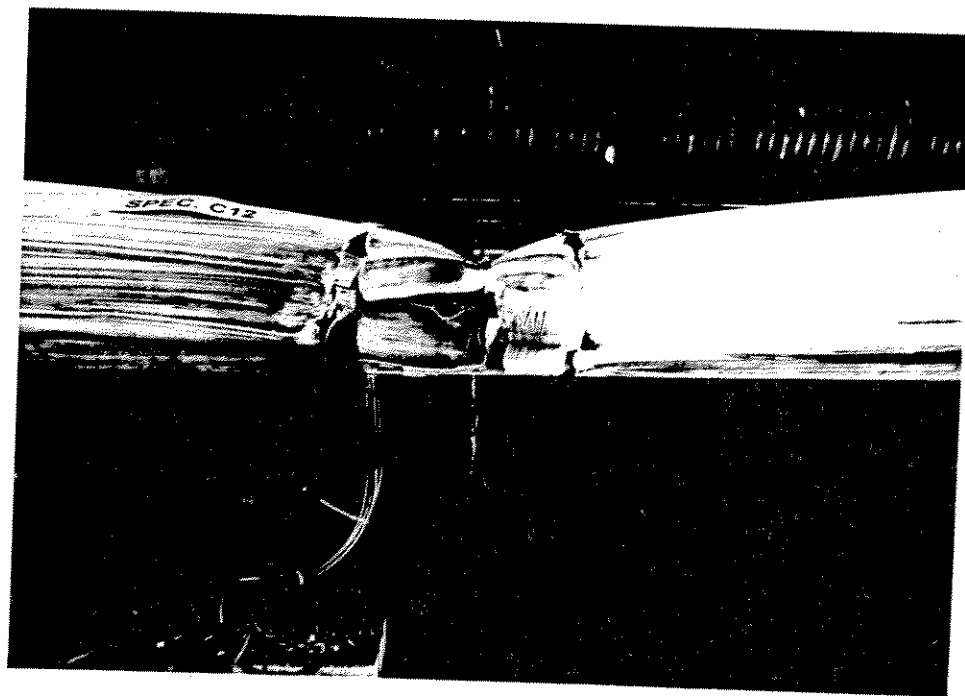


Figure 3.37 - Specimen C12 at Peak Axial Load

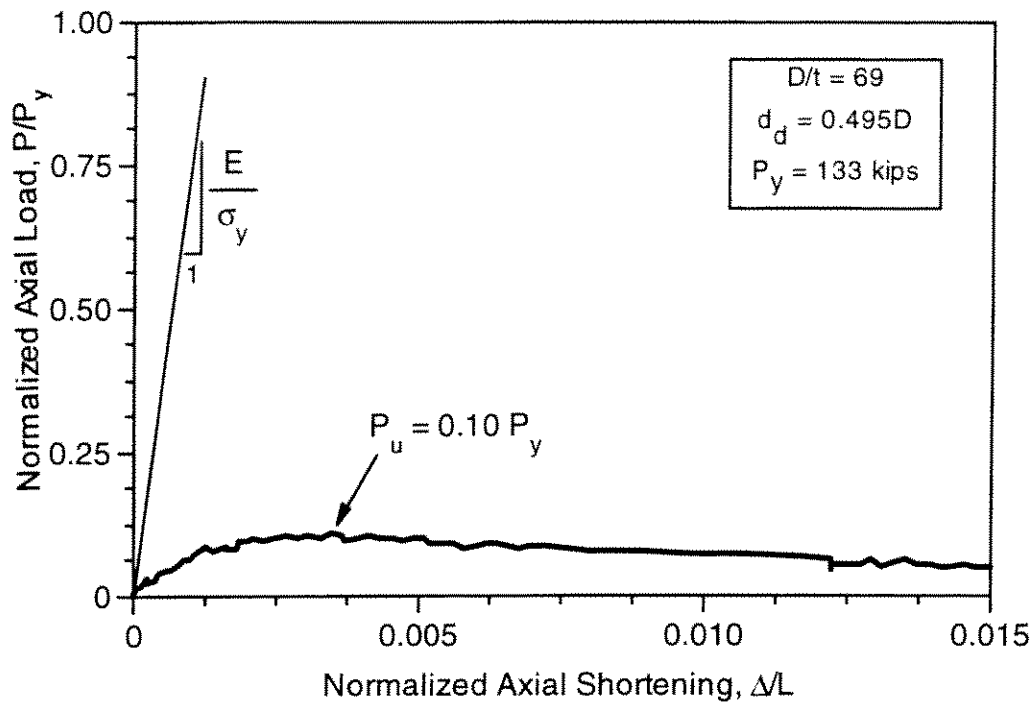


Figure 3.34 - Normalized Axial Load-Shortening Response of Specimen C12

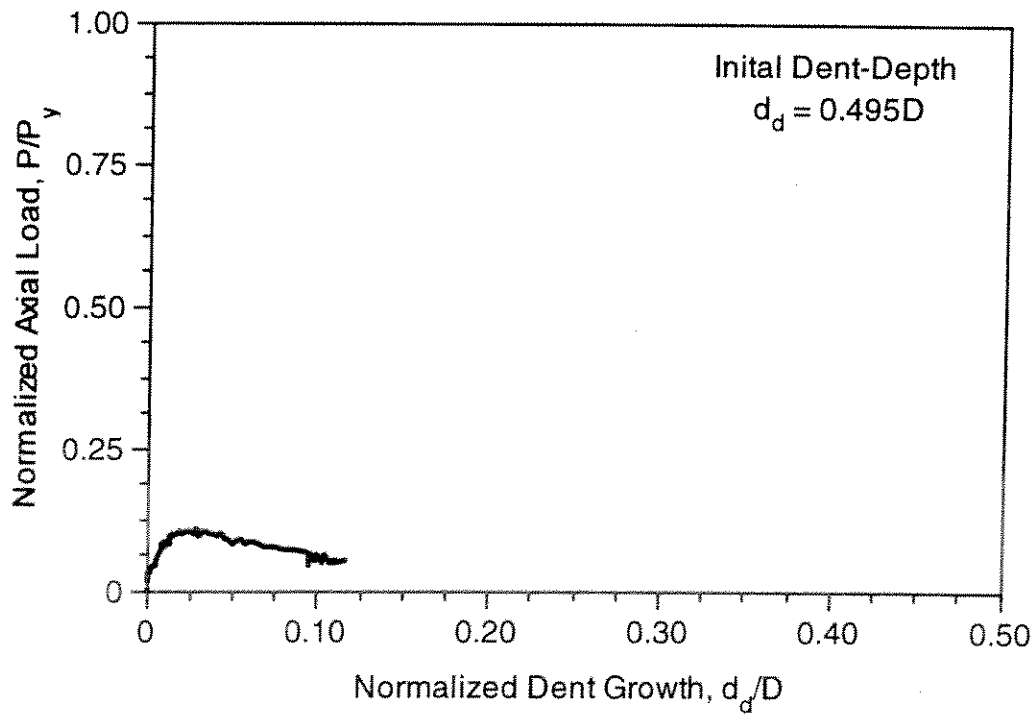


Figure 3.35 - Normalized Dent Growth of Specimen C12

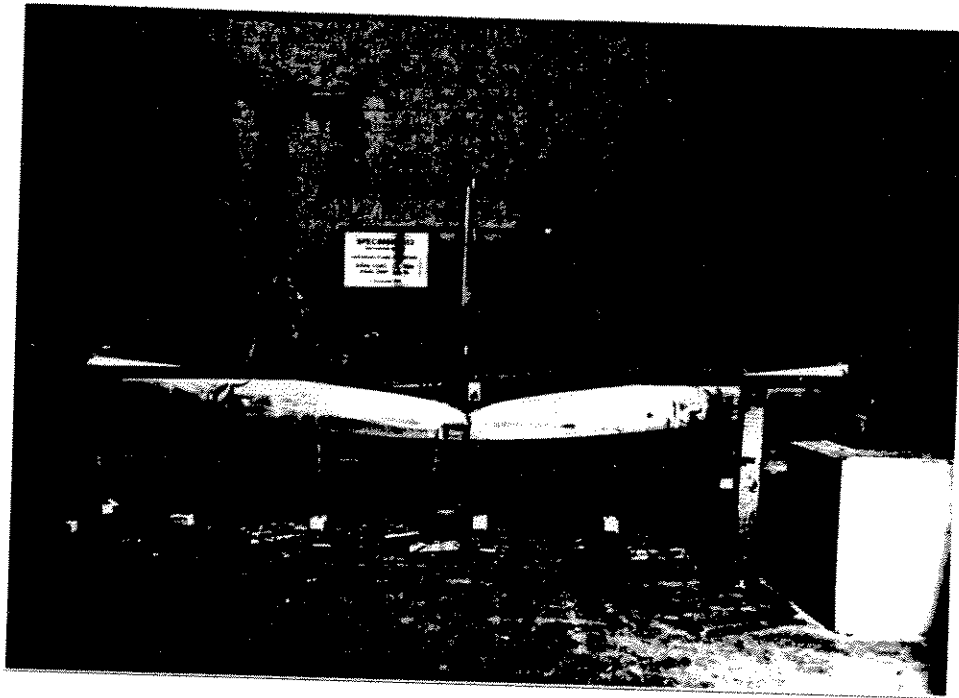


Figure 3.32 - Specimen A12 at End of Test

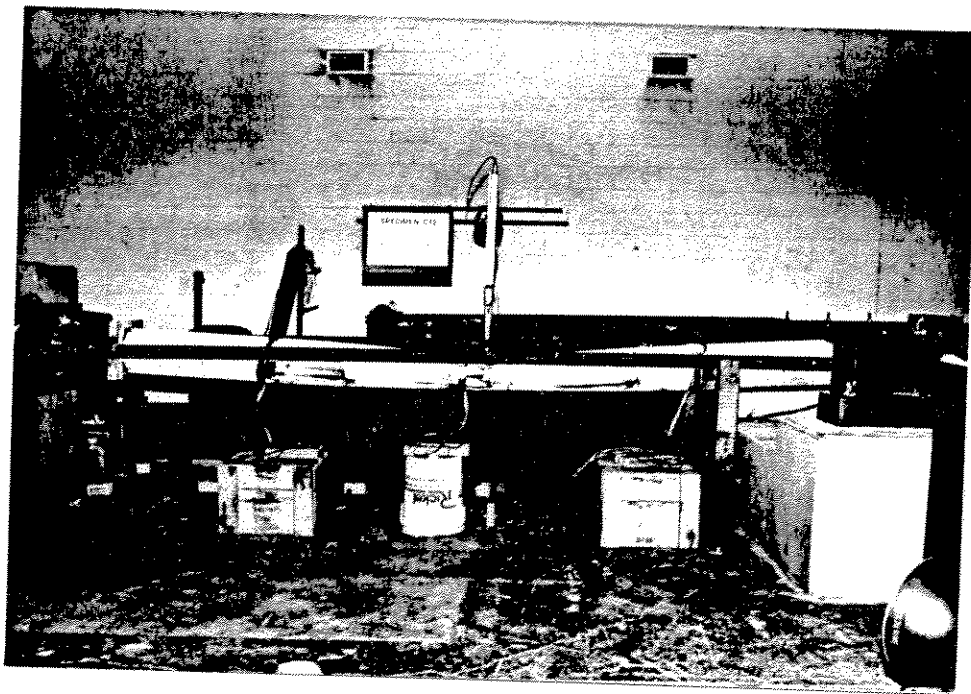


Figure 3.33 - Specimen C12 Prior to Testing



Figure 3.30 - Specimen A12 at Peak Axial Load

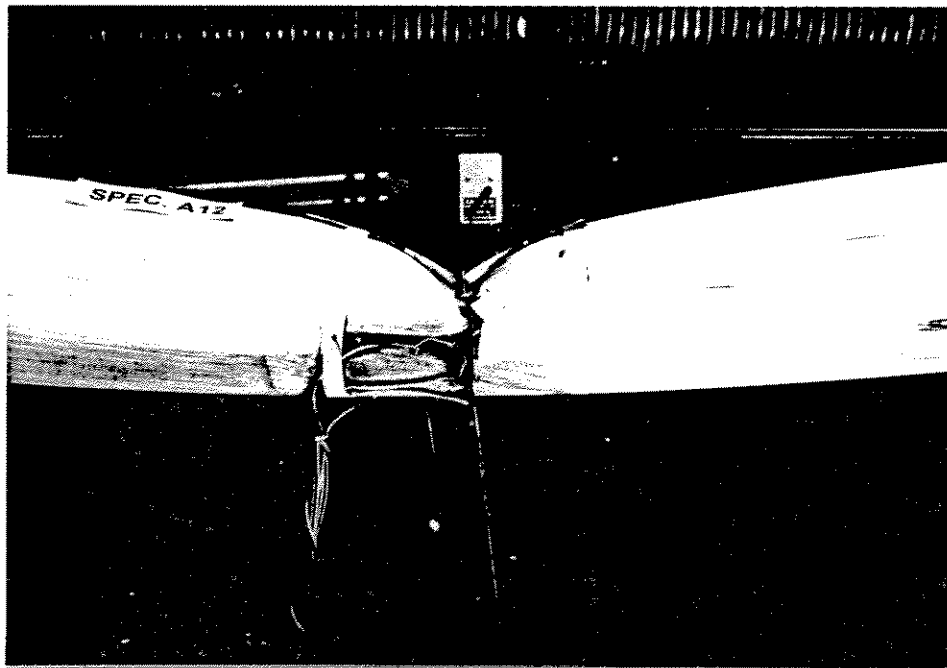


Figure 3.31 - Dented Region of Specimen A12 After Achieving Peak Axial Load

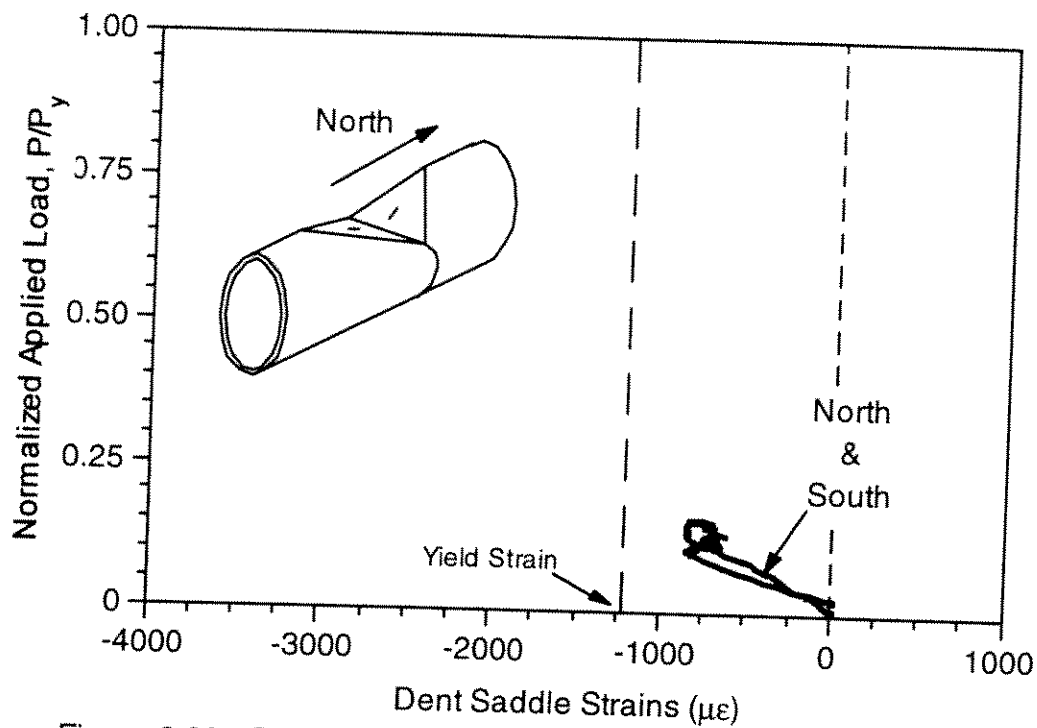


Figure 3.28 - Strain History Inside Dent Saddle of Specimen A12

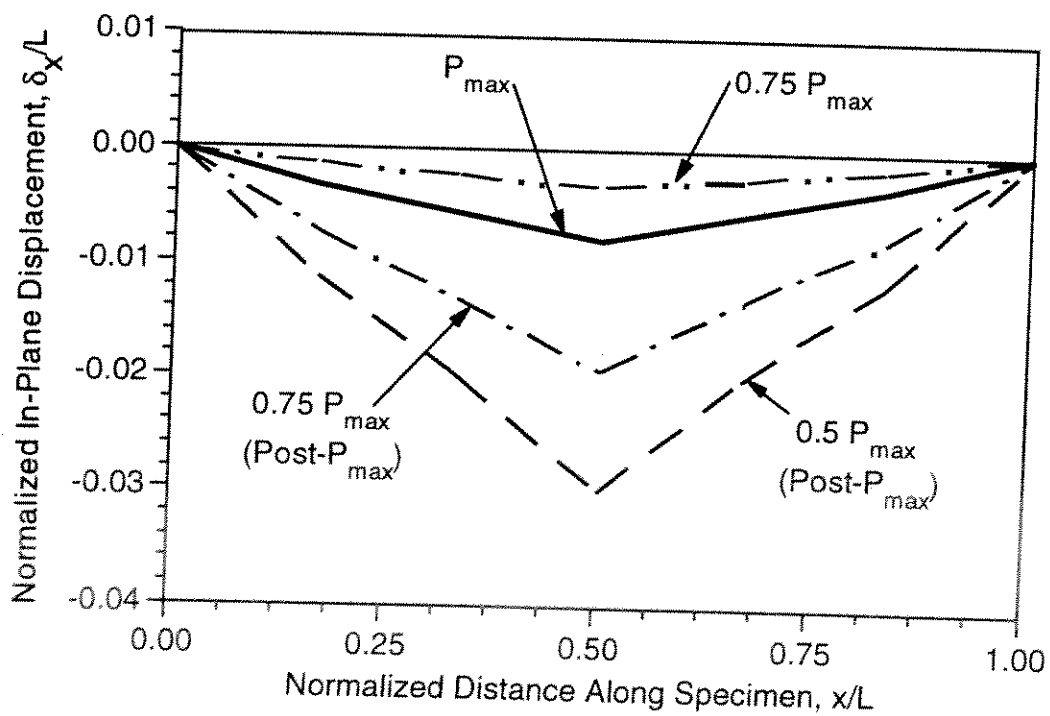


Figure 3.29 - Measured In-Plane Displacements of Specimen A12 at Various Stages of Loading

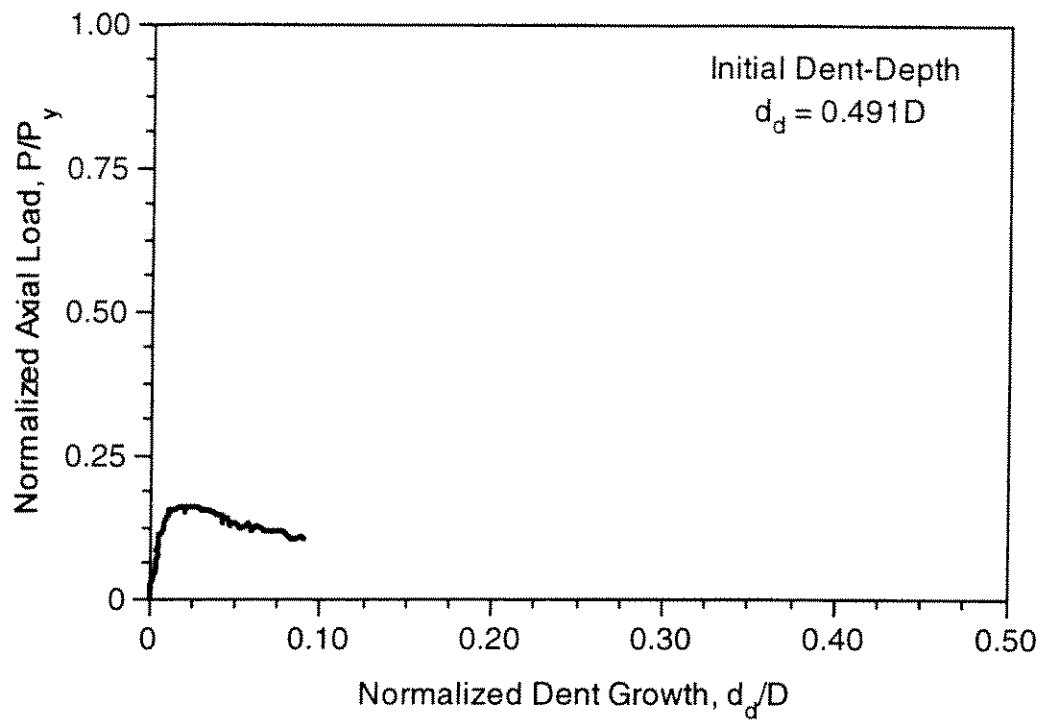


Figure 3.26 - Normalized Dent Growth of Specimen A12

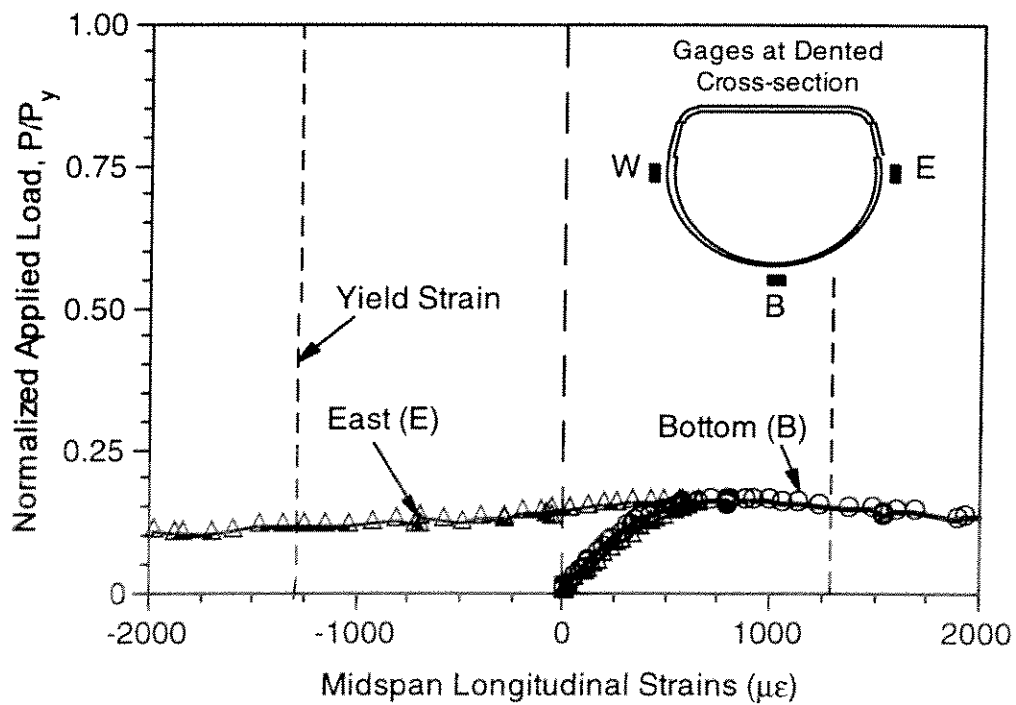


Figure 3.27 - Strain History at Midspan Dent of Specimen A12  
(West-Side Gage Malfunctioned)

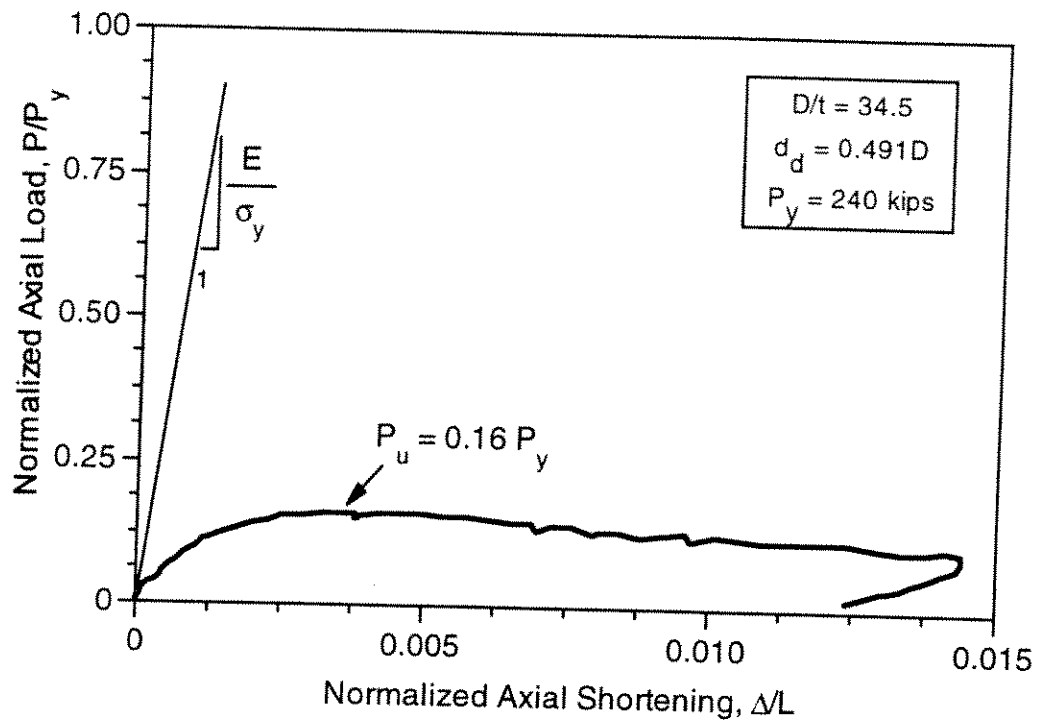


Figure 3.24 - Normalized Axial Load-Shortening Response of Specimen A12

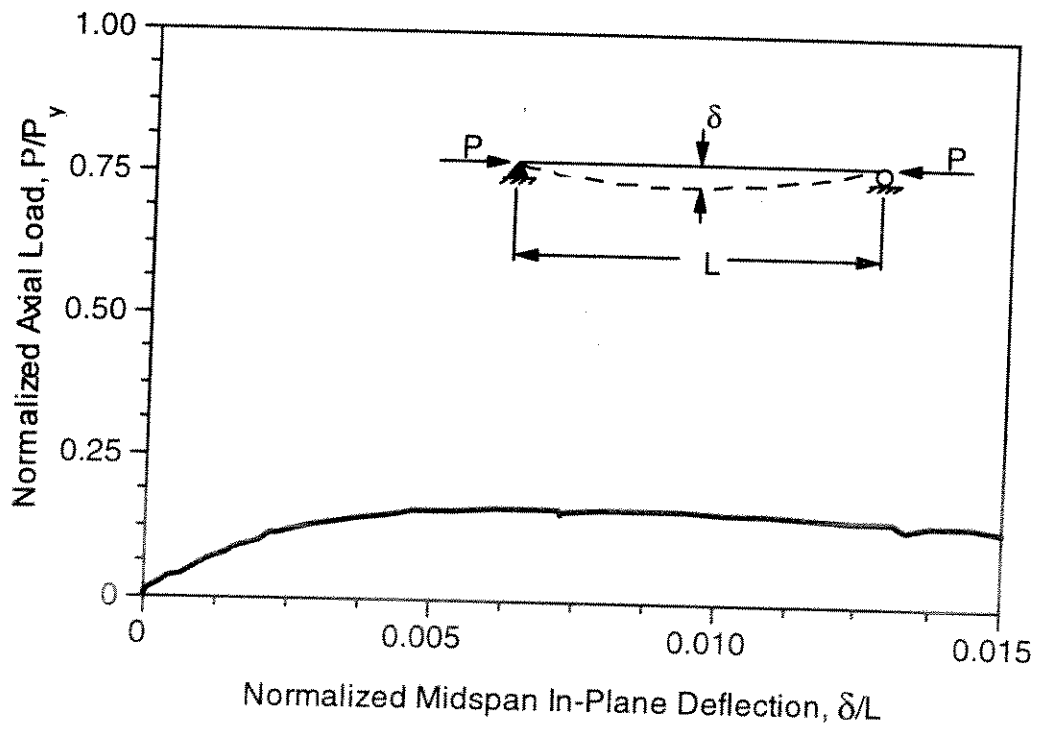


Figure 3.25 - Axial Load-Midspan Deflection Response of Specimen A12



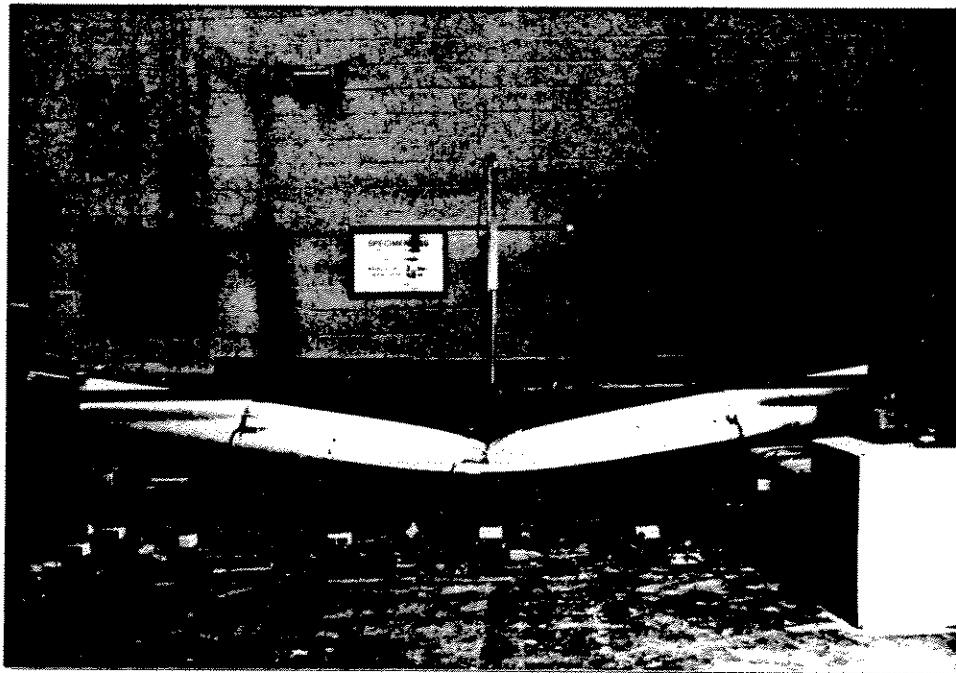


Figure 3.22 - Specimen C10 at End of Test

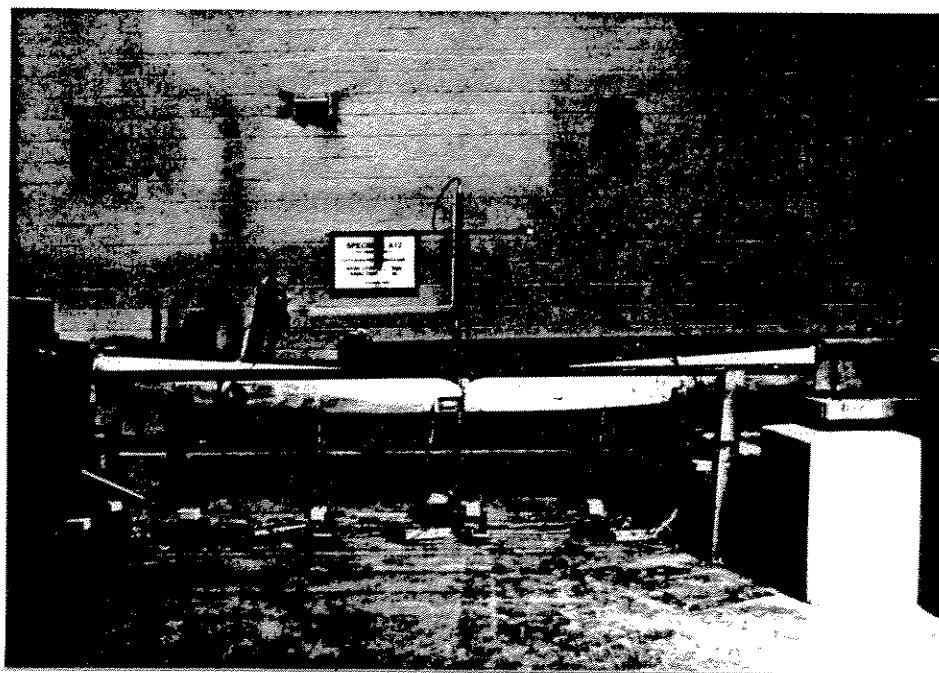


Figure 3.23 - Specimen A12 Prior to Testing

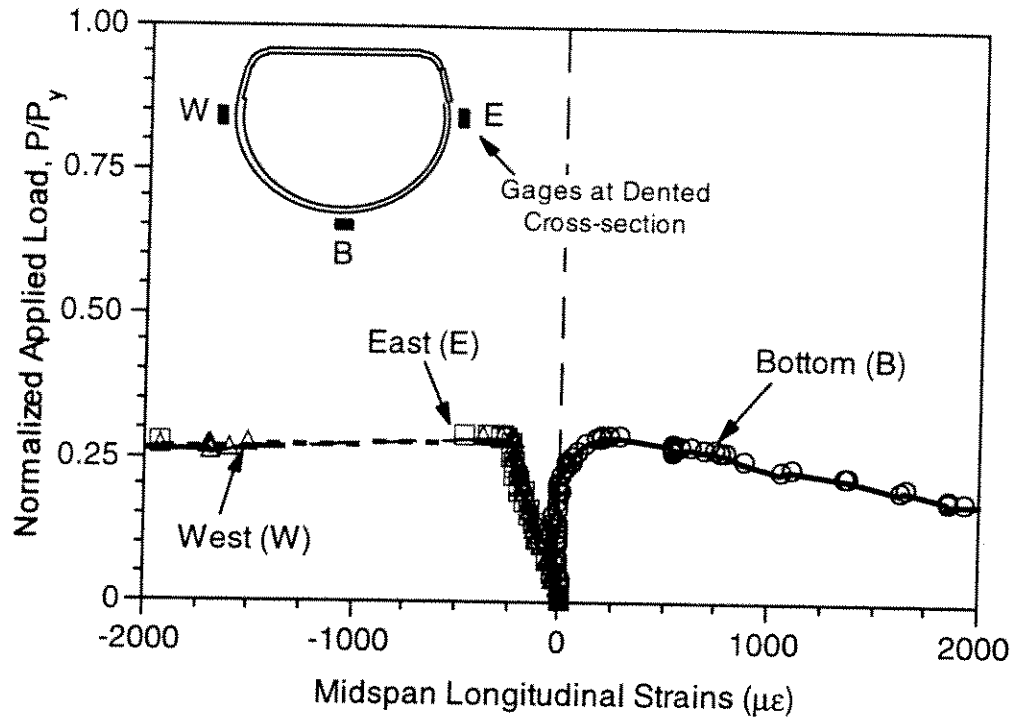


Figure 3.20 - Strain History at Midspan Dent of Specimen C10

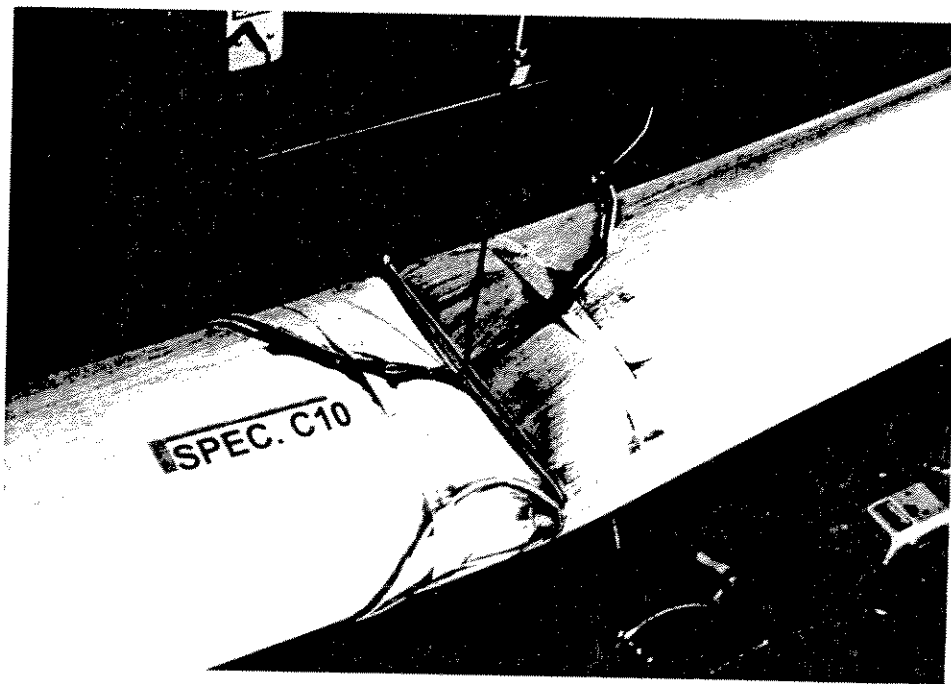


Figure 3.21 - Dented Region of Specimen C10 Near End of Test

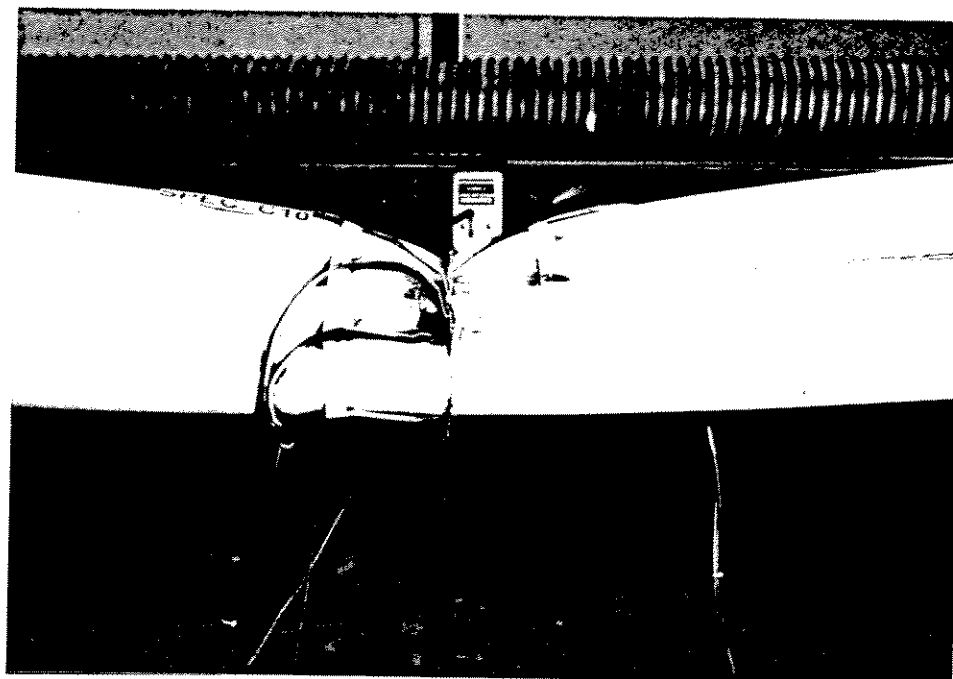


Figure 3.18 - Dented Region of Specimen C10 After Developing Peak Axial Load

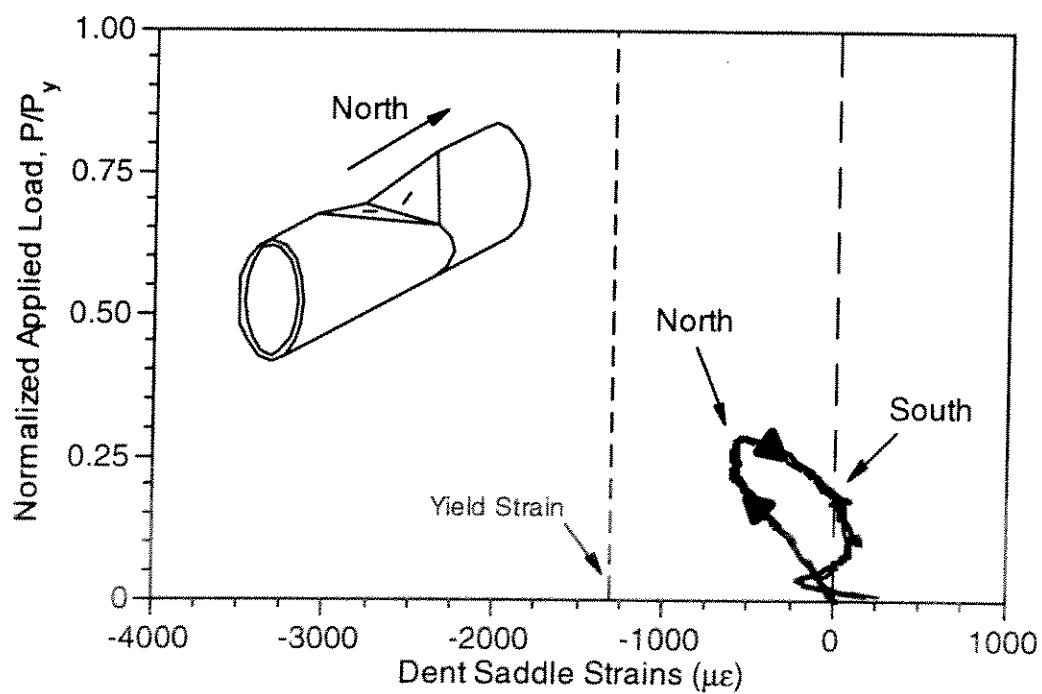


Figure 3.19 - Strain History Inside Dent Saddle of Specimen C10

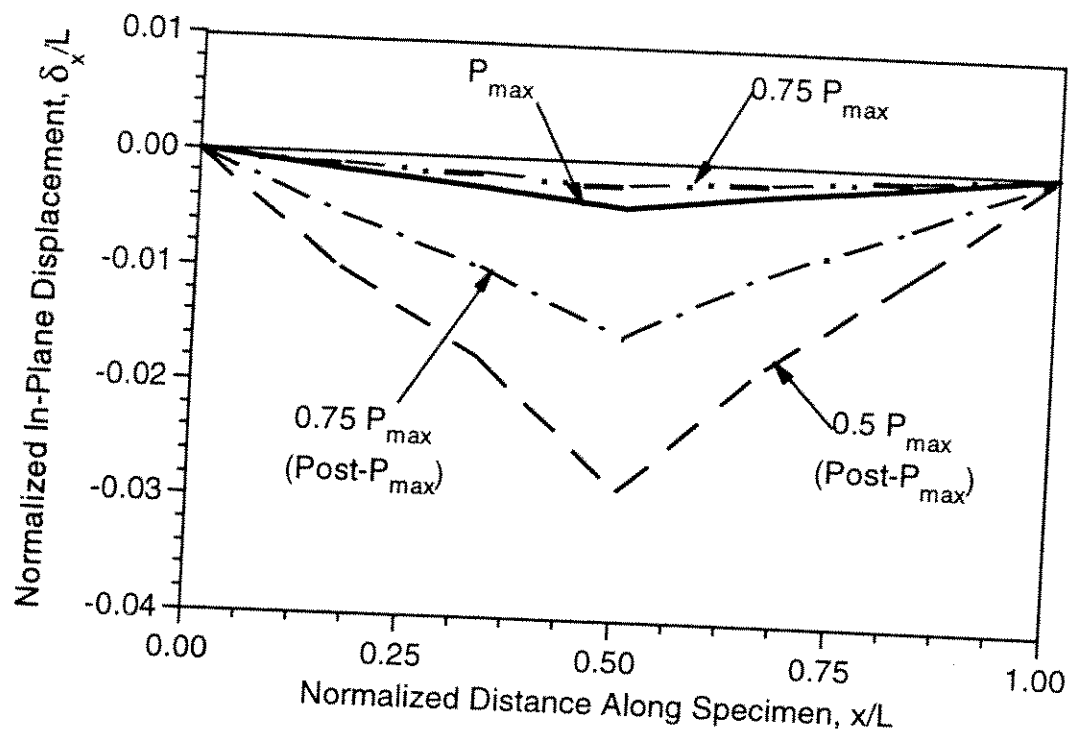


Figure 3.16 - Measured In-Plane Displacements of Specimen C10 at Various Stages of Loading

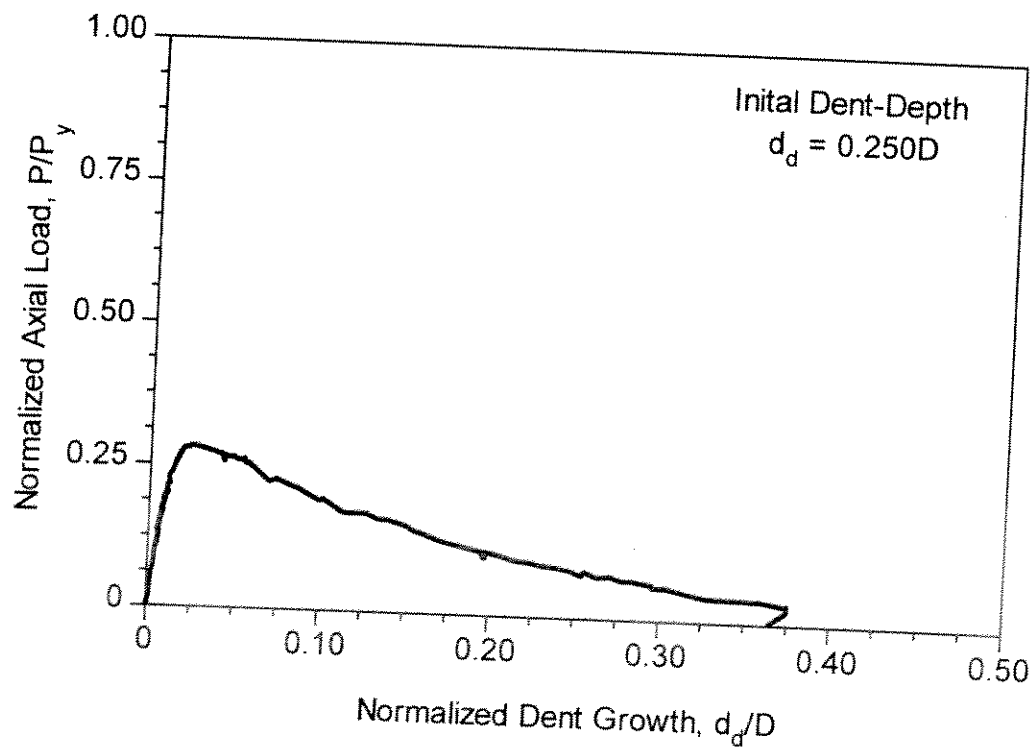


Figure 3.17 - Normalized Dent Growth of Specimen C10

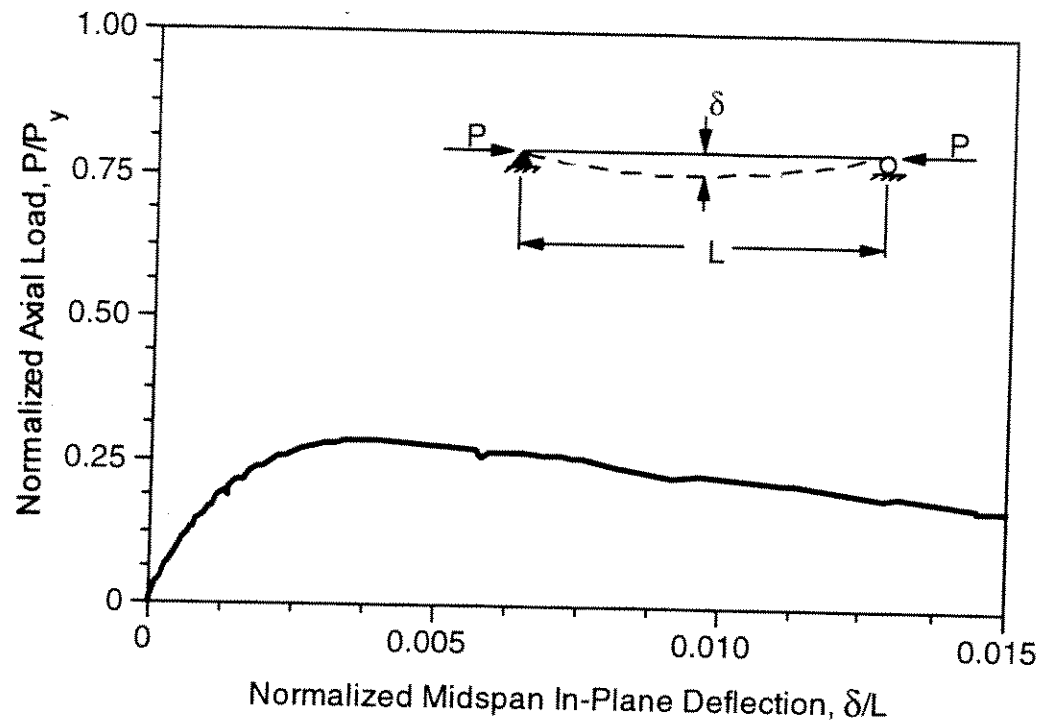


Figure 3.14 - Axial Load-Midspan Deflection Response of Specimen C10

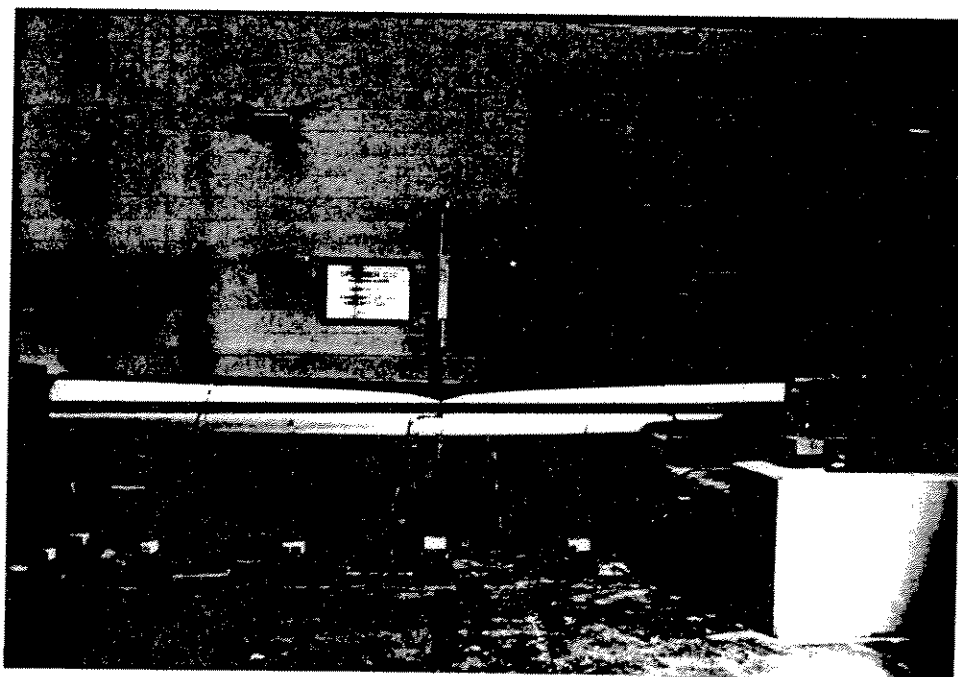


Figure 3.15 - Specimen C10 at Peak Applied Axial Load

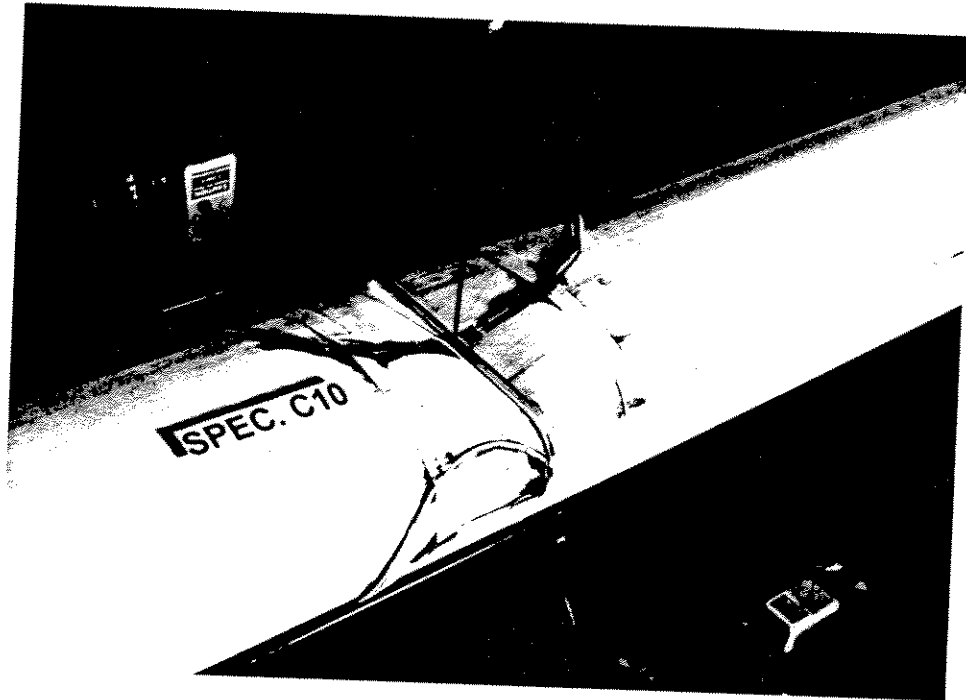


Figure 3.12 - Specimen C10 Dented Region Prior to Testing

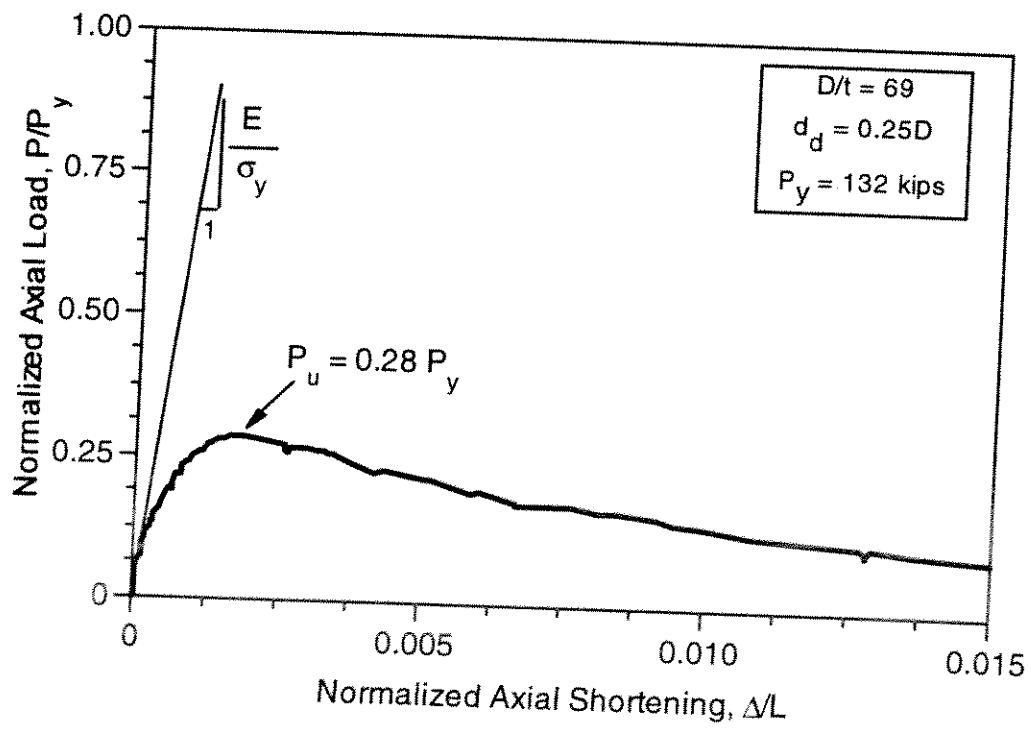


Figure 3.13 - Normalized Axial Load-Shortening Response of Specimen C10

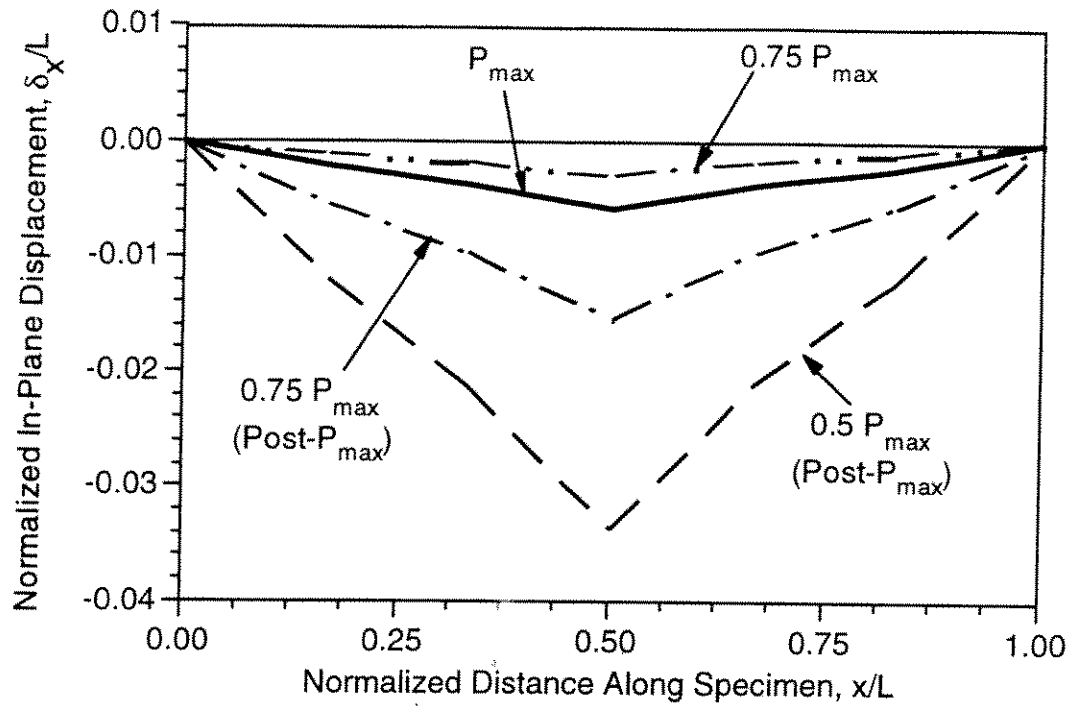


Figure 3.10 - Measured In-Plane Displacements of Specimen A10 at Various Stages of Loading

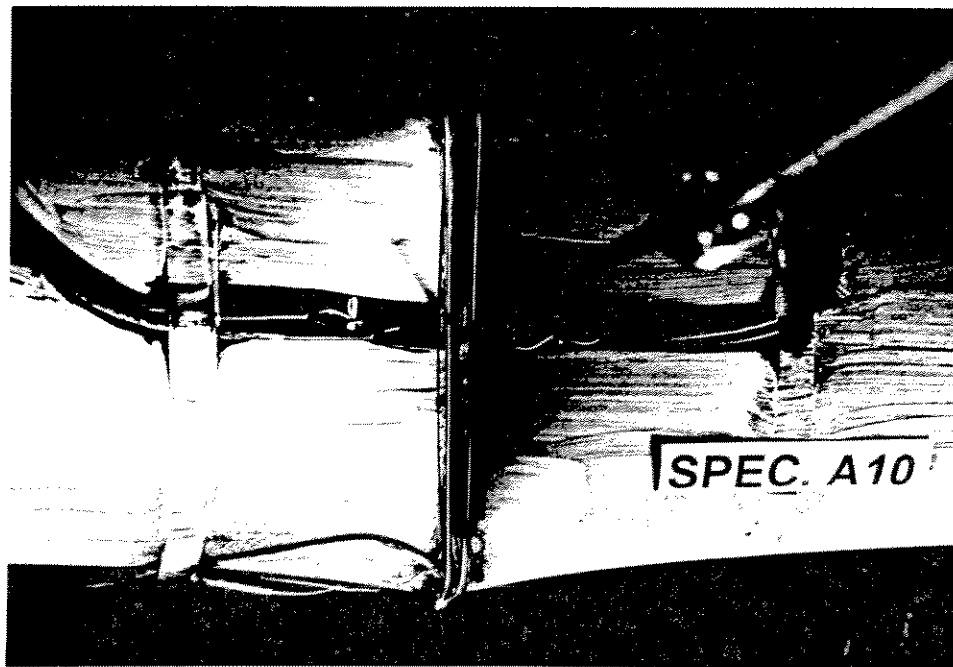


Figure 3.11 - Top View of Dented Region After Formation of Plastic Hinge

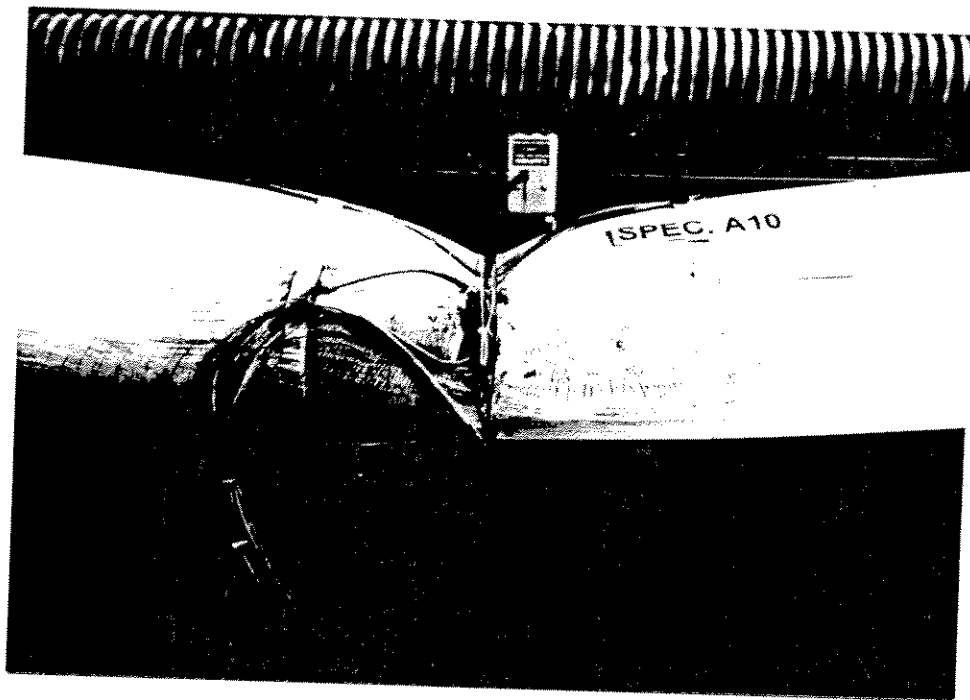


Figure 3.8 - Yielding and Dent-Growth in Dented Region Following Development of Peak Axial Load

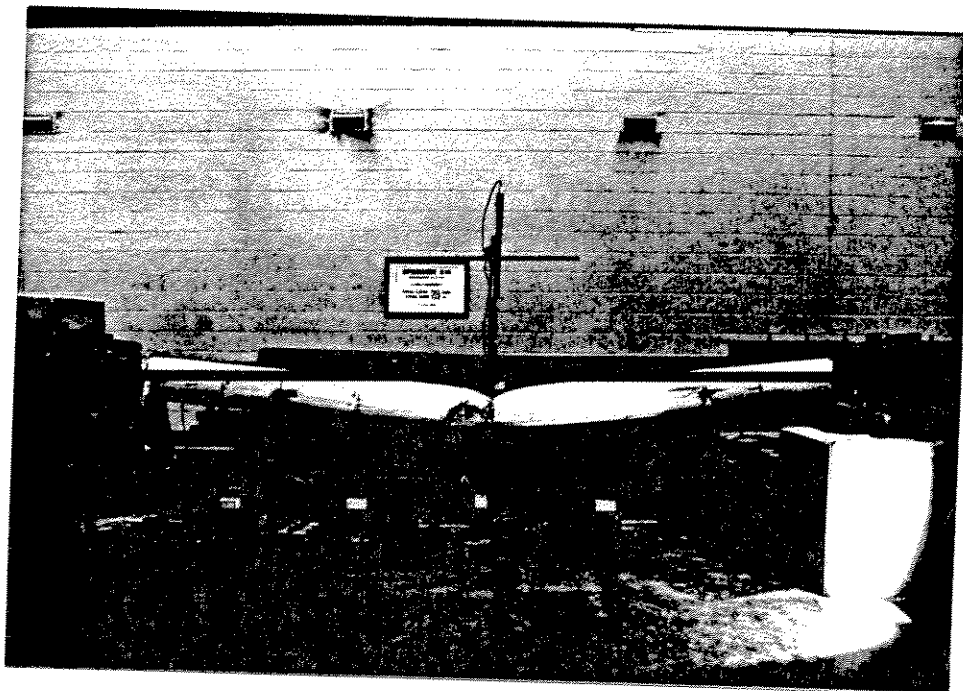


Figure 3.9 - Deflected Shape of Specimen A10 Following Development of Peak Axial Load



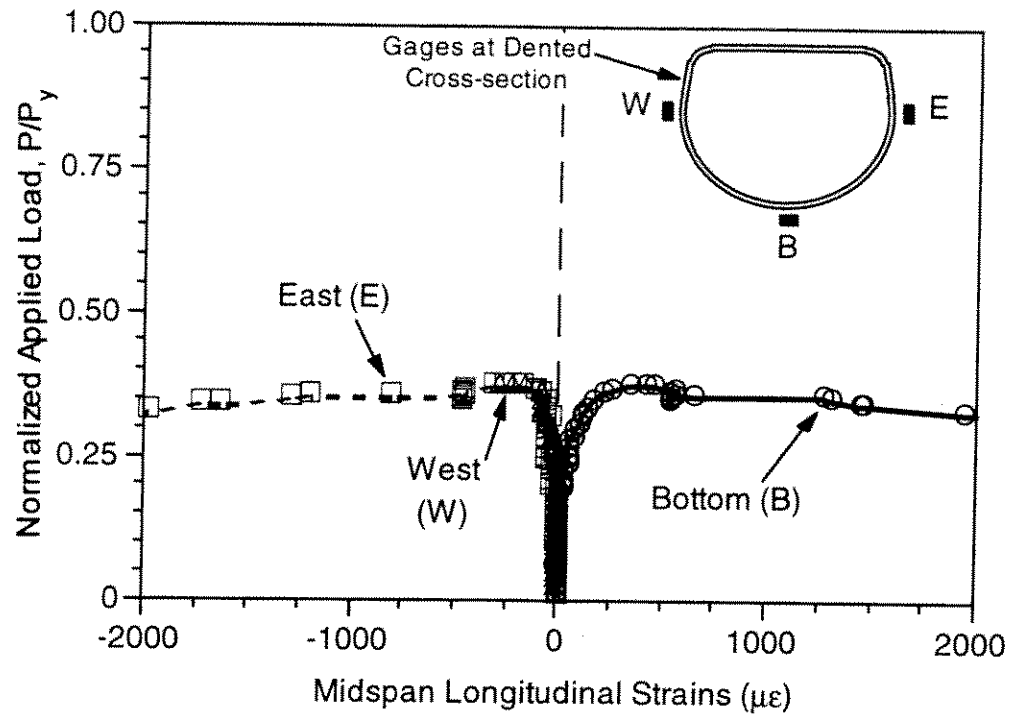


Figure 3.6- Strain History at Midspan Dent of Specimen A10

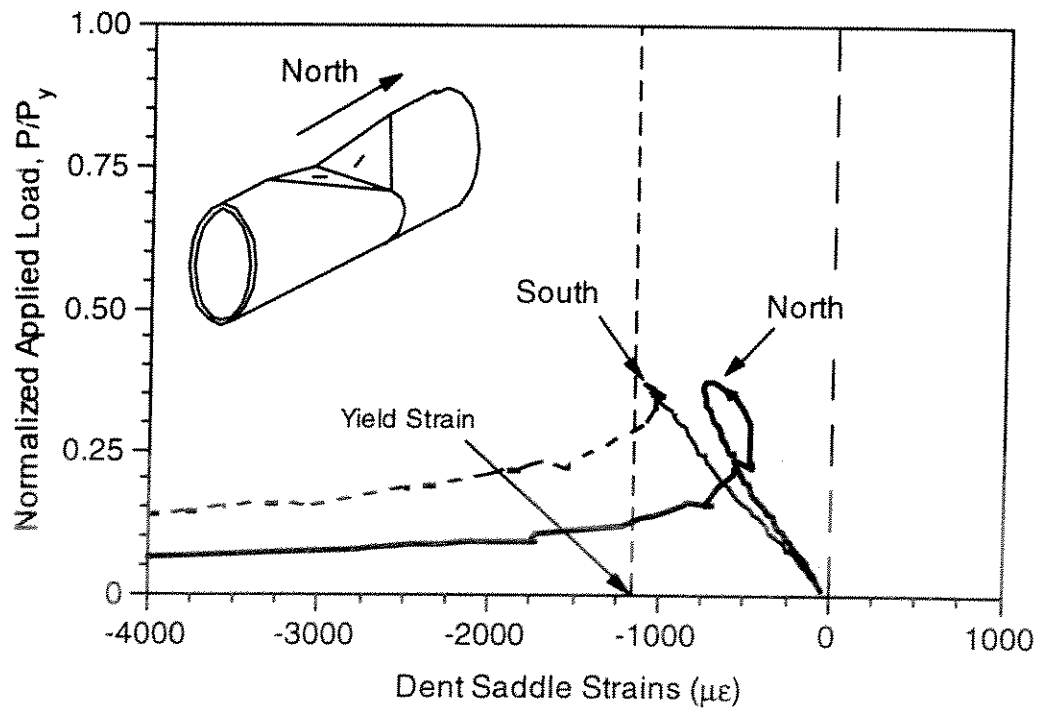


Figure 3.7 - Strain History Inside Dent Saddle of Specimen A10

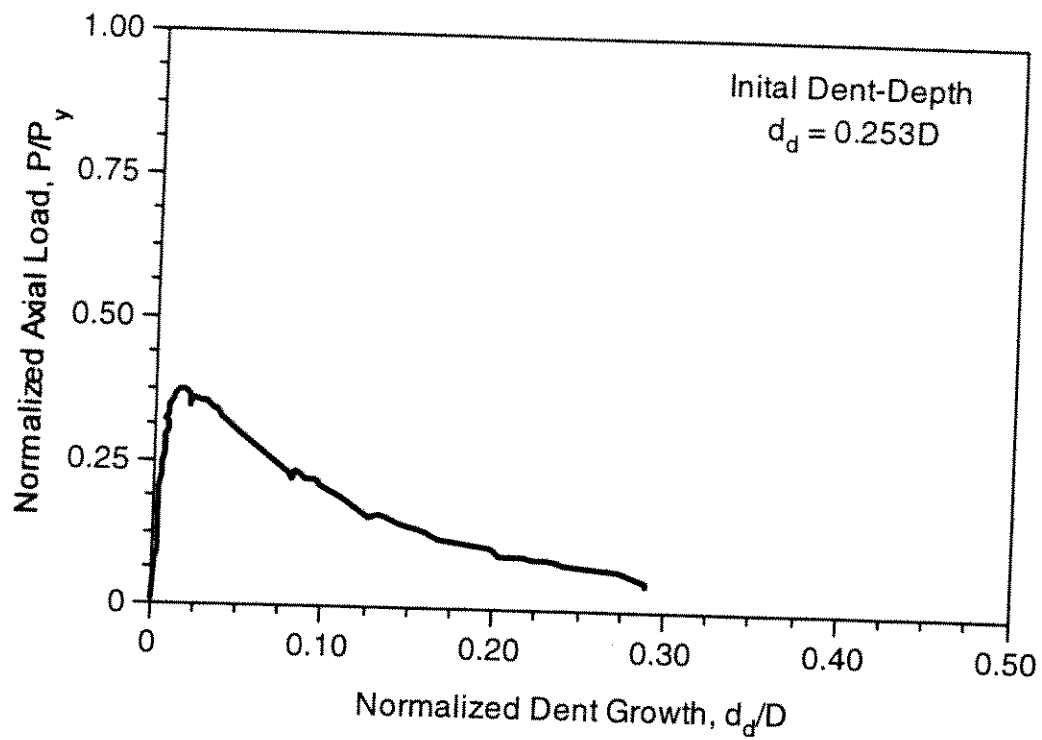


Figure 3.4 - Normalized Dent Growth of Specimen A10

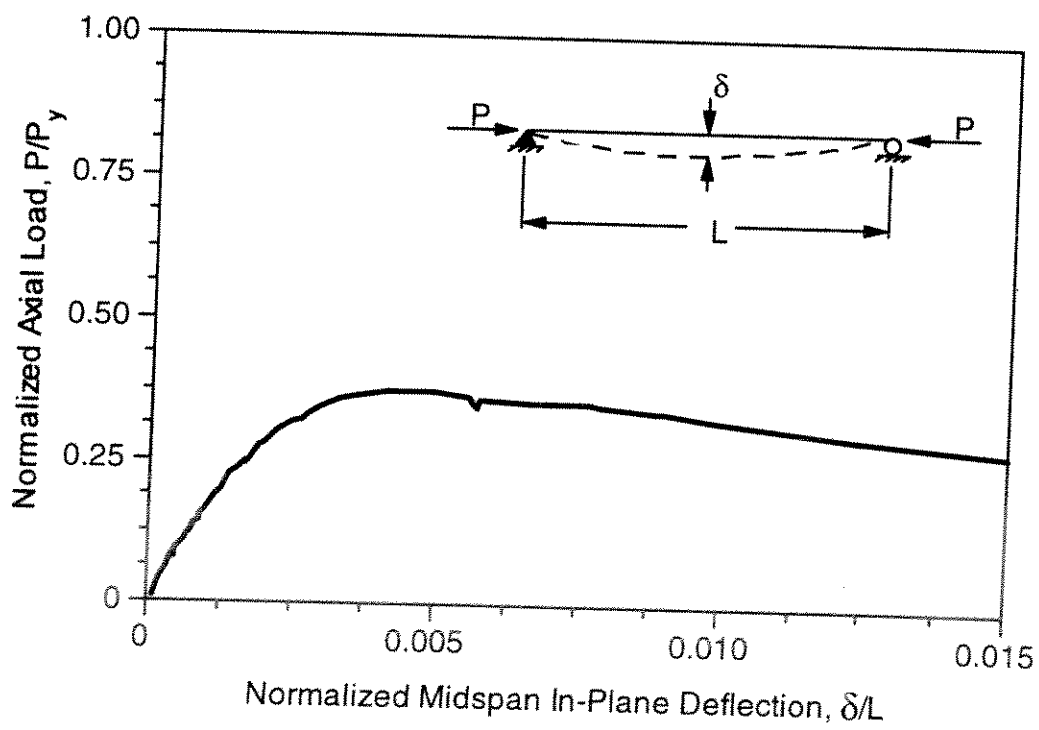


Figure 3.5 - Axial Load-Midspan Deflection Response of Specimen A10

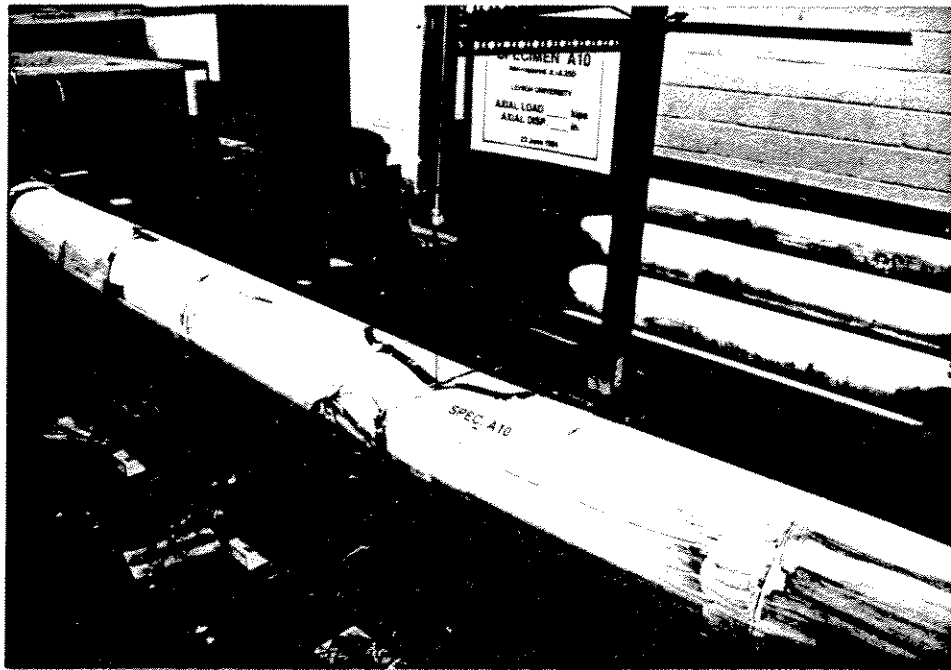


Figure 3.2 - Specimen A10 Prior to Testing

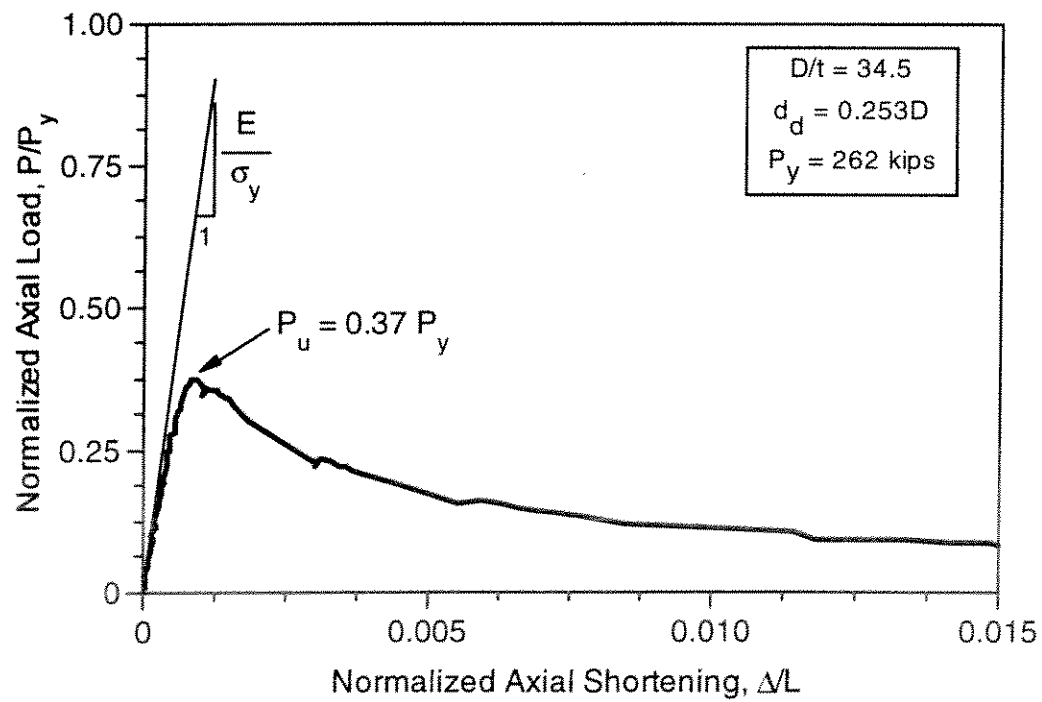


Figure 3.3 - Normalized Axial Load-Shortening Response of Specimen A10

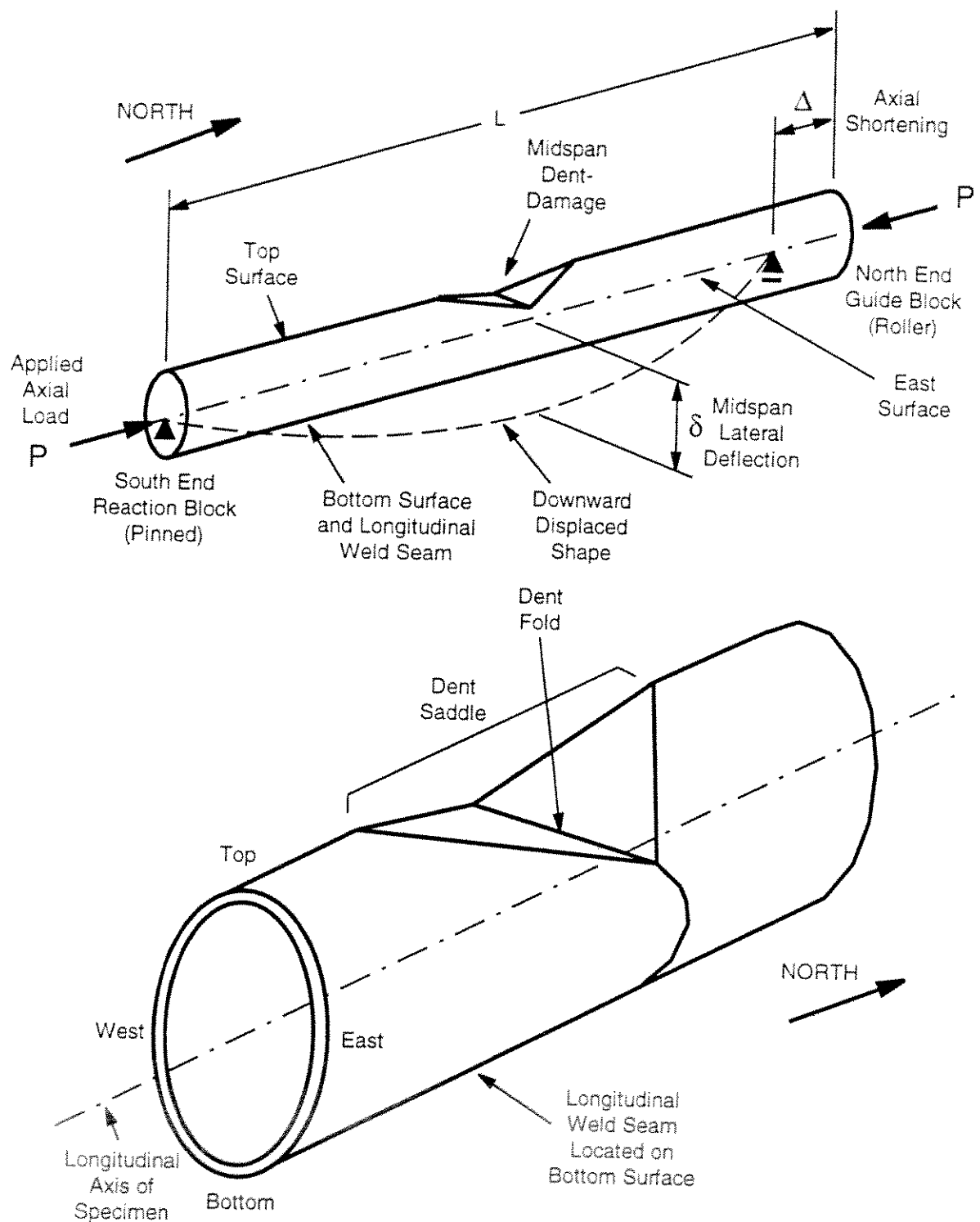


Figure 3.1 - Nomenclature Describing the Orientation, Specific Features, and Response Quantities of a Typical Test Specimen

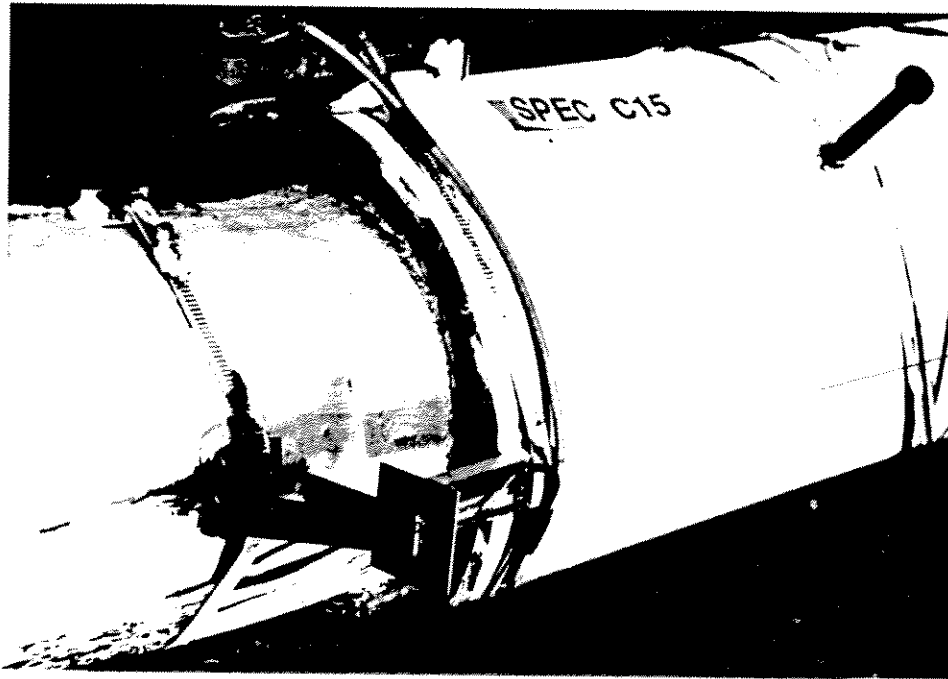


Figure 2.36 - Photograph of Slip Gage Instrumentation

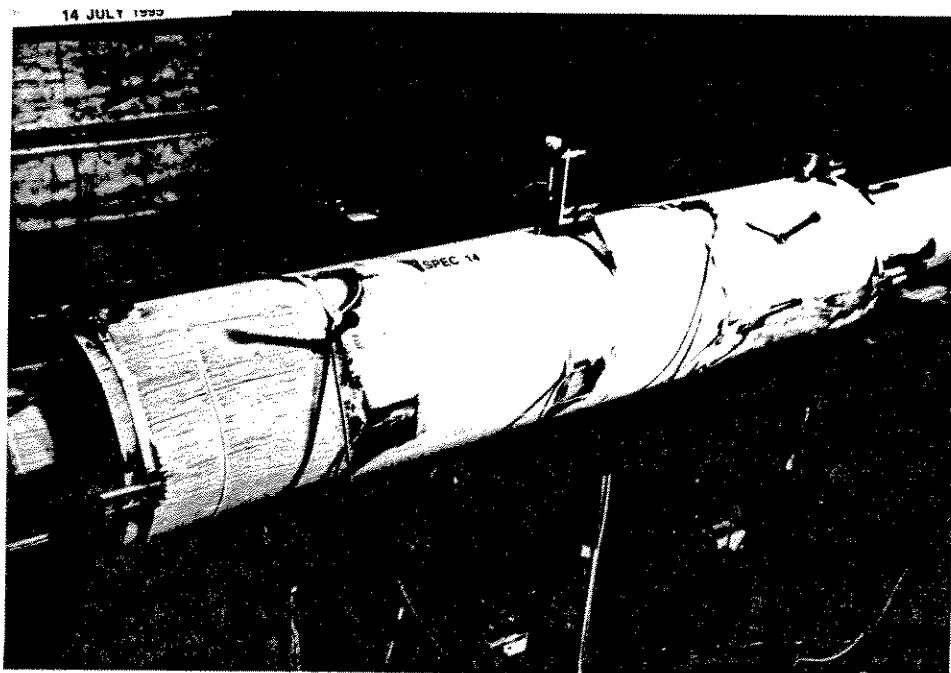


Figure 2.37 - Photograph of Dent Depth Growth Instrumentation

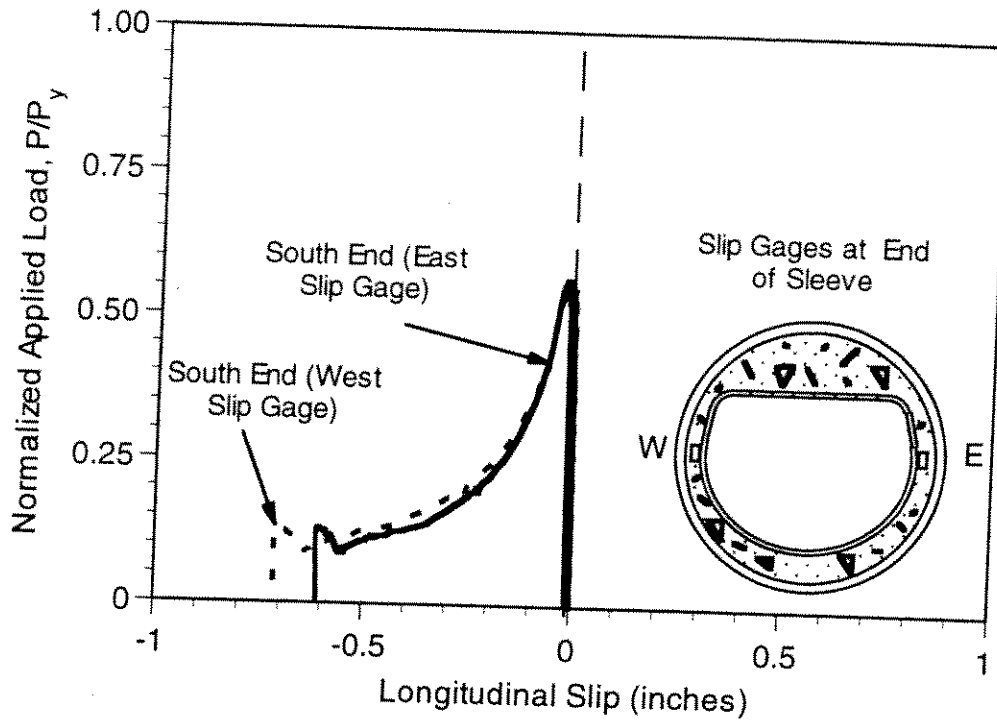


Figure 3.92 - Slip History at Each End of Sleeve, Specimen C15

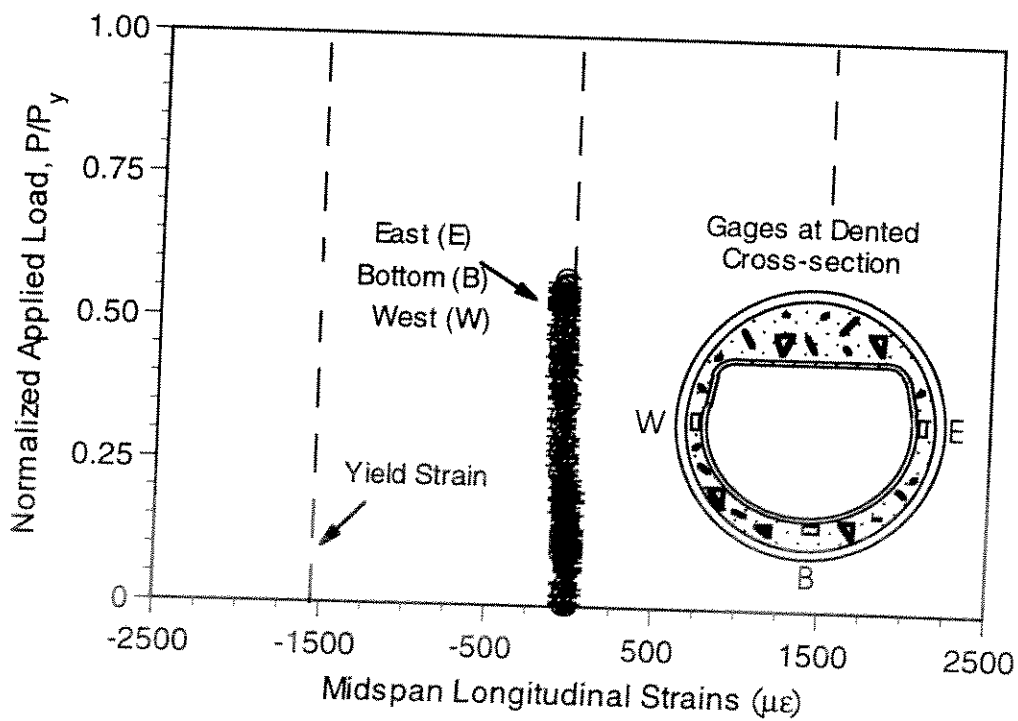


Figure 3.93 - Tube Strain History at Midspan Dent of Specimen C15



Figure 3.90 - Local Buckle in Tube at South End of Grouted Sleeve

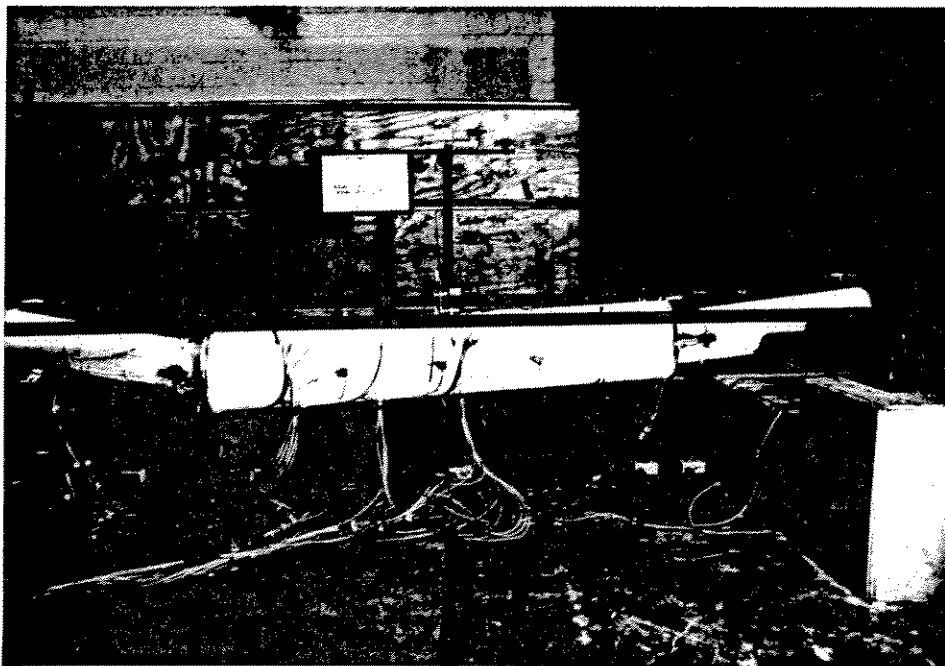


Figure 3.91 - Specimen C15 Lateral Displacement After Developing Local Buckling in Tube at South (Left) End of Sleeve

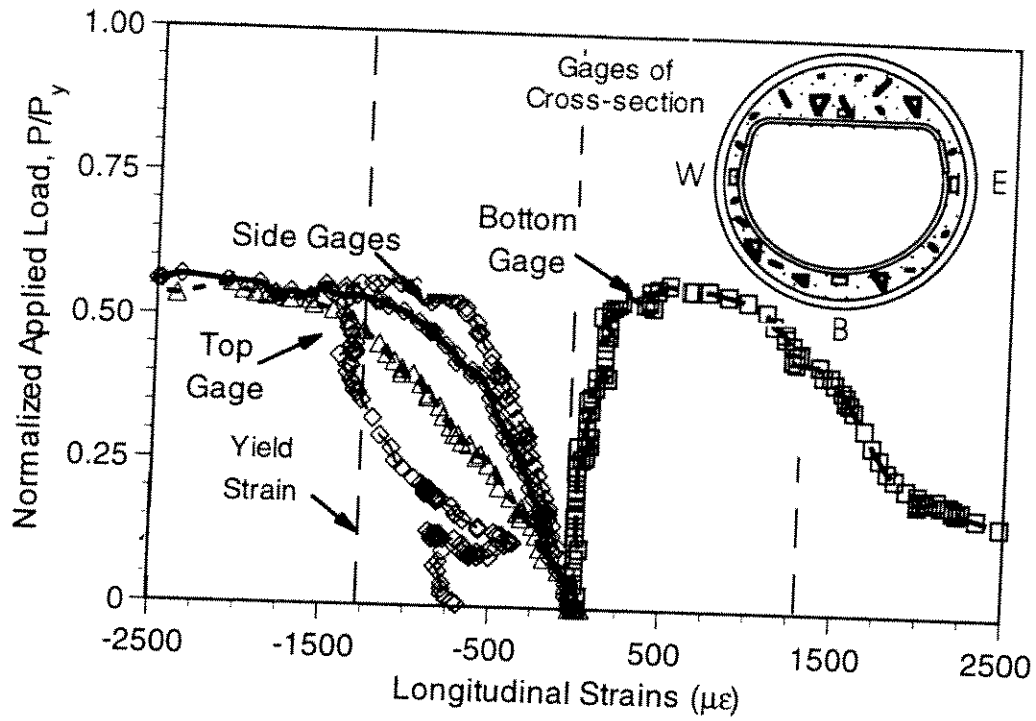


Figure 3.88 - Tube Strain History at  $x=0.17L$  of Specimen C15

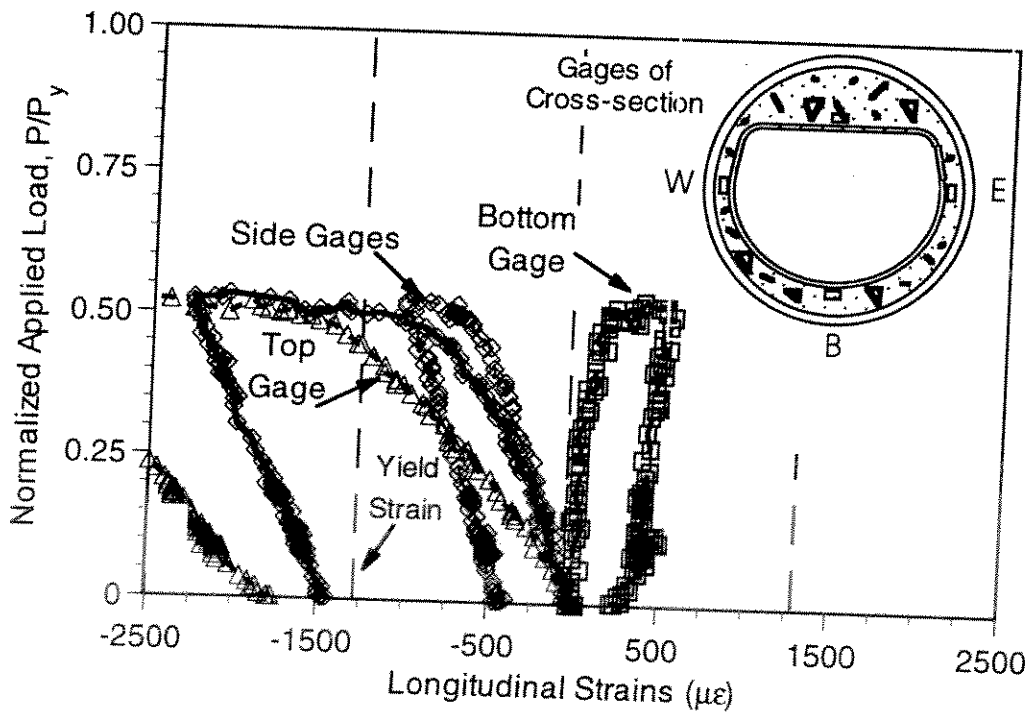


Figure 3.89 - Tube Strain History at  $x=0.83L$  of Specimen C15



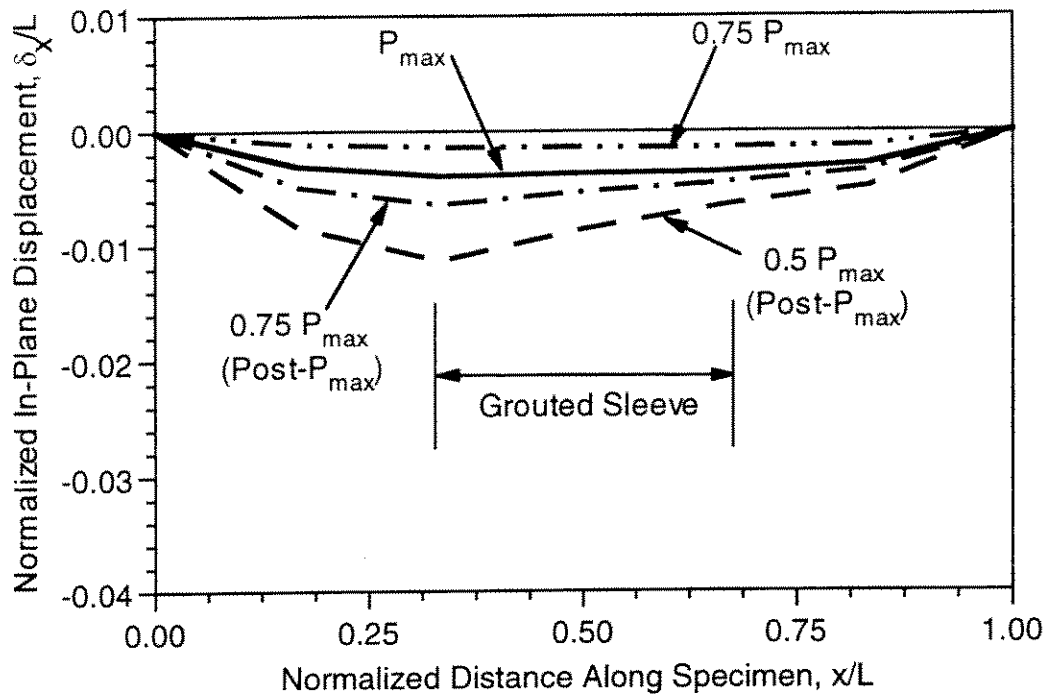


Figure 3.86 - Measured Lateral Displacements of Specimen C15 at Various Stages of Loading

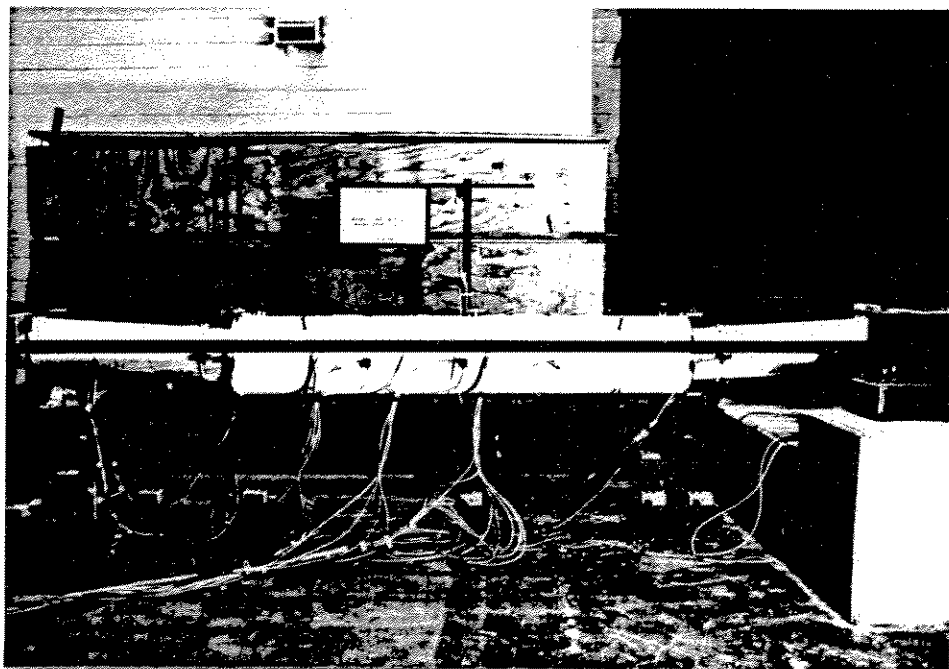


Figure 3.87 - Specimen C15 Near Ultimate Load

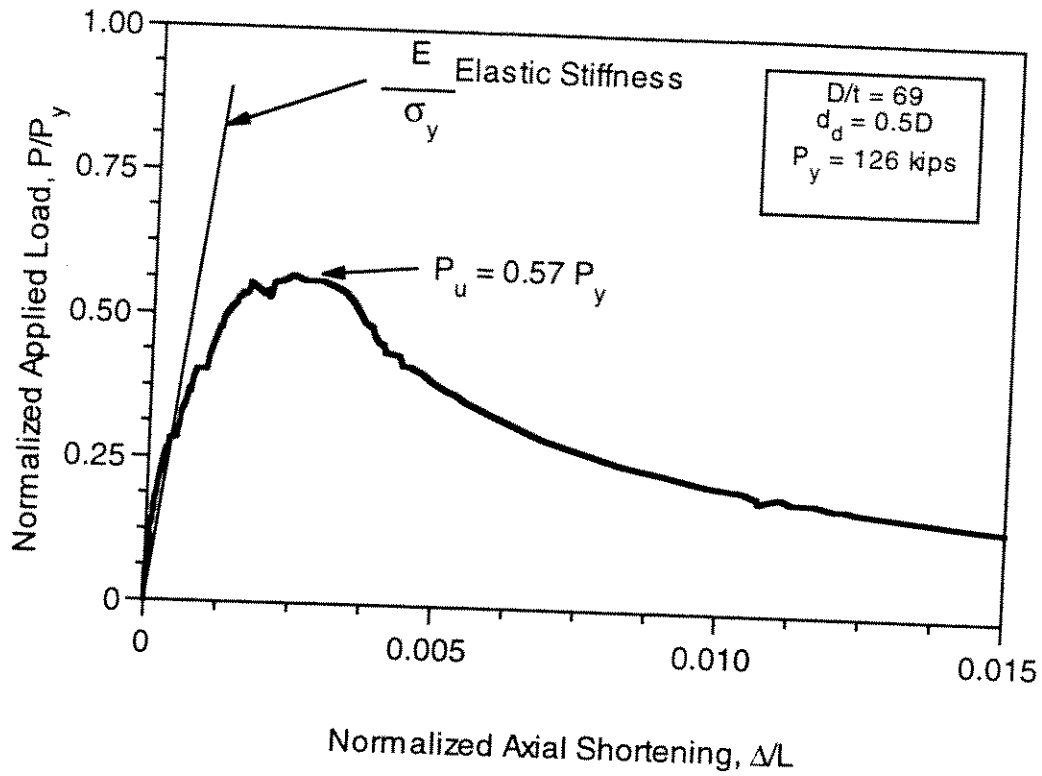


Figure 3.84 - Normalized Axial Load-Shortening Response of Specimen C15

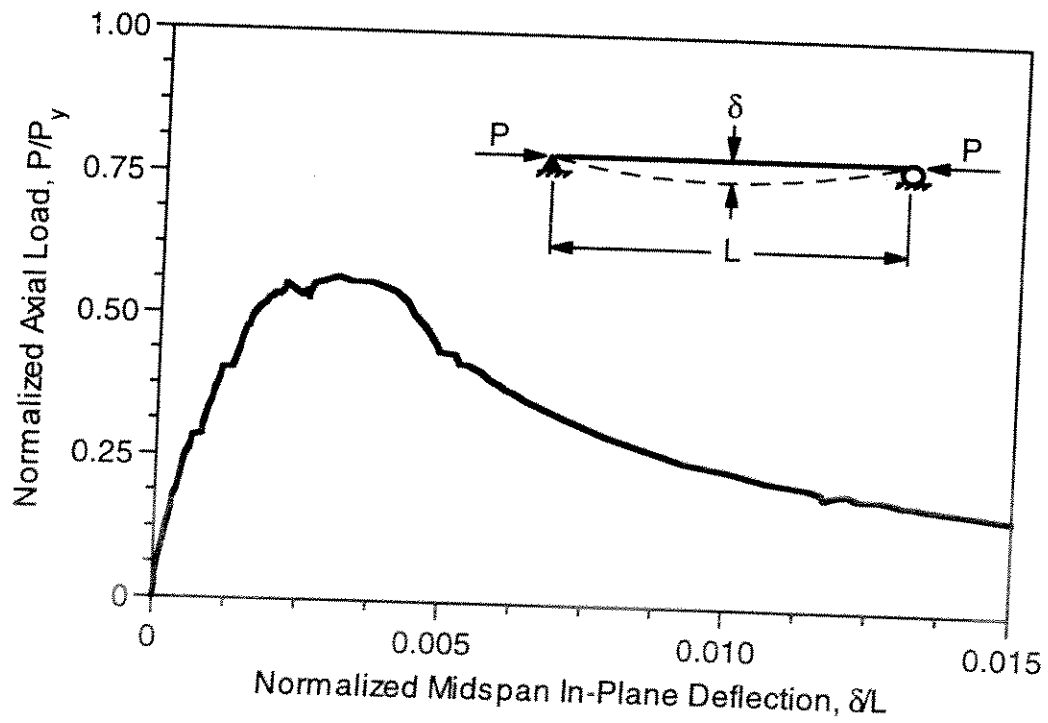


Figure 3.85 - Axial Load-Midspan Deflection Response of Specimen C15

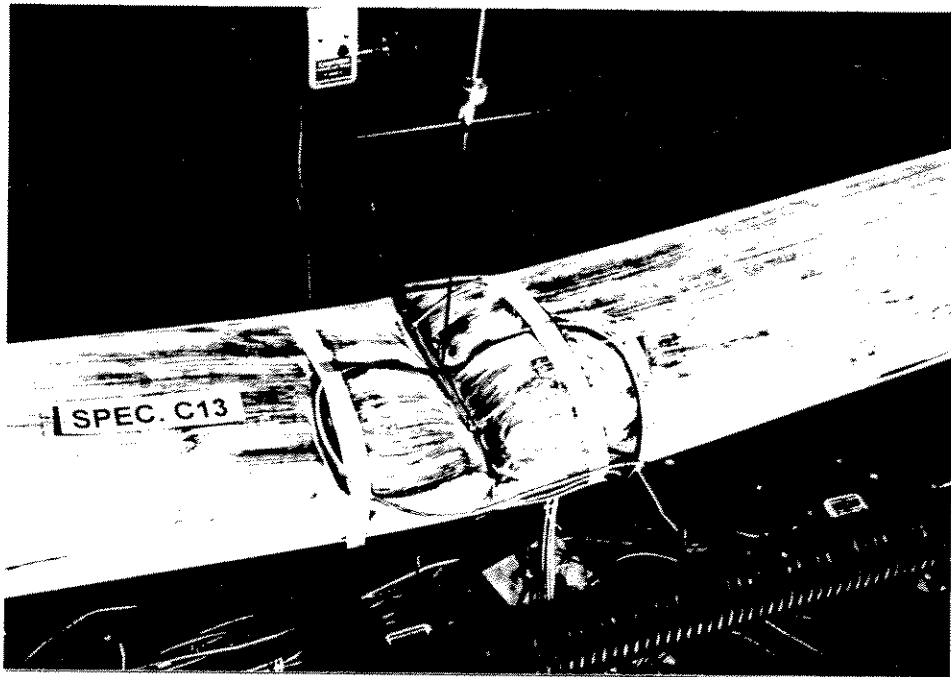


Figure 3.82 - Dented Region of Specimen C13 at End of Test

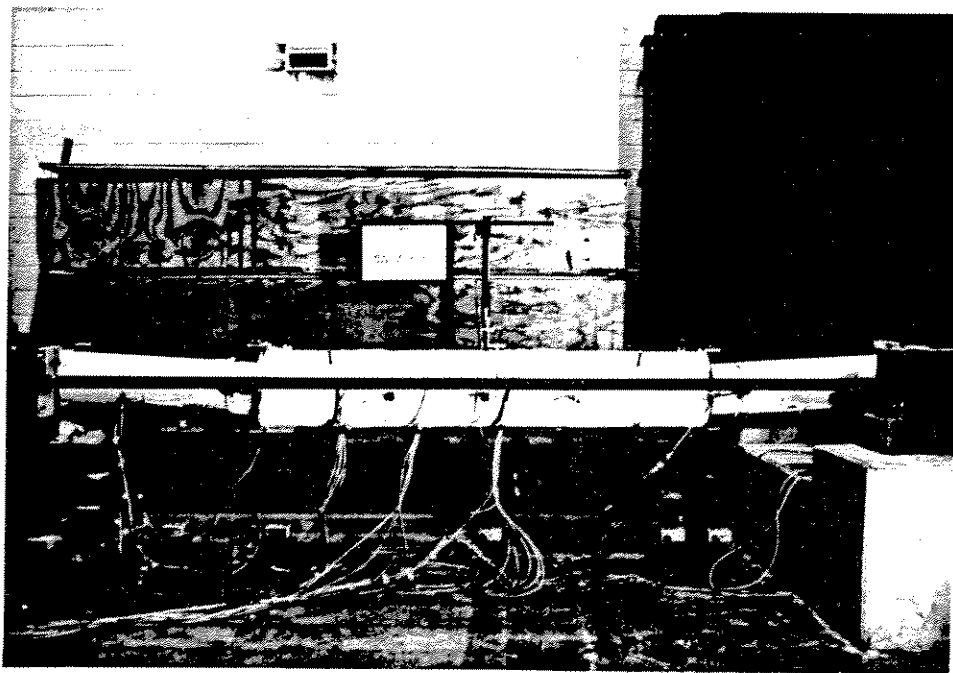


Figure 3.83 - Specimen C15 Prior to Testing

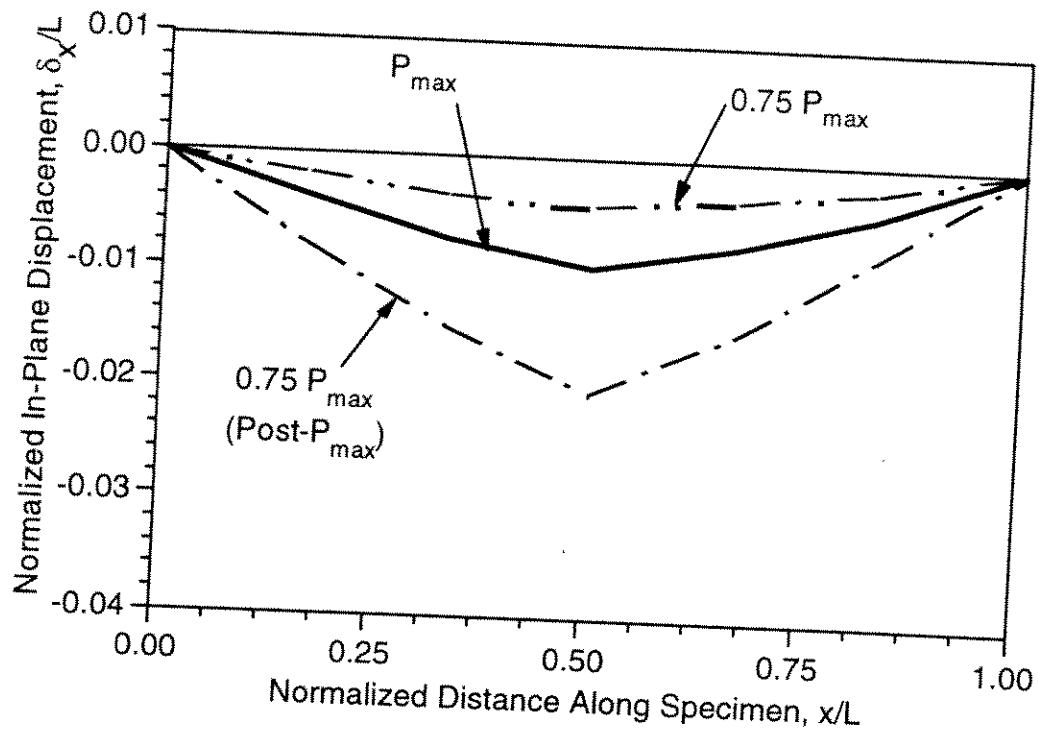


Figure 3.80 - Measured Lateral Displacements of Specimen C13 at Various Stages of Loading

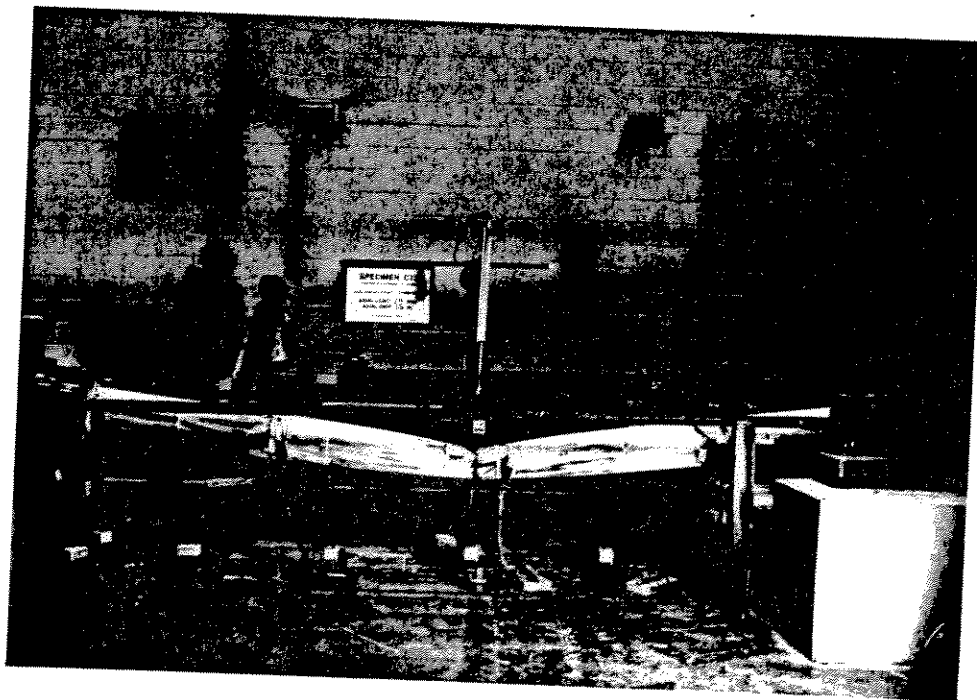


Figure 3.81 - Specimen C13 at End of Test

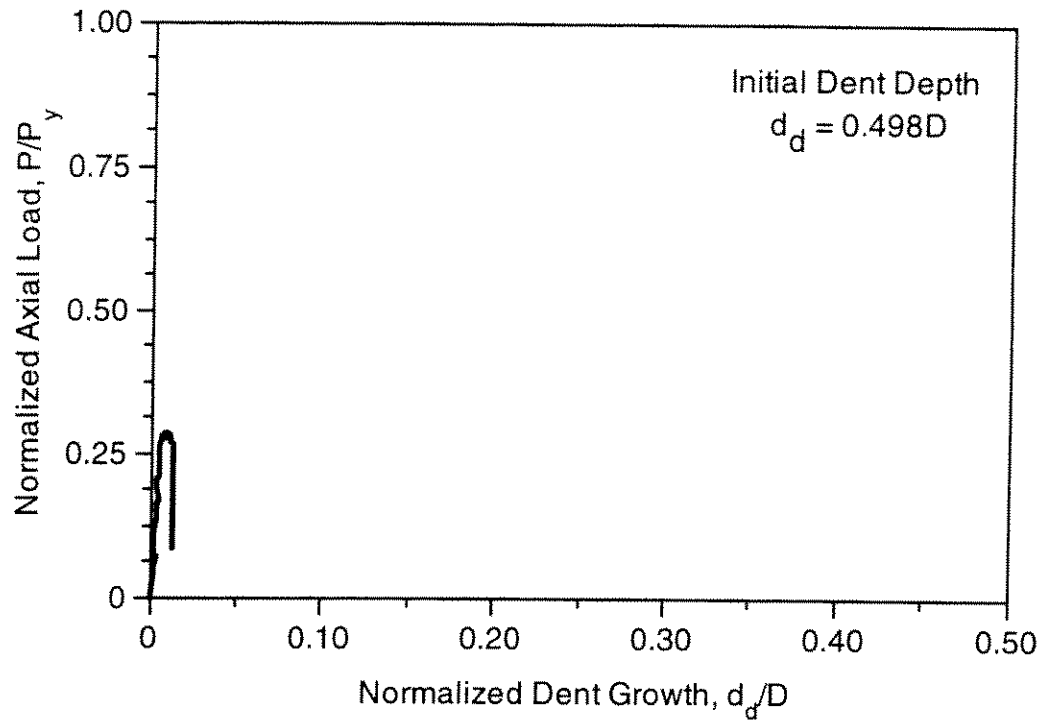


Figure 3.78 - Normalized Dent Growth of Specimen C13

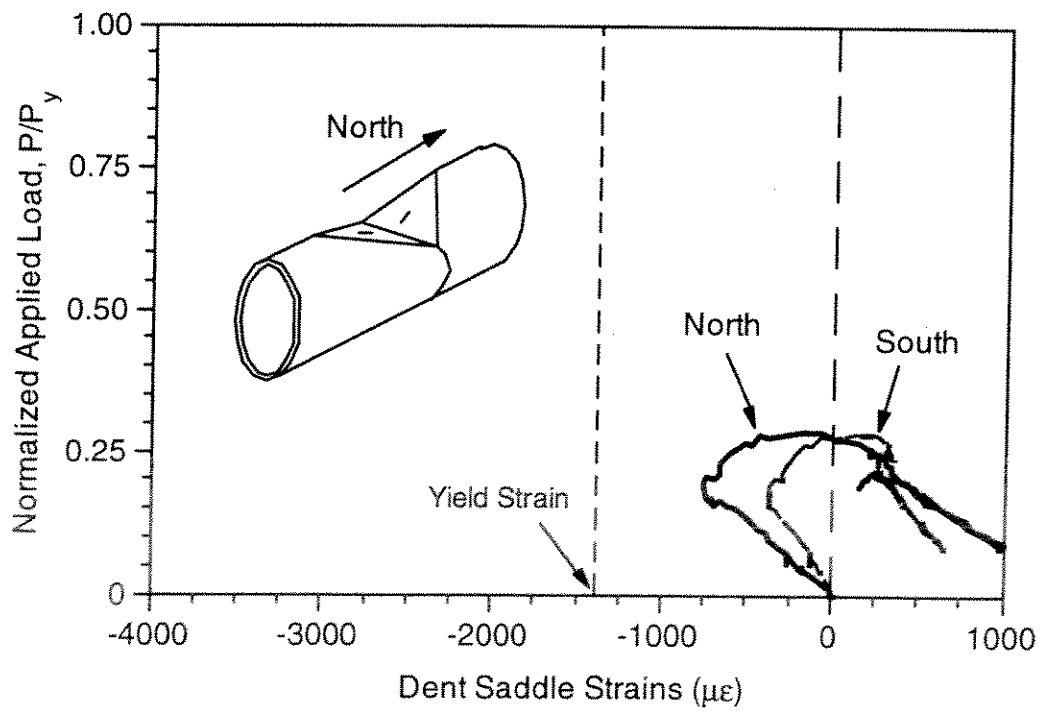


Figure 3.79 - Strain History Inside Dent Saddle of Specimen C13

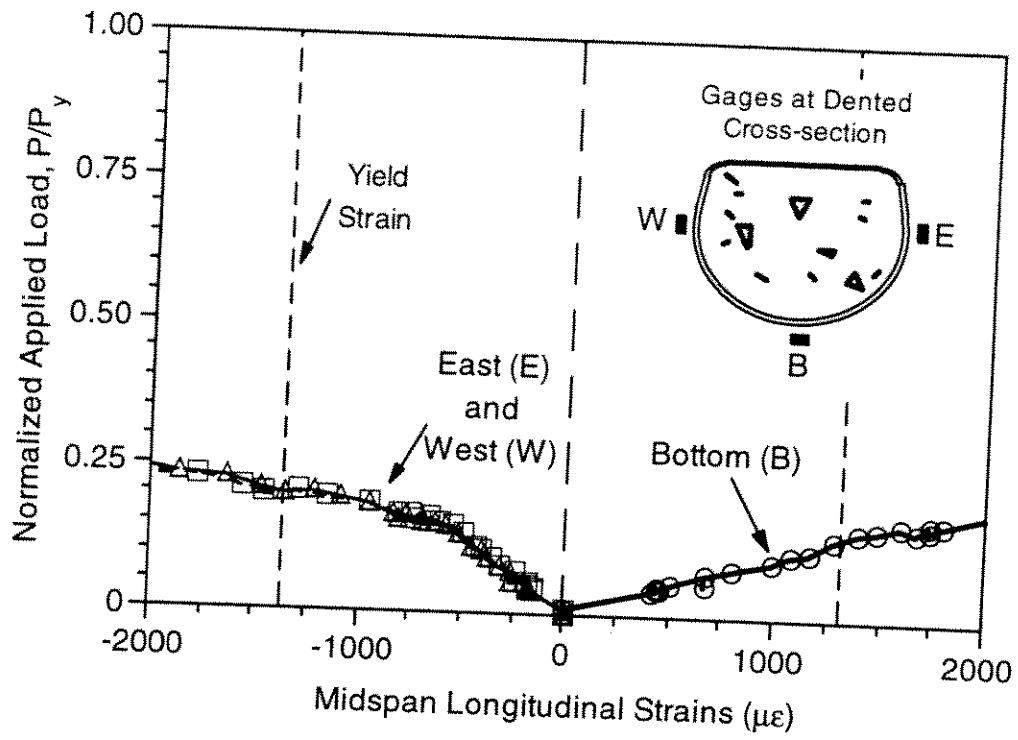


Figure 3.76 - Strain History at Midspan Dent of Specimen C13

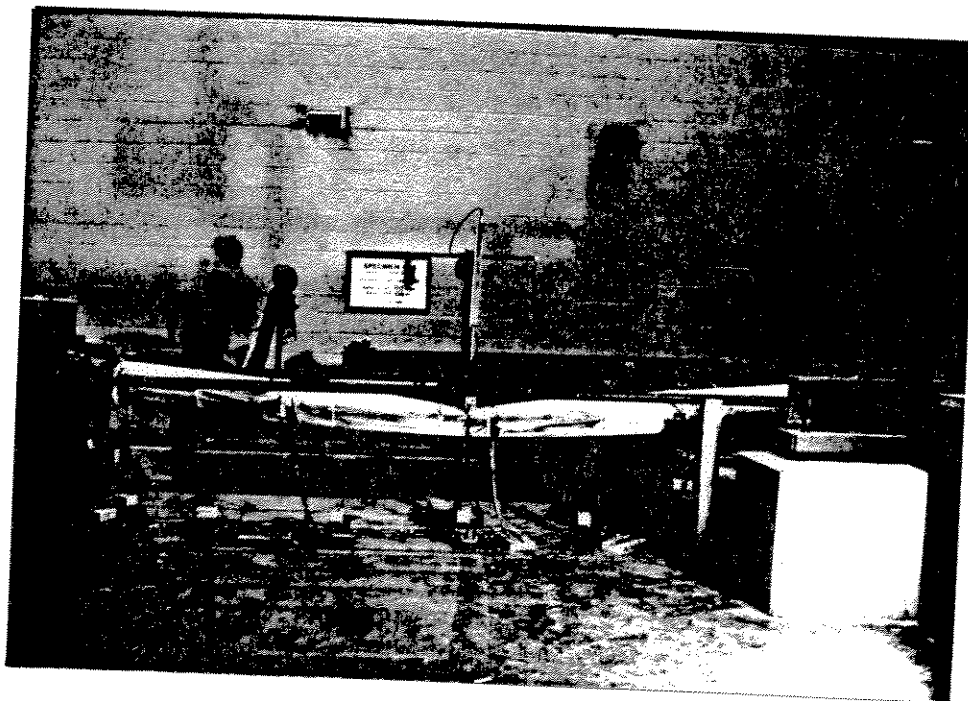


Figure 3.77 - Specimen C13 at Application of Maximum Axial Load

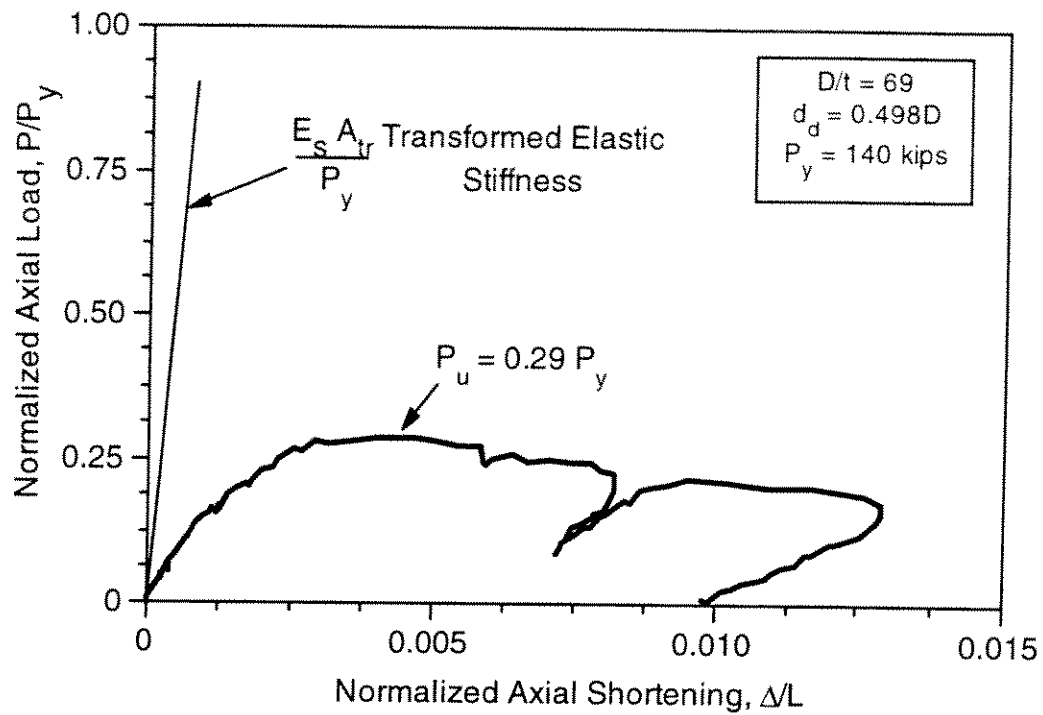


Figure 3.74 - Normalized Axial Load-Shortening Response of Specimen C13

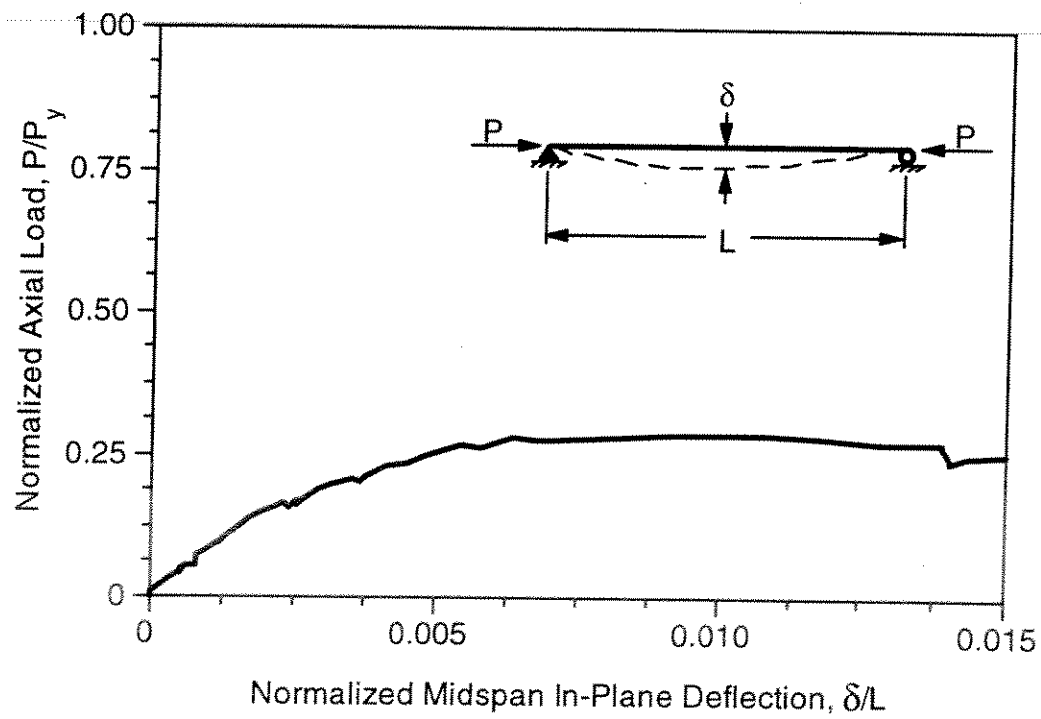


Figure 3.75 - Axial Load-Midspan Deflection Response of Specimen C13

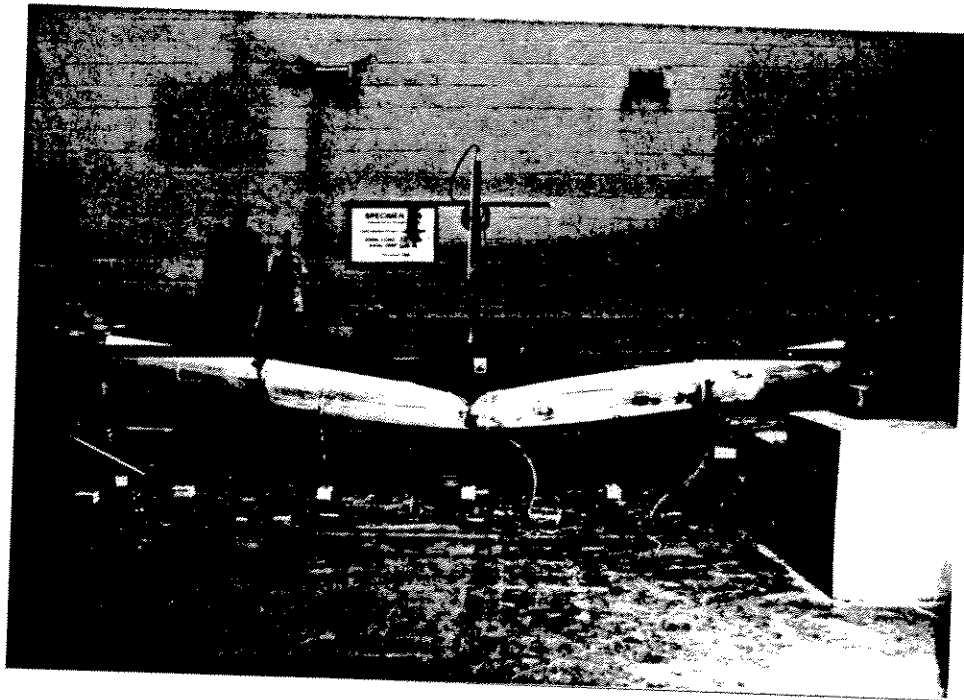


Figure 3.72 - Overall View of Specimen A13 at End of Test

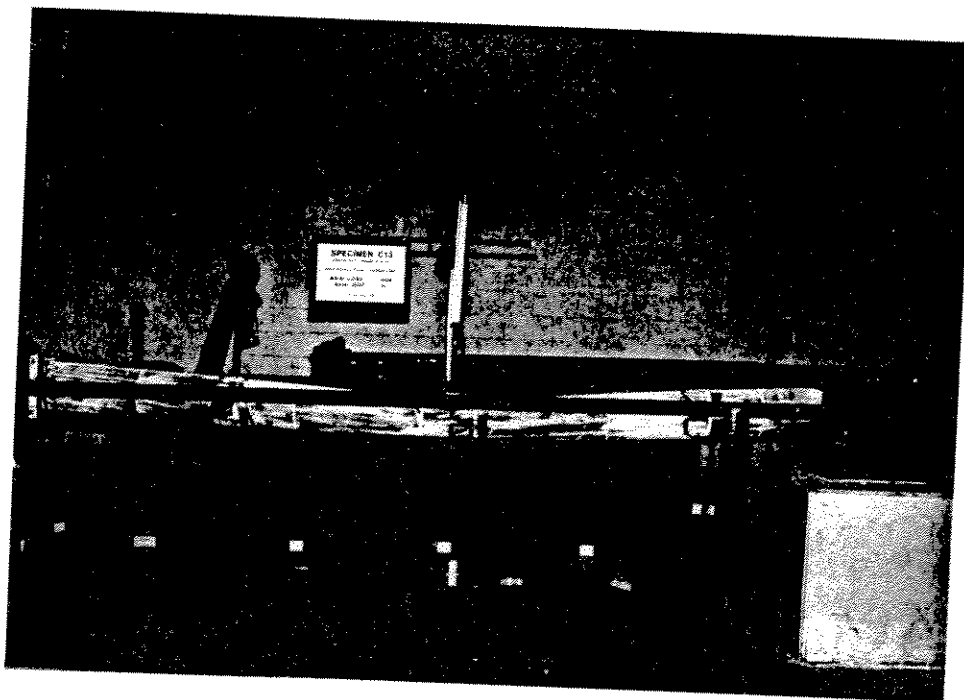


Figure 3.73 - Specimen C13 Prior to Test



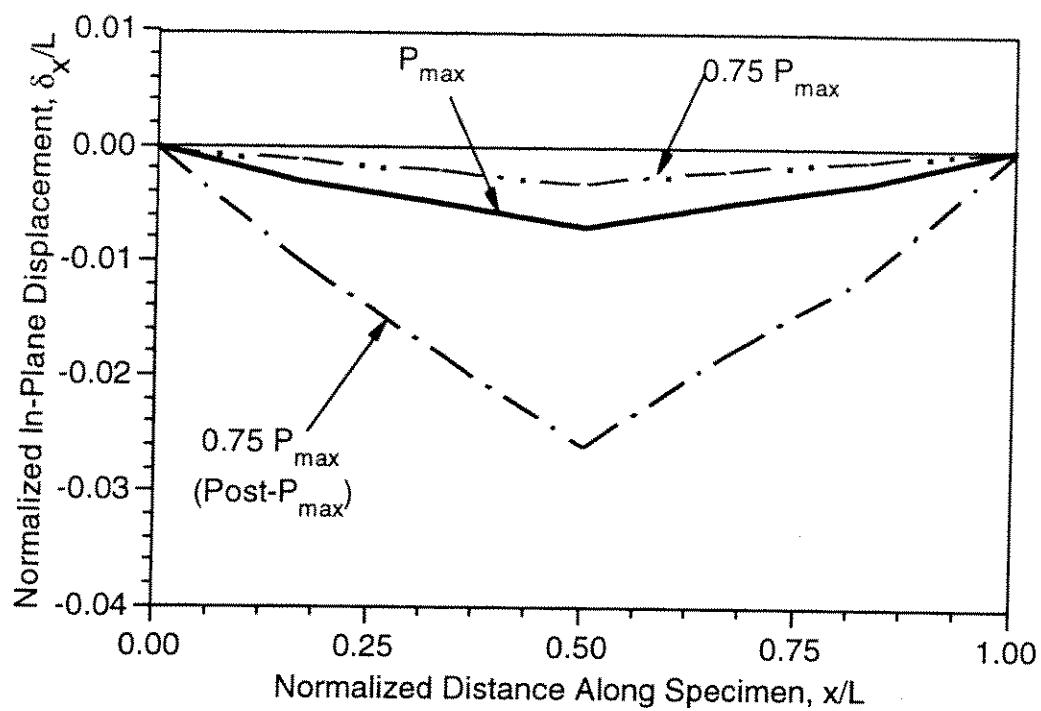


Figure 3.70 - Measured Lateral Displacements of Specimen A13 at Various Stages of Loading

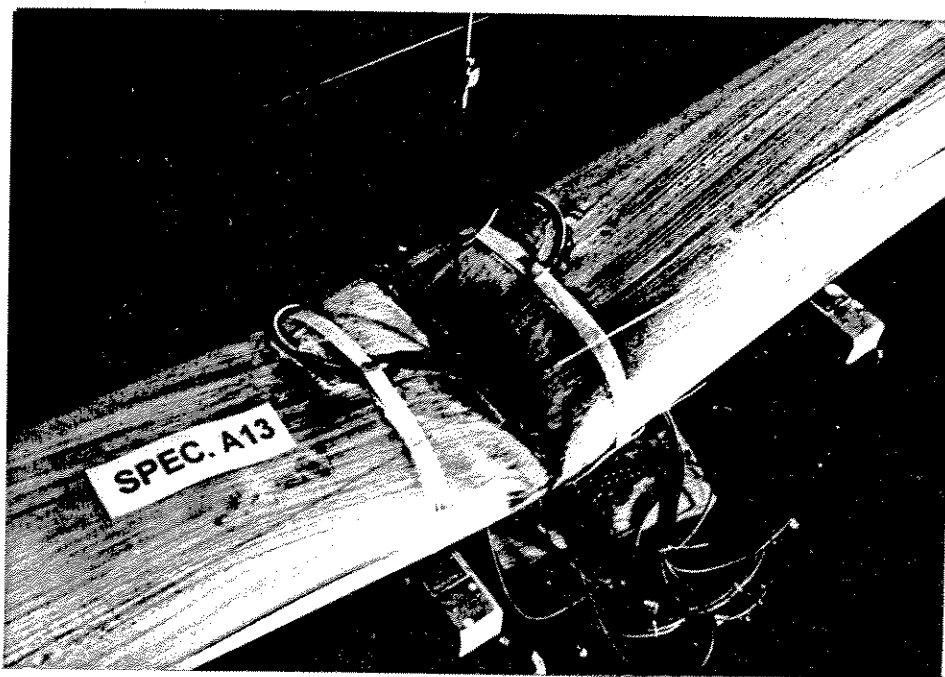


Figure 3.71 - Dented Region of Specimen A13 at End of Test

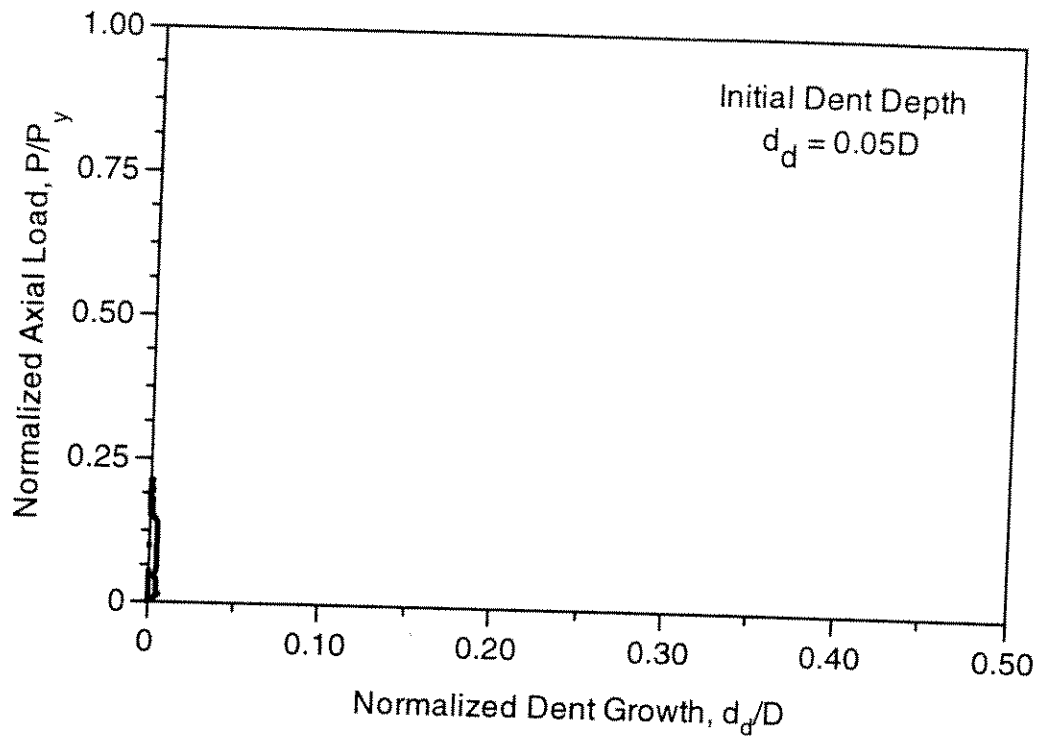


Figure 3.68 - Normalized Dent Growth of Specimen A13

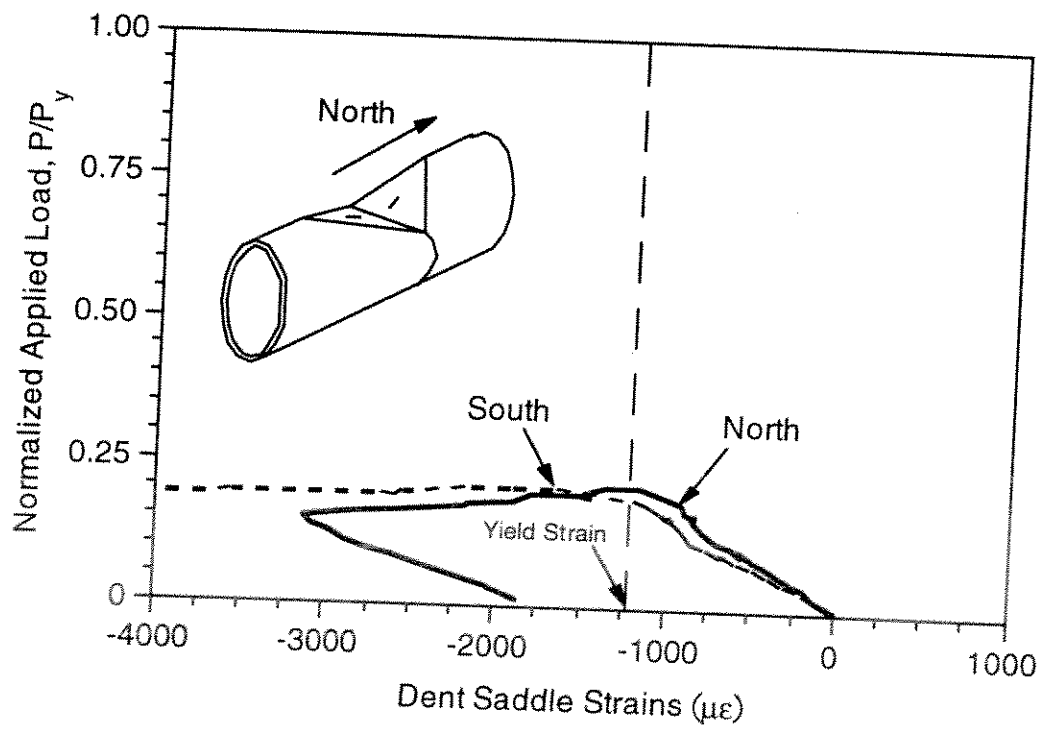


Figure 3.69 - Strain History Inside Dent Saddle of Specimen A13

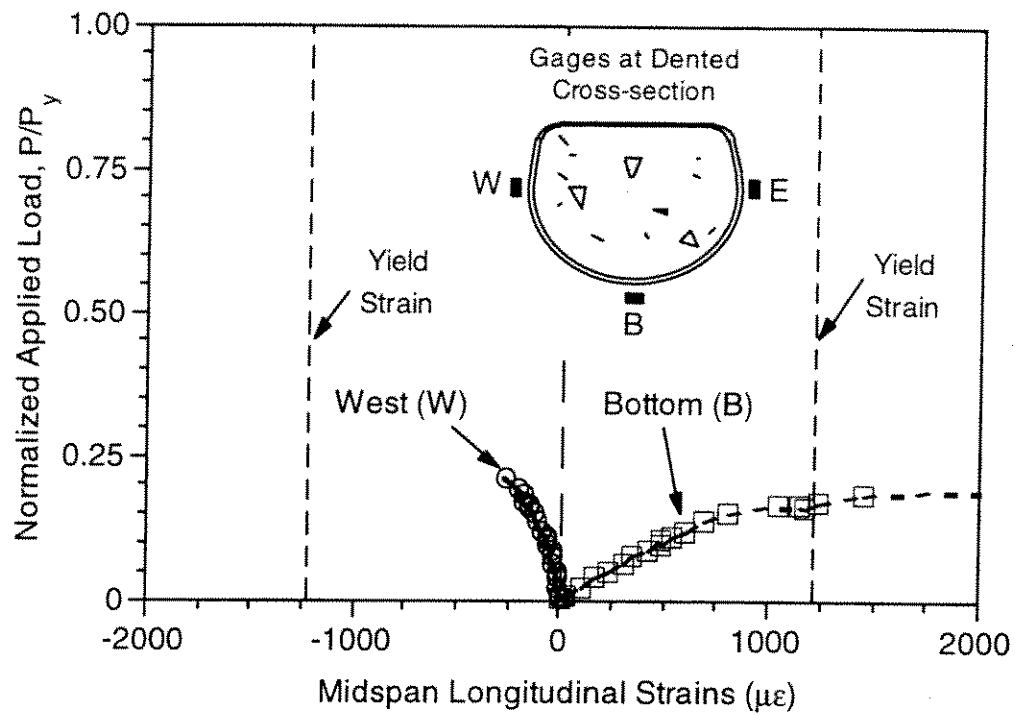


Figure 3.66 - Strain History at Midspan Dent of Specimen A13  
(East Gage Malfunctioned)



Figure 3.67 - Specimen A13 at Application of Maximum Axial Load

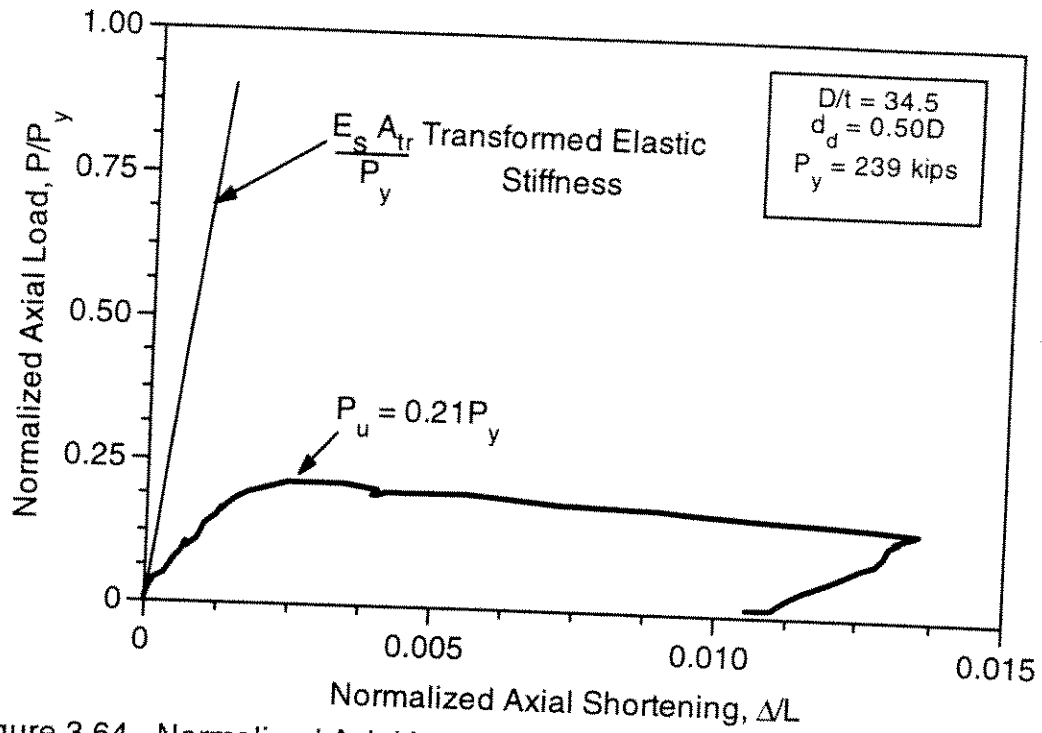


Figure 3.64 - Normalized Axial Load-Shortening Response of Specimen A13

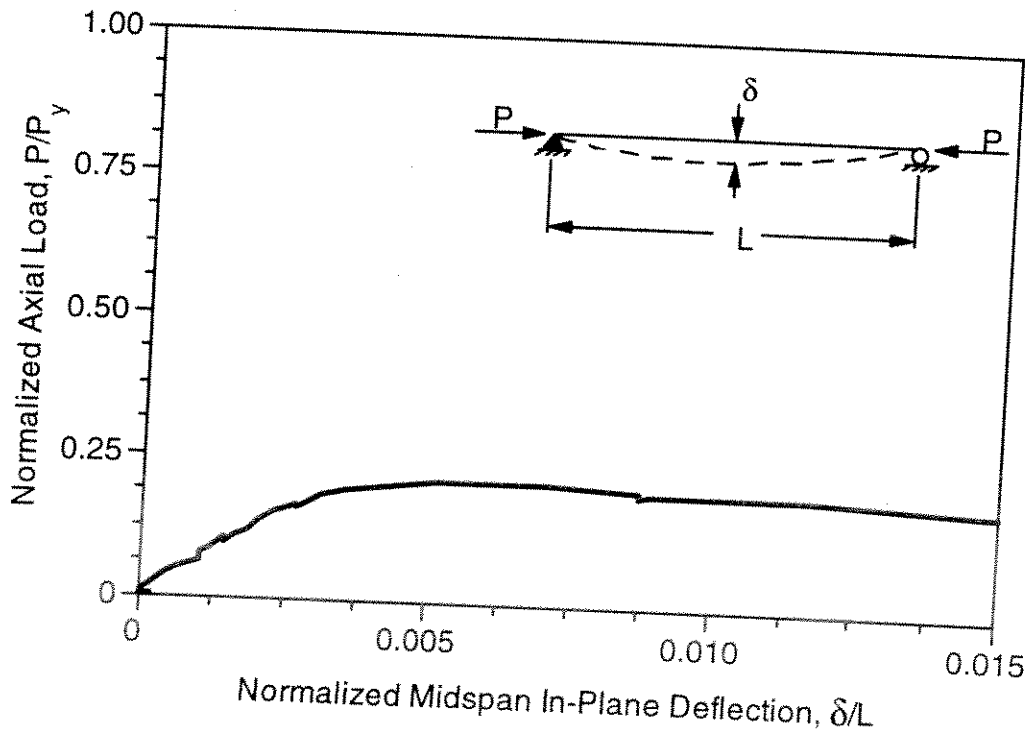


Figure 3.65 - Axial Load-Midspan Deflection Response of Specimen A13

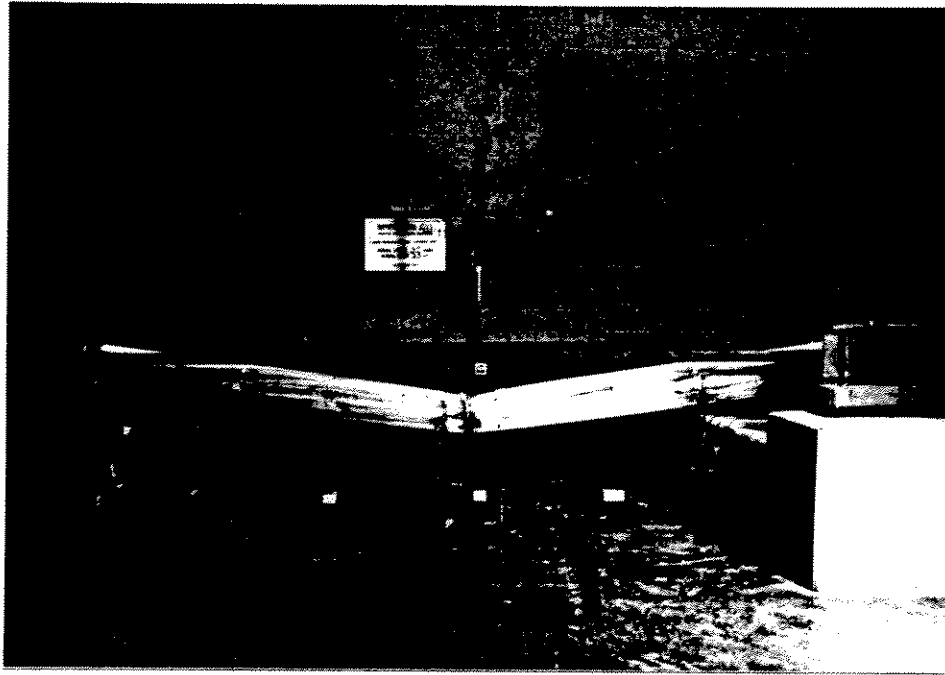


Figure 3.62 - Specimen C11 at End of Test

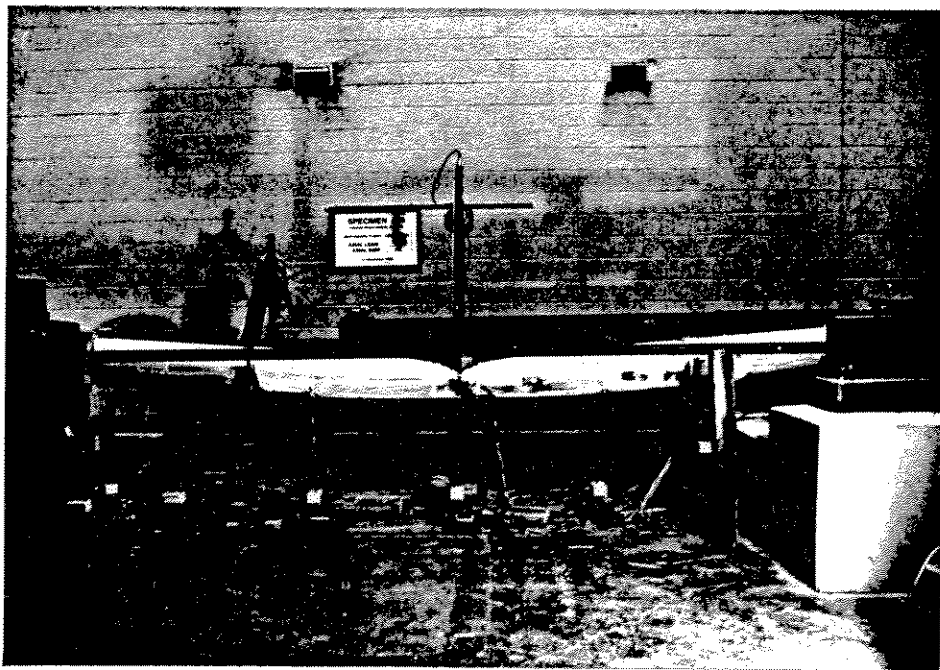


Figure 3.63 - Specimen A13 Prior to Test



Figure 3.60 - Specimen C11 After Achieving Maximum Axial Load (  $\delta = 0.01L$  )

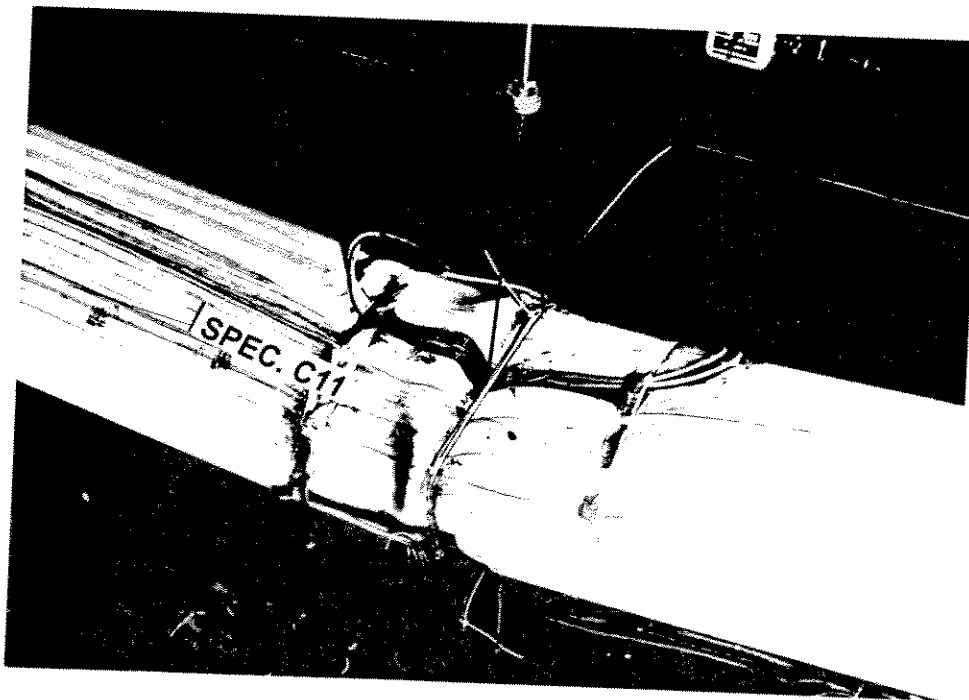


Figure 3.61 - Dented Region of Specimen C11 After Developing Maximum Load (  $\Delta = 0.0089L$  )

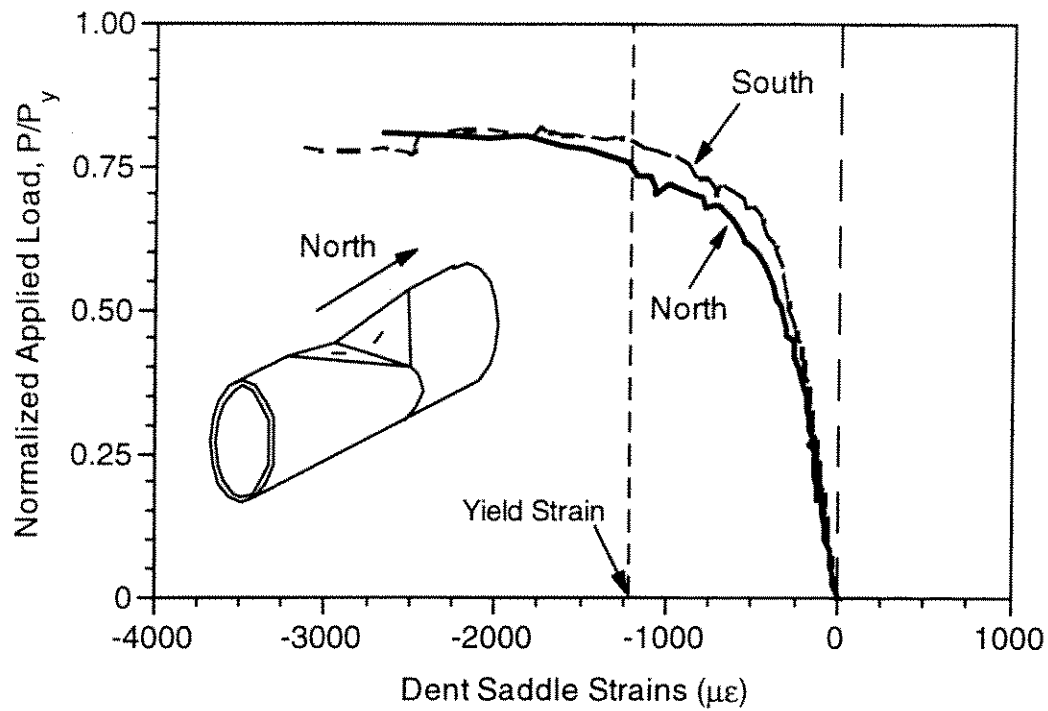


Figure 3.58 - Strain History Inside Dent Saddle of Specimen C11

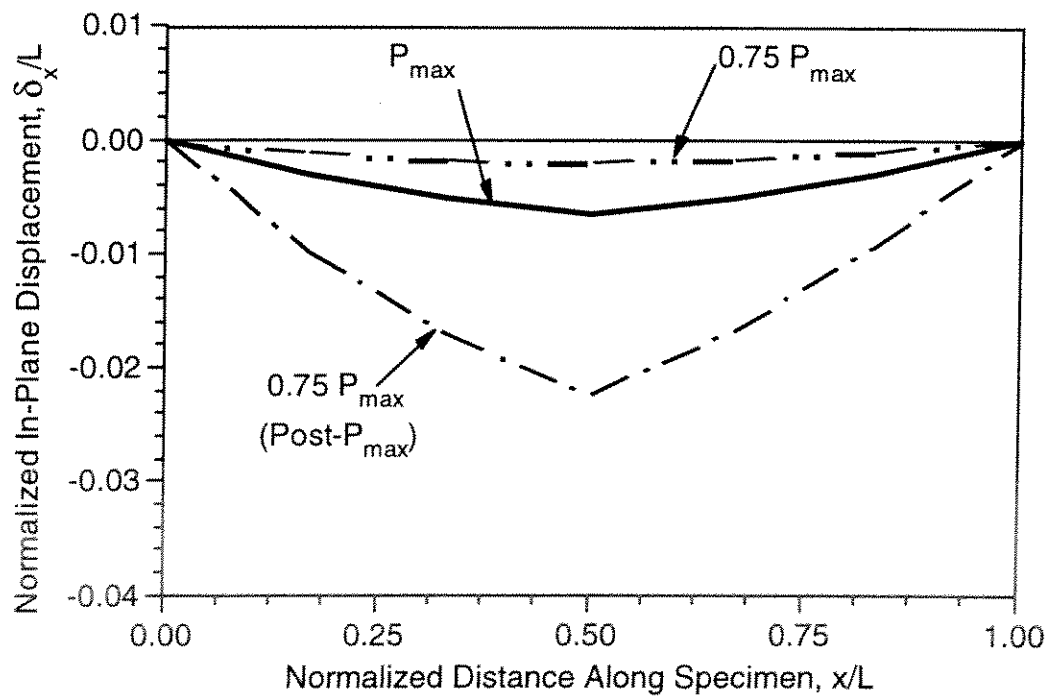


Figure 3.59 - Measured Lateral Displacements of Specimen C11 at Various Stages of Loading

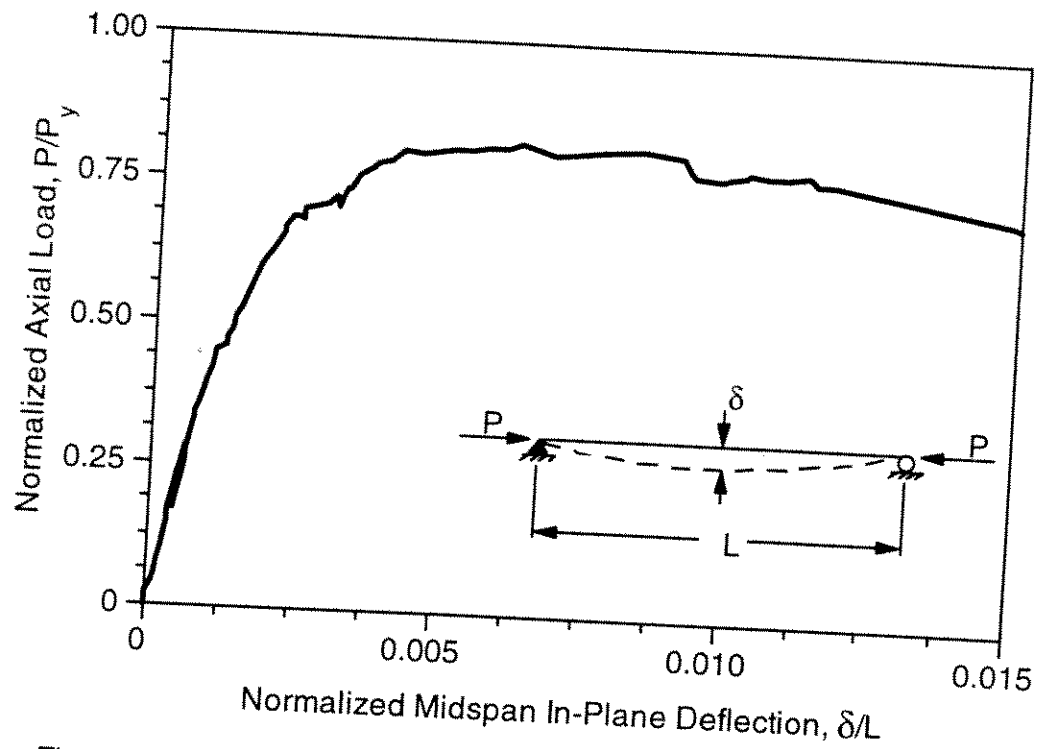


Figure 3.56 - Axial Load-Midspan Deflection Response of Specimen C11

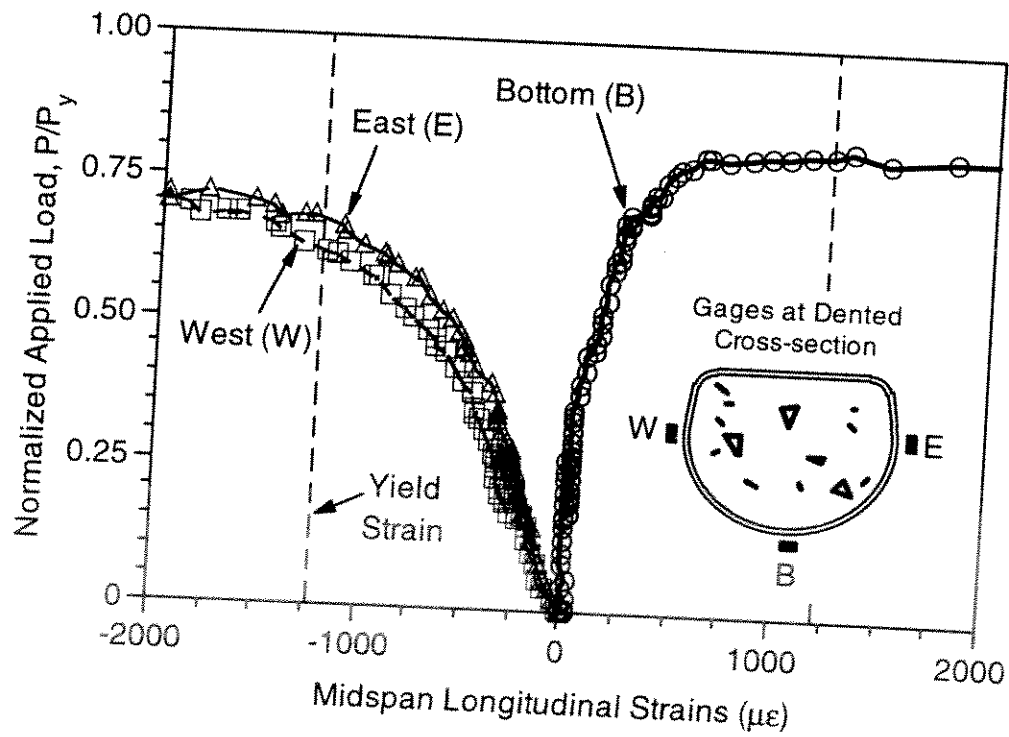


Figure 3.57 - Strain History at Midspan Dent of Specimen C11



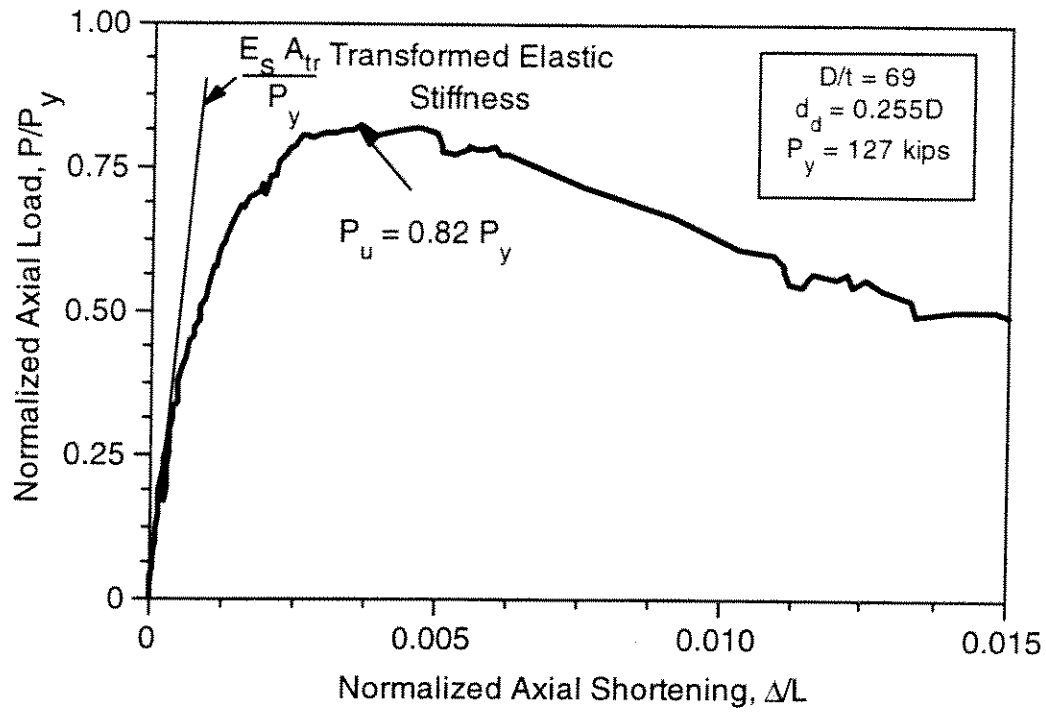


Figure 3.54 - Normalized Axial Load-Shortening Response of Specimen C11

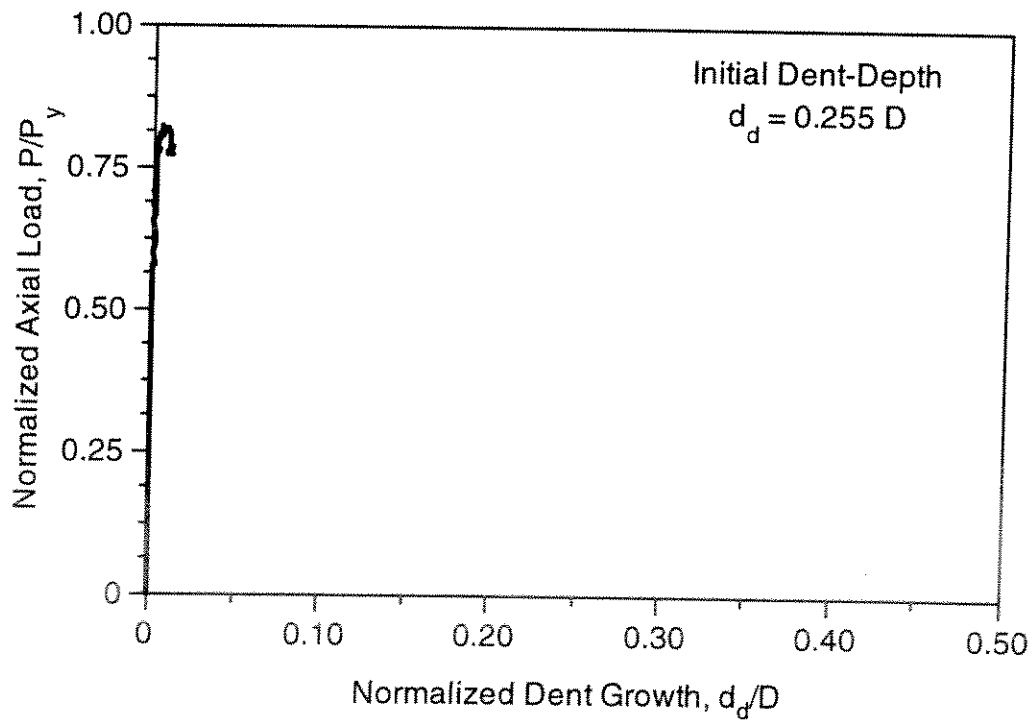


Figure 3.55 - Normalized Dent Growth of Specimen C11

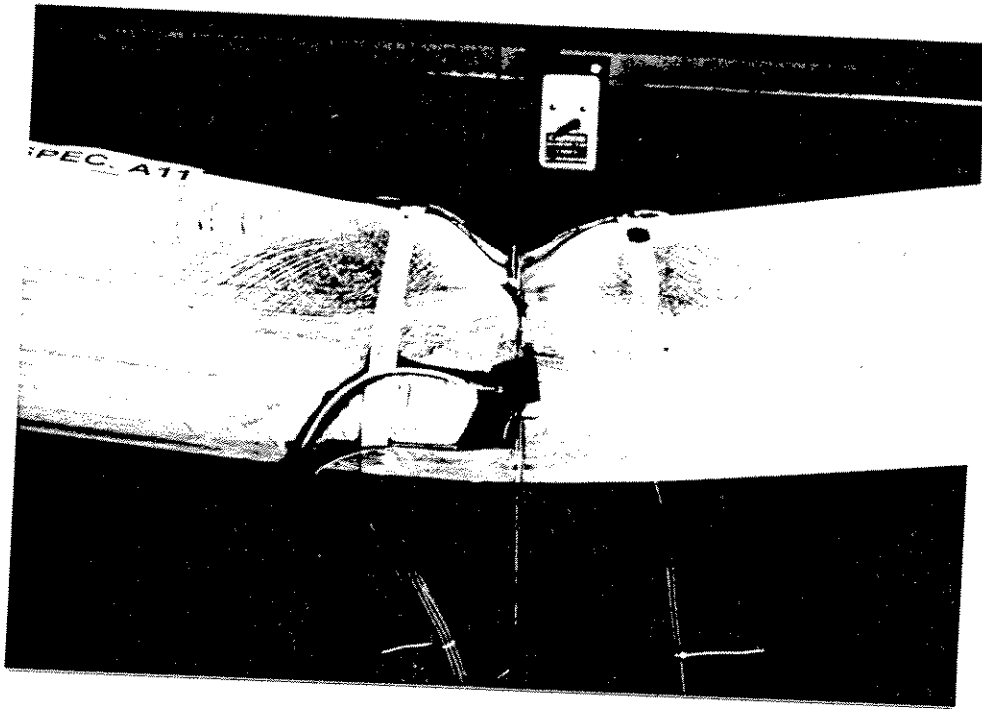


Figure 3.52 - Side View of Dented Region of Specimen A11 Near End of Test



Figure 3.53 - Specimen C11 Prior to Testing

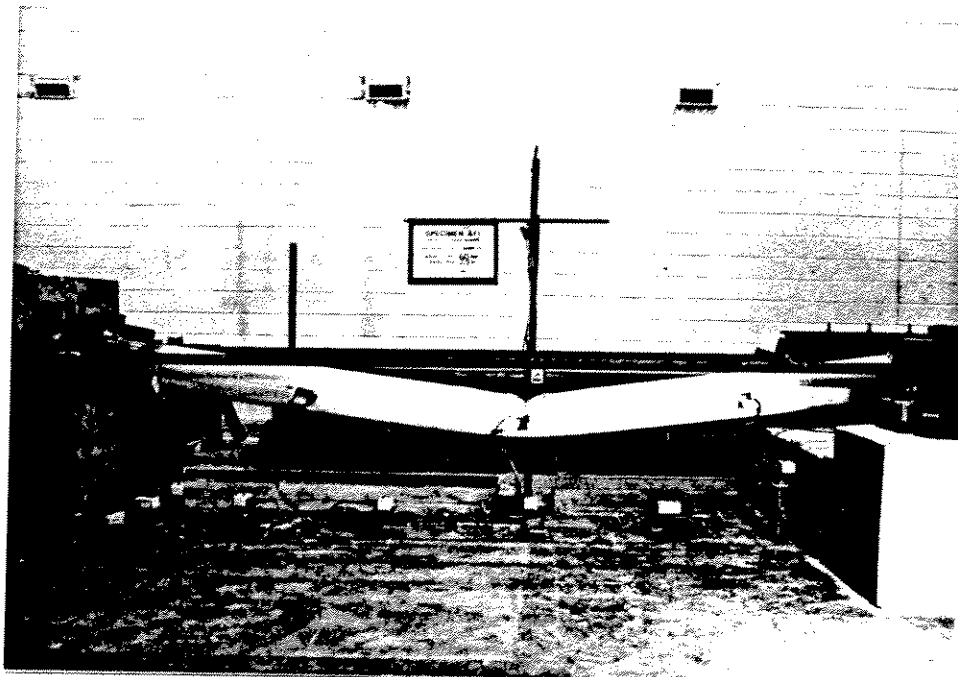


Figure 3.50 - Specimen A11 Following Application of Maximum Axial Load

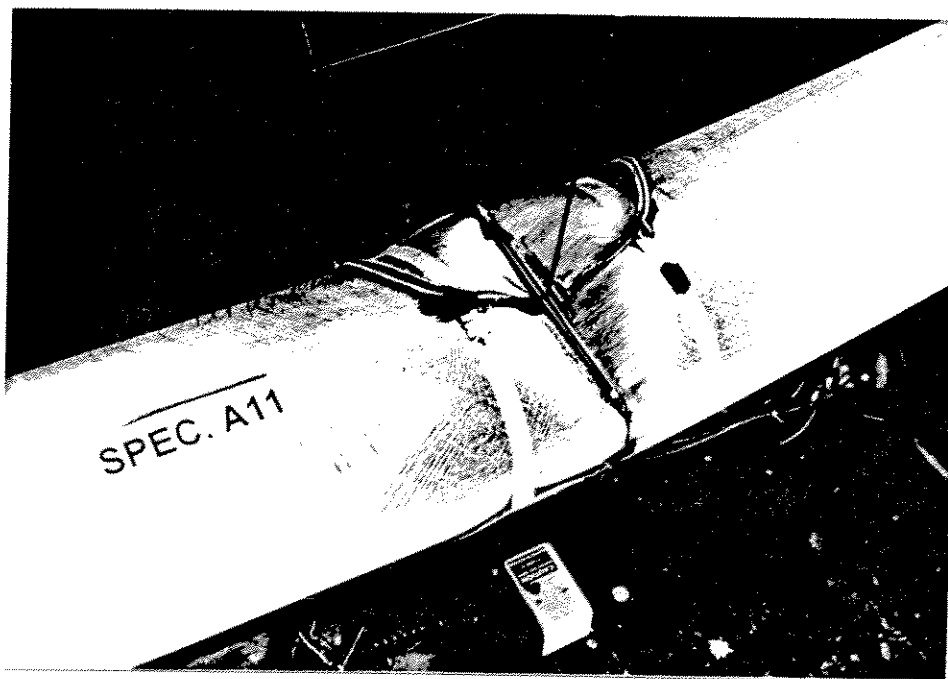


Figure 3.51 - Dented Regions of Specimen A11 Near End of Test

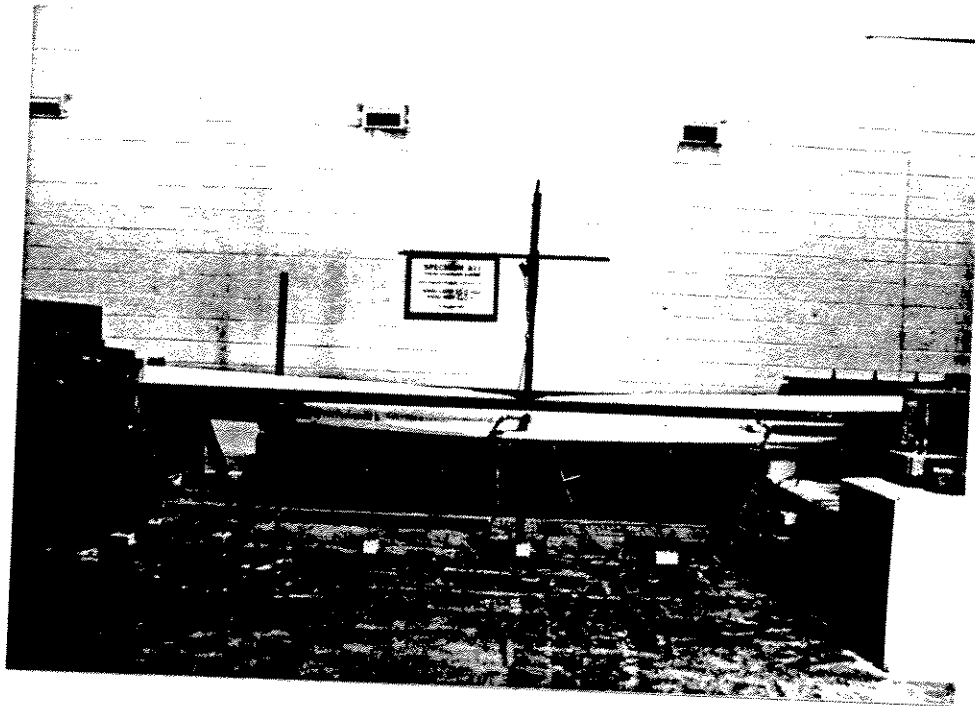


Figure 3.48 - Specimen A11 at Maximum Applied Axial Load

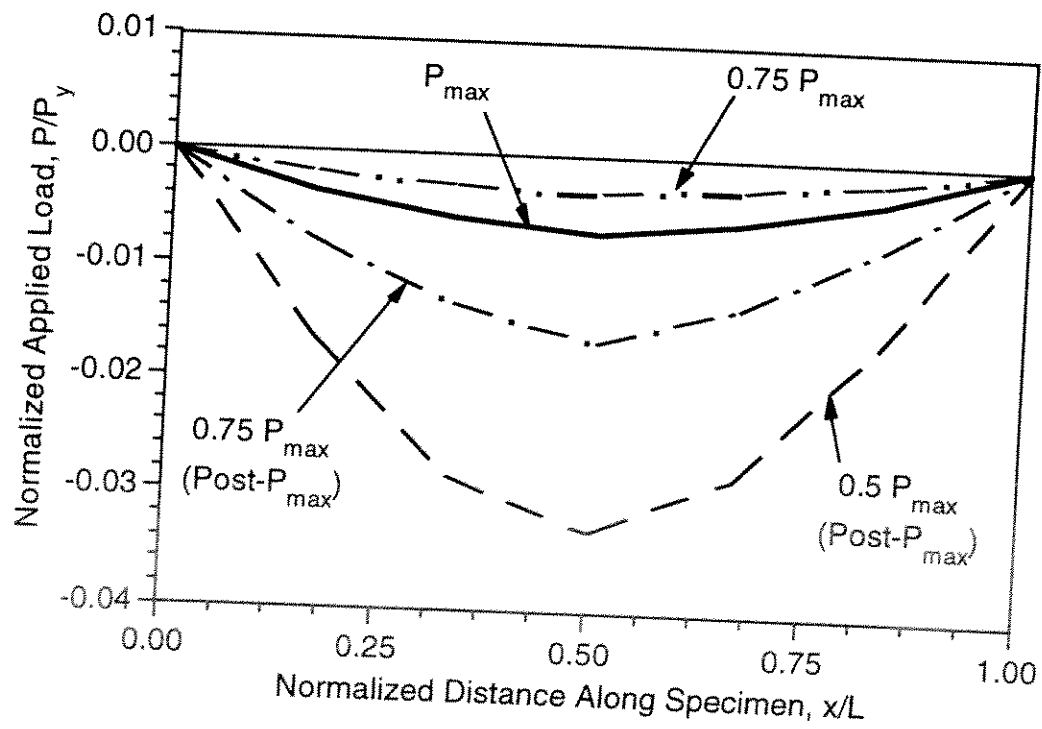


Figure 3.49 - Measured Lateral Displacements of Specimen A11 at Various Stages of Loading

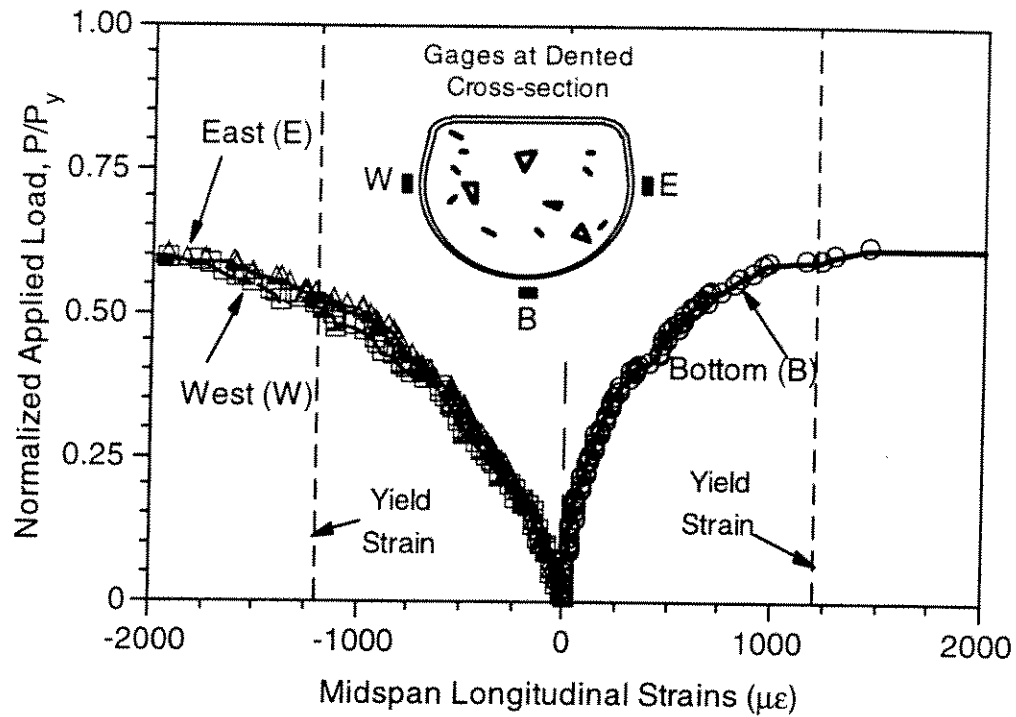


Figure 3.46 - Strain History at Midspan Dent of Specimen A11

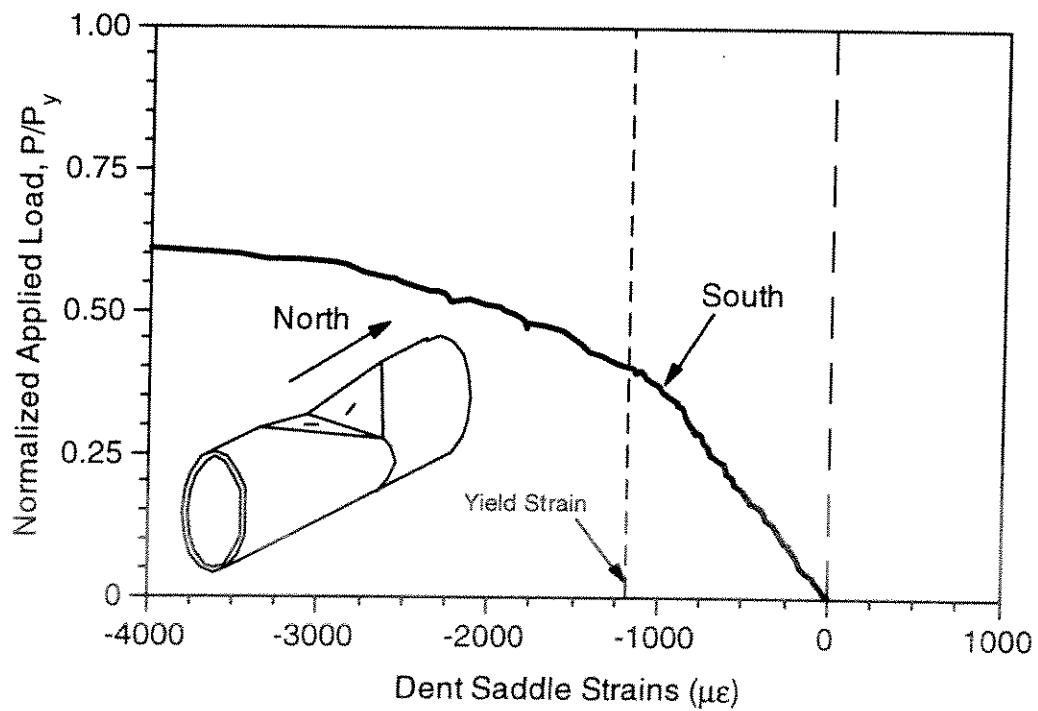


Figure 3.47 - Strain History Inside Dent Saddle of Specimen A11  
(North Gage Malfunctioned)

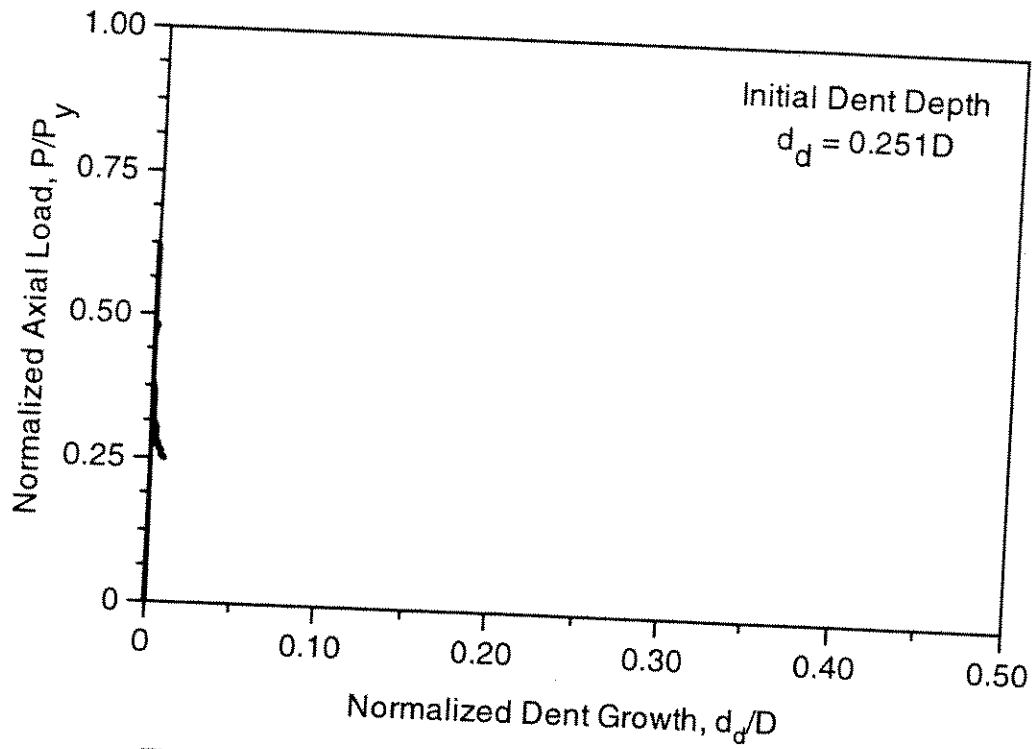


Figure 3.44 - Normalized Dent Growth of Specimen A11

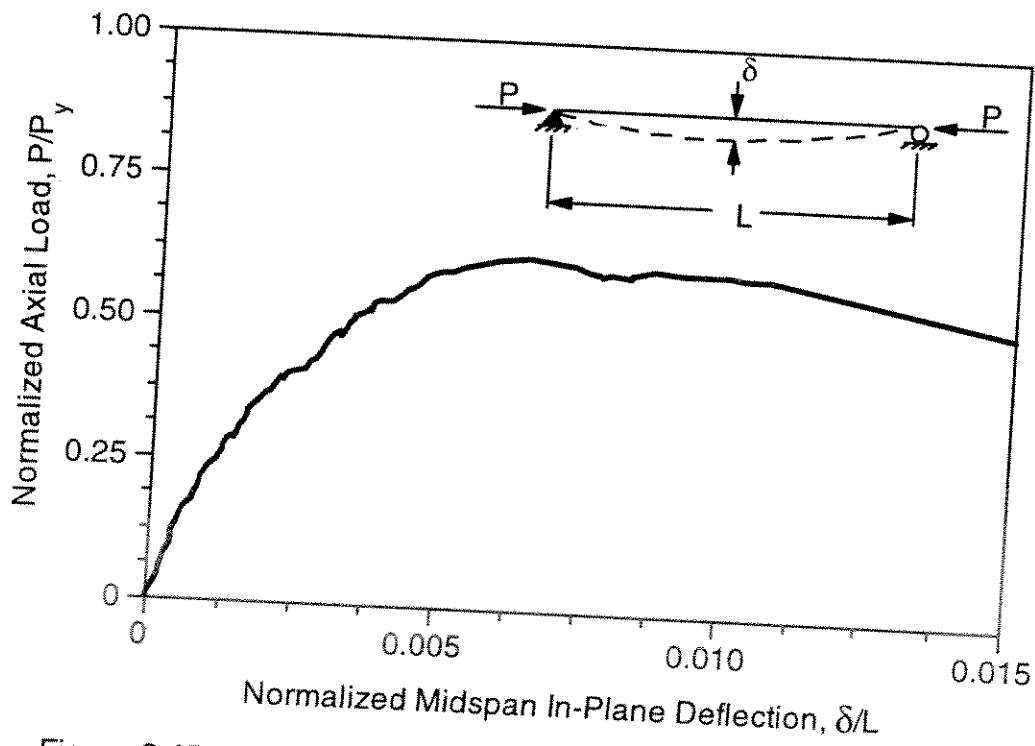


Figure 3.45 - Axial Load-Midspan Deflection Response of Specimen A11

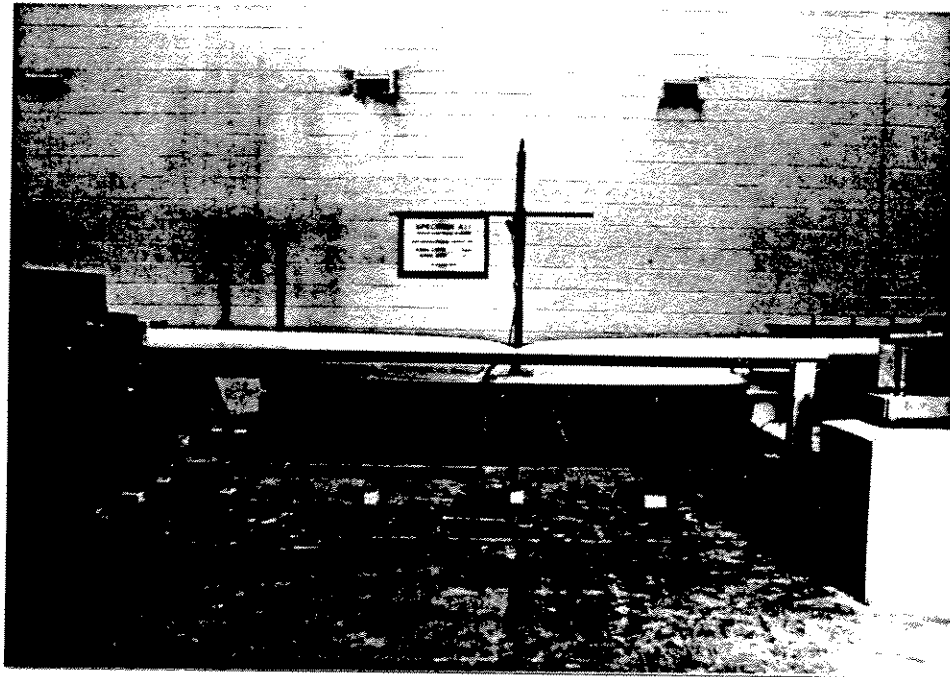


Figure 3.42 - Specimen A11 Prior to Testing

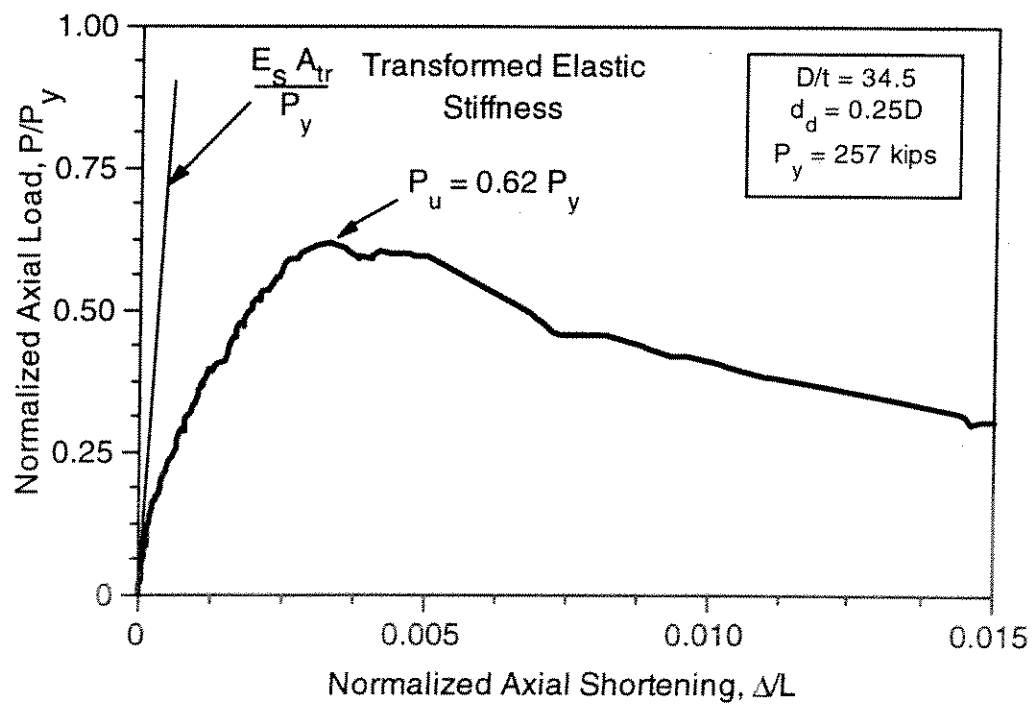


Figure 3.43 - Normalized Axial Load-Shortening Response of Specimen A11

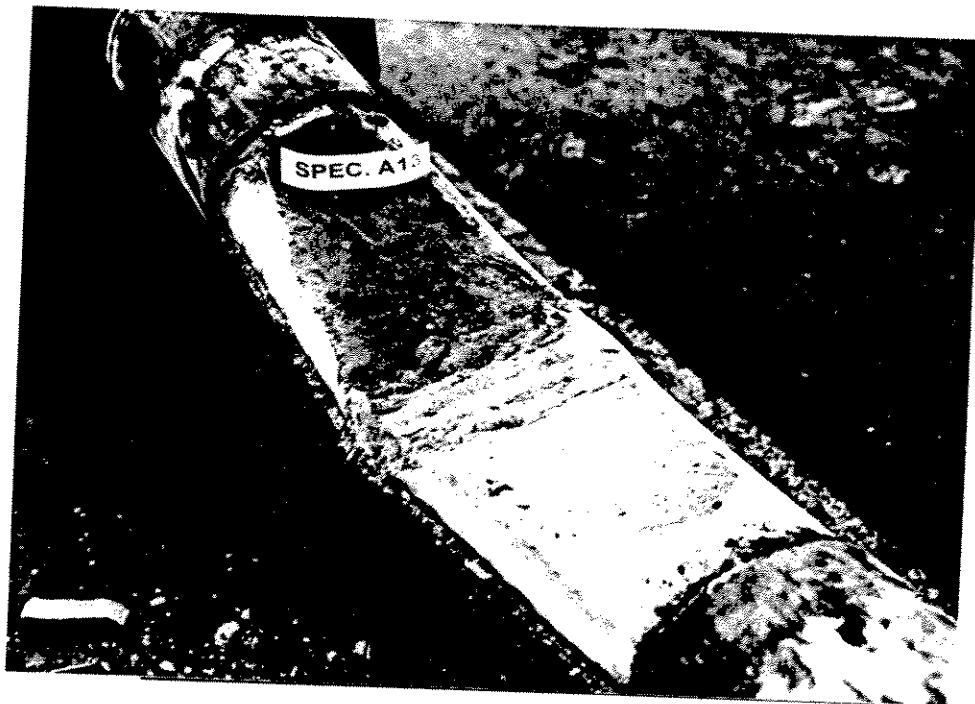


Figure 3.107 - Exposed Grout in Dented Zone of Specimen A13 After Completion of Testing



Figure 3.108 - Exposed Grout in Dented Zone of Specimen C13 After Completion of Testing





Figure 3.105 - Exposed Grout in Dented Zone of Specimen A11 After Completion of Testing



Figure 3.106 - Exposed Grout in Dented Zone of Specimen C11 After Completion of Testing

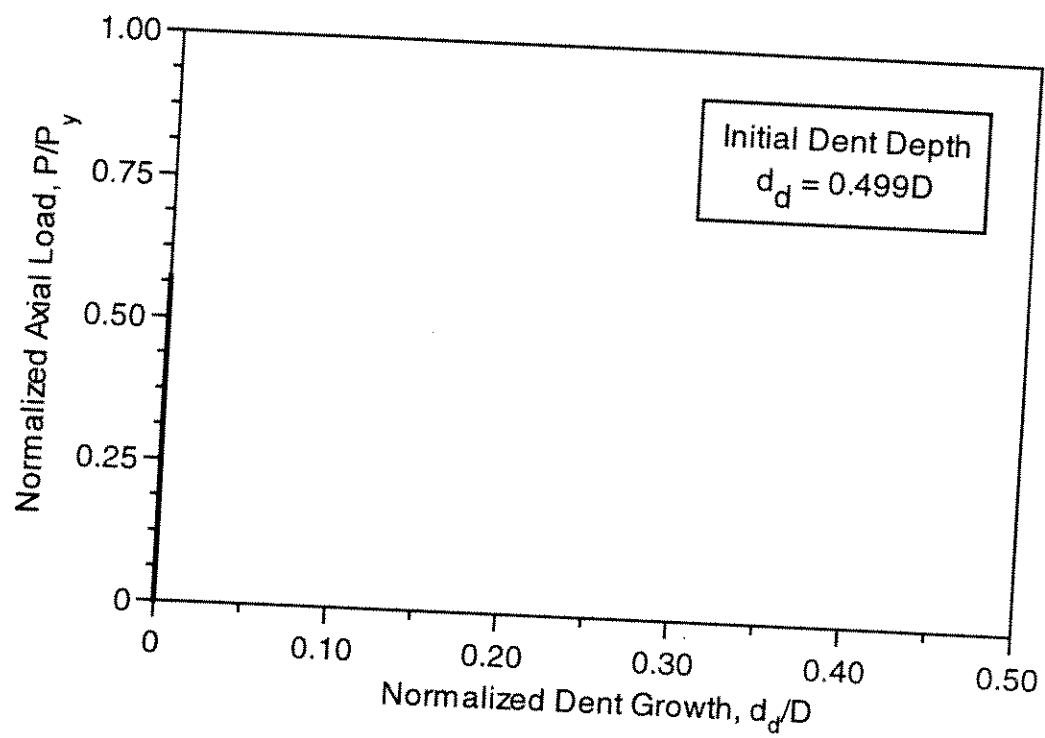


Figure 3.104 - Normalized Dent Growth of Specimen C15

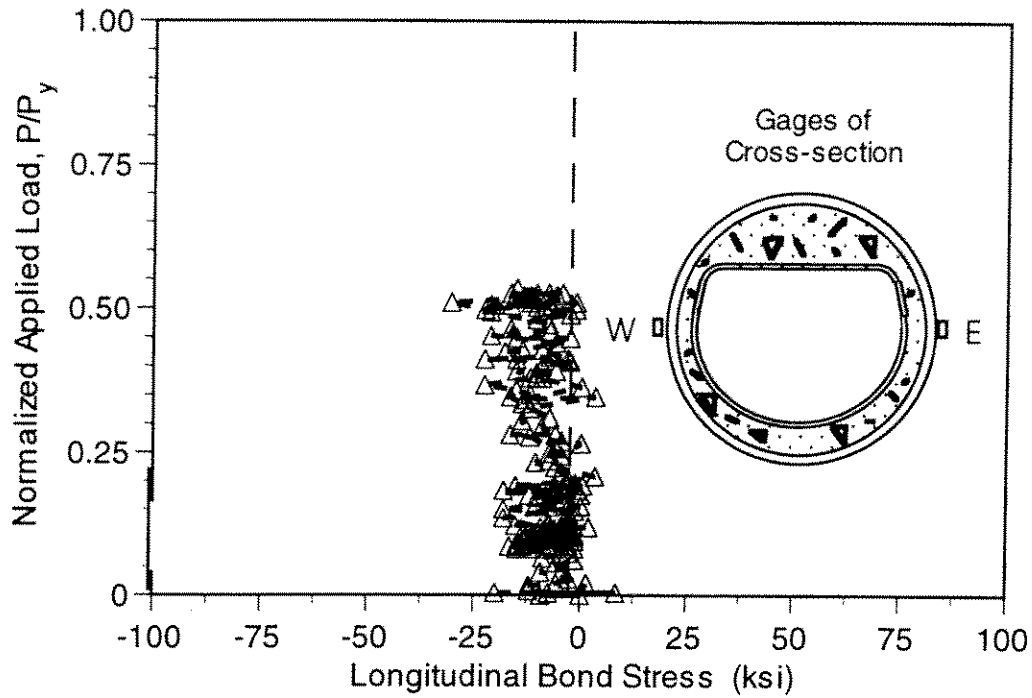


Figure 3.102 - Sleeve Bond Stress History at 15 inches South of Dent, Specimen C15 (Average of East and West Gages)

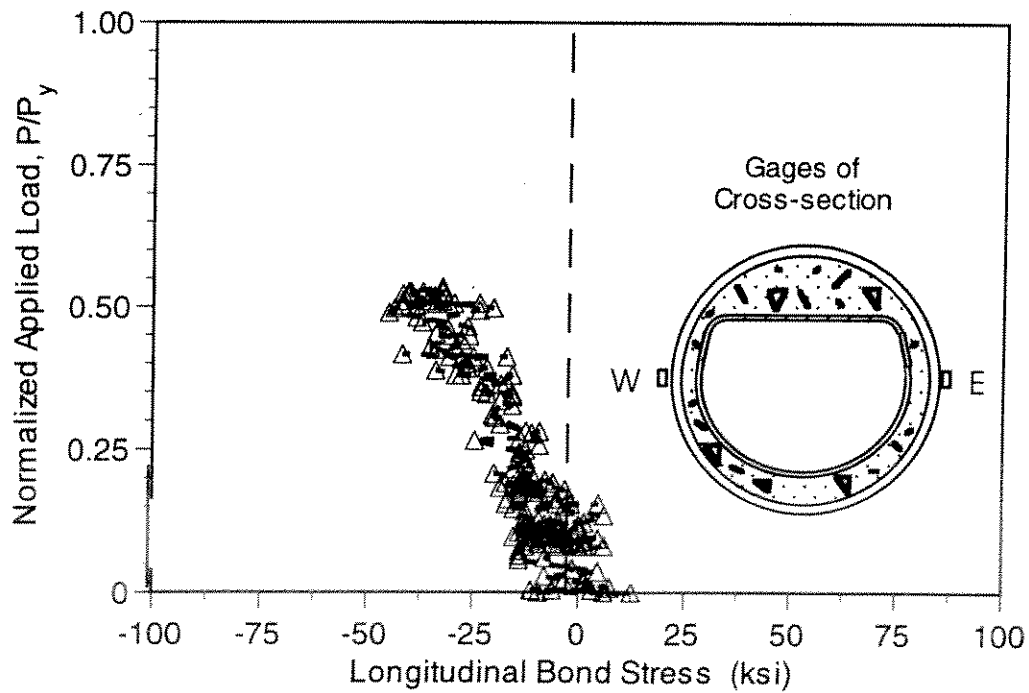


Figure 3.103 - Sleeve Bond Stress History at 15 inches North of Dent, Specimen C15 (Average of East and West Gages)

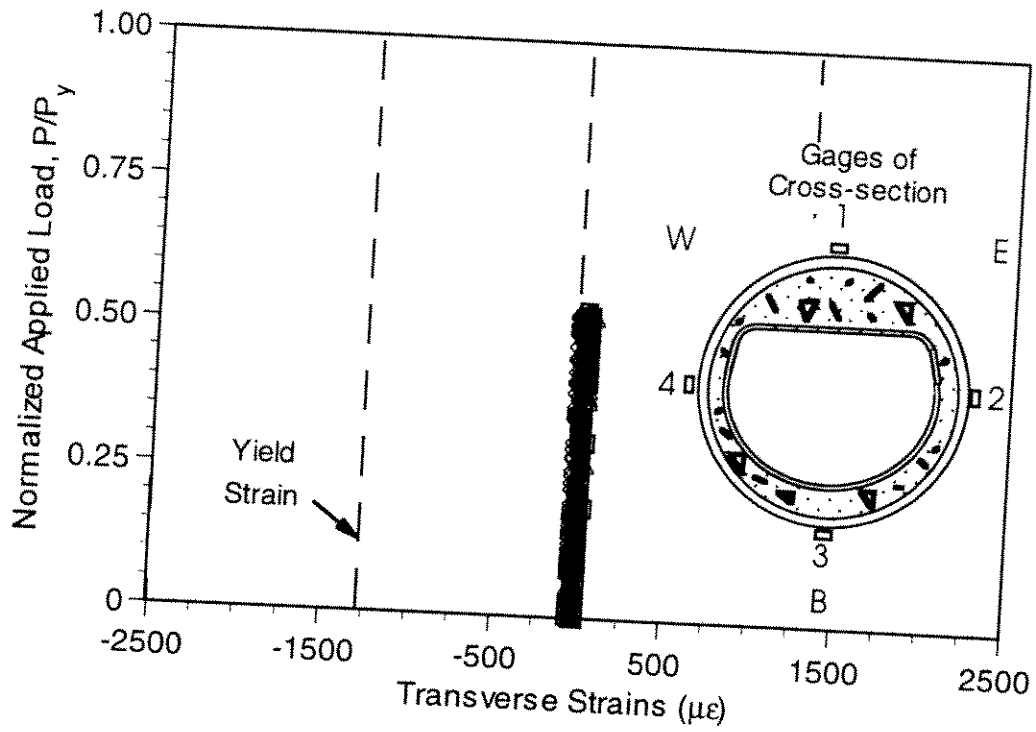


Figure 3.100 - Sleeve Strain History at Dent of Specimen C15

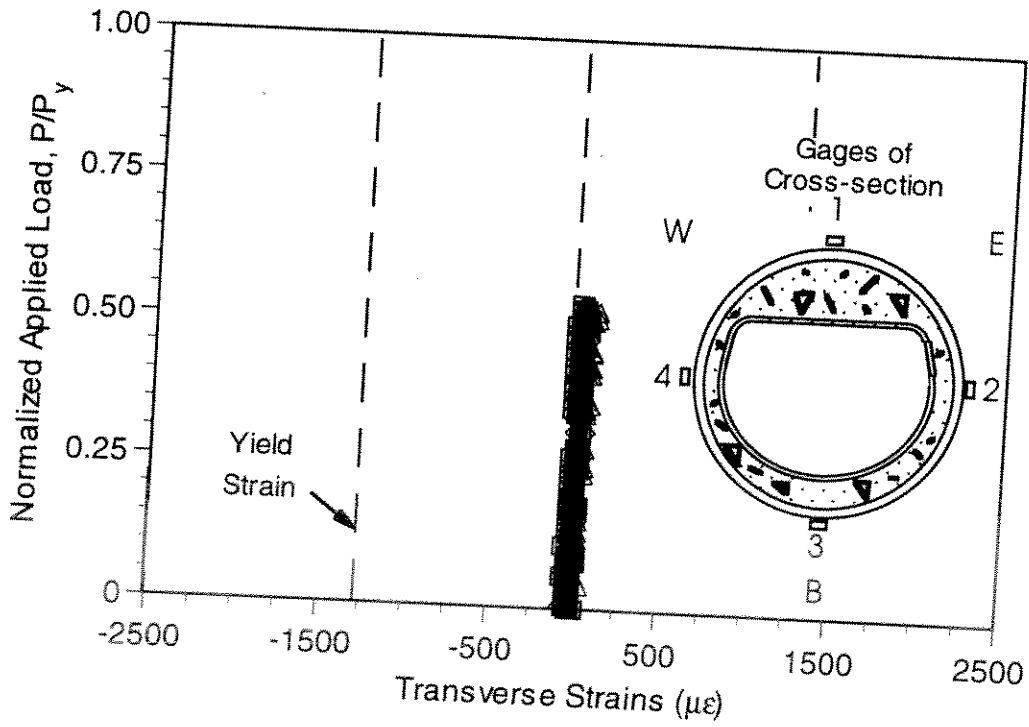


Figure 3.101 - Sleeve Strain History at  $x=0.58L$  of Specimen C15

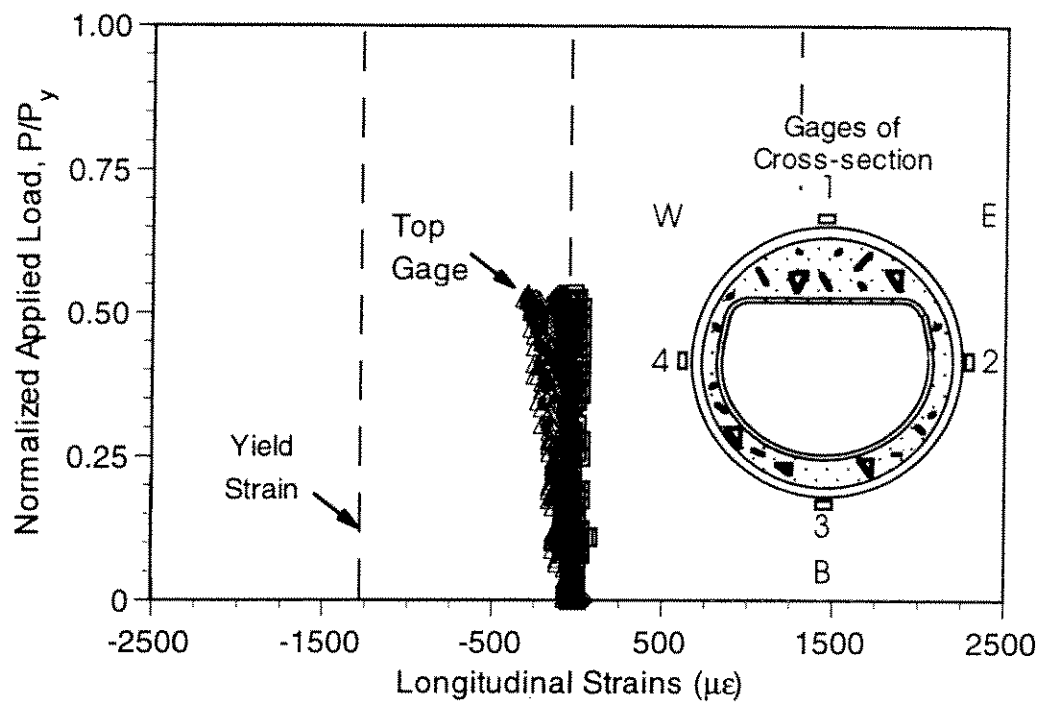


Figure 3.98 - Sleeve Strain History at  $x=0.58L$  of Specimen C15

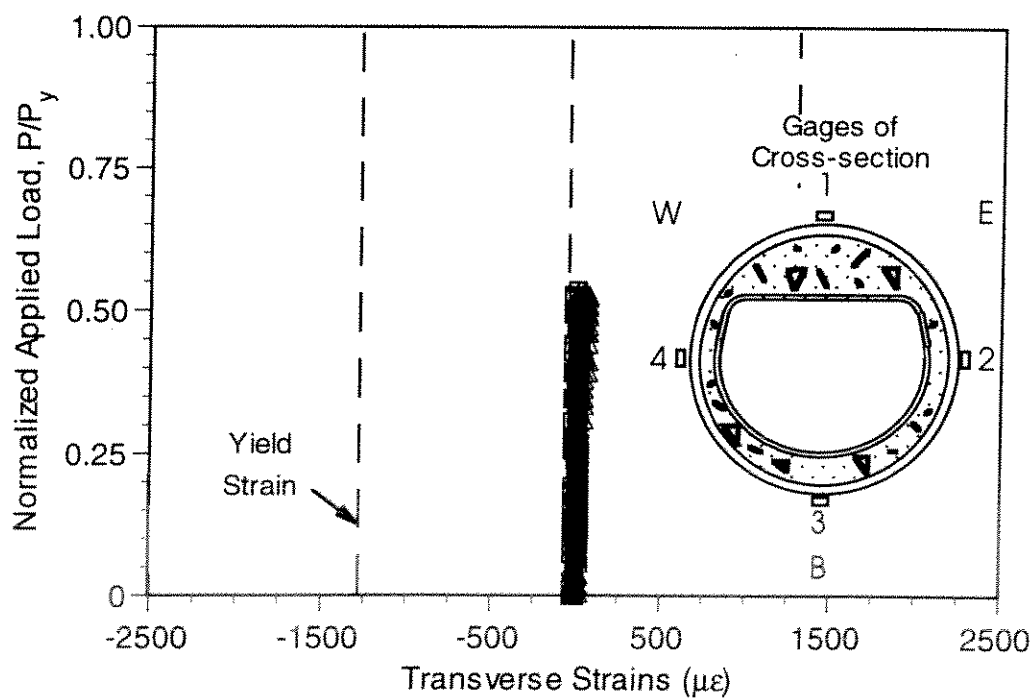


Figure 3.99 - Sleeve Strain History at  $x=0.42L$  of Specimen C15

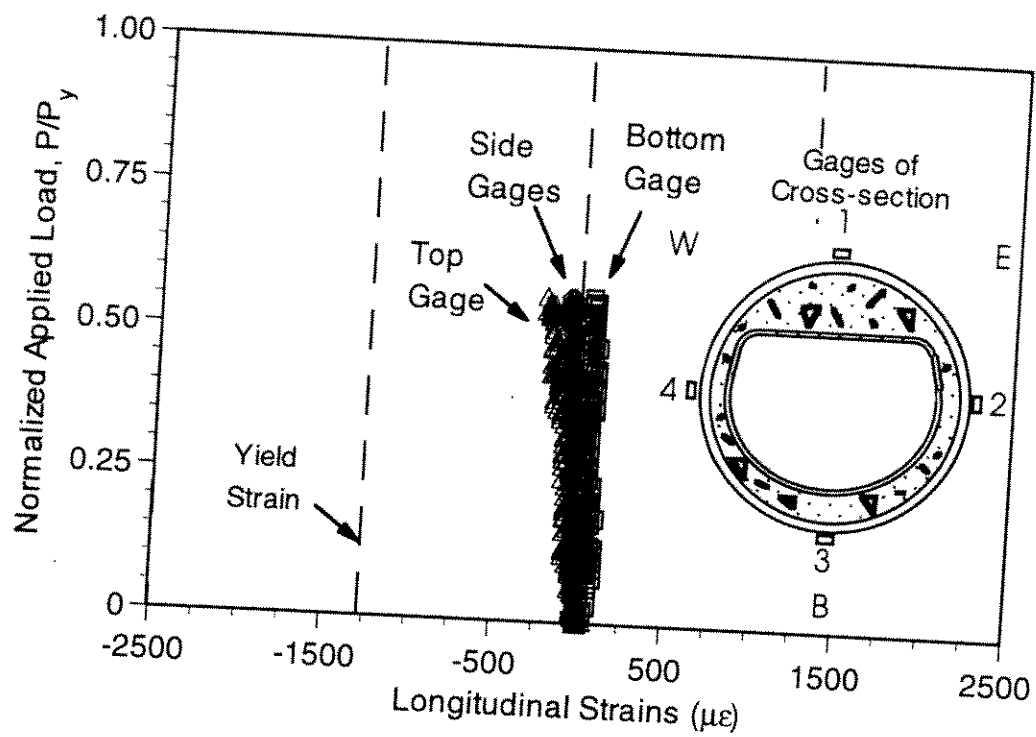


Figure 3.96 - Sleeve Strain History at  $x=0.42L$  of Specimen C15

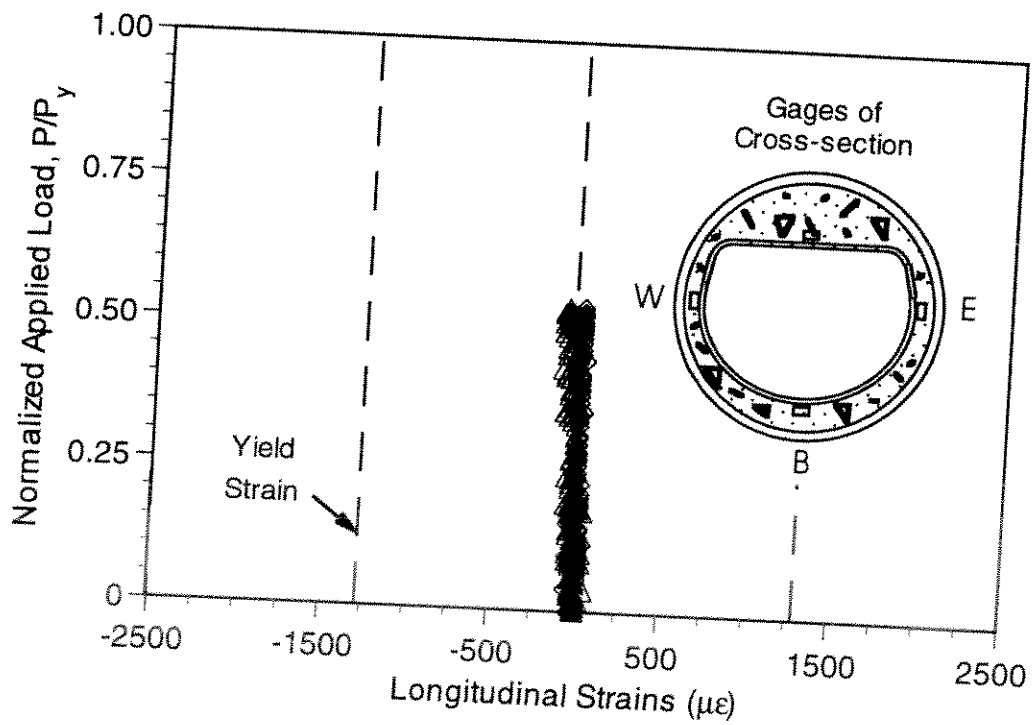


Figure 3.97 - Tube Strain History at  $x=0.58L$  of Specimen C15

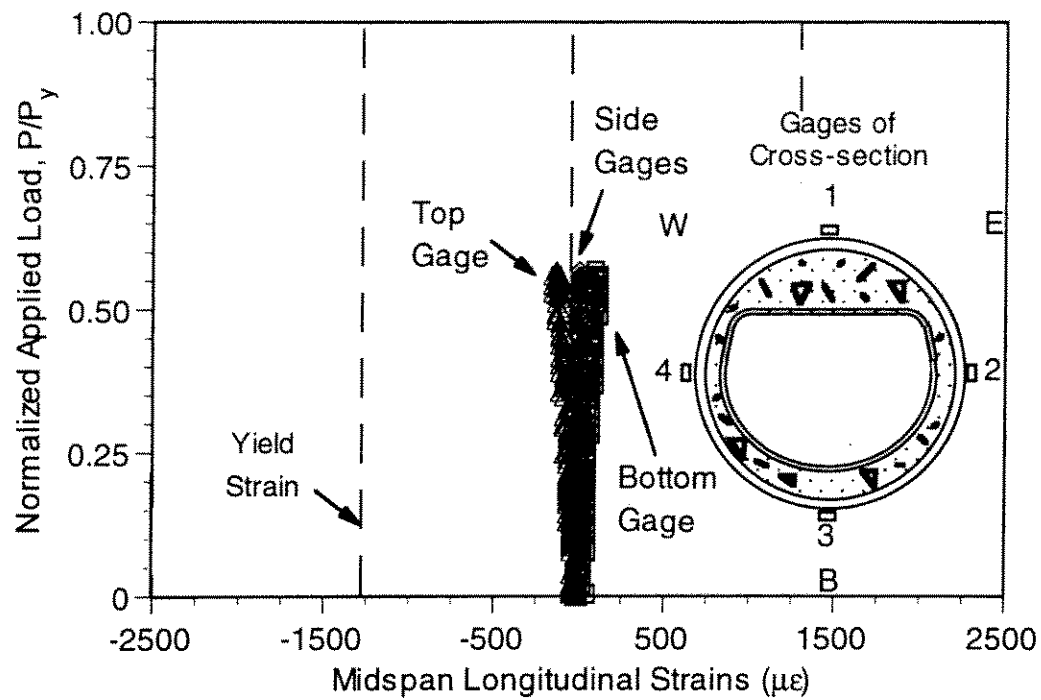


Figure 3.94 - Sleeve Strain History at Dent of Specimen C15

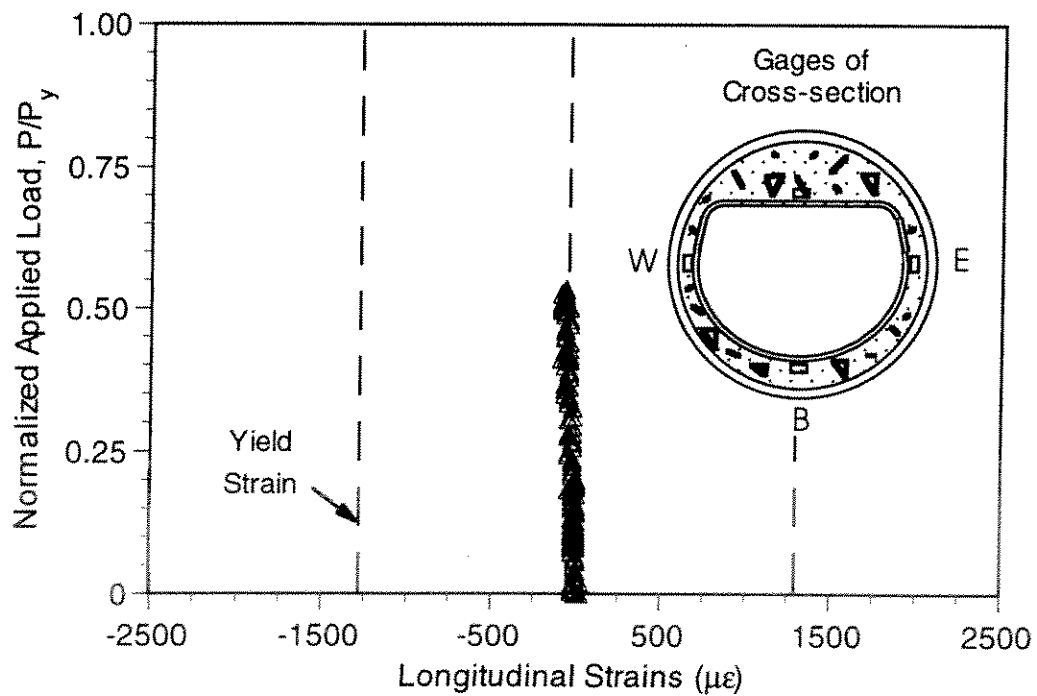


Figure 3.95 - Tube Strain History at  $x=0.42L$  of Specimen C15

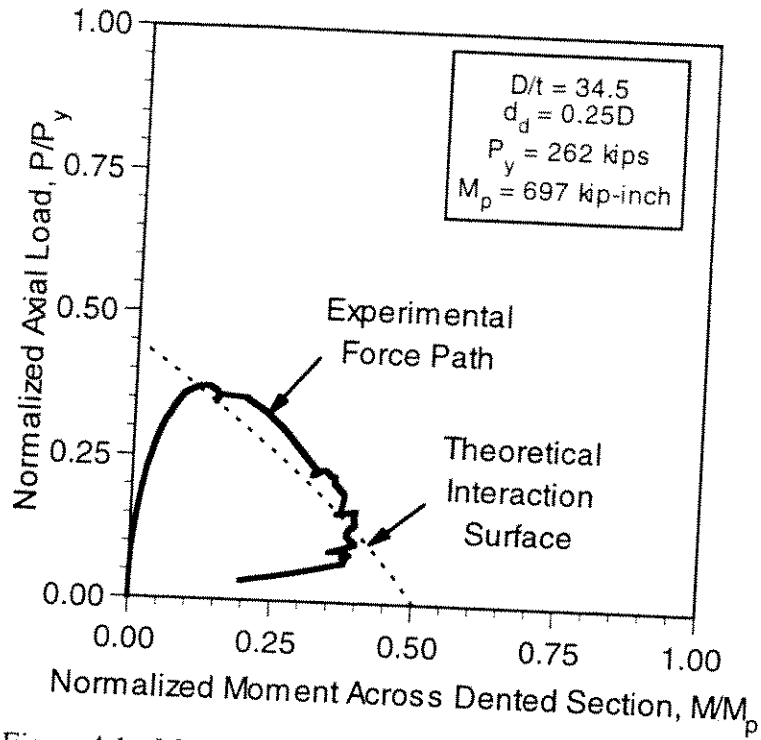


Figure 4.1 - Moment-Axial Load Interaction for Specimen A10

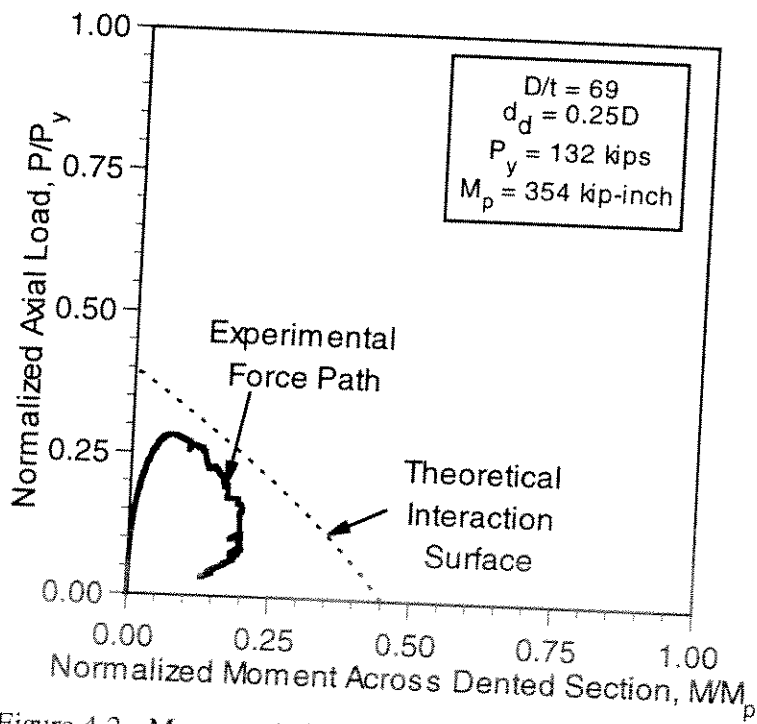


Figure 4.2 - Moment-Axial Load Interaction for Specimen C10



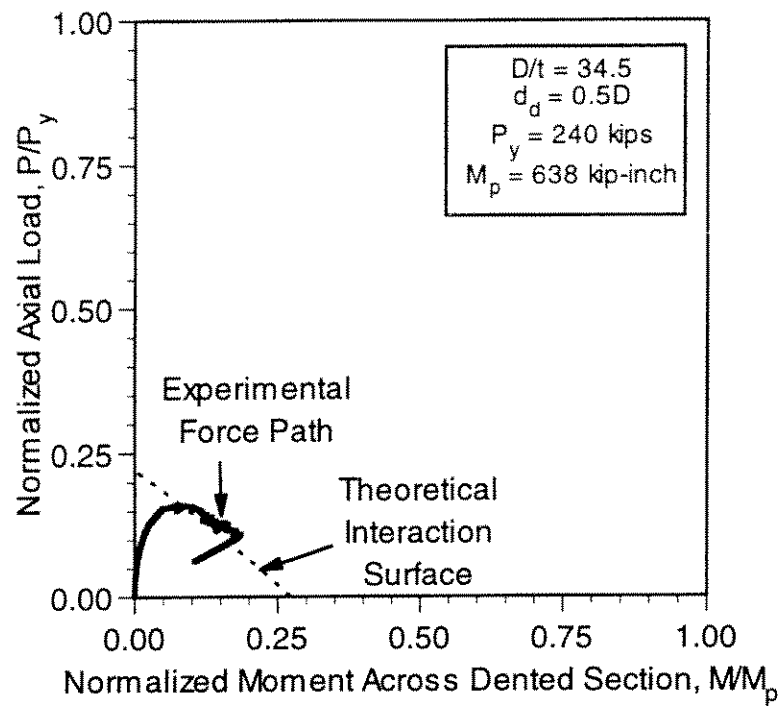


Figure 4.3 - Moment-Axial Load Interaction for Specimen A12

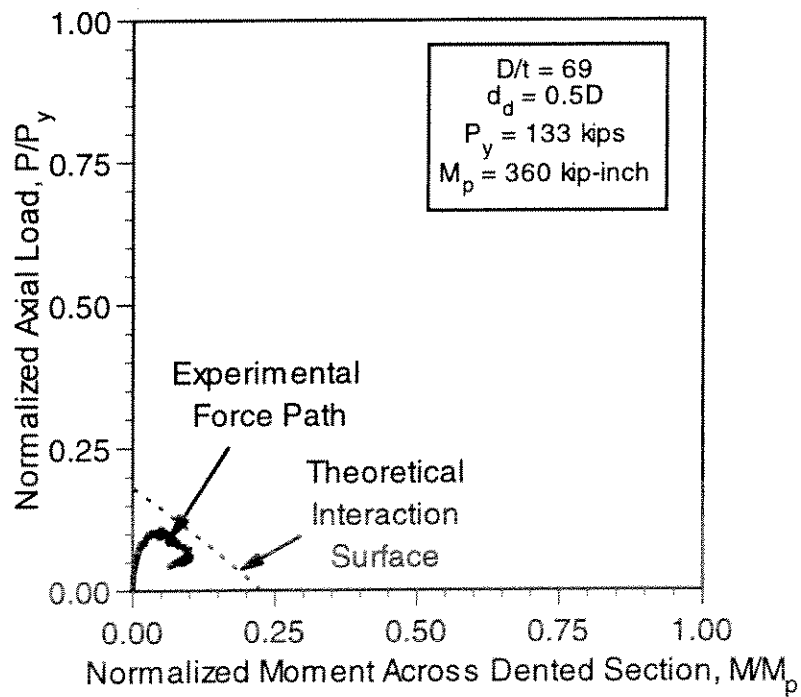


Figure 4.4 - Moment-Axial Load Interaction for Specimen C12

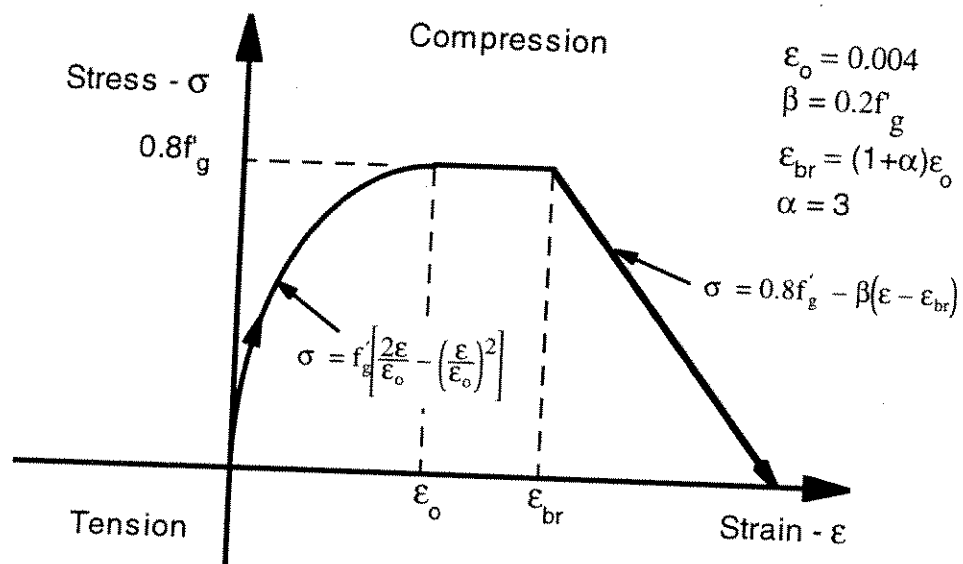


Figure 4.5 - Fiber Stress-Strain Relationships for Grout (after Ricles et al. 1997)

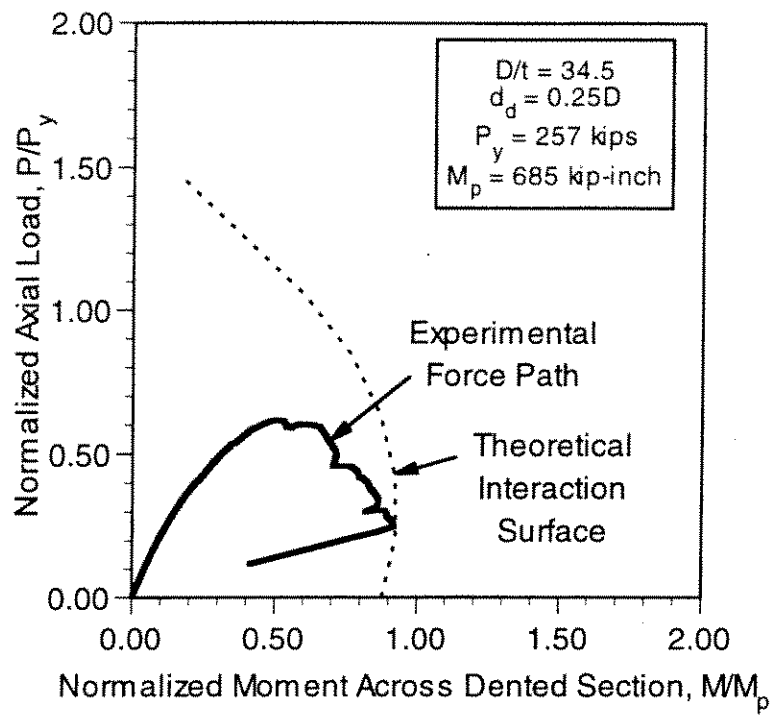


Figure 4.6 - Moment-Axial Load Interaction for Specimen A11

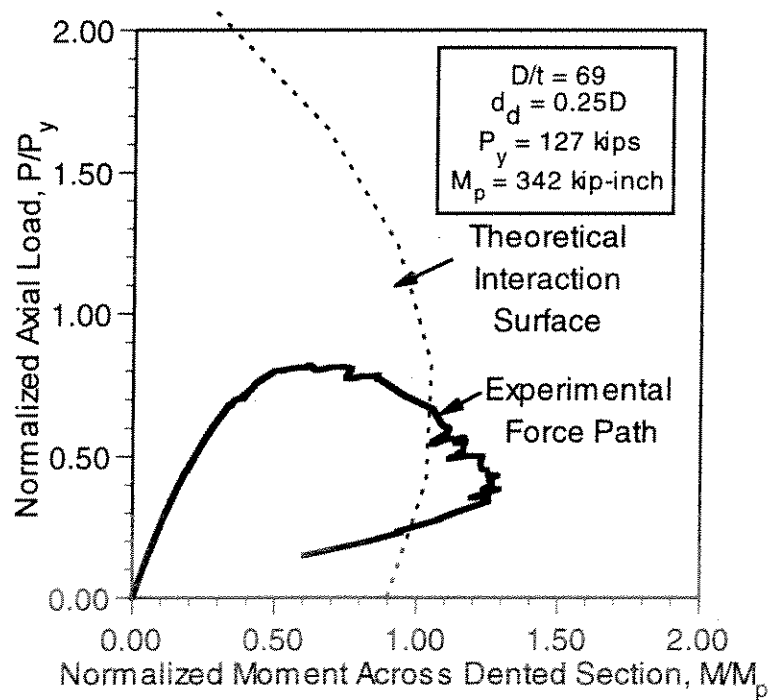


Figure 4.7 - Moment-Axial Load Interaction for Specimen C11

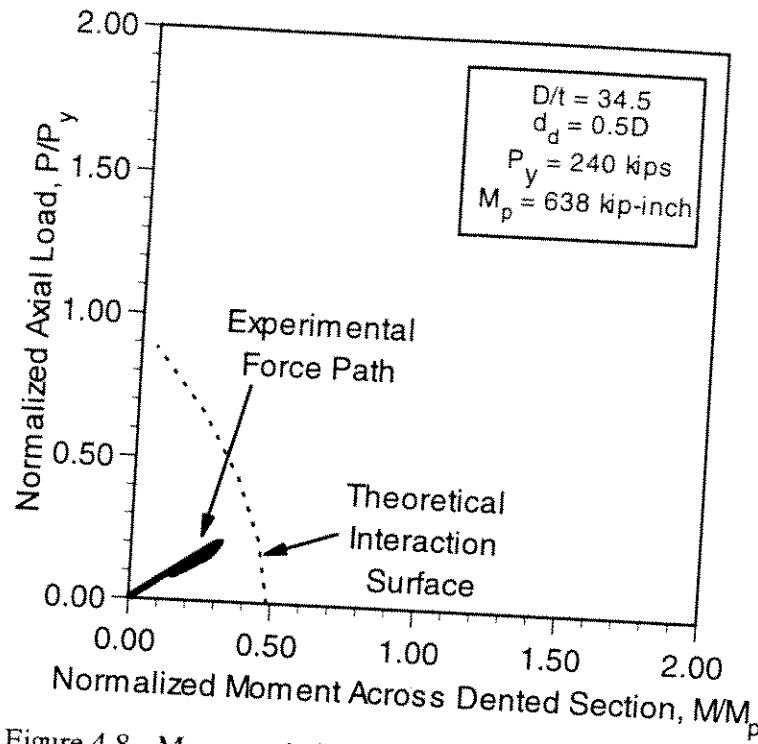


Figure 4.8 - Moment-Axial Load Interaction for Specimen A13

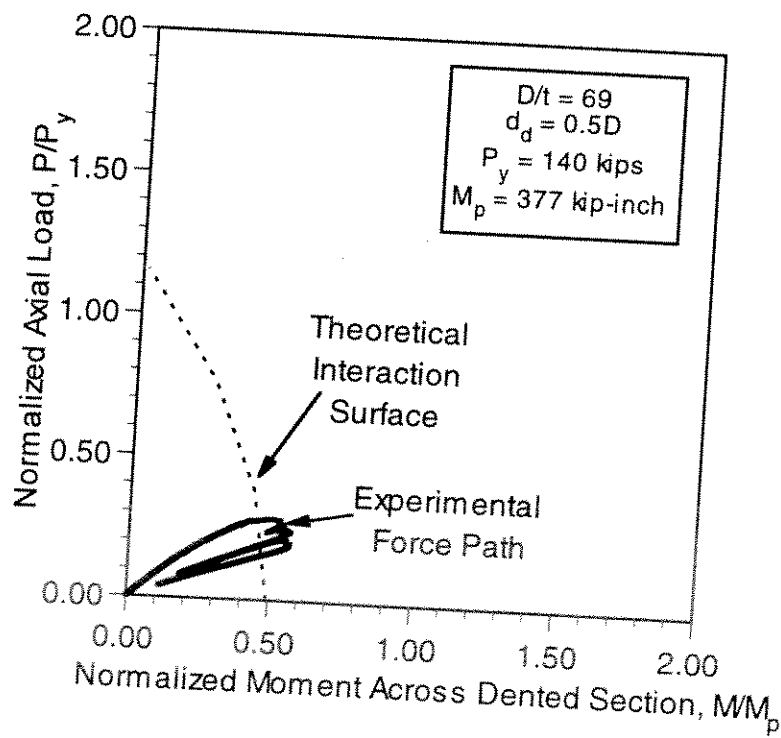


Figure 4.9 - Moment-Axial Load Interaction for Specimen C13

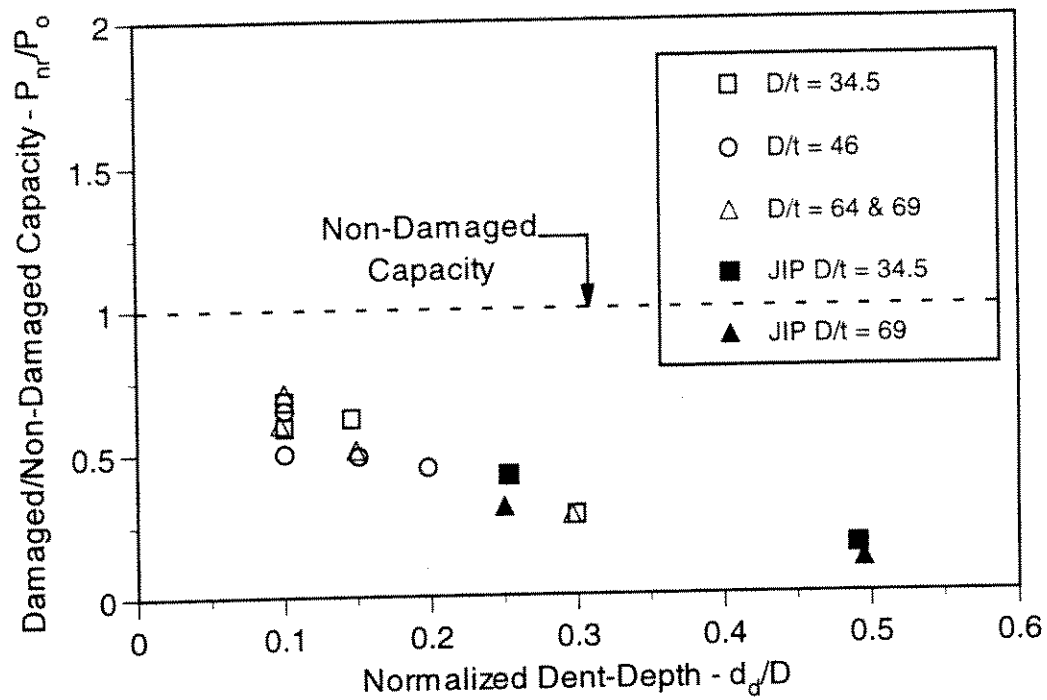


Figure 4.10- Effect of Dent-Damage on Specimen Ultimate Capacity (Previous Experimental Data from Ricles et al. [1992, 1997] Included)

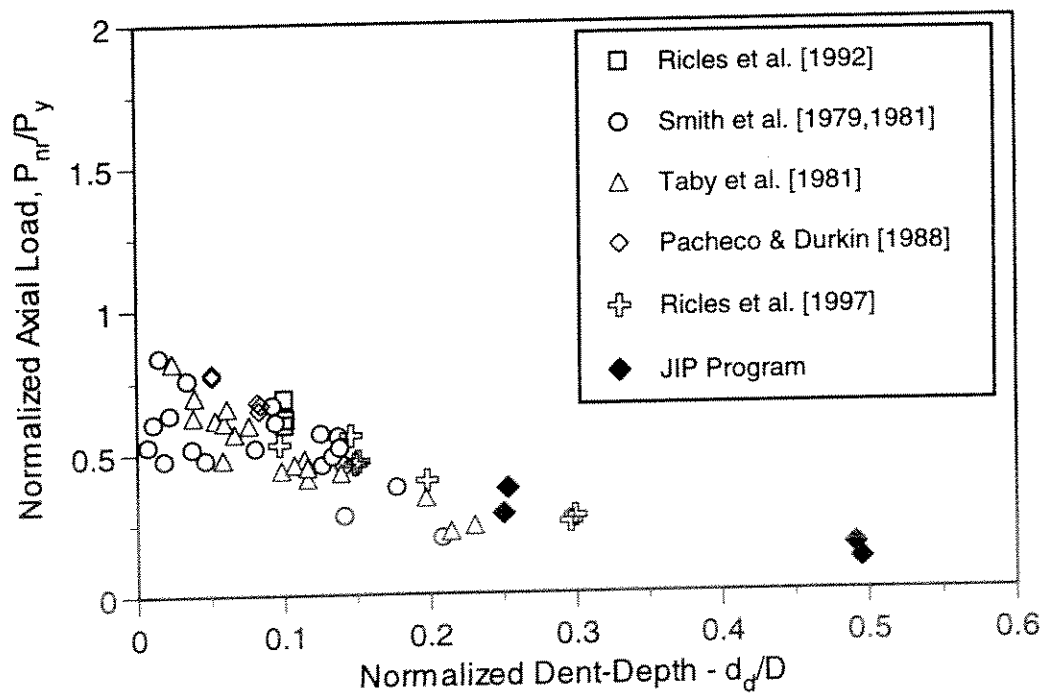


Figure 4.11 - Effect of Dent-Damage on Specimen Ultimate Axial Capacity

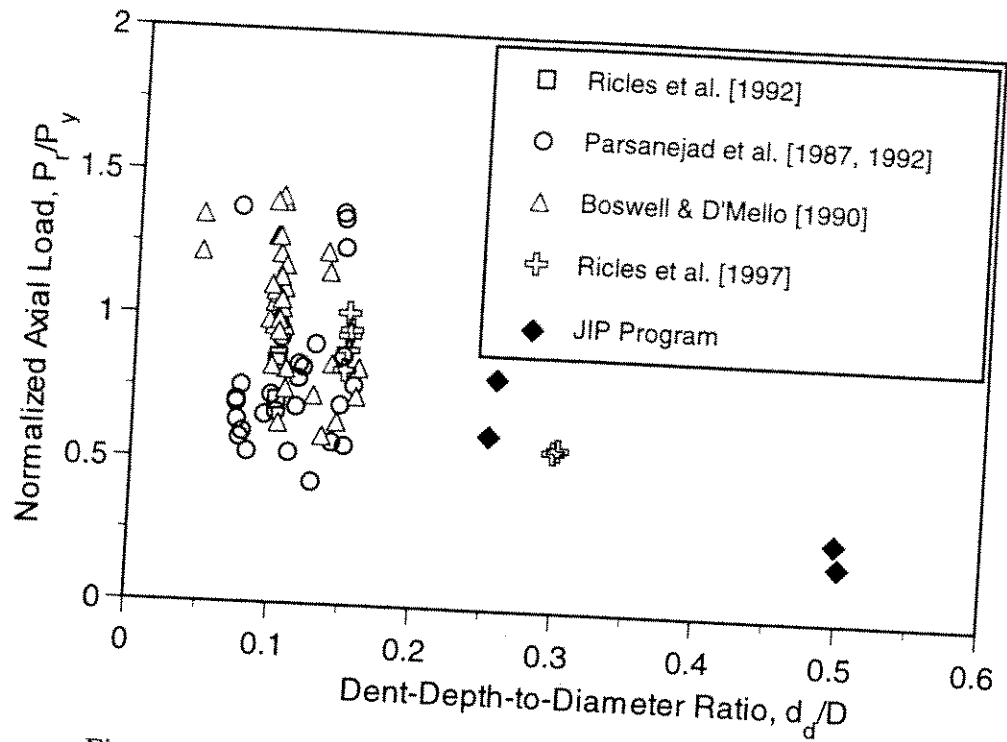


Figure 4.12 - Effect of Internal Grout Repair on Ultimate Axial Capacity

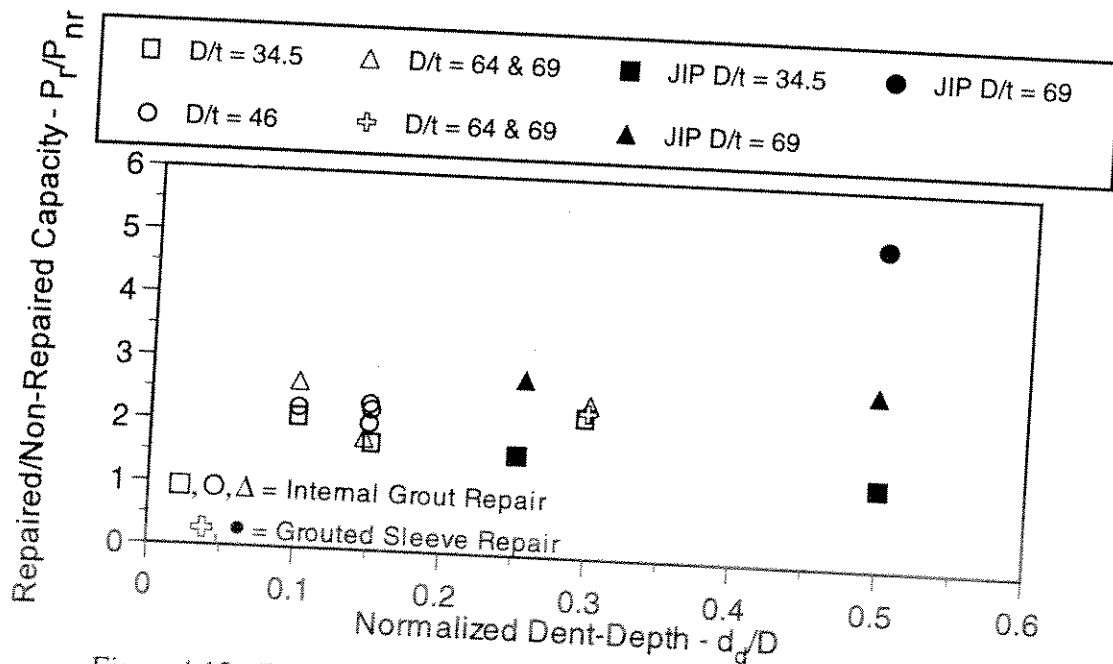


Figure 4.13 - Relative Increase in Dent-Damaged Axial Load Capacity After Grout Repair (Previous Experimental Data from Ricles et al. [1992, 1997] Included)

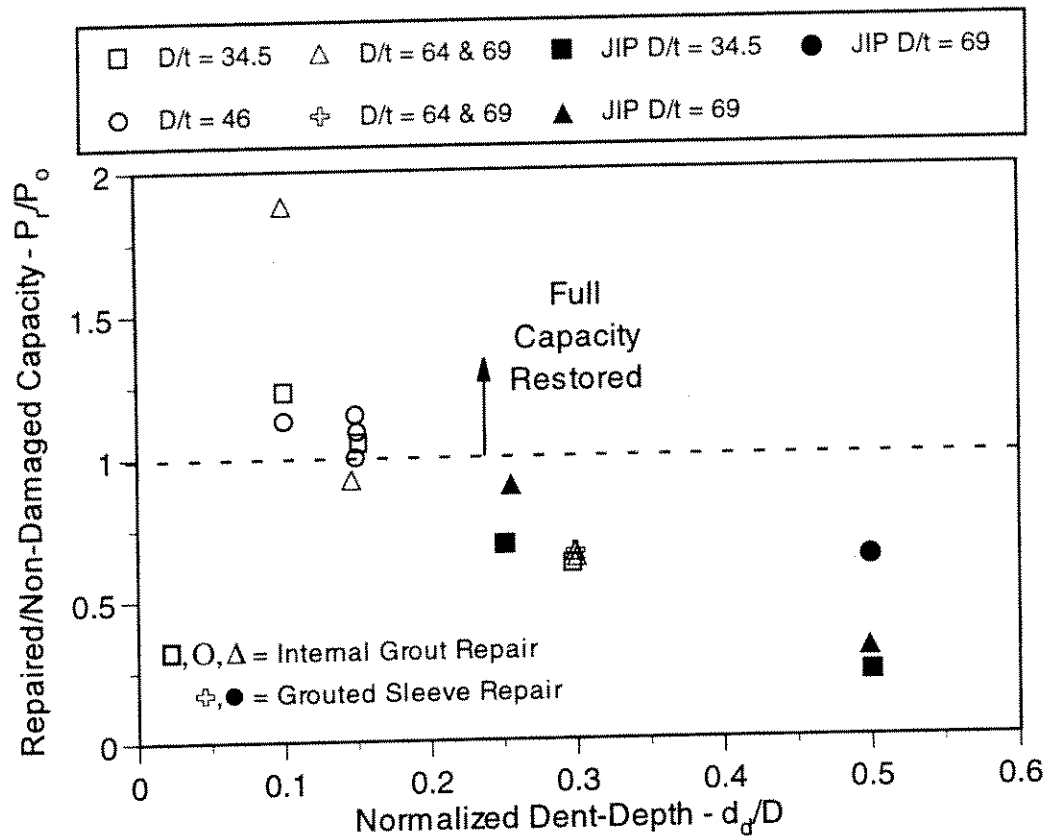


Figure 4.14 - Effectiveness of Axial Capacity Restoration by Grout Repair  
(Previous Experimental Data from Ricles et al. [1992, 1997] Included)

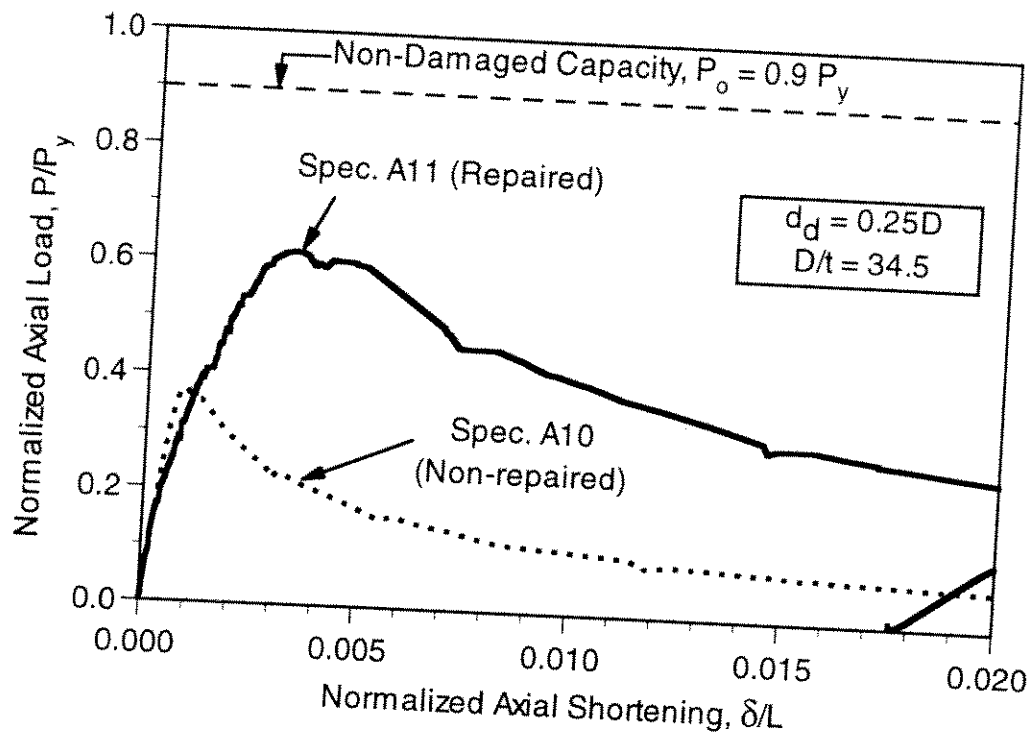


Figure 4.15 - Comparison of Axial Load-Shortening Response for Internal Grout Repaired and Non-repaired Specimens,  $d_d = 0.25D$  &  $D/t = 34.5$

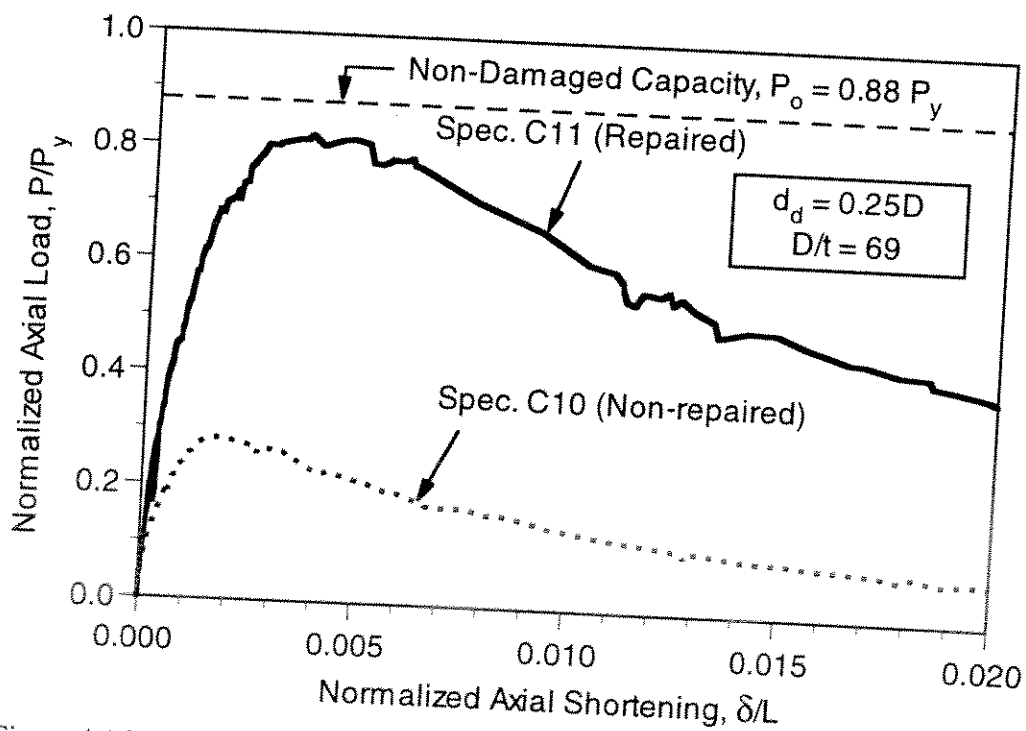


Figure 4.16 - Comparison of Axial Load-Shortening Response for Internal Grout Repaired and Non-repaired Specimens,  $d_d = 0.25D$  &  $D/t = 69$



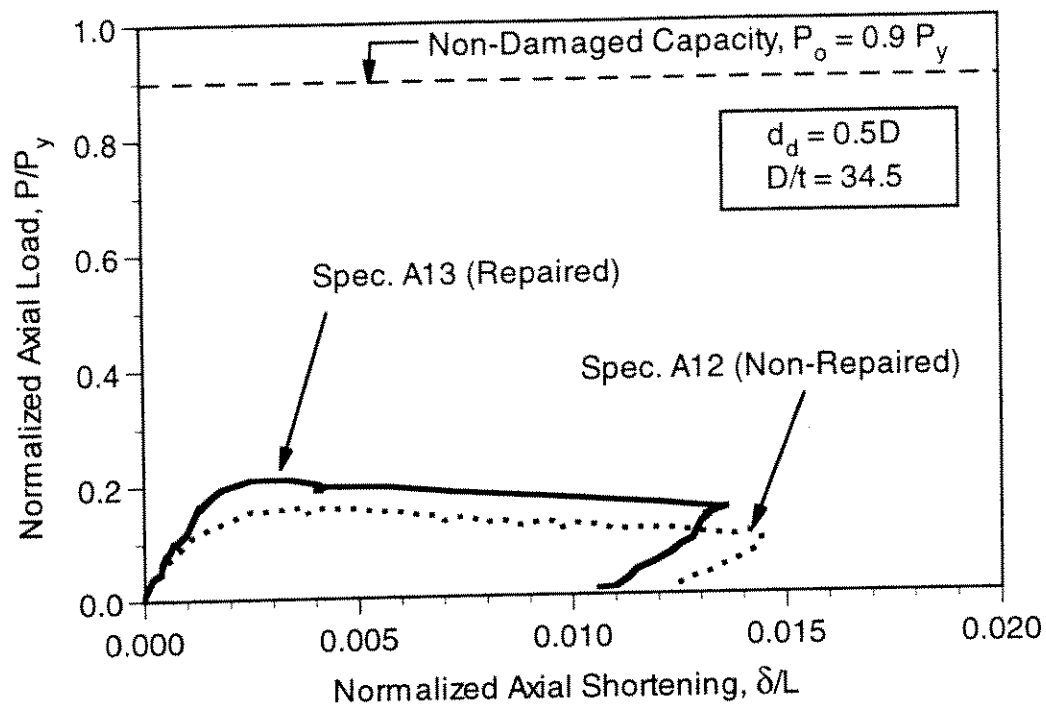


Figure 4.17 - Comparison of Axial Load-Shortening Response for Internal Grout Repaired and Non-repaired Specimens,  $d_d = 0.5D$  &  $D/t = 34.5$

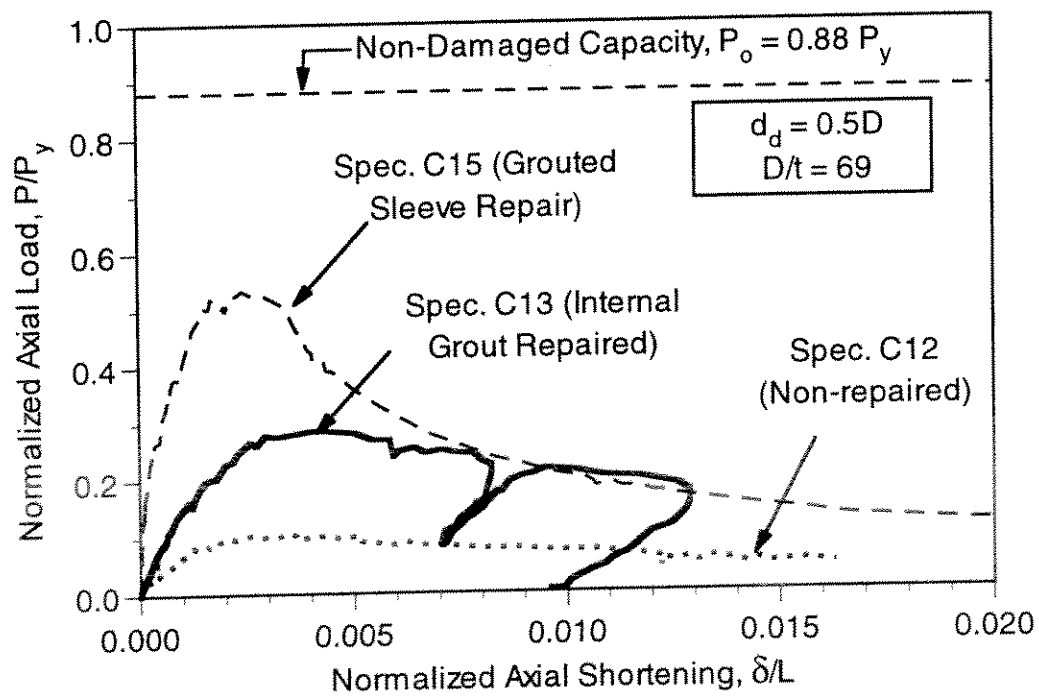


Figure 4.18 - Comparison of Axial Load-Shortening Response for Internal Grout Repaired and Non-repaired Specimens,  $d_d = 0.5D$  &  $D/t = 69$

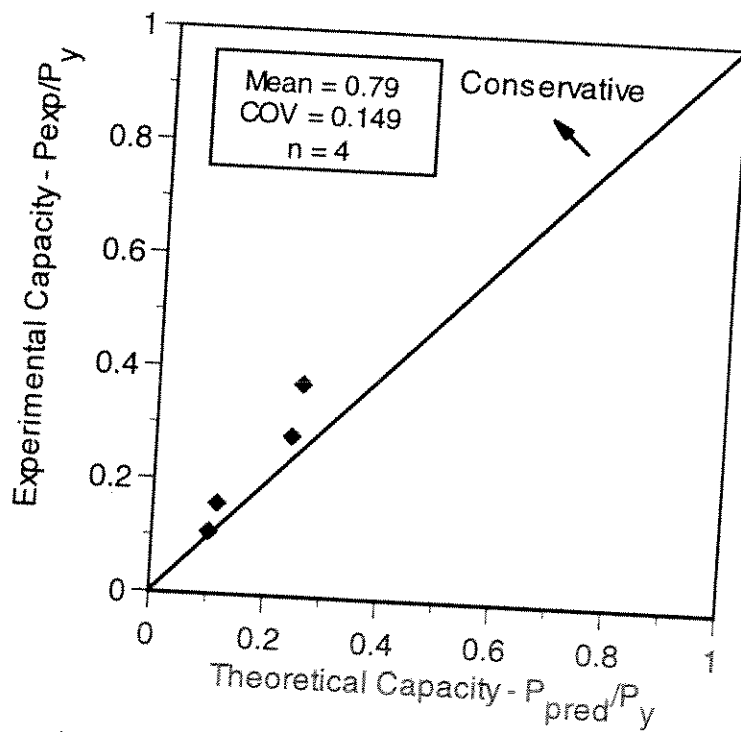


Figure 4.19 - Comparison of Ellinas Strength Equation Predictions with Experimental Results for Current Test Program

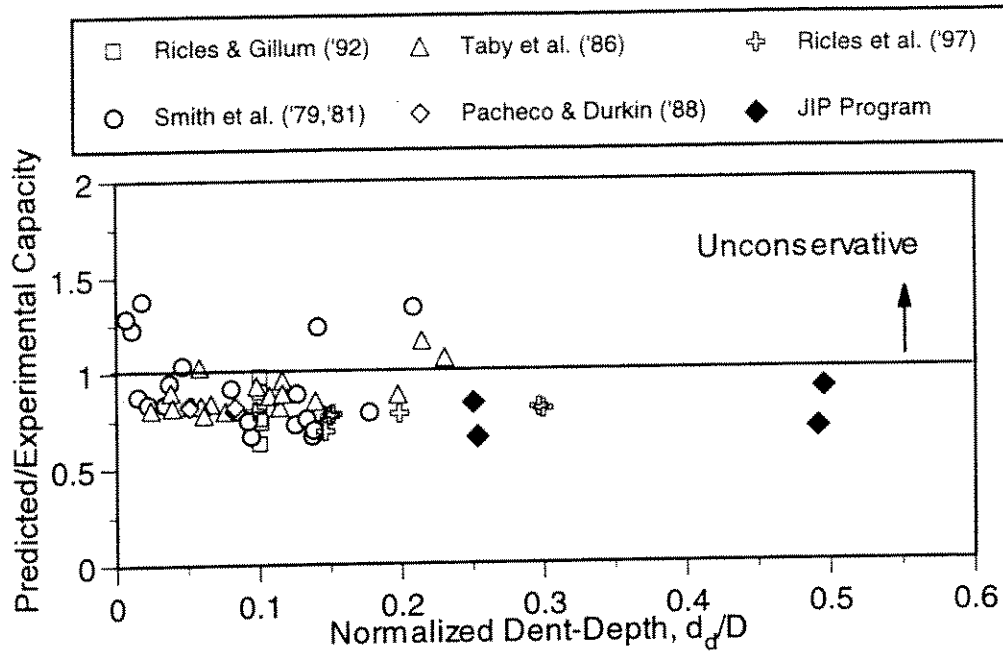


Figure 4.20 - Sensitivity of Ellinas Strength Equation to Depth of Applied Dent-Damage for Specimens with Simply-Supported Boundary Conditions

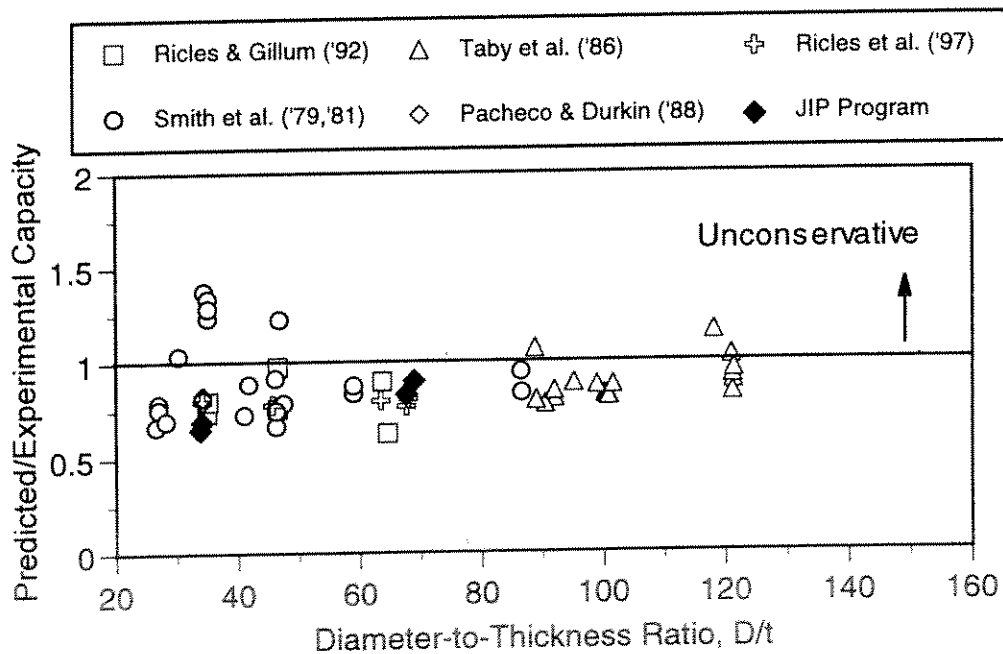


Figure 4.21 - Sensitivity of Ellinas Strength Equation to Diameter-to-Thickness Ratio for Specimens with Simply-Supported Boundary Conditions

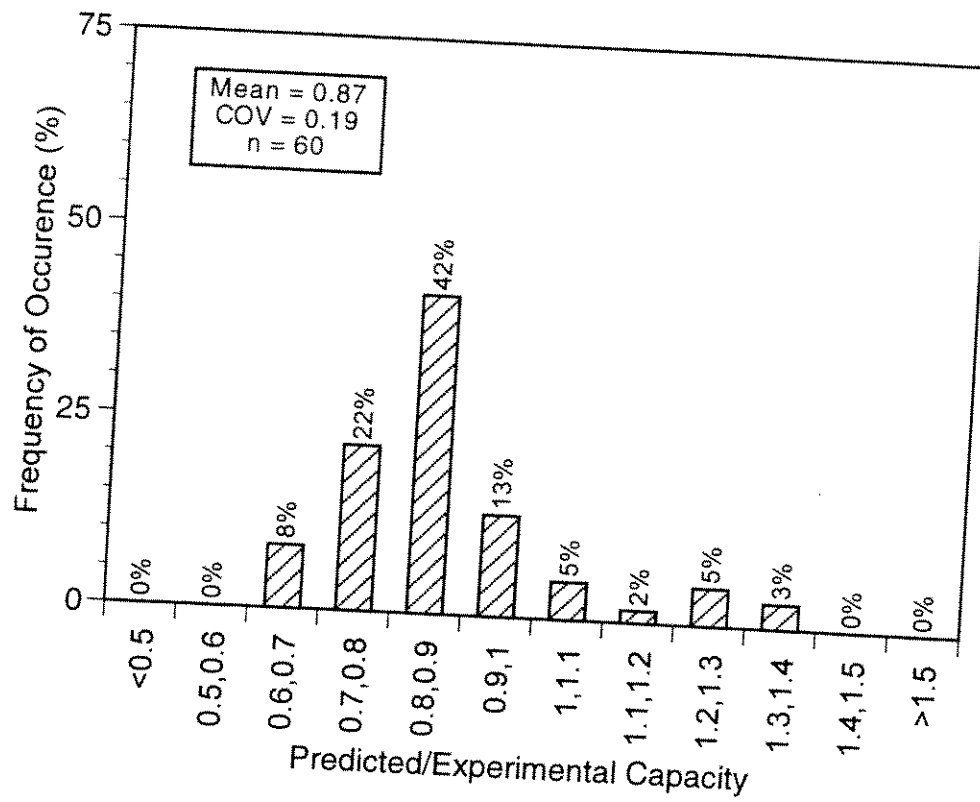


Figure 4.22 - Histogram of Predicted-to-Measured Capacity Ratio for the Ellinas Strength Equation (Includes Current and Previous Experimental Data)

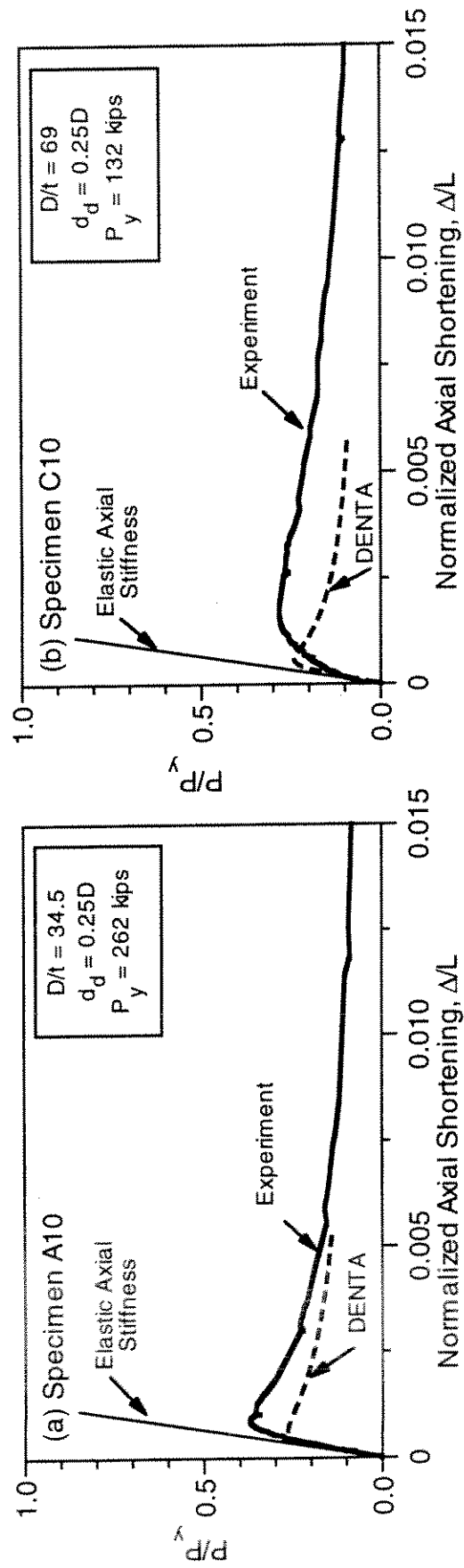


Figure 4.23 - Comparison of DENTA II and Experimental Results for the Axial Load-Shortening Response of Non-repaired Specimens

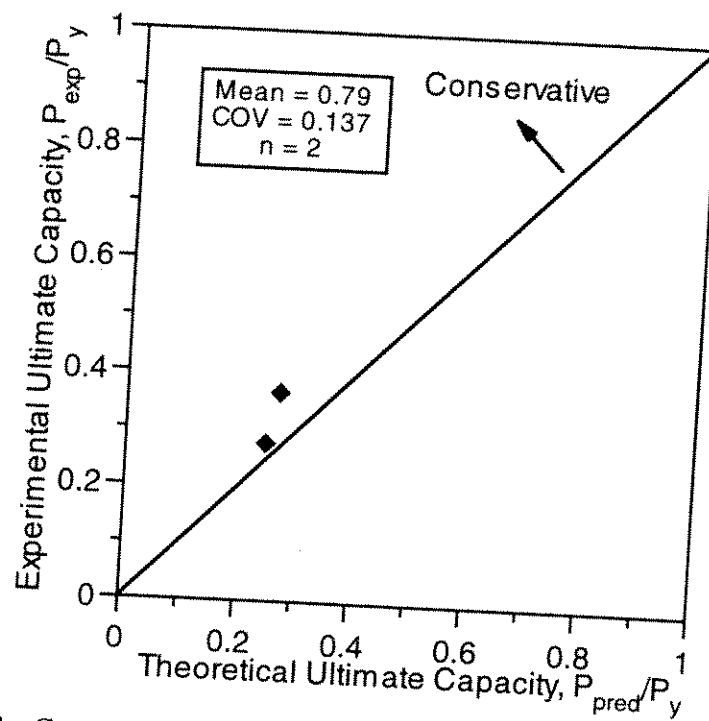


Figure 4.24 - Comparison of DENTA II Predictions with Experimental Results of Current Test Program

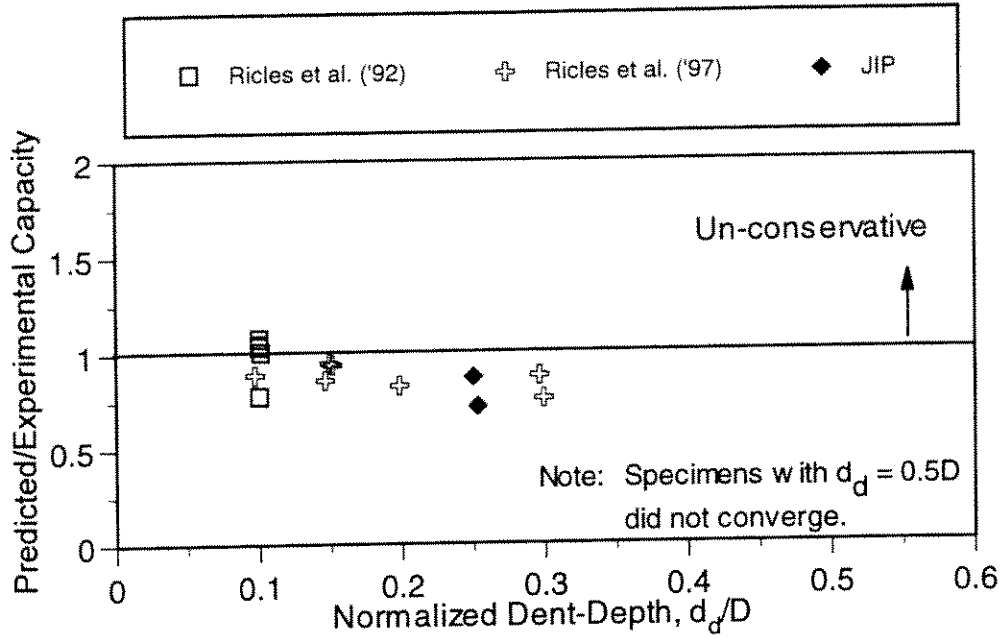


Figure 4.25 - Sensitivity of DENTA II to Depth of Applied Dent-Damage for Specimens with Simply-Supported Boundary Conditions

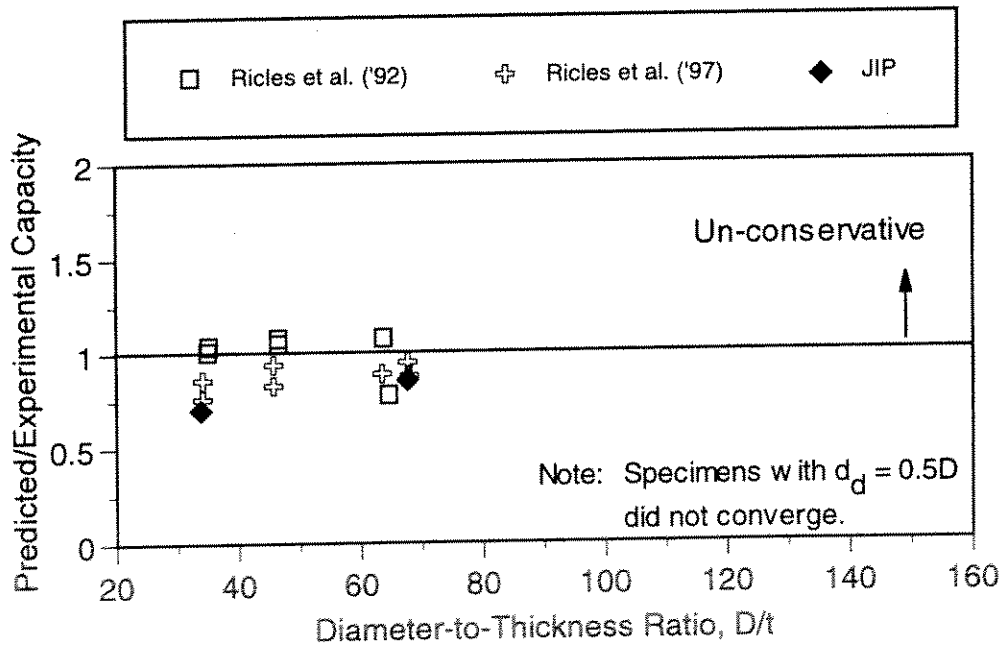


Figure 4.26 - Sensitivity of DENTA II to Diameter-to-Thickness Ratio for Specimens with Simply-Supported Boundary Conditions

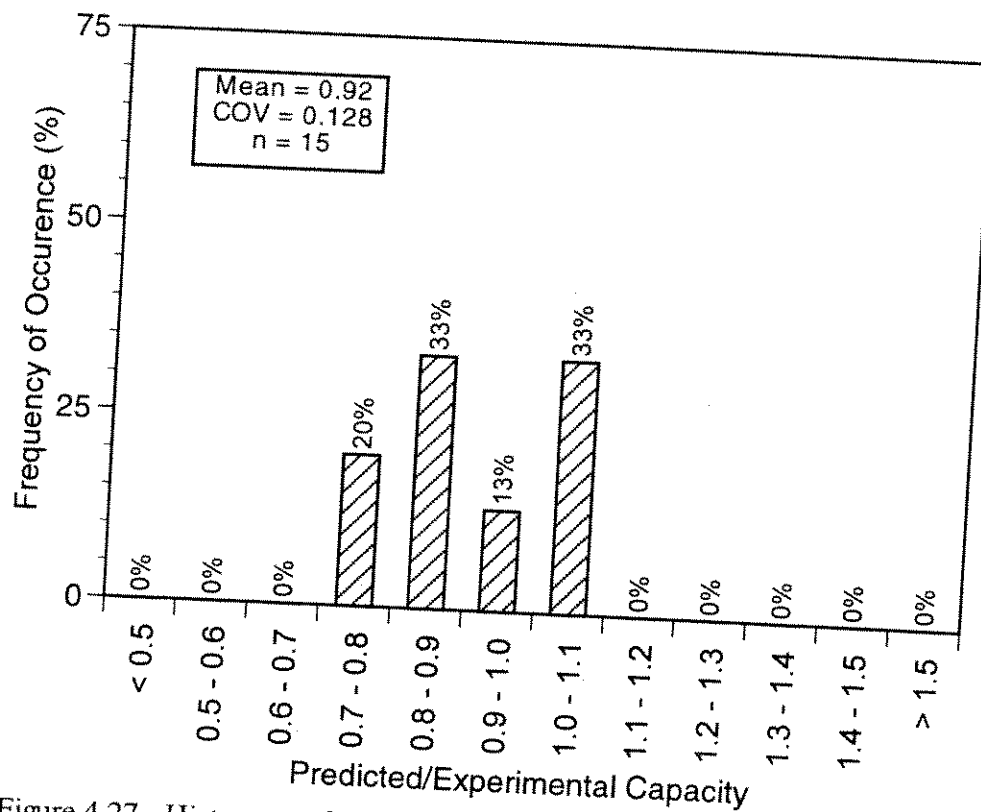


Figure 4.27 - Histogram of Predicted-to-Measured Capacity Ratio for DENTA II  
(Includes Data from Current Program and Ricles et al. [1992, 1997])



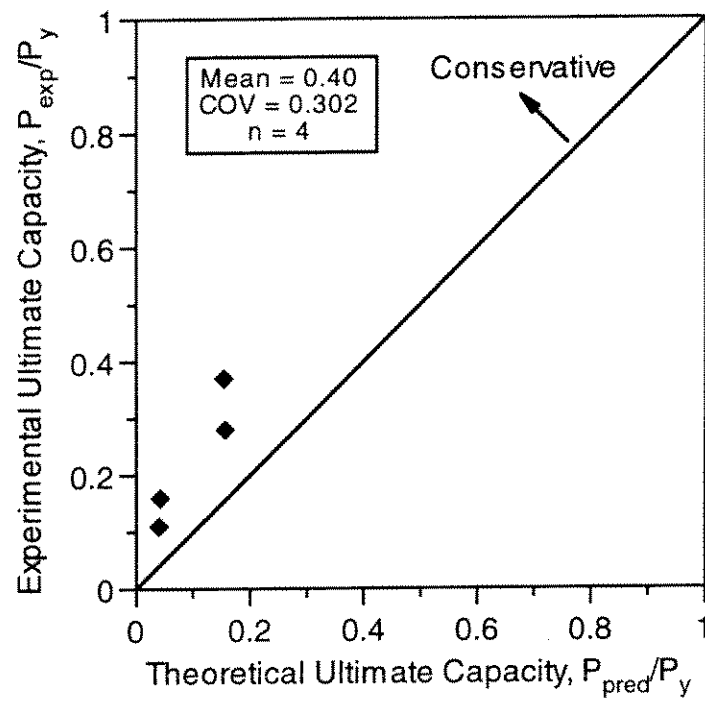


Figure 4.28 - Comparison of UCDENT Equation with Experimental Results from Current Test Program

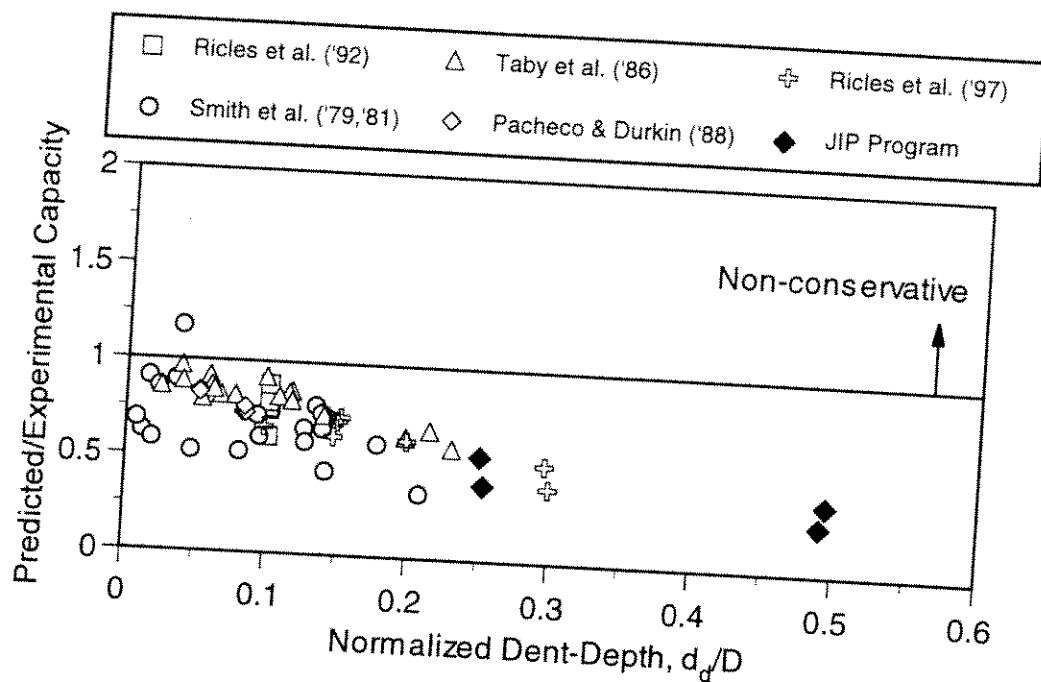


Figure 4.29 - Sensitivity of UCDENT to Depth of Applied Dent-Damage for Specimens with Simply-Supported Boundary Conditions

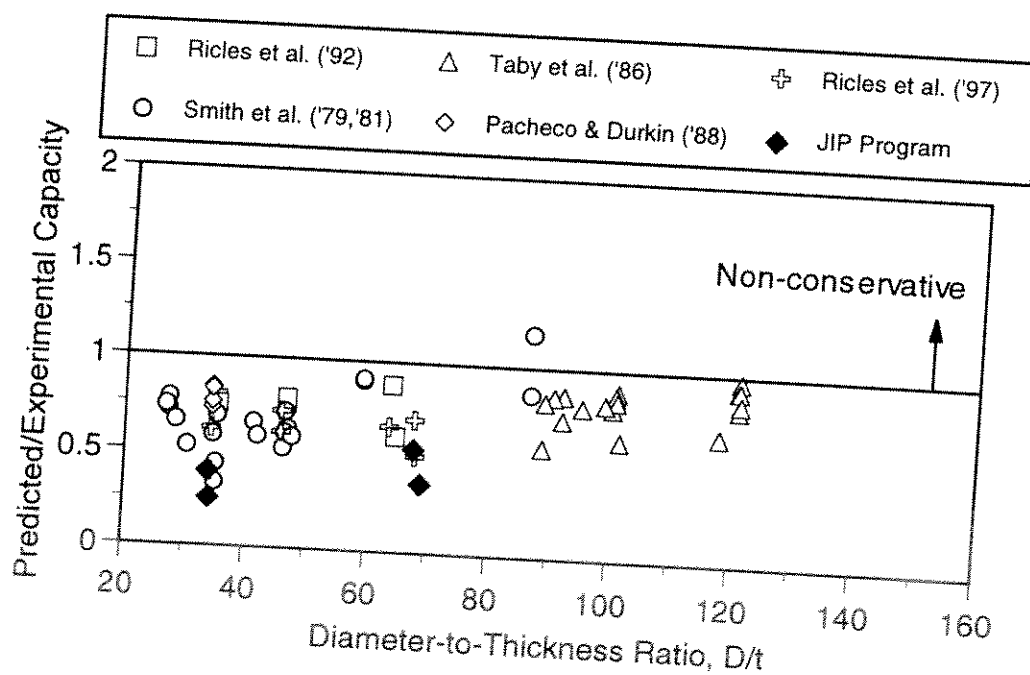


Figure 4.30 - Sensitivity of UCDENT to Diameter-to-Thickness Ratio for Specimens with Simply-Supported Boundary Conditions

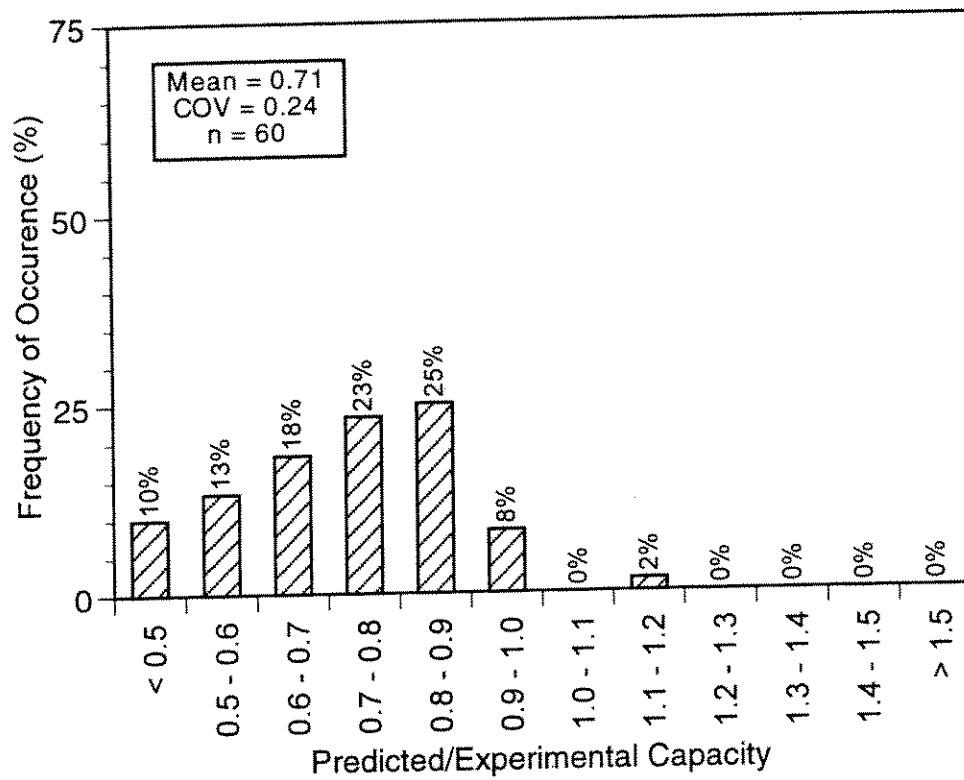


Figure 4.31 - Histogram of Predicted-to-Measured Capacity Ratio for UCDENT (Includes Current and Previous Experimental Data)

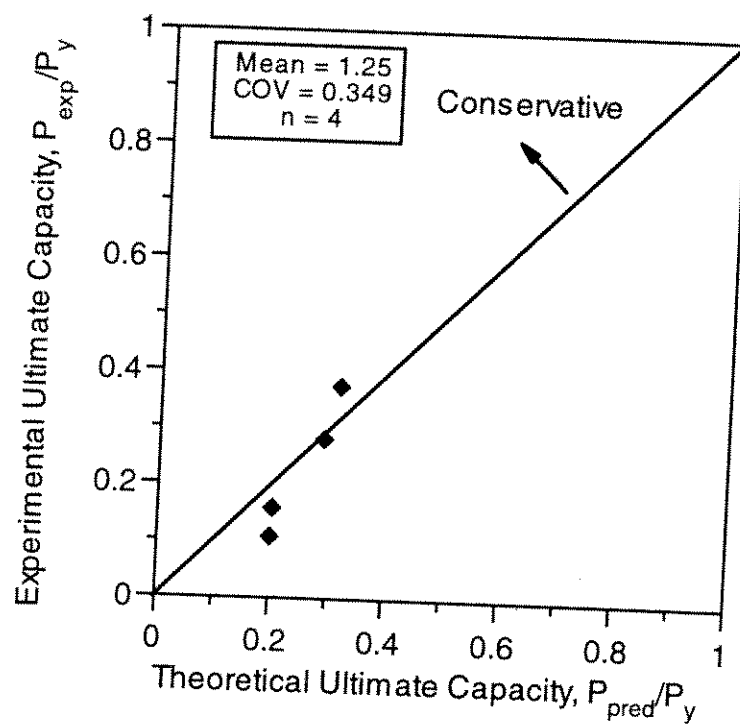


Figure 4.32 - Comparison of Loh Unity Check (Stability) Equation with Experimental Results from Current Test Program

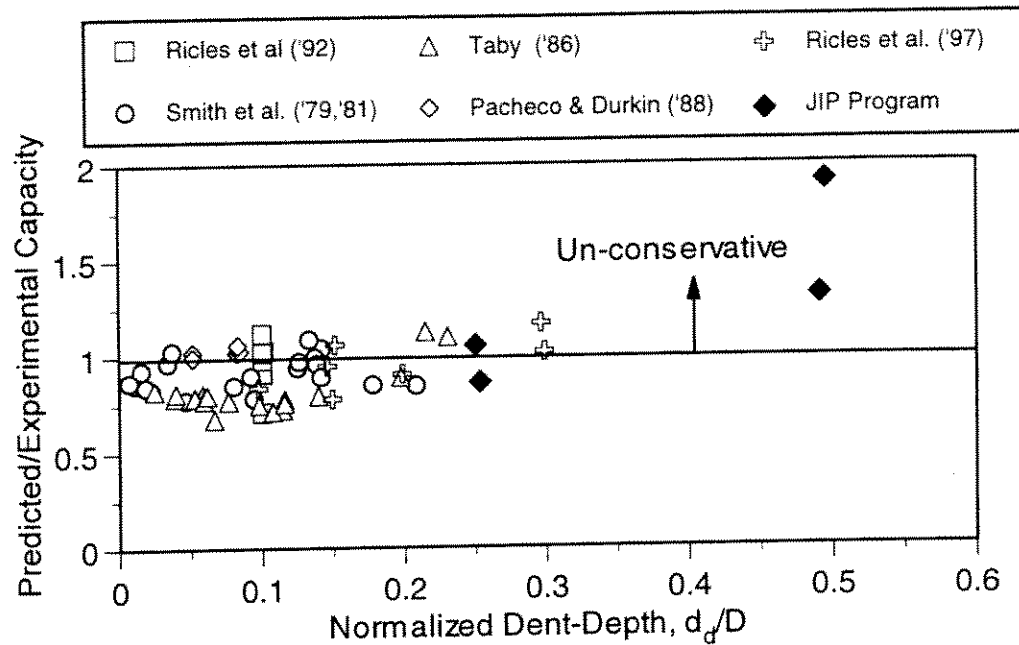


Figure 4.33 - Sensitivity of Loh Unity Check (Stability) Equation to Depth of Applied Dent-Damage for Specimens with Simply-Supported Boundary Conditions

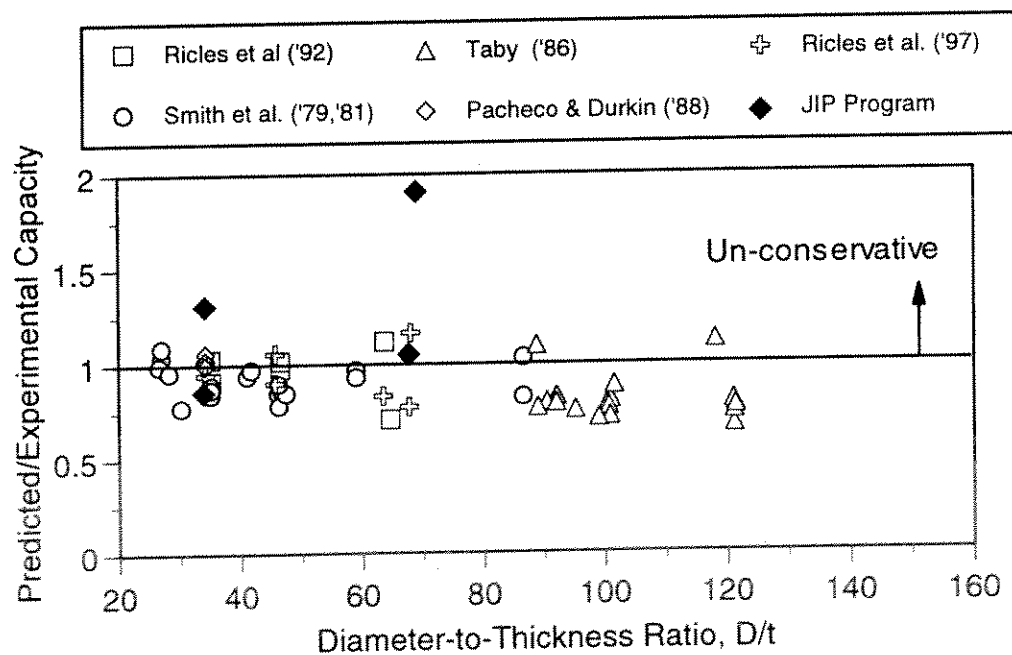


Figure 4.34 - Sensitivity of Loh Unity Check (Stability) Equation to Diameter-to-Thickness Ratio for Specimens with Simply-Supported Boundary Conditions

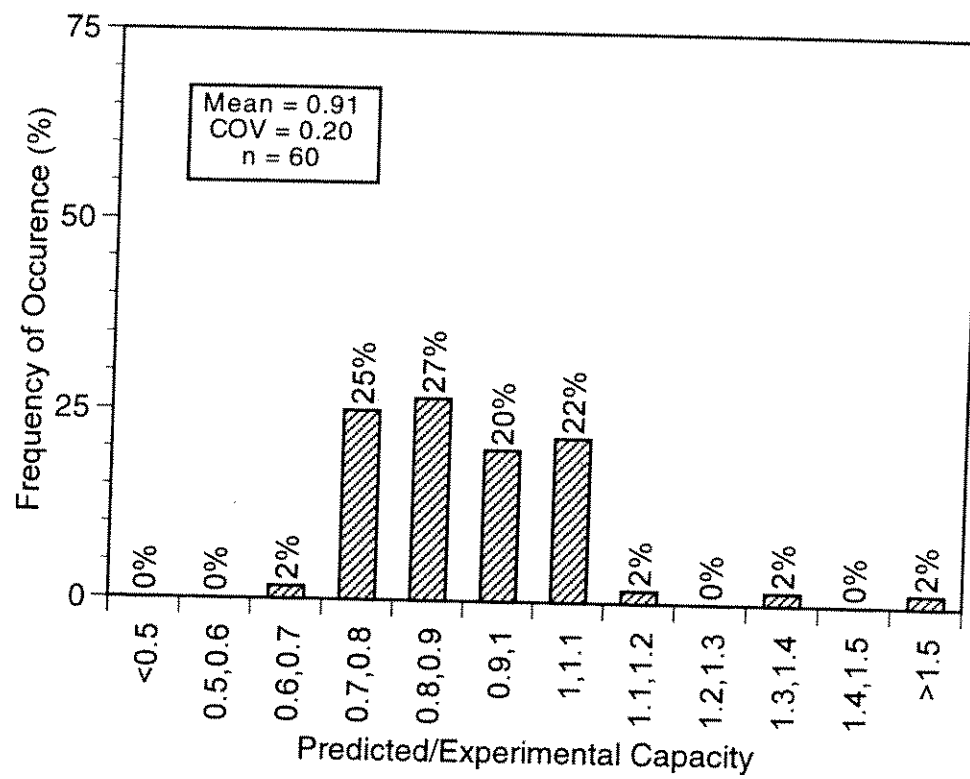


Figure 4.35 - Histogram of Predicted-to-Measured Capacity Ratio for Loh Unity Check Equation (Includes Current and Previous Experimental Data)

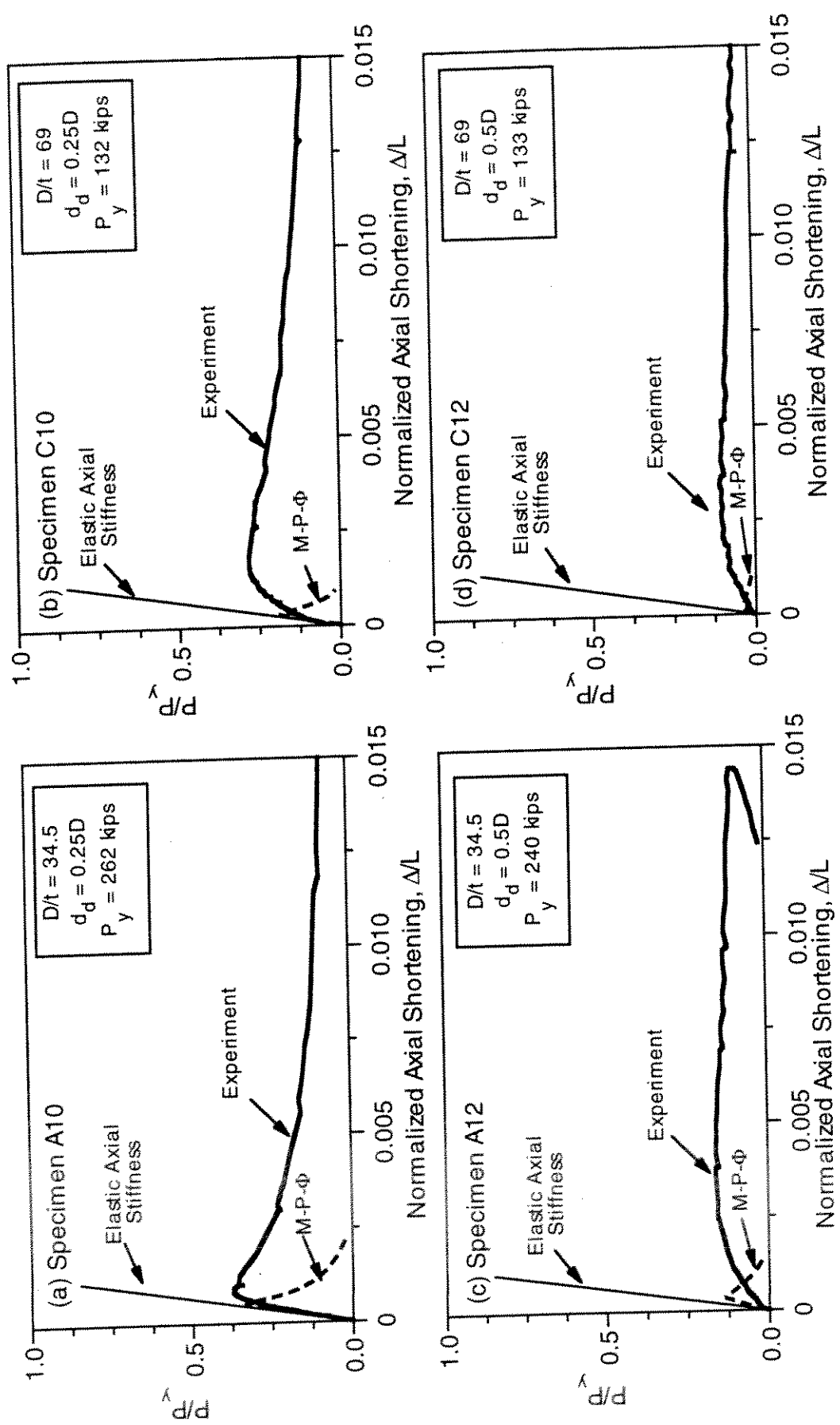


Figure 4.36 - Comparison of M-P- $\Phi$  Based Method and Experimental Results for the Axial Load-Shortening Response of Non-repaired Specimens

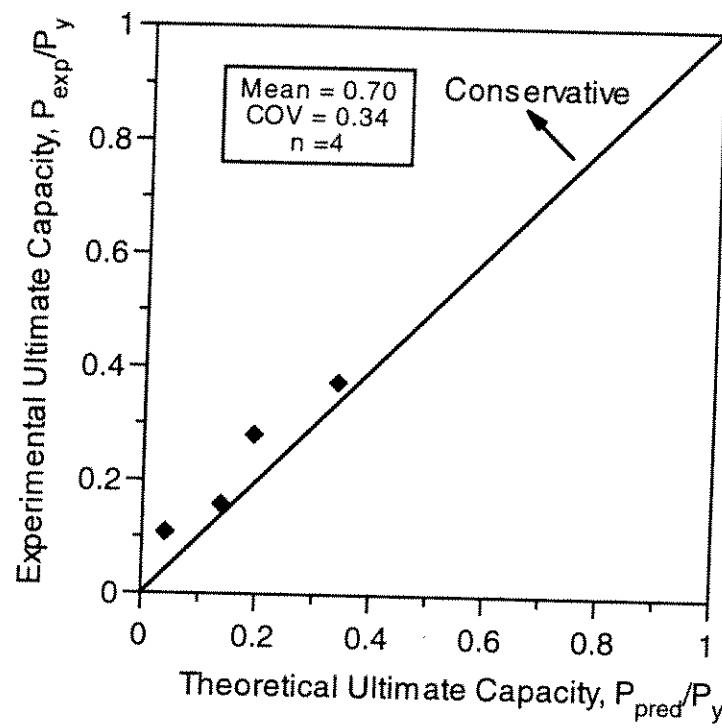


Figure 4.37 - Comparison of M-P- $\Phi$  Based Predictions with Experimental Results of Current Test Program



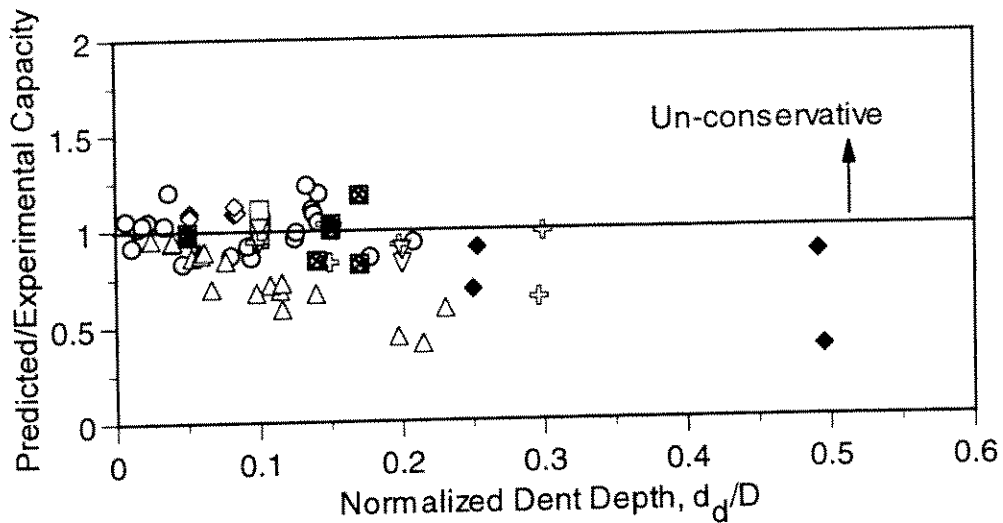
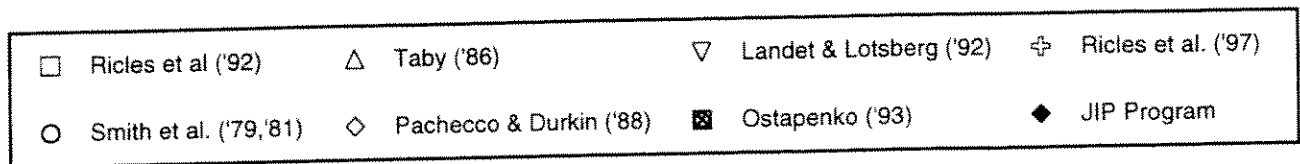


Figure 4.38 - Sensitivity of M-P- $\Phi$  Based Method to Depth of Applied Dent-Damage for Specimens with Simply-Supported Boundary Conditions and Dent at Midspan

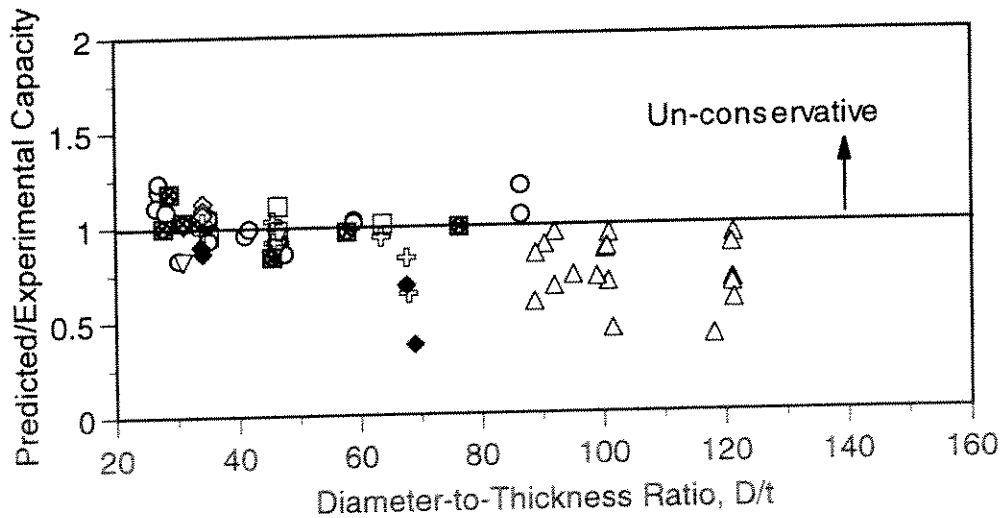
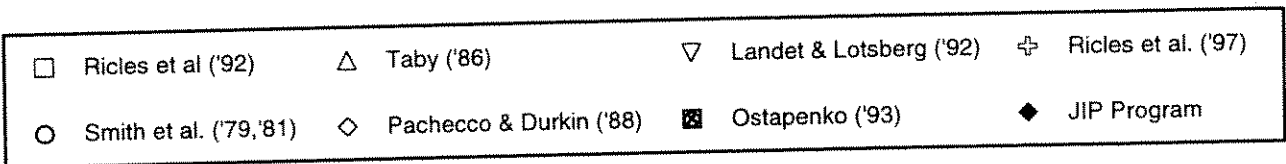


Figure 4.39 - Sensitivity of M-P- $\Phi$  Based Method to Diameter-to-Thickness Ratio for Specimens with Simply-Supported Boundary Conditions and Dent at Midspan

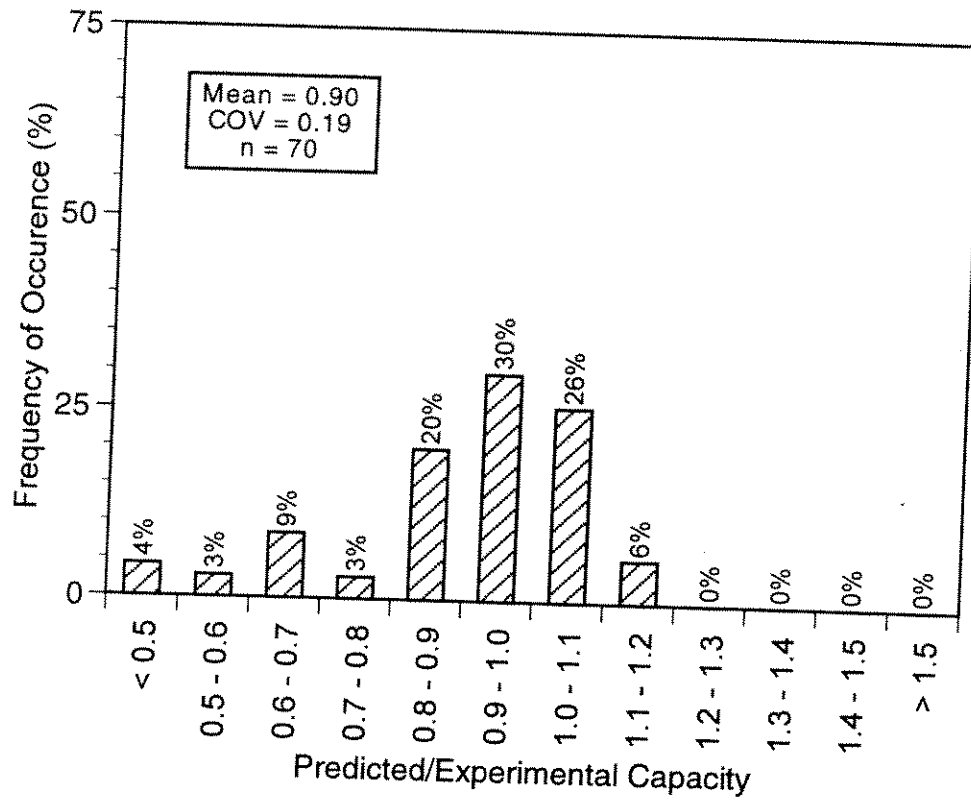


Figure 4.40 - Histogram of Predicted-to-Measured Capacity Ratio for M-P- $\Phi$  Based Method (Includes Current and Previous Experimental Data)

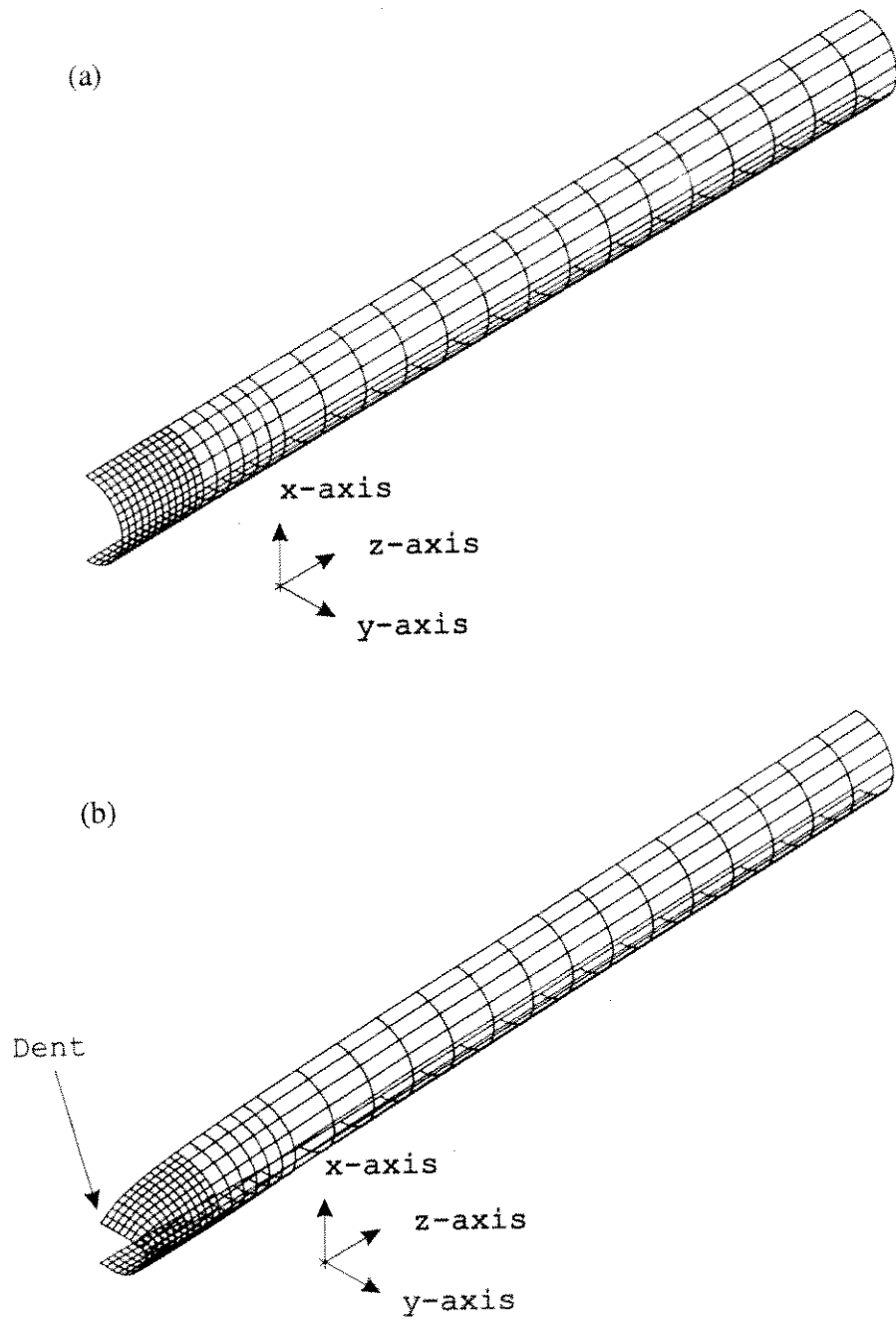


Figure 4.41 - Typical Finite Element Mesh for Non-repaired Specimens, (a) Undeformed Prior to Denting, and (b) Deformed Model Following Denting (after Ricles et al. 1997)

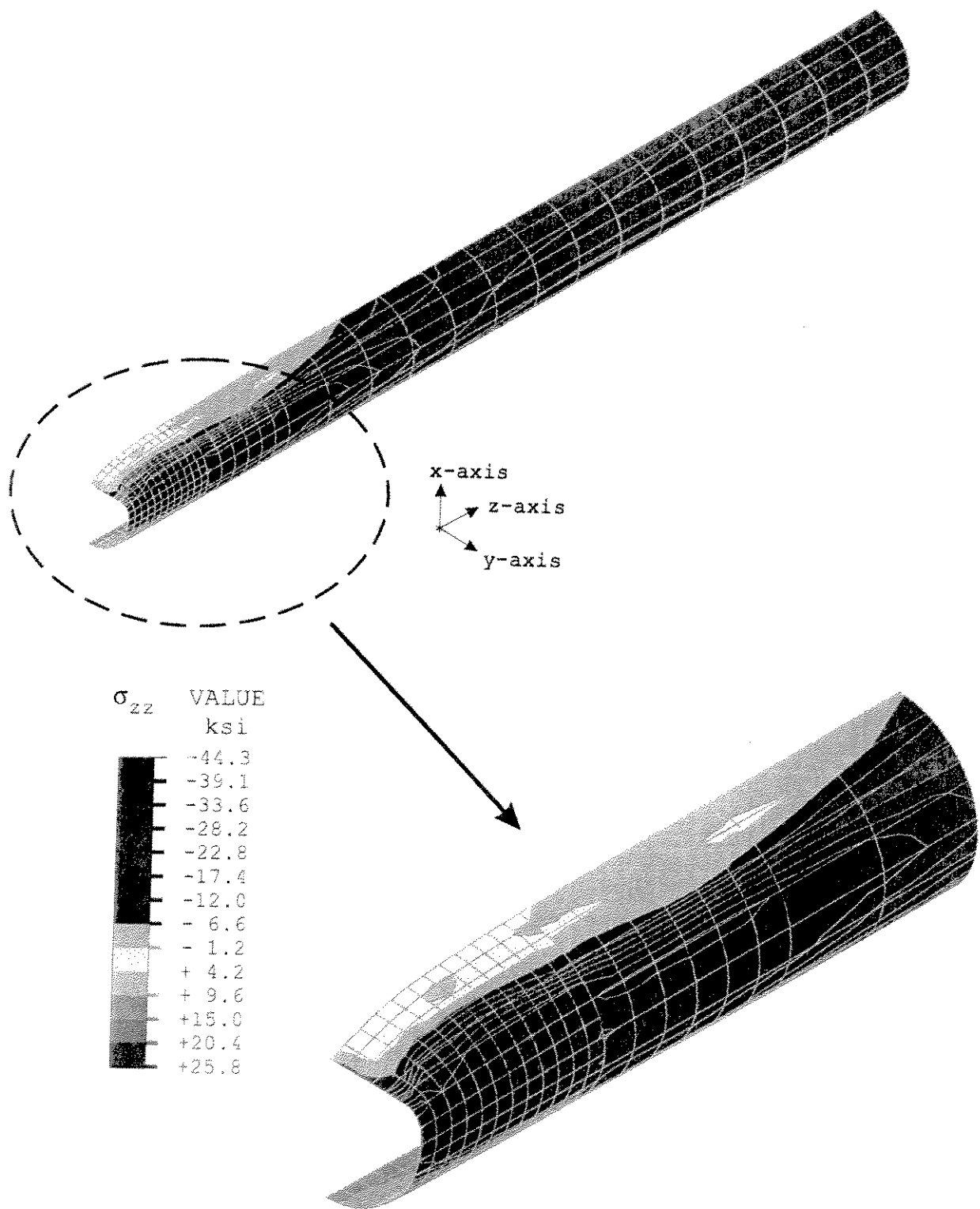


Figure 4.42 Longitudinal Stress Contour of Steel Tube of Specimen A10 at Maximum Axial Load in Analysis



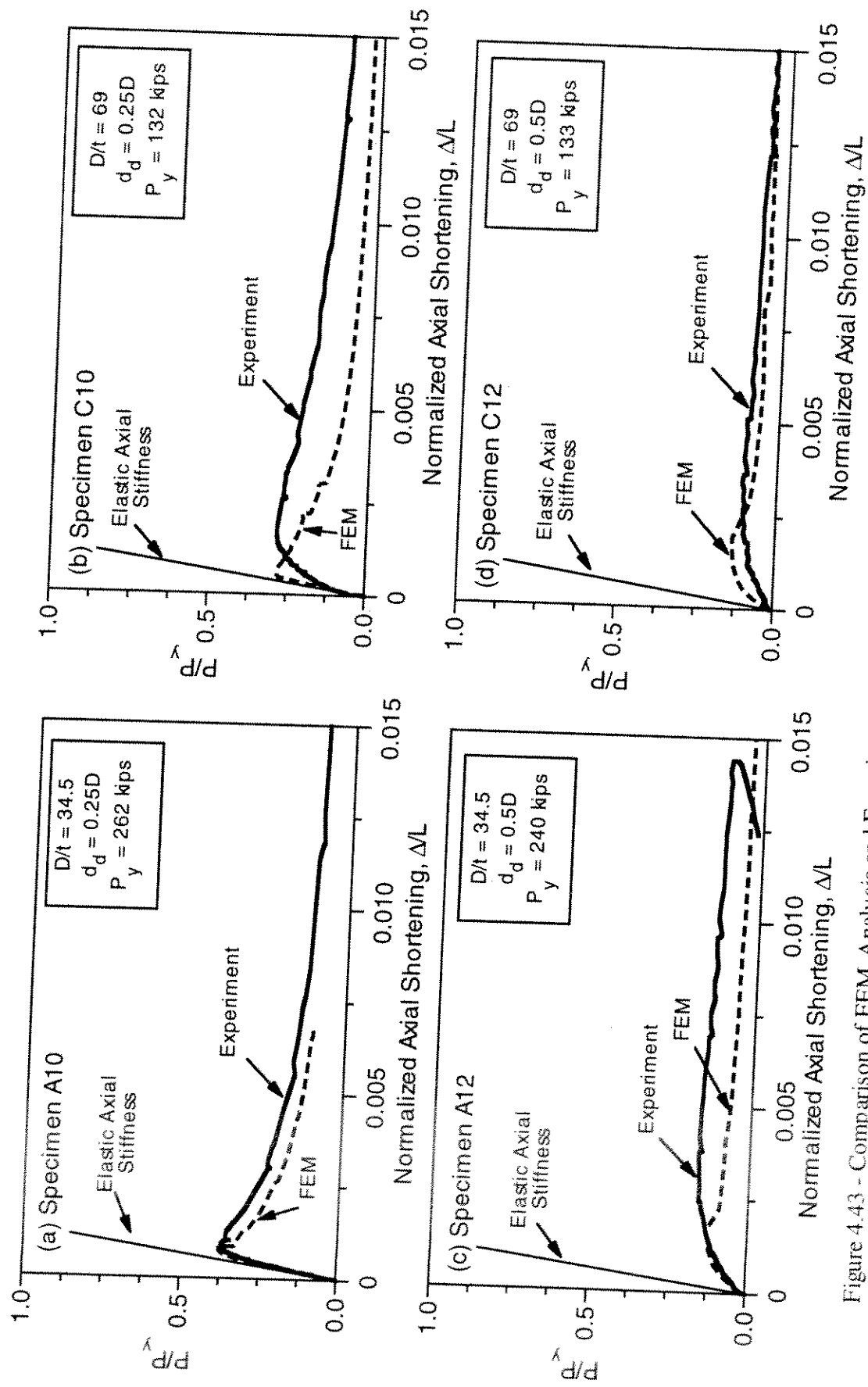


Figure 4.43 - Comparison of FEM Analysis and Experimental Results for the Axial Load-Shortening Response of Non-repaired Specimens

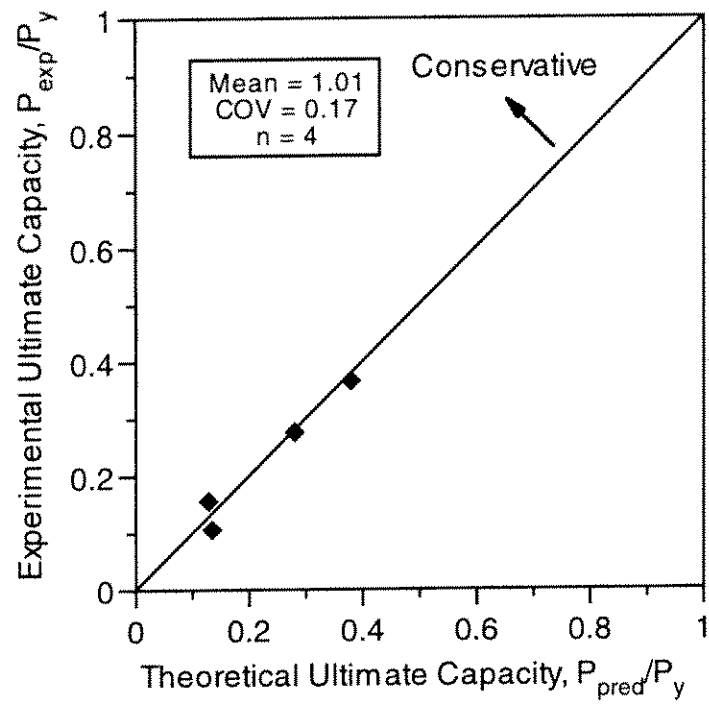


Figure 4.44 - Comparison of FEM Predictions with Experimental Results from Current Program

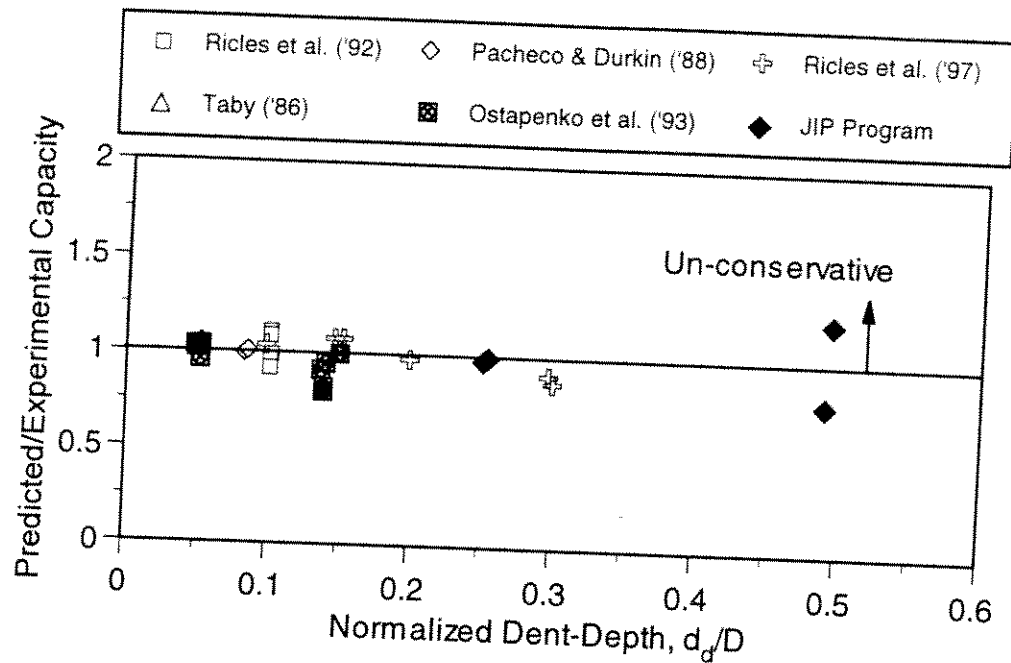


Figure 4.45 - Sensitivity of FEM Analysis to Depth of Applied Dent-Damage for Specimens with Simply-Supported Boundary Conditions

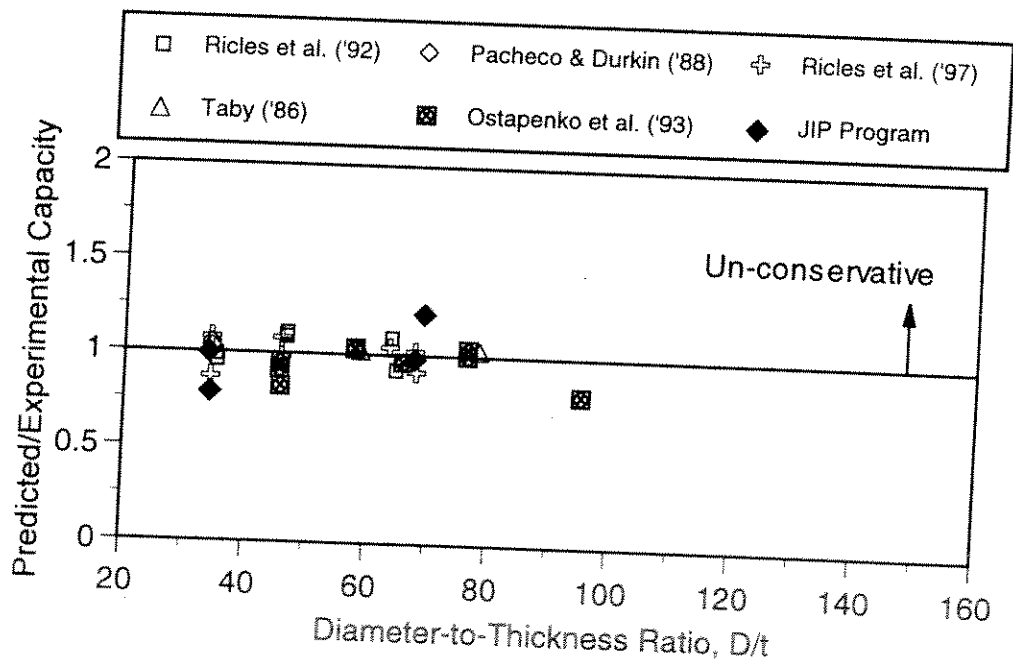


Figure 4.46 - Sensitivity of FEM Analysis to Diameter-to-Thickness Ratio for Specimens with Simply-Supported Boundary Conditions



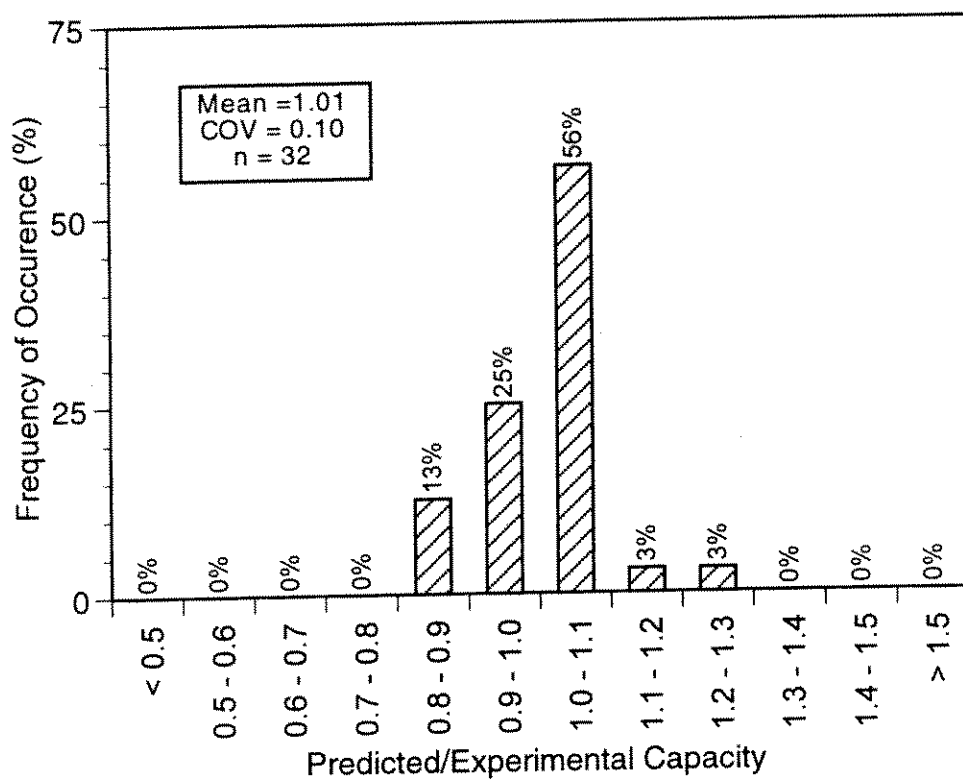


Figure 4.47 - Histogram of Predicted-to-Measured Capacity Ratio for FEM Analysis (Includes Current and Previous Experimental Data)

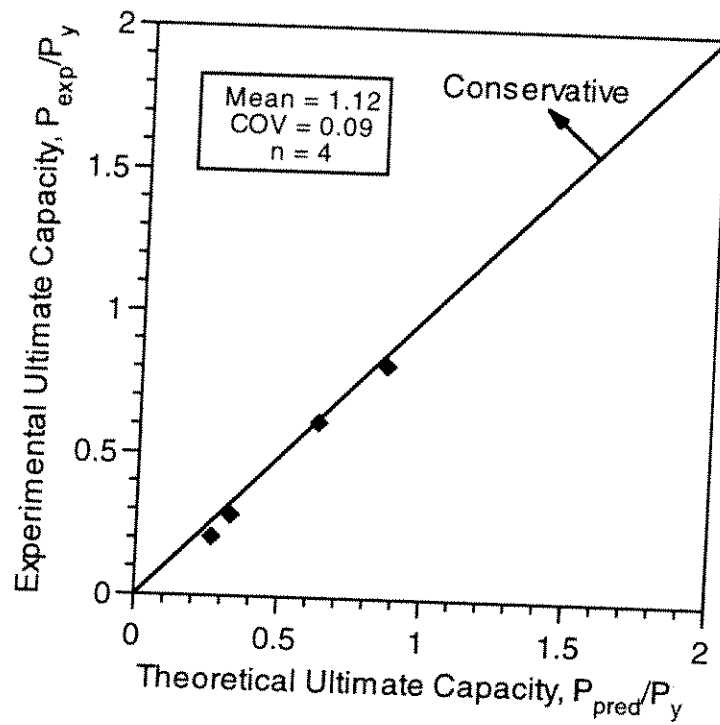


Figure 4.48 - Comparison of Parsanejad's Equation with Experimental Results of Internally Grouted Specimens from Current Program

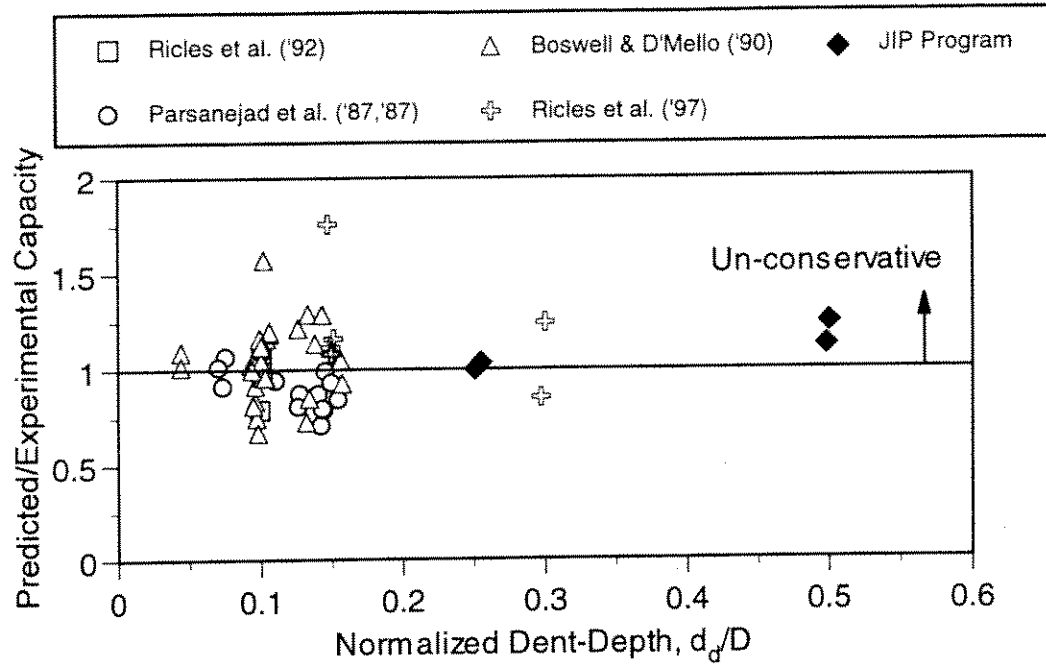


Figure 4.49 - Sensitivity of Parsanejad's Equation to Depth of Applied Dent-Damage for Internal Grout Repaired Specimens

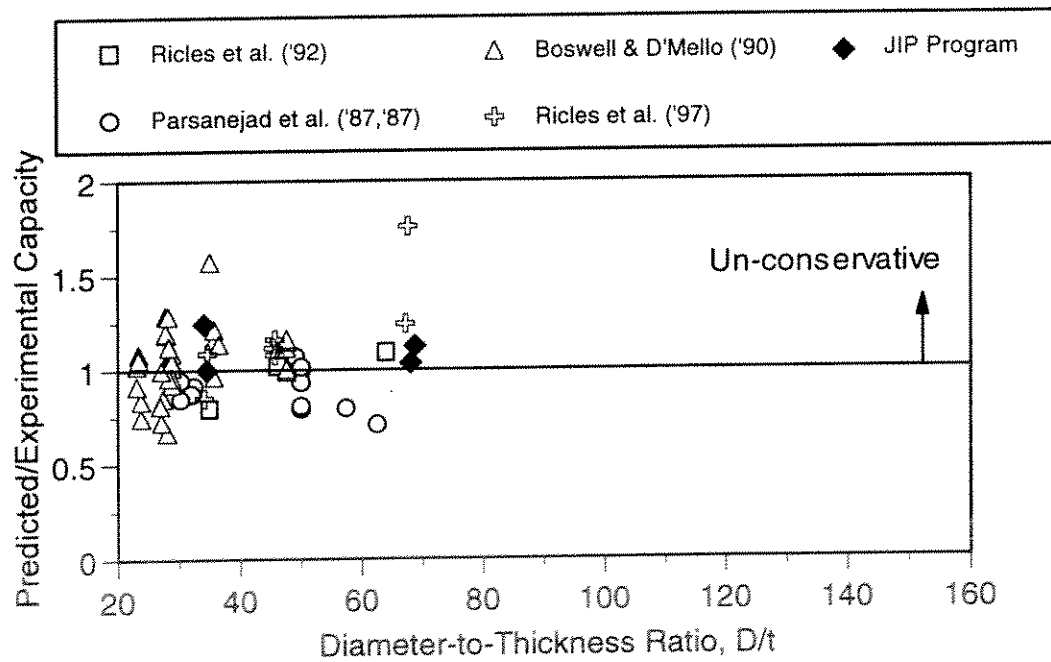


Figure 4.50 - Sensitivity of Parsanejad's Equation to Diameter-to-Thickness Ratio for Internal Grout Repaired Specimens

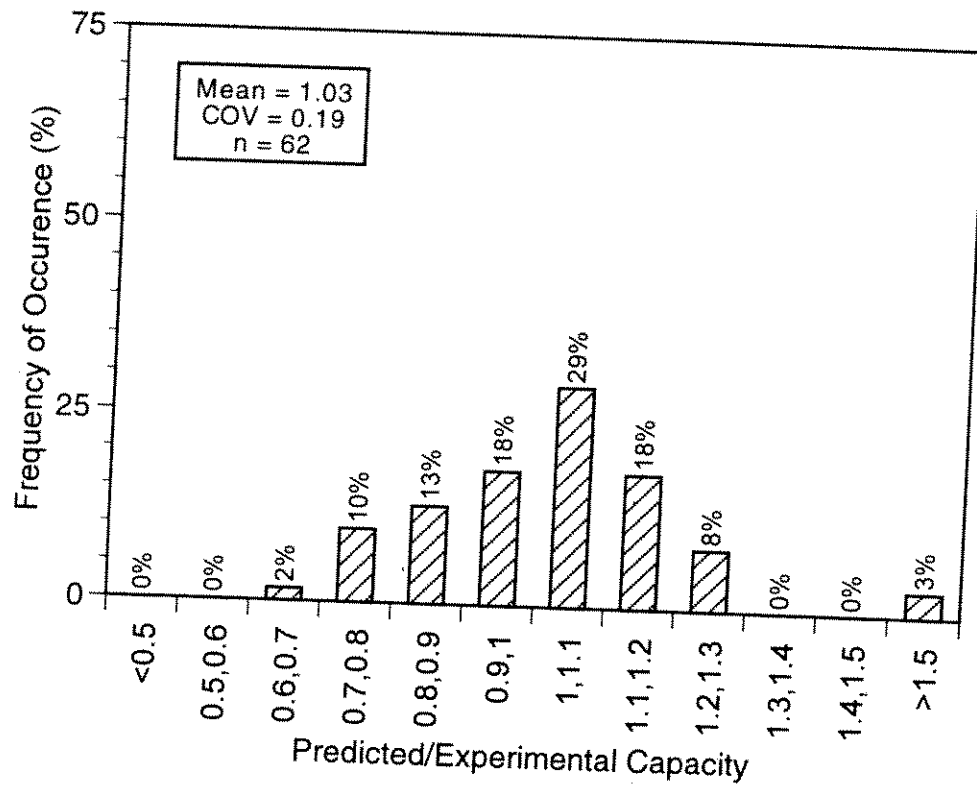


Figure 4.51 - Histogram of Predicted-to-Measured Capacity Ratio for Parsanejad's Equation (Includes Current and Previous Experimental Data)

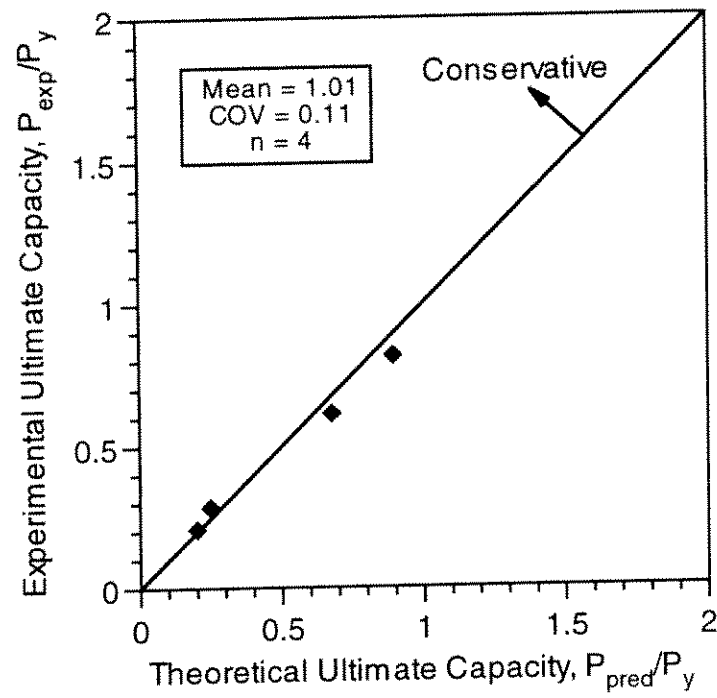


Figure 4.52 - Comparison of Loh's Modified AISC-LRFD Strength Equation with Experimental Results of Internally Grouted Specimens from Current Program

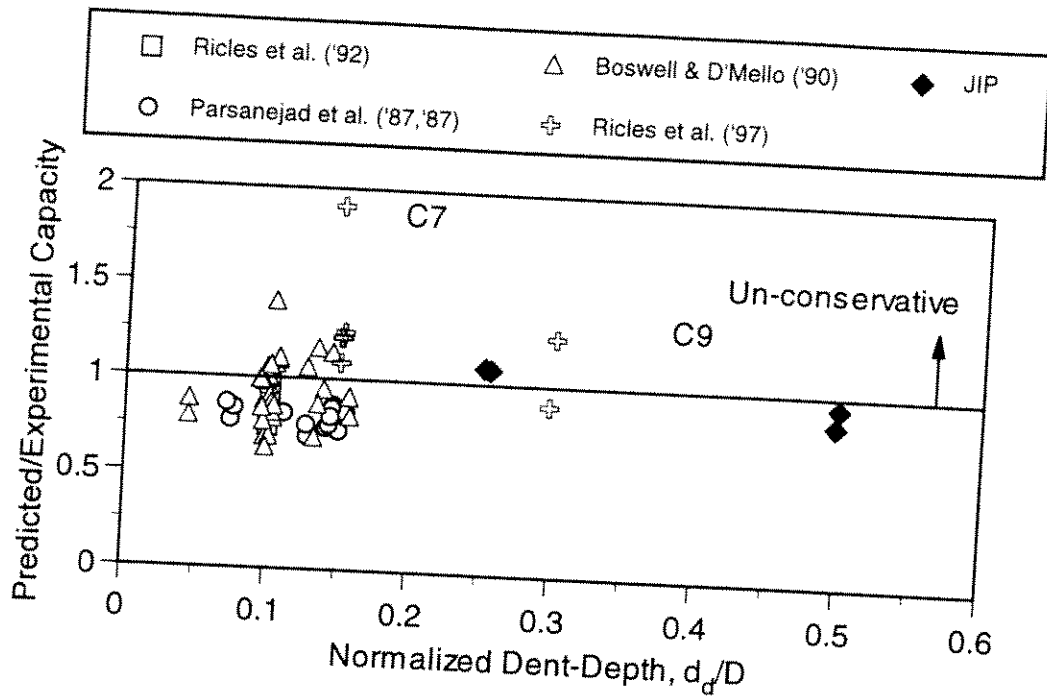


Figure 4.53 - Sensitivity of Loh's Modified AISC-LRFD Equation to Depth of Applied Dent-Damage for Internal Grout Repaired Specimens

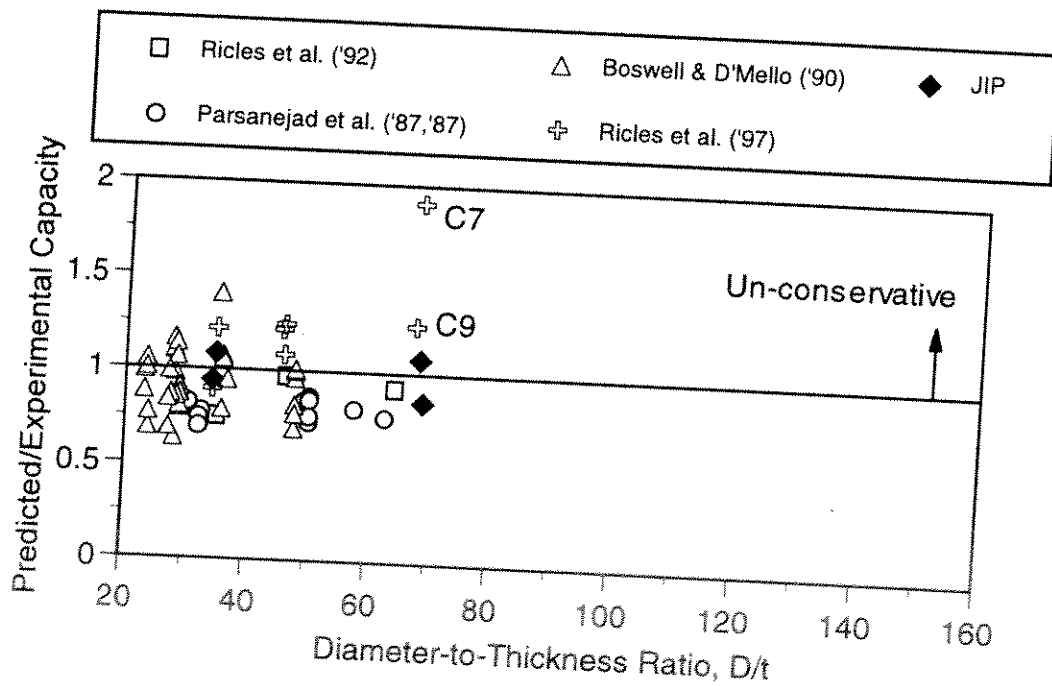


Figure 4.54 - Sensitivity of Loh's Modified AISC-LRFD Equation to Diameter-to-Thickness Ratio for Internal Grout Repaired Specimens

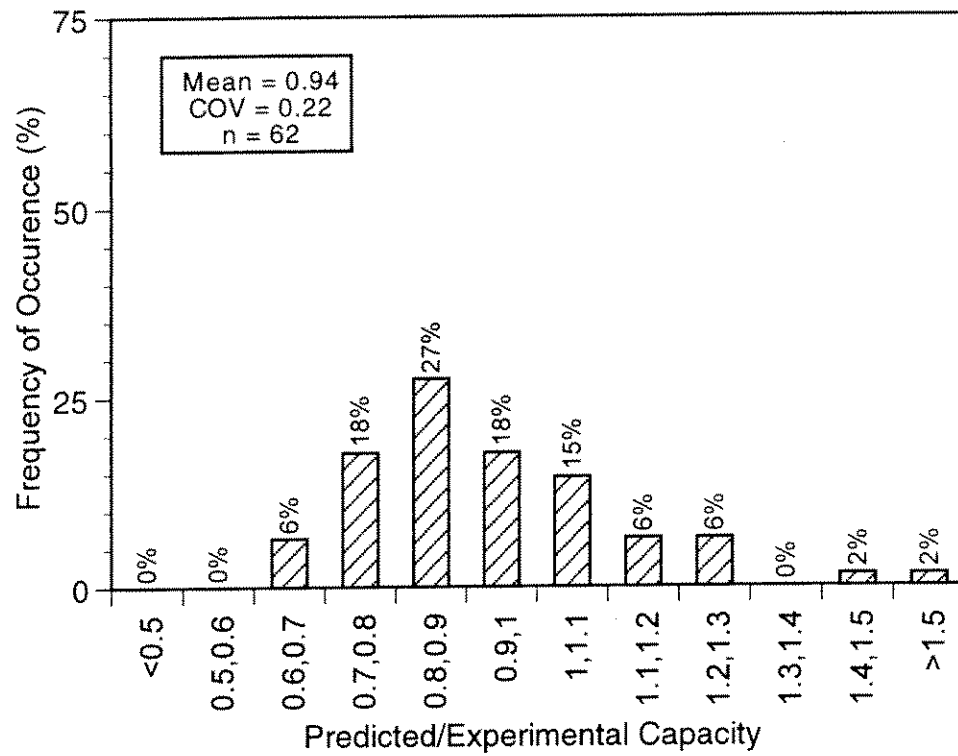
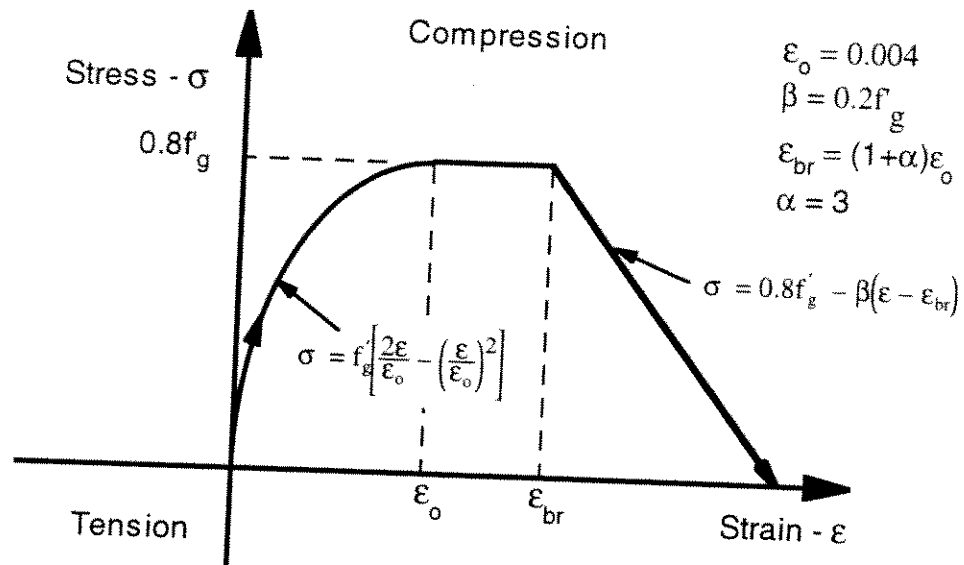
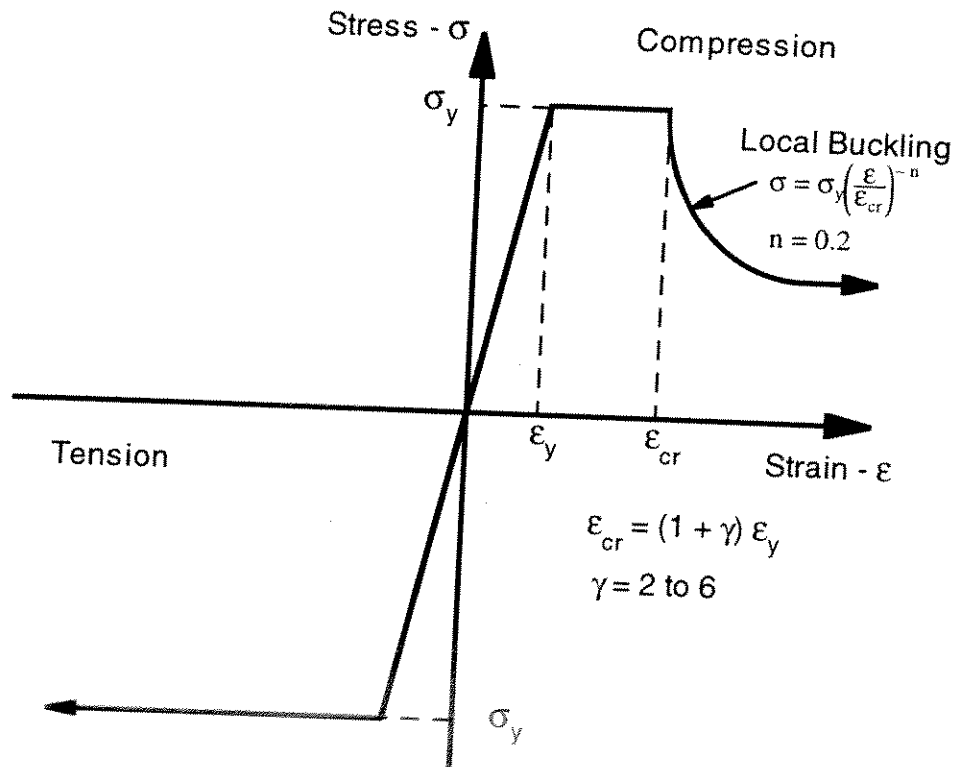


Figure 4.55 - Histogram of Predicted-to-Measured Capacity Ratio for Loh's Modified AISC-LRFD Equation (Includes Current and Previous Experimental Data)



(a) Fiber Stress-Strain Relationship for Grout



(b) Fiber Stress-Strain Relationship for Steel

Figure 4.56 - Fiber Stress-Strain Relationships for (a) Grout and (b) Steel  
 (after Ricles et al. 1997)



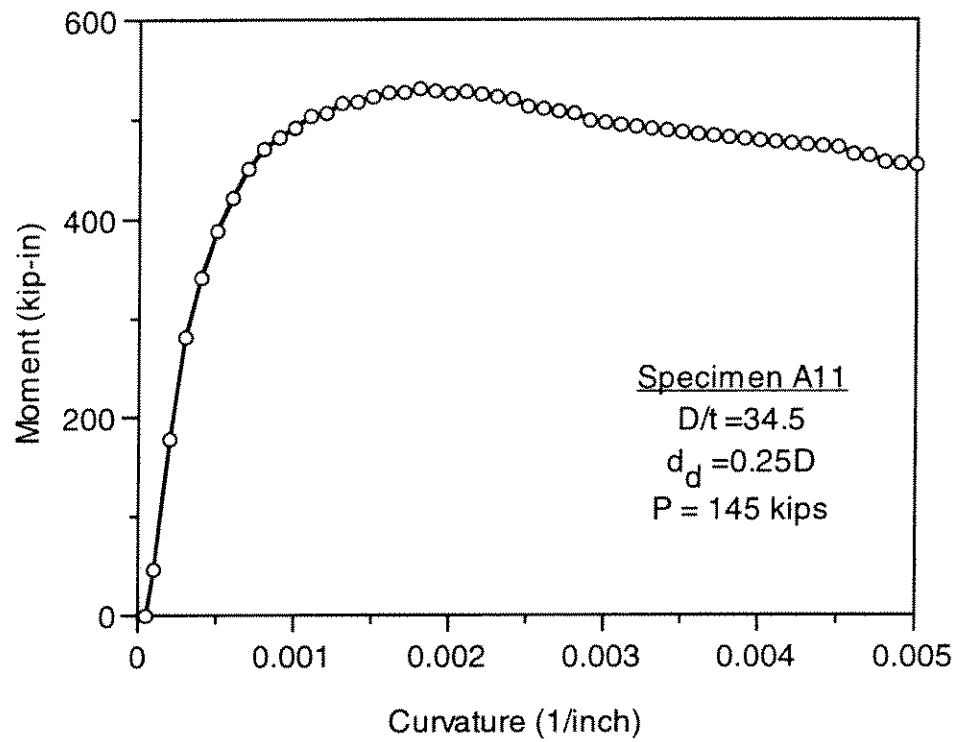


Figure 4.57 - Typical Moment-Curvature (M- $\phi$ ) Relationship for an Internal Grout Repaired Specimen (Moment Referenced at Centroid of Undented Cross-Section).

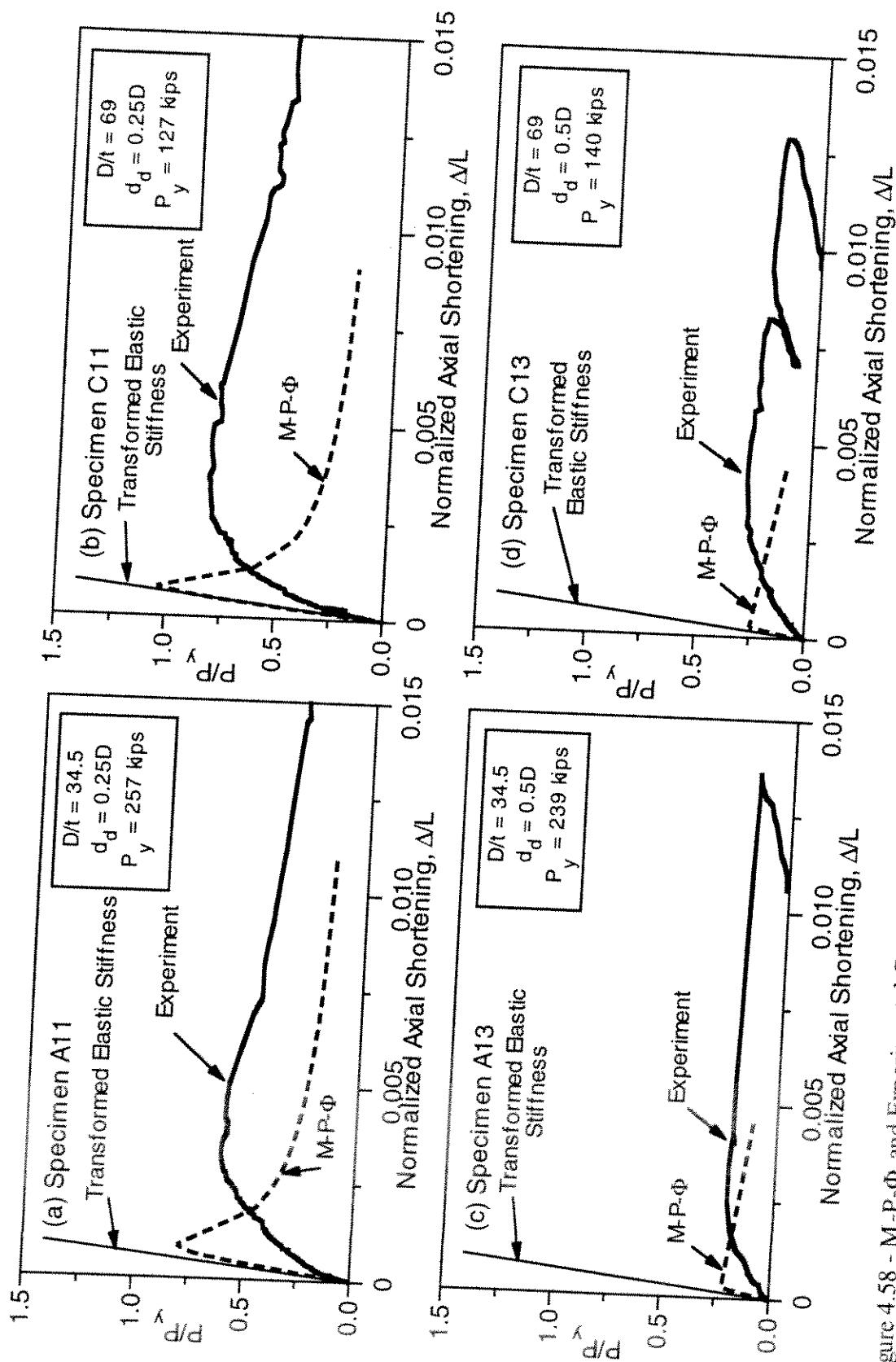


Figure 4.58 - M-P- $\phi$  and Experimental Comparison for the Axial Load-Shortening Response of Internal Grout Repaired Specimens  
(M-P- $\phi$  Analysis Based on Grout Modulus per Eqn (2.1))

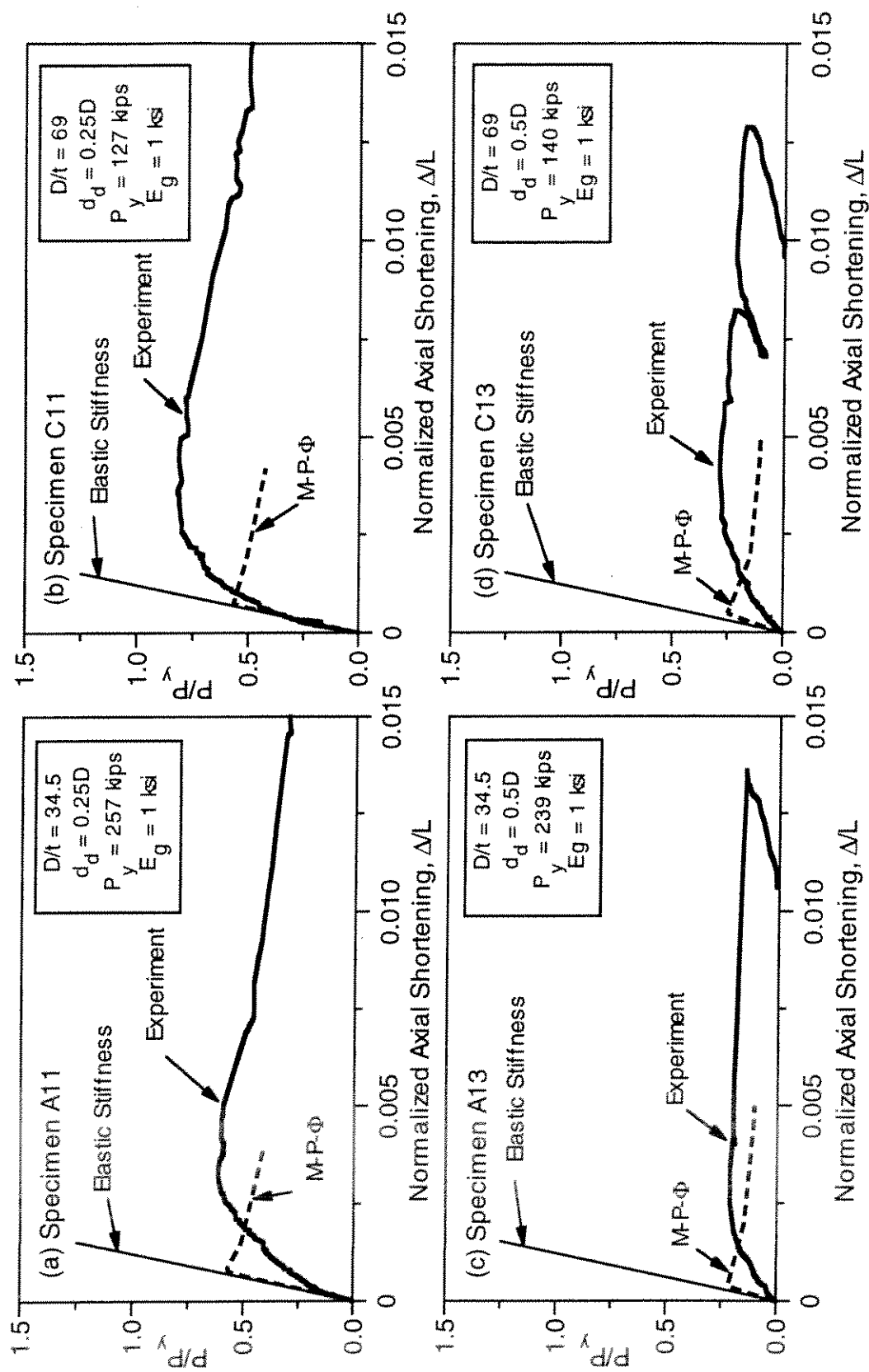


Figure 4.59 - M-P- $\Phi$  and Experimental Comparison for the Axial Load-Shortening Response of Internal Grout Repaired Specimens  
(M-P- $\Phi$  Analysis Based on Reduced Grout Modulus  $E_g = 1 \text{ ksi}$ )

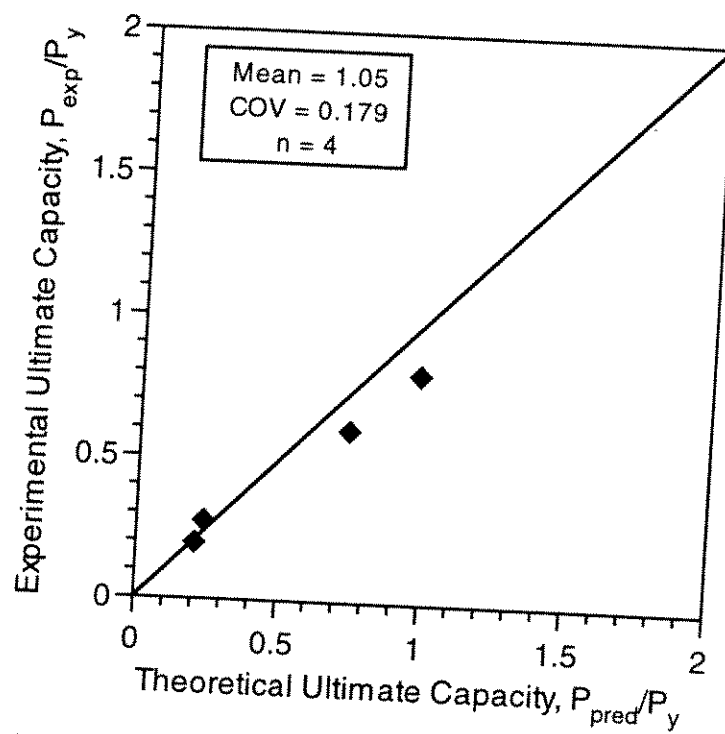


Figure 4.60 - Comparison of M-P- $\Phi$  Based Method with Experimental Results of Internally Grouted Specimens from Current Program (Analysis Based on Measured Grout Modulus).

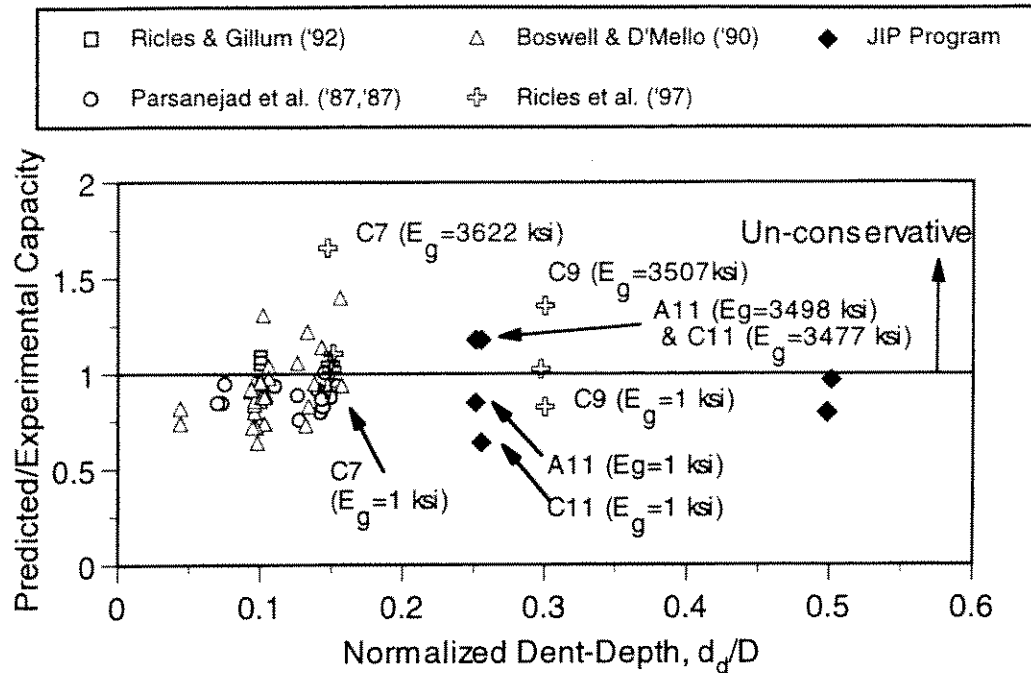


Figure 4.61 - Sensitivity of M-P- $\Phi$  Based Method to Depth of Applied Dent-Damage for Internal Grout Repaired Specimens

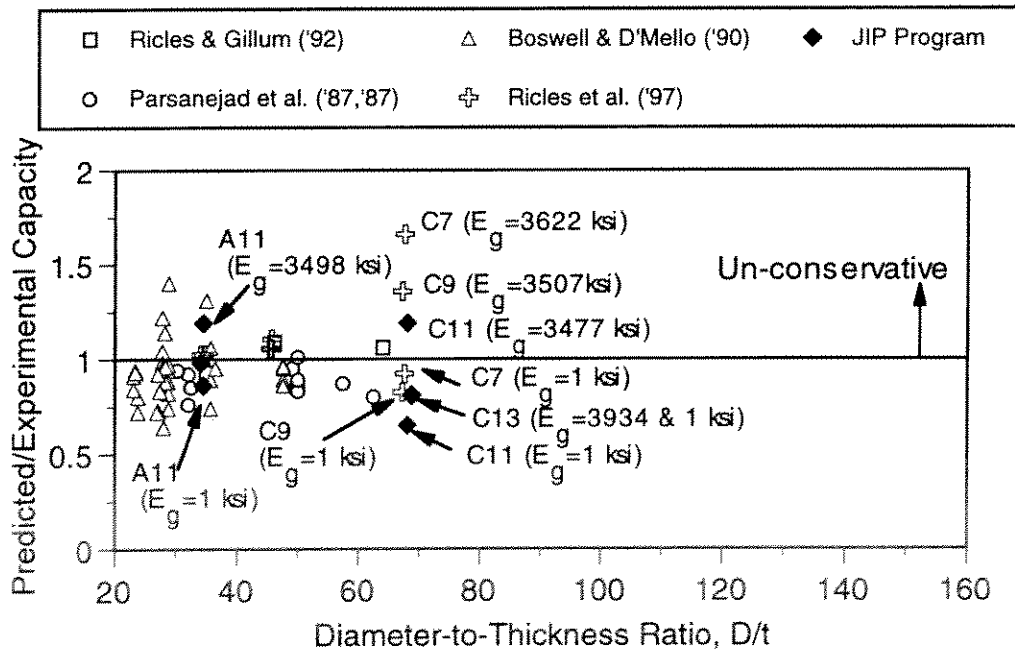


Figure 4.62 - Sensitivity of M-P- $\Phi$  Based Method to Diameter-to-Thickness Ratio for Internal Grout Repaired Specimens

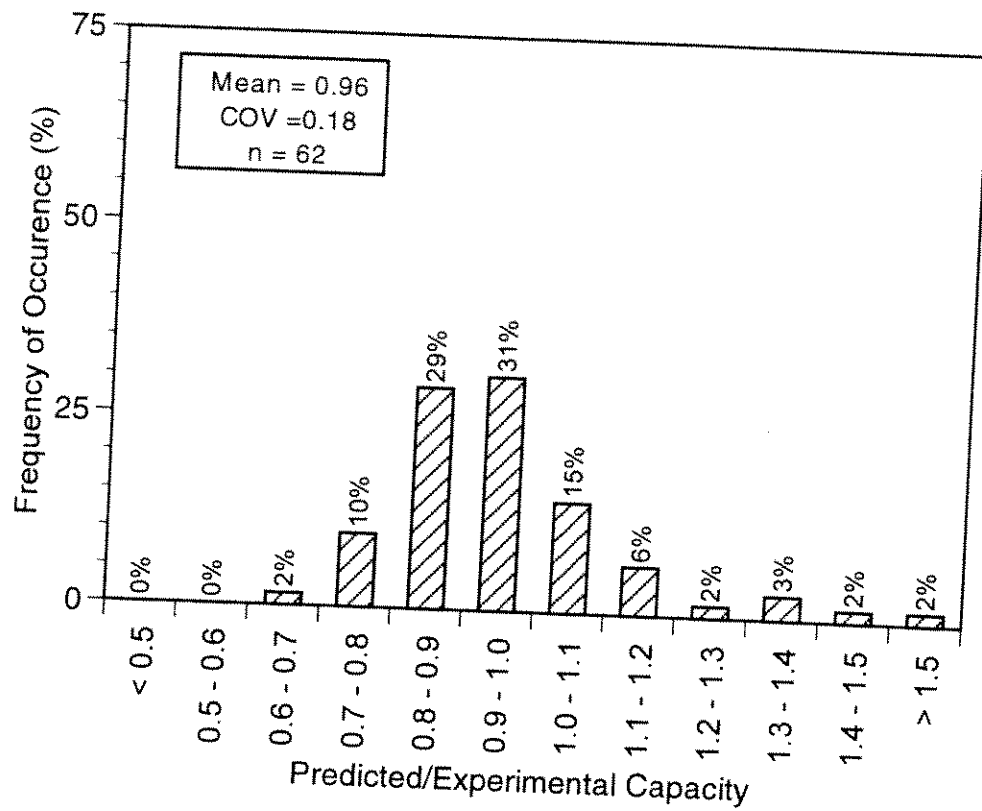


Figure 4.63 - Histogram of Predicted-to-Measured Capacity Ratio for M-P- $\Phi$  Based Method (Includes Previous Experimental Data)

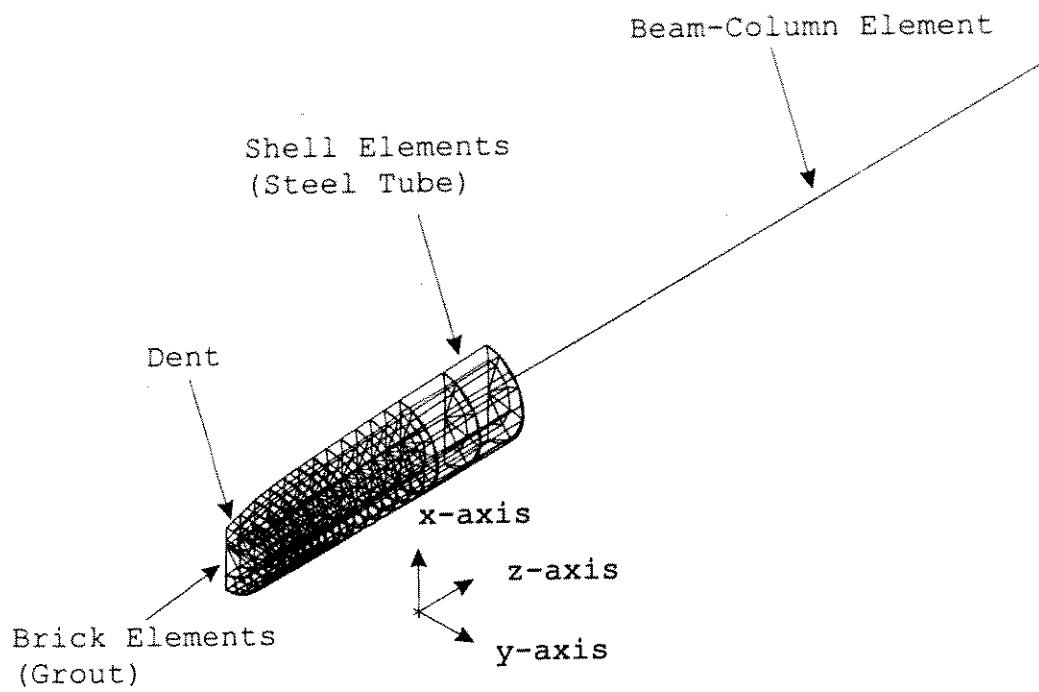


Figure 4.64 - Typical Finite Element Mesh for Internal Grout Repaired Specimens, Deformed Model Following Denting and Definition of Grout Elements (after Ricles et al. 1997)

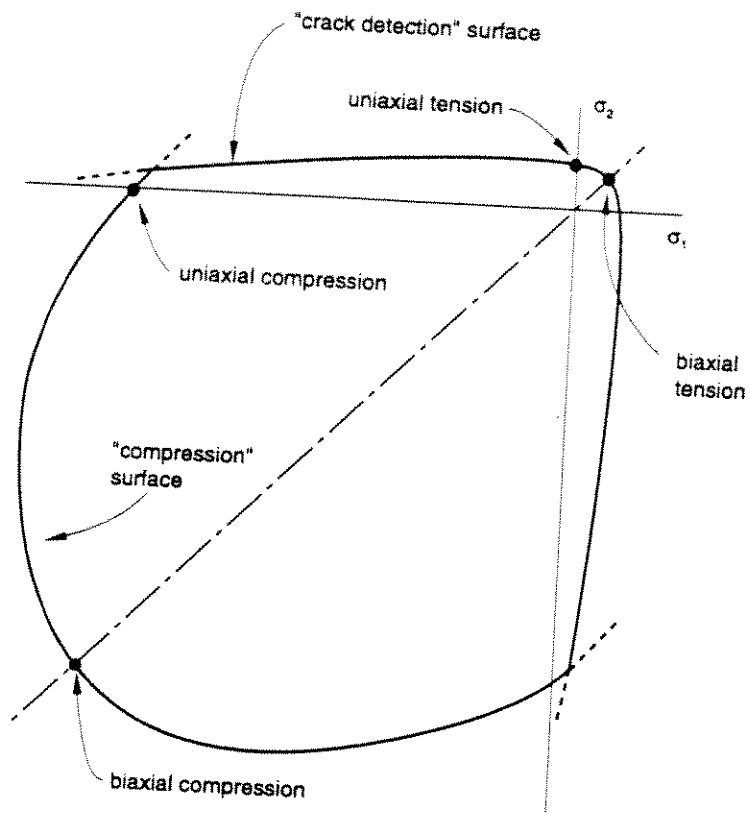


Figure 4.65 - Concrete Failure Surfaces in Plane Stress for Modeling Grout  
(after ABAQUS 1993)



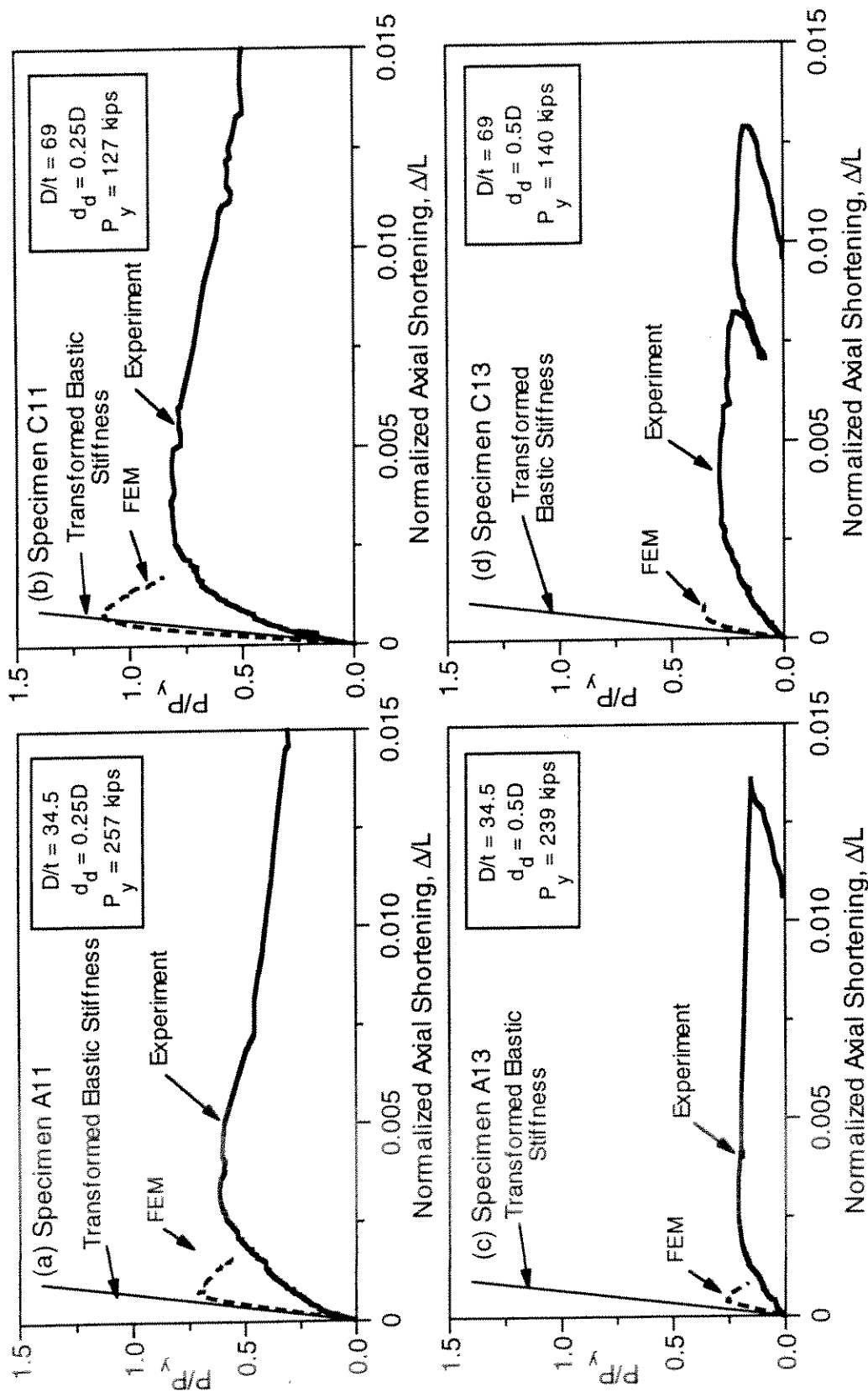


Figure 4.66 - FEM and Experimental Comparison for the Axial Load-Shortening Response of Internal Grout Repaired Specimens  
(FEM Analysis Based on Grout Modulus per Eqn (2.1))

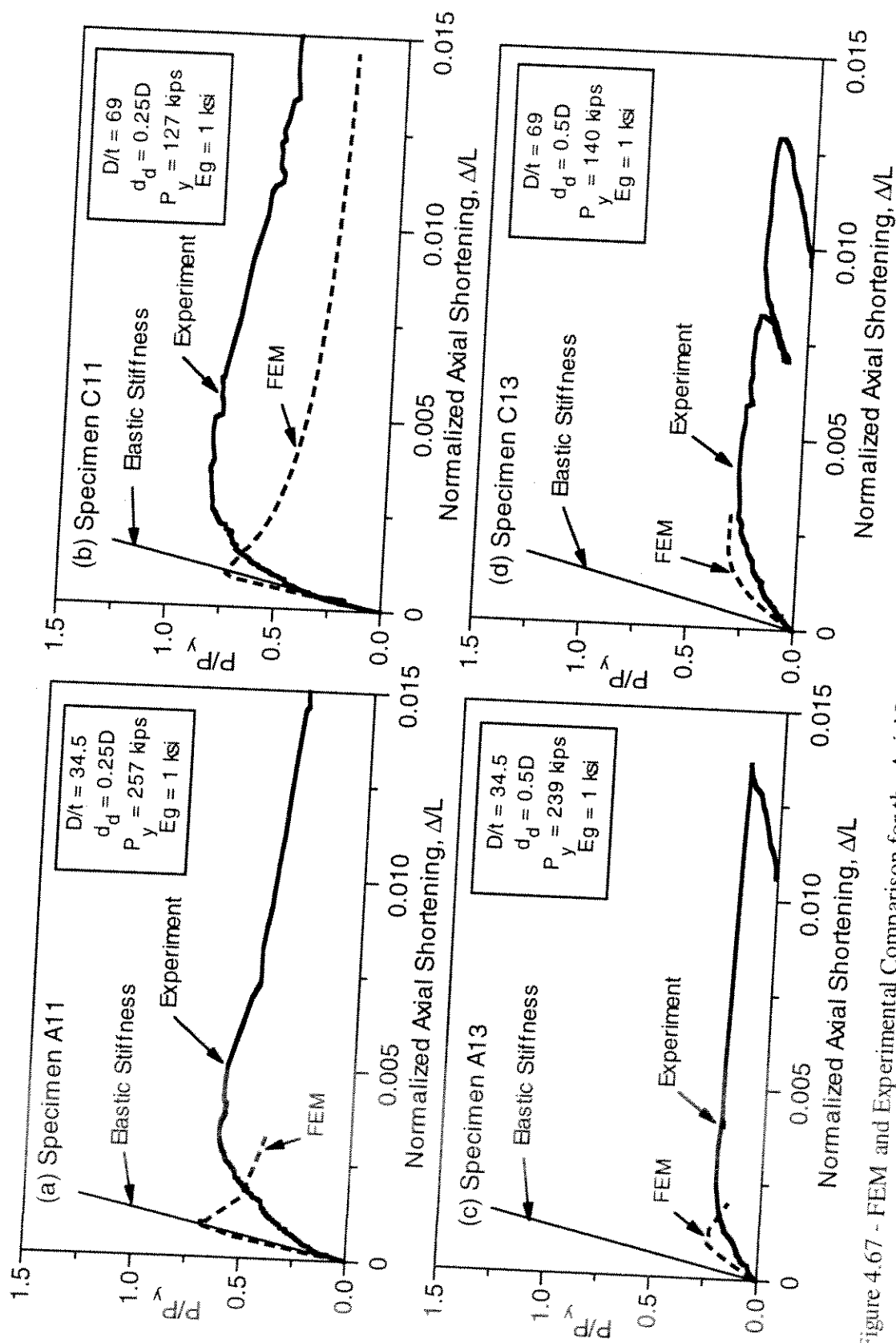


Figure 4.67 - FEM and Experimental Comparison for the Axial Load-Shortening Response of Internal Grout Repaired Specimens  
(FEM Analysis Based on Reduced Grout Modulus  $E_g = 1$  ksi)



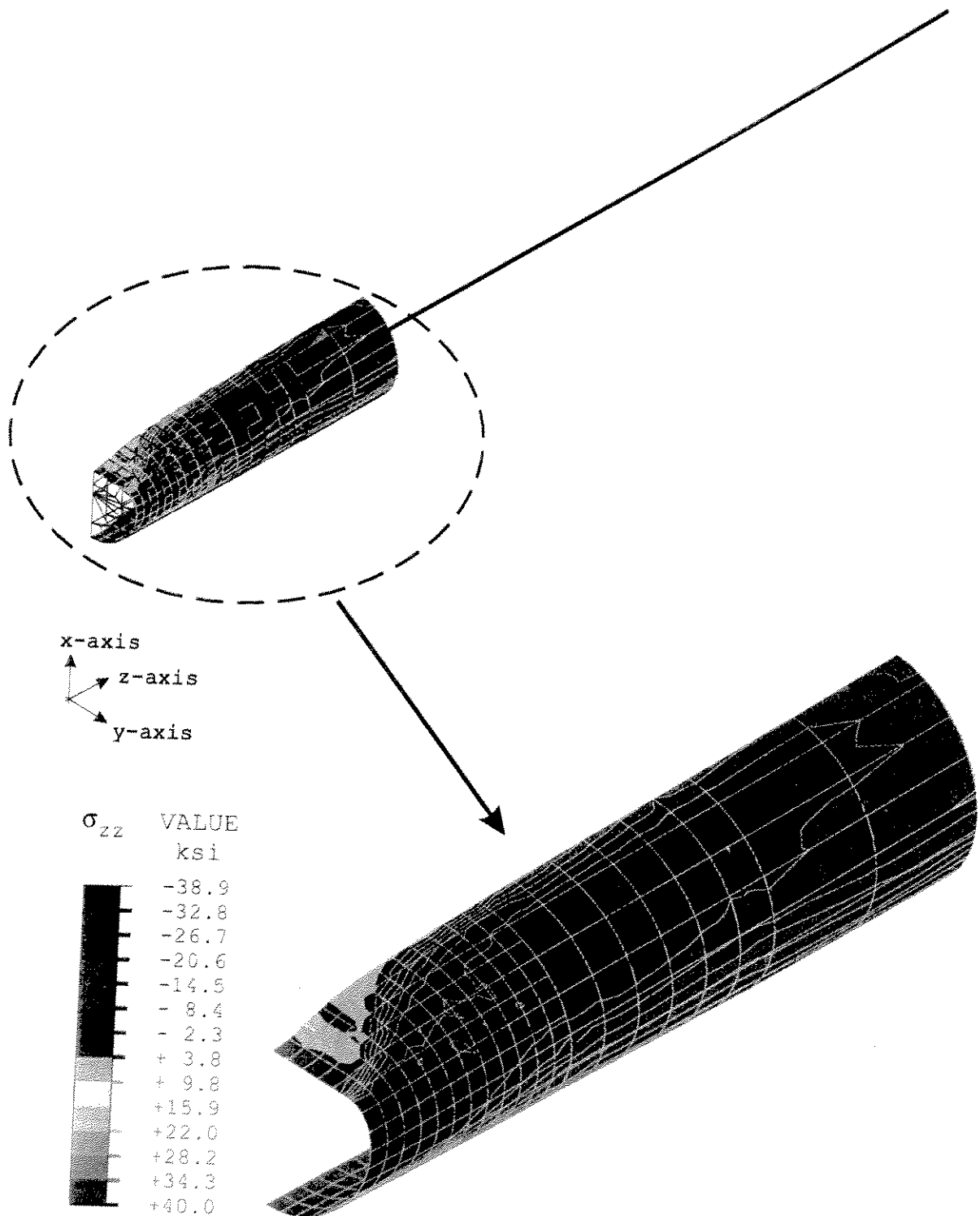


Figure 4.68 Longitudinal Stress Contour of Steel Tube of Specimen A11 Just After Maximum Axial Load in Analysis Was Achieved



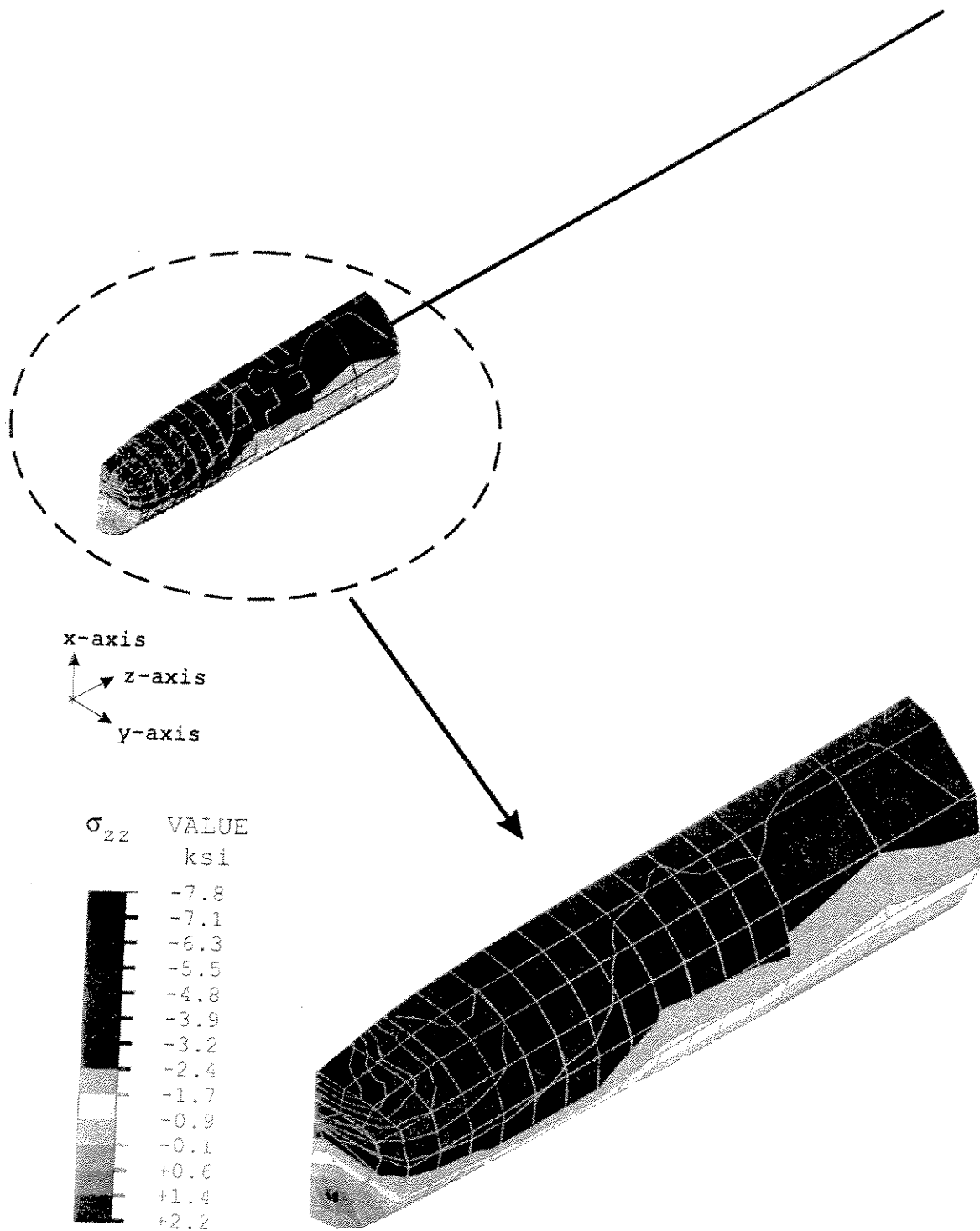


Figure 4.69 Longitudinal Stress Contour of Internal Grout of Specimen A11 Just After Maximum Axial Load in Analysis Was Achieved



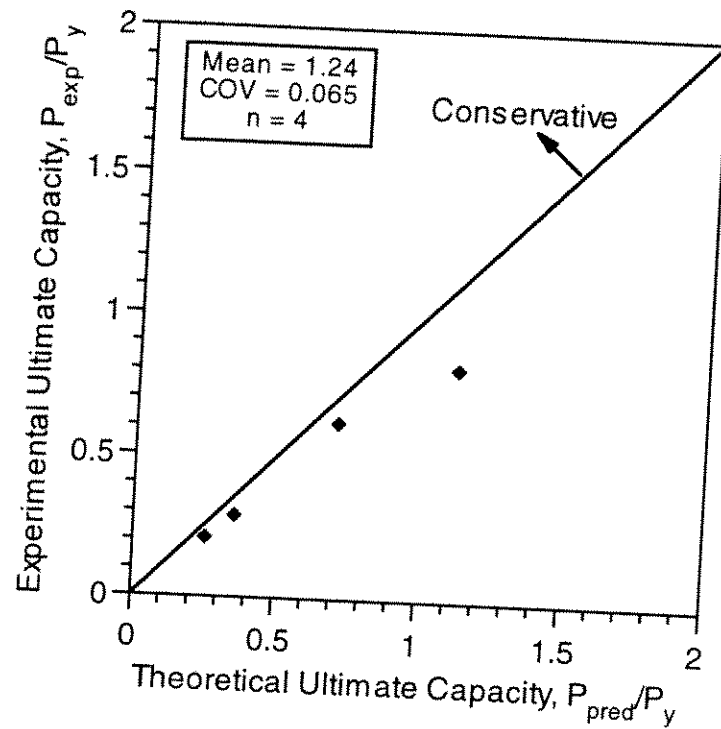


Figure 4.70 - Comparison of FEM Analysis with Experimental Results of Internally Grouted Specimens from Current Program (Grout Modulus Based on Eqn (2.1)).



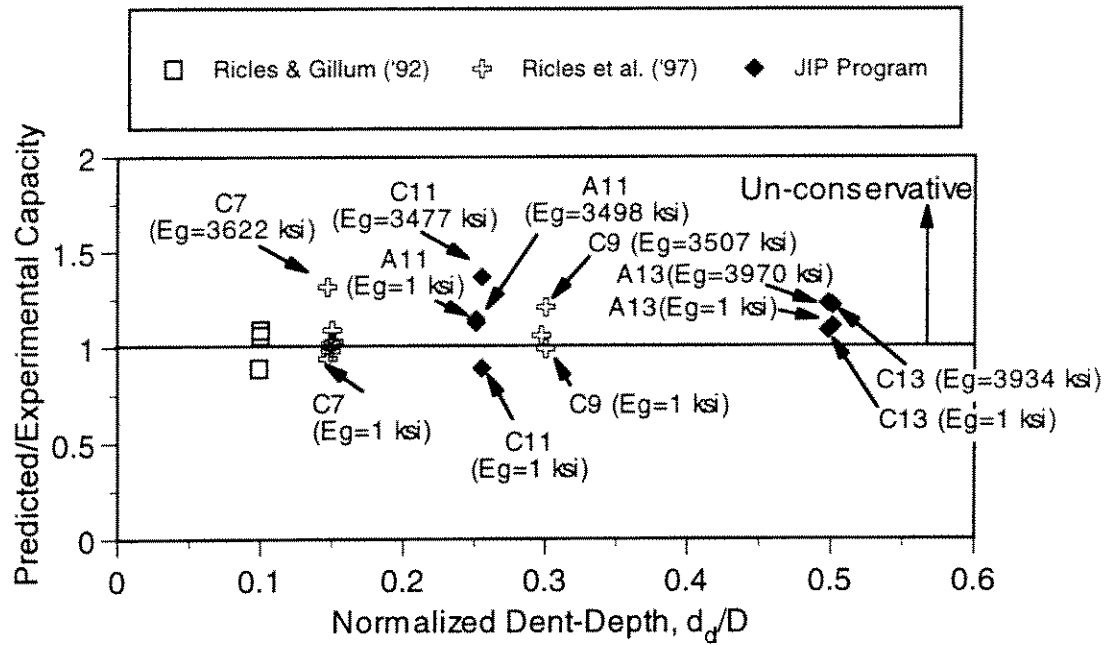


Figure 4.71 - Sensitivity of FEM Analysis to Depth of Applied Dent-Damage for Internal Grout Repaired Specimens

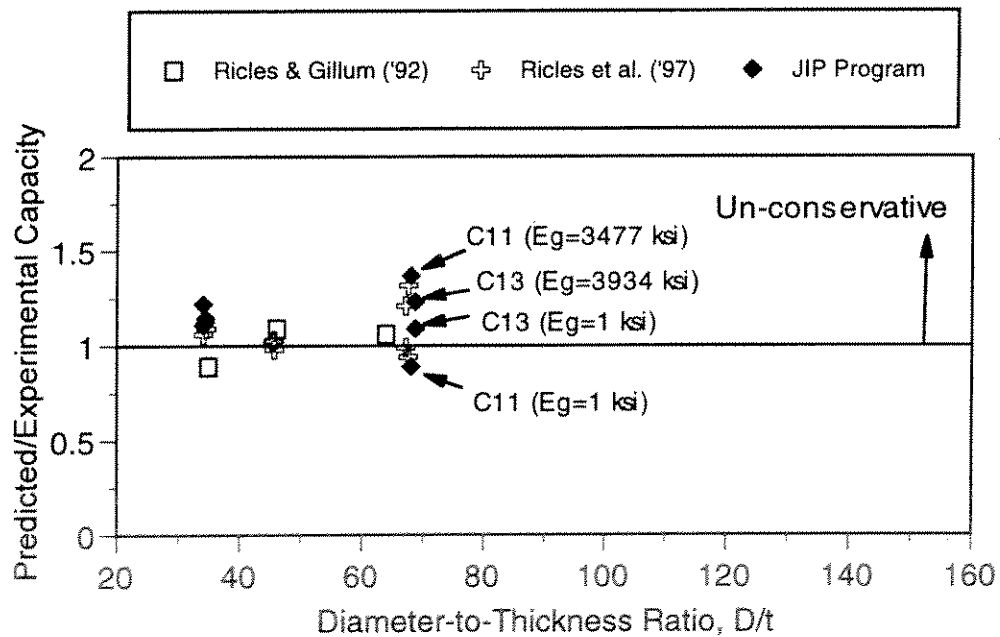


Figure 4.72 - Sensitivity of FEM Analysis to Diameter-to-Thickness Ratio for Internal Grout Repaired Specimens

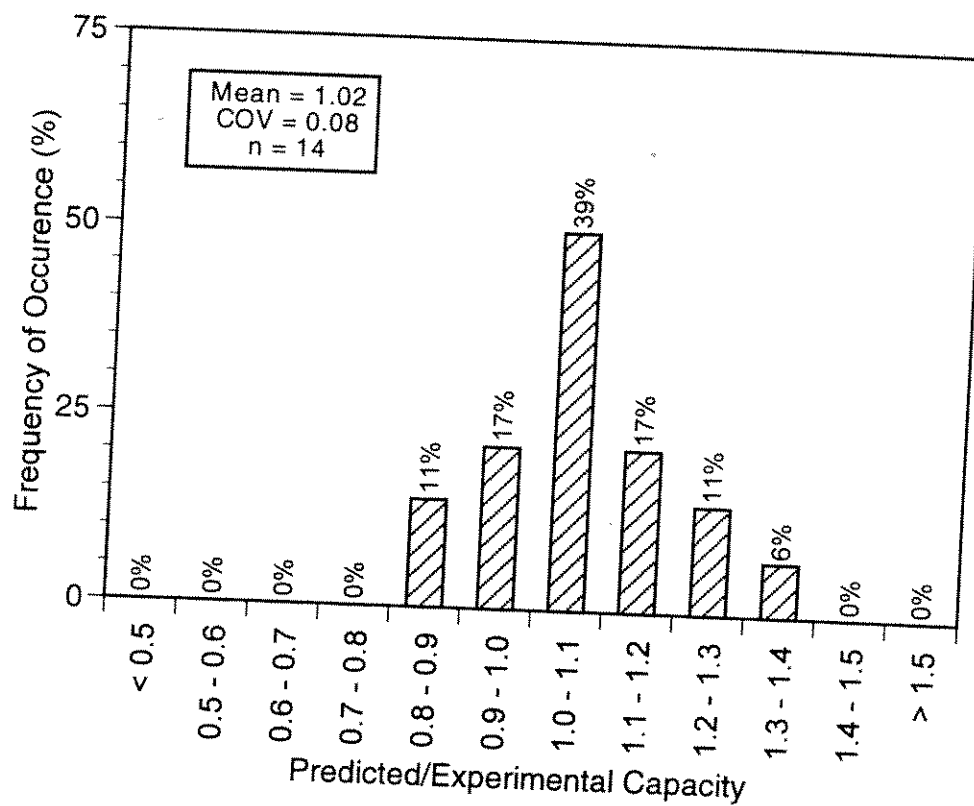


Figure 4.73 - Histogram of Predicted-to-Measured Capacity Ratio for FEM Analysis (Includes Previous Experimental Data from Ricles et al. ['92,'97], Analysis Based on Reduced Grout Modulus for Current Study)

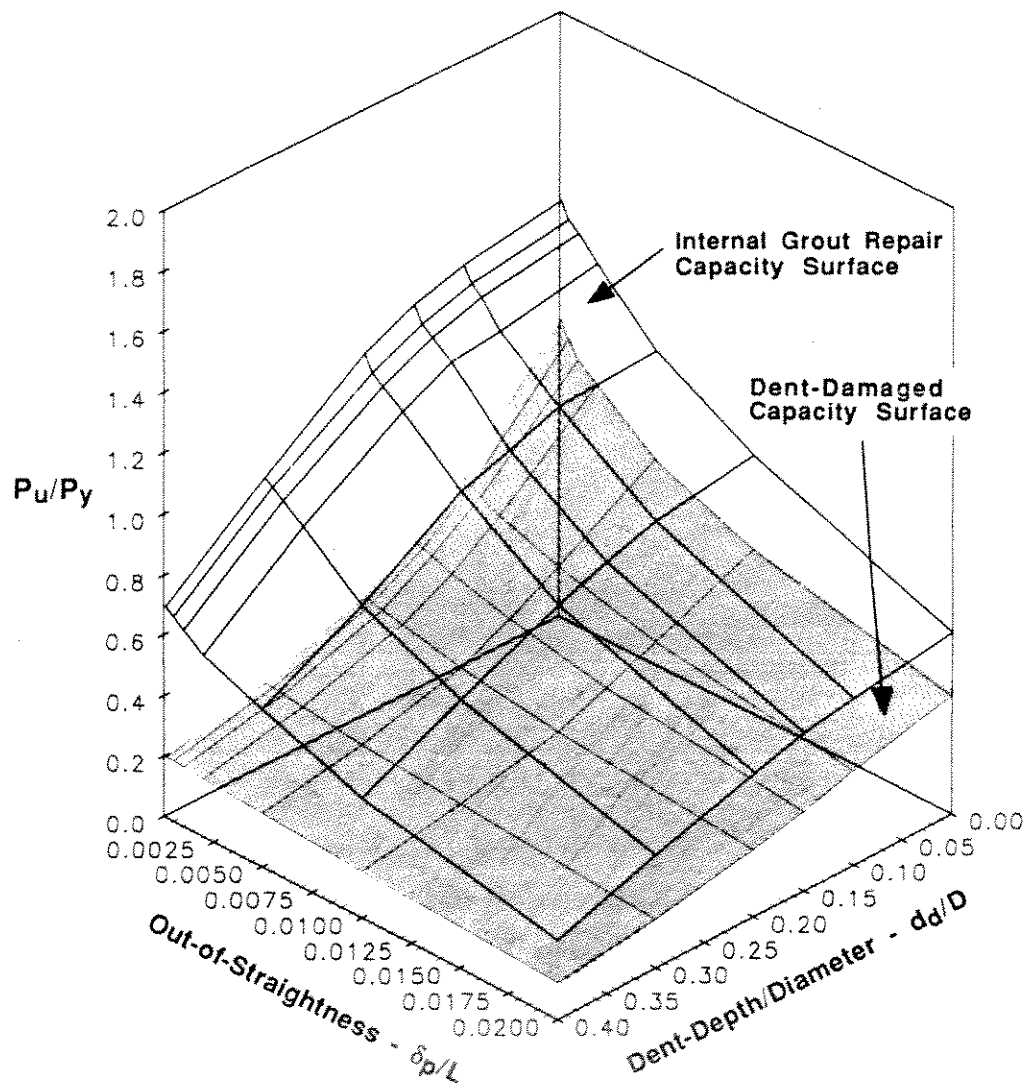


Figure 4.74 - Comparison of Residual Strength with Repaired Strength for  $kL/r = 60$  and  $D/t = 34.5$  ( $f'_g = 5.0$  ksi and  $\sigma_y = 34.8$  ksi) [after Ricles et al. 1997]

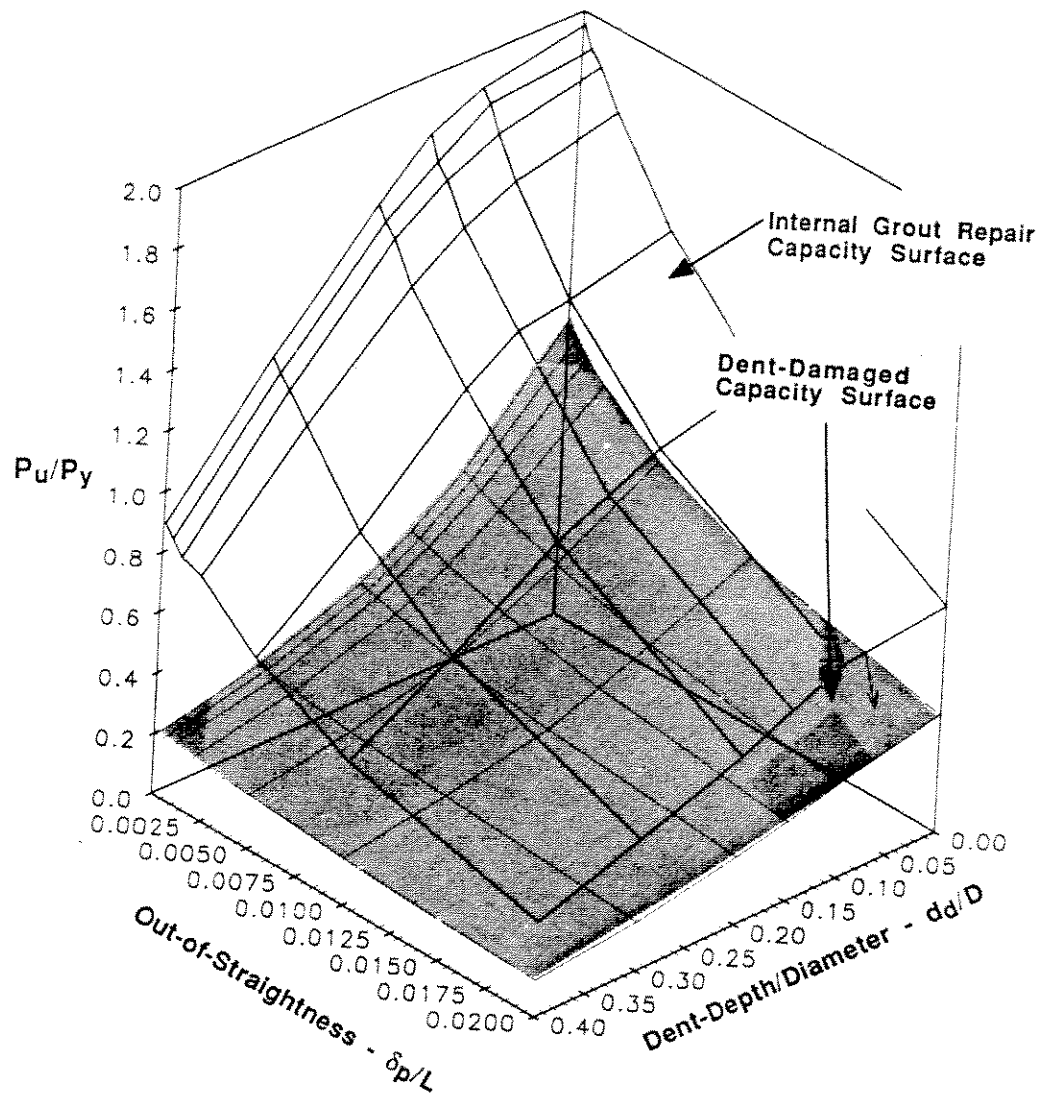


Figure 4.75 - Comparison of Residual Strength with Repaired Strength for  $kL/r = 60$  and  $D/t = 69$  ( $f'_g = 5.0$  ksi and  $\sigma_y = 34.8$  ksi) [after Ricles et al. 1997]

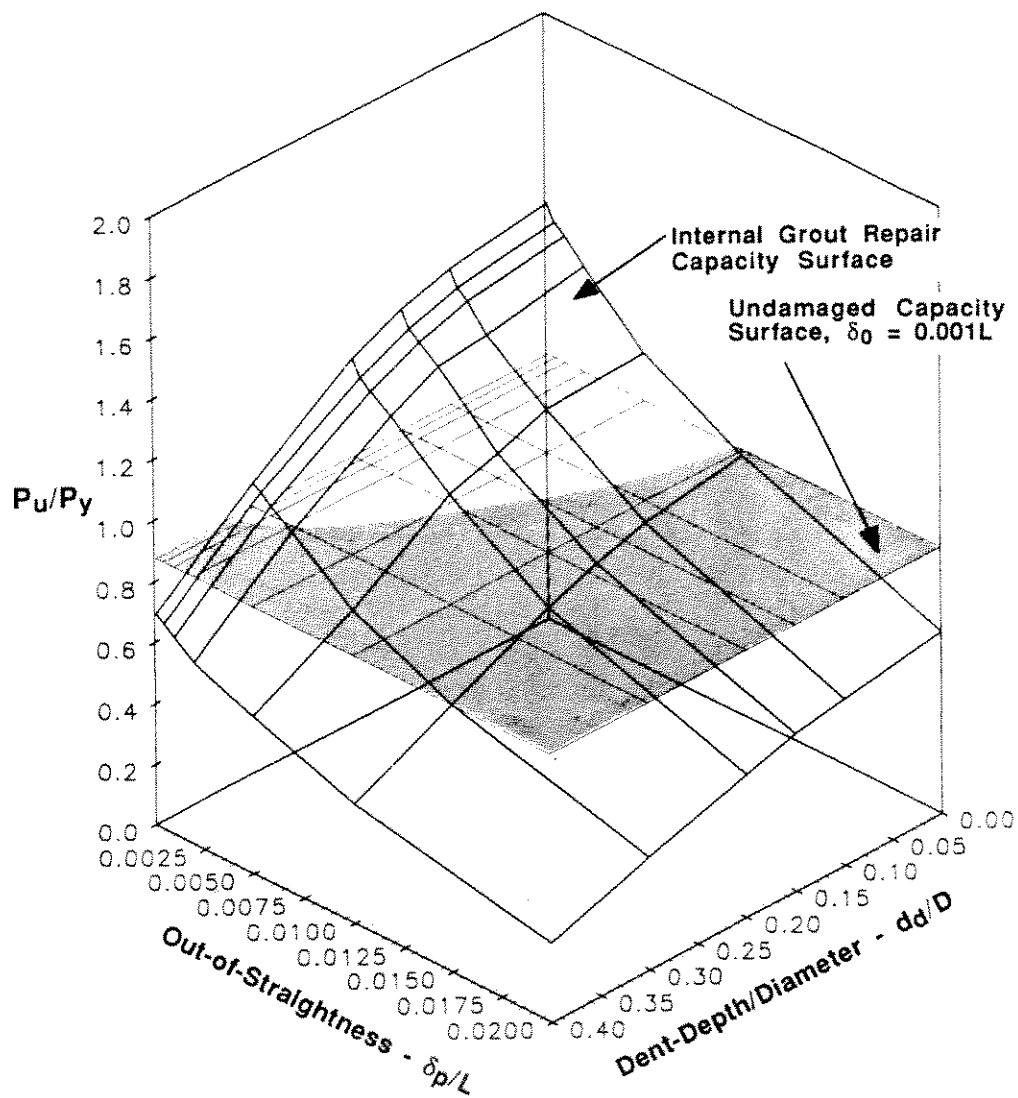


Figure 4.76 - Comparison of Residual Strength with Non-Damaged Capacity for  $kL/r = 60$  and  $D/t = 34.5$  ( $F_g = 5.0$  ksi and  $\sigma_y = 34.8$  ksi) [after Ricles et al. 1977]

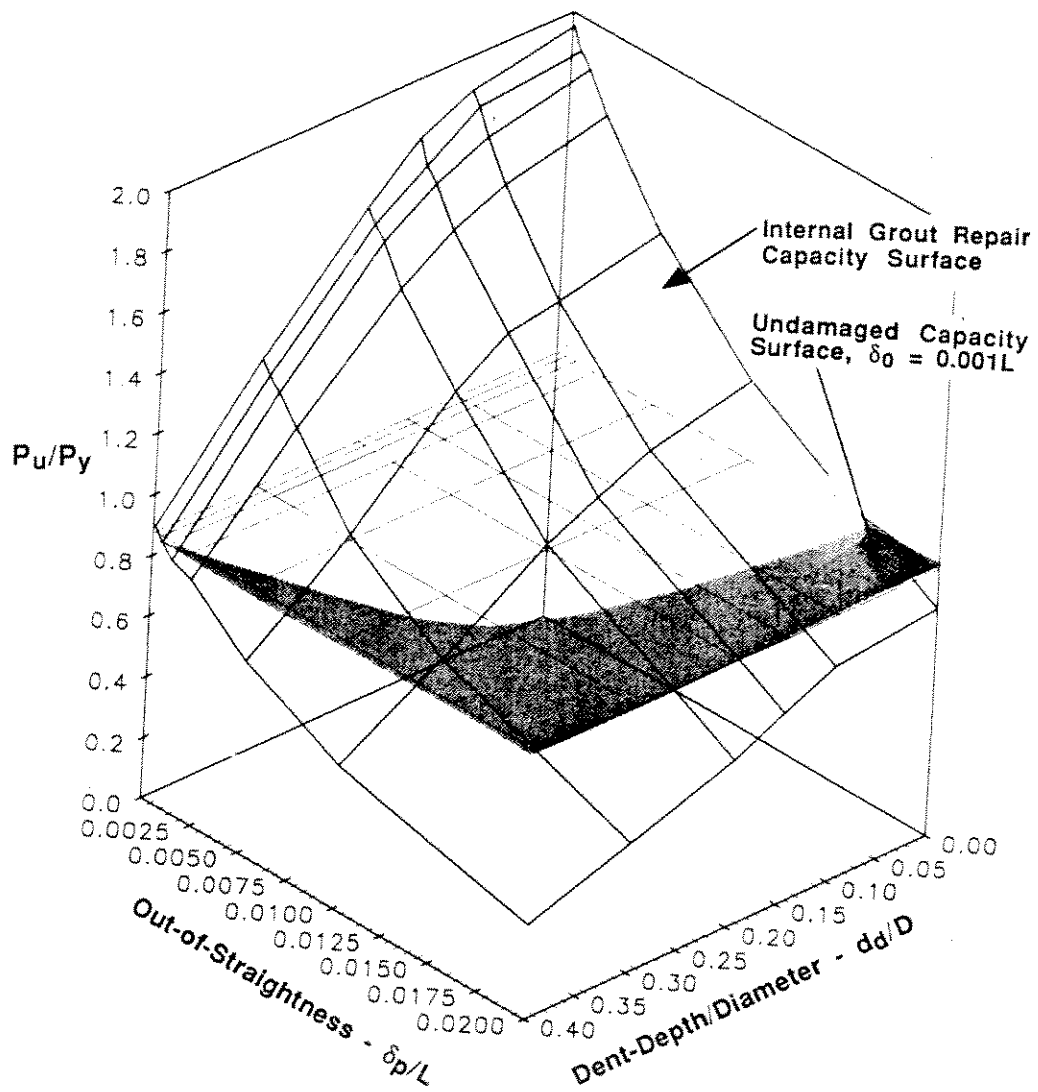


Figure 4.77 - Comparison of Residual Strength with Non-Damaged Capacity for  $kL/r = 60$  and  $D/t = 69$  ( $F_g = 5.0$  ksi and  $\sigma_y = 34.8$  ksi) [after Ricles et al. 1977]

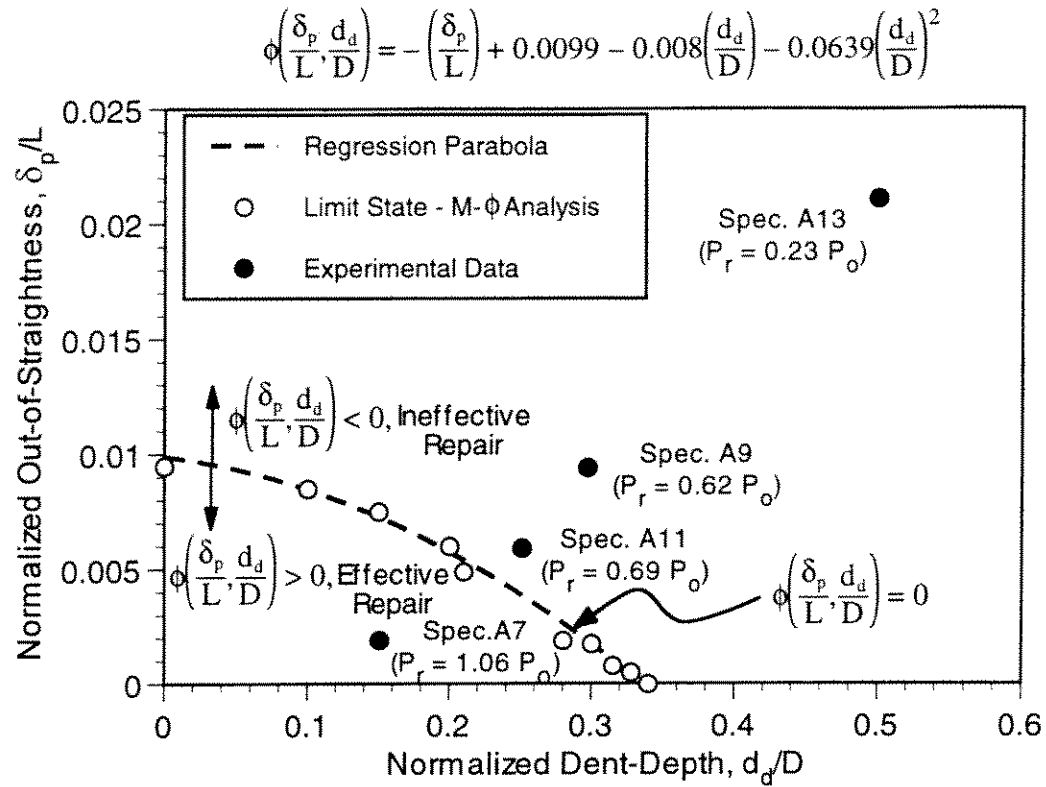


Figure 4.78 - Regression Analysis Showing the Limit of Repairability by Internal Grouting of Dent-Damaged Members with  $D/t = 34.5$  and  $KL/r = 60$

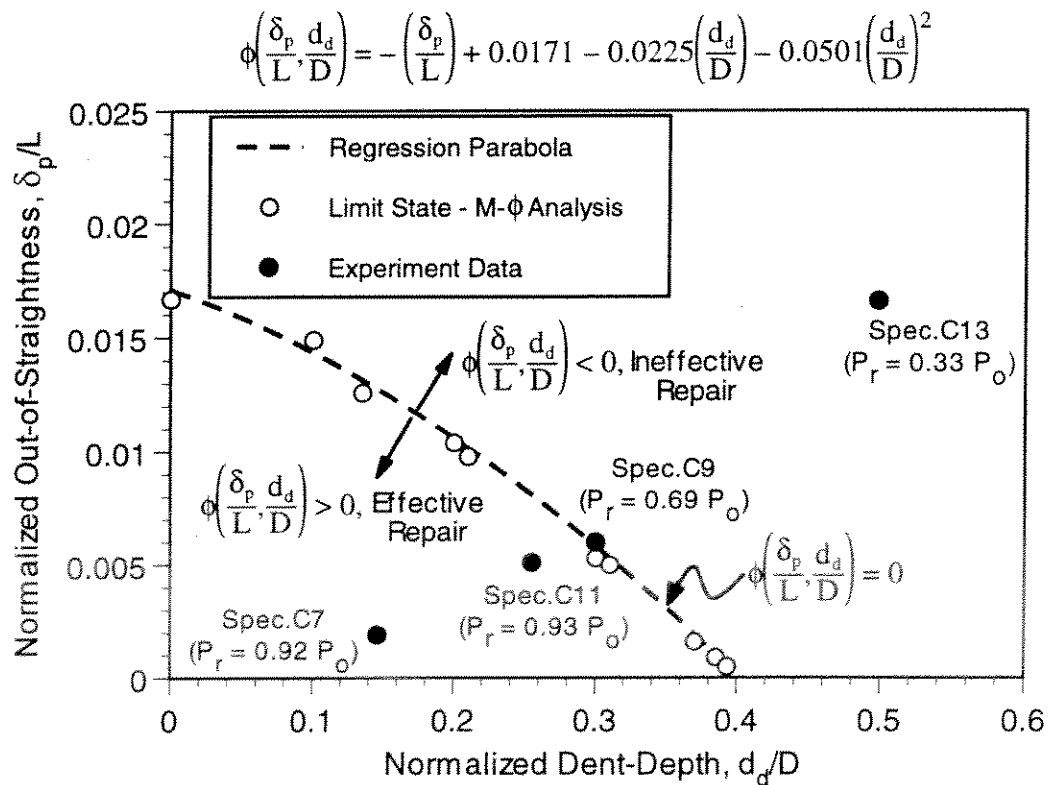


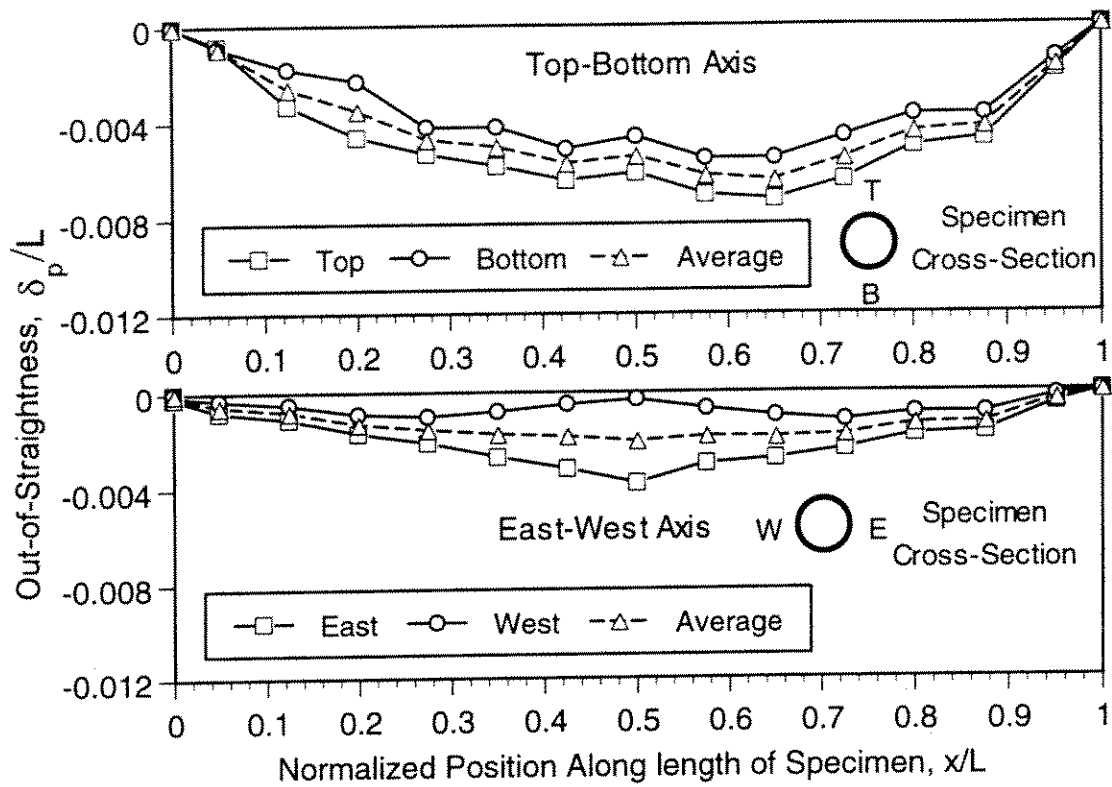
Figure 4.79 - Regression Analysis Showing the Limit of Repairability by Internal Grouting of Dent-Damaged Members with  $D/t = 69$  and  $KL/r = 60$

## **APPENDIX A**

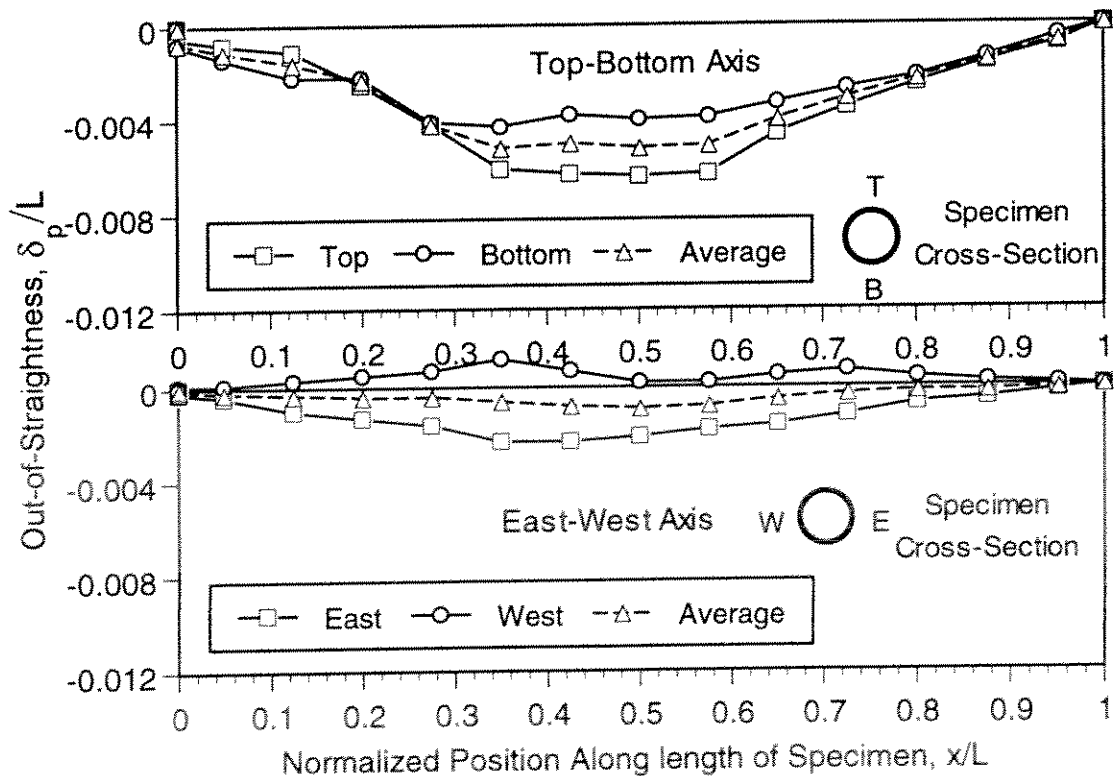
### **SPECIMEN MEASURED OUT -OF-STRAIGHTNESS FOLLOWING DENTING**



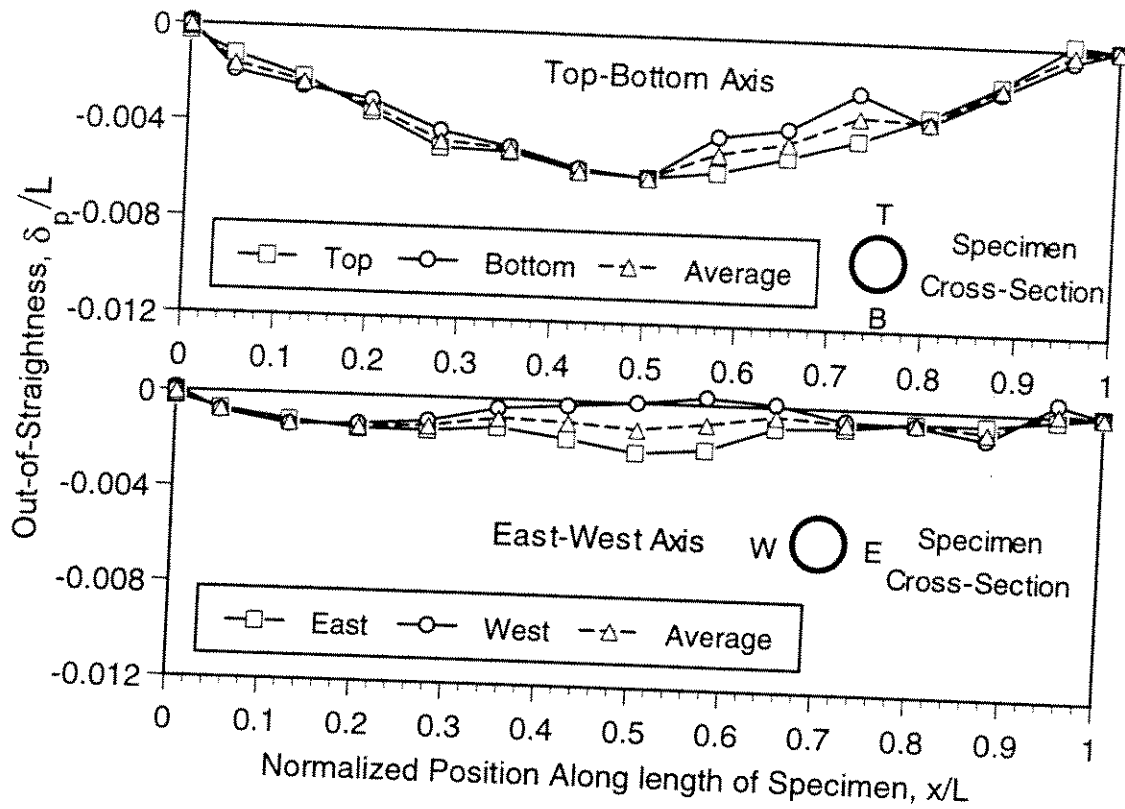
### Specimen A10



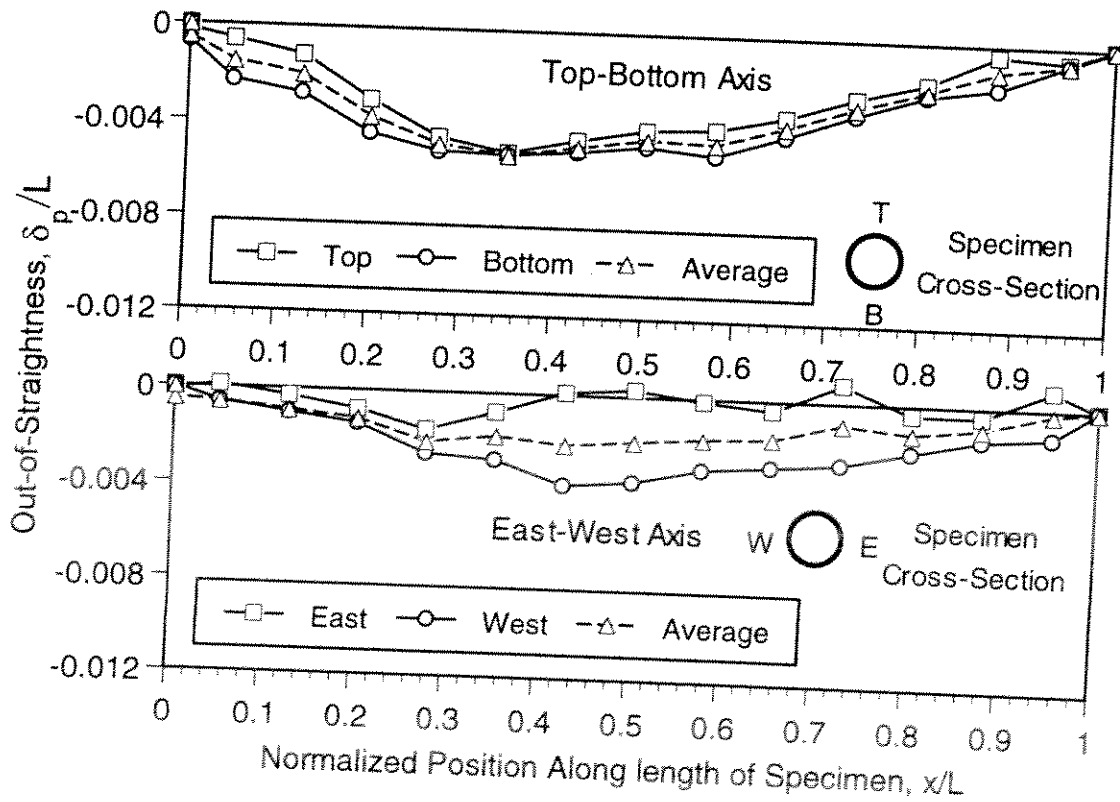
### Specimen C10



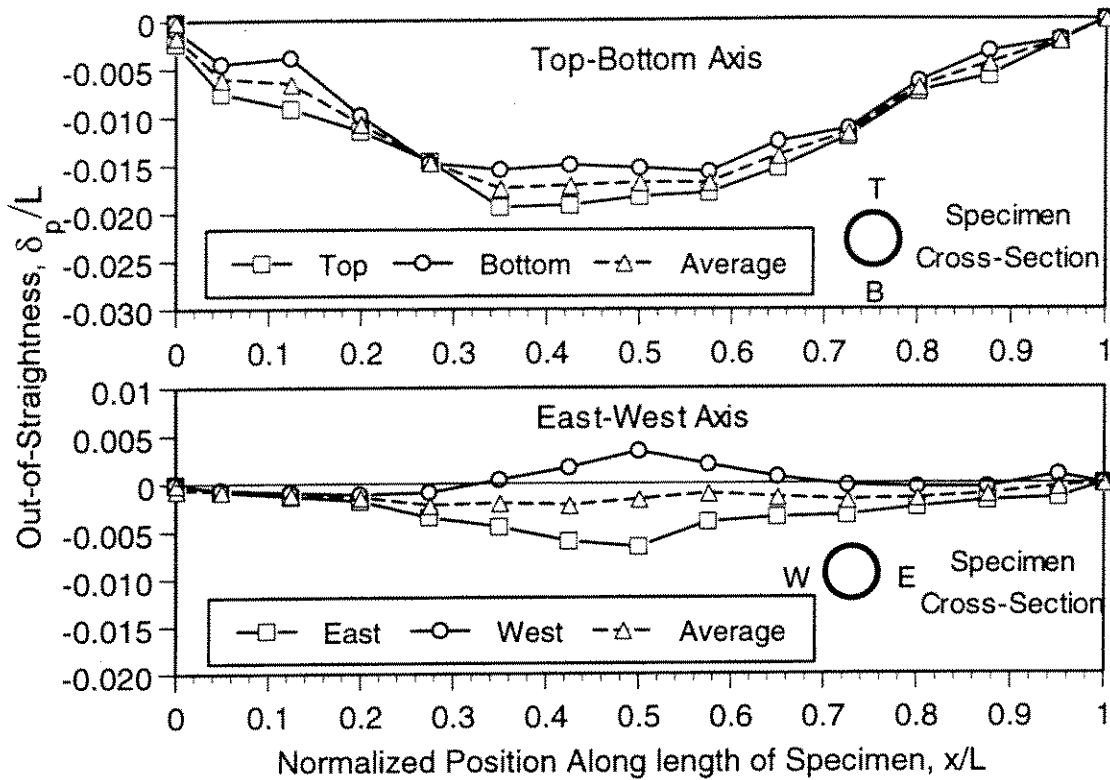
**Specimen A11**



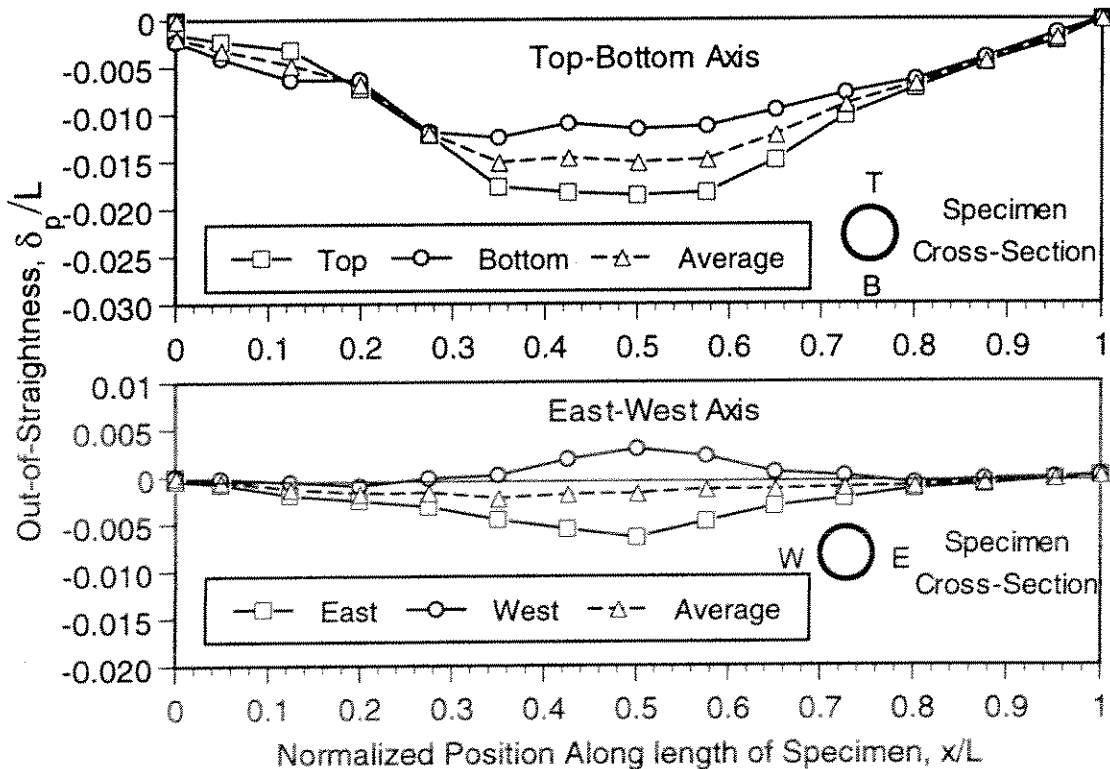
**Specimen C11**



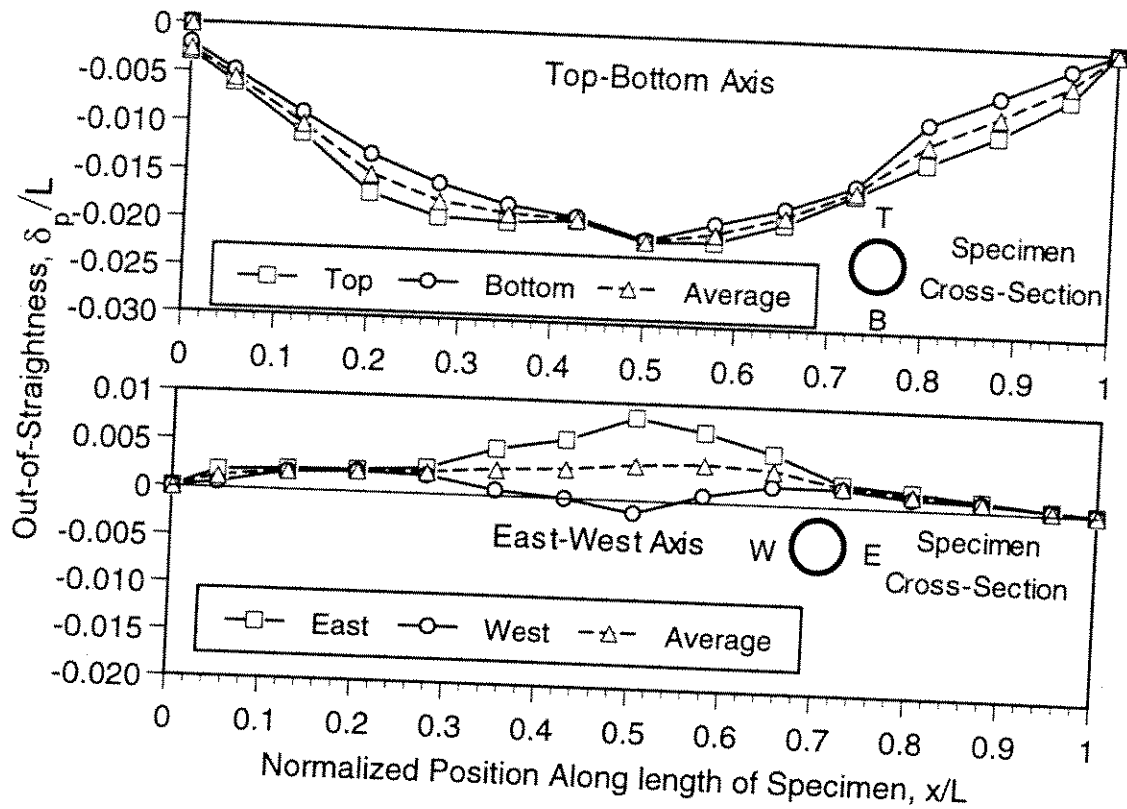
**Specimen A12**



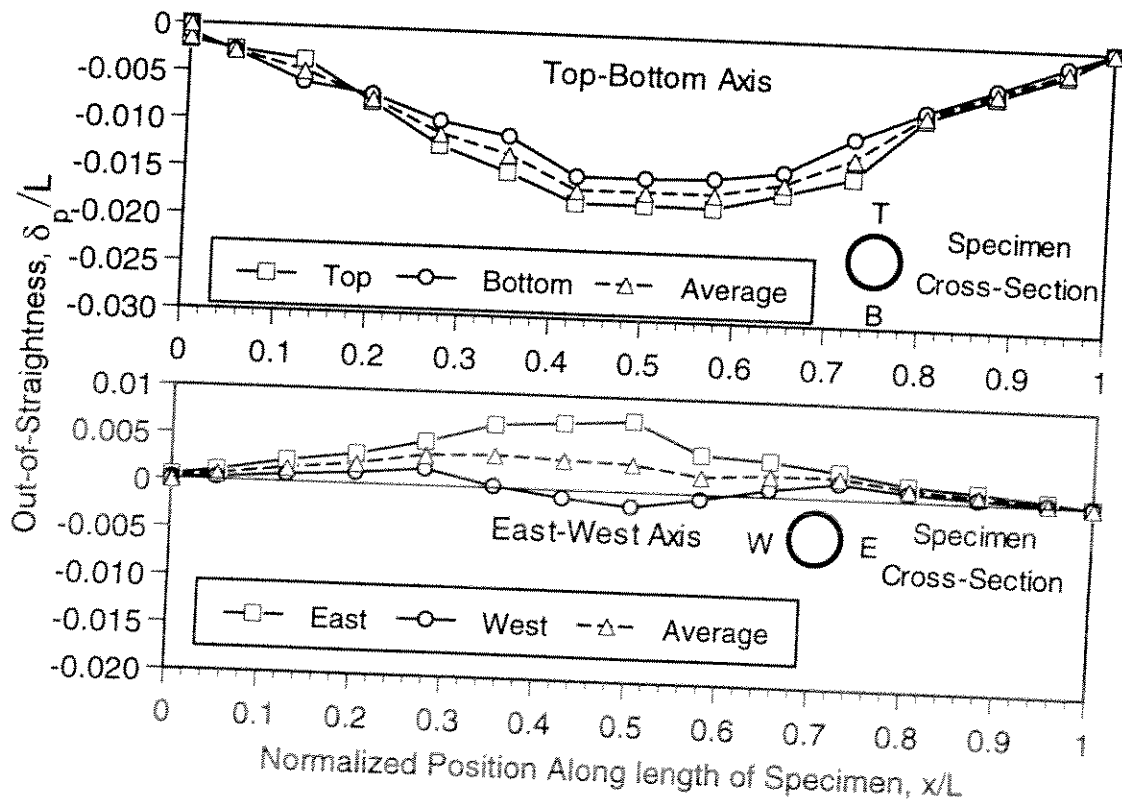
**Specimen C12**



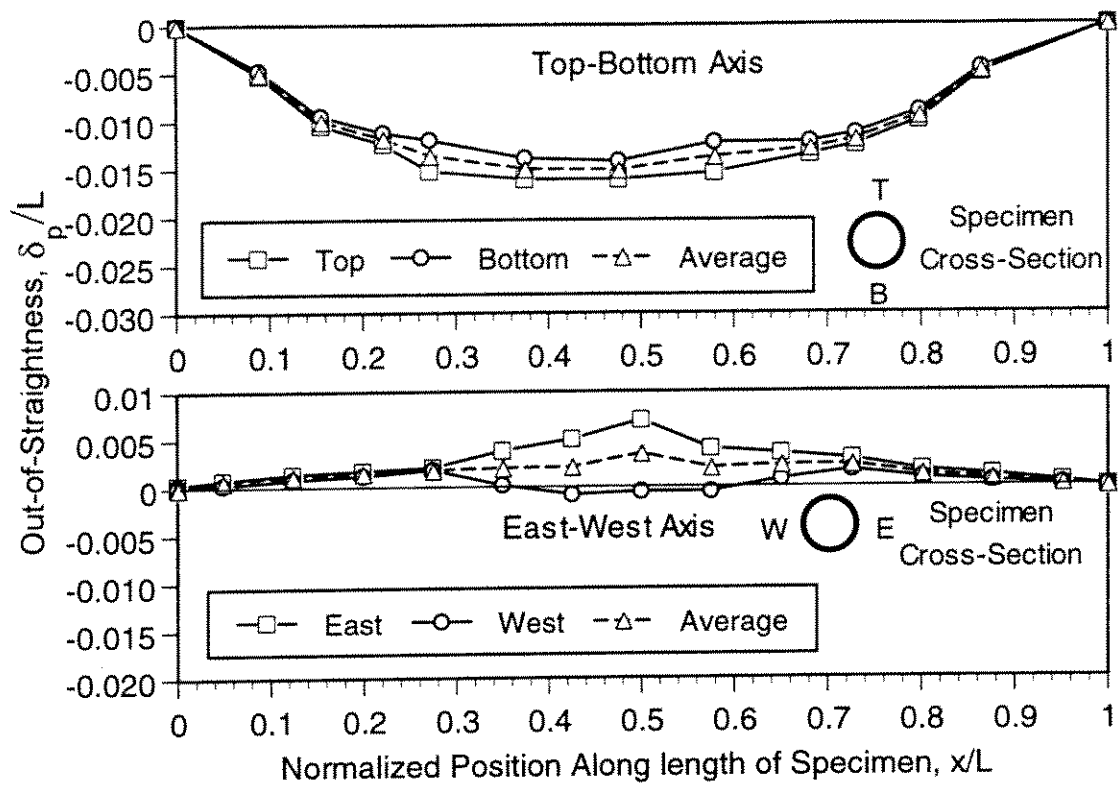
**Specimen A13**



**Specimen C13**



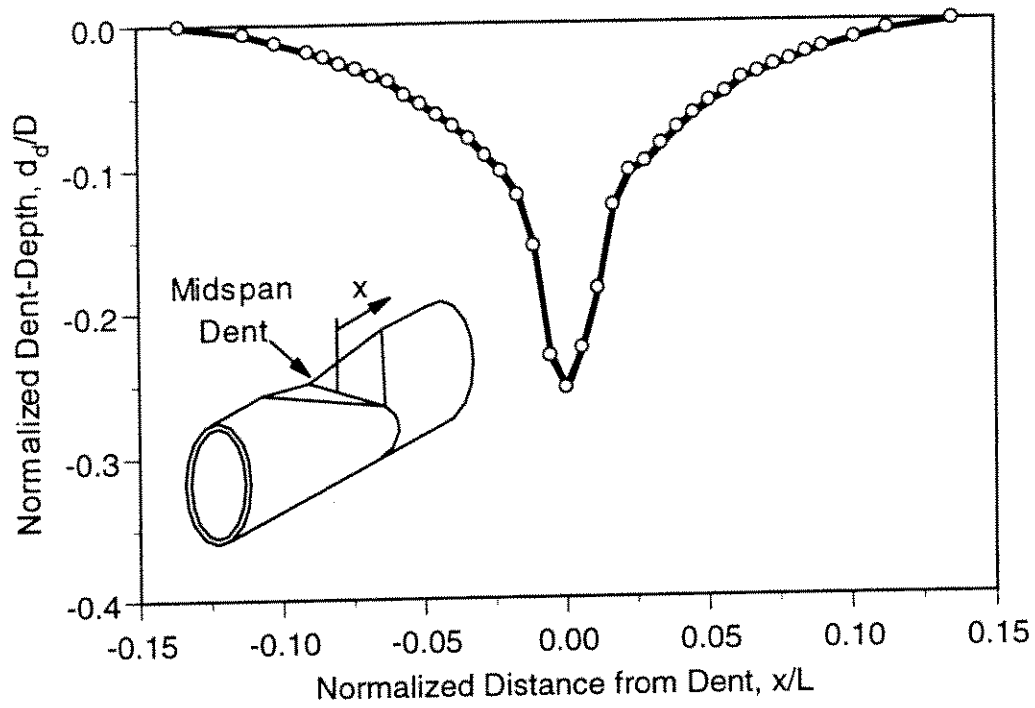
# Specimen C15



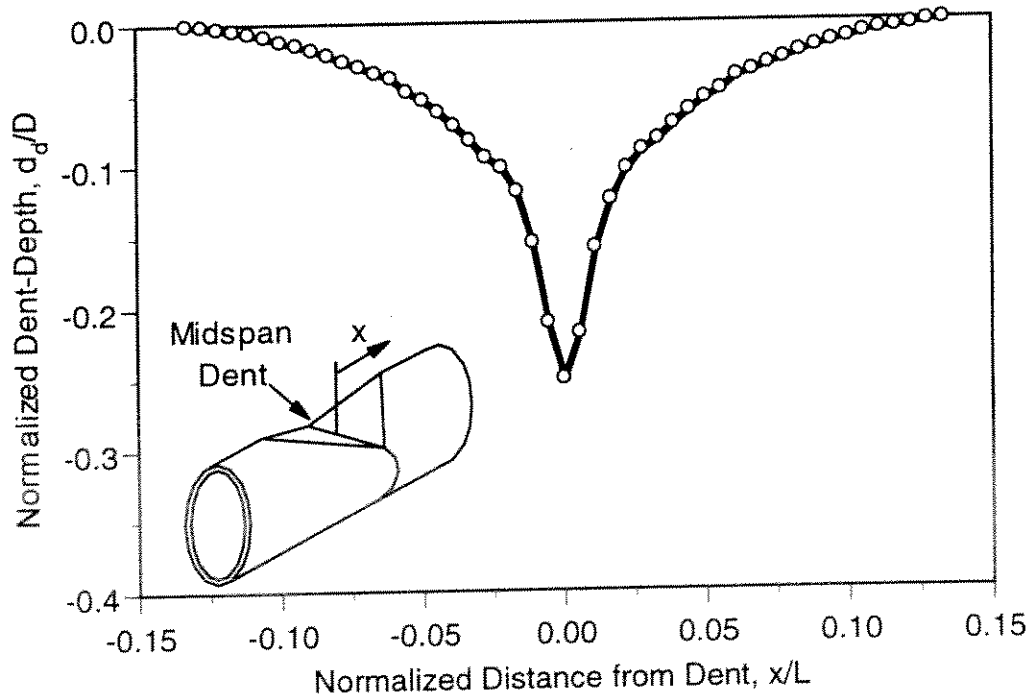
## **APPENDIX B**

### **SPECIMEN MEASURED DENT PROFILES**

Specimen A10



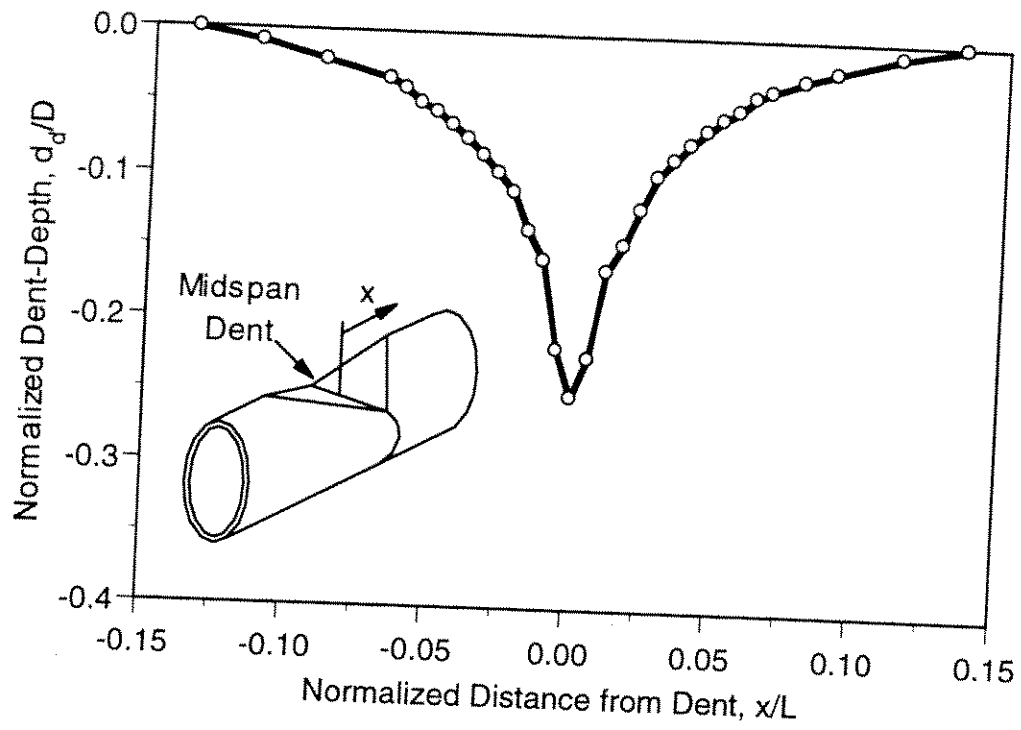
Specimen C10



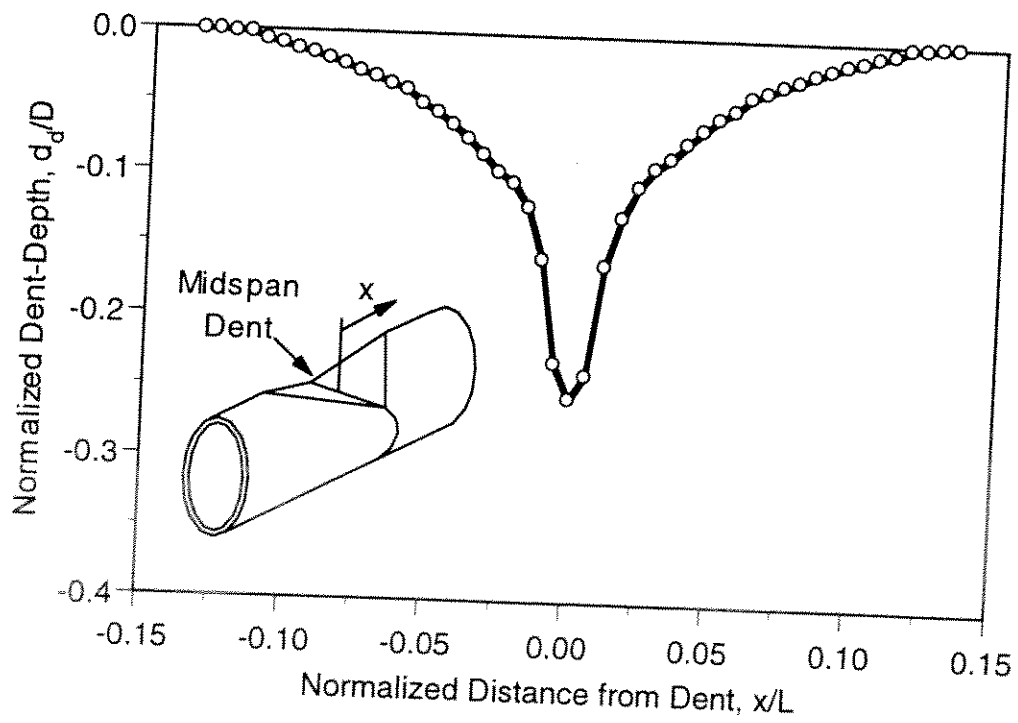




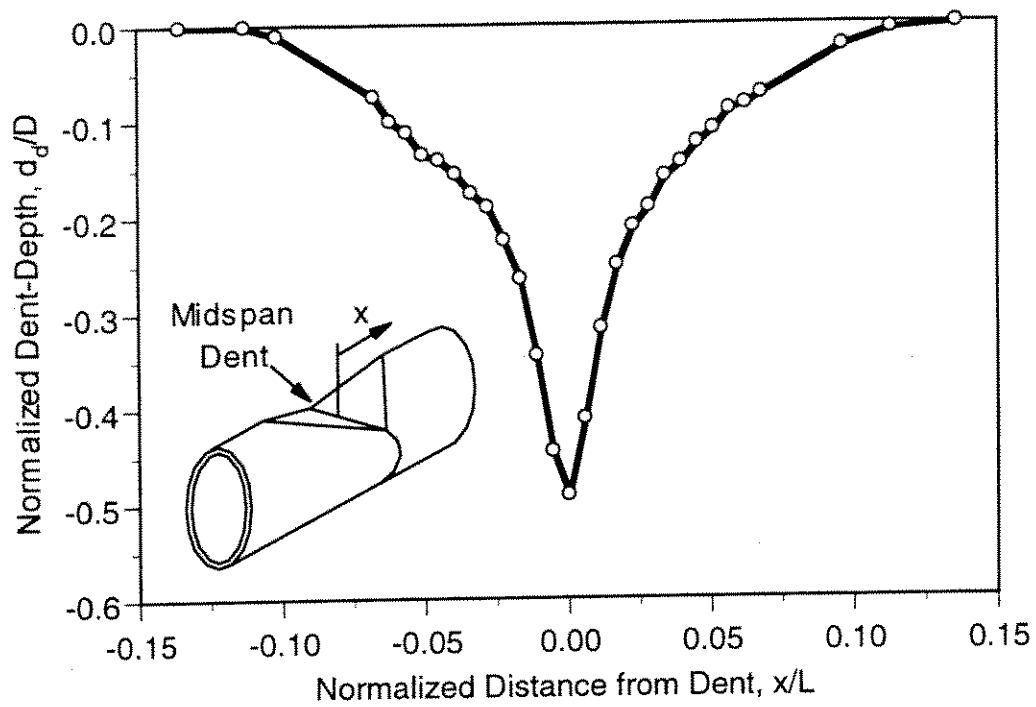
Specimen A11



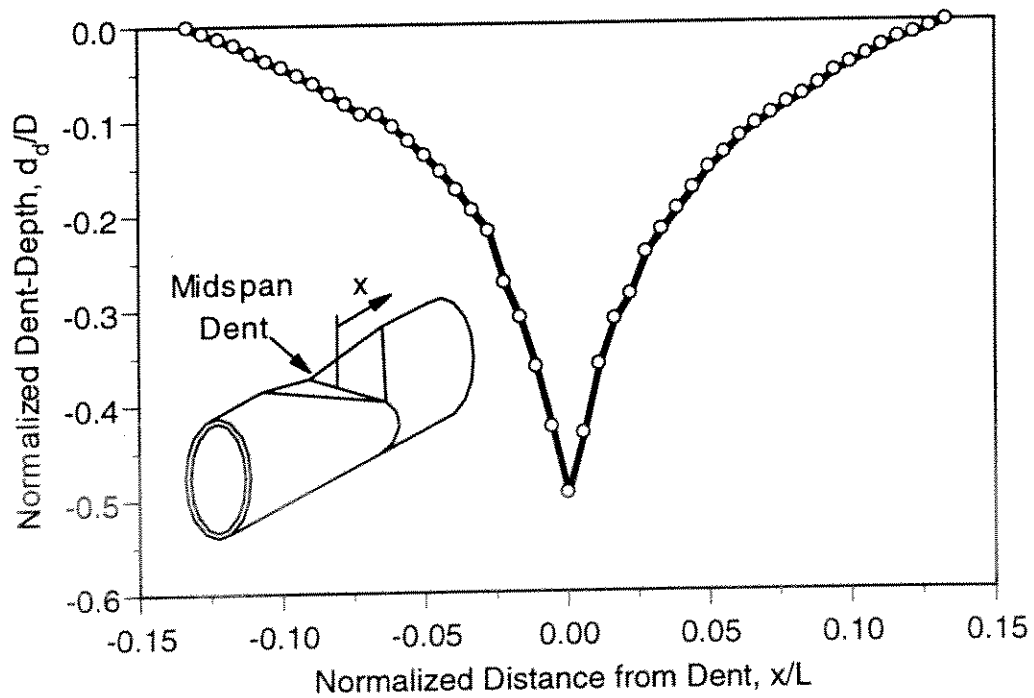
Specimen C11



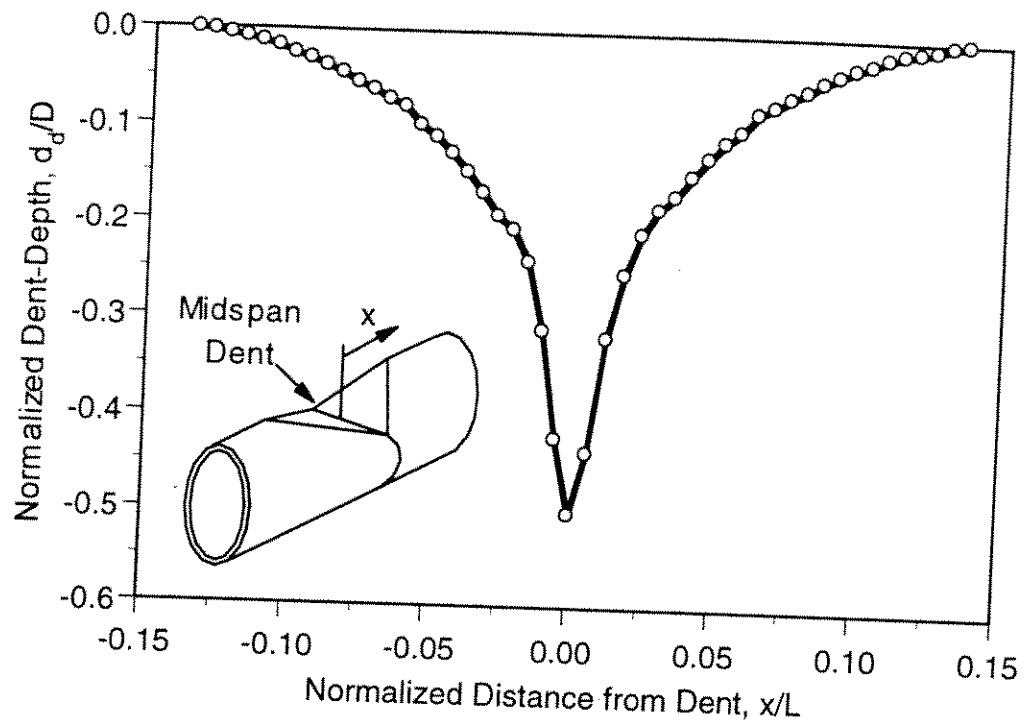
Specimen A12



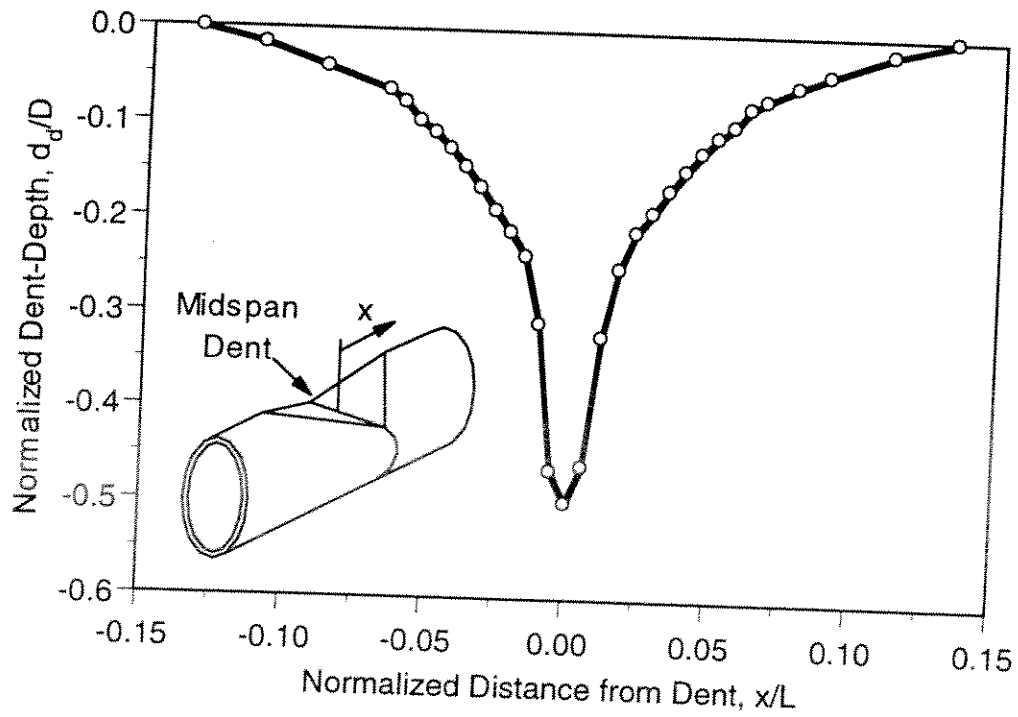
Specimen C12



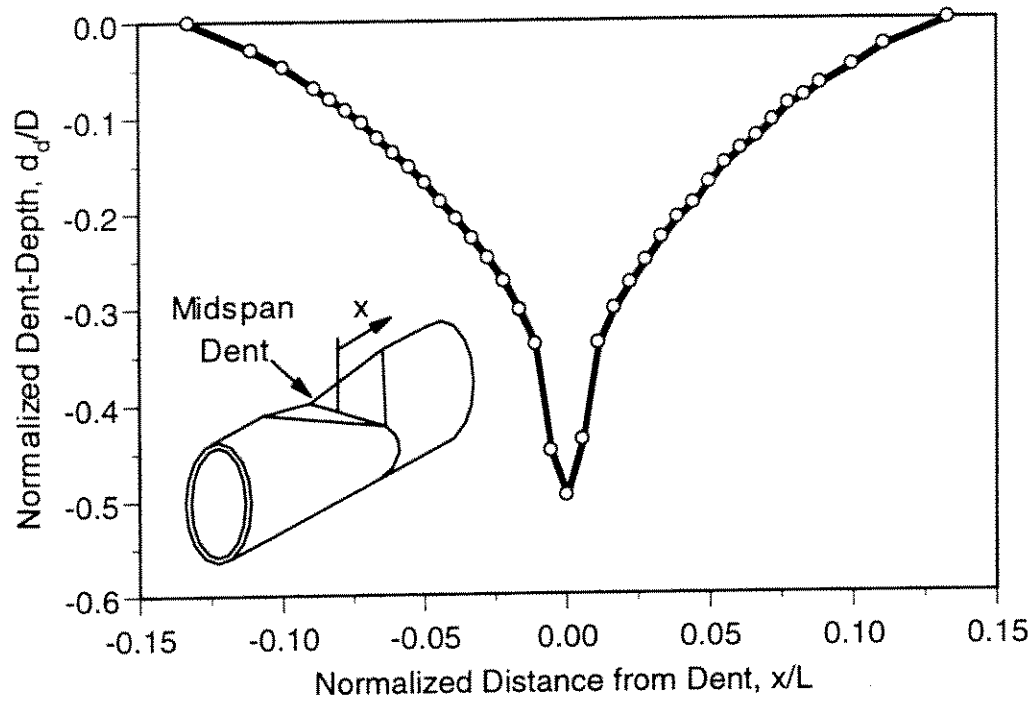
**Specimen A13**



**Specimen C13**



Specimen C15



## **APPENDIX C**

### **ABAQUS Input File for Specimen A10 - Dented, Non-repaired Specimen Analysis**



```

DENT,END,228,37
**
**C An element named MASTER at the end of tube with 0% eccentricity.
**C This element is used for load/displacement application.
**
*NODE,NSET=MASTER
9999,0.,0.,89.6
**
** .....
** ..... ELEMENT DEFINITION .....
** .....
**C Elements generation, 8 noded shell element is used.
**
*ELEMENT,TYPE=S8R5,ELSET=ETUBE
1,1,3,77,75,2,40,76,38
217,889,893,1041,1037,891,967,1039,963
271,1777,1781,2225,2221,1779,2003,2223,1999
**
**C Element generation
*ELGEN,ELSET=ETUBE
1,18,2,1,12,74,18
217,9,4,1,6,148,9
271,9,4,1,15,444,9
**
** .....RIGID KNIFE INDENTOR
**
**C Nodes to define rigid knife indenter. Nodes 10001 through 10017 define the nodes
**C for the rigid knife indenter.
**
*NODE, NSET=KNIFE
10001,4.1895,0.0000,0.
10002,4.1895,0.365139,0.
10003,4.1895,0.727499,0.
10004,4.1895,1.084322,0.
10005,4.1895,1.432893,0.
10006,4.1895,1.770559,0.
10007,4.1895,2.09475,0.
10008,4.1895,2.402998,0.
10009,4.1895,2.692959,0.
10010,4.1895,2.962424,0.
10011,4.1895,3.209343,0.
10012,4.1895,3.431837,0.
10013,4.1895,3.628212,0.
10014,4.1895,3.796976,0.
10015,4.1895,3.936842,0.
10016,4.1895,4.046746,0.
10017,4.1895,4.125852,0.
**
**C Gap element GAPUNI is used to connect the knife indenter and the cylinder.
**C Elements 501 through 517 are the elements defining the knife indenter.
**
**C For example. Element 501 is formed by nodes 10001 and 1. Element 501 is
**C of type GAPUNI (unidirectional gap element) and is labelled as element
**C set GAPI

```

```

**
*ELEMENT,TYPE=GAPUNI,ELSET=GAP1
501,10001,1
*ELEMENT,TYPE=GAPUNI,ELSET=GAP2
502,10002,2
*ELEMENT,TYPE=GAPUNI,ELSET=GAP3
503,10003,3
*ELEMENT,TYPE=GAPUNI,ELSET=GAP4
504,10004,4
*ELEMENT,TYPE=GAPUNI,ELSET=GAP5
505,10005,5
*ELEMENT,TYPE=GAPUNI,ELSET=GAP6
506,10006,6
*ELEMENT,TYPE=GAPUNI,ELSET=GAP7
507,10007,7
*ELEMENT,TYPE=GAPUNI,ELSET=GAP8
508,10008,8
*ELEMENT,TYPE=GAPUNI,ELSET=GAP9
509,10009,9
*ELEMENT,TYPE=GAPUNI,ELSET=GAP10
510,10010,10
*ELEMENT,TYPE=GAPUNI,ELSET=GAP11
511,10011,11
*ELEMENT,TYPE=GAPUNI,ELSET=GAP12
512,10012,12
*ELEMENT,TYPE=GAPUNI,ELSET=GAP13
513,10013,13
*ELEMENT,TYPE=GAPUNI,ELSET=GAP14
514,10014,14
*ELEMENT,TYPE=GAPUNI,ELSET=GAP15
515,10015,15
*ELEMENT,TYPE=GAPUNI,ELSET=GAP16
516,10016,16
*ELEMENT,TYPE=GAPUNI,ELSET=GAP17
517,10017,17
**
**C The *GAP command specifies the initial clearance between the gaps.
**C Note that the rigid knife indenter is tangent to the tube at node 1.
**C The element set is GAP1 for the gap element between node 1 and the indenter.
**C Therefore, the clearance for element set GAP1 is 0.0
**C The clearance for the other element set is calculated using geometry.
**
*GAP,ELSET=GAP1
0.,-1.,0.,0.
*GAP,ELSET=GAP2
0.01594,-1.,0.,0.
*GAP,ELSET=GAP3
0.066365,-1.,0.,0.
*GAP,ELSET=GAP4
0.14275,-1.,0.,0.
*GAP,ELSET=GAP5
0.252658,-1.,0.,0.
*GAP,ELSET=GAP6
0.392524,-1.,0.,0.
*GAP,ELSET=GAP7

```



0.561287,-1.,0.,0.  
 \*GAP,ELSET=GAP8  
 0.757663,-1.,0.,0.  
 \*GAP,ELSET=GAP9  
 0.980157,-1.,0.,0.  
 \*GAP,ELSET=GAP10  
 1.227076,-1.,0.,0.  
 \*GAP,ELSET=GAP11  
 1.496541,-1.,0.,0.  
 \*GAP,ELSET=GAP12  
 1.786502,-1.,0.,0.  
 \*GAP,ELSET=GAP13  
 2.09475,-1.,0.,0.  
 \*GAP,ELSET=GAP14  
 2.418941,-1.,0.,0.  
 \*GAP,ELSET=GAP15  
 2.75661,-1.,0.,0.  
 \*GAP,ELSET=GAP16  
 3.10518,-1.,0.,0.  
 \*GAP,ELSET=GAP17  
 3.462,-1.,0.,0.

\*\*

\*\*

\*\*

\*\*

#### SHELL ELEMENT THICKNESS AND MATERIAL TYPE DEFINITION

\*\*C Defining the thickness of the shell element and 5 (default) integration points  
 \*\*C through the thickness

\*\*

\*SHELL SECTION,ELSET=ETUBE,MATERIAL=STEEL1  
 0.255

\*\*

\*\*.....ELASTIC PLASTIC ANALYSIS

\*\*

\*\* The tube (ELSET=ETUBE) is assumed to be an  
 \*\* elastic plastic material. The material constitutive  
 \*\* properties from test data are used.

\*\*

\*MATERIAL, NAME=STEEL1

\*ELASTIC

29510.,0.3

\*PLASTIC

36.0,0.

36.5,0.015

37.0,0.3

\*\*

\*\*

\*\*

\*\*

#### BOUNDARY CONDITIONS

\*\*C Defining additional element sets needed to impose boundary conditions  
 \*\*

\*\* NSET CRADLE is the node set defining the nodes where the  
 \*\* hydrostone support along the bottom half of the tube section  
 \*\* is provided during the indentation process. The support spans

```

** from the mid-span for about 24 inches.
**
** Note that only the bottom part of the tube, subtended by
** an arc of 90 degrees (and not the bottom half of the tube
** subtended by an arc of 180 deg) is supported. For this
** reason, the node set CRADLE starts from node 29 and not
** from node 19.
**
*NSET,NSET=CRADLE,GENERATE
**19,2239,37
**20,2240,37
**21,2241,37
**22,2242,37
**23,2243,37
**24,2244,37
**25,2245,37
**26,2246,37
**27,2247,37
**28,2248,37
29,2249,37
30,2250,37
31,2251,37
32,2252,37
33,2253,37
34,2254,37
35,2255,37
36,2256,37
37,2257,37
**
** NSET TOP and BOTTOM are the node sets along the top and bottom edges
** of the tube. These node sets define the symmetrical axis. NSET ENDTWO is
** the same as NSET END except that the inactive nodes (e.g, 8438, 8440)
** are not included.
**
*NSET,NSET=TOP,GENERATE
1,8437,37
**
*NSET,NSET=BOT,GENERATE
37,8473,37
**
*NSET,NSET=END2,GENERATE
8437,8473,2
**
*BOUNDARY
DENT,ZSYMM
TOP,YSYMM
BOT,YSYMM
KNIFE,2,3
CRADLE,1
**
** .....
** MULTI-POINT CONSTRAINTS
** .....
**
**C Multi-point constraints.

```

\*\*C The mesh around the dented areas are finer than elsewhere. The boundaries between  
 \*\*C the fine and coarse mesh can have nodes that are not shared between the adjacent  
 \*\*C elements. These nodes are constrained to displace in a parabolic manner. The  
 \*\*C parabola is defined by the nodes that are shared by adjacent elements. For  
 \*\*C example, the displacement of Node 58 and Node 132 are constrained  
 \*\*C by a 2nd order polynomial (parabola) passing through Nodes 21, 95 & 169.  
 \*\*C Nodes 21, 95 and 169 are shared by the adjacent elements of the fine and  
 \*\*C coarse mesh. Nodes 58 and 132 are for defining the fine mesh only.  
 \*\*

\*MPC

2,890,889,891,893  
 2,892,889,891,893  
 2,894,893,895,897  
 2,896,893,895,897  
 2,898,897,899,901  
 2,900,897,899,901  
 2,902,901,903,905  
 2,904,901,903,905  
 2,906,905,907,909  
 2,908,905,907,909  
 2,910,909,911,913  
 2,912,909,911,913  
 2,914,913,915,917  
 2,916,913,915,917  
 2,918,917,919,921  
 2,920,917,919,921  
 2,922,921,923,925  
 2,924,921,923,925  
 \*\*

\*\* The load is applied by imposing a displacement on the  
 \*\* MASTER node. The nodes at the ends of the tube are  
 \*\* slaved, i.e. constrained to move as a rigid body  
 \*\* with respect to the MASTER node. The \*EQUATION command  
 \*\* imposes the Master-Slave relationship between the nodes.  
 \*\*

\*EQUATION

3

8437,3,1.,9999,3,-1.,9999,5,4.1895

\*EQUATION

3

8439,3,1.,9999,3,-1.,9999,5,4.12585

\*EQUATION

3

8441,3,1.,9999,3,-1.,9999,5,3.93684

\*EQUATION

3

8443,3,1.,9999,3,-1.,9999,5,3.628213

\*EQUATION

3

8445,3,1.,9999,3,-1.,9999,5,3.20934

\*EQUATION

3

8447,3,1.,9999,3,-1.,9999,5,2.69296

\*EQUATION

3

```

8449,3,1.,9999,3,-1.,9999,5,2.09475
*EQUATION
3
8451,3,1.,9999,3,-1.,9999,5,1.432893
*EQUATION
3
8453,3,1.,9999,3,-1.,9999,5,0.727499
*EQUATION
3
8455,3,1.,9999,3,-1.,9999,5,0.0
*EQUATION
3
8457,3,1.,9999,3,-1.,9999,5,-0.727499
*EQUATION
3
8459,3,1.,9999,3,-1.,9999,5,-1.432893
*EQUATION
3
8461,3,1.,9999,3,-1.,9999,5,-2.09475
*EQUATION
3
8463,3,1.,9999,3,-1.,9999,5,-2.69296
*EQUATION
3
8465,3,1.,9999,3,-1.,9999,5,-3.20934
*EQUATION
3
8467,3,1.,9999,3,-1.,9999,5,-3.628213
*EQUATION
3
8469,3,1.,9999,3,-1.,9999,5,-3.93684
*EQUATION
3
8471,3,1.,9999,3,-1.,9999,5,-4.12585
*EQUATION
3
8473,3,1.,9999,3,-1.,9999,5,-4.1895
**
** The following EQUATION command constraints the nodes at the end
** (called node set END2) to have the same amount of transverse
** displacement as the MASTER element.
**
*EQUATION
2
END2,1,1,9999,1,-1
**
**
**DATA CHECK
**
*****
**C                                     Step 1
*****
**
**C In step 1, the rigid knife indenter is displaced 2.4 inches
**C towards the tube to simulate the indentation process. It is a strain

```

```

**C control simulation. The movement is displaced using the *BOUNDARY command.
**C The 2.4 inch displacement results in an indentation to diameter (d/D)
**C ratio of 0.25 after unloading the knife edge.
**
*STEP,NLGEOM,INC=300
APPLICATION OF LATERAL DISPLACEMENT TO CREATE DENT
*STATIC
0.01,1.,1.E-8,0.1
*CONTROLS, PARAMETERS=FIELD, FIELD=DISPLACEMENT
0.01, 1.0,,100.
*CONTROLS, PARAMETERS=FIELD, FIELD=ROTATION
0.05, 1.0,,100.
*BOUNDARY
KNIFE,1.,-2.4
*EL PRINT,FREQ=0,SUMMARY=NO
*PRINT,CONTACT=YES,RESIDUAL=NO
*END STEP
*****
**C
Step 2
*****
**C In step 2, the applied displacement of the rigid knife indenter is removed.
**C The removal is also strain control and is specified by the *BOUNDARY command.
**
**C Read restart file from Step 1 and write restart file for step 3 (this has been commented
**C out below, and is optional in the analysis).
**
**RESTART, READ, STEP=1, INC=74, WRITE, FREQUENCY=999
**
*STEP,NLGEOM,INC=50
REMOVING KNIFE EDGE LOADING
*STATIC
0.01,1.,1.E-4,0.2
*BOUNDARY
KNIFE,1.,0.0
*EL PRINT,FREQ=0,SUMMARY=NO
*PRINT,CONTACT=YES,RESIDUAL=NO
*END STEP
*****
**C
Step 3
*****
**C In step 3, the elements defining the rigid knife indenter (GAP1 through
**C GAP 17) are removed using the *MODEL CHANGE command. New boundary
**C conditions are defined in *BOUNDARY, OP=NEW. The support along the
**C circumference below the dent (element set CRADLE) is removed. The
**C boundary that defines the symmetry of the member remains unchanged.
**C The ends of the tube is not allowed to move in the 1 and 2 (x and y)
**C directions as defined by *BOUNDARY,OP=NEW,FIXED command. The
**C parameter FIXED specifies that the values of the variables are to remain
**C unchanged from the last steps.
**
*STEP,NLGEOM,INC=10
REMOVAL OF KNIFE EDGE LOADING AND APPLYING NEW BC
*STATIC

```

```

1.0,1.,1.E-4,1.0
*MODEL CHANGE,REMOVE
GAP1,GAP2,GAP3,GAP4,GAP5,GAP6,GAP7,GAP8,GAP9,GAP10,GAP11,
GAP12,GAP13,GAP14,GAP15,GAP16,GAP17
*BOUNDARY,OP=NEW, FIXED
DENT,ZSYMM
TOP,YSYMM
BOT,YSYMM
MASTER,1,2
*NODE PRINT,NSET=MASTER,SUMMARY=NO
U1,U2,U3,UR2
*NODE PRINT,NSET=END2,SUMMARY=NO
U1,U2,U3
*NODE PRINT,GLOBAL=YES,NSET=DENT,TOTALS=YES,SUMMARY=NO
U1,U2,RF1,RF3
*EL PRINT,FREQ=0,SUMMARY=NO,POSITION=NODES
*PRINT,CONTACT=YES,RESIDUAL=NO
*END STEP
*****
**C                                     Step 4
*****
**
**C In this step, a concentrated load is applied at the MASTER element set.
**C The RIKS solution method is used. Write out to restart file for post processing
**C of the results obtained in Step 4
**
*RESTART, WRITE, FREQUENCY=18
*STEP,NLGEOM,INC=125
APPLICATION OF AXIAL LOAD
*STATIC, RIKS
0.005,1.,1.E-8,0.1
*CONTROLS, PARAMETERS=FIELD, FIELD=DISPLACEMENT
0.01, 1.0,,100.
*CONTROLS, PARAMETERS=FIELD, FIELD=ROTATION
0.05, 1.0,,100.
*CLOAD, OP=NEW
9999,3,-100.0
*NODE PRINT,NSET=MASTER,SUMMARY=NO
U1,U2,U3,UR2,CF3
*NODE FILE,NSET=MASTER, FREQUENCY=1
U,CF
*NODE FILE, NSET=END2, FREQUENCY=1
U
*NODE PRINT,NSET=END2,SUMMARY=NO
U1,U2,U3
*NODE PRINT,GLOBAL=YES,NSET=DENT,TOTALS=YES,SUMMARY=NO
U1,U2,RF1,RF3
*EL PRINT,POSITION=AVERAGED AT NODES,FREQ=0
*PRINT,CONTACT=YES
*END STEP

```

## **APPENDIX D**

### **ABAQUS Input File for Specimen A11 - Dented, Internal Grout Repaired Specimen Analysis**

```

*****
**          MODEL DEFINITION OF TUBE A11
**          Dented, Internal Grout Repair tubular with dent depth = 0.251D,
**          damaged out-of-straightness = 0.0059L
**          File created by T.K. Sooi and J.M. Ricles
**          August 1996
**          Lehigh University
*****
**FILE NAME: A11_jmr2.inp
**JOB NAME: A11
**ABAQUS Version 5.5
**C The analysis is broken into four steps.
** Stage 1: The coordinates for the steel shell elements and grout brick
**           elements are read from a file created from a previous analysis.
** Stage 2: Model definition (element connectivity, material properties, boundary
**           conditions, multi-point constraints, etc.).
** Stage 3: Reading of the initial strain and assignment to the steel shell elements
**           to simulate the effects of dent damage.
** Stage 4: Application of axial load (referred to as Step 1)
**
*HEADING
SPECIMEN A11
**
*RESTART, WRITE, FREQUENCY=12
**
*****
**          NODAL DEFINITION
*****
**-----**
** Steel tube and Grout          **
**-----**
** Nodes for the steel tube and grout for layers 1 and 2
** are read in from input file named Node25.inp.
** This file is created by running an analysis of an undented tubular
** to obtain the nodal coordinates and initial strain for the steel shell
** elements
**
*NODE, INPUT=Node25.inp
**
**-----**
** Center of specimen          **
**-----**
** Nodes 400001 through 402665 are for solid elements
** Nodes 402665 through 402670 are for beam elements
**
*NODE
400001, 0., 0., 0.
402665, 0.1272, 0.0, 28.5
402666, 0.246, 0.0, 40.0
402667, 0.375, 0.0, 50.0
402668, 0.525, 0.0, 60.0
402669, 0.691, 0.0, 70.0
402670, 0.868, 0.0, 80.0
402671, 1.05, 0.0, 90.0

```



```

**
*NGEN, NSET=CENTER
400001, 402665, 148
**
*NSET, NSET=NBEAM, GENERATE
402665, 402670, 1
**
**-----**
** Load Application Point **
**-----**
*NSET, NSET=LDPOINT, GENERATE
402671, 402671
*NSET, NSET=GAGEPT, GENERATE
402669, 402669, 1
**
*****
**
ELEMENT DEFINITION
*****
**
**-----**
** 8 noded shell element to model the steel tube **
**-----**
**
*ELEMENT, TYPE=S8R5, ELSET=ETUBE
1, 1, 3, 77, 75, 2, 40, 76, 38
217, 889, 893, 1041, 1037, 891, 967, 1039, 963
271, 1777, 1781, 2225, 2221, 1779, 2003, 2223, 1999
**
*ELGEN, ELSET=ETUBE
1, 18, 2, 1, 12, 74, 18
217, 9, 4, 1, 6, 148, 9
271, 9, 4, 1, 2, 444, 9
**
**-----**
** Solid elements to model the grout **
**-----**
**Note:
** Elements 1001 through 1063 are defined such that they can be 'unbonded'
** to the steel tube if necessary. At this time, the model is such that
** they are completely bond.
** Elements 1055 through 1118 are defined such that they are completely
** bonded to the steel.
** 4 noded brick element
**
*ELEMENT, TYPE=C3D8
1001, 100001, 200001, 200149, 100149, 100005, 200005, 200153, 100153
1055, 100889, 200889, 201037, 1037, 100893, 200893, 201041, 1041
1064, 1037, 201037, 201185, 1185, 1041, 201041, 201189, 1189
1109, 1777, 201777, 202221, 2221, 1781, 201781, 202225, 2225
1110, 1781, 201781, 202225, 2225, 1789, 201789, 202233, 2233
**
** 6 noded pie element
**
*ELEMENT, TYPE=C3D6, ELSET=L3-A
2001, 200001, 200005, 400001, 200149, 200153, 400149

```

2002, 200005, 200009, 400001, 200153, 200157, 400149  
 2003, 200009, 200013, 400001, 200157, 200161, 400149  
 2004, 200013, 200017, 400001, 200161, 200165, 400149  
 2005, 200017, 200021, 400001, 200165, 200169, 400149  
 2006, 200021, 200029, 400001, 200169, 200177, 400149  
 2007, 200029, 200037, 400001, 200177, 200185, 400149

\*\*

2085, 201777, 201781, 401777, 202221, 202225, 402221  
 2086, 201781, 201789, 401777, 202225, 202233, 402221  
 2087, 201789, 201797, 401777, 202233, 202241, 402221  
 2088, 201797, 201805, 401777, 202241, 202249, 402221  
 2089, 201805, 201813, 401777, 202249, 202257, 402221

\*\*

\*ELGEN, ELSET=LAYER1A

1001, 9, 4, 1, 6, 148, 9

1055, 9, 4, 1

1064, 9, 4, 1, 5, 148, 9

\*ELGEN, ELSET=LAYER2A

2001, 12, 148, 7

2002, 12, 148, 7

2003, 12, 148, 7

2004, 12, 148, 7

2005, 12, 148, 7

2006, 12, 148, 7

2007, 12, 148, 7

\*\*

\*ELGEN, ELSET=LAYER1B

1109, 2, 444, 5

1110, 4, 8, 1, 2, 444, 5

\*ELGEN, ELSET=LAYER2B

2085, 2, 444, 5

2086, 2, 444, 5

2087, 2, 444, 5

2088, 2, 444, 5

2089, 2, 444, 5

\*\*

\*\* Additional element set

\*\* -----

\*ELSET, ELSET=LAYER1

LAYER1A, LAYER1B

\*\*

\*ELSET, ELSET=LAYER2

LAYER2A, LAYER2B

\*\*

\*ELSET, ELSET=ESLD

LAYER1, LAYER2

\*\*

\*\* Beam elements

\*\* -----

\*ELEMENT, TYPE=B33

601, 402665, 402666

\*\*

\*ELGEN, ELSET=EBEAM

601, 5, 1, 1

\*\*

```

*ELEMENT, TYPE=B33, ELSET=SLEEVE
606, 402670, 402671
**
*****
**
                SHELL ELEMENT THICKNESS AND MATERIAL TYPE DEFINITION
*****
**
** Shell section for steel tube
**-----
*SHELL SECTION,ELSET=ETUBE,MATERIAL=STEEL1
0.2497
**
** Solid section to define grout
**-----
*SOLID SECTION, ELSET=ESLD, MATERIAL=GROUT
**
** Composite section for beam element
**-----
*BEAM SECTION, ELSET=EBEAM, MATERIAL=STEEL1, SECTION=PIPE
3.88, 0.2172
**4.1875, 0.127
0.0, 1.0, 0.0
**
*BEAM SECTION, ELSET=SLEEVE, MATERIAL=STEEL1, SECTION=PIPE
3.88, 0.2172
**4.1875, 0.127
0.0, 1.0, 0.0
**
*****
**
                CONSTITUTIVE RELATIONSHIPS
*****
**
** Steel tube.
**-----
** The data are from tension tests
*MATERIAL, NAME=STEEL1
*ELASTIC
29500.,0.3
*PLASTIC
36.0
36.5, 0.015
37.0, 0.03
**
**GROUT
**-----
** Use material type *CONCRETE provided by ABAQUS.
** The data are from grout tests. Use 80% of cube strength
** and assume elastic response up to 70% of the stress-strain compressive
** strength used in the analysis (i.e., 0.56 times the original cube strength)
**
*MATERIAL, NAME=GROUT
*ELASTIC, TYPE=ISO
3498., 0.18
*CONCRETE

```

```

3.34, 0.
4.78, 0.0035
*FAILURE RATIOS
1.16, 0.02
**
**---Assume 3% of tension stress remains across the cracked element
*TENSION STIFFENING
1.0, 0.
0.03, 0.0003
**
**
*****
**                                     **
**                               BOUNDARY CONDITIONS                               **
**                               *****                               **
*****
**                                     **
**-----**
** Defining additional element sets needed to impose boundary conditions **
**-----**
** DENT
** ----
*NSET, NSET=DENT, GENERATE
1,37,1
**
** TOP, BOTTOM, NEND
** -----
** Node sets along the top, bottom and end edges of shell elements.
*NSET, NSET=TOP, GENERATE
1,852,37
889, 1629, 148
1777, 2665, 444
**
*NSET, NSET=BOT, GENERATE
37,888,37
925, 1665, 148
1813, 2701, 444
**
*NSET, NSET=NEND, GENERATE
2665,2701,2
**
** NGRTSYM
** -----
** Nodes that describe the symmetric half of the grout about the long axis
*NSET, NSET=GRT_SYM, GENERATE
100001, 100889, 148
200001, 201777, 148
400001, 401777, 148
200037, 201813, 148
100037, 100925, 148
**
202221, 202665, 444
202257, 202701, 444
**
*NSET, NSET=NGRTSYM
GRT_SYM, 402221
**

```

```

** DENT-G
** -----
** Nodes that describe the symmetric half of the grout about the mid-span.
*NSET, NSET=N_L1L2, GENERATE
100001, 100037, 4
200001, 200021, 4
200021, 200037, 8
*NSET, NSET=DENT-G
N_L1L2, 400001
**
** -----**
** Set boundary conditions **
** -----**
*BOUNDARY
DENT,ZSYMM
DENT-G, ZSYMM
TOP,YSYMM
BOT,YSYMM
NGRTSYM, YSYMM
LDPOINT, 1, 2
**
*****
**
MULTI-POINT CONSTRAINTS **
*****
**
** -----**
** Shell Elements **
** -----**
*MPC
QUADRATIC,890,889,891,893
QUADRATIC,892,889,891,893
QUADRATIC,894,893,895,897
QUADRATIC,896,893,895,897
QUADRATIC,898,897,899,901
QUADRATIC,900,897,899,901
QUADRATIC,902,901,903,905
QUADRATIC,904,901,903,905
QUADRATIC,906,905,907,909
QUADRATIC,908,905,907,909
QUADRATIC,910,909,911,913
QUADRATIC,912,909,911,913
QUADRATIC,914,913,915,917
QUADRATIC,916,913,915,917
QUADRATIC,918,917,919,921
QUADRATIC,920,917,919,921
QUADRATIC,922,921,923,925
QUADRATIC,924,921,923,925
**
** -----**
** Grout **
** -----**
**
** Constraints between the fine and coarse mesh at the tension side of tube
** -----
** Define Node sets and use them to apply MPC

```

```

**
*NSET, NSET=FIX_1, GENERATE
200021, 201649, 148
*NSET, NSET=FIX_2, GENERATE
200029, 201657, 148
*NSET, NSET=FIX_3, GENERATE
200037, 201665, 148
*NSET, NSET=FREE_1, GENERATE
200025, 201653, 148
*NSET, NSET=FREE_2, GENERATE
200033, 201661, 148
**

*MPC
LINEAR, FREE_1, FIX_1, FIX_2
LINEAR, FREE_2, FIX_2, FIX_3
**

** Constraints between fine and coarse mesh at 3 diameter away from dent
** -----
*MPC
LINEAR, 201785, 201781, 201789
LINEAR, 201793, 201789, 201797
LINEAR, 201801, 201797, 201805
LINEAR, 201809, 201805, 201813
**
*****
**
EQUATION CONSTRAINTS
*****
**
** ----- **
** EQUATION commands constraints the shell elements at
** the beam junction to remain as plane section.
** The displacement fields of the beam and shell must be
** compatible.
** ----- **
**
**
*EQUATION
** Degree of Freedom 4, 5 and 6 rotation about x, Y and Z-axis
** -----
2
402665, 4, 1.0, 2665, 4, -1.0
2
NEND, 5, 1.0, 402665, 5, -1.0
2
402665, 6, 1.0, 2665, 6, -1.0
**
** Degree of freedom 1 and 2, displacement about X and Y-axis
** -----
3
402665, 1, 1.0, 2665, 1, -0.5, 2701, 1, -0.5
2
402665, 2, 1.0, 2665, 2, -1.0
**
** Degree of freedom 3, displacement in Z-axis
** -----

```

```

3
2665, 3, 1.0, 402665, 3, -1.0, 402665, 5, 4.1895
3
2669, 3, 1.0, 402665, 3, -1.0, 402665, 5, 3.93684
3
2673, 3, 1.0, 402665, 3, -1.0, 402665, 5, 3.20934
3
2677, 3, 1.0, 402665, 3, -1.0, 402665, 5, 2.09475
3
2681, 3, 1.0, 402665, 3, -1.0, 402665, 5, 0.727499
3
2685, 3, 1.0, 402665, 3, -1.0, 402665, 5, -0.727499
3
2689, 3, 1.0, 402665, 3, -1.0, 402665, 5, -2.09475
3
2693, 3, 1.0, 402665, 3, -1.0, 402665, 5, -3.20934
3
2697, 3, 1.0, 402665, 3, -1.0, 402665, 5, -3.93684
3
2701, 3, 1.0, 402665, 3, -1.0, 402665, 5, -4.1895
**
**-----**
** Constrains between Shell elements (Tube), solid elements (Grout) **
**-----**
**First, generate nodal sets
**
**TUBE
**----
*NSET, NSET=II_a, GENERATE
1, 889, 148
37, 925, 148
*NSET, NSET=II_b, GENERATE
5, 893, 148
9, 897, 148
13, 901, 148
17, 905, 148
21, 909, 148
25, 913, 148
29, 917, 148
33, 921, 148
*NSET, NSET=II
II_a, II_b
**
**GROUT
**----
*NSET, NSET=JJ_a, GENERATE
100001, 100889, 148
100037, 100925, 148
*NSET, NSET=JJ_b, GENERATE
100005, 100893, 148
100009, 100897, 148
100013, 100901, 148
100017, 100905, 148
100021, 100909, 148
100025, 100913, 148

```

```

100029, 100917, 148
100033, 100921, 148
*NSET, NSET=JJ
JJ_a, JJ_b
**
*EQUATION
2
II, 1, 1, JJ, 1, -1
2
II_b, 2, 1, JJ_b, 2, -1
**
*****
**          Read Initial Stress from file          **
**          File name: Res_10.inp                  **
*****
**
**INITIAL CONDITIONS, TYPE=STRESS, INPUT=Res_10.inp
**
**VIEWPOINT
**1,1,1
**SHRINK
**DRAW
**DATA CHECK
**
*****
**C                      Step 1
*****
**C In this step, a concentrated load is applied at the MASTER element set.
**C The RIKS solution method is used. Write out to restart file for post processing
**C of the results obtained in Step 1
*STEP,NLGEOM,INC=150
APPLICATION OF AXIAL LOAD
*STATIC, RIKS
0.025,1.0,1.E-12,0.1
*CONTROLS, PARAMETERS=FIELD, FIELD=DISPLACEMENT
0.05,1.0,,100.
*CONTROLS, PARAMETERS=FIELD, FIELD=ROTATION
0.1,1.0,,100.
*CLOAD
LDPOINT,3,-100.
*NODE PRINT,NSET=LDPOINT,SUMMARY=NO
U1,U2,U3,UR2,CF3
*NODE FILE,NSET=LDPOINT, FREQUENCY=1
U,CF
*NODE FILE, NSET=GAGEPT, FREQUENCY=1
U
*NODE FILE, NSET=DENT, FREQUENCY=1
U
*NODE PRINT,GLOBAL=YES,NSET=DENT,TOTALS=YES,SUMMARY=NO
U1,U2,RF1,RF3
*NODE PRINT, GLOBAL=YES, NSET=DENT-G, TOTAL=YES
U1, U2, RF1, RF3
*EL PRINT,POSITION=AVERAGED AT NODES,FREQ=0
*PRINT, RESIDUAL=YES
*END STEP

```



## **APPENDIX E**

### **DATABASE OF UNREPAIRED AND INTERNAL GROUT REPAIRED DENT-DAMAGED TEST SPECIMENS**

**Table E.1 Non-Repaired Specimen Geometry**

Ref.	Spec.	D (in.)	t (in.)	d <sub>s</sub> (in.)	L (in.)	$\delta_p$ (in.)	E <sub>s</sub> (ksi)	F <sub>y</sub> (ksi)	end eccent. (in.)	P <sub>exp</sub> (kip)
8	A1	8.626	0.247	0.868	178.800	0.125	29071	34.800	0.000	141.0
8	A2	8.624	0.246	0.861	178.800	0.107	29071	34.800	1.725	91.0
8	B1	8.631	0.186	0.862	178.900	0.161	30714	33.400	0.000	99.0
8	B2	8.636	0.186	0.861	178.900	0.465	30714	33.400	1.725	52.0
8	C1	8.642	0.134	0.861	180.100	0.216	30800	39.400	0.000	97.0
8	C2	8.643	0.136	0.861	180.100	0.126	30800	39.400	1.725	46.0
10	A3	2.504	0.083	0.116	84.650	0.466	28716	32.800	0.000	9.9
10	B3	3.131	0.068	0.250	84.650	0.423	31037	28.700	0.000	9.7
10	B4	3.130	0.067	0.034	84.650	0.423	28281	29.000	0.000	11.4
10	C3	4.005	0.068	0.135	84.650	0.034	28571	33.800	0.000	21.5
10	C4	4.005	0.068	0.061	84.650	0.043	30022	36.500	0.000	25.9
10	D3	3.544	0.041	0.130	84.650	0.026	33647	68.000	0.000	16.1
10	D4	3.545	0.041	0.078	84.650	0.085	32052	69.200	0.000	20.1
11	F2	15.980	0.390	1.990	305.300	0.550	31037	42.490	0.000	462.4
11	F2S	2.626	0.063	0.330	52.170	0.261	30022	39.740	0.000	9.2
12	P1A	1.754	0.038	0.165	42.400	0.081	30022	51.340	0.000	6.4
12	R1A	1.754	0.065	0.248	35.430	0.081	30022	69.470	0.000	11.1
12	R1B	1.754	0.065	0.233	35.430	0.050	30022	69.470	0.000	11.8
12	R1C	1.755	0.066	0.240	35.430	0.032	30022	69.470	0.000	13.6
12	R2A	1.747	0.062	0.241	35.430	0.074	30022	68.890	0.000	11.8
12	P1C	1.754	0.037	0.311	42.400	0.157	30022	51.340	0.000	3.9
12	P2C	1.754	0.038	0.161	21.220	0.028	30022	51.340	0.000	7.1
13	Q1A	1.752	0.051	0.032	35.430	0.365	30022	71.070	0.000	9.3
13	Q1B	1.751	0.050	0.247	35.430	0.624	30022	71.070	0.000	5.4
13	Q1C	1.751	0.050	0.364	35.430	1.028	30022	71.070	0.000	3.8
13	Q2A	1.751	0.050	0.012	35.430	0.244	30022	83.540	0.000	11.8
14	1ABB	4.728	0.039	0.182	98.425	0.051	29500	42.060	0.000	15.2
14	1ACB	4.717	0.039	0.274	98.425	0.171	29500	42.060	0.000	11.7
14	1ACC	4.722	0.039	0.313	98.425	0.117	29500	42.060	0.000	13.8
14	1ADB	4.721	0.039	0.461	98.425	0.116	29500	42.060	0.000	10.7
14	1ADC	4.730	0.039	0.547	98.425	0.192	29500	42.060	0.000	9.8
14	1AEC	4.720	0.040	1.012	98.425	0.701	29500	42.060	0.000	5.5
14	1BBB	4.943	0.049	0.195	98.425	0.046	29500	45.250	0.000	23.8
14	1BCB	4.912	0.049	0.259	98.425	0.126	29500	45.250	0.000	21.2
14	1BCC	4.928	0.049	0.290	98.425	0.074	29500	45.250	0.000	20.6
14	1BDB	4.938	0.049	0.564	98.425	0.092	29500	45.250	0.000	16.3
14	1BDC	4.946	0.050	0.531	98.425	0.158	29500	45.250	0.000	16.0
14	1BEC	5.073	0.050	1.000	98.425	0.438	29500	45.250	0.000	12.1
14	1CBB	5.335	0.058	0.130	98.425	0.048	29500	42.780	0.000	33.6
14	1CCB	5.331	0.059	0.327	98.425	0.038	29500	42.780	0.000	27.7
14	1CCC	5.331	0.060	0.406	98.425	0.074	29500	42.780	0.000	25.7
14	1CDB	5.324	0.056	0.615	98.425	0.186	29500	42.780	0.000	18.0
14	1CDC	5.331	0.058	0.743	98.425	0.235	29500	42.780	0.000	17.8
14	1CEC	5.320	0.060	1.225	98.425	0.859	29500	42.780	0.000	10.1
9	A6	8.637	0.253	1.257	177.880	0.343	29510	38.000	0.000	141.0
9	B6	8.621	0.189	1.301	179.190	0.274	29940	38.000	0.000	90.0
9	C6	8.590	0.127	1.280	180.500	0.320	30220	40.000	0.000	62.0
9	A8	8.625	0.253	2.575	177.250	1.761	29510	34.000	0.000	62.0
9	C8	8.625	0.127	2.555	180.500	1.080	30220	39.000	0.000	33.0
9	C1a	8.619	0.136	0.839	183.750	0.472	30800	44.000	0.000	85.0
9	B17	8.617	0.189	1.707	179.000	0.568	29940	42.000	0.000	84.0
9	A10	8.629	0.255	2.185	177.190	1.140	29510	39.000	0.000	98.0
9	C10	8.585	0.127	2.146	180.500	0.944	30220	39.000	0.000	37.0
9	A12	8.625	0.253	4.235	177.000	3.075	29510	36.000	0.000	38.0
9	C12	8.608	0.125	4.258	180.000	2.732	30220	40.000	0.000	14.4
4	1-A1	5.5157	0.1614	0.4528	78.74	0.1398	29007	40.6	0	74.5
4	2-A1	5.5157	0.1614	0.4646	78.74	0.1378	29000	40.6	0	73.6
4	3-A1	5.5157	0.1614	0.4567	78.74	0.1319	29000	40.6	0	71.9
4	4-A2	5.5157	0.1614	0.2835	78.74	0.0547	29000	40.6	0	84.4
4	5-A2	5.5157	0.1614	0.2835	78.74	0.0547	29000	40.6	0	86.1

**Table E.1(cont'd) Non-Repaired Specimen Geometry**

Ref.	Spec.	D (in.)	t (in.)	d <sub>a</sub> (in.)	L (in.)	$\delta_p$ (in.)	E <sub>s</sub> (ksi)	F <sub>y</sub> (ksi)	end eccent. (in.)	P <sub>exp</sub> (kip)
3	P1P	15.00	0.26	0.71	35.35	0.300	29500	42.7	0.60	328.0
3	P1F	15.00	0.26	0.74	35.29	0.370	29500	42.7	0.00	415.0
3	P1PS	3.94	0.06	0.20	9.42	0.000	29500	38.5	0.00	23.3
3	P2P	17.03	0.375	2.37	34.85	0.660	29500	57.1	0.25	516.0
3	P2F	17.01	0.375	2.31	34.79	0.940	29500	57.1	0.00	768.0
3	P2PS	5.38	0.118	0.74	11.33	0.380	29500	42.1	0.00	43.4
3	P3PA	24.50	0.321	1.26	34.35	0.020	29500	59.3	0.30	950.0
3	P3PB	24.50	0.321	3.64	34.35	0.300	29500	59.3	0.40	620.0
3	P4P	18.75	0.197	2.58	31.35	0.980	29500	55.3	0.00	283.0
2	D1-32	5.33	0.178	0.53	105.4	0.445	30297	50.8	0.00	83.2
2	D1-33	5.33	0.178	1.06	105.4	1.181	30297	49.3	0.00	56.3
2	D1-35	5.52	0.118	0.55	105.4	0.433	31080	53.4	0.00	56.5
2	D1-36	5.52	0.118	1.10	105.4	0.945	31080	58.0	0.00	33.5

**Table E.2 Internal Grout Repaired Specimen Geometry**

Ref.	Spec.	D (in.)	t (in.)	d <sub>g</sub> (in.)	L (in.)	δ <sub>p</sub> (in.)	E <sub>s</sub> (ksi)	F <sub>y</sub> (ksi)	f' <sub>g</sub> (ksi)	E <sub>g</sub> (ksi)	end eccent. (in.)	P <sub>exp</sub> (k)
9	A7	8.65	0.25	1.3	178	0.331	29500	39	5.54	3610	0	243
9	B7	8.63	0.19	1.29	180	0.335	29900	41	5.64	3650	0	211
9	B7-A	8.63	0.189	1.3	180	0.38	29900	42	5.97	3750	0	203
9	B7-B	8.63	0.189	1.29	179	0.395	29900	41	2.51	2430	0	183
9	C7	8.59	0.127	1.26	181	0.347	30200	40	6.4	3890	0	111
9	A9	8.63	0.253	2.56	178	1.67	29500	37	5.38	3560	0	139
9	C9	8.6	0.128	2.58	181	1.06	29500	42	6	3760	0	81
9	A11	8.63	0.25	2.17	178	1.05	29500	39	5.97	3750	0	158
9	C11	8.58	0.126	2.19	181	0.912	30200	38	5.9	3730	0	104
9	A13	8.63	0.253	4.32	178	3.75	29500	36	7.69	4260	0	50
9	C13	8.6	0.125	4.28	180	2.98	30200	42	7.55	4220	0	40
8	A3	8.63	0.247	0.857	179	0.107	29100	34.8	4.38	2910	1.73	191
8	B3	8.63	0.187	0.863	179	0.197	30700	33.4	3.89	3070	1.73	117
8	C3	8.64	0.135	0.86	180	0.162	30800	39.4	6.89	3080	1.73	122
5	A2	1.75	0.054	0.127	49.4	0.049	29500	85.1	4.63	2390	0.024	13.8
5	B1	1.76	0.055	0.246	49.4	0.013	29500	81.7	4.63	2390	0.088	10.7
5	B2	1.76	0.055	0.223	49.4	0.223	29500	83.6	4.63	2390	0.037	27.9
5	C2	2.75	0.056	0.207	73.2	0.005	29500	77.6	4.63	2390	0.039	23.3
5	D1	2.75	0.055	0.398	73.2	0.031	29500	71.5	4.63	2390	0.081	19.7
5	D2	2.75	0.055	0.411	73.2	0.31	29500	75.1	4.63	2390	0.019	8.8
5	E1	1.75	0.058	0.192	49.4	0.256	29500	53.4	4.28	2270	0.008	12.1
5	E2	1.75	0.058	0.27	49.4	0.007	29500	50.9	4.28	2270	0.004	5.4
6	F1	1.75	0.028	0.248	52.6	0.087	29500	26	2.28	2160	0.003	20.5
6	G1	2.75	0.055	0.193	75	0.004	29500	31.8	2.28	2160	0.008	19.5
6	G2	2.75	0.055	0.396	75	0.044	29500	33.6	2.28	2160	0.01	14.2
6	G3	2.75	0.055	0.346	75	0.32	29500	33.5	2.28	2160	0.009	28.8
6	H1	3.5	0.061	0.5	75	0.166	29500	32.4	2.28	2160	0	12.7
1	A1	1.75	0.05	0.179	35.4	0.046	29500	75.2	6.23	1590	0	19.2
1	A2	1.75	0.049	0.182	35.4	0.036	29500	75.2	10.7	1590	0	14.4
1	A3	1.75	0.049	0.221	35.4	0.07	29500	75.2	6.23	1590	0	16.2
1	A4	1.75	0.048	0.242	35.4	0.072	29500	75.2	10.7	1590	0	21.7
1	A5	1.75	0.049	0.181	35.4	0.062	29500	75.2	10.7	1590	0	18.7
1	B1	1.75	0.063	0.185	35.4	0.05	29500	75	6.23	1590	0	20.6
1	B2	1.75	0.063	0.185	35.4	0.042	29500	75	6.23	1590	0	14.8
1	B3	1.75	0.063	0.232	35.4	0.088	29500	75	6.23	1590	0	15.9
1	B4	1.75	0.062	0.251	35.4	0.075	29500	75	10.7	1590	0	84.3
1	C1	3	0.104	0.131	61.4	0.021	29500	72.9	10.7	1590	0	93.5
1	C2	3	0.104	0.131	61.4	0.011	29500	72.9	10.7	1590	0	50.4
1	D1	3	0.104	0.468	61.4	0.185	29500	73.3	10.7	1590	0	57.7
1	D2	3	0.104	0.472	61.4	0.171	29500	73.3	10.7	1590	0	83.4
1	F1	3	0.126	0.292	71.3	0.086	29500	67.3	10.7	1590	0	74.4
1	F2	3	0.126	0.289	71.3	0.088	29500	67.3	10.7	1590	0	82.1
1	G1	3	0.13	0.28	61	0.043	29500	70.5	10.7	1590	0	87.2
1	G2	3	0.13	0.288	61	0.069	29500	70.5	10.7	1590	0	85.7
1	H1	3	0.128	0.293	50.8	0.053	29500	68.4	10.7	1590	0	86.1
1	H2	3	0.128	0.287	50.8	0.066	29500	68.4	10.7	1590	0	44.3
1	J1	3	0.063	0.307	72.8	0.073	29500	74	10.7	1590	0	42.7
1	J2	3	0.063	0.299	72.8	0.129	29500	74	10.7	1590	0	53.8
1	K1	3	0.063	0.288	62.2	0.093	29500	72.4	10.7	1590	0	51.5
1	K2	3	0.063	0.297	62.2	0.047	29500	72.4	10.7	1590	0	59.1
1	L1	3	0.063	0.301	52	0.055	29500	72.7	10.7	1590	0	59.9
1	L2	3	0.063	0.297	52	0.044	29500	72.7	10.7	1590	0	58.2
1	M1	3	0.107	0.288	71.7	0.069	29500	71.9	10.7	1590	0	89.3
1	M2	3	0.107	0.293	71.7	0.063	29500	71.9	10.7	1590	0	63.4
1	N1	3	0.104	0.3	61.4	0.108	29500	70.8	10.7	1590	0	71.3
1	N2	3	0.104	0.304	61.4	0.08	29500	70.8	10.7	1590	0	79.4
1	O1	3	0.106	0.309	51.2	0.11	29500	69.8	10.7	1590	0	76.4
1	O2	3	0.106	0.3	51.2	0.047	29500	69.8	10.7	1590	0	442
1	Q1	8.64	0.315	1.16	193	0.3	29500	46.3	10.7	1590	0	

Table E.2(cont'd) Internal Grout Repaired Specimen Geometry

Ref.	Spec.	D (in.)	t (in.)	d <sub>g</sub> (in.)	L (in.)	δ <sub>p</sub> (in.)	E <sub>s</sub> (ksi)	F <sub>y</sub> (ksi)	f' <sub>g</sub> (ksi)	E <sub>g</sub> (ksi)	end eccent. (in.)	P <sub>exp</sub> (k)
1	Q2	8.64	0.319	1.14	193	0.522	29500	46.3	10.7	1590	0	476
1	Q3	8.64	0.319	0.809	193	0.269	29500	46.3	10.7	1590	0	430
1	Q4	8.64	0.321	0.818	193	0.22	29500	46.3	10.7	1590	0	544
7	J1	2.7	0.056	0.248	64.2	0.199	25900	36.4	5.18	1980	0	11.1
7	J2	2.7	0.056	0.194	64.2	0.257	27100	38.1	5.18	1980	0	12.5
7	J3	2.7	0.056	0.208	64.2	0.238	25200	44.1	5.18	1980	0	12.4
7	J4	2.7	0.057	0.194	64.2	0.244	25200	37.8	5.18	1980	0	12.5
7	J5	2.7	0.055	0.319	64.2	0.013	25600	36.9	5.18	1980	0	14
7	J6	2.7	0.055	0.311	64.2	0.011	26200	37.5	5.18	1980	0	14.4
7	K1	2.7	0.056	0.203	89.8	0.359	26200	36.8	5.18	1980	0	9.9
7	K2	2.7	0.055	0.219	89.8	0.341	25800	38.5	5.18	1980	0	9.3
7	K3	2.7	0.056	0.311	89.8	0.007	26200	38.5	5.18	1980	0	14.1
7	K4	2.7	0.056	0.308	89.8	0.02	25600	37.8	5.18	1980	0	12.1
7	I1	2.7	0.052	0.275	75.8	0.212	26200	33.4	2.73	2160	0	13.5
7	I2	2.7	0.053	0.259	75.8	0.235	27500	33.3	2.73	2160	0	10.7
7	I3	2.7	0.054	0.27	75.8	0.243	29100	33.6	2.73	2160	0	10.1
7	H2	2.7	0.06	0.394	75.8	0.053	34300	31.7	2.27	2160	0	13.8

### Database Reference List

1. Boswell, L.F. and D'Mello, C.A. (1990) "Residual and Fatigue Strength of Grout-Filled Damaged Tubular Members," OTH 88 314, Offshore Technology Report, United Kingdom Department of Energy.
2. Landet, E. and Lotsburg, I. (1992), "Laboratory Testing of Ultimate Capacity Dented Tubular Members", *Journal of Structural Engineering*, ASCE, Vol. 118, No. 4.
3. Ostapenko, A., Wood, B.A., Chowdury, A., and Hebor, M.F. (1993), "Residual Strength of Damaged Tubular Members in Offshore Structures", Volume 1, ATLSS Report 93-03, ATLSS Engineering Research Center, Lehigh University, Bethlehem, PA.
4. Pacheco, L.A. and Durkin, S. (1988) "Denting and Collapse of Tubular Members - A Numerical and Experimental Study," *International Journal of Mechanical Sciences*, Vol. 30, No. 5.
5. Parsanejad, S., (1987) "Strength of Grout-Filled Damaged Tubular Members," *Journal of Structural Engineering*, ASCE, Vol. 113, No. 3.
6. Parsanejad, S., Tyder, S., and Chin, K.Y., (1987) "Experimental Investigation of Grout-Filled Damaged Tubular Members," *Proceedings on Steel and Aluminum Structures*, University College, Cardiff, England.
7. Parsanejad, S., and Gusheh, P. (1992) "Behavior of Partially Grout-Filled Damaged Tubular Members," *Journal of Structural Engineering*, ASCE, Vol. 118, No. 11.
8. Ricles, J.M., Gillum, T., and Lamport, W. (1992) "Residual Strength and Grout Repair of Dented Offshore Tubular Bracing," ATLSS Report No. 92-14, Lehigh University, Bethlehem, PA.
9. Ricles, J., Bruin, W., and Sooi, T. K (1997), "Residual Strength and Grout Repair of Dent-Damaged Offshore Tubular Bracing - Phase II Study", ATLSS Report No. 97-12, ATLSS Engineering Research Center, Lehigh University, Bethlehem, Pennsylvania (in press).
10. Smith, C.S., Kirkwood, W., and Swan J.W. (1979) "Buckling Strength and Post-Collapse Behavior of Tubular Bracing Members Including Damage Effects," *Proceedings of the 2nd International Conference of the Behavior of Offshore Structures* (BOSS '79), Imperial College, London, England.
11. Smith, C.S., Somerville, W.L., and Swan J.W. (1981) "Residual Strength and Stiffness of Damaged Steel Bracing Members," *Proceedings of the Offshore Technology Conference*, OTC Paper 3981, Houston, Texas.
12. Smith, C.S. (1983) "Assessment of Damage in Offshore Steel Platforms," *Proceedings of the International Conference of Offshore and Marine Safety*, Glasgow, Scotland.
13. Smith, C.S. (1986) "Residual Strength of Tubulars Containing Combined Bending and Dent-Damage," *Proceedings of the 9th Annual Energy Sources Technology Conference*, New Orleans, Louisiana.
14. Taby, J. (1986) "Experiments with Damaged Tubulars," Report No. 6.07, ID STF71-A86067, SINTEF, The Foundation for Scientific and Industrial Research, Norwegian Institute of Technology, Trondheim, Norway.